Electrocatalysts for Fuel Cells and Water Electrolyzers: From Synthesis to Performance Evaluation at Realistic Reaction Conditions

Inaugural dissertation
of the Faculty of Science,
University of Bern

presented by

Johanna Schröder

from Germany

Supervisor of the doctoral thesis:

Prof. Dr. Matthias Arenz

Department of Chemistry, Biochemistry,
and Pharmaceutical Sciences

Electrocatalysts for Fuel Cells and Water Electrolyzers: From Synthesis to Performance Evaluation at Realistic Reaction Conditions

Inaugural dissertation
of the Faculty of Science,
University of Bern

presented by

Johanna Schröder

from Germany

Supervisor of the doctoral thesis:

Prof. Dr. Matthias Arenz

Department of Chemistry, Biochemistry,
and Pharmaceutical Sciences

Accepted by the Faculty of Science.

Bern, 04.10.2021

The Dean
Prof. Dr. Zoltan Balogh

Summary

Fuel cells and electrolyzers are key aspects for the storage and conversion of renewable energy. Due to the kinetic hindered oxygen reactions at the cathode or anode of fuel cells and electrolyzers, respectively, the improvement of those Pt and Ir based nanoparticle (NP) based catalysts is crucial for their application. In a first step an understanding of the NP synthesis including a size control is necessary, then the investigation of the activity and stability of the catalysts. Therefore, this dissertation deals with "Electrocatalysts for Fuel Cells and Water Electrolyzers: From Synthesis to Performance Evaluation at Realistic Reaction Conditions".

The polyol process enables the synthesis of "surfactant-free" NPs with tailored catalyst properties like the control of the particle size. A mechanistic investigation of the Pt NP synthesis in the polyol process can be achieved by slowing down the reduction process inducing the particle formation process by visible light. The particle size control by the OH^-/Pt ratio as described previously in the polyol process can be confirmed in the visible-light-induced reduction. By systematically reducing different precursors in presence of the bases NaOH or Na(acac) it can be shown that the size of Pt NPs can be controlled additionally by the $acac^-$/Pt ratio reaching a comparable size control at the respective OH^-/Pt ratio. Besides the control by the anion/Pt ratio the character of the precursor seems to determine the particle size.

The gas diffusion electrode (GDE) setup is presented as a straightforward testing device enabling the performance of accelerated stress tests (ASTs) of Pt/C catalysts under realistic conditions with respect to catalyst loading and temperature close to the conditions applied in fuel cells. The coupling to *ex situ* small angle X-ray scattering (SAXS) enables degradation studies comparing the change of the particle size and the electrochemically active surface area (ECSA) during the ASTs. Applying ASTs on catalysts with different initial particle sizes revealed similar end-of-treatment sizes. For a deeper understanding of the degradation mechanism, *operando* SAXS is performed during the application of ASTs. One of the main challenges in coupling SAXS to ASTs is the recording of a suitable background. In this work, the background measurement in transmission configuration is achieved by the vertical movement of the cell of the gas diffusion layer (GDL) experiencing the same electrochemical treatment. Thus, a bimodal catalyst consisting of two size populations, so that the electrochemical Ostwald ripening should be induced, could be studied. The same bimodal catalyst was investigated at a synchrotron in an *operando* SAXS study in grazing incidence configuration enabling the establishment of a depth profile of the degradation within the catalyst layer. Surprisingly, both studies are not clearly evidencing the expected electrochemical Ostwald ripening.

"Surfactant-free" Ir NPs were synthesized with the colloidal so-called Co4Cat process performed in low boiling point solvents. These Ir NPs can be used as potential electrolyzer catalysts. Efforts to control the obtained particle size were performed by adjusting different synthesis parameters such as the temperature or water content.

Furthermore, the GDE setup was adjusted to obtain a straightforward performance testing setup for electrolyzer catalysts reaching comparable results as compared to the rotating disk electrode (RDE) method, which is currently the standard testing device in basic research. It is shown that the used carbon based GDL is stable enough to perform performance tests. In addition, a straightforward way to prepare catalyst films on top of titanium based porous transport layers

(PTLs) typically used in electrolyzers was developed. Using a simple hot-pressing of a Nafion membrane to the catalyst layer leads to comparable activity results as generated using a GDL. Kinetic studies assuming Arrhenius behavior enabled the determination of the electrochemical activation energy and the estimation of the exchange current density.

List of Publications

Publications Included in the Thesis

The same numbering as in the discussion of the manuscripts appended to this dissertation is used.

I. J. Schröder, S. Neumann, S. Kunz, Visible-Light-Induced Synthesis of "Surfactant-Free" Pt Nanoparticles in Ethylene Glycol as a Synthetic Approach for Mechanistic Studies on Nanoparticle Formation, *J. Phys. Chem. C*, **2020**, *124*, 21798-21809. https://doi.org/10.1021/acs.jpcc.0c06361

II. J. Schröder, S. Neumann, J. Quinson, M. Arenz, S. Kunz, Anion Dependent Particle Size Control of Platinum Nanoparticles Synthesized in Ethylene Glycol, *Nanomaterials*, **2021**, *11*, 2092. https://doi.org/10.3390/nano11082092 (Open Access)

III. J. Schröder, J. Quinson, J. K. Mathiesen, J. J. K. Kirkensgaard, S. Alinejad, V. A. Mints, K. M. Ø. Jensen, M. Arenz, A new approach to probe the degradation of fuel cell catalysts under realistic conditions: combining tests in a gas diffusion electrode setup with small angle X-ray scattering, *J. Electrochem. Soc.*, **2020**, *167*, 134515. https://doi.org/10.1149/1945-7111/abbdd2 https://doi.org/10.26434/chemrxiv.12263804.v2 (Open Access Preprint)

IV. J. Schröder,[*] J. Quinson,[*] J. J. K. Kirkensgaard, M. Arenz, *Operando* SAXS Study of a Pt/C Fuel Cell Catalyst with an X-ray Laboratory Source, *J. Phys. D: Appl. Phys*, **2021**, *54*, 294004. [*]equally contributing. https://doi.org/10.1088/1361-6463/abfa39 https://doi.org/10.26434/chemrxiv.14283788.v1 (Open Access Preprint)

V. J. Schröder, R. K. Pittkowski, I. Martens, R. Chattot, J. Drnec, J. Quinson, J. J. K. Kirkensgaard, M. Arenz, Tracking the Catalyst Layer Depth-Dependent Electrochemical Degradation of a Bimodal Pt/C Fuel Cell Catalyst: A Combined Operando Small- and Wide-Angle X-Ray Scattering Study, **2021**, *in preparation*.

VI. J. Quinson, L. Kacenauskaite, J. Schröder, S. B. Simonsen, L. Theil Kuhn, T. Vosch, M. Arenz, UV-induced syntheses of surfactant-free precious metal nanoparticles in alkaline methanol and ethanol, *Nanoscale Adv.*, **2020**, *2*, 2288-2292. https://doi.org/10.1039/D0NA00218F (Open Access)

VII. J. Schröder, V. A. Mints, A. Bornet, E. Berner, M. Fathi Tovini, J. Quinson, G. K. H. Wiberg, F. Bizzotto, H. A. El-Sayed, M. Arenz, The Gas Diffusion Electrode Setup as Straightforward Testing Device for Proton Exchange Membrane Water Electrolyzer Catalysts, *JACS Au*, **2021**, *1*, 247-251. https://doi.org/10.1021/jacsau.1c00015 (Open Access)

Publications Not Included in the Thesis

The numbering is following the publication times.

i. S. Neumann, J. Schröder, F. Bizzotto, M. Arenz, A. Dworzak, M. Oezaslan, M. Bäumer, S. Kunz, Halide-Induced Leaching of Pt Nanoparticles – Manipulation of Particle Size by Controlled Ostwald Ripening, *ChemNanoMat*, **2019**, *5*, 462-471.
https://doi.org/10.1002/cnma.201800550

ii. S. Alinejad, M. Inaba, J. Schröder, J. Du, J. Quinson, A. Zana, M. Arenz, Testing fuel cell catalysts under more realistic reaction conditions: accelerated stress tests in a gas diffusion electrode setup, *JPhys Energy*, **2020**, *2*, 024003.
https://doi.org/10.1088/2515-7655/ab67e2 (Open Access)

iii. J. Quinson, J. K. Mathiesen, J. Schröder, A. Dworzak, F. Bizzotto, A. Zana, S. B. Simonsen, L. Thiel Kuhn, M. Oezaslan, K. M. Ø. Jensen, M. Arenz, Teaching old precursors new tricks: Fast room temperature synthesis of surfactant-free colloidal platinum nanoparticles, *J. Colloid Interface Sci.*, **2020**, *577*, 319-328.
https://doi.org/10.1016/j.jcis.2020.05.078

iv. S. Alinejad, J. Quinson, J. Schröder, J. J. K. Kirkensgaard, M. Arenz, Carbon-supported platinum electrocatalysts probed in a gas diffusion setup with alkaline environment: How particle size and mesoscopic environment influence the degradation mechanism, *ACS Catal.*, **2020**, *10*, 13040-13049.
https://doi.org/10.1021/acscatal.0c03184
https://doi.org/10.26434/chemrxiv.13047710.v2 (Open Access Preprint)

v. J. K. Mathiesen, J. Quinson, A. Dworzak, T. Vosch, M. Juelsholt, E. T. S. Kjær, J. Schröder, J. J. K. Kirkensgaard, M. Oezaslan, M. Arenz, K. M. Ø. Jensen, Insights from In Situ Studies on the Early Stages of Platinum Nanoparticle Formation, *J. Phys. Chem. Lett.*, **2021**, *12*, 3224-3231.
https://doi.org/10.1021/acs.jpclett.1c00241

vi. F. Bizzotto, J. Quinson, J. Schröder, A. Zana, M. Arenz, Surfactant-Free Colloidal Strategies for Highly Dispersed and Active Supported IrO_2 Catalysts: Synthesis and Performance Evaluation for the Oxygen Evolution Reaction, *J. Catal.*, **2021**, *in press*.
https://doi.org/10.1016/j.jcat.2021.07.004 (Open Access)
https://doi.org/10.26434/chemrxiv.13643807.v1 (Open Access Preprint)

List of Abbreviations

$acac^-$	Acetylacetonate anion
Al_2O_3	Aluminum oxide, alumina
Ar	Argon
AEC	Alkaline electrolysis cell
AST	Accelerated stress test
Br^-	Bromide anion
C	Carbon
CCM	Catalyst coated membrane
CE	Counter electrode
Cl^-	Chloride anion
CO	Carbon monoxide
CS^+	Cesium cation
CV	Cyclic voltammogram/voltammetry
e^-	Electron
ECSA	Electrochemical active surface area
ESRF	European Synchrotron Radiation Facility
EDS	Energy-dispersive X-ray spectroscopy
EG	Ethylene glycol
FCCJ	Fuel cell commercialization conference of Japan
FTIR	Fourier transform infrared spectroscopy
GDE	Gas diffusion electrode
GDL	Gas diffusion layer
H^+	Proton
H_2	Hydrogen molecule
H_2O	Water molecule
$HClO_4$	Perchloric acid
HER	Hydrogen evolution reaction
HOR	Hydrogen oxidation reaction
H_{upd}	Hydrogen under potential deposition
IL-TEM	Identical location transmission electron microscopy
Ir	Iridium
K^+	Potassium cation
Li^+	Lithium cation
MEA	Membrane electrode assembly
MPL	Microporous layer
Na^+	Sodium cation
NP	Nanoparticle
O_2	Oxygen molecule
OER	Oxygen evolution reaction
OH^-	Hydroxide anion
ORR	Oxygen reduction reaction
PEMFC	Proton exchange membrane fuel cell
PEMWE	Proton exchange membrane water electrolyzer

PCTFE	Polychlorotrifluoroethylene
PGM	Platinum group metal
PTFE	Polytetrafluoroethylene
Pt	Platinum
PTL	Porous transport layer
RDE	Rotating disk electrode
RE	Reference electrode
RHE	Reversible hydrogen electrode
SAXS	Small angle X-ray scattering
SEM	Scanning electron microscopy
SiO_2	Silicon dioxide, silica
TEM	Transmission electron microscopy
Ti	Titanium
TiO_2	Titanium dioxide, titania
UV	Ultraviolet
Vis	visible
WAXS	Wide angle X-ray scattering
WE	Working electrode
XAS	X-ray absorption spectroscopy

List of Contents

1. Introduction and Outline of the Thesis

1.1. Introduction

For future energy storage and renewable energy conversion electrolyzers and fuel cells are playing a key role. The excess of electricity produced from renewable energy carriers can be used for the splitting of water (electrolysis). The formed oxygen and hydrogen can then be recombined in fuel cells via the opposite reaction by regenerating water, e.g., as alternative to combustion engines in vehicles.[1,2]

The two devices, electrolyzers and fuel cells are operated under alkaline or acidic conditions.[3,4] Under acidic conditions proton exchange membrane are used. The devices are then called proton exchange membrane water electrolyzers (PEMWEs)[3] and proton exchange membrane fuel cells (PEMFCs)[4]. In PEMWEs and PEMFCs higher power densities can be reached than in alkaline electrolyzers[3] and fuel cells[5] and the nowadays often used Nafion® membranes are very stable.[5] However, the catalyst materials are mostly limited to precious metals, i.e., Pt group metals (PGM).[6] In alkaline environment non-precious metals (non-PGMs), can be used as catalysts for the oxygen reaction,[7] however the employment of liquid electrolyte is necessary[3] due to limitations of alkaline membranes.[6,8] Furthermore, the durability of the PGM[9] and non-PGM catalysts under alkaline conditions is limited.[10]

The water splitting process in PEMWEs consists of the oxygen evolution reaction (OER) and H^+ formation at the anode:[11]

$$\mathbf{H_2O} \rightarrow \frac{1}{2}\,\mathbf{O_2} + 2\,H^+ + 2\,e^- \qquad (1)$$

The H^+ is passing through the membrane and hydrogen is evolved, i.e., the hydrogen evolution reaction (HER), at the cathode[11] via

$$2\,H^+ + 2\,e^- \rightarrow \mathbf{H_2} \qquad (2)$$

In the PEMFCs the hydrogen is split into H^+, i.e., the hydrogen oxidation reaction (HOR, the reversed direction of reaction (2)), at the anode.[4] H^+ is passing the membrane and forms water by the reduction of oxygen, i.e., the oxygen reduction reaction (ORR, the reversed of reaction (1)), at the cathode.[4] The oxygen reduction and oxidation are kinetically hindered, while the hydrogen reduction and evolution are very fast.[12–14] Due to the poor kinetics of the oxygen half-cell reactions, ORR and OER, a large overpotential is necessary to reach high currents.[14] Therefore, the conversion efficiency of electrolyzers or fuel cells is limited by the sluggish OER or ORR, respectively, and the research focuses on the improvement of catalysts for those oxygen reactions.[14,15]

The catalysts used in electrolyzers and fuel cells consist of nanoparticles (NPs) as a small size of 1-5 nm enormously increases the surface area to volume ratio as compared to bulk material[16] and hence less material is needed. The electrode material for the HER or HOR is typically Pt showing however limitations in the use of impure gas as by CO poisining.[5] Despite the rareness of Ir, the OER is performed using Ir NPs and alloys with, e.g., Ru due to the compromise of low overpotential and stability.[17,18] For the ORR Pt NPs and its alloys are the most active catalysts[19] according to the volcano plot, i.e., the catalyst activity is plotted depending on the oxygen binding energy.[20] Thereby, it is tried to form alloys with less rare and less expensive metals for

the catalysts of OER and ORR to reduce the amount of precious metals needed.[19] The NPs are usually supported to avoid agglomeration and to increase the dispersion of the particles and hence to ensure a high surface area.[21,22] Supports used in fuel cells are high-surface area carbons (C) due to their good electric conductivity.[5] In electrolyzers alternatively, e.g., titanium oxide (TiO_2) is used to obtain high stability at high potentials.[23] The supported catalysts are, e.g., sprayed on the proton exchange membrane, i.e., catalyst coated membrane (CCM), and then hot-pressed on C or Ti based substrates, in fuel cells[15] or electrolyzers[23], respectively.

Due to the sluggish oxygen reactions and thus the research focus on the investigation of the ORR or OER, electrochemical setups investigating only the half-cell reaction of fuel cells or electrolyzers, i.e. ORR or OER, respectively, are often used.[14,15] The standard testing device is the rotating disk electrode (RDE) setup.[24] Because of mass transport limitations in a RDE setup for ORR testing, Zalitis *et al.*[25] designed a floating electrode. The recently introduced gas diffusion electrode setup simulates additionally conditions close to the fuel cell.[26–28] (I was involved in the work of reference 28 that I repeatedly refer to in the introduction. In order to highlight such cases of "self-reference", in the following such cases are marked without interrupting the flow for the reader.) Therefore, setups simulating realistic conditions but being straightforward in handling are preferentially used for catalyst testing.[28,29] Due to the long time research focus on activity improvement, many highly active catalysts were developed.[30,31] However, besides a high activity additionally a decent stability of the catalysts is equally important for the applications.[32,33] To increase the catalyst degradation simulating application conditions accelerated stress tests (ASTs) are performed.[34–36] Hence, the combination of AST protocols in gas diffusion electrode (GDE) setups seems to be reasonable or even evident.[28] Unfortunately, the analysis of the catalyst layer in the GDE setup, i.e., gas diffusion electrode layer (GDL), is at the moment often limited to *ex situ* measurements. Coupling of a GDE setup to an ICP-MS presented recently by Ehelebe *et al.*[37] to measure the metal dissolution is hence from outstanding importance. *Operando* techniques enable the understanding of degradation mechanisms to thus deduce considerations for improved catalyst design.

1.2. Outline of the Thesis

In the following second chapter the experimental methods that I used are discussed and compared to literature.

1. The “surfactant-free” NP syntheses approaches for Pt and Ir NPs are discussed.
2. Concerning the gas diffusion electrode setup, it is pointed out why this electrocatalytic testing device simulates realistic conditions close to PEMFCs and PEMWEs in contrast to the RDE setup, the standard testing tool.
3. The electrochemical characterization methods and characterization techniques I was working with are presented and used characterization protocols are discussed as compared to literature.

Afterwards in the third chapter the seven appended manuscripts are discussed. During my PhD I was focusing on the nanoparticle formation mechanisms and degradation studies of fuel cell catalysts. Therefore, I start to discuss the manuscripts I to V related to the topic of fuel cell

catalysts.

I. The synthesis mechanism of Pt NPs as a potential cathode material for fuel cells based on a visible light induced reduction in the polyol process is discussed.

II. The influence of precursor anions and the base anions in the size control of Pt NPs synthesized in the polyol process are shown.

III. Degradation studies of fuel cell catalysts under realistic conditions in a GDE setup performing *ex situ* small angle X-ray scattering (SAXS) analysis are presented.

IV. The manuscript is about degradation studies by performed *operando* SAXS using a lab X-ray source.

V. In this manuscript a degradation study coupling *operando* SAXS and wide-angle X-ray scattering (WAXS) at a synchrotron source is presented.

At the end of my PhD time, I was working on the topic of electrolysis, discussed in the manuscripts VI and VII.

VI. UV-light induced Ir NP synthesis as potential anode material for PEMWEs is shown.

VII. The manuscript deals with the performance testing of an Ir catalyst under realistic conditions of a PEMWE in a GDE setup.

2. Experimental Methods

In the second chapter the important experimental methods I used for the preparation of the results from the appended manuscripts (based on their descriptions from the experimental sections) are discussed and compared to literature.

1. Discussion of the “surfactant-free” NP syntheses approaches for Pt and Ir NPs.
2. Presentation of the gas diffusion electrode setup by pointing out why realistic conditions close to PEMFCs and PEMWEs are simulated in contrast to commonly used testing devices as the RDE setup.
3. Presentation of the electrochemical characterization methods and characterization techniques I was working with and discussion of used characterization protocols.

2.1. "Surfactant-Free" Nanoparticle Synthesis

Standard colloidal methods need polymers as "surfactants" (e.g., PVP) to obtain small and stable colloids.[38–40] Their removal demands harsh conditions as high temperature[41] or ozone treatment that might alter the catalyst, the NP size, and the support.[42] As alternative two different "surfactant-free" nanoparticle synthesis approaches were studied.

2.1.1. Polyol Synthesis

The ethylene glycol (EG) based synthesis of NPs under alkaline conditions (i.e., polyol synthesis) enables the preparation of "surfactant-free" colloids with narrow particle size distributions.[43,44] As tailoring of physical properties (i.e., particle size, particle loading, and support) of the NPs and the catalyst is possible, the approach is very attractive for the preparation of catalysts.[45]

In general in the polyol synthesis, the metal precursor (e.g., H_2PtCl_6, H_2BrCl_6) is reduced in alkaline EG to form colloids, while the solvent EG is oxidized.[44] By changing the precursors, besides Pt NPs additionally Ir, Ru, and Rh NPs can be formed (I was involved in one of the cited studies).[46–48] As most investigations were done about Pt NPs and during my PhD time I synthesized only Pt NPs with the polyol process, I focus on details about the Pt particle synthesis. The reduction of the metal salt can be induced thermally (by a heated oil bath or microwave radiation) or UV light.[44,49–51] In the reduction process the solvent EG is oxidized to glycolaldehyde, glycol acid, oxalaldehyde, and/or oxalic acid. Additionally, EG can degrade by forming two CO molecules absorbing to the Pt NP surface.[44,52] The protons formed during the reduction of the metal precursor and the oxidation of the EG are reacting with the OH^-, that is present due to the alkaline conditions, to form water.[49] For the stabilization of the formed NPs an excess of OH^- is needed.[44,50] However, due to the high viscosity and boiling point of the synthesis media EG, it needs to be removed for further processing of the NPs. By lowering the pH adding HCl the NPs can be flocculated and redispersed in several organic solvents with high vapor pressures (as isopropanol, ethanol, acetone), while maintaining the particle size.[53] Afterwards, those NPs can be used for the preparation of heterogeneous catalysts by deposition of the particles onto support material (e.g., alumina (Al_2O_3), silica (SiO_2), carbon (C)). The polyol approach can therefore be used to prepare catalysts for heterogenous catalysis as CO oxidation (I was involved in one of the cited studies, that I frequently refer to in this chapter)[54,55] or as fuel cell cathode material.[50,56] After flocculation the NPs are merely covered by CO, but no organic residuals can be identified.[44] In solid-state NMR spectroscopy this finding was further confirmed for supported catalysts prepared from such colloids.[55] In contrast to the surfactants as polymers that are typically used in colloidal chemistry,[57] CO coverage in supported NPs can be easily replaced by OH^- by adding alkaline water.[53]

Furthermore, it was shown in different studies that OH^- is not only important to stabilize the NPs but also that the particle size is determined by the amount of OH^- during the reduction, i.e., the particle size increases reducing the OH^- amount.[44,50] Quinson *et al.*[58] showed that in the polyol approach the use of the cations of lithium (Li^+), sodium (Na^+), potassium (K^+), and cesium (Cs^+) in the hydroxide base do not influence neither the particle size nor the stability. In the thermal reduction of H_2PtCl_6 or H_2PtBr_6 in presence of NaOH the NP size can be

increased additionally due to halide induced leaching (i.e., the halides from the precursors) and subsequent Ostwald ripening during a time period for 17 h at 150 °C. Reducing H_2PtBr_6 instead of H_2PtCl_6, the higher leaching ability of bromide as compared to chloride results thereby in larger particles.[54] In the same work Neumann *et al.*[54] showed that the thermal reduction of the halide-free precursor $Pt(acac)_2$ ($acac^-$ abbreviation for acetylacetonate anion) in presence of NaOH leads even at the long time period of 17 h to a constant large NP size of 3 nm. The missing aspect regarding the size control is a closer investigation of the anion influence of the precursor and the base that is discussed in manuscript II, see chapter 3.2.

The several reports discussed above show that the polyol process is thoroughly investigated and demonstrate that independent of the user reproducible results concerning the size control can be generated in different laboratories. Therefore, it was surprising that, when I started my PhD, mechanistic investigations about the polyol approach were still missing. Quinson *et al.*[50] proposed the ratio of OH^- to Pt surface atoms as size determining aspect in the synthesis and the interrupting of the growth process due to OH^- without a further discussion of the NP formation mechanism. In the discussion of manuscript I, see chapter 3.1, details are found about a proposed particle formation mechanism based on the precursor reduction induced by visible light.

In the polyol approach for further processing the solvent EG, due to its high viscosity and high boiling point, needs to be removed. This is normally done by flocculating the particles by adding HCl and redispersing the particles in solvents with lower boiling points as, e.g., acetone.[44,50] Chloride is however a well-known leaching agent for Pt NPs, especially in electrochemistry, and hence it should be avoided in the preparation of electrocatalysts (I was involved in one of the cited studies).[54,59]

2.1.2. Synthesis in Low Boiling Point Solvents

An alternative synthesis approach is the so-called Co4Cat method[60] being performed in the low-boiling point solvents methanol or ethanol where the flocculation step of the polyol process is redundant.[61] Therefore processing of the particles formed by the Co4Cat process is much faster while narrow size distributions are obtained as known from the polyol process.[61]

In the Co4Cat technology Pt or Ir NPs can be synthesized by reducing metal precursors as H_2PtCl_6 or $IrCl_3$ in alkaline low boiling point solvents. While the Pt NP formation process was thoroughly investigated (I was involved in two of the cited studies, I refer to again in this chapter),[58,61–65] only few reports are found about Ir NPs (I was involved in one of the cited studies, I refer to again in this chapter).[61,66] In literature different aspects to understand the Pt NP formation mechanism are investigated inducing the reduction thermally (heated oil bath or microwave based) or by UV-light.[62] However, the use of methanol or ethanol as compared to EG changes the particle properties and behavior. It is shown that a size control of Pt NPs in MeOH can be generated by adding water.[61,62] A size increase from ca. 2 to ca. 5 nm can be obtained in the reduction of H_2PtCl_6 in alkaline aqueous methanol (75 % water, 25 % methanol) by decreasing the NaOH/Pt ratio from 100 to 5, respectively.[62] The change of the cation of the base leads to less stable Pt NPs in the order $Li^+ \gg Na^+ > K^+ > Cs^+$ in methanol while in EG no impact is observed.[58] The use of an aged H_2PtCl_6 precursor solution in methanol by daylight shows a substantial faster reduction due to the presence of Pt(II) complexes.[63] The investigation

of the reduction of H_2PtCl_6 in ethanol or methanol combining several analysis techniques revealed in ethanol a fast reduction from Pt(IV) to Pt(II) followed by the nucleation and a strong growth process or sintering with less surface bonded CO. In methanol only moderate growth is observed while a strong CO band in the Fourier transform infrared spectroscopy (FTIR) spectrum showing that many CO is bond to the particle surface.[64] *In situ* studies of the H_2PtCl_6 reduction revealed polynuclear $Pt_xCl_yO_z$ complexes were the coordination number of Pt-Cl decreases when the reduction is proceeding.[65]

In the few reports about Ir NP synthesis[61,66] a size control and the reduction induced by UV-light are still missing. The tries of a size control in the Ir NP synthesis induced by UV-light is discussed in manuscript VI, see chapter 3.6.

2.1.3. LaMer Growth Model and Seed Mediated Growth

The NP formation is usually proposed to follow the kinetic LaMer model and its suitability was shown for specific systems.[67–70] In the LaMer model first monomers are formed by the reduction of the dissolved metal precursor. Small, instable nuclei are formed when supersaturation is achieved. At a critical concentration due to further increase of the monomer concentration large enough nuclei are formed that remain stable under the given conditions. When the monomer concentration falls below the nucleation threshold this continuous nucleation is stopped and the deposition of the monomers on stable nuclei leads to particle growth.[71,72] According to the LaMer model it is possible to generate seed mediated growth when NPs are exposed to a monomer solution with a concentration that is low enough not to induce nucleation as competitive reaction pathway.[73] In kinetic studies at ambient temperature Kunz *et al.*[74] showed an size increase of AuPd NPs by adding different amounts of Au precursor solution to Pd NPs. The particle size increase was predicted by assuming that the initial size distribution of the Pd clusters is changing evenly by adding the same amount of Au precursor in a given time period. In the work of Kunz *et al.*[74] the particle size predictions based on a pure seed-mediated mechanism are in good agreement with the measured NP sizes. The same approach of seed-mediated growth by exposing NPs to a more noble precursor solution[74] is presented by Hwang *et al.*[75] for RuPt NPs.

Such seed-mediated growth experiments were tried in the polyol process by adding a partially reduced H_2PtCl_6 solution as monomer, i.e., irradiation of H_2PtCl_6 in alkaline EG with 400 nm for 4 h resulting in a colorless solution, to thermally formed Pt NPs. Thermally formed Pt NPs were used (a) as-prepared, (b) redispersed in EG, or (c) supported on C (the two latter to reduce the amount of OH^-) and exposed to room light and room temperature for a week. (d) The reaction mixture of (a) was exposed to 500 nm for 3 h at room temperature. The seed-mediated growth experiments of Pt NPs in the polyol process tried to be induced by irradiation with 500 nm are discussed in manuscript I in chapter 3.1.

Additionally, seed-mediated growth experiments in the Co4Cat process adding monomers of $IrCl_3$ (obtained by short UV treatment) to Ir NPs (formation induced by UV light or microwaves) were tried at 40 °C for 6 h. The seed-mediated growth experiments of Ir NPs in the Co4Cat process tried to be induced in reducing (hydrogen) atmosphere and under UV light are discussed in manuscript VI in chapter 3.6.

2.2. Gas Diffusion Electrode Setup

To investigate catalysts for PEMFCs or PEMWEs the most realistic way would be the use of membrane electrode assemblies (MEAs) in proper device. However, special equipment is needed for the assembling and due to the complexity of the setup as well as the film preparation of the MEAs, several repeats are rarely performed. Additionally, typically a few grams of catalyst material are required for the testing under realistic fuel cell conditions.[76] Last but not least, a separate analysis of both catalyst layers (cathode and anode) and the separation of the side reaction is difficult. Therefore, testing devices only focusing on the half-cell reaction are preferred that require a limited amount of catalyst material and are straightforward to perform. As alternative to MEA setups, traditionally RDE setups are used for the initial catalyst testing, compare Figure 1, as only a small amount of catalyst is necessary. However, in a RDE setup the conditions of the catalyst testing are often far away from realistic conditions.[76] Furthermore, reproducibility of the catalyst films is barely controlled (due to catalyst drop casting, see chapter 2.2.1) and still the rotator as special equipment is necessary.

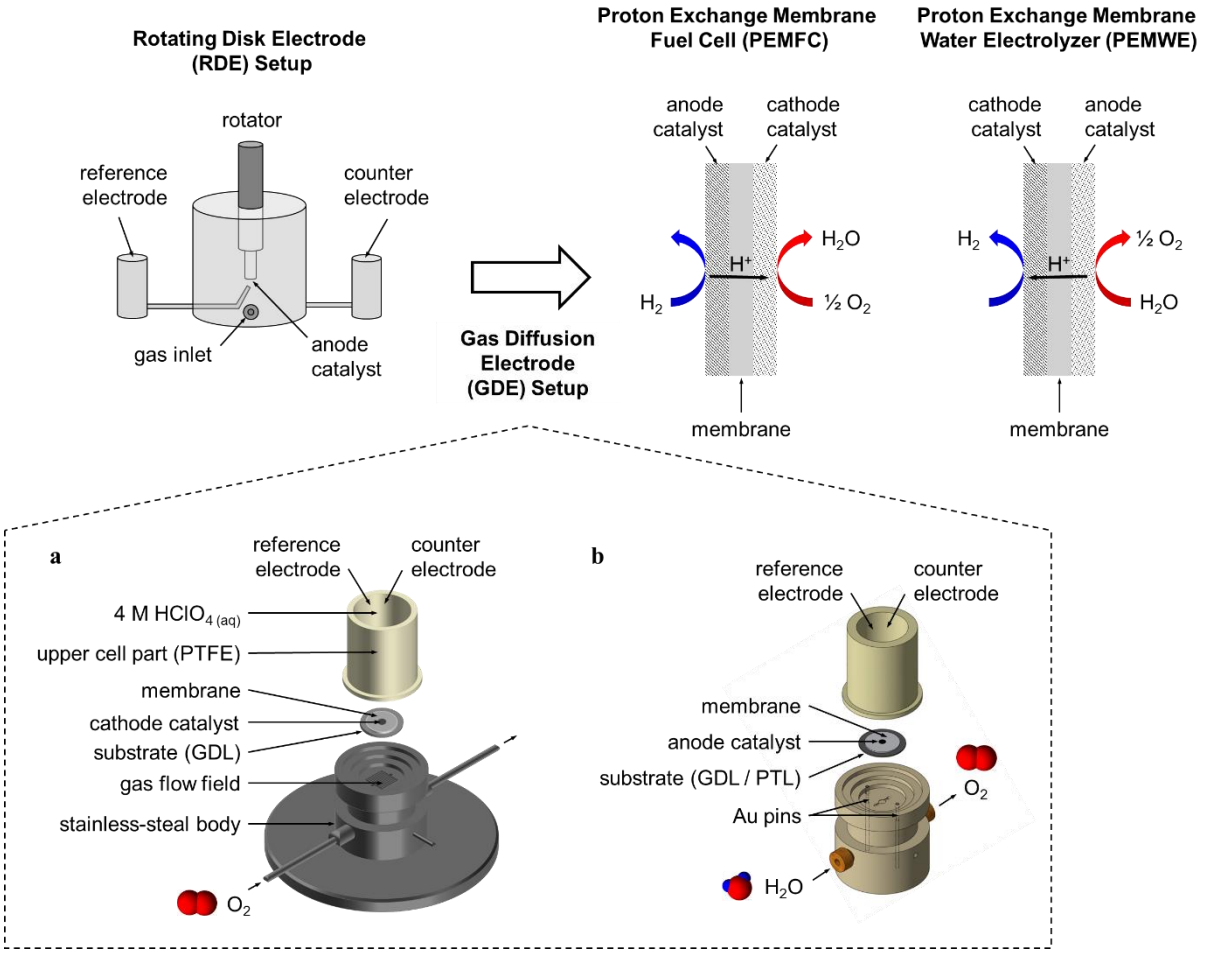

Figure 1. In-house developed gas diffusion electrode (GDE) setups for the a) ORR degradation studies and b) OER activity measurements as compared to the rotating disk electrode (RDE) setup (top left), proton exchange membrane fuel cells (PEMFCs), and water electrolyzers (PEMWEs) (top right). Reprinted with permission from *JACS Au* **2021**, *1*, 247-251. Copyright 2021 The Authors. Published by American Chemical Society.

A new half-cell that fills the gap between basic research testing, i.e., RDE, and the realistic but complicated MEA testing, is the recently presented GDE setup for the ORR (I was involved in one of the cited studies, that I frequently refer to within the discussion of this chapter)[26–28], see

Figure 1a. Two further advantages of the GDE setup in the ORR are the reduced mass transport limitation and the possibility to reach higher current densities as compared to the standard RDE setup.[37] The design of the GDE setup presented in Figure 1a is described in the following: A Nafion® membrane is placed on a catalyst layer that is deposited on a GDL, i.e. working electrode (WE), as used in MEAs.[28] The Nafion® membrane is additionally avoiding the leaking of the electrolyte into the GDE. The reactant oxygen (O_2) gas can pass the GDL reaching the catalyst and forming together with protons from the electrolyte water according to the back reaction of equation (1). The gas needs to be humidified to guarantee a humidification of the Nafion®.[27,28] The upper cell part above the Nafion® membrane is made of polytetrafluoroethylene (PTFE). A platinum (Pt) wire is used as a counter electrode (CE) and a hydrogen trapped reference electrode (RE), i.e., reversible hydrogen electrode (RHE). The CE is placed inside a glass capillary with a glass frit on the bottom to avoid the trapping of gas bubbles from the counter reaction in the hole of the Teflon cell, prevent an interaction of the CE products with the WE, and hence help to improve the reproducibility of the measurement.[28] All potentials in the studies of manuscript III are referred to the RHE potential and perchloric acid ($HClO_4$, 10 mL, 4 M) was used as electrolyte. For a controlled temperature (30 or 50 °C) during the subsequent electrochemical measurements a fan in an isolated Faraday cage was used.

An alternative GDE setup design was presented by Pinaud *et al.*[76] that was adjusted by Ehelebe *et al*.[29,37] The principle between all three setups is the same, i.e. a catalyst layer is deposited on a GDL and the O_2 gas (reactant for ORR) is flowing through the GDL reaching the catalyst that is in contact with the electrolyte. In the cell design there are however some differences. The GDE cell of Pinaud *et al.*[76] is placed in a beaker of electrolyte, that is increasing the amount of electrolyte. The WE is arranged vertically and the gas is introduced from the top of the cell, that is free of electrolyte. A catalyst layer of 3 cm^2 is necessary, hence the performance of professional hot pressing seems to be unavoidable to guarantee the contact between membrane and catalyst layer. The high amount of catalyst leads to high currents of 1.5 A/cm^2 but this necessitates an exact determination of the iR drop as this determines the measurement error. Therefore, an iR correction cannot be performed based on cell resistance measurements at a constant frequency.[76] In the adapted GDE cell of Ehelebe *et al*.[29,37] the WE assembly is located next to the electrolyte reservoir, a catalyst layer of 4 cm^2, and again a large amount of electrolyte are used. Both cells of Pinaud *et al.*[76] and Ehelebe *et al*.[29,37] were so fare surprisingly only used for measurements at room temperature.

For OER studies the stainless-steel body from the ORR measurement was replaced by polychlorotrifluoroethylene (PCTFE) for enhanced chemical stability at high voltages (see Figure 1b). The GDE was placed on top of the flow field with the Nafion® membrane upwards as before for ORR testing. In the GDE setup for the OER two Au pins were placed vertical inside the cell body and a plastic disc as pedestal was screwed into the cell body to push the Au pins into the GDE. In the ORR setup the contacting to the WE was obtained via the stainless-steel body. The upper cell part (Teflon) with the electrolyte (15 ml 4 M $HClO_4$) had a hole in the same size as the WE (Ø 3 mm). The induced gas, e.g., O_2, was transported the reactant water that reacted according to equation (1). In manuscript VII the GDE setup was used for OER activity tests with the same assembly of the CE and RHE as described before for the ORR AST in the GDE setup. The temperature control (30, 40, 50, or 60 °C) in the subsequent electrochemical measurements was reached by placing the cell in a metal box on top of a heating plate.

2.2.1. Gas Diffusion Electrode Preparation

The preparation of the GDE consist of firstly the deposition of the catalyst film onto a substrate and secondly attaching a Nafion® membrane. In the following, the procedures for the use of a C based GDL or a Ti based porous transport layer (PTL) as substrates are discussed.

Catalyst film preparation with C based GDL

The catalyst films on a GDL for electrocatalytic investigations in GDE setups can be done by drop casting, spray coating, or vacuum filtration. Prior to the film preparation, a catalyst ink dispersion needs to be prepared. Drop casting of a catalyst dispersion is typically done to prepare catalyst films for electrocatalytic measurements in RDE setups[66,77] using stable and well dispersed catalysts with carbon support in a mixture of H_2O to isopropanol of 3:1.[77] Comparable to the catalyst films for RDE measurements drop casting could be a possibility for the preparation of GDEs. However, drop casting can lead to varying film qualities in repeating measurements. Therefore, Inaba *et al.*[27] and Alinejad *et al.*[28] prepared catalyst films for measurements in the GDE setup via spray coating of GDLs generating loadings as used in RDE testing. With drop casting or the spray coating method the reached loadings are however far away from realistic loadings of 0.2 $mg_{Pt}\ cm^{-2}_{geo}$ in fuel cells[78] or 1.0 $mg_{Pt}\ cm^{-2}_{geo}$ in electrolyzers[79].

The vacuum filtration method introduced by Yarlagadda *et al.*[80] enables the preparation of catalyst films deposited on a GDL with realistic catalyst loadings. Furthermore, various samples can be punched out to obtain reproducible catalyst films for repeatable measurements. In the ink for the vacuum filtration Nafion® was added to ensure proton conductivity in the catalyst layer.[27] The vacuum filtration was used to prepare catalyst films for the manuscripts III to V and VII, see chapters 3.3 to 3.5 and 3.7.

Nafion® membrane activation

Before attaching the Nafion® membrane to the catalyst layer the membrane was first activated: The Nafion® membrane (stored in water and cut in the right circle size) was cleaned from organic impurities[81] by a treatment in 5 wt.% H_2O_2 (30 min, 80 °C). After treating in Milli-Q water (30 min, 80 °C) to remove the H_2O_2 the cutoff membranes were protonated[81] by a treatment in 8 wt.% H_2SO_4 (30 min, 80 °C). After final rinsing of the cutoff membranes with Milli-Q water, they were kept in a glass vial filled with Milli-Q water. This procedure was used for the Nafion® membrane activation in the manuscripts III and VII, see chapter 3.3 and 3.7.

Pressing of GDL with Nafion® membrane

The attaching of the Nafion® membrane was necessary by pressing in a pellet press as otherwise sometimes a bubble during the assembly of the GDE setup was formed and hence the electrical contact during the electrochemical testing was lost. The Nafion® membrane was pressed on top of the GDE, see Figure 2, by placing a Teflon or paper sheet on top of a Teflon block and afterwards the GDL (Ø 2 cm with a hole of Ø 3 mm) and the catalyst deposited on the GDL obtained by the vacuum filtration (Ø 3 mm) in the hole. A Nafion® membrane was rinsed with

Milli-Q water and placed on top of the GDL, followed by a second Teflon or paper sheet and a second Teflon block. Everything was placed between two metal blocks and the pressing was performed at 2 tons for 10 min. This pressing procedure was used in the manuscripts III and VII.

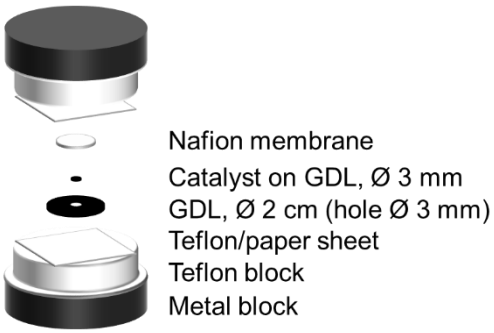

Figure 2. Preparation of the WE by placing the catalyst layer deposited by vacuum filtration onto a GDL (Ø 3 mm) into the hole (Ø 3 mm) of a GDL (Ø 2 cm) and pressing a Nafion® membrane onto it by applying 2 t for 10 min between two Teflon or paper sheets, two Teflon blocks, and two metal blocks.

Catalyst film preparation and hot-pressing with Ti based PTL

Instead of a Nafion® membrane pressed to a catalyst layer that was deposited on a carbon based GDL, a catalyst layer on top of a Nafion® membrane (CCMs) pressed to a Ti based substrate, i.e., PTL, are used in PEMWEs.[23,82] However, for the CCM preparation special equipment is needed, that is not accessible in all laboratories for catalyst testing experiments. The highly porous PTL makes the performance of vacuum filtration or drop casting of the isopropanol-water ink, as used in the GDL preparation described above, impossible. A simple alternative to the fabrication of CCMs is the use of a glycerol-based catalyst ink due to the substantial higher viscosity of glycerol as compared to water and isopropanol. However, drop casting the glycerol-based ink does not completely avoid the permeation of the ink into the PTL. Comparing the structure of the PTL to the one of the GDL it becomes apparent that the hydrophobicity of the GDL is generated by the Teflon containing microporous layer (MPL). Therefore, Teflon was sprayed on top of the PTL before the drop casting to prevent the permeation of the glycerol-based ink into the PTL.

To avoid after the assembling of the GDE cell a poor electric connection between the PTL and the Nafion® membrane resulting sometimes in high resistances of several hundred ohms, the temperature during pressing needed to be increased by performing a simple hot-pressing. This approach of hot-pressing of the Nafion® membrane (activated as described in the previous paragraph) to the PTL (with glycerol-based ink deposited onto it) was performed for the PTL preparation in manuscript VII, see chapter 3.7.

2.2.2. ORR Degradation Protocols and Degradation Mechanisms

Stability investigations of fuel cell catalysts are done simulating the catalyst use under realistic conditions and simultaneously accelerating the catalyst degradation by performing ASTs. Alinejad *et al.*[28] simulated (1) load-cycles, (2) start-up/shutdown conditions, and (3) a combination of both of PEMFCs in vehicles by stress test protocols recommended by the Fuel Cell

Commercialization Conference of Japan (FCCJ)[83,84] in the gas diffusion electrode setup. The three protocols consist in details of the following procedure:

1. In the load-cycle conditions the potential is stepped between 0.6 and 1.0 V_{RHE}, e.g., holding each potential for 3 s. In manuscript III in *ex situ* SAXS analysis after degradation measurements in a GDE setup 9000 cycles at 25 °C or 5000 cycles at 50 °C under load-cycle conditions were performed, see chapter 3.3 for details. The temperature was controlled by a fan in an isolated Faraday cage to reach 30 or 50 °C (as in manuscript III, see chapter 3.3). Furthermore, those load-cycle conditions were performed in manuscript IV and V in *operando* SAXS studies at room temperature, see chapter 3.4 and 3.5, respectively.
2. Alinejad *et al.*[28] showed that under start-up/shutdown conditions, performing cyclic voltammograms between the potentials 1.0 and 1.5 V_{RHE}, in the GDE setup a strong carbon corrosion of the investigated Pt/C catalyst occurs. This makes an analysis of the electrochemical active surface area (ECSA, see chapter 2.3.1) questionable leading to ambiguous conclusions concerning the degradation of the Pt NPs.
3. In the combination protocol, e.g., 500 load-cycles are applied holding each potential for 3 s, followed by 10 cycles of start-up/shutdown conditions.[28] Between the three presented protocols the combination protocol is simulating the most realistic driving conditions of fuel cell vehicles.

During the AST the NPs (a) can migrate followed by a coalescence and potentially sintering, (b) dissolve as metal ions, (c) experience electrochemical Ostwald ripening, i.e., large particles grow at the expense of small ones, and (d) detach from the support.[85] The degradation mechanisms (a)-(d) reduce the ECSA of the catalyst and (a)-(c) change the particle size.

2.2.3. OER Activity Protocol

In RDE testing normally cyclic voltammetry is performed as a protocol to test catalyst activities[86–88] although PEMWEs are used in galvanostatic mode.[11] In addition, in potentiodynamic or potentiostatic modes the catalyst comparison is complicated as both the measured current and due to iR correction the applied potential change. Therefore, a galvanostatic protocol was chosen for the performance testing including the holding of different mass specific current densities for 2 min.

To measure reasonable activity data a good temperature control is necessary. This was done in a metal box placed on top of a heating plate to work at 30, 40, 50, or 60 °C (as in manuscript VII, see chapter 3.7). After assembling the setup, it was allowed enough time to reach the desired temperature before starting any experiment. The successful assembling of the cell was verified by recording one cyclic voltammogram while purging the electrode with humidified gas, O_2 or Ar, (with a scan rate of 10 mV s^{-1}, 1.2-1.6 V_{RHE}). Bizzotto *et al.*[66] showed that the homemade IrO_2/C is only partially oxidized after the NP synthesis. Hence for guaranteeing the complete oxidation of the Ir based catalyst the electrode potential was hold at 1.6 V_{RHE} for 5 min. The resistance during the measurement was determined online using an AC signal (5 kHz, 5 mV) as during the activity measurements the applied current densities were below 200 mA mg_{Ir}^{-1}.[89]

2.3. Electrochemical Characterization and Characterization Techniques

2.3.1. ECSA Determination of Pt Based ORR Catalysts

The ECSA can be determined by CO stripping due to the chemical adsorption of CO on Pt atoms.[90] By subtracting the cyclic voltammogram (CV) performed in Argon (Ar) and using a baseline correction between the chosen peak limits as shown by Inaba *et al.*[91] any influence of capacitive currents from the carbon support can be avoided. The change in surface area, i.e., the surface loss during the AST, together with the knowledge of the change in particle size allows to draw conclusions about the degradation mechanism. The determination of ECSA was used in the degradation studies performed in a gas diffusion electrode setup discussed in manuscript III in chapter 3.3.

2.3.2. OER Activity Determination

The activity in OER catalyst testing performed in the GDE setup was analyzed of the iR corrected data averaging the potential of the last 60 s of each current step, see chapter 2.2.3 for details. The potential was not used of the 2 min in total of the galvanostatic measurement as it was not from the begin on constant. Each measurement was repeated three times preparing a new WE from the same catalyst film obtained by vacuum filtration, see chapter 2.2.1 for details. The determination of the OER activity was used in performance testing of a commercial OER catalyst in a gas diffusion electrode setup discussed in manuscript VII in chapter 3.7.

2.3.3. UV/vis Spectroscopy

UV/vis spectroscopy can be used to identify compounds, e.g., in a reaction mixture. Exposing the sample to ultraviolet and visible light, the intensity of the transmitted light through the sample I is compared to the reference (background) spectrum I_0. When the ground state of a compound in the sample is excited by the induced UV/vis light of a certain wavelength the intensity of the transmitted light is reduced as compared to the reference spectrum. At that certain wavelength is then an absorbance maximum found based on Lambert-Beer's law with the absorbance A, the transmission T, the molar decadic extinction coefficient ε, the concentration of the absorbing compound c, and the pathlength of the sample:[92,93]

$$A = -\log(T) = -\log\left(\frac{I}{I_0}\right) = \varepsilon\, c\, d \qquad (3)$$

When the sample is enough diluted to enable the light transmission, those absorbance maxima can be assigned to certain compounds of the sample (but not every time unambiguously).

To trace the reduction of the reaction mixture and identify intermediates in the polyol process UV/vis spectroscopy was used in manuscript I, see chapter 3.1. The measurement was done in a Quartz cuvette using the solvent EG as background spectrum and for the dilution of the sample.

2.3.4. Transmission and Scanning Electron Microscopy

Different techniques to analyze the particle size are used in the field of heterogenous (electro)catalysis. In the electron microscopy an electron beam is induced and the interaction of the electrons with the sample (electron scattering) is displayed.[94] In general it is distinguished between the two different setups of transmission and scanning electron microscopes.

Transmission electron microscopy (TEM)

The most common technique is TEM. Metal NPs or metal particles supported on carbon are deposited onto a carbon film of a TEM grid.[95] Due to the higher mass of the metal particles as compared to the carbon, more electrons are scattered, hence a less intense electron beam reaches the image plane and the metal particles are seen darker than the carbon areas.[94] The particle size of spherical particles can be determined by measuring the diameters of the dark spots on the TEM images. A statistical evaluation is often done by measuring typically at least 200 particles (I was involved in one of the cited studies).[9,63,96] TEM was intensely used for particle size determinations in the manuscripts I and II in chapter 3.1 and 3.2, and in the manuscripts III and V, see chapter 3.3 and 3.5, to show the particle size for the pristine catalysts as compared to SAXS results.

Additionally identical location (IL) TEM of electrocatalysts is performed in literature to investigate particle size changes of certain particles on so called finder grids, i.e., the grid is marked with letters, in electrochemical studies.[97,98] The TEM grid is used as WE and the particles on the marked spots are analyzed before and after the electrochemical treatment. Thereby, the degradation mechanisms, that the NPs on the marked spots of the electrocatalysts experience, can be identified (I was involved in one of the cited studies).[28,35,99–103]

There are serval limitations found in TEM imaging as particle size analysis technique: The 3D catalyst film are shown as a 2D image, so thin films are needed transmitting enough electrons.[94] Such thin films are reached, e.g., by intense dilution of a NP dispersion or catalyst ink. In addition, it is only possible to investigate very small parts of the sample, hence TEM is a very local technique,[56,94,101] and the selection of the images of the NPs or catalyst being analyzed is user dependent. Furthermore, depending on the quality of the TEM images, i.e., contrast and resolution, as well as the user measuring the particles sizes, the results of the particle diameters can variate.

Scanning electron microscopy (SEM)

SEM by comparison achieves less resolution than TEM, hence size measurements of small NPs is not possible. However, 3D microscopic imagining is possible.[94] In SEM different phenomena of electron interactions with the sample as secondary or backscattering electrons scattering through large angles are used to change, e.g., the contrast or surface-sensitivity on the image by using different detectors.[94,104] As the higher mass of elements leads to higher yields of backscattering electrons, lighter spots as compared to lighter elements are seen on the SEM image when the detector for backscattering electrons is used. On the contrary, the contrast in images yielding from secondary electrons cannot be clearly interpretated.[104]

Additionally, it is often possible to perform energy-dispersive X-ray spectroscopy (EDS) in an SEM instrument. The electron beam injects electrons from the inner shells. By filling that hole with an electron from an upper shell an X-ray with a characteristic energy per element according to the energy difference of the two orbitals from the different shells is emitted.[104] In manuscript VII EDS element mapping of a SEM cross-section of an Ir catalyst film deposited onto the C based GDL is investigated, see chapter 3.7.

2.3.5. Small Angle X-Ray Scattering (SAXS)

While TEM is a local technique, SAXS permits the particle size analysis over the whole catalyst,[56,101] thus SAXS was established as analysis technique in the last years.[28,50,77,101] In SAXS the scattering intensity of the sample in a certain range of the scattering vector q (unit $Å^{-1}$) is detected. Before an analysis of those scattering data is possible after sample preparation, a calibration of the SAXS instrument, and a proper background subtraction are required.

Sample preparation and calibration

As compared to TEM a larger amount of sample is needed. The catalyst films prepared by vacuum filtration as described in chapter 2.2.1 with a realistic PEMFC loading[78] of 0.2 mg_{Pt} cm^{-2} can be used as-prepared for SAXS measurements. In manuscript III it is shown that it is even possible to measure *ex situ* SAXS with the Nafion® membrane on top of the catalyst film.

Before starting the measurement the sample-detector distance needs to be calibrated that is typically done by using silver behenate as it is scattering strongly with defined spacings between the diffraction peaks[105,106] as presented for the first time by Huang *et al.*[107] Additionally, an important step is the scaling of the intensity to enable the extraction of information about the volume fractions, the surface area, or the number of particles.[108] The scaling can be done by a direct calibration or using, e.g., glassy carbon as secondary calibration standard.[108,109] The obtained calibration factor is then multiplied with the measured intensity to generate the intensity in absolute units.[109]

Background subtraction

For SAXS measurements, a crucial aspect is the background subtraction and hence the background measurement. At synchrotron facilities anomalous SAXS[110] or measurements in the grazing incidence configuration[111–113] (as used in manuscript V, see chapter 3.5) can be performed *operando*. However, those techniques are not available at all SAXS synchrotron beamlines and not at laboratory X-ray sources. Alternatively, background measurements can be done in a separate experiment leading often to difficulties in data normalization.[110]

A new WE design enables that the catalyst layer and substrate are experiencing the same AST treatment. This spot on the substrate can be measured as background by *operando* SAXS, see Figure 3. By preparing a catalyst film by vacuum filtration homogenous catalyst films are generated, where punchouts with defined catalyst amounts can be used in electrochemical testing, as described in chapter 2.2.1. Such a punchout consisting of a catalyst layer deposited on a GDL

was placed in the middle of a frame of catalyst free GDL and both were glued to Kapton tape, see Figure 3. Next to the catalyst layer metal free spots experience the same AST protocol in the *operando* cell presented by Binninger *et al.*[114] By moving the cell this metal-free spots can be moved into the beam for *operando* background measurements. This technique was presented and used in manuscript IV in *operando* SAXS measurements at a laboratory X-ray source but can also be used in synchrotron studies especially when anomalous SAXS and the grazing incidence mode are not possible.

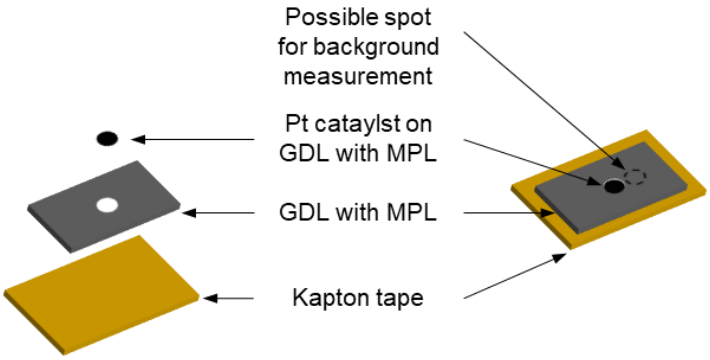

Figure 3. Sketch of the new designed WE (diameter 5 mm) with a Pt/C catalyst deposited on a GDL placed in the middle of a GDL that were glued to Kapton tape enabling background measurements of a spot experiencing the same treatment as the sample, e.g., at an X-ray lab source.

Fitting of scattering data

After background correction the SAXS data are fitted, e.g., by a model of polydisperse spheres where it is assumed that the total volume of particles of a certain size is log-normal distributed, i.e., the distribution is volume-weighted. Based on that model for a bimodal catalyst consisting of two distinguishable size population the fitting is done according to

$$I(q) = A \cdot q^{-n} + C_1 \int P_{S1}(q, R)\, V_1(R)\, D_1(R)\, dR + C_2 \int P_{S1}(q, R)\, V_2(R)\, D_2(R)\, dR \qquad (4)$$

I(q) is the radially averaged intensity as a function of the scattering vector q that is defined with the wavelength λ and the scattering angle 2θ as[115]

$$q = 4\pi \cdot \sin(\theta) / \lambda \qquad (5)$$

The free parameters A, n, R_1, R_2, σ_1, σ_2, C_1, C_2 from equation (4) used in the fitting of the model of two polydisperse spheres and volume-weighted log-normal distributions are discussed in detail in the following:

1. The term $A \cdot q^{-n}$ is the power law to consider the behavior at low q values (i.e, large particle sizes) with A and n as free parameters and the scattering vector q.[116]
2. C_1 and C_2 are scaling constants.
3. P_{S1} and P_{S1} are the hard-sphere form factors[117–119] normalized by the particle volume V_1 or V_2 defined by

$$P_s(q,R)= \left(3\frac{\sin(qR)-qR\cos(qR)}{(qR)^3}\right)^2 \quad (6)$$

4. D_1 and D_2 are the log-normal distributions of the two polydisperse spheres[120,121]:

$$D(R)=\frac{1}{R\sigma\sqrt{2\pi}}\exp\left(-\frac{1}{2}\left(\frac{\ln(R)-\ln(R_0)}{\sigma}\right)^2\right) \quad (7)$$

5. σ^2 is the variance of the log-normal distribution[121]:

$$\sigma^2=(\exp(\sigma^2)-1)\exp(2\ln(R_0)+\sigma^2) \quad (8)$$

6. R_0 is the geometric mean radius of the log-normal distribution[121] (in Å):

$$R_0=\exp\left(\ln(R_0)+\frac{\sigma^2}{2}\right) \quad (9)$$

   To determine the mean particle size, i.e., diameter, and standard deviation $\sigma=\sqrt{\sigma^2}$ in nm a factor of 0.2 needs to be multiplied to the equations (8) and (9).

The use of two individual populations for the fitting of the background subtracted SAXS data of the bimodal catalyst (with two distinguishable particle sizes) necessitates a weighting of the scaling factors of the two populations to obtain a merged probability density. Depending on this weighting, e.g., by the surface contribution of the two size populations the electrochemical contribution of the populations is pointed out in the intensities of the probability densities.

3. Discussion of Appended Manuscripts

In the third chapter seven manuscripts, I was involved in, that are appended to this dissertation, are discussed starting with a description, followed by specifying my contribution to the work, and finally presenting the most important findings.

Manuscript I to **V** are about the topic of PEMFCs.

- **Manuscript I** is discussing the synthesis mechanism of Pt NPs in the polyol process as a potential cathode material for fuel cells based on a visible light induced reduction.
- **Manuscript II** is studying the precursor and base anion influence on the particle size control in the polyol synthesis of Pt NPs.
- **Manuscript III** deals with degradation studies of fuel cell catalysts under realistic conditions in a GDE setup performing *ex situ* SAXS analysis.
- **Manuscript IV** and **V** are about degradation studies by *operando* SAXS using a lab X-ray source or coupled to *operando* WAXS at a synchrotron, respectively.

Manuscript VI and **VII** deal with the topic of electrolysis.

- **Manuscript VI** is about UV-light induced Ir NP synthesis as potential anode material for PEMWEs.
- **Manuscript VII** deals with the performance testing of an Ir catalyst under realistic conditions of a PEMWE in a GDE setup.

3.1. Manuscript I:

The results shown in this chapter are excerpts from the publication

J. Schröder, S. Neumann, S. Kunz

Visible-Light-Induced Synthesis of "Surfactant-Free" Pt Nanoparticles in Ethylene Glycol as a Synthetic Approach for Mechanistic Studies on Nanoparticle Formation

J. Phys. Chem. C, **2020**, *124*, 21798-21809.

https://doi.org/10.1021/acs.jpcc.0c06361

Articles on request author-directed link

Description

The preparation of "surfactant-free" Pt NPs by the polyol process in alkaline conditions induced thermally (in a heated oil bath or by microwaves), or by UV-light was thoroughly investigated.[44,49,50,58] Schrader *et al.*[44] and Quinson *et al.*[50] reported a size control of the Pt NPs by varying the amount of OH^-. Additionally, the stability and size influences due to the cations of the base was investigated by Quinson *et al.*[58] Despite many reports and the great potential for catalytic applications[43,122–124] the mechanism of the Pt NP formation in the polyol process is poorly understood.[72] Usually NP formation is proposed to follow the LaMer model as described in chapter 2.1.3.[67–70] Reducing the dissolved metal precursors leads to the so-called monomers. The simple kinetic LaMer model is suitably describing specific systems.[67–70] However, reports question its validity for the polyol process.[50] Quinson *et al.*[50] described that the OH^- does not only stabilize the "surfactant-free" Pt NPs, but the authors suggest that it also stops the growth process during the synthesis. The formation mechanism was in that study not further discussed but the ratio of OH^- to Pt surface atoms seem to be constant.[50] This indicated that rather the OH^-/Pt ratio determines the final particle size than the kinetics as in the LaMer model. However, a clear understanding of the determining factor for the particle size is still missing.

Due to the indication that the particle size is not controlled by kinetics a slowing down of the particle formation would be beneficial to investigate intermediates during the synthesis. Previous reports showed that the reduction by UV-light is slowing down the formation process (to ca. 2 h)[49] as compared to the thermal- or microwave-induced synthesis (ca. 3 min)[44]. Those reports were proposing that the NP formation is induced by UV light as part of the daylight as the absorbance maximum of the used precursor H_2PtCl_6 is found in the UV light region (at ca. 265 nm).[51] Showing that visual light can be used to induce Pt NP formation, a reduction and particle growth mechanism for the polyol synthesis using H_2PtCl_6 and H_2PtBr_6 as metal precursors is proposed.

Contribution to the Work

I synthesized the Pt NPs and designed the experiments together with S. Kunz. I performed the UV/vis and FTIR spectroscopy and prepared the TEM samples. I analyzed the TEM images that were taken by S. Neumann. I analyzed mass spectroscopy data that were taken by the spectrometry services at the University of Bremen (Institute of Organic and Analytical Chemistry) and University of Bern (Department of Chemistry and Biochemistry). S. Kunz and I wrote the first draft of the manuscript, which was read and commented by all authors.

Most Important Findings

<u>Visible-light-induced reduction of H_2PtCl_6 under varying wavelength</u>

Exposing H_2PtCl_6 in presence of NaOH in EG with different wavelengths (400-650 nm) shows that NP formation is possible over a long range of visible light despite previous reports.[49,51] This is unexpected as the precursor has an absorbance maximum in the UV range at 265 nm.[51] As compared to UV light induced syntheses[49] the reduction takes up to 24 h. The observed NP formation rate changes depending on the wavelength of the exposed light with a maximum at

500 nm, see Figure 4. In the reduction of H_2PtCl_6 the irradiation after 24 h with wavelengths of 600 and 650 or 400 nm does not lead to NPs or not enough to process, respectively. The optical analysis of the reaction mixture during the reduction shows three distinguishable reduction phases: The yellow precursor solution (bordered in yellow in Figure 4) is first reduced to a colorless solution (bordered in blue) before the brown dispersion indicating the NP formation is reached. The NP formation can be followed by UV/vis spectroscopy as the absorbance maximum of the precursor solution is at 265 nm[51], while the formed intermediate is not showing a UV/vis absorbance, and due to the scattering of the NPs a substantial increase of absorbance is seen after particle formation, see Figure 5. The particle size of 1.3 ± 0.5 nm after exposure with 500 nm for 24 h is comparable to thermally formed NPs[44].

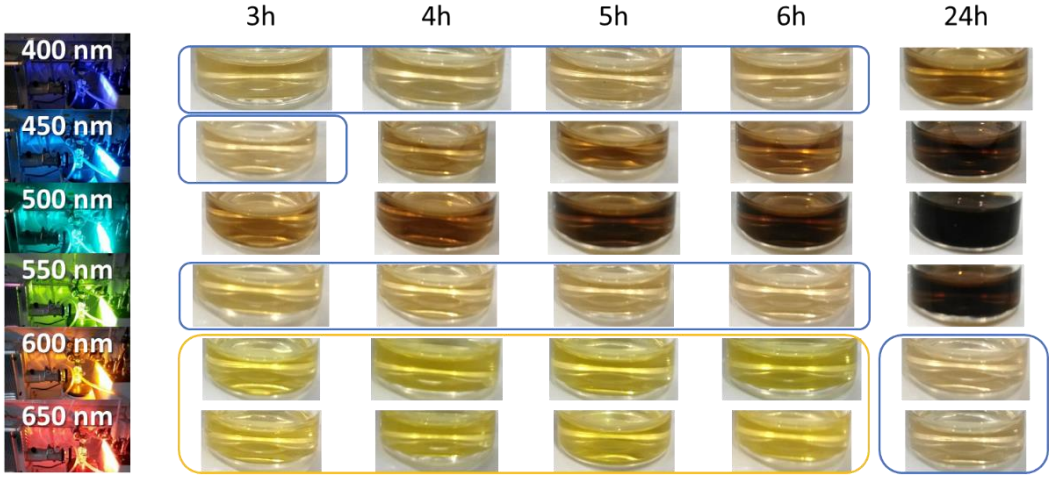

Figure 4. Photos of the reaction mixtures of H_2PtCl_6 in EG using an OH^-/Pt ratio of 24.4 after exposure with 400, 450, 500, 550, 600, and 650 nm for 3, 4, 5, 6, and 24 h. The yellow precursor solution (bordered in yellow) is reduced to a colorless intermediate (bordered in blue) before the brown NP dispersion is formed. Reprinted with permission from *J. Phys Chem. C* **2020**, *124 (39)*, 21798-21809. Copyright 2020 American Chemical Society.

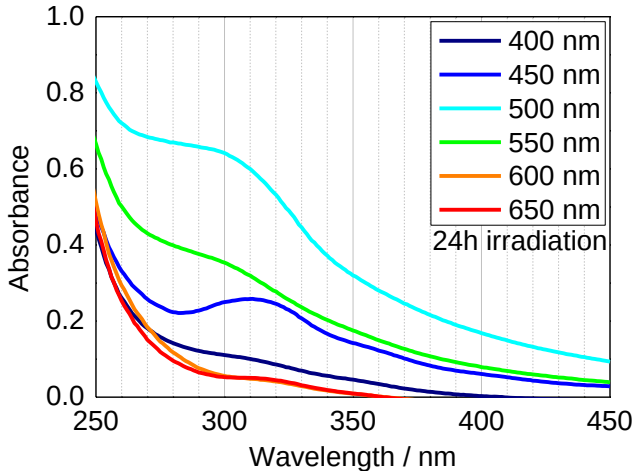

Figure 5. UV/vis spectra of the reaction mixtures of H_2PtCl_6 in EG and an OH^-/Pt ratio of 24.4 after exposure with 400, 450, 500, 550, 600, and 650 nm for 24 h. Reprinted with permission from *J. Phys Chem. C* **2020**, *124 (39)*, 21798-21809. Copyright 2020 American Chemical Society.

Visible-light-induced reduction of H_2PtBr_6 under varying wavelength

Reducing H_2PtBr_6 by visible light using wavelengths between 400 and 600 nm leads to stable

NP dispersions after 24 h. The maximum reduction rate is found again at a wavelength of 450 or 500 nm. Although the reduction rate in the visible light induced reduction of H_2PtBr_6 is increased as compared to the reduction of H_2PtCl_6, the particle sizes are comparable (between 1.4 ± 0.3 and 1.6 ± 0.4 nm as compared to 1.3 ± 0.5 nm for the reduction of H_2PtBr_6 as compared to H_2PtCl_6, respectively). Therefore, the particle formation is halide independent although the particle formation rate (the intermediate reduction) is precursor dependent. As discussed in chapter 2.1.3 the LaMer model is a kinetic model, hence if the particle formation is following the LaMer model, only kinetics determines the final particle size. According to the LaMer model, at a low reduction rate, as in the visible light induced synthesis, the monomer concentration is only slowly increasing. Thus, the consumption rate of the monomer due to nucleation should be higher as the monomer formation rate resulting in a rapid fall of the monomer concentration below the nucleation threshold. The LaMer model therefore predicts small particle for high reduction rates and large particle at a low reduction rate. However, despite different time scales (24 h in visible light induced reduction) the particle sizes are comparable to NPs prepared by a thermal (90 min)[44] or microwave based (3 min)[50] reduction. Hence, it seems that the LaMer model does not correctly describe the reduction mechanism for the polyol process.

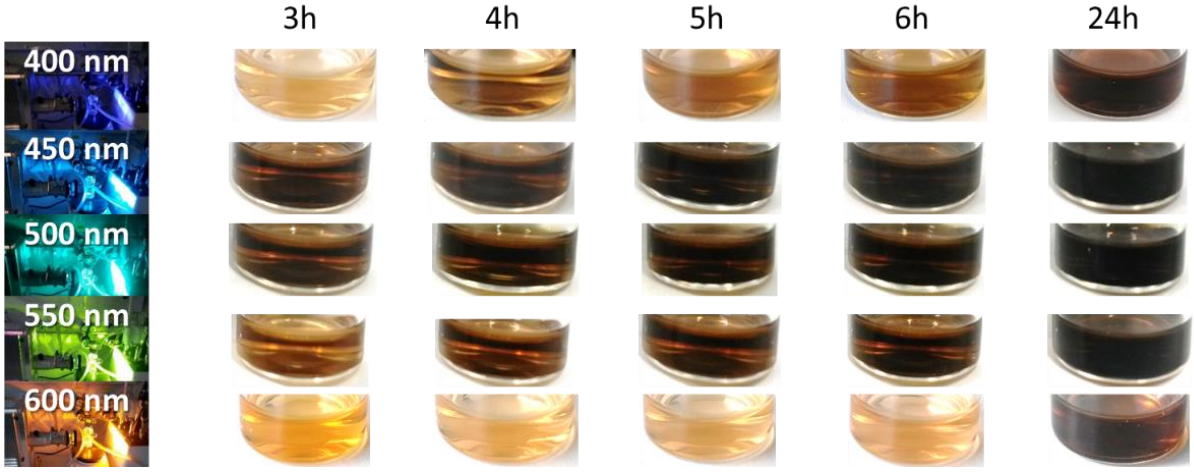

Figure 6. Photos of the reaction mixtures of H_2PtBr_6 in EG using an OH^-/Pt ratio of 24.4 after exposure with 400, 450, 500, 550, 600, and 650 nm for 3, 4, 5, 6, and 24 h. Reprinted with permission from *J. Phys Chem. C* **2020**, *124 (39)*, 21798-21809. Copyright 2020 American Chemical Society.

Visible-light-induced reduction of H_2PtCl_6 at different OH^-/Pt ratios

Additionally, the change of OH^-/Pt ratio in the reduction of H_2PtCl_6 influences the NP formation rate in visible light induced NP synthesis. Decreasing the OH^-/Pt ratio from 24.4 to 5.3 in the reduction of H_2PtCl_6 leads to a decrease of the reduction rate, see Figure 7. In previous investigations in the thermal reduction of H_2PtCl_6 no particle formation was observed below an OH^-/Pt ratio of six.[44] This ratio is necessary to neutralize the OH^- formed during the reaction. Therefore, the use of OH^-/Pt ratios above six led to the expected alkaline pH after the reduction resulting in stable particle for several weeks. At an OH^-/Pt ratio of 3.0 no NPs are formed, hence a certain amount of OH^- seems to be necessary to initiate the nucleation. However, at OH^-/Pt ratios of 4.6 and 5.3 stable particles are formed showing that the visible light induced reduction enables the NP formation at low OH^-/Pt ratios that are not accessible in thermal reduction.[44]

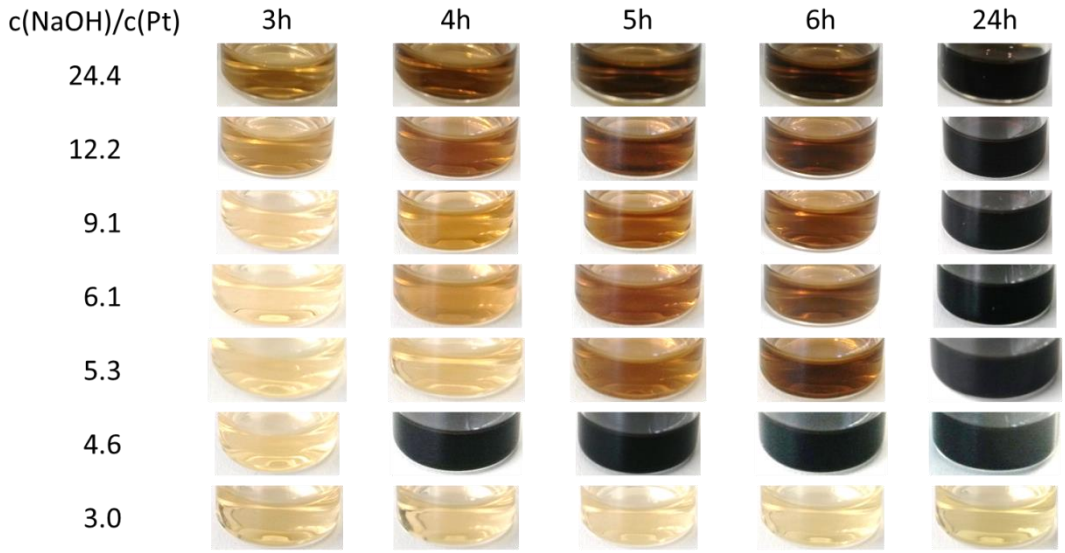

Figure 7. Photos of the reaction mixtures of H_2PtCl_6 in EG after exposure with 500 nm for 3, 4, 5, 6, and 24 h using OH^-/Pt ratios of 24.4, 12.2. 9.1, 6.1, 5.3, 4.6, and 3.0. Reprinted with permission from *J. Phys Chem. C* **2020**, *124 (39)*, 21798-21809. Copyright 2020 American Chemical Society.

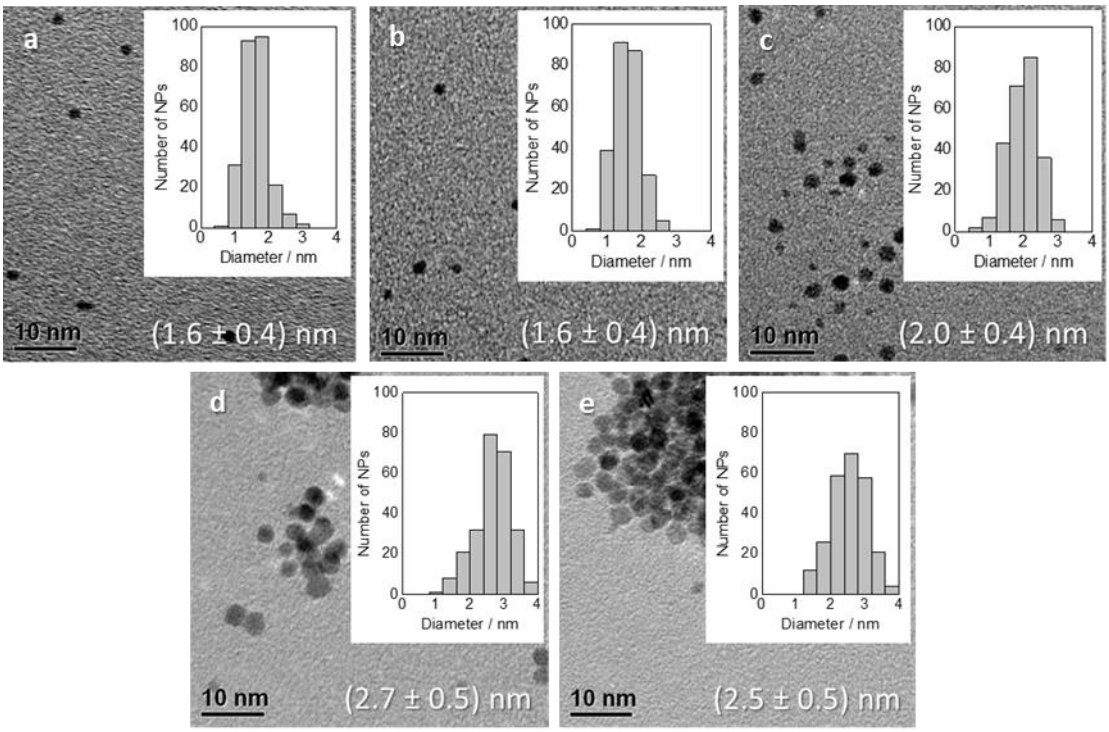

Figure 8. Representative TEM images, averaged NP sizes, and size distributions after exposure with 500 nm for 24 h using OH^-/Pt ratios of (a) 12.2, (b) 9.1, (c) 6.1, (d) 5.3, and (e) 4.6. The TEM images (d) and (e) show particle agglomeration. Reprinted with permission from *J. Phys Chem. C* **2020**, *124 (39)*, 21798-21809. Copyright 2020 American Chemical Society.

The visible light induced synthesis leads to a particle size increase from 1.3 ± 0.5 nm to 2.0 ± 0.4 nm decreasing the OH^-/Pt ratio from 24.4 to 6.1, see Figure 8. Interestingly, the same trend is observed in the thermal (oil bath[44] or microwave[50]) and UV light induced[49] reduction of H_2PtCl_6. The same size control despite different time scales indicates again that the LaMer model is not suitable to describe the polyol process.

Visible-light-induced reduction of H_2PtBr_6 at different OH^-/Pt ratios

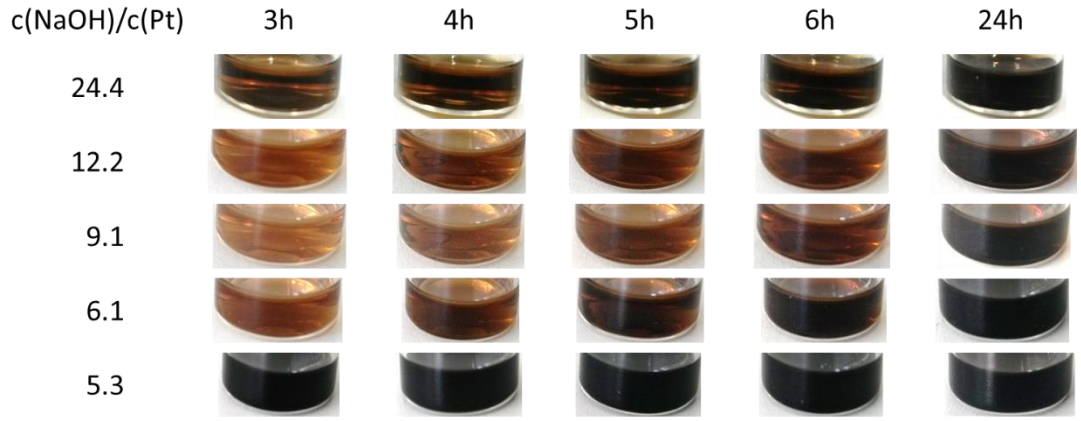

Figure 9. Photos of the reaction mixtures of H_2PtCl_6 in EG after exposure with 500 nm for 3, 4, 5, 6, and 24 h using OH^-/Pt ratios of 24.4, 12.2. 9.1, 6.1, and 5.3. Reprinted with permission from *J. Phys Chem. C* **2020**, *124 (39)*, 21798-21809. Copyright 2020 American Chemical Society.

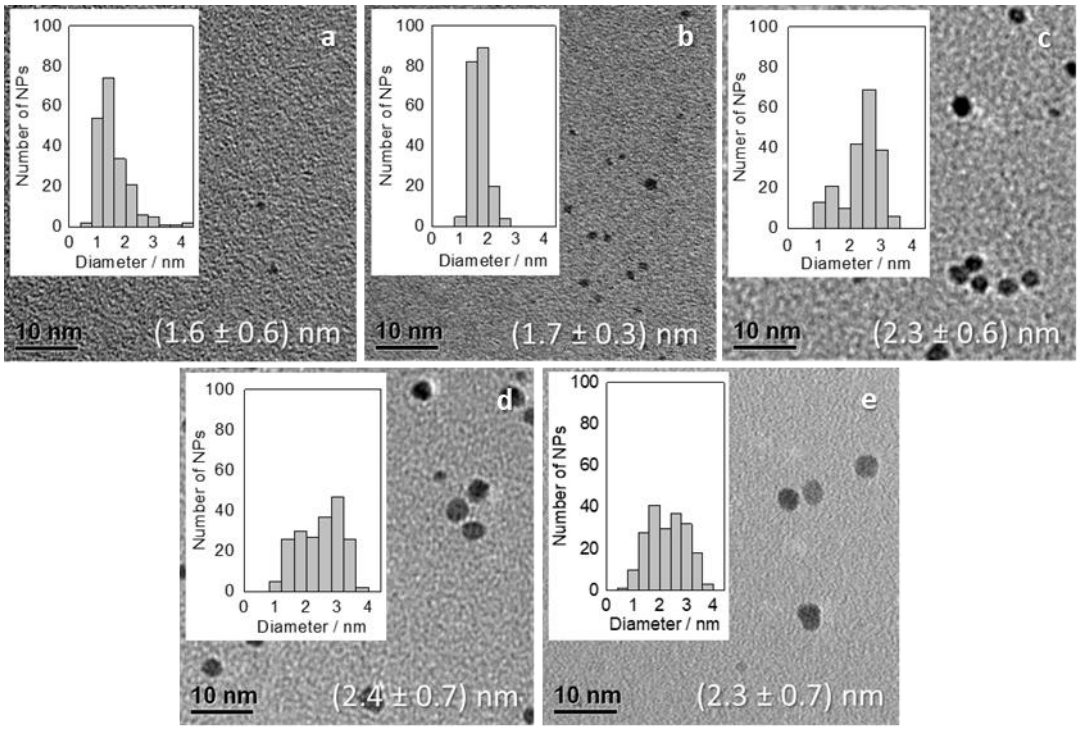

Figure 10. Representative TEM images, averaged NP sizes, and size distributions after exposure with 500 nm for 24 h using OH^-/Pt ratios of (a) 12.2, (b) 9.1, (c) 6.1, (d) 5.3, and (e) 5.3 after 3 h of irradiation. Reprinted with permission from *J. Phys Chem. C* **2020**, *124 (39)*, 21798-21809. Copyright 2020 American Chemical Society.

In the visible light induced reduction of H_2PtBr_6 the change of the OH^-/Pt ratio influences the NP formation rate as well. Decreasing the OH^-/Pt ratio from 24.4 to 6.1 shows again a decrease in the reduction rate, see Figure 9. The strongly increased formation rate is observed at the OH^-/Pt ratio of 5.3 as compared to the reduction of H_2PtCl_6. Interestingly, despite different formation rates of the reduction of H_2PtBr_6 as compared to H_2PtCl_6 in the visible-light-induced synthesis and different time scales as compared to a thermal or microwave-based reduction the decreased OH^- amount results in a comparable size control, see Figure 10.[50]

Proposed NP formation mechanism

This work supports the work of Quinson *et al.*[50] proposing that the particle size is determined by the ratio of OH^- to Pt surface atoms. However, the finding of this work that the particle size control is independent of the reduction rate, i.e., kinetics, cannot be explained by the LaMer model. Therefore, a new NP formation mechanism is proposed, see Figure 11. As no particles or not stable particles are formed without[49] or at very low NaOH concentrations[44], OH^- seems to play a crucial role.

(I) In a first step the halide ligands from the precursor are probably exchanged by OH^- forming halide hydroxy mixed platinum complexes. Not Ostwald ripening (this occurs at higher temperatures, i.e., 150 °C, after 17 h (a study I was involved in is cited)[54]) but other thermodynamic aspects depending on the hydroxide concentration determine the finial particle size. Already the first formed Pt^0 are supposed to be influenced by this dependency of OH^- to Pt surface atoms.

(II) It is assumed that the halide hydroxy platinum complex is reduced to form the monomers. It is shown in the time-dependent UV/vis spectra that at room temperature under exposure to visible light the intermediate is fast formed, while the complete reduction to NPs takes a long time. Additionally, the UV/vis absorption maximum of the intermediate in the reduction of H_2PtBr_6 is observable for a long time (6 h) (noted that the intermediate in the reduction of H_2PtCl_6 is not visible in UV/vis spectroscopy). As the formation step of the monomer is slow as compared to the intermediate, the monomer formation (fully reduced precursor) seems to be the kinetically relevant step and not the intermediate formation (partially formed precursor). Furthermore, the monomer formation seems to preferentially occur under light exposure with a wavelength of 500 nm.

(III) Freshly formed single Pt atoms try to bind further Pt atoms or ligands instead if no Pt is available. OH^- binds facile to Pt in alkaline solutions.[125] During the begin of the reduction a few monomers are expressed to a high OH^- concentration, hence enough OH^- is present to stabilize the monomers. Afterwards, the formed Pt monomers can according to the equilibrium reaction react back to the intermediate or coalesce with other Pt atoms stabilized by OH^- forming dimers, trimers, etc. The formation to Pt bulk is thermodynamically preferred to the oxidation forming the intermediate as Pt is a noble metal. Therefore, the monomers favorably form NPs which size is limited by the ratio of OH^- to Pt surface atoms. Although it was shown before that CO is additionally bonding to the Pt surface[44,50] it is not understood when this starts to happen. The strong CO band in FTIR spectroscopy above 2000 cm^{-2} known from the thermal reduction,[44] is not observable for the Pt NPs synthesized by visible light. The stabilization by CO seems hence only be happing at high temperatures.

Besides the size control due to OH^- the amount of OH^- is also stabilizing the NPs. As in the thermal reduction of H_2PtCl_6 at low OH^- concentrations no stable particles can be formed, CO alone does not seem to sufficiently stabilizes particles.[44] Bromide on the other hand seems to stabilize NPs additionally being in line with the stronger bonding of bromide to Pt as compared to chloride.[125] Therefore, the

proposed NP formation mechanism is not valid at low OH^- concentrations.

The unsuccessful seed-mediated growth experiments performed for this study, see chapter 2.1.3 for experimental details, are explainable within the proposed mechanism. At high OH^-/Pt ratios it is assumed that no seed growth but reduction of the precursor forming particles with a size determined by the amount of OH^- is occurring. At low enough OH^-/Pt ratios that should allow particle growth, the missing growing of the NPs is explainable by the lack of free OH^- in the reaction mixture. The OH^- added by the as-prepared NP dispersion is bond to the particles and hence not accessible to form the reactive intermediate. Consequently, based on the suggested reduction mechanism the reaction is stopped and again no particle size increase is observed.

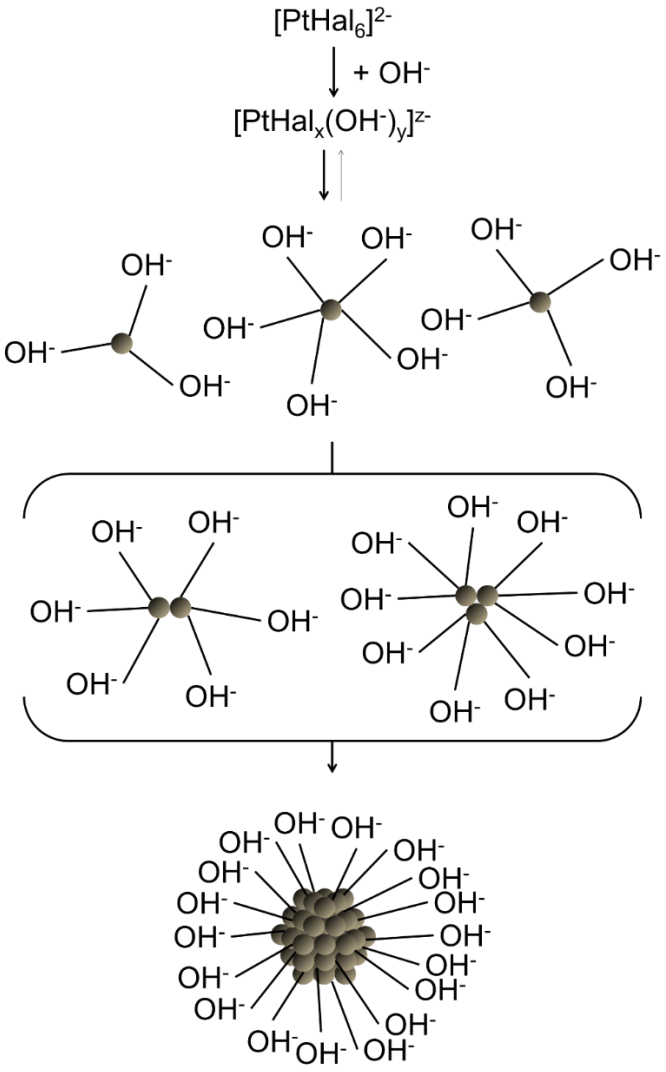

Figure 11. Proposed NP formation mechanism by (I) forming an intermediate by a partial substitution of the halides by hydroxide ions, (II) further reduction to Pt^0 atoms stabilized by hydroxide, and (III) dimer and trimer formation of Pt^0 leading to the final NPs with a size determined by the ratio of hydroxide to Pt surface atoms. Reprinted with permission from *J. Phys Chem. C* **2020**, *124 (39)*, 21798-21809. Copyright 2020 American Chemical Society.

3.2. Manuscript II:

The results shown in this chapter are excerpts from the publication

J. Schröder, S. Neumann, J. Quinson, M. Arenz, S. Kunz

Anion Dependent Particle Size Control of Platinum Nanoparticles Synthesized in Ethylene Glycol

Nanomaterials, **2021**, *11*, 2092.

https://doi.org/10.3390/nano11082092 (Open Access)

Description

The versatile polyol approach enables the synthesis of "surfactant-free" Pt NPs to prepare tailored[53,122,124] CO oxidation (I was involved in one of the cited studies, that I frequently refer to in the discussion of manuscript II)[54,55] or fuel cell[50,56] catalysts. While the metal salt (i.e., precursor, as H_2PtCl_6) is reduced in presence of a base (e.g., NaOH) the solvent EG oxidates forming glycolaldehyde, glycol acid, oxalaldehyde, and oxalic acid or two CO molecules that adsorb to the Pt NP surface.[44,52] The protons formed during the reduction are neutralized by OH^- forming water.[49] The importance of OH^- stabilizing and determining the NP size in the reduction of the precursor H_2PtCl_6 in EG was shown by Schrader *et al.*[44] and Quinson *et al.*[50]. Additionally, it is shown in literature that the Li^+, Na^+, K^+, or Cs^+ cations in the hydroxide base do not affect the size or stability of the particles in EG.[58] However, the thermal reduction of H_2PtCl_6 or H_2PtBr_6 for a time period of 17 h (NaOH as base, 150 °C) leads to an increase in particle size due to halide induced leaching and subsequent Ostwald ripening. The size of the NPs synthesized from the halide-free precursor $Pt(acac)_2$ ($acac^-$ is the abbreviation of the acetylacetonate anion) remains constant during the same period.[54] The higher leaching ability of bromide as compared to chloride leads to a larger particle size in the thermal reduction of H_2PtBr_6, but the halide-free $Pt(acac)_2$ results in particles with a size of 3 nm.[54] In manuscript I, see chapter 3.1, the reduction of H_2PtCl_6 or H_2PtBr_6 in the visible light induced reduction at room temperature in presence of NaOH, where Ostwald ripening is excluded, a comparable size control depending on the OH^-/Pt ratio is observed that was used for mechanistic investigations of the polyol approach. Both results together can be seen as an indication for particle size control by the base anion in the polyol method. The NP size control in the reduction of the precursors H_2PtCl_6[44,50] (and Manuscript I) or $Pt(acac)_2$[54] in presence of NaOH was studied before. As compared to those results the reduction of the precursors H_2PtCl_6 or $Pt(acac)_2$ in presence of different amounts of the base Na(acac) is investigated in the presently discussed manuscript. Furthermore, another halide-free precursor $H_2Pt(OH)_6$ is reduced in presence of different amounts of the bases NaOH or Na(acac).

Contribution to the Work

I designed the experiments together with S. Kunz. S. Neumann and J. Quinson took TEM images that I analyzed. S. Kunz and M. Arenz supervised the research. S. Kunz and I wrote the first draft of the manuscript, that was read, and commented by all authors.

Most Important Findings

Thermal reduction in presence of NaOH

The size control by OH^- was so far studied in the presence of varying cations[58] or halides.[54] Therefore, in the discussed manuscript the reduction of the halide free precursor $H_2Pt(OH)_6$ is investigated in presence of varying amounts of OH^- to see if the size is again controlled by the OH^-/Pt ratio. Unfortunately, the dissolution and reduction steps of $H_2Pt(OH)_6$ cannot be separated as the turbid reaction mixture changed in color from white to yellow and further to brown before obtaining the brown NP dispersion. Nevertheless, it is tried to use a comparable protocol as in the thermal reduction of H_2PtCl_6 and H_2PtBr_6 by stirring $H_2Pt(OH)_6$ in presence of NaOH

in EG in a preheated oil bath at 150 °C. The amount of OH^- is thereby considered in the calculation of the to be added amount of NaOH to generate the wanted OH^-/Pt ratios. Using an OH^-/Pt ratio of 48.8 does not lead to a stable NP dispersion as observed before in the thermal reduction of H_2PtCl_6.[44] Reducing $H_2Pt(OH)_6$ thermally the OH^-/Pt ratio of 24.4 shows after 25-90 min of heating at 150 °C a few flocculated NPs while the majority remains stable after three days of storage. In contrast the NPs using OH^-/Pt ratios of 12.2 (10-90 min of heating), 9.2 and 7.6 (5-90 min of heating) remain stable during storing. While in the thermal reduction of H_2PtCl_6 the particle formation, i.e., the color change to dark brown, is independent of the OH^-/Pt ratio observed after ca. 3 min,[44,50] it occurs faster the lower the OH^-/Pt ratio in the reduction of $H_2Pt(OH)_6$, e.g., after ca. 25 min or ca. 1 min at an OH^-/Pt ratio of 24.4 or 7.6, respectively. The different reduction behavior might indicate that in the absence of halides an alternative mechanism to the one proposed in manuscript I for the polyol approach. After a short heating period of 5-10 min narrow size distributions with a constant averaged particle size between 1.2 ± 0.4 or 1.4 ± 0.3 nm for the OH^-/Pt ratios between 12.2 and 7.6 are obtained, see Figure 12.

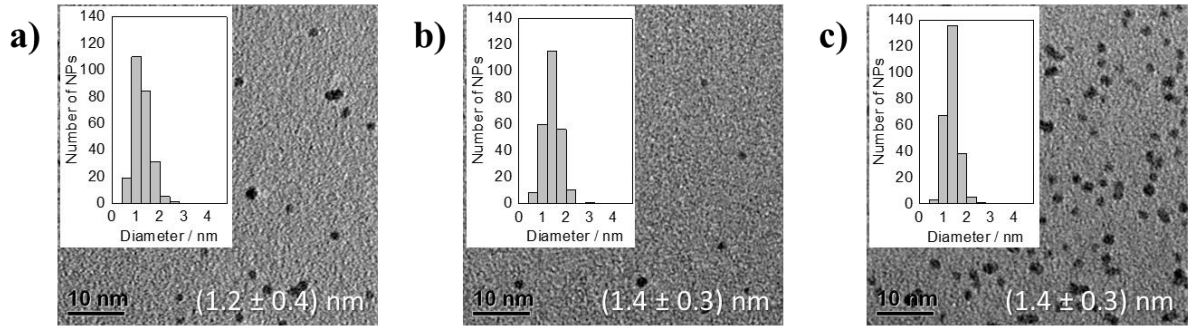

Figure 12. TEM images, particle size distributions, and averaged sizes with standard deviations of the thermally formed Pt NPs in the reduction of $H_2Pt(OH)_6$ in presence of varying OH^-/Pt ratios of a) 12.2 (10 min of heating at 150 °C), b) 9.2 (5 min), and c) 7.6 (5 min). Reprinted with permission from *Nanomaterials*, **2021**, *11*, 2092.

Continuing heating the reaction mixtures for 90 min in total leads to an increase in particle size and quite large size distributions, see Figure 13. The particle size of 1.6 ± 0.4 nm observed at an OH^-/Pt ratio of 24.4 is comparable to size results reported before (also in manuscript I) in other polyol syntheses at the same OH^-/Pt ratio.[44,50,54,58] Decreasing the OH^-/Pt ratio to 12.2 results in a NP size of 2.0 ± 0.7 nm being larger as compared to 1.4 ± 0.3 nm (OH^-/Pt ratio of 12.5) described for the reduction of H_2PtCl_6 by Quinson *et al.*[50] Below an OH^-/Pt ratio of 9.2 a constant particle size of around 2.5 is reached, while in the chloride containing system particle sizes of 2.1 ± 0.6 and 2.5 ± 0.3 for OH^-/Pt ratios of 10 and 6.3 are observed, respectively.[50] The larger standard deviations of the size distributions and the slightly different particle size results might be explainable by the absence of chloride leading to a reduced amount of leached Pt species[54] or the missing separation of the dissolving and reducing steps of $H_2Pt(OH)_6$.

To sum up, in the thermal reduction of $H_2Pt(OH)_6$ in presence of NaOH a size control depending on the OH^-/Pt ratios can be reached that is slightly differing as compared to the before described[44,50,54,58] chloride containing system. The change of the precursor anion from chloride to OH^- is hence only little influencing the size. In contrast, the use of $acac^-$ as precursor anion, i.e., the precursor $Pt(acac)_2$, is according to Neumann *et al.*[54] substantially increasing the particle size to ca. 3 nm. The comparison of the NP size results observed in the reduction of the three

different precursors H_2PtCl_6, $H_2Pt(OH)_6$, and $Pt(acac)_2$ in presence of NaOH might be an indication that the reduction process is influenced by the precursor anion.

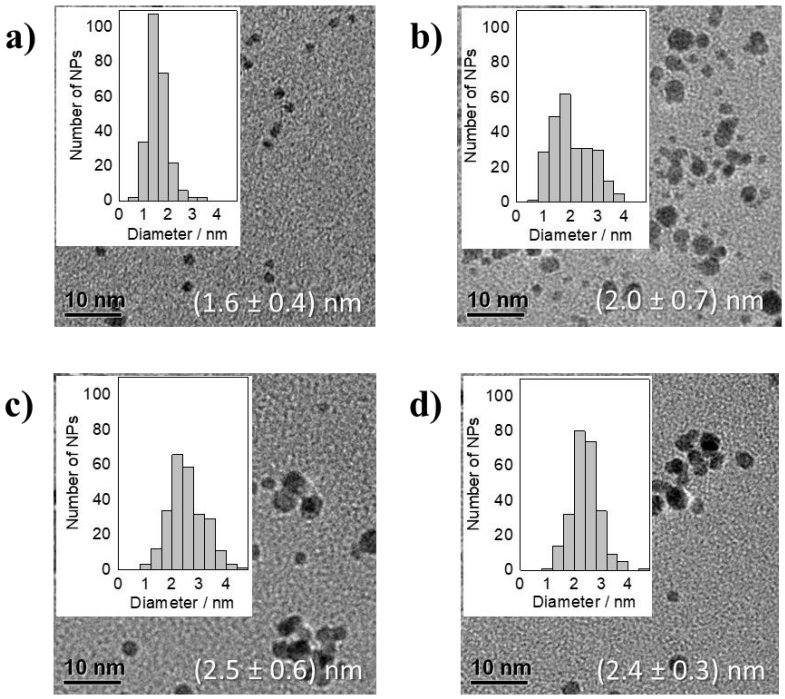

Figure 13. TEM images, particle size distributions, and averaged sizes with standard deviations of the thermally formed Pt NPs in the reduction of $H_2Pt(OH)_6$ in presence of varying OH^-/Pt ratios of a) 24.4, b) 12.2, c) 9.2, and d) 7.6 after 90 min of heating at 150 °C in total. Reprinted with permission from *Nanomaterials*, **2021**, *11*, 2092.

Thermal reduction in presence of Na(acac)

The anion $acac^-$ in the precursor $Pt(acac)_2$, that is an organic anion and substantial larger as compared to OH^- or chloride, results in larger particle sizes of ca. 3 nm as describe before.[54] Based on the different character of the anion it could be assumed that the presence of the anion $acac^-$ leads to the size increase. Therefore, in the second part of the manuscript the thermal reduction of the three precursors H_2PtCl_6, $H_2Pt(OH)_6$, and $Pt(acac)_2$ in presence of Na(acac) as base (instead of NaOH) is investigated. The question is if the amount of the base anion $acac^-$ leads to comparable trends in particle size depending on the precursor anion as observed for OH^- or if comparable large NPs are obtained as observe in the reduction of $Pt(acac)_2$ in presence of NaOH due to the presence of $acac^-$.

The thermal reduction of H_2PtCl_6 in presence of Na(acac) is substantially faster (ca. 1 min) as compared to NaOH (ca. 3 min[44,50]) and after more than 20 min of synthesis time sintering and flocculation of the particles are observed. Based on these different observations it seems that the stabilization role of OH^- cannot be taken over by $acac^-$ and chloride. Based on that, the assumption could be that the NPs are less protected against a chloride attack leading to Ostwald ripening and hence larger particles as compared to the reaction mixture in presence of NaOH. However, after 10 min of reduction for $acac^-$/Pt ratios between 5.4-48.8 stable particles with a size between 1.4-1.9 nm are obtained, see Figure 14, while after longer reduction periods the NPs are sintering. Using $acac^-$/Pt ratios below 5.4 result in sintered NPs already during the synthesis, while the high $acac^-$/Pt ratio of 48.8 leads to particles that are stable for several days.

Although, in the reduction of H_2PtCl_6 the presence of Na(acac) as compared to NaOH is influencing the rate and the stability, a comparable particle size without Ostwald ripening is seen in presence of the base Na(acac) as compared to reduction when NaOH is present. This could be explained by a possible chloride induced leaching without the following Ostwald ripening that was described after long heating periods by Neumann *et al.*[54]

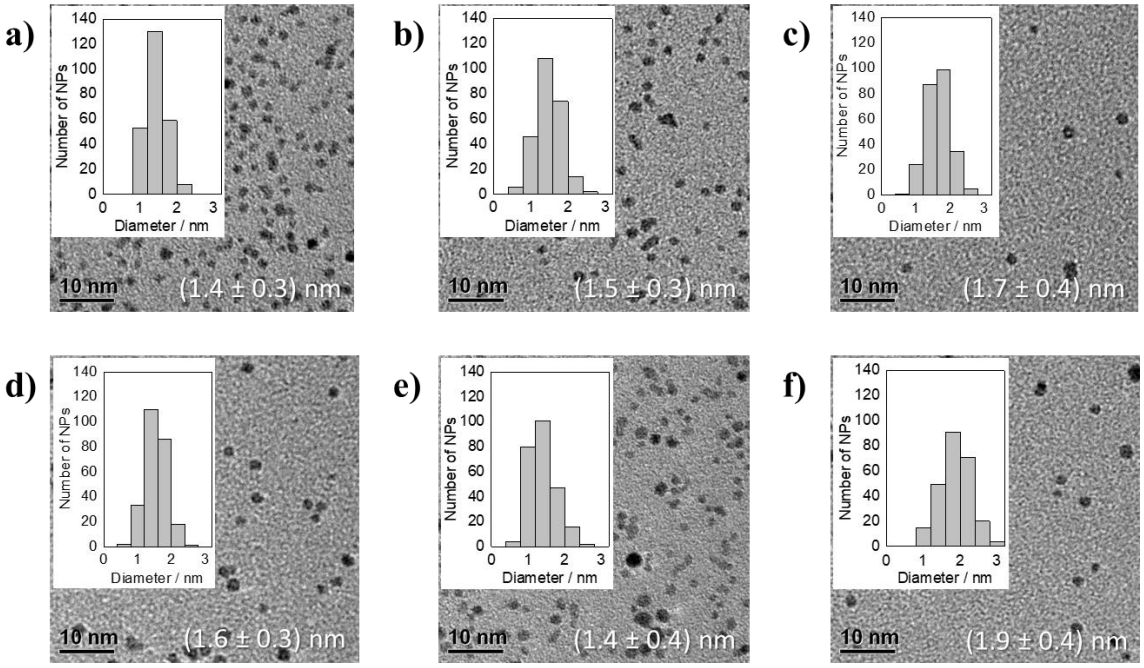

Figure 14. TEM images, particle size distributions, and averaged sizes with standard deviations of the thermally formed Pt NPs in the reduction of H_2PtCl_6 in presence of varying $acac^-$/Pt ratios of a) 48.8, b) 24.4, c) 12.2, d) 9.2, e) 6.1, and f) 5.4 after 10 min of heating at 150 °C. Reprinted with permission from *Nanomaterials*, **2021**, *11*, 2092.

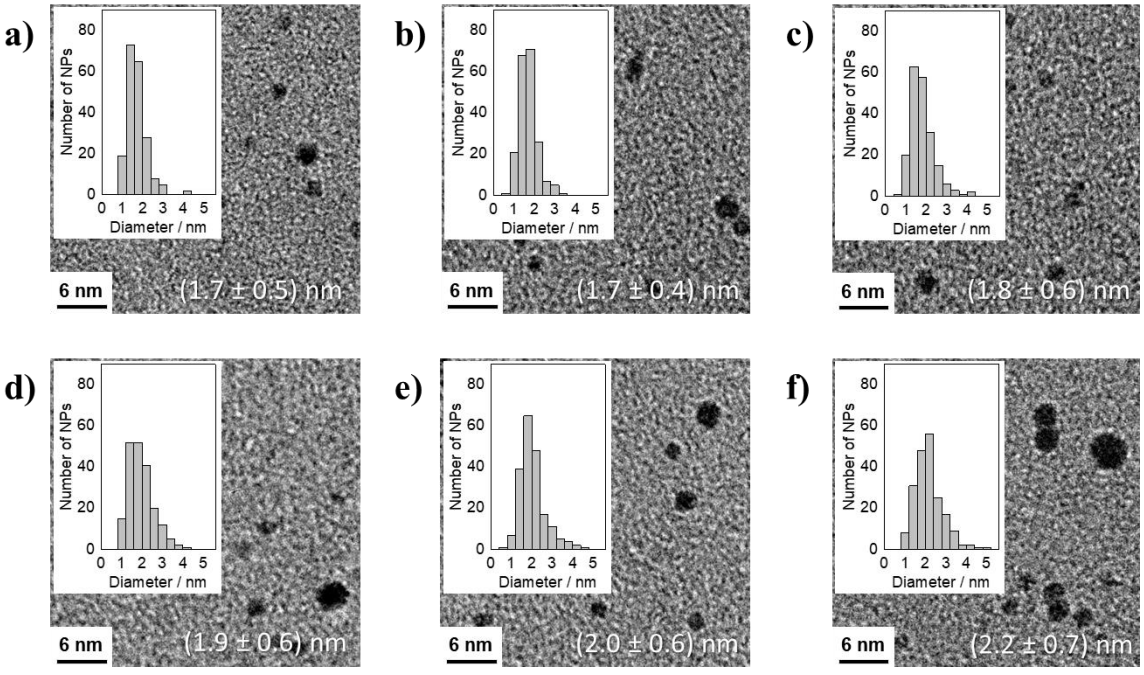

Figure 15. TEM images, particle size distributions, and averaged sizes with standard deviations of the thermally formed Pt NPs in the reduction of $H_2Pt(OH)_6$ in presence of varying $acac^-$/Pt ratios of a) 48.8, b) 24.4, c) 12.2, d) 9.2, e) 6.1, and f) 4.6 after 90 min of heating at 150 °C. Reprinted with permission from *Nanomaterials*, **2021**, *11*, 2092.

The thermal reduction of $H_2Pt(OH)_6$ in presence of Na(acac) results in stable NPs after 90 min using $acac^-$/Pt ratios between 4.6 and 48.8. At high $acac^-$/Pt ratios of 48.8 and 24.4 a constant particle size of 1.7 ± 0.5 and 1.7 ± 0.4 nm is obtained, see Figure 15. The decrease of the $acac^-$/Pt ratio to 4.6 leads to a size increase to 2.2 ± 0.7 nm. This size increase is comparable to the results observed in the first part of the manuscript in the reduction of $H_2Pt(OH)_6$ in presence of NaOH. There might be a slight trend reaching smaller particles at a certain $acac^-$/Pt ratio as compared to the same OH^-/Pt ratio. The same amount of OH^- is used by changing the $acac^-$/Pt ratio, hence the slightly smaller particles could be explained by the "ligand" interaction of $acac^-$ and OH^- that are stabilizing the particle surface.

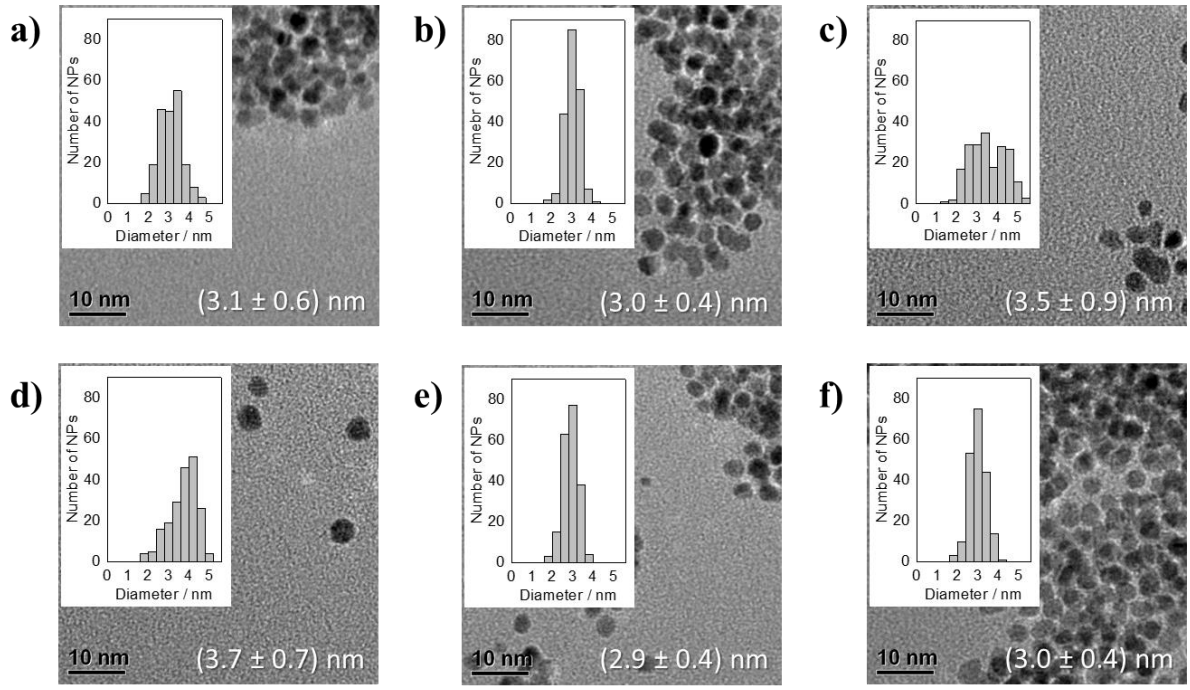

Figure 16. TEM images, particle size distributions, and averaged sizes with standard deviations of the thermally formed Pt NPs in the reduction of $Pt(acac)_2$ in presence of varying $acac^-$/Pt ratios of a) 24.4, b) 12.2, c) 9.1, d) 6.1, e) 5.4, and f) 4.6 after 150 min of heating at 150 °C. Reprinted with permission from *Nanomaterials*, **2021**, *11*, 2092.

The thermal reduction of $Pt(acac)_2$ in the presence of Na(acac) results in NPs that remain stable for several hours, although particle agglomeration is seen on the TEM images, see Figure 16. Most of the samples show after a day of storage yellow to light brown solids precipitated on the wall and bottom of the glass vials that is without further characterization assumed to contain organic compounds as $acac^-$ that are insoluble in EG at room temperature. While at an $acac^-$/Pt ratio of 48.9 no stable particles can be obtained, in the range between $acac^-$/Pt ratios of 24.4 and 4.6 the NP size is found to be between 2.9 ± 0.4 and 3.7 ± 0.7 nm (at $acac^-$/Pt ratios of 5.4 and 6.1, respectively). To reach particle sizes above 3 nm in the reduction of H_2PtCl_6 in presence of NaOH Quinson *et al.*[50] show that substantial reduced OH^-/Pt ratios of 5.5 or lower are necessary leading to agglomeration on the TEM grid. This difference might be originated in the larger size of $acac^-$ as compared to OH^- as less $acac^-$ anions are located on the surface of the Pt particles due to their sterically hindering. Therefore, the particle surface is even at high $acac^-$ concentrations fast saturated with substantial less anions leading to less negative charge situated on the particle surface that reduces the Coulomb repulsion between the particles and hence increase the probability of agglomeration.

The large particle sizes generated by reducing $Pt(acac)_2$ in presence of Na(acac) are in agreement with 3.0 ± 0.3 nm reported by Neumann *et al.*[54] for the reduction of $Pt(acac)_2$ in presence of NaOH as base. Therefore, the large particle sizes are obtained independent of the amount of the base anion and only due to the use of the precursor $Pt(acac)_2$. Comparing the results of the six before discussed combinations of the precursors H_2PtCl_6, $H_2Pt(OH)_6$, and $Pt(acac)_2$ in presence of the bases NaOH or Na(acac), the particle sizes seem to be controlled by the character of the precursor while the base anion seem to be less important. The character of the precursor is expected to be only at the beginning of the NP formation process important, so the size control by the precursor could be explained as follows. The reduction rate is influenced by the Pt salt, i.e., the required time for a "ligand" exchange with the base anion or the Pt reduction. The rate of the "ligand" exchange is determined by the anion equilibrium and the binding strength of the anions (OH^-, $acac^-$, or chloride) to the Pt surface. Because of the expected location of the anions on or binding to the surface the bond properties of the anions are important in the continuing reduction and growth process. The experimental observations are that smaller NPs are obtained when smaller anions (i.e., OH^-) are present while larger particles arise from less small or large anions (i.e., OH^- or $acac^-$, respectively). When larger ligands are used, less of them can be located at or bond to the Pt surface. Therefore, even at high anion concentrations of the sterically demanding $acac^-$ ligands their availability to stabilize the NPs is reduced due to less present charge on the surface resulting in larger particles. The same large particles are obtained independent of the amount of NaOH or Na(acac) in the reduction of $Pt(acac)_2$, hence $acac^-$ (from the precursor) seem to bind strongly to the Pt and determines the particle size independent of the present anions. Consequently, not the bonding length but the shielding of the $acac^-$ seem to be the size determining step by reducing the amount of bound $acac^-$ to the Pt surface or preventing a ligand exchange by OH^- in the presence of the base NaOH.

3.3. Manuscript III:

The results shown in this chapter are excerpts from the publication

J. Schröder, J. Quinson, J. K. Mathiesen, J. J. K. Kirkensgaard, S. Alinejad, V. A. Mints, K. M. Ø. Jensen, M. Arenz

A new Approach to Probe the Degradation of Fuel Cell Catalysts under Realistic Conditions: Combining Tests in a Gas Diffusion Electrode Setup with Small Angle X-Ray Scattering

J. Electrochem. Soc., **2020**, *167*, 134515.

https: doi.org/10.1149/1945-7111/abbdd2

https://doi.org/10.26434/chemrxiv.12263804.v2 (Open Access Preprint)

Description

As a promising alternative to replace combustion engines in vehicles, PEMFCs using Pt alloys[126,127] as catalysts, e.g., PtCo in the Mirai automobile from Toyota,[1] supported on high surface carbon, are developed.[33,128] The research was focusing for a long time on the development of highly active fuel cell catalysts[129] but stability is equally important.[32,33] Thereby, it is desired to perform stability tests under realistic conditions that are based on statistical statements. The catalyst use under realistic conditions and the acceleration of the degradation is simulated by performing ASTs (a study I was involved in is cited that I frequently refer to in the discussion of manuscript III),[28,130] e.g., following protocols recommended by the Fuel Cell Commercialization Conference of Japan (FCCJ).[83,84] Such AST measurements are usually done in classical RDE setups[131] or in MEAs.[132] Although a fast screening is possible in RDE measurements, unrealistic conditions as liquid electrolyte are applied. Due to small catalyst amounts in RDE measurements many repeats are necessary to obtain enough material for a SAXS analysis. MEAs on the other hand are used under realistic conditions but substantially more advanced equipment is required. Furthermore, the time consuming MEA testing is rarely performed with several repeats of a sample nor different catalysts are compared. A new approach to combine the advantages of both cell types for stability tests under realistic conditions is a GDE setup.[27,28] Alinejad *et al.*[28] investigated the loss in surface area depending on the AST protocol in a GDE setup and the catalyst, i.e., 2-3 nm and 4-5 nm Pt/C.

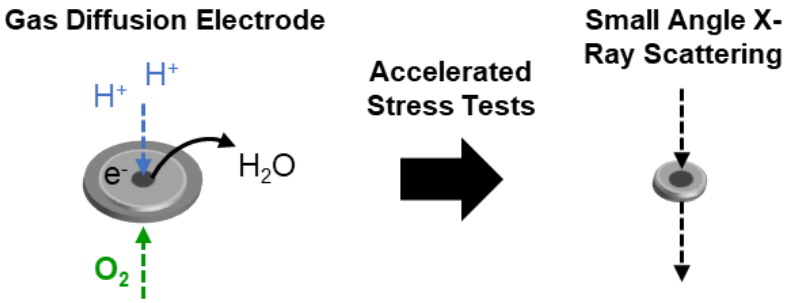

Figure 17. Scheme describing the structure of the used GDE setup where the O_2 is passing the GDL, reaching the Pt catalyst, and reacting with the protons from the $HClO_4$ electrolyte that are passing the Nafion® membrane and the electrons to water (left side) and the performance of *ex situ* SAXS on the cutouts of the GDE consisting of the catalyst layer and the Nafion® membrane (right side) after the performed accelerated stress tests.

In the following discussed manuscript the GDE approach presented before[27,28] is combined with the analysis of the particle size by SAXS before and after the AST, see Figure 17. Load-cycle conditions, i.e., steps between 0.6 and 1.0 V_{RHE}, as described in chapter 2.2.2 are applied. Three different commercial Tanaka Pt/C catalysts that are often used as benchmark catalysts in RDE studies[133] are investigated, i.e., 1-2 nm, 2-3 nm, and 4-5 nm Pt/C. The suitability of the GDE setup for AST studies was shown before using loadings comparable to RDE measurements but fare from realistic loadings in fuel cells.[28] The use of vacuum filtration, see chapter 2.2.1, enables the repeat of several measurements with equal catalyst film quality and realistic fuel cell loadings in contrast to RDE measurements. Comparing the loss of ECSA obtained in electrochemical measurements, see chapter 2.3.1, and the changes of particle size via SAXS enables conclusions about the degradation mechanism depending on the operation temperature. Additionally, due to the investigation of the PEMWE half-cell reaction in the GDE setup, the SAXS analysis is possible without further disassembling of the GDE, i.e., the Nafion® membrane does

not need to be removed while MEAs do not allow a simple separation of the catalyst films of anode and cathode. Therefore, this manuscript demonstrates the GDE setup as a straightforward and fast testing device under realistic conditions enabling mechanistic insights by the coupling to SAXS, see Figure 17.

Contribution to the Work

M. Arenz and I designed the electrochemical experiments, which were prepared and performed by me. I prepared the samples for SAXS measurements and participated in the SAXS data analysis. J. Quinson performed the TEM and SAXS measurements and analysis. J. J. K. Kirkensgaard supervised the SAXS data acquisition and analysis. S. Alinejad gave advice for the GDE preparation, provided surface area data for low loading GDE and participated in the discussion of the GDE results. V. Mints gave advice for the vacuum filtration and the GDE preparation. J. Quinson and J. K. Mathiesen collected the X-ray total scattering data which were analyzed by J. K. Mathiesen. M. Arenz and K. M. Ø. Jensen supervised the research. M. Arenz and I wrote the first draft of the manuscript, which was read and commented by all authors.

Most Important Findings

The ECSA determined from the CO stripping curves before and after the AST are compared, see Figure 18. Before AST the smaller NPs are leading as expected to higher ECSAs of 109 ± 4, 81 ± 1, and 57 ± 1 for the 1-2 nm, 2-3 nm, and 4-5 nm Pt/C catalysts at 25 °C, respectively, see Table 1. The ECSA is comparable to results obtained by RDE measurements[133] confirming a full utilization of the catalyst layer. At 50 °C as compared to 25 °C the CO stripping peak potential is shifting to lower potentials, see Figure 18, and the ECSA is slightly reduced, see Table 1. This is expected due to the reduced CO equilibrium coverage and the facilitated CO oxidation at higher temperature.[134] The catalyst with small NPs has not only a higher ECSA before the AST but additionally experiences a higher surface loss by the AST of 43 ± 1 and 34 ± 1 % for 4-5 nm and 2-3 nm Pt/C as compared to 4 ± 1 % of 1-2 nm Pt/C at 25 °C. Increasing the temperature to 50 °C leads to higher surface loss, although the number of potential steps during the AST is reduced from 9000 to 5000. Interestingly, the 4-5 nm Pt/C is rather stable, i.e., a surface loss below 5 % at 25 °C and at 50 °C the surface loss is increased but still substantially less as observed for the two other catalysts with smaller particle size.

Comparing the surface loss at 25 °C to data generated by Alinejad *et al.*[28] in a GDL setup using lower loadings typical for RDE studies,[77] i.e., ca. 8 vs 200 µg cm^{-2}_{geo}, showed interestingly substantial higher ECSA losses: 48 ± 2 and 18 ± 1 % at lower loading for the 2-3 nm and 4-5 Pt/C catalysts, respectively, as compared to 34 ± 1 and 4 ± 1 % in this study. Such a degradation depending on the catalyst film thickness was observed before in SFC measurements coupled to ICP-MS.[135,136] The change in Pt dissolution depending on the catalyst layer thickness was explained by varying redeposition probabilities of the Pt ions.[135] This catalyst loading dependent surface loss, although an equal trend between the different catalysts is observed, is pointing out the importance of ASTs under realistic conditions.

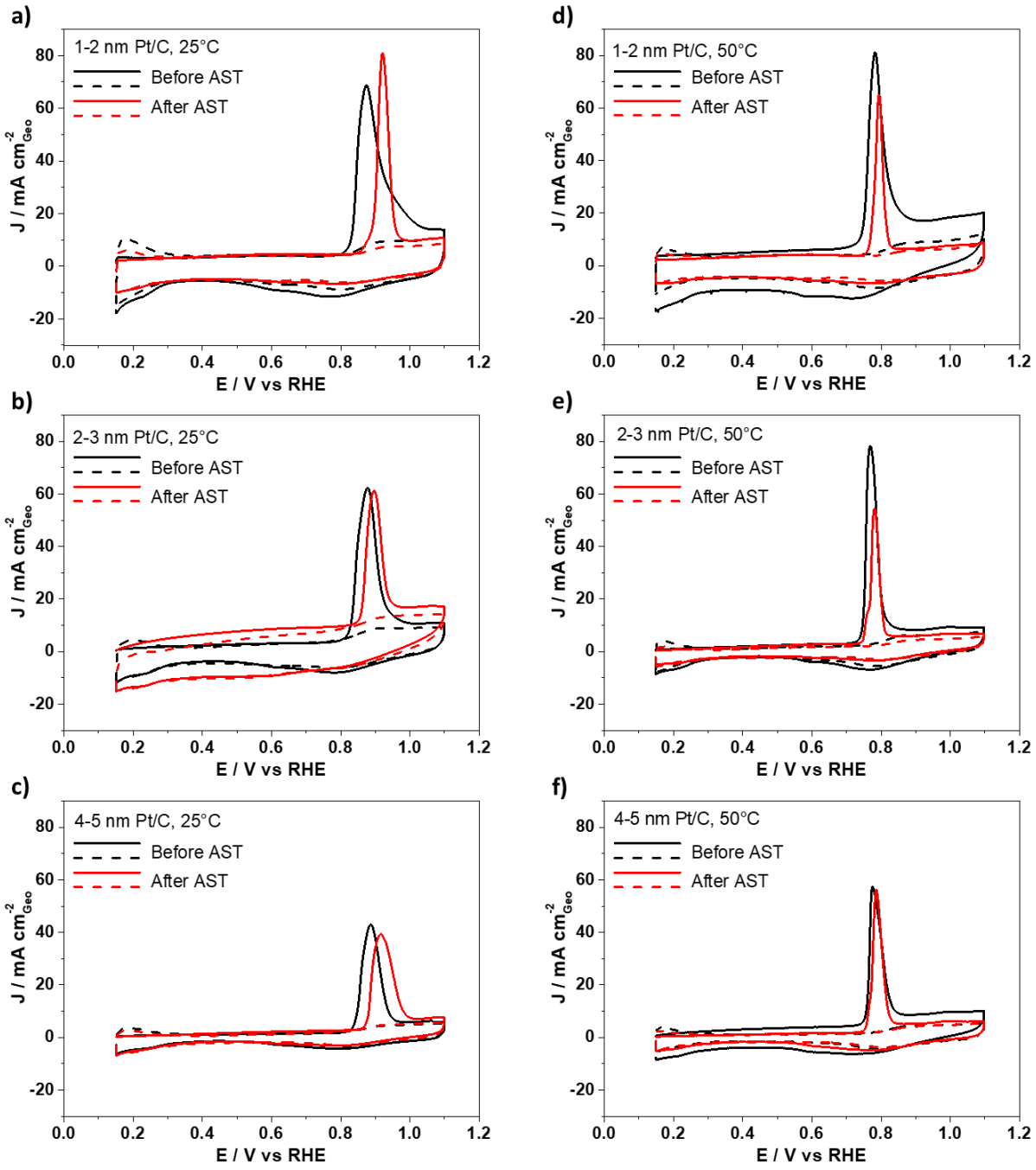

Figure 18. Representative CO stripping curves (solid lines) and Ar backgrounds (dashed lines) before (black lines) and after the AST (red lines) applying potential steps between 0.6 and 1.0 V_{RHE} (2 s holding per potential) at 25 °C ((a)-(c), 9000 steps) and 50 °C ((a)-(c), 5000 steps).

The electrochemical characterization of the ECSA is combined with *ex situ* SAXS data analysis to investigate the particle size changes after the ASTs. Figure 19 shows representative probability densities obtained by SAXS. The particles size described in the following is the average particle diameter (calculated from the mean particle sizes of three repeated measurements) and the error is the standard deviations relative to this average particle size. It is important to notice that unlike size histograms generated from TEM, small changes in the SAXS fitting parameters, based on the fitting model used in this study, result in relatively large deviations in the log-normal distributions. This can be mistaken as large size deviations between repeating

measurements despite comparable average particle sizes. The applied AST protocol at 25 and 50 °C leads to consistent repeated measurements of comparable average diameters and deviations with only one exception for a repeat of the 2-3 nm Pt/C catalyst at 50 °C.

Table 1. ECSA determined from the CO stripping curves before and after the AST (9000 or 5000 steps between 0.6 and 1.0 V_{RHE} at 25 or 50 °C, respectively, in oxygen) and ECSA loss with the standard deviations of three reproducible repeats.

T / ° C	Pt/C Catalysts	ECSA / $m^2\ g^{-1}_{Pt}$		Surface loss / %
		Before AST	After AST	
25	1-2 nm	109 ± 4	62 ± 3	43 ± 1
	2-3 nm	81 ± 1	54 ± 1	34 ± 1
	4-5 nm	57 ± 1	55 ± 1	4 ± 1
50	1-2 nm	90 ± 2	43 ± 2	53 ± 1
	2-3 nm	67 ± 4	35 ± 3	48 ± 2
	4-5 nm	50 ± 2	42 ± 1	16 ± 1

Applying the AST protocol leads to an increase in average diameter as expected from the CO stripping results showing a loss of ECSA. The most substantial size increase from 2.08 ± 0.04 to 4.86 ± 0.43 (AST in O_2 at 25 °C) and to 6.06 ± 0.54 nm (AST in O_2 at 50 °C) is observed for the 1-2 nm Pt/C catalyst. The 2-3 nm Pt/C catalyst shows an increase from 2.97 ± 0.09 to 5.24 ± 0.02 (25 °C) and to 5.58 ± 1.67 nm (50 °C) while for the 4-5 nm Pt/C catalyst the increase is only moderate from 5.88 ± 0.13 to 6.25 ± 0.47 (25 °C) and to 6.63 ± 0.03 nm (50 °C). As expected, the most dramatic degradation is experienced by the small particles.[137] After the AST at 50 °C interestingly an equal "end of treatment" size is found in the range between 5.6-6.6 nm. A comparison of the obtained size changes to literature is unfortunately difficult due to differing applied protocols. Kocha *et al.*[138] or Mayrhofer *et al.*[139] applied potential scanning on a 2-3 nm Pt/C catalyst on Vulcan C (0.025-1.0 V_{RHE}) or Ketjen black (0.4-1.4 V_{RHE}), respectively. Load cycle conditions following the FCCJ protocols using a homemade catalyst were applied by Speder *et al.*[101,140] or Zana *et al.*[35] by performing IL-TEM. Yano *et al.*[141] observed after load cycles performed in MEA a comparable size increase from 2.2 ± 0.5 to 6.5 ± 2.3 nm, while Tamaki *et al.*[142] were reporting an increase from 3.2 ± 0.8 to 7.9 ± 4.6 nm after 10,000 cycles.

In the discussed study in the GDE setup, the same "end of treatment" size of around 6 nm independent of the initial particle size but temperature dependent is observed. The result of comparable size distributions after the applied AST protocol at 50 °C for all three catalysts is important regarding the aim of increasing the power density for mobile PEMFC applications. At high current densities (< 1 A cm^{-2}) currently high performance losses are observed and the oxygen mass transport resistance is suggested to be reduced by increasing the ECSA and

improving the catalyst dispersion, i.e., using small NPs.[78] Based on the presented results the strategy of particle size decrease will only be successful when a way to avoid the size increase is found.

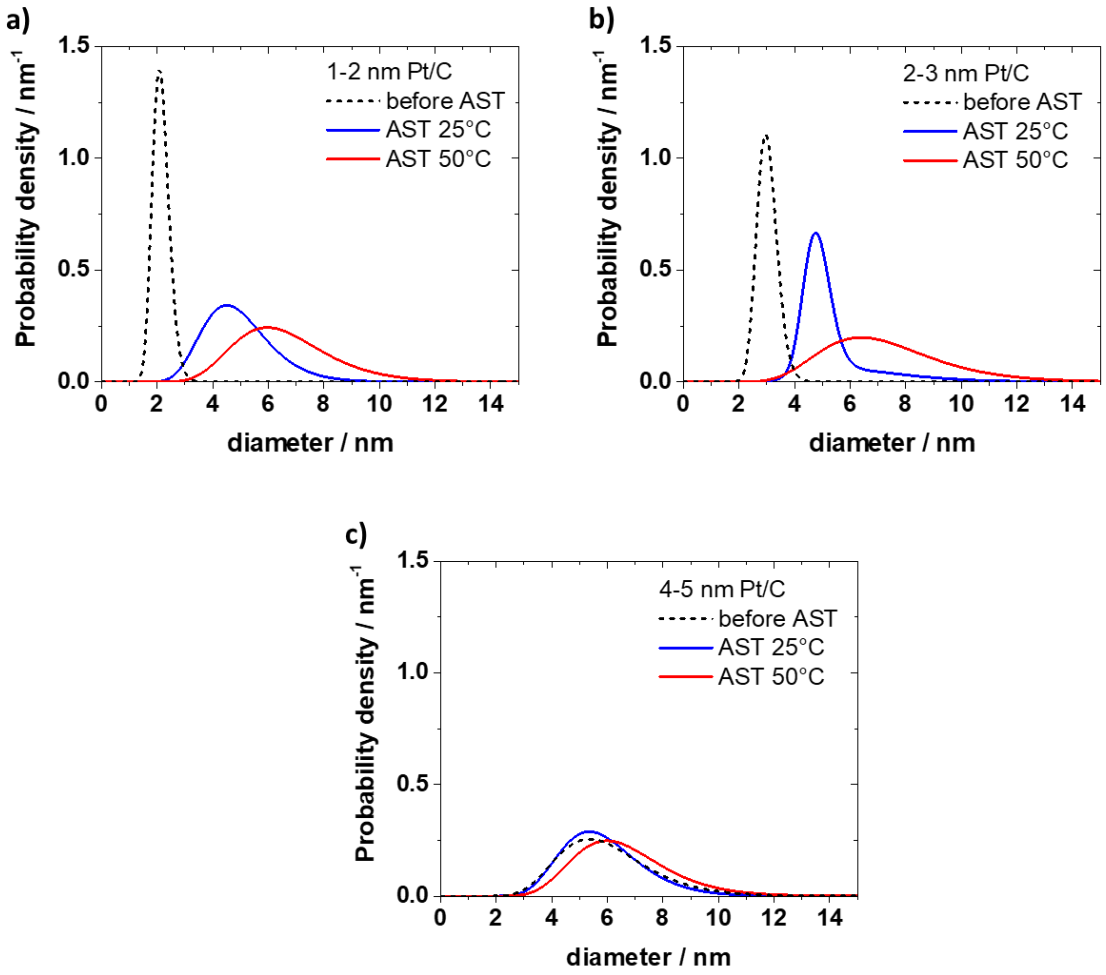

Figure 19. Representative SAXS probability densities for the 1-2 nm, 2-3 nm, and 4-5 nm Pt/C catalysts. Before after the AST protocol after 25 and 50 °C. © The Electrochemical Society. Reproduced with permission from *J. Electrochem. Soc.*, **2020**, *167*, 134515. All rights reserved.

Discussing the degradation mechanism first the particles size increase after AST, see Figure 19, is consistent with the observed loss in ECSA, see Table 1. The surface loss could be a consequence of all four degradation mechanisms, i.e., migration/coalescence, particle dissolution, electrochemical Ostwald ripening, NP detachment, see chapter 2.2.2. However, the particle size increase is only explainable by coalescence of NPs or Ostwald ripening. Due to the ECSA loss depending on catalyst layer thickness Ostwald ripening seems essentially contribute to the catalyst degradation but coalescence cannot be excluded. The 4-5 nm Pt/C catalyst might experience some NP detachment as the ECSA is decreased maintaining an almost constant particle size as reported by Mayrhofer *at al.*[139] for the same catalyst performing IL-TEM. However, the presented results in the GDE setup cannot clearly show particle detachment. The last degradation mechanism of NP dissolution would result in a particle size decrease in the case that no following redeposition of dissolved Pt ions is happening. In MEAs such a redeposition in the Nafion® membrane occurs due to hydrogen crossover through the membrane. As in the GDE setup the electrolyte is not purged with hydrogen and the gas flow rates measured at the gas inlet and outlet are comparable, a hydrogen crossover and hence redeposition are unlikely.

3.4. Manuscript IV:

The results shown in this chapter are excerpts from the publication

J. Schröder,* J. Quinson,* J. J. K Kirkensgaard, M. Arenz

*equally contributing

Operando SAXS Study of a Pt/C Fuel Cell Catalyst with an X-ray Laboratory Source

J. Phys. D: Appl. Phys., **2021**, *54*, 294004.

https://doi.org/10.1088/1361-6463/abfa39

https://doi.org/10.26434/chemrxiv.14283788.v1 (Open Access Preprint)

Description

The catalysts with Pt or Pt alloy NPs[1,2] used in PEMFCs, e.g., as alternative to combustion engines for large vehicles,[143–145] require not only a high activity but also sufficient stability. Therefore, the degradation of catalysts is investigated in ASTs. Recently, ASTs in a GDE setup were performed (a study I was involved in is cited)[28] (see also manuscript III) comparing the effect of simulated load-cycle and start-stop conditions recommended by the FCCJ[83,84] on commercial Pt catalysts. To investigate the change in particle size over the whole catalyst layer, SAXS can be performed as shown in manuscript III. *Ex situ* measurements as performed in manuscript III however lead to a poor time resolution as only a few points, i.e., pristine and end-of-treatment size, can be collected. For a complete understanding of the degradation mechanism the number of *ex situ* sampled would need to be strongly increased. A higher time-resolution without an enormously number of samples can be generated by performing *in situ*[146–148] or *operando* SAXS[114,116,149] measurements. Such studies are often done at synchrotron X-ray sources. However, beamtime at synchrotrons for *operando* SAXS measurements is limited, i.e., proposals are challenging to get accepted, and granting of proposal typically takes time. Additionally, equipment shipment can lead to challenges in cost and logistic and makes measurements quite inflexible. Due to travel restrictions during the Covid-19 pandemic, synchrotron measurements were postponed or performed in even more challenging remote operation. However, *operando* studies at lab X-ray source have some general advantages also under normal situations. Travel and research costs can be saved, experiments can be better designed, and measurements can be faster repeated while it can take month at synchrotrons.

In the following manuscript an *operando* cell introduced before for X-ray absorption spectroscopy (XAS) measurements[150] is used at a laboratory X-ray source. The change of particle size of a bimodal catalyst with two distinguishable size populations after performing ASTs is analyzed. For generating reasonable SAXS data the background subtraction is a crucial aspect. Usually the background measurements at laboratory X-ray source is done in a separate experiment leading often to difficulties in data normalization.[110] At synchrotrons alternatively anomalous SAXS[110] or measurements in the grazing incidence mode[111–113] are performed that are not available at laboratory X-ray sources. In the discussion of this manuscript, a new WE design is presented where catalyst layer and substrate are experiencing the same AST treatment, thus a suitable background measurement by *operando* SAXS is enabled, see Figure 3. This new technique allows not only the performance of suitable *operando* SAXS measurements at laboratory X-ray source, but it can also be used in *operando* studies at synchrotrons.

Contribution to the Work

M. Arenz, J. Quinson, and I designed the electrochemical experiments, which were prepared (catalyst films, assembling the cell) and performed by me. J. J. K. Kirkensgaard and J. Quinson were setting up the installation of the SAXS instrument. J. Quinson and I performed the SAXS measurements and J. Quinson the SAXS analysis. J. J. K. Kirkensgaard supervised the SAXS data acquisition and analysis. M. Arenz and I wrote the first draft of the manuscript, which was read and commented by all authors.

Most Important Findings

A proper background subtraction for *operando* SAXS measurement is challenging at laboratory X-ray sources as often separate background measurements are performed.[110] In this manuscript the background is measured from a metal-free spot next to the catalyst film experiencing the same AST protocol as the sample by moving the cell, see chapter 2.3.5 for details. This approach is tested analyzing the particle size change of a bimodal catalyst consisting of a mixture of two commercial Pt NP/C catalysts with two distinguishable size populations. Reports about dissolution rates[151,152] or degradation mechanisms[153] depending on the NP size are found. With such a bimodal catalyst the effect of the presented background subtraction of a range of NP size can be studied. Furthermore, in the bimodal catalyst Ostwald ripening, i.e., the growth of small particles at the expense of large one,[154] is expected to be the preferred degradation mechanism.

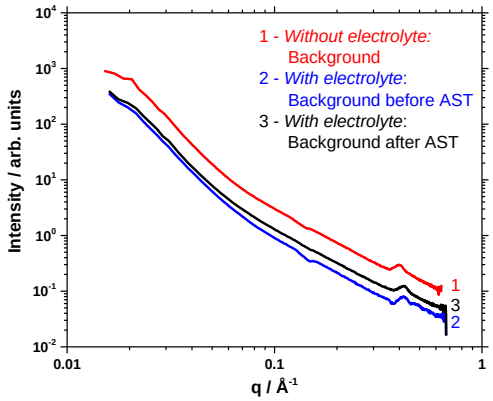

Figure 20. Intensity differences between different backgrounds (1) without electrolyte (red), with electrolyte (2) before (blue) and (3) after (black) the applied AST protocol.

In the described design of the WE different background measurements were performed without electrolyte inside the cell (red line), after filling the cell with electrolyte (blue line), and after the applied AST protocol (black line) with potential steps between 0.6 and 1.0 V_{RHE} (3 s holding), see Figure 20. Subtracting the different backgrounds has a substantial influence on the probability density of the particle size distributions of the bimodal Pt catalyst, see Figure 21. Using the background recorded before the AST with electrolyte in the cell shows the two distinguishable size populations, see Figure 21a. However, the probability density of the pristine catalyst is strongly differing from the sample before the AST after introducing electrolyte including a substantial increase of the mean particle size of the small population. Explanations could be that a steady state of the electrolyte was not reached or that the spot for the background measurement was not chosen properly. As the SAXS intensity increases with the square of the NP volume, the sensitivity of smaller particles to additional scattering or absorption by the added electrolyte is higher. Consequently, the particle size of the NPs is erroneously estimated (using the background before AST), see Figure 21a, and the probability density of the large population seems to be increased at the expense of the small one in presence of the electrolyte (using the background after AST), see Figure 21b. Additionally, in contrast to the observations in manuscript III, see Figure 19 in chapter 3.3, the particle sizes of both populations seem to remain rather constant, see Figure 21a.

The use of the background measurement taken after the AST, see Figure 21b, leads to the same mean particle size for the pristine catalyst and after adding the electrolyte before the AST. After

contact to the electrolyte the probability density of the small population increases at the expense of the large particles that could be explained by NP dissolution and subsequent Ostwald ripening. Inductively coupled plasma mass spectrometry measurements in scanning flow cells revealed indeed Pt dissolution of Pt/C catalysts after contact to electrolyte.[36,155] During the AST the size of the large size population is remaining constant at 5.0 ± 1.4 before and 5.0 ± 1.1 nm after 900 AST steps, while the small population is growing in size from 2.0 ± 0.5 to 2.6 ± 0.6 nm. The size increase of the 1-2 nm Pt/C catalyst and stable 4-5 nm Pt/C catalyst is seen before in manuscript III in Figure 19, see chapter 3.3, where the degradation mechanisms of Pt dissolution with followed Ostwald repining and NP coalescence could not be distinguished. Comparing both results, i.e., *ex situ* measurements in a GDE setup in manuscript III and *in situ* SAXS in an *operando* cell in the presently discussed manuscript, seem to reveal that the adding of a second size population is not affecting the degradation mechanism. Due to the continuous size increase and decrease of the probability density of the small NPs as well as a continuous increase of the probability density of the large population in *operando* SAXS, particle dissolution seems to be more likely than particle coalescence.

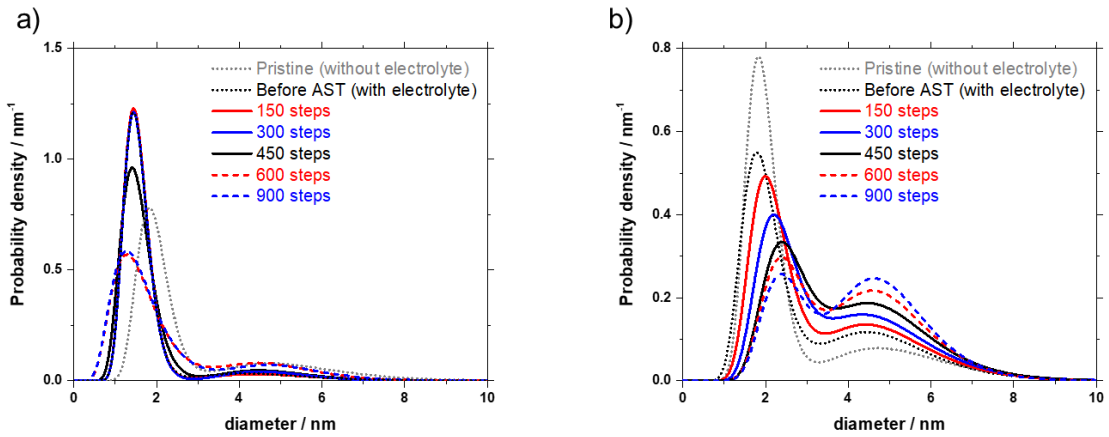

Figure 21. Probability density functions obtained by SAXS using scattering data as background with electrolyte (a) before and (b) after the AST.

3.5. Manuscript V:

The results shown in this chapter are excerpts from the publication

J. Schröder, R. K. Pittkowski, I. Martens, R. Chattot, J. Drnec, J. Quinson, J. J. K. Kirkensgaard, M. Arenz

Tracking the Catalyst Layer Depth Dependent Electrochemical Degradation of a Bimodal Pt/C Fuel Cell Catalyst: A Combined *Operando* Small- and Wide-Angle X-Ray Scattering Study

In preparation.

Description

As discussed before PEMFCs require besides a high activity sufficient stability.[32,33] ASTs are performed for investigations of the electrochemical degradation mechanisms (a study I was involved in is cited that I repeatedly refer to in the description of manuscript V)[28,130] that are all affecting the NP size of the catalyst.[85,156] As mentioned before to investigate the particle size of the whole catalyst layer and not only locally as in (S)TEM PEMFC catalysts were analyzed in the last years by SAXS.[28,50,77,101] Despite many AST studies, the degradation mechanism of Ostwald ripening could not be clearly identified by (S)TEM nor SAXS.[139,157] In the following study as for manuscript IV, see chapter 3.4, a bimodal catalyst of two distinguishable Pt particle size distributions that should be favored for Ostwald ripening[154] is investigated. The bimodal catalyst is prepared by mixing two commercial Pt/C catalysts locating the distinguishable size populations on different C flakes. As AST protocol load cycle conditions of PEMFEs, as recommended by the Fuel Cell Commercialization Conference of Japan (FCCJ),[83,84] are simulated. While in manuscript IV the bimodal catalyst was investigated in an *operando* cell in transmission mode at an X-ray laboratory source, in the presently discussed manuscript the bimodal catalyst is studies in an *operando* cell using grazing incidence configuration at the European Synchrotron Radiation Facility (ESRF) in Grenoble. As in manuscript IV the mean particle size of both populations can be determined by *operando* SAXS but the quantification of the ratios of the two size populations is difficult.

Therefore, in the present manuscript additionally WAXS data are analyzed. Using the crystallite size and the phase fraction as free parameters for the Rietveld refinement of the WAXS data results in a single population with an average coherent domain size. The combination of SAXS and WAXS analysis instead enables the determination of the phase fractions of the two population by using the mean particle sizes determined via SAXS as input values for the crystallite size during the Rietveld refinement. Furthermore, due to performed grazing incidence mode in the present manuscript the degradation depending on the depth profile of the catalyst layer can be investigated. This approach of the combination of *operando* SAXS and WAXS is used to investigate the catalyst layer depth dependence of the degradation. Cyclic voltammetry is performed between AST cycles for an overview of the status of degradation by comparing the hydrogen under potential deposition (H_{upd}) peak. As expected, the determined mean particle sizes obtained by SAXS are not affected by the CV, thus the change of the NP size is originated in the AST. Comparing the particle size at two different positions (at the same depth) on the catalyst layer shows that the change of NP size is position independent and hence data representative for the catalyst layer are analyzed. Finally, the combination of *operando* SAXS and WAXS, i.e., the comparison on the mean NP size and the phase fractions of the crystallite sizes of the two size populations, enables the observation of different degradation phenomena depending on the depth in the catalyst layer.

Contribution to the Work

M. Arenz and I designed the electrochemical experiments. I prepared the catalyst film. Due to the COVID restrictions the measurements at the synchrotron were performed in remote mode by I. Martens, R. Chattot, and J. Drnec in discussion with M. Arenz, J. Quinson and me. The SAXS data analysis was done by me, some initial analysis was done by J. Quinson. The WAXS

data analysis was performed by R. Pittkowski supported by I. Martens. J. J. K. Kirkensgaard supervised the SAXS data acquisition and analysis. M. Arenz and I wrote the first draft of the manuscript, which was send to all authors to be read and commented.

Most Important Findings

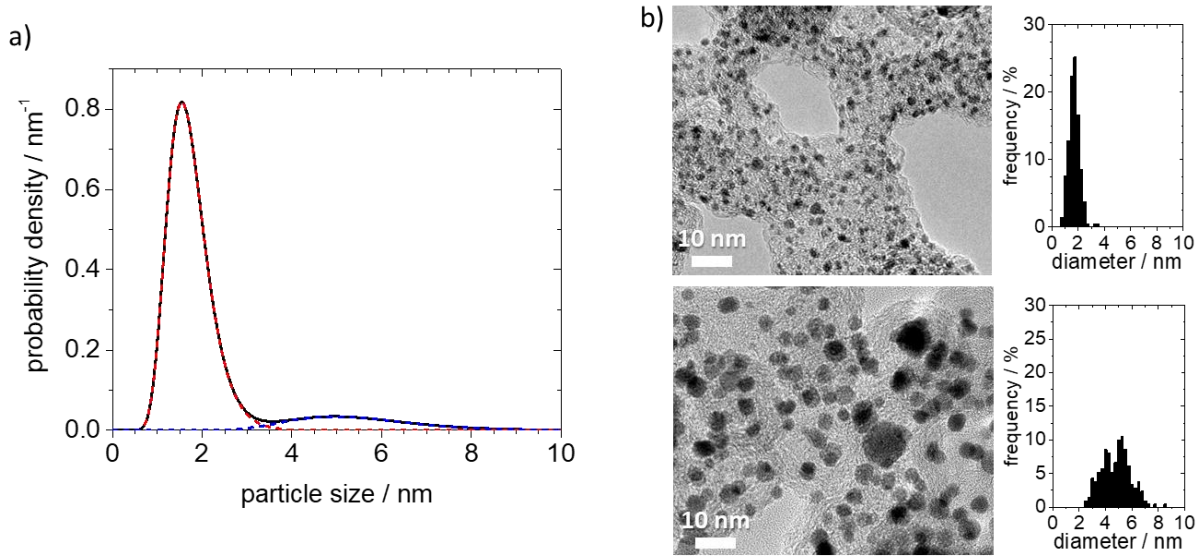

Figure 22. a) Calculated probability density function of the as-prepared bimodal Pt/C catalyst obtained from SAXS data in a depth close to the electrolyte-catalyst-interface together with the individual probability densities of the two size populations (dashed red and blue of the smaller and larger size population, respectively). b) Individual TEM images and size histograms of the two commercial Pt/C catalysts that were mixed to generate the bimodal catalyst.

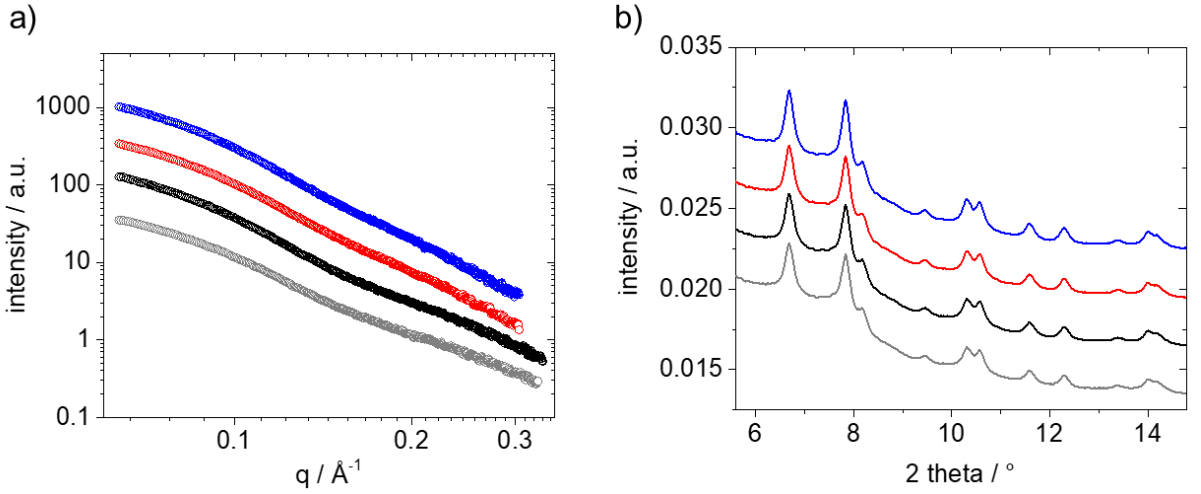

Figure 23. a) Background subtracted SAXS scattering data and b) corresponding WAXS diffractograms in a depth close to the electrolyte-catalyst interface: initial (grey), after catalyst cleaning (black), after 2500 AST cycles (red), and after 5000 AST cycles (blue). To improve visibility the different datasets are presented with a vertical offset.

The two size populations, in the following referred to as “smaller” and “larger” population, can be well distinguished via SAXS as shown in the calculated probability density function of the particle sizes of the bimodal catalyst before the AST protocol, see Figure 22. The bimodal catalyst should favor the degradation mechanism of electrochemical Ostwald ripening, i.e., the growth of the large particles at the expense of the small ones.[154] Due to the performed grazing

incidence mode a selection of different spots on and different depths within the catalyst layer by performing z-scans[158] is possible allowing to study the degradation depending on the distance to the electrolyte-catalyst interface.

Before discussing the influence of the AST protocol on the catalyst particles, the approach of the combination of SAXS and WAXS analysis is introduced investigating the pristine catalyst in a depth (z-direction) close to the electrolyte-catalyst interface, see scattering and diffraction data in grey in Figure 23. The mean particle sizes and phase fractions of the two populations in the bimodal Pt/C catalyst can be compared to the "expected values" as the bimodal catalyst is a mixture of two individually characterized Pt/C catalysts (in a known metal ratio of 0.4:0.6). It is possible to determine the mean particle sizes by SAXS but quantification of the relative number of particles in the two populations is difficult. The mean particle sizes and their standard deviations of the long-normal distributions determined via SAXS are 1.7 ± 0.5 and 5.5 ± 1.5 nm, see Figure 22a and Figure 24a. The retrieved particle diameters are in good agreement with the averaged particle sizes obtained from the individual catalysts via TEM of ca. 2 and ca. 5 nm, see Figure 23b. The expected relative number of particles should be theoretical accessible based on the SAXS data, however simulations of such a bimodal catalyst showed that there is no one-to-one correspondence regarding the intensity of the scattering data and the fitting. Thus, while the relative number of particles could not be determined during the simulations, the mean particle size remained similar even when bimodal catalyst with different phase fractions were simulated.

The analysis of the *operando* WAXS data should remedy this limitation. The peaks of the Pt fcc phase can be clearly seen in the WAXS diffraction patters in Figure 23b. The fraction of the two populations is estimated by refining the full pattern (starting from 6° 2θ) with two Pt phases of different domain size as structural model. However, the Rietveld refinement of both the fraction and particle size as free parameters for the two populations results in a single population with an average coherent domain size due to the interdependence of both parameters. Using only WAXS analysis hence is also not enough for the determination of the mean crystallite size and the phase fractions. Hence, the mean particle sizes of the two populations from *operando* SAXS were used in the Rietveld refinement of the *operando* WAXS data as input values for the crystallite sizes as the two parameters are although not identical closely related[159] allowing to estimate the phase fractions of the two populations. The approach is based on the assumptions of negligibility of the instrument profile on the diffraction pattern and that the peak boarding is not a result of strain effects.[22] Using this approach phase fractions of 0.44:0.56 of the smaller to the larger populations in the pristine sample close to electrolyte-catalyst interface were obtained that are in good agreement with the theoretical mass ratio of 0.4:0.6. Therefore, the combination of *operando* SAXS and WAXS enables the simultaneous investigation of the progression of the particle size and phase fractions, i.e., mass ratios, of the two Pt/C populations during the AST protocol.

Before Pt/C catalysts are used in electrochemical experiments they typically need to be cleaned by electrode potential cycling. The insertion of the electrolyte into the cell and performance of the potential cycles for catalyst cleaning slightly change the starting conditions of the catalyst. This is seen in the fraction increase of the smaller NP size populations from 0.44:0.56 to 0.48:0.52 with respect to the larger NPs, see Figure 24b, while the mean particle sizes from the SAXS fitting remain similar, see Figure 24a. Preferential dissolution and particle loss could

explain this result. Pizzutilo *et al.*[36] described Pt dissolution after electrochemical contacting by coupling scanning flow cells (SFC) with ICP-MS. Unexpectedly, the phase fraction results indicate a phenomenon including a preferred loss of the larger particles. A mechanism of preferential detachment of the large particles due to support oxidation was proposed before for the exact same catalyst as used in manuscript V.[99,139] Figure 24a confirms that after electrolyte contact and the typically performed Pt/C catalyst cleaning no substantial change in particle size occurs. In addition, the overlap of the blue filled circles (after CV) and the blue open circles in Figure 24a show that no change in particle size is observed after applying CVs (to confirm electrochemical contact) periodically subsequent to the AST cycles. Thus, the changes observed during the measurement are related to the performed AST.

The discussion of the effect of the AST protocol on the catalyst NPs is done first in a depth close to the electrolyte-catalyst interface. Figure 23 shows representative *operando* SAXS and WAXS data of the initial Pt/C catalyst, after catalyst cleaning, after 2500, and after 5000 AST cycles. The changes of the mean particle sizes allow three main observations at a depth close to the electrolyte-catalyst interface, see Figure 24a:

1. The size of both populations increases.
2. The size increase is more pronounced at the beginning of the AST.
3. The size increase of the smaller particle population is more pronounced from 1.76 ± 0.48 to 2.42 ± 0.79 (size increase of around 50 %) as compared to the increase of the larger population from 5.48 ± 1.45 to 5.87 ± 1.61 nm (size increase of around 7 %).

The observation that the size increase is more pronounced at the beginning of the AST treatment is in agreement with previous findings.[32,35,36] The size increase of both populations is unexpected and not obviously in line with electrochemical Ostwald ripening. In the case of Ostwald ripening occurring between the two size populations based on a preferential dissolving of the small particles, a size decrease of the smaller population would be expected. The increase in mean particle size of the smaller population could be explained by a phenomenon of a preferential dissolution of the smaller particles *within* that population. On the other hand, the increase in size of the larger population is explainable by electrochemical Ostwald ripening or the described phenomenon of a preferential dissolution of the smaller particles *within* the larger population. Hence, a dissolution of the small particles followed by Ostwald ripening seems to happen *within* the two populations and not between them. The phenomenon of Ostwald ripening is a local process in the nanometer scale without redepositing of dissolved Pt ions on neighboring catalyst flakes that is in agreement with a mechanism of mobile Pt special on the support as described by Ferreira *et al.*[132]

Ostwald ripening between the two populations would lead to a substantial change of the relative particle numbers of both populations. The analyzed phase fractions show indeed the decrease of the phase fraction of the smaller population. As the change of the phase fractions is relatively small the preferential dissolution of the smaller particles *within* both populations seems to be more likely. This phenomenon would additionally explain the increase of the mean particle sizes of both populations. To better understand the described phenomenon the change in particle sizes and phase fractions is furthermore analyzed in a “middle depth” with respect to the electrolyte-catalyst interface.

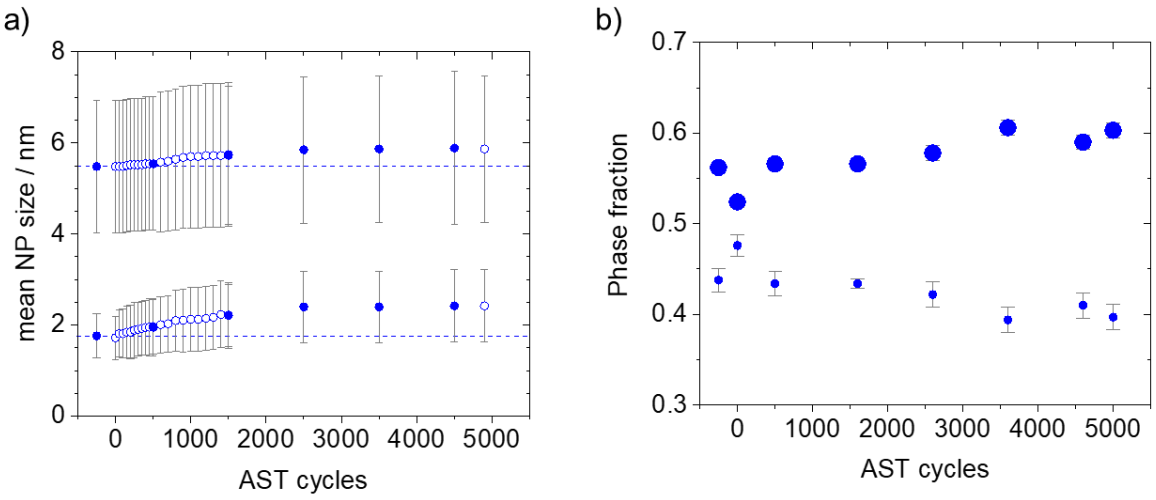

Figure 24. a) Mean particle size and standard deviation of a long-normal distribution obtained by *operando* SAXS of the bimodal Pt/C catalyst in a depth close to the electrolyte-catalyst interface applying load cycle conditions as AST protocol in an *operando* cell after the AST cycles (blue empty circles) and after the subsequent CVs (blue filled cycles). b) Phase fractions of the smaller and larger population (shown as small and large circles, respectively) of the bimodal catalyst in the middle catalyst layer obtained via Rietveld refinement from the WAXS data using the SAXS mean particle sizes as input values for the crystallite size.

The increase of the mean size of the two populations in both depths (close and in a middle depth with respect to the electrolyte-catalyst interface) during the AST treatment confirms the electrochemical connection of the complete catalyst layer. Based on the change in particle size four similarities are found for the two analyzed depths:

1. The particle sizes and changes within the larger populations are similar during the AST in both depths.
2. The size increase of the smaller population is more pronounced as compared to the increase of the larger population (from 2.43 ± 0.67 to 3.52 ± 0.68 nm (size increase of around 45 %) and from 5.50 ± 1.17 to 5.99 ± 1.15 nm (size increase of around 9 %) in the middle catalyst layer depth).
3. Comparable relative size increases in both depths of 7 and 50 % for the smaller and larger population close to the electrolyte-catalyst interface and 9 and 45 % in the middle of the catalyst layer are seen.
4. The particle size change of the larger population seems to be depth independent.

A strong difference between both depths is the slightly smaller particle size of the smaller population in the depth closer to the electrolyte-catalyst interface (already before the start of the AST).

The determined ratio of 0.46:0.54 of the smaller to larger population in the pristine sample in the middle catalyst depths, see Figure 25b, is in good agreement with the theoretical ratio of 0.4:0.6. After the electrolyte contact and the cleaning CVs the ratio increases to 0.51:0.49 while the mean particle sizes do not change. This observation reminds of the phenomenon described in the depths close to the electrolyte-catalyst interface. However, in the middle depth the phase fraction of the smaller population continues to increase during the AST reaching a ratio of 0.6:04 at the end of treatment, see Figure 25b, while the particle size of both populations is increasing, see Figure 25a.

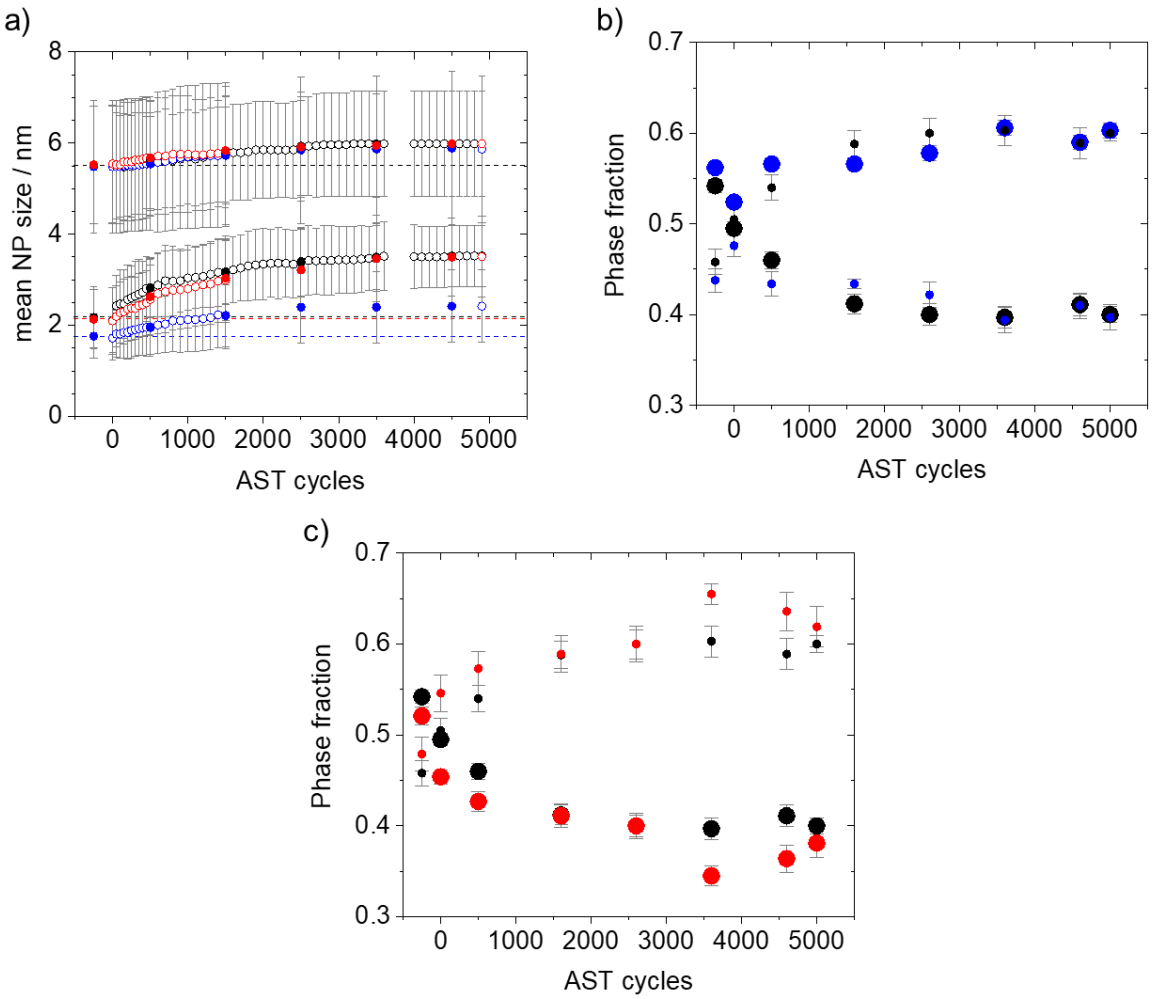

Figure 25. a) Mean particle size and standard deviation of a long-normal distribution obtained by *operando* SAXS of the bimodal Pt/C catalyst in an *operando* cell after the load cycle conditions as AST protocol (circles) and after the subsequent CVs (filled cycles) close to the electrolyte (blue), in the middle (black), and deeper inside the catalyst layer (red). Phase fractions of the smaller and larger population (shown as small and large circles, respectively) of the bimodal catalyst obtained via Rietveld refinement from the WAXS data using the SAXS mean particle sizes as input values for the crystallite size b) at a middle depth of the catalyst layer (black) and close to the electrolyte (blue), c) at a middle depth of the (black) and deeper inside the catalyst layer (red) (due to an overlap of the red and black filled circles, the red are placed in front of the black ones).

This observation in the middle depth is unexpected. Therefore, a third depth (different z-direction) even deeper inside the catalyst layer was analyzed showing the same unexpected results in change of the particle size and phase fraction as seen in the middle depths, see Figure 25a. As the crystallite size of the Rietveld refinement are not identical (but closely related) to the mean particle sizes, in addition, the influence of slight changes of the input values of the smaller population (shifted by ± 0.5 nm) was studied, see Figure 26a. It was confirmed that the observed trends of the phase fraction changes are not artifacts originated from the mean particle sizes, see Figure 26b and c.

The described observations can be explained by different degradation mechanisms. However, enhanced dissolving of the particles of the larger population and the migration of the smaller particles from the upper catalyst layer seem to be unlikely. A mechanism of preferential detachment of the particles from the larger population due to the oxidation of the support as described before of the same catalyst as used in manuscript V[99,139] could explain the observations.

For interpretating the observed results of an increase in phase fraction and size of the small population, it needs to be pointed out that the determined phase fractions are relative and not absolute values. An increase of the fraction of the smaller population can therefore result from an absolute increase in number of the same particles or a decrease in number of the larger population that would be observed in the case of preferred particle loss of the larger NPs. Mayrhofer *et al.*[139] and Hartl *et al.*[99] observed such a particle detachment with a subsequent particle dissolution without redeposition in an RDE setup via IL-TEM of the large particles of the exact same catalyst as used in manuscript V. Based on a larger contact area of larger particles a stronger support-particle interaction could be suggested and thus no preferred detachment from the support.[160] However, the support-particle interaction is not only size dependent but also determined by the graphitization degree of the carbon support of a catalyst.[161] The preferred detachment of the large particles observed in the results of manuscript V indicates degradation scenarios depending on both the particle and the support property. The large NPs that are assumed to preferably detach from the support (due to a weaker anchoring) have during their pathway through the pores of the catalyst layer a certain redeposition probability, leading to a decrease of the large population within the catalyst layer but an increase closer to the electrolyte. Via electrochemical Ostwald ripening the small particles are dissolving and redepositing onto the small and large NPs, hence a large size increase of the small population is observed that is limited close to the electrolyte due to a decreased redeposition probability.

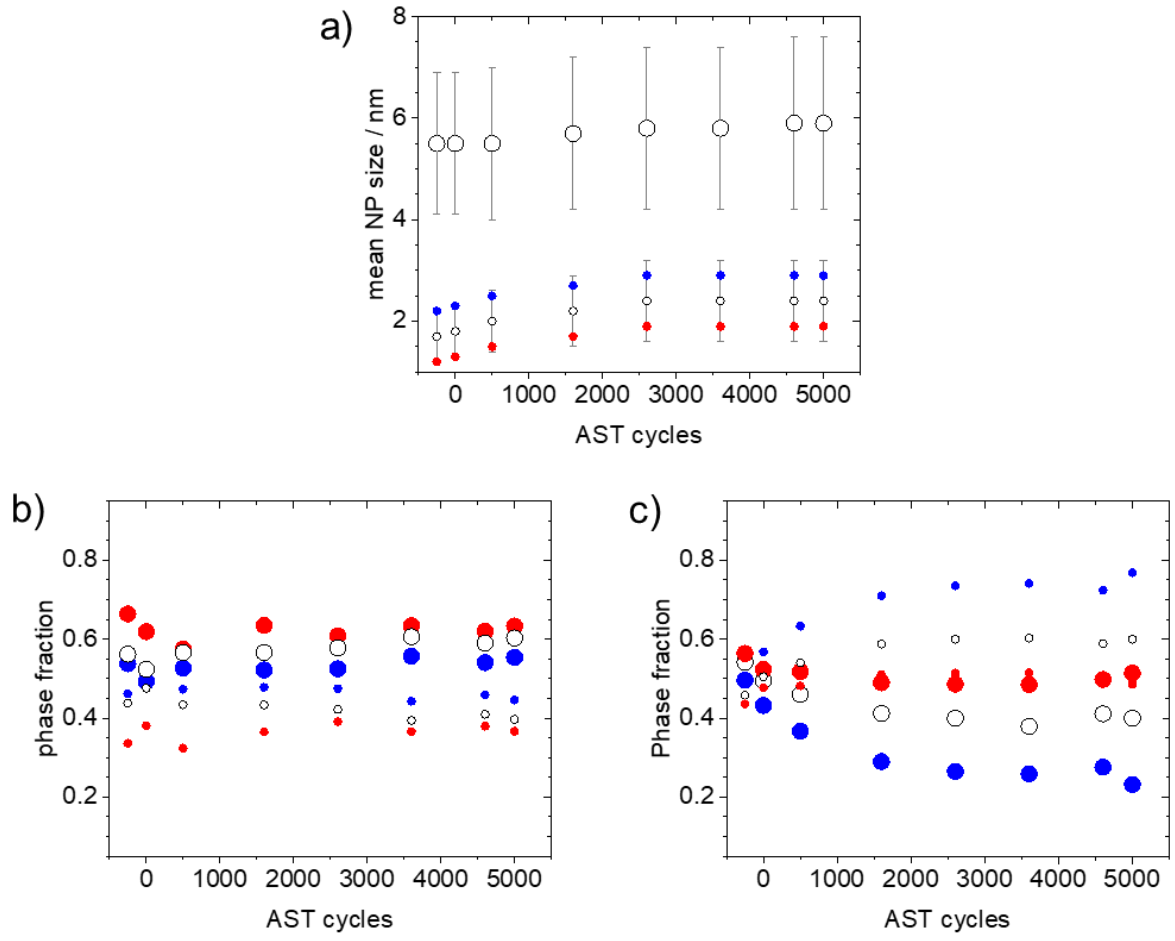

Figure 26. a) The change of the mean particle sizes of the smaller population (+ 0.5 nm (blue), – 0.5 nm (red)) obtained by SAXS as input values for the crystallite size during the Rietveld refinement and corresponding phase fractions for the depth b) closest to the electrolyte and c) in the middle of the catalyst layer.

3.6. Manuscript VI:

The results shown in this chapter are excerpts from the publication

J. Quinson, L. Kacenauskaite, J. Schröder, S. B. Simonsen, L. Theil Kuhn, T. Vosch, M. Arenz

UV-Induced Syntheses of Surfactant-Free Precious Metal Nanoparticles in Alkaline Methanol and Ethanol

Nanoscale Advances, **2020**, *2*, 2288-2292.

https://doi.org/10.1039/D0NA00218F (Open Access)

Description

The synthesis of "surfactant-free" Pt NPs introduced by Wang *et al.*[43] as catalyst for PEMFCs was thoroughly investigated in EG (I was involved in one of the cited studies)[44,50,53,54,162] and by the Co4Cat process in low boiling points solvents like ethanol and methanol (I was involved in one of the cited studies)[58,61–63,148,162]. The Pt NPs were mostly synthesized by a thermal or microwave based reduction and only few reports are found about light induced synthesis limited to EG.[49,51] Concerning "surfactant-free" Ir NP syntheses for PEMWE catalysts only a few reports are found, which are limited to a thermal or microwave-based reduction.[61,66] The Ir NP syntheses are leading independent of the used solvent, i.e., EG, methanol, or ethanol, to small particles with a particle size of about 1 nm. The question about a size control via the Co4Cat for Ir NPs as reported for Pt[61] came up. As for the Co4Cat process light induced synthesis were not reported, the discussion of manuscript V fills up this gab of UV-light-induced particle synthesis. The focus is on the discussion of the Ir NP synthesis and the misleading tries of a size control including seed-mediated growth experiments as that is my contribution to the manuscript VI. The results are compared to the Pt NP synthesis generated by Dr. J. Quinson and L. Kacenauskaite.

Contribution to the Work

I did not perform the synthesis nor the analysis of the UV-light-induced Pt NPs. I performed the Ir NP synthesis of the H_2IrCl_6 precursor shown in Figure 27 (in the SI in the manuscript). I supervised and planed the experiments of the Ir NP synthesis that were mostly performed by N. Schären. J. Quinson took the TEM images of the TEM samples prepared by N. Schären and me. J. Quinson and I analyzed the TEM images. M. Arenz supervised the research. J. Quinson and I wrote the first draft of Ir chapter of the manuscript, the whole manuscript was read and commented by all authors.

Most Important Findings

The UV-light-induced synthesis is a suitable procedure to form very small Ir NPs. Changing different synthesis parameters as the precursor (Na_2IrCl_6, H_2IrCl_6, or $IrCl_3$), solvent (EtOH, MeOH, H_2O), amounts of water (10-25 % in volume), NaOH concentration (0-44 mM), temperature (10-40 °C), times of synthesis (up to 24 h) and gas atmosphere (air, 5 % H2 in Ar, Ar, CO) lead to Ir particle sizes in the same range of 1.0-1.7 nm, see Figure 27 for some examples. Different seed-mediated growth approaches were not successful but resulted in small Ir NP sizes. Despite comparable particle sizes, different particle formation rates are observed. The NP formation rate in ethanol is often substantially increased as compared to methanol. Adding NaOH leads to a slightly and in Ar gas atmospheres a substantially faster NP formation, while a CO atmosphere slows down the NP formation. Independent of the NP formation kinetics, i.e., different time scales, and the change of reaction parameters NPs in the same size range are generated. Hence, also the UV-light-induced reduction cannot solve the challenge of size control of Ir NPs but is presented as an excellent approach to generate small Ir NPs independent of the tested synthesis conditions.

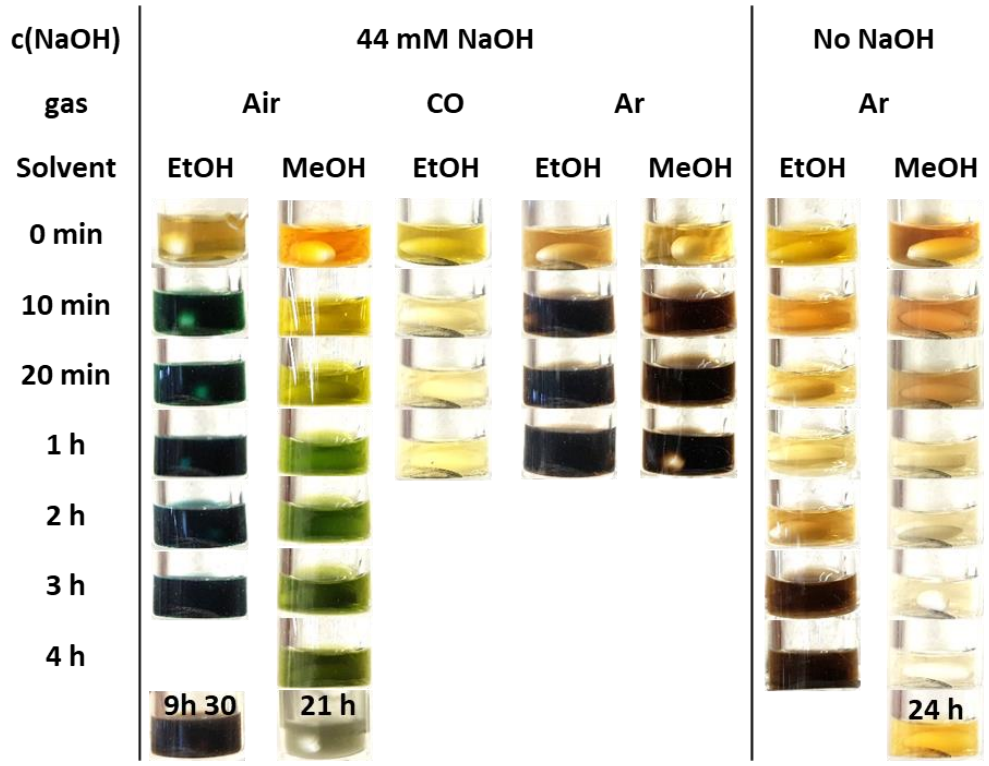

Figure 27. The synthesis mixture after different times in the reduction of the precursor H_2IrCl_6 in ethanol and methanol by irradiation with UV-C light. Reproduced from *Nanoscale Adv.* **2020**, *2 (6)*, 2288-2292 with permission from the Royal Society of Chemistry.

In contrast the UV-induced reduction of H_2PtCl_6 is behaving differently in methanol as compared to ethanol. While also in ethanol no size control is possible by changing the NaOH content, in methanol the increase to a NaOH/Pt content of 25 leads to an increase in particle size to 3.3 ± 1.1 nm. The change of water content to at least 50 % during the Pt NP synthesis leads only to a fine size control.

Due to the different behavior in particle size in the synthesis of Ir as compared to Pt NPs reaching comparable small Ir particles sizes independent of the reduction conditions is even more astonishing. When the reduction of the Ir precursors to NPs is induced by UV-light the Co4Cat process seem to be basically infallible. Such a lack of error prone can be seen as an advantage and strength of the Co4Cat process but it still remains poorly understood.

3.7. Manuscript VII:

The results shown in this chapter are excerpts from the publication

J. Schröder, V. A. Mints, A. Bornet, E. Berner, M. Fathi Tovini, J. Quinson, G. K. H. Wiberg, F. Bizzotto, H. A. El-Sayed, M. Arenz

The Gas Diffusion Electrode Setup as Straightforward Testing Device for Proton Exchange Membrane Water Electrolyzer Catalysts

JACS Au, **2021**, *1*, 247-251.

https://pubs.acs.org/doi/10.1021/jacsau.1c00015 (Open Access)

Description

The coupling of PEMWEs to renewable energy sources, e.g., wind, solar, is a promising technology for energy conversion and long-term storage. Thereby the use of PEMWEs enables higher current densities and in contrast to alkaline electrolysis cells (AECs) no liquid electrolyte is needed.[3,6,11] The preferred anode materials for PEMWEs are Ir and Ir alloys due to the compromise between activity and stability of IrO_2.[17,18,163] Performance testing of OER catalysts for PEMWEs is normally done in RDE measurements[66,86,164] or a MEA assembled as PEMWE.[165–167] However, using the RDE as compared to MEA it is challenging to measure at high temperatures close to operation temperature. Additionally, only thin catalyst films and an aqueous electrolyte can be used in RDE setups. Measuring under realistic conditions in MEAs on the other hand is time consuming to assembly and special equipment is needed: the preparation of catalyst films on the membrane (CCMs), hot-pressing of the membrane to the porous Ti based substrate, i.e., PTL, and the MEA operation. Additionally, performance contradictions in stability tests of RDE as compared to MEA measurements were described.[168,169] Therefore, a device filling the gap between RDE and MEA testing is desired. After successful establishing of the GDE setup in ORR studies under realistic fuel cell conditions (I was involved in one of the cited studies)[27,28] (see also discussion of manuscript IV, chapter 3.4) the question was if it is possible to test OER catalysts with the GDE approach.

In the following discussion the GDE setup is presented the first time for OER screening experiments. In the presented manuscript the reactant, i.e., water, is introduced to the GDE by humidified gas. Therefore, it was important that it could be shown that the reaction rate is independent over a large range of the gas flow rate. As the data obtained in the GDE setup are comparable to RDE measurements, the GDE approach can be seen as a straightforward testing device much easier to operate than an MEA. The investigation of the gas atmosphere (Ar versus O_2) shows the impact of the O_2 pressure in the Nernst equation. The possibility of using a Ti PTL instead of a carbon GDL confirms the realistic PEMWE testing conditions as compared to RDE measurements. Due to the high costs of PTLs and the difficulties in mechanical and electrochemical processing, the use of PTLs for screening experiments is questionable. Instead, the use of GDLs should be recommended. The short-term stability of the GDL in the presented activity measurements and the possibility of the catalyst film preparation by vacuum filtration supports the approach of using GDLs for performance tests. Finally, the presented opportunity to perform kinetic studies enabling the estimation the exchange current density j_0 and the electrochemical activation energy E_A complete the testing possibilities in the GDE as compared to the RDE setup.

Contribution to the Work

G. K. H. Wiberg designed the GDE setup for the OER measurements. M. Arenz, H. A. El-Sayed, and I designed the electrochemical experiments in the GDE setup, prepared and performed by me. V. A. Mints performed the RDE measurements. I prepared the samples for TEM and XPS measurements. J. Quinson performed TEM and M. Fathi Tovini XPS measurements and analysis. E. Berner did the SEM and EDS measurements. A. Bornet did initial tests on the hot-pressing. F. Bizzotto did initial OER tests in the GDE setup. H. A. El-Sayed and M. Arenz supervised the research. M. Arenz and I wrote the first draft of the manuscript, that was read,

and commented by all authors.

Most Important Findings

The catalyst film used in the GDE measurements is a commercial IrO_2 catalyst deposited by vacuum filtration as introduced by Yarlagadda *et al.*[80] on top of the MPL of the GDL. Performing EDS element mapping of a SEM cross-section shows a clear separation of the deposited catalyst film, the carbon containing MPL, and the carbon fibers of the GDL, see Figure 28. Hence the vacuum filtration is a suitable technique for the preparation of reproducible films with catalyst loading comparable to PEMWEs.[24,81]

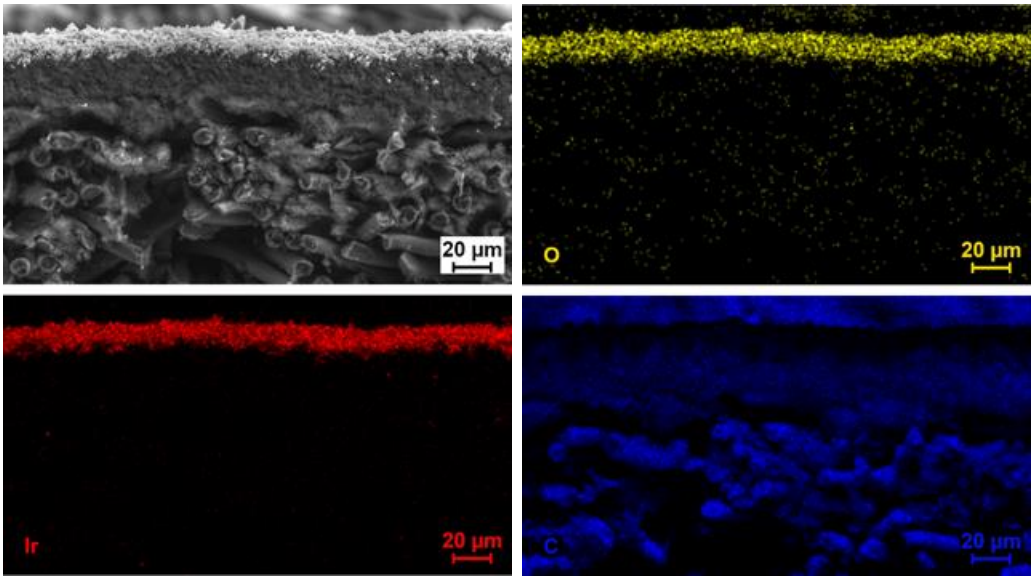

Figure 28. EDS element mapping of a SEM cross-section of an active IrO_2 catalyst prepared by vacuum filtration on top of a GDL: iridium (Ir, red), oxygen (O, yellow), and carbon (C, blue). The clear separation of the catalyst film deposited on the carbon containing MPL, and the carbon fibers of the GDL are apparent. Reprinted with permission from *JACS Au* **2021**, *1*, 247-251. Copyright 2021 The Authors. Published by American Chemical Society.

The influence of different parameters as the gas flow rate, gas atmosphere (Ar, O_2), substrate (GDL, PTL), and the temperature (30-60 °C) on the OER catalyst performance are investigated in the GDL setup to establish a measurement protocol. The use of humidified Ar as reactant gas reveals an independence in Tafel slope of 41.4 ± 0.9 mV dec^{-1} by changing the gas flow rate over a wide range between 40-190 mL min^{-1}. Only a low flow rate (10 ml min^{-1}) leads to a nonlinear Tafel slope behavior indicating mass transport limitations as the lack of water transported to the catalyst or difficulties to remove the formed O_2 from the catalyst surface.

A measurement protocol for the OER catalyst testing applying current steps, normalized to the mass of the precious metal amount, is established in the GDE setup. The performance test in the GDE setup is compared to the conventional OER catalyst testing device, the RDE setup. The comparison of data at 30 °C between both setups reveals comparable results in activity, i.e., 4.3 and 4.9 mA mg_{Ir}^{-1} at 1.48 V_{RHE} in galvanostatic GDE as compared to potentiostatic RDE measurements, respectively, see Figure 29a. Those activities are compared to data reported by Alia *et al.*[86,170] At 60 °C the catalyst is slightly less active in the GDE as compared to the RDE setup, see Figure 29b. However, substantial deviations in the current density *j* are

observed in the RDE measurement. These deviations can be explained by a possible catalyst degradation, e.g., catalyst detachment, as during the performance of CV a clear deactivation could be observed. Performing the GDE measurements at 60 °C in Ar as compared to O_2 leads to an apparent higher activity at lower current densities, see Figure 29b, due to the influence of the O_2 partial pressure in the Nernst equation. This effect also explains the substantial increase in Tafel slope at higher current densities due to O_2 bubble formation[87,88] resulting in an apparent deactivation in Ar at higher current densities, and thus an approaching to the activity measured in O_2.

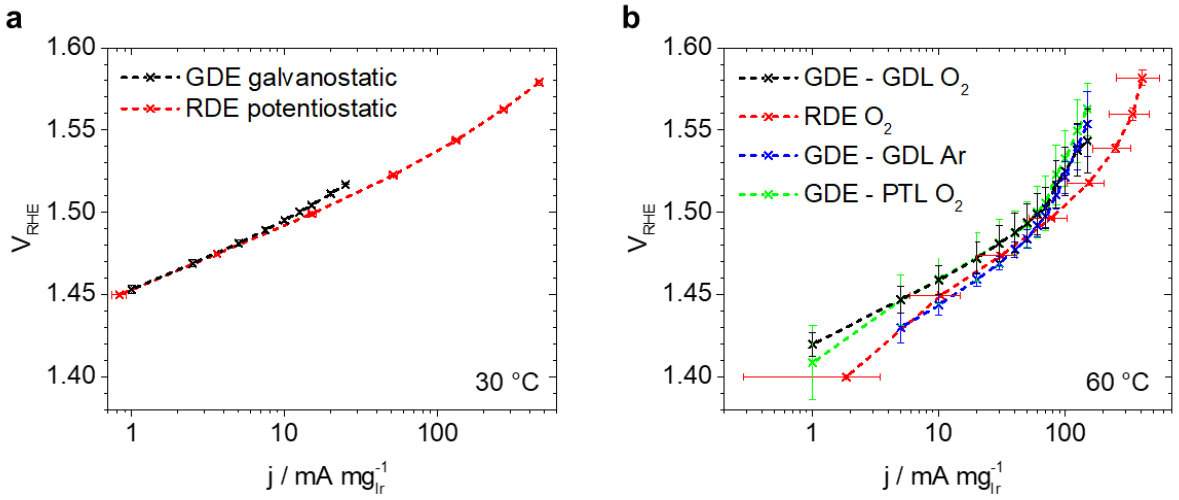

Figure 29. Tafel plots of OER mass activity *j* of the commercial IrO_2 catalyst. Comparison of measurements generated in the RDE as compared to the GDE setup (a) at 30 °C using a GDL in O_2 and (b) at 60 °C using a GDL in O_2 or Ar and a PTL in O_2. Reprinted with permission from *JACS Au* **2021**, *1*, 247-251. Copyright 2021 The Authors. Published by American Chemical Society.

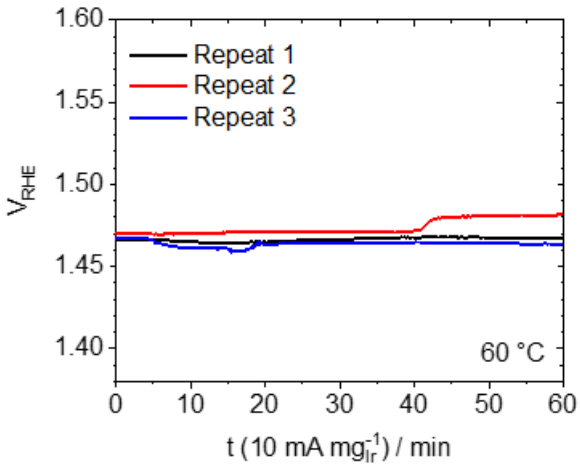

Figure 30. Stability test of three repeats of IrO_2/GDL applying 10 mA mg_{Ir}^{-1} for 1 h. Reprinted with permission from *JACS Au* **2021**, *1*, 247-251. Copyright 2021 American Chemical Society.

Performing the activity test protocol in the GDE setup with a catalyst film deposited onto a Ti PTL instead of the carbon GDL interestingly generate comparable results. Ti PTLs are usually used in PEMWEs due to long-term stability problems of carbon. However, the preparation of the PTL is substantial more complex as the GDL, see chapter 2.2.1 for preparation details. This presents the performance of the GDE setup with the GDL as a substantially less complex testing approach of PEMWE catalysts as compared to MEAs. To confirm that carbon corrosion is not

affecting the activity measurements in the GDE setup the current density was increased stepwise from 1 to 10 mA mg_{Ir}^{-1} and kept constant at 10 mA mg_{Ir}^{-1} for 1 h. The three independent repeats of the IrO_2 catalyst deposited on a GDL in Figure 30 shows that it is possible to perform stability studies as suggested by Spöri *et al.*[171] Although the potential increase in repeat 2 might be traced back to bubble formation or carbon degradation, the GDL substrate is suitable for screening tests. To perform long-term stability investigations under harsher conditions the use of CCMs pressed to PTLs might be necessary.[23,82]

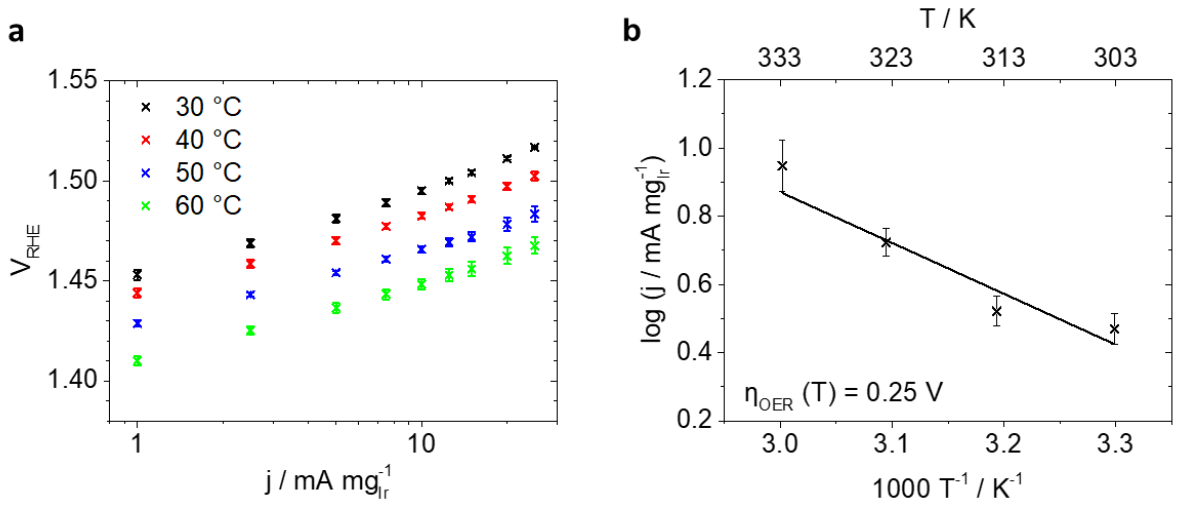

Figure 31. (a) Tafel plot of OER mass activity *j* of the commercial IrO_2 catalyst applying current steps at the temperatures of 30, 40, 50, and 60 °C generated in a GDE setup. (b) The corresponding Arrhenius plot at an overpotential η_{OER} of 0.25 V. Reprinted with permission from *JACS Au* **2021**, *1*, 247-251. Copyright 2021 The Authors. Published by American Chemical Society.

Finally, the temperature influence is investigated by applying the temperatures 30, 40, 50, and 60 °C) consecutively (measuring three independent samples). The Tafel plot shows as expected an increase in the OER rate with temperature.[172] The linear and parallel Tafel slopes at low current densities indicate that the OER reaction mechanism in the investigated temperature range is the same. Due to the precise Tafel slopes the linear fits can be extrapolated to the exchange current densities j_0 and the electrochemical activation energy E_A can be estimated assuming Arrhenius behavior, see Figure 31b. For the determination of j_0 and E_A the temperature dependance of the reversible potential according to an equation of Parthasarathy *at al.*[173] is considered. The obtained j_0 of 10.6 ± 6.0, 3.5 ± 1.8, 2.1 ± 1.2, and 7.2 ± 3.8 × 10^{-9} A mg_{Ir}^{-1} for 30, 40, 50, and 60 °C, respectively, are comparable to 7.3 × 10^{-9} A mg_{Ir}^{-1} calculated from Lu *et al.*[174] The increase of j_0 from 50 to 60 °C shows the limitation of the extrapolation. From the linear fit of the Arrhenius plot at an overpotential of 0.25 V, see Figure 31, E_A of 28.5 ± 6.6 kJ mol^{-1} can be determined. The difference to 47 kJ mol^{-1} reported by Suermann *et al.*[167] in a PEMWE mainly results from the measurement at 30 °C. Although measurements at four temperatures only allows a rough estimation, the GDE setup is presented as straightforward approach for kinetic studies.

4. Conclusions and Perspectives

4.1. Conclusions

4.1.1. Pt Nanoparticle Synthesis by the Polyol Approach

In manuscript I the visible-light-induced NP synthesis enabled mechanistic investigations of the reduction of the H_2PtCl_6 and H_2PtBr_6 precursors in the polyol process. Reducing H_2PtCl_6 or H_2PtBr_6 in presence of NaOH led to comparable particle sizes at a constant OH-/Pt ratio of 24.4 independent of the wavelength of the exposed visible light. Despite the slowing down of the reduction process (to 24 h) as compared to the thermally induced reduction (by microwaves (3 min) or in a heated oil bath (90 min)) comparable results in particle size were obtained in the reduction of H_2PtCl_6 by reducing the OH-/Pt ratio. The conditions used in the visible-light-induced reduction at room temperature were showing that in absence of Ostwald ripening, also the reduction of H_2PtBr_6 results in a comparable size control as compared to the use of the precursor H_2PtCl_6. The same particle size results despite different reduction conditions leading to different reduction rates were in contradiction to the kinetic LaMer model that is typically used to explain the NP formation process. The visibility of the reduction intermediates due to different colors by the slowing down of the NP synthesis enabled the proposition of a new reduction and NP formation mechanism.

The size control by the OH^-/Pt ratio could be confirmed using a $H_2Pt(OH)_6$ as precursor in the thermal reduction in EG (manuscript II). This observation of a size control could be extended to the $acac^-$/Pt in the reductions of H_2PtCl_6 or $H_2Pt(OH)_6$ in presence of the base Na(acac) as compared to the regular used NaOH. The use of the precursor $Pt(acac)_2$ in the thermal reduction resulted in the polyol process in substantial larger particles independent of the amount of the bases NaOH or Na(acac) used during the synthesis. Those results revealed that the size control is strongly depending on the character of the precursor and its anion before the OH^-/Pt or $acac^-$/Pt are determining the size.

4.1.2. Degradation Studies of Fuel Cell Catalysts

The straightforward handling of the GDE setup was once more confirmed by the coupling to *ex situ* SAXS measurements to determine the particle size changes during ASTs (manuscript III). AST protocols were applied in the GDE setup using catalyst films that were prepared via vacuum filtration to generate similar loadings as common in fuel cells. This straightforward way of film preparation together with the performance of ASTs at 50 °C demonstrated the GDE setup as a testing device working close to realistic fuel cell application conditions. The combination of ECSA loss and the particle size change analyzed by SAXS were used to investigate the degradation mechanisms during the AST (simulating load cycle conditions) depending on the initial particle size and temperature. The results showed that despite different initial particle sizes a similar end of treatment size was obtained. Those results are questioning the strategy to use smaller particles to reach higher currents densities due to the higher surface area and hence decreasing the amount of used precision metals.

For a deeper understanding of the degradation mechanism a continuous observation of the particle size is desired. As *ex situ* SAXS would have enormously increased the number of samples,

SAXS was performed in *operando* using realistic fuel cell loadings generated again by vacuum filtration and stimulating load cycle conditions by an AST protocol. The results of manuscript IV were generated at an X-ray lab source performing the crucial aspect of a suitable background measurements by vertical moving of the operando cell to a GDL spot that was experiencing the same AST protocol as the catalyst. A bimodal catalyst consisting of a mixture of two commercial catalysts with distinguishable size populations was used that should favor electrochemical Ostwald ripening as degradation mechanism, i.e., the growth of the large particles at the expense of the small ones. The analysis of the mean particle sizes revealed a growth of the small population while the size of the large particles remained similar. This is in agreement with the *ex-situ* SAXS observations after performing ASTs in the GDE setup showing that the smaller particles experienced a substantial more pronounced size increase as compared to the large NPs. *Operando* measurements at the ESRF (manuscript V) of the bimodal catalyst simulating load cycle conditions were performed in grazing incidence mode enabling the investigation of the degradation depending on the depth profile of the catalyst layer. The combination of *operando* SAXS with WAXS made it possible to easily estimate the phase fractions of the two populations using the mean particle size obtained by SAXS as input for the crystallite size. Despite the bimodal system that should be favored for electrochemical Ostwald ripening this degradation mechanism was once more not clearly identified in both manuscript IV and V.

4.1.3. Ir Nanoparticle Synthesis by the Co4Cat Process

UV-light-induced synthesis parameters and conditions as precursor, solvent, gas atmosphere, temperature, base concentration, and water content were varied as well as seed-mediated growth experiments were performed trying without success to change and control the particle size of the Ir NPs by the Co4Cat process in manuscript VI.

4.1.4. Testing of Electrolyzer Catalysts in a GDE Setup

The GDE setup was presented in manuscript VII as a straightforward performance testing device of electrolyzer catalysts using realistic catalyst loadings reached by vacuum filtration. As the reactant water was introduced by humidified gas it was important to show the independence of catalyst performance over a large range of gas flow rate as soon as it is high enough. In addition, it could be shown that at 30 °C the GDE setup is showing a comparable performance as in the RDE setup, while differences at 60 °C are assumed to occur due to catalyst degradation. Therefore, the GDE setup can be presented as straightforward techniques enabling performance testing under a realistic temperature as used in PEMWEs. Investigating the influence of the gas atmosphere revealed that at lower current densities a lower activity is observed in Ar as compared to O_2 atmosphere. Due to the O_2 partial pressure in the Nernst equation the activity in Ar atmosphere increases to a comparable performance as working in an O_2 atmosphere. In the performance tests in manuscript VII the activity is tested using C based GDLs that show stability limitations at high potentials and hence the performance of the investigated catalysts could be influenced. The GDL stability during the time of the performance measurements could be confirmed, hence the use of the GDL is demonstrated to be suitable for the activity testing. In addition, it is shown that even the use of a Ti based PTL as typically used in PEMWEs is

possible in a GDE setup. Increasing the ink viscosity using glycerol and increasing the hydrophobicity by spraying Teflon on top of the Ti PTL enables the preparation of a catalyst film without permeation of the catalyst into the PTL. After performing a simple hot-pressing electric contact was guaranteed and an activity comparable to the results obtained using a C GDL was reached. Finally, a kinetic study between 30 and 60 °C was performed allowing the determination of the electrochemical activation energy assuming Arrhenius behavior and the estimation of the exchange current density at a certain overpotential.

4.2. Perspectives

4.2.1. Synthesis and Degradation Studies of Fuel Cell Catalysts

To further understand the NP formation mechanism and differences in reduction between the precursors, *in situ* studies would be necessary as done by Mathiesen *et al.* (a study I was involved in is cited)[65] for Pt NPs prepared by the Co4Cat process. For a comparable study, high concentrations of about 50 mM Pt (double the concentration used in manuscript I and II) would be necessary. In addition, during *in situ* experiments it is important to exclude the interaction of the analysis technique with the sample. Unfortunately, in the case of EG as solvent and reducing agent X-ray beam induced reduction occurs leading to very different size results[175] as compared to the before observed size control depending on the OH^-/Pt ratio.[44,49,50] Therefore, a further investigation of NP formation process seems to be challenging by the common techniques.

However, the polyol process as a colloidal approach has its strength to control the particle size and the support independent of each other. Therefore, the polyol process could be used to synthesis a homemade bimodal catalyst enabling to investigate the degradation mechanism depending on the used supports instead of working with a commercial catalyst mixture with unknown synthesis and treatment conditions. Investigating the catalyst by performing ASTs should be done *operando* but under more realistic conditions than in a flow cell in liquid electrolyte as it was done in manuscript IV and V. I would suggest using a gas diffusion electrode setup and implementing the option of using a Nafion® membrane as the environment of the catalyst is expected to strongly affect its degradation. The analysis of the *operando* SAXS data to investigate the particle size changes during AST protocols should be adjusted by not anymore assuming a model with spheric particle shapes nor a log-normal size distribution of the degraded particles. The combination of *operando* SAXS and WAXS for bimodal systems (not only two Pt populations but also composite catalysts with reduced amount of precious metals) is from my point of view very helpful to get not only information about size changes but also the phase fractions. The possibility to investigate fuel cell catalysts is in general unlimited to all systems. However, a next step would be from my point of view comparing different degradation protocols of the Pt/C bimodal catalyst in *operando* studies.

4.2.2. Synthesis of Electrolyzer Catalysts

A last idea trying to control the particle size of Ir NPs in the Co4Cat process would be the use of surfactants. But a next step is clearly trying to understand the particle formation mechanism,

thereby *in situ* studies are indispensable. A study combining different *in situ* X-ray techniques as done by Mathiesen *et al.*[65] is in progress, where I was involved in data collection. Based on those results, it is hoped to get new insights, e.g., in the intermediates, to systematically adjust the reduction parameters that might enable a size control.

4.2.3. Testing of Electrolyzer Catalysts in a GDE Setup

The next step for testing of electrolyzer catalysts in a GDE setup is from my point of view to establish this technique as testing device. It is therefore inevitable to enable long-time stability measurements with Ti based PTLs. Another topic would be the flushing of water instead of humidified gas through the GDE setup. Due to the lack of hydrophobicity and hence an expected flooding of the uncoated lower part of the GDE, also in the experiment of flushing water through the cell a Ti PTL should be used. A last aspect would be to enable the use of CCMs pressed to Ti PTLs in the GDE setup. For all future experiments, the optimization of the hot-pressing procedure used in manuscript VII is necessary that might include a collaboration to perform professional hot-pressing as done for MEA testing.

5. Acknowledgement

I would like to thank Sebastian Kunz for his excellent supervision and support during the first time of my PhD even in the process of leaving University of Bremen. Furthermore, I would like to thank Matthias Arenz for his excellent supervision and support at University of Bern, for always taking his time to discuss results, to motivate, and to give advice. Additionally, I would like to thank Jonathan Quinson from Copenhagen University for great discussions and collaborations as well as Jacob J. K. Kirkensgaard from Copenhagen University for his support in SAXS data acquisition and analysis.

Thank you very much to my present and former colleagues Shima, Jia, Vlad, Etienne, Nicolas, Aline, Damin, Ilya, Francesco, Alessandro, Jan, Gustav from University of Bern, Rebecca, Jette, Kirsten from Copenhagen University, Sarah, David, Daniel, Jan, as well as Martin, Conny, Vera, Brigitte, Volkmar, Marcus from University of Bremen. In addition, I would like to thank the workshop and the mass spectroscopy service from University of Bern, the mass spectroscopy service from University of Bremen, and Isaac, Jakub, and Raphael from ERSF in Grenoble.

Finally, I want to thank my parents, brothers, and friends for supporting me but also distracting me in the right moments.

6. References

(1) Yoshida, T.; Kojima, K. Toyota MIRAI Fuel Cell Vehicle and Progress Toward a Future Hydrogen Society. *Electrochem. Soc. Interface* **2015**, *24* (2), 45–49. https://doi.org/10.1149/2.F03152if.

(2) Pollet, B. G.; Kocha, S. S.; Staffell, I. Current Status of Automotive Fuel Cells for Sustainable Transport. *Current Opinion in Electrochemistry*. Elsevier August 1, 2019, pp 90–95. https://doi.org/10.1016/j.coelec.2019.04.021.

(3) Schmidt, O.; Gambhir, A.; Staffell, I.; Hawkes, A.; Nelson, J.; Few, S. Future Cost and Performance of Water Electrolysis: An Expert Elicitation Study. *Int. J. Hydrogen Energy* **2017**, *42* (52), 30470–30492. https://doi.org/10.1016/j.ijhydene.2017.10.045.

(4) Daud, W. R. W.; Rosli, R. E.; Majlan, E. H.; Hamid, S. A. A.; Mohamed, R.; Husaini, T. *PEM Fuel Cell System Control: A Review*; Pergamon, 2017; Vol. 113, pp 620–638. https://doi.org/10.1016/J.RENENE.2017.06.027.

(5) Carrette, L.; Friedrich, K. A.; Stimming, U. Fuel Cells - Fundamentals and Applications. *Fuel Cells* **2001**, *1* (1), 5–39. https://doi.org/10.1002/1615-6854(200105)1:1<5::AID-FUCE5>3.0.CO;2-G.

(6) Babic, U.; Suermann, M.; Büchi, F. N.; Gubler, L.; Schmidt, T. J. Critical Review—Identifying Critical Gaps for Polymer Electrolyte Water Electrolysis Development. *J. Electrochem. Soc.* **2017**, *164* (4), F387–F399. https://doi.org/10.1149/2.1441704jes.

(7) He, Q.; Cairns, E. J. Review—Recent Progress in Electrocatalysts for Oxygen Reduction Suitable for Alkaline Anion Exchange Membrane Fuel Cells. *J. Electrochem. Soc.* **2015**, *162* (14), F1504–F1539. https://doi.org/10.1149/2.0551514jes.

(8) Gottesfeld, S.; Dekel, D. R.; Page, M.; Bae, C.; Yan, Y.; Zelenay, P.; Kim, Y. S. Anion Exchange Membrane Fuel Cells: Current Status and Remaining Challenges. *J. Power Sources* **2018**, *375*, 170–184. https://doi.org/10.1016/j.jpowsour.2017.08.010.

(9) Lafforgue, C.; Maillard, F.; Martin, V.; Dubau, L.; Chatenet, M. Degradation of Carbon-Supported Platinum-Group-Metal Electrocatalysts in Alkaline Media Studied by in Situ Fourier Transform Infrared Spectroscopy and Identical-Location Transmission Electron Microscopy. *ACS Catal.* **2019**, 5613–5622. https://doi.org/10.1021/acscatal.9b00439.

(10) Roche, I.; Chaînet, E.; Chatenet, M.; Vondrák, J. Durability of Carbon-Supported Manganese Oxide Nanoparticles for the Oxygen Reduction Reaction (ORR) in Alkaline Medium. *J. Appl. Electrochem.* **2008**, *38* (9), 1195–1201. https://doi.org/10.1007/s10800-008-9537-z.

(11) Buttler, A.; Spliethoff, H. Current Status of Water Electrolysis for Energy Storage, Grid Balancing and Sector Coupling via Power-to-Gas and Power-to-Liquids: A Review. *Renew. Sustain. Energy Rev.* **2018**, *82*, 2440–2454. https://doi.org/10.1016/j.rser.2017.09.003.

(12) Gasteiger, H. A.; Panels, J. E.; Yan, S. G. Dependence of PEM Fuel Cell Performance on Catalyst Loading. *J. Power Sources* **2004**, *127* (1–2), 162–171. https://doi.org/10.1016/j.jpowsour.2003.09.013.

(13) Mathias, M. F.; Makharia, R.; Gasteiger, H. A.; Conley, J. J.; Fuller, T. J.; Gittleman, C. J.; Kocha, S. S.; Miller, D. P.; Mittelsteadt, C. K.; Xie, T.; Van, S. G.; Yu, P. T. Two Fuel Cell Cars in Every Garage? *Electrochemical Society Interface*. September 1, 2005, pp 24–35. https://doi.org/10.1149/2.f05053if.

(14) Hong, W. T.; Risch, M.; Stoerzinger, K. A.; Grimaud, A.; Suntivich, J.; Shao-Horn, Y. Toward the Rational Design of Non-Precious Transition Metal Oxides for Oxygen Electrocatalysis. *Energy and Environmental Science*. 2015, pp 1404–1427. https://doi.org/10.1039/c4ee03869j.

(15) Gasteiger, H. A.; Kocha, S. S.; Sompalli, B.; Wagner, F. T. Activity Benchmarks and Requirements for Pt, Pt-Alloy, and Non-Pt Oxygen Reduction Catalysts for PEMFCs. *Applied Catalysis B: Environmental*. Elsevier March 10, 2005, pp 9–35. https://doi.org/10.1016/j.apcatb.2004.06.021.

(16) Antolini, E. Structural Parameters of Supported Fuel Cell Catalysts: The Effect of Particle Size, Inter-Particle Distance and Metal Loading on Catalytic Activity and Fuel Cell Performance. *Applied Catalysis B: Environmental*. Elsevier February 1, 2016, pp 298–313. https://doi.org/10.1016/j.apcatb.2015.08.007.

(17) Fabbri, E.; Habereder, A.; Waltar, K.; Kötz, R.; Schmidt, T. J. Developments and Perspectives of Oxide-Based Catalysts for the Oxygen Evolution Reaction. *Catal. Sci. Technol.* **2014**, *4* (11), 3800–3821. https://doi.org/10.1039/c4cy00669k.

(18) Antolini, E. Iridium as Catalyst and Cocatalyst for Oxygen Evolution/Reduction in Acidic Polymer Electrolyte Membrane Electrolyzers and Fuel Cells. *ACS Catalysis*. American Chemical Society May 2, 2014, pp 1426–1440. https://doi.org/10.1021/cs4011875.

(19) Stacy, J.; Regmi, Y. N.; Leonard, B.; Fan, M. The Recent Progress and Future of Oxygen Reduction Reaction Catalysis: A Review. *Renew. Sustain. Energy Rev.* **2017**, *69*, 401–414. https://doi.org/10.1016/j.rser.2016.09.135.

(20) Nørskov, J. K.; Rossmeisl, J.; Logadottir, A.; Lindqvist, L.; Kitchin, J. R.; Bligaard, T.; Jónsson, H. Origin of the Overpotential for Oxygen Reduction at a Fuel-Cell Cathode. *J. Phys. Chem. B* **2004**, *108* (46), 17886–17892. https://doi.org/10.1021/jp047349j.

(21) Wilson, M. S.; Gottesfeld, S. *Thin-Film Catalyst Layers for Fuel Cell Electrodes Polymer Electrolyte*; 1992; Vol. 22.

(22) Speder, J.; Spanos, I.; Zana, A.; Kirkensgaard, J. J. K.; Mortensen, K.; Altmann, L.; Bäumer, M.; Arenz, M. From Single Crystal Model Catalysts to Systematic Studies of Supported Nanoparticles. *Surf. Sci.* **2015**, *631*, 278–284. https://doi.org/10.1016/j.susc.2014.05.024.

(23) Bühler, M.; Holzapfel, P.; McLaughlin, D.; Thiele, S. From Catalyst Coated Membranes to Porous Transport Electrode Based Configurations in PEM Water Electrolyzers. *J. Electrochem. Soc.* **2019**, *166* (14), F1070–F1078. https://doi.org/10.1149/2.0581914jes.

(24) Pan, L.; Ott, S.; Dionigi, F.; Strasser, P. Current Challenges Related to the Deployment of Shape-Controlled Pt Alloy Oxygen Reduction Reaction Nanocatalysts into Low Pt-Loaded Cathode Layers of Proton Exchange Membrane Fuel Cells. *Curr. Opin. Electrochem.* **2019**, *18*, 61–71. https://doi.org/10.1016/j.coelec.2019.10.011.

(25) Zalitis, C. M.; Kramer, D.; Kucernak, A. R. Electrocatalytic Performance of Fuel Cell Reactions at Low Catalyst Loading and High Mass Transport. *Phys. Chem. Chem. Phys.* **2013**, *15* (12), 4329–4340. https://doi.org/10.1039/c3cp44431g.

(26) Wiberg, G. K. H.; Fleige, M.; Arenz, M. Gas Diffusion Electrode Setup for Catalyst Testing in Concentrated Phosphoric Acid at Elevated Temperatures. *Rev. Sci. Instrum.* **2015**, *86* (2), 024102. https://doi.org/10.1063/1.4908169.

(27) Inaba, M.; Jensen, A. W.; Sievers, G. W.; Escudero-Escribano, M.; Zana, A.; Arenz,

M. Benchmarking High Surface Area Electrocatalysts in a Gas Diffusion Electrode: Measurement of Oxygen Reduction Activities under Realistic Conditions. *Energy Environ. Sci.* **2018**, *11* (4), 988–994. https://doi.org/10.1039/C8EE00019K.

(28) Alinejad, S.; Inaba, M.; Schröder, J.; Du, J.; Quinson, J.; Zana, A.; Arenz, M. Testing Fuel Cell Catalysts under More Realistic Reaction Conditions: Accelerated Stress Tests in a Gas Diffusion Electrode Setup. *J. Phys. Energy* **2020**, *2* (2), 024003. https://doi.org/10.1088/2515-7655/ab67e2.

(29) Ehelebe, K.; Seeberger, D.; Paul, M. T. Y.; Thiele, S.; Mayrhofer, K. J. J.; Cherevko, S. Evaluating Electrocatalysts at Relevant Currents in a Half-Cell: The Impact of Pt Loading on Oxygen Reduction Reaction. *J. Electrochem. Soc.* **2019**, *166* (16), F1259–F1268. https://doi.org/10.1149/2.0911915jes.

(30) Han, B.; Carlton, C. E.; Kongkanand, A.; Kukreja, R. S.; Theobald, B. R.; Gan, L.; O'Malley, R.; Strasser, P.; Wagner, F. T.; Shao-Horn, Y. Record Activity and Stability of Dealloyed Bimetallic Catalysts for Proton Exchange Membrane Fuel Cells. *Energy Environ. Sci.* **2015**, *8* (1), 258–266. https://doi.org/10.1039/c4ee02144d.

(31) Ma, Z.; Zhang, Y.; Liu, S.; Xu, W.; Wu, L.; Hsieh, Y. C.; Liu, P.; Zhu, Y.; Sasaki, K.; Renner, J. N.; Ayers, K. E.; Adzic, R. R.; Wang, J. X. Reaction Mechanism for Oxygen Evolution on RuO2, IrO2, and RuO2@IrO2 Core-Shell Nanocatalysts. *J. Electroanal. Chem.* **2018**, *819*, 296–305. https://doi.org/10.1016/j.jelechem.2017.10.062.

(32) Marcu, A.; Toth, G.; Kundu, S.; Colmenares, L. C.; Behm, R. J. Ex Situ Testing Method to Characterize Cathode Catalysts Degradation under Simulated Start-up/Shutdown Conditions – A Contribution to Polymer Electrolyte Membrane Fuel Cell Benchmarking. *J. Power Sources* **2012**, *215*, 266–273. https://doi.org/10.1016/j.jpowsour.2012.05.010.

(33) Katsounaros, I.; Cherevko, S.; Zeradjanin, A. R.; Mayrhofer, K. J. J. J. Oxygen Electrochemistry as a Cornerstone for Sustainable Energy Conversion. *Angew. Chemie - Int. Ed.* **2014**, *53* (1), 102–121. https://doi.org/10.1002/anie.201306588.

(34) Speder, J.; Zana, A.; Arenz, M. The Colloidal Tool-Box Approach for Fuel Cell Catalysts: Systematic Study of Perfluorosulfonate-Ionomer Impregnation and Pt Loading. *Catal. Today* **2016**, *262*, 82–89. https://doi.org/10.1016/j.cattod.2015.09.021.

(35) Zana, A.; Speder, J.; Roefzaad, M.; Altmann, L.; Baumer, M.; Arenz, M.; Bäumer, M.; Arenz, M. Probing Degradation by IL-TEM: The Influence of Stress Test Conditions on the Degradation Mechanism. *J. Electrochem. Soc.* **2013**, *160* (6), F608–F615. https://doi.org/10.1149/2.078306jes.

(36) Pizzutilo, E.; Geiger, S.; Grote, J.-P.; Mingers, A.; Mayrhofer, K. J. J.; Arenz, M.; Cherevko, S. On the Need of Improved Accelerated Degradation Protocols (ADPs): Examination of Platinum Dissolution and Carbon Corrosion in Half-Cell Tests. *J. Electrochem. Soc.* **2016**, *163* (14), F1510–F1514. https://doi.org/10.1149/2.0731614jes.

(37) Ehelebe, K.; Knöppel, J.; Bierling, M.; Mayerhöfer, B.; Böhm, T.; Kulyk, N.; Thiele, S.; Mayrhofer, K. J. J.; Cherevko, S. Platinum Dissolution in Realistic Fuel Cell Catalyst Layers. *Angew. Chemie Int. Ed.* **2020**. https://doi.org/10.1002/anie.202014711.

(38) Harada, M.; Einaga, H. Formation Mechanism of Pt Particles by Photoreduction of Pt Ions in Polymer Solutions. *Langmuir* **2006**, *22* (5), 2371–2377. https://doi.org/10.1021/la052378m.

(39) Wang, W.; Chen, X.; Cai, Q.; Mo, G.; Jiang, L. S.; Zhang, K.; Chen, Z. J.; Wu, Z. H.; Pan, W. In Situ SAXS Study on Size Changes of Platinum Nanoparticles with

Temperature. *Eur. Phys. J. B* **2008**, *65* (1), 57–64. https://doi.org/10.1140/epjb/e2008-00322-7.

(40) Steinfeldt, N. In Situ Monitoring of Pt Nanoparticle Formation in Ethylene Glycol Solution by SAXS-Influence of the NaOH to Pt Ratio. *Langmuir* **2012**, *28* (36), 13072–13079. https://doi.org/10.1021/la3026232.

(41) Cargnello, M.; Chen, C.; Diroll, B. T.; Doan-Nguyen, V. V. T.; Gorte, R. J.; Murray, C. B. Efficient Removal of Organic Ligands from Supported Nanocrystals by Fast Thermal Annealing Enables Catalytic Studies on Well-Defined Active Phases. *J. Am. Chem. Soc.* **2015**, *137* (21), 6906–6911. https://doi.org/10.1021/jacs.5b03333.

(42) Huang, W.; Hua, Q.; Cao, T. Influence and Removal of Capping Ligands on Catalytic Colloidal Nanoparticles. *Catal. Letters* **2014**, *144* (8), 1355–1369. https://doi.org/10.1007/s10562-014-1306-5.

(43) Wang, Y.; Ren, J.; Deng, K.; Gui, L.; Tang, Y. Preparation of Tractable Platinum, Rhodium, and Ruthenium Nanoclusters with Small Particle Size in Organic Media. *Chem. Mater.* **2000**, *9*, 1622–1627. https://doi.org/10.1021/cm0000853.

(44) Schrader, I.; Warneke, J.; Neumann, S.; Grotheer, S.; Swane, A. A.; Kirkensgaard, J. J. K.; Arenz, M.; Kunz, S. Surface Chemistry of "Unprotected" Nanoparticles: A Spectroscopic Investigation on Colloidal Particles. *J. Phys. Chem. C* **2015**, *119* (31), 17655–17661. https://doi.org/10.1021/acs.jpcc.5b03863.

(45) Comotti, M.; Li, W. C.; Spliethoff, B.; Schüth, F. Support Effect in High Activity Gold Catalysts for CO Oxidation. *J. Am. Chem. Soc.* **2006**, *128* (3), 917–924. https://doi.org/10.1021/ja0561441.

(46) Wang, Y.; Ren, J.; Deng, K.; Gui, L.; Tang, Y. Preparation of Tractable Platinum , Rhodium , and Ruthenium Nanoclusters with Small Particle Size in Organic Media Preparation of Tractable Platinum , Rhodium , and Ruthenium Nanoclusters with Small Particle Size in Organic Media. *Chem. Mater.* **2000**, No. 9, 1622–1627. https://doi.org/10.1021/cm0000853.

(47) Arminio-Ravelo, J. A.; Quinson, J.; Pedersen, M. A.; Kirkensgaard, J. J. K.; Arenz, M.; Escudero-Escribano, M. Synthesis of Iridium Nanocatalysts for Water Oxidation in Acid: Effect of the Surfactant. *ChemCatChem* **2020**, *12* (5), 1282–1287. https://doi.org/10.1002/cctc.201902190.

(48) Bizzotto, F.; Quinson, J.; Schröder, J.; Zana, A.; Arenz, M. Surfactant-Free Colloidal Strategies for Highly Dispersed and Active Supported IrO2 Catalysts: Synthesis and Performance Evaluation for the Oxygen Evolution Reaction. *J. Catal.* **2021**. https://doi.org/10.1016/J.JCAT.2021.07.004.

(49) Kacenauskaite, L.; Quinson, J.; Schultz, H.; Kirkensgaard, J. J. K.; Kunz, S.; Vosch, T.; Arenz, M. UV-Induced Synthesis and Stabilization of Surfactant-Free Colloidal Pt Nanoparticles with Controlled Particle Size in Ethylene Glycol. *ChemNanoMat* **2017**, *3* (2), 89–93. https://doi.org/10.1002/cnma.201600313.

(50) Quinson, J.; Inaba, M.; Neumann, S.; Swane, A. A.; Bucher, J.; Simonsen, S. B.; Theil Kuhn, L.; Kirkensgaard, J. J. K.; Jensen, K. M. Ø.; Oezaslan, M.; Kunz, S.; Arenz, M. Investigating Particle Size Effects in Catalysis by Applying a Size-Controlled and Surfactant-Free Synthesis of Colloidal Nanoparticles in Alkaline Ethylene Glycol: Case Study of the Oxygen Reduction Reaction on Pt. *ACS Catal.* **2018**, *8* (7), 6627–6635. https://doi.org/10.1021/acscatal.8b00694.

(51) Kacenauskaite, L.; Swane, A. A.; Kirkensgaard, J. J. K.; Fleige, M.; Kunz, S.; Vosch,

T.; Arenz, M. Synthesis Mechanism and Influence of Light on Unprotected Platinum Nanoparticles Synthesis at Room Temperature. *ChemNanoMat* **2016**, *2* (2), 104–107. https://doi.org/10.1002/cnma.201500118.

(52) Bock, C.; Paquet, C.; Couillard, M.; Botton, G. A.; MacDougall, B. R. Size-Selected Synthesis of PtRu Nano-Catalysts: Reaction and Size Control Mechanism. *J. Am. Chem. Soc.* **2004**, *126* (25), 8028–8037. https://doi.org/10.1021/ja0495819.

(53) Neumann, S.; Grotheer, S.; Tielke, J.; Schrader, I.; Quinson, J.; Zana, A.; Oezaslan, M.; Arenz, M.; Kunz, S. Nanoparticles in a Box: A Concept to Isolate, Store and Re-Use Colloidal Surfactant-Free Precious Metal Nanoparticles. *J. Mater. Chem. A* **2017**, *5* (13), 6140–6145. https://doi.org/10.1039/C7TA00628D.

(54) Neumann, S.; Schröder, J.; Bizzotto, F.; Arenz, M.; Dworzak, A.; Oezaslan, M.; Bäumer, M.; Kunz, S. Halide-Induced Leaching of Pt Nanoparticles – Manipulation of Particle Size by Controlled Ostwald Ripening. *ChemNanoMat* **2019**, *5*, 462–471. https://doi.org/10.1002/cnma.201800550.

(55) Neumann, S.; Gutmann, T.; Buntkowsky, G.; Paul, S.; Thiele, G.; Sievers, H.; Bäumer, M.; Kunz, S. Insights into the Reaction Mechanism and Particle Size Effects of CO Oxidation over Supported Pt Nanoparticle Catalysts. *J. Catal.* **2019**, *377*, 662–672. https://doi.org/10.1016/j.jcat.2019.07.049.

(56) Speder, J.; Altmann, L.; Roefzaad, M.; Bäumer, M.; Kirkensgaard, J. J. K. K.; Mortensen, K.; Arenz, M. Pt Based PEMFC Catalysts Prepared from Colloidal Particle Suspensions – a Toolbox for Model Studies. *Phys. Chem. Chem. Phys.* **2013**, *15* (10), 3602. https://doi.org/10.1039/c3cp50195g.

(57) Toshima, N.; Yonezawa, T. Bimetallic Nanoparticles—Novel Materials for Chemical and Physical Applications. *New J. Chem.* **1998**, *22* (11), 1179–1201. https://doi.org/10.1039/a805753b.

(58) Quinson, J.; Bucher, J.; Simonsen, S. B.; Kuhn, L. T.; Kunz, S.; Arenz, M. Monovalent Alkali Cations: Simple and Eco-Friendly Stabilizers for Surfactant-Free Precious Metal Nanoparticle Colloids. *ACS Sustain. Chem. Eng.* **2019**, *7* (16), 13680–13686. https://doi.org/10.1021/acssuschemeng.9b00681.

(59) Mayrhofer, K. J. J.; Kreuzer, J.; Arenz, M.; Ashton, S. J. An Electrochemical Cell Configuration Incorporating an Ion\nConducting Membrane Separator between Reference And\nWorking Electrode. *Int. J. Electrochem. Sci.* **2009**, *4* (1), 1–8.

(60) Kunz, S.; Arenz, M.; Quinson, J. Improved Precious Metal Nanoparticles. EP332990A1, US20190308155A1, November 29, 2017.

(61) Quinson, J.; Neumann, S.; Wannmacher, T.; Kacenauskaite, L.; Inaba, M.; Bucher, J.; Bizzotto, F.; Simonsen, S. B.; Theil Kuhn, L.; Bujak, D.; Zana, A.; Arenz, M.; Kunz, S. Colloids for Catalysts: A Concept for the Preparation of Superior Catalysts of Industrial Relevance. *Angew. Chemie Int. Ed.* **2018**, *57* (38), 12338–12341. https://doi.org/10.1002/anie.201807450.

(62) Quinson, J.; Kacenauskaite, L.; Bucher, J.; Simonsen, S. B.; Theil Kuhn, L.; Oezaslan, M.; Kunz, S.; Arenz, M. Controlled Synthesis of Surfactant-Free Water-Dispersible Colloidal Platinum Nanoparticles by the Co4Cat Process. *ChemSusChem* **2019**, *12* (6), 1229–1239. https://doi.org/10.1002/cssc.201802897.

(63) Quinson, J.; Mathiesen, J. K.; Schröder, J.; Dworzak, A.; Bizzotto, F.; Zana, A.; Simonsen, S. B.; Theil Kuhn, L.; Oezaslan, M.; Jensen, K. M. Ø.; Arenz, M. Teaching Old Precursors New Tricks: Fast Room Temperature Synthesis of Surfactant-Free

Colloidal Platinum Nanoparticles. *J. Colloid Interface Sci.* **2020**, *577*, 319–328. https://doi.org/10.1016/j.jcis.2020.05.078.

(64) Quinson, J.; Neumann, S.; Kacenauskaite, L.; Bucher, J.; Kirkensgaard, J. J. K.; Simonsen, S. B.; Theil Kuhn, L.; Zana, A.; Vosch, T.; Oezaslan, M.; Kunz, S.; Arenz, M. Solvent-Dependent Growth and Stabilization Mechanisms of Surfactant-Free Colloidal Pt Nanoparticles. *Chem. – A Eur. J.* **2020**, *26* (41), 9012–9023. https://doi.org/10.1002/chem.202001553.

(65) Mathiesen, J. K.; Quinson, J.; Dworzak, A.; Vosch, T.; Juelsholt, M.; Kjær, E. T. S.; Schröder, J.; Kirkensgaard, J. J. K.; Oezaslan, M.; Arenz, M.; Jensen, K. M. Ø. Insights from In Situ Studies on the Early Stages of Platinum Nanoparticle Formation. *J. Phys. Chem. Lett.* **2021**, *12* (12), 3224–3231. https://doi.org/10.1021/acs.jpclett.1c00241.

(66) Bizzotto, F.; Quinson, J.; Zana, A.; Kirkensgaard, J. J. K.; Dworzak, A.; Oezaslan, M.; Arenz, M. Ir Nanoparticles with Ultrahigh Dispersion as Oxygen Evolution Reaction (OER) Catalysts: Synthesis and Activity Benchmarking. *Catal. Sci. Technol.* **2019**, *9* (22), 6345–6356. https://doi.org/10.1039/C9CY01728C.

(67) Sugimoto, T.; Shiba, F.; Sekiguchi, T.; Itoh, H. Spontaneous Nucleation of Monodisperse Silver Halide Particles from Homogeneous Gelatin Solution I: Silver Chloride. *Colloids Surfaces A Physicochem. Eng. Asp.* **2000**, *164* (2–3), 183–203. https://doi.org/10.1016/S0927-7757(99)00366-0.

(68) Sugimoto, T.; Shiba, F. Spontaneous Nucleation of Monodisperse Silver Halide Particles from Homogeneous Gelatin Solution II: Silver Bromide. *Colloids Surfaces A Physicochem. Eng. Asp.* **2000**, *164* (2–3), 205–215. https://doi.org/10.1016/S0927-7757(99)00365-9.

(69) Park, B. K.; Jeong, S.; Kim, D.; Moon, J.; Lim, S.; Kim, J. S. Synthesis and Size Control of Monodisperse Copper Nanoparticles by Polyol Method. *J. Colloid Interface Sci.* **2007**, *311* (2), 417–424. https://doi.org/10.1016/J.JCIS.2007.03.039.

(70) Chee, S. S.; Lee, J. H. Preparation and Oxidation Behavior of Ag-Coated Cu Nanoparticles Less than 20 Nm in Size. *J. Mater. Chem. C* **2014**. https://doi.org/10.1039/c4tc00509k.

(71) Thanh, N. T. K.; Maclean, N.; Mahiddine, S. Mechanisms of Nucleation and Growth of Nanoparticles in Solution. *Chem. Rev.* **2014**, *114* (15), 7610–7630. https://doi.org/10.1021/cr400544s.

(72) Polte, J. Fundamental Growth Principles of Colloidal Metal Nanoparticles – a New Perspective. *CrystEngComm* **2015**, *17* (36), 6809–6830. https://doi.org/10.1039/C5CE01014D.

(73) Xia, Y.; Gilroy, K. D.; Peng, H. C.; Xia, X. Seed-Mediated Growth of Colloidal Metal Nanocrystals. *Angew. Chemie - Int. Ed.* **2017**, *56* (1), 60–95. https://doi.org/10.1002/anie.201604731.

(74) Kunz, S.; Iglesia, E. Mechanistic Evidence for Sequential Displacement-Reduction Routes in the Synthesis of Pd-Au Clusters with Uniform Size and Clean Surfaces. *J. Phys. Chem. C* **2014**, *118* (14), 7468–7479. https://doi.org/10.1021/jp500537v.

(75) Hwang, B.-J.; Sarma, L. S.; Chen, C.-H.; Bock, C.; Lai, F.-J.; Chang, S.-H.; Yen, S.-C.; Liu, D.-G.; Sheu, H.-S.; Lee, J.-F. Controlled Synthesis and Characterization of Ru $_{Core}$−Pt $_{Shell}$Bimetallic Nanoparticles. *J. Phys. Chem. C* **2008**, *112* (50), 19922–19929. https://doi.org/10.1021/jp807154a.

(76) Pinaud, B. A.; Bonakdarpour, A.; Daniel, L.; Sharman, J.; Wilkinson, D. P. Key

Considerations for High Current Fuel Cell Catalyst Testing in an Electrochemical Half-Cell. *J. Electrochem. Soc.* **2017**, *164* (4), F321–F327. https://doi.org/10.1149/2.0891704jes.

(77) Inaba, M.; Quinson, J.; Arenz, M. PH Matters: The Influence of the Catalyst Ink on the Oxygen Reduction Activity Determined in Thin Film Rotating Disk Electrode Measurements. *J. Power Sources* **2017**, *353*, 19–27. https://doi.org/10.1016/j.jpowsour.2017.03.140.

(78) Kongkanand, A.; Mathias, M. F. The Priority and Challenge of High-Power Performance of Low-Platinum Proton-Exchange Membrane Fuel Cells. *J. Phys. Chem. Lett.* **2016**, *7* (7), 1127–1137. https://doi.org/10.1021/acs.jpclett.6b00216.

(79) Carmo, M.; Fritz, D. L.; Mergel, J.; Stolten, D. A Comprehensive Review on PEM Water Electrolysis. *Int. J. Hydrogen Energy* **2013**, *38* (12), 4901–4934. https://doi.org/10.1016/j.ijhydene.2013.01.151.

(80) Yarlagadda, V.; McKinney, S. E.; Keary, C. L.; Thompson, L.; Zulevi, B.; Kongkanand, A. Preparation of PEMFC Electrodes from Milligram-Amounts of Catalyst Powder. *J. Electrochem. Soc.* **2017**, *164* (7), F845–F849. https://doi.org/10.1149/2.1461707jes.

(81) Carmo, M.; Fritz, D. L.; Mergel, J.; Stolten, D. A Comprehensive Review on PEM Water Electrolysis. *Int. J. Hydrogen Energy* **2013**, *38* (12), 4901–4934. https://doi.org/10.1016/j.ijhydene.2013.01.151.

(82) Rakousky, C.; Reimer, U.; Wippermann, K.; Carmo, M.; Lueke, W.; Stolten, D. An Analysis of Degradation Phenomena in Polymer Electrolyte Membrane Water Electrolysis. *J. Power Sources* **2016**, *326*, 120–128. https://doi.org/10.1016/J.JPOWSOUR.2016.06.082.

(83) Park, Y.-C.; Kakinuma, K.; Uchida, M.; Tryk, D. A.; Kamino, T.; Uchida, H.; Watanabe, M. Investigation of the Corrosion of Carbon Supports in Polymer Electrolyte Fuel Cells Using Simulated Start-up/Shutdown Cycling. *Electrochim. Acta* **2013**, *91*, 195–207. https://doi.org/10.1016/j.electacta.2012.12.082.

(84) Ohma, A.; Shinohara, K.; Iiyama, A.; Yoshida, T.; Daimaru, A. Membrane and Catalyst Performance Targets for Automotive Fuel Cells by FCCJ Membrane, Catalyst, MEA WG. *ECS Trans.* **2011**, *41* (1), 775–784. https://doi.org/10.1149/1.3635611.

(85) Meier, J. C.; Galeano, C.; Katsounaros, I.; Topalov, A. A.; Kostka, A.; Schüth, F.; Mayrhofer, K. J. J. Degradation Mechanisms of Pt/C Fuel Cell Catalysts under Simulated Start–Stop Conditions. *ACS Catal.* **2012**, *2* (5), 832–843. https://doi.org/10.1021/cs300024h.

(86) Alia, S. M.; Rasimick, B.; Ngo, C.; Neyerlin, K. C.; Kocha, S. S.; Pylypenko, S.; Xu, H.; Pivovar, B. S. Activity and Durability of Iridium Nanoparticles in the Oxygen Evolution Reaction. *J. Electrochem. Soc.* **2016**, *163* (11), F3105–F3112. https://doi.org/10.1149/2.0151611jes.

(87) El-Sayed, H. A.; Weiß, A.; Olbrich, L. F.; Putro, G. P.; Gasteiger, H. A. OER Catalyst Stability Investigation Using RDE Technique: A Stability Measure or an Artifact? *J. Electrochem. Soc.* **2019**, *166* (8), F458–F464. https://doi.org/10.1149/2.0301908jes.

(88) Hartig-Weiss, A.; Tovini, M. F.; Gasteiger, H. A.; El-Sayed, H. A. OER Catalyst Durability Tests Using the Rotating Disk Electrode Technique: The Reason Why This Leads to Erroneous Conclusions. *ACS Appl. Energy Mater.* **2020**, *3* (11), 10323–10327. https://doi.org/10.1021/acsaem.0c01944.

(89) Wiberg, G. K. H.; Mayrhofer, K. J. J.; Arenz, M. Investigation of the Oxygen Reduction Activity on Silver - A Rotating Disc Electrode Study. *Fuel Cells* **2010**, *10* (4), 575–581. https://doi.org/10.1002/fuce.200900136.

(90) Chang, S. C.; Leung, L. W. H.; Weaver, M. J. Comparisons between Coverage-Dependent Infrared Frequencies for Carbon Monoxide Adsorbed on Ordered Pt(111), Pt(100), and Pt(110) in Electrochemical and Ultrahigh-Vacuum Environments. *J. Phys. Chem.* **1989**, *93* (14), 5341–5345. https://doi.org/10.1021/j100351a006.

(91) Inaba, M.; Quinson, J.; Bucher, J. R.; Arenz, M. On the Preparation and Testing of Fuel Cell Catalysts Using the Thin Film Rotating Disk Electrode Method. *J. Vis. Exp.* **2018**, *133* (133), e57105. https://doi.org/10.3791/57105.

(92) Perkampus, H.-H. Principles. In *UV-VIS Spectroscopy and Its Applications*; Springer Berlin Heidelberg: Berlin, Heidelberg, 1992; pp 3–9. https://doi.org/10.1007/978-3-642-77477-5_2.

(93) WORKMAN, J. OPTICAL SPECTROMETERS. In *Applied Spectroscopy: A Compact Reference for Practitioners*; Workman, J., Ed.; Elsevier, 1998; pp 3–28. https://doi.org/10.1016/B978-012764070-9/50003-2.

(94) Williams, D. B.; Carter, C. B. *Transmission Electron Microscopy: A Textbook for Materials Sciences*; Springer US: Boston, MA, 2009. https://doi.org/10.1007/978-0-387-76501-3.

(95) Arenz, M.; Zana, A. Fuel Cell Catalyst Degradation: Identical Location Electron Microscopy and Related Methods. *Nano Energy* **2016**, *29*, 299–313. https://doi.org/10.1016/j.nanoen.2016.04.027.

(96) Quinson, J.; Kacenauskaite, L.; Christiansen, T. L.; Vosch, T.; Arenz, M.; Jensen, K. M. Ø. Spatially Localized Synthesis and Structural Characterization of Platinum Nanocrystals Obtained Using UV Light. *ACS Omega* **2018**, *3* (8), 10351–10356. https://doi.org/10.1021/acsomega.8b01613.

(97) Perez-Alonso, F. J.; Elkjær, C. F.; Shim, S. S.; Abrams, B. L.; Stephens, I. E. L.; Chorkendorff, I. B. Identical Locations Transmission Electron Microscopy Study of Pt/C Electrocatalyst Degradation during Oxygen Reduction Reaction. *J. Power Sources* **2011**, *196* (15), 6085–6091. https://doi.org/10.1016/j.jpowsour.2011.03.064.

(98) Schlögl, K.; Mayrhofer, K. J. J.; Hanzlik, M.; Arenz, M. Identical-Location TEM Investigations of Pt/C Electrocatalyst Degradation at Elevated Temperatures. *J. Electroanal. Chem.* **2011**, *662* (2), 355–360. https://doi.org/10.1016/j.jelechem.2011.09.003.

(99) Hartl, K.; Hanzlik, M.; Arenz, M. IL-TEM Investigations on the Degradation Mechanism of Pt/C Electrocatalysts with Different Carbon Supports. *Energy Environ. Sci.* **2011**, *4* (1), 234–238. https://doi.org/10.1039/C0EE00248H.

(100) Hodnik, N.; Zorko, M.; Bele, M.; Hočevar, S.; Gaberšček, M. Identical Location Scanning Electron Microscopy: A Case Study of Electrochemical Degradation of PtNi Nanoparticles Using a New Nondestructive Method. *J. Phys. Chem. C* **2012**, *116* (40), 21326–21333. https://doi.org/10.1021/jp303831c.

(101) Speder, J.; Zana, A.; Spanos, I.; Kirkensgaard, J. J. K. K.; Mortensen, K.; Hanzlik, M.; Arenz, M. Comparative Degradation Study of Carbon Supported Proton Exchange Membrane Fuel Cell Electrocatalysts - The Influence of the Platinum to Carbon Ratio on the Degradation Rate. *J. Power Sources* **2014**, *261*, 14–22. https://doi.org/10.1016/j.jpowsour.2014.03.039.

(102) Arán-Ais, R. M.; Yu, Y.; Hovden, R.; Solla-Gullón, J.; Herrero, E.; Feliu, J. M.;

Abruña, H. D. Identical Location Transmission Electron Microscopy Imaging of Site-Selective Pt Nanocatalysts: Electrochemical Activation and Surface Disordering. *J. Am. Chem. Soc.* **2015**, *137* (47), 14992–14998. https://doi.org/10.1021/jacs.5b09553.

(103) Arenz, M.; Zana, A. Fuel Cell Catalyst Degradation: Identical Location Electron Microscopy and Related Methods. *Nano Energy* **2016**, *29*, 299–313. https://doi.org/10.1016/j.nanoen.2016.04.027.

(104) Zhou, W.; Wang, Z. L. *Scanning Microscopy for Nanotechnology: Tequniques and Applications*; Zhou, W., Wang, Z. L., Eds.; Springer: New York, 2006. https://doi.org/10.1007/978-0-387-39620-0.

(105) Raftery, T.; Gilles, R. JCPDS-International Centre for Diffraction Data Round Robin Study of Silver Behenate. A Possible Low-Angle X-Ray Diffraction Calibration Standard. *Powder Diffr.* **1995**, *10* (2), 91–95. https://doi.org/10.1017/S0885715600014421.

(106) Grishaev, A. Sample Preparation, Data Collection, and Preliminary Data Analysis in Biomolecular Solution X-Ray Scattering. *Curr. Protoc. Protein Sci.* **2012**, *1* (SUPPL.70), Unit17.14. https://doi.org/10.1002/0471140864.ps1714s70.

(107) Huang, T. C.; Toraya, H.; Blanton, T. N.; Wu, Y. X-Ray Powder Diffraction Analysis of Silver Behenate, a Possible Low-Angle Diffraction Standard. *J. Appl. Crystallogr.* **1993**, *26* (pt 2), 180–184. https://doi.org/10.1107/S0021889892009762.

(108) Pauw, B. R. Everything SAXS: Small-Angle Scattering Pattern Collection and Correction. *J. Phys. Condens. Matter* **2014**, *26* (23). https://doi.org/10.1088/0953-8984/26/23/239501.

(109) Dreiss, C. A.; Jack, K. S.; Parker, A. P. On the Absolute Calibration of Bench-Top Small-Angle X-Ray Scattering Instruments: A Comparison of Different Standard Methods. *J. Appl. Crystallogr.* **2006**, *39* (1), 32–38. https://doi.org/10.1107/S0021889805033091.

(110) Binninger, T.; Garganourakis, M.; Han, J.; Patru, A.; Fabbri, E.; Sereda, O.; Kötz, R.; Menzel, A.; Schmidt, T. J. Particle-Support Interferences in Small-Angle X-Ray Scattering from Supported-Catalyst Materials. *Phys. Rev. Appl.* **2015**, *3* (2), 024012(6). https://doi.org/10.1103/PhysRevApplied.3.024012.

(111) Chaâbane, N.; Lazzari, R.; Jupille, J.; Renaud, G.; Avellar Soares, E. CO-Induced Scavenging of Supported Pt Nanoclusters: A GISAXS Study. *J. Phys. Chem. C* **2012**, *116* (44), 23362–23370. https://doi.org/10.1021/jp306496t.

(112) Ruge, M.; Drnec, J.; Rahn, B.; Reikowski, F.; Harrington, D. A.; Carlà, F.; Felici, R.; Stettner, J.; Magnussen, O. M. Structural Reorganization of Pt(111) Electrodes by Electrochemical Oxidation and Reduction. *J. Am. Chem. Soc.* **2017**, *139* (12), 4532–4539. https://doi.org/10.1021/jacs.7b01039.

(113) Khalakhan, I.; Bogar, M.; Vorokhta, M.; Kúš, P.; Yakovlev, Y.; Dopita, M.; Sandbeck, D. J. S.; Cherevko, S.; Matolínová, I.; Amenitsch, H. Evolution of the PtNi Bimetallic Alloy Fuel Cell Catalyst under Simulated Operational Conditions. *ACS Appl. Mater. Interfaces* **2020**, *12* (15), 17602–17610. https://doi.org/10.1021/acsami.0c02083.

(114) Binninger, T.; Fabbri, E.; Patru, A.; Garganourakis, M.; Han, J.; Abbott, D. F.; Sereda, O.; Kötz, R.; Menzel, A.; Nachtegaal, M.; Schmidt, T. J. Electrochemical Flow-Cell Setup for in Situ X-Ray Investigations: I. Cell for SAXS and XAS at Synchrotron Facilities. *J. Electrochem. Soc.* **2016**, *163* (10), H906–H912. https://doi.org/10.1149/2.0201610jes.

(115) Li, T.; Senesi, A. J.; Lee, B. Small Angle X-Ray Scattering for Nanoparticle Research.

Chem. Rev. **2016**, *116* (18), 11128–11180. https://doi.org/10.1021/acs.chemrev.5b00690.

(116) Tillier, J.; Binninger, T.; Garganourakis, M.; Patru, A.; Fabbri, E.; Schmidt, T. J.; Sereda, O. Electrochemical Flow-Cell Setup for In Situ X-Ray Investigations II. Cell for SAXS on a Multi-Purpose Laboratory Diffractometer. *J. Electrochem. Soc.* **2016**, *163* (10), H913–H920. https://doi.org/10.1149/2.0211610jes.

(117) Kajiwara, K.; Hiragi, Y. Chapter 6 Structure Analysis by Small-Angle X-Ray Scattering. *Anal. Spectrosc. Libr.* **1996**, *7* (C), 353–404. https://doi.org/10.1016/S0926-4345(96)80007-1.

(118) Callejas-Fernández, J.; Ramos, J.; Sanz, O.; Forcada, J.; Ortega-Vinuesa, J. L.; Martín-Molina, A.; Rodríguez-Valverde, M. A.; Tirado-Miranda, M.; Schmitt, A.; Sierra-Martin, B.; Maldonadovaldivia, A.; Fernández-Barbero, A.; Pons, R.; Capitán-Vallvey, L. F.; Salinas-Castillo, A.; Lapresta-Fernández, A.; Vázquez, B.; Aguilar, M. R.; San Román, J.; Maldonado-Valdivia, A.; Fernández-Barbero, A.; Pons, R.; Capitán-Vallvey, L. F.; Salinas-Castillo, A.; Lapresta-Fernández, A.; Vázquez, B.; Aguilar, M. R.; San Román, J. *Experimental Techniques Used for the Characterization of Soft Nanoparticles*; 2014. https://doi.org/10.1039/9781782625216-00019.

(119) Garcia, P. R. A. F.; Prymak, O.; Grasmik, V.; Pappert, K.; Wlysses, W.; Otubo, L.; Epple, M.; Oliveira, C. L. P. An in Situ SAXS Investigation of the Formation of Silver Nanoparticles and Bimetallic Silver–Gold Nanoparticles in Controlled Wet-Chemical Reduction Synthesis. *Nanoscale Adv.* **2020**, *2* (1), 225–238. https://doi.org/10.1039/C9NA00569B.

(120) Haubold, H. G.; Wang, X. H.; Jungbluth, H.; Goerigk, G.; Schilling, W. In Situ Anomalous Small-Angle X-Ray Scattering and X-Ray Absorption near-Edge Structure Investigation of Catalyst Structures and Reactions. *J. Mol. Struct.* **1996**, *383* (1–3), 283–289. https://doi.org/10.1016/S0022-2860(96)09300-3.

(121) Sinharay, S. Continuous Probability Distributions. In *International Encyclopedia of Education*; Elsevier, 2010; pp 98–102. https://doi.org/10.1016/B978-0-08-044894-7.01720-6.

(122) Wang, Y.; Zhang, J.; Wang, X.; Ren, J.; Zuo, B.; Tang, Y. Metal Nanoclusters Stabilized with Simple Ions and Solvents - Promising Building Blocks for Future Catalysts. *Top. Catal.* **2005**, *35* (1–2), 35–41. https://doi.org/10.1007/s11244-005-3811-7.

(123) Corain, B.; Schmid, G.; Toshima, N. *Metal Nanoclusters in Catalysis and Materials Science: The Issue of Size Control*; Elsevier, 2008. https://doi.org/10.1016/B978-0-444-53057-8.X5001-6.

(124) Wang, X.; Sonström, P.; Arndt, D.; Stöver, J.; Zielasek, V.; Borchert, H.; Thiel, K.; Al-Shamery, K.; Bäumer, M. Heterogeneous Catalysis with Supported Platinum Colloids: A Systematic Study of the Interplay between Support and Functional Ligands. *J. Catal.* **2011**, *278* (1), 143–152. https://doi.org/10.1016/j.jcat.2010.11.020.

(125) Markoví, N. M.; Ross, P. N. Surface Science Studies of Model Fuel Cell Electrocatalysts. *Surf. Sci. Rep.* **2002**, *45*, 117–229. https://doi.org/10.1016/s0167-5729(01)00022-x.

(126) Stamenkovic, V. R.; Mun, B. S.; Arenz, M.; Mayrhofer, K. J. J.; Lucas, C. A.; Wang, G.; Ross, P. N.; Markovic, N. M. Trends in Electrocatalysis on Extended and Nanoscale Pt-Bimetallic Alloy Surfaces. *Nat. Mater.* **2007**, *6* (3), 241–247. https://doi.org/10.1038/nmat1840.

(127) Wang, D.; Xin, H. L.; Hovden, R.; Wang, H.; Yu, Y.; Muller, D. A.; DiSalvo, F. J.; Abruña, H. D. Structurally Ordered Intermetallic Platinum–Cobalt Core–Shell Nanoparticles with Enhanced Activity and Stability as Oxygen Reduction Electrocatalysts. *Nat. Mater.* **2013**, *12* (1), 81–87. https://doi.org/10.1038/nmat3458.

(128) Debe, M. K. Electrocatalyst Approaches and Challenges for Automotive Fuel Cells. *Nature* **2012**, *486* (7401), 43–51. https://doi.org/10.1038/nature11115.

(129) Han, B.; Carlton, C. E.; Suntivich, J.; Xu, Z.; Shao-Horn, Y. Oxygen Reduction Activity and Stability Trends of Bimetallic Pt0.5M0.5 Nanoparticle in Acid. *J. Phys. Chem. C* **2015**, *119* (8), 3971–3978. https://doi.org/10.1021/jp5129904.

(130) Zana, A.; Speder, J.; Reeler, N. E. A.; Vosch, T.; Arenz, M. Investigating the Corrosion of High Surface Area Carbons during Start/Stop Fuel Cell Conditions: A Raman Study. *Electrochim. Acta* **2013**, *114*, 455–461. https://doi.org/10.1016/j.electacta.2013.10.097.

(131) Nagai, T.; Murata, H.; Morimoto, Y. Influence of Experimental Conditions on the Catalyst Degradation in the Durability Test. *J. Electrochem. Soc.* **2014**, *161* (6), F789–F794. https://doi.org/10.1149/2.109406jes.

(132) Ferreira, P. J.; la O', G. J.; Shao-Horn, Y.; Morgan, D.; Makharia, R.; Kocha, S.; Gasteiger, H. A.; La O', G. J.; Shao-Horn, Y.; Morgan, D.; Makharia, R.; Kocha, S.; Gasteiger, H. A. Instability of Pt/C Electrocatalysts in Proton Exchange Membrane Fuel Cells. *J. Electrochem. Soc.* **2005**, *152* (11), A2256. https://doi.org/10.1149/1.2050347.

(133) Nesselberger, M.; Ashton, S.; Meier, J. C.; Katsounaros, I.; Mayrhofer, K. J. J.; Arenz, M. The Particle Size Effect on the Oxygen Reduction Reaction Activity of Pt Catalysts: Influence of Electrolyte and Relation to Single Crystal Models. *J. Am. Chem. Soc.* **2011**, *133* (43), 17428–17433. https://doi.org/10.1021/ja207016u.

(134) Herrero, E.; Feliu, J. M.; Blais, S.; Radovic-Hrapovic, Z.; Jerkiewicz, G. Temperature Dependence of CO Chemisorption and Its Oxidative Desorption on the Pt(111) Electrode. *Langmuir* **2000**, *16* (11), 4779–4783. https://doi.org/10.1021/la9907432.

(135) Keeley, G. P.; Cherevko, S.; Mayrhofer, K. J. J. The Stability Challenge on the Pathway to Low and Ultra-Low Platinum Loading for Oxygen Reduction in Fuel Cells. *ChemElectroChem* **2016**, *3* (1), 51–54. https://doi.org/10.1002/celc.201500425.

(136) Kasian, O.; Geiger, S.; Mayrhofer, K. J. J.; Cherevko, S. *Electrochemical On-Line ICP-MS in Electrocatalysis Research*; John Wiley and Sons Inc., 2019; Vol. 19, pp 2130–2142. https://doi.org/10.1002/tcr.201800162.

(137) Holby, E. F.; Sheng, W.; Shao-Horn, Y.; Morgan, D. Pt Nanoparticle Stability in PEM Fuel Cells: Influence of Particle Size Distribution and Crossover Hydrogen. *Energy Environ. Sci.* **2009**, *2* (8), 865. https://doi.org/10.1039/b821622n.

(138) Kocha, S. S.; Shinozaki, K.; Zack, J. W.; Myers, D. J.; Kariuki, N. N.; Nowicki, T.; Stamenkovic, V.; Kang, Y.; Li, D.; Papageorgopoulos, D. Best Practices and Testing Protocols for Benchmarking ORR Activities of Fuel Cell Electrocatalysts Using Rotating Disk Electrode. *Electrocatalysis* **2017**, *8* (4), 366–374. https://doi.org/10.1007/s12678-017-0378-6.

(139) Mayrhofer, K. J. J.; Meier, J. C.; Ashton, S. J.; Wiberg, G. K. H.; Kraus, F.; Hanzlik, M.; Arenz, M. Fuel Cell Catalyst Degradation on the Nanoscale. *Electrochem. commun.* **2008**, *10* (8), 1144–1147. https://doi.org/10.1016/j.elecom.2008.05.032.

(140) Speder, J.; Zana, A.; Spanos, I.; Kirkensgaard, J. J. K. K.; Mortensen, K.; Arenz, M. On the Influence of the Pt to Carbon Ratio on the Degradation of High Surface Area Carbon Supported PEM Fuel Cell Electrocatalysts. *Electrochem. commun.* **2013**, *34*,

153–156. https://doi.org/10.1016/j.elecom.2013.06.001.

(141) Yano, H.; Watanabe, M.; Iiyama, A.; Uchida, H. Particle-Size Effect of Pt Cathode Catalysts on Durability in Fuel Cells. *Nano Energy* **2016**, *29*, 323–333. https://doi.org/10.1016/j.nanoen.2016.02.016.

(142) Tamaki, T.; Minagawa, A.; Arumugam, B.; Kakade, B. A.; Yamaguchi, T. Highly Active and Durable Chemically Ordered Pt–Fe–Co Intermetallics as Cathode Catalysts of Membrane–Electrode Assemblies in Polymer Electrolyte Fuel Cells. *J. Power Sources* **2014**, *271*, 346–353. https://doi.org/10.1016/j.jpowsour.2014.08.005.

(143) Gröger, O.; Gasteiger, H. A.; Suchsland, J. P. Review-Electromobility: Batteries or Fuel Cells? *J. Electrochem. Soc.* **2015**, *162* (14), A2605–A2622. https://doi.org/10.1149/2.0211514jes.

(144) Stacy, J.; Regmi, Y. N.; Leonard, B.; Fan, M. The Recent Progress and Future of Oxygen Reduction Reaction Catalysis: A Review. *Renewable and Sustainable Energy Reviews*. 2017, pp 401–414. https://doi.org/10.1016/j.rser.2016.09.135.

(145) Nazir, H.; Muthuswamy, N.; Louis, C.; Jose, S.; Prakash, J.; Buan, M. E. M.; Flox, C.; Chavan, S.; Shi, X.; Kauranen, P.; Kallio, T.; Maia, G.; Tammeveski, K.; Lymperopoulos, N.; Carcadea, E.; Veziroglu, E.; Iranzo, A.; M. Kannan, A. Is the H2 Economy Realizable in the Foreseeable Future? Part III: H2 Usage Technologies, Applications, and Challenges and Opportunities. *International Journal of Hydrogen Energy*. Elsevier Ltd October 30, 2020, pp 28217–28239. https://doi.org/10.1016/j.ijhydene.2020.07.256.

(146) Harada, M.; Tamura, N.; Takenaka, M. Nucleation and Growth of Metal Nanoparticles during Photoreduction Using in Situ Time-Resolved SAXS Analysis. *J. Phys. Chem. C* **2011**, *115* (29), 14081–14092. https://doi.org/10.1021/jp203119a.

(147) Wu, L.; Willis, J. J.; McKay, I. S.; Diroll, B. T.; Qin, J.; Cargnello, M.; Tassone, C. J. High-Temperature Crystallization of Nanocrystals into Three-Dimensional Superlattices. *Nature* **2017**, *548* (7666), 197–201. https://doi.org/10.1038/nature23308.

(148) Quinson, J.; Neumann, S.; Kacenauskaite, L.; Bucher, J.; Kirkensgaard, J. J. K.; Simonsen, S. B.; Theil Kuhn, L.; Zana, A.; Vosch, T.; Oezaslan, M.; Kunz, S.; Arenz, M. Solvent-Dependent Growth and Stabilization Mechanisms of Surfactant-Free Colloidal Pt Nanoparticles. *Chem. - A Eur. J.* **2020**, *26* (41), 9012–9023. https://doi.org/10.1002/chem.202001553.

(149) Povia, M.; Herranz, J.; Binninger, T.; Nachtegaal, M.; Diaz, A.; Kohlbrecher, J.; Abbott, D. F.; Kim, B.-J.; Schmidt, T. J. Combining SAXS and XAS To Study the Operando Degradation of Carbon-Supported Pt-Nanoparticle Fuel Cell Catalysts. *ACS Catal.* **2018**, *8* (8), 7000–7015. https://doi.org/10.1021/acscatal.8b01321.

(150) Binninger, T.; Fabbri, E.; Patru, A.; Garganourakis, M.; Han, J.; Abbott, D. F.; Sereda, O.; Kötz, R.; Menzel, A.; Nachtegaal, M.; Schmidt, T. J. Electrochemical Flow-Cell Setup for In Situ X-Ray Investigations. *J. Electrochem. Soc.* **2016**, *163* (10), H906–H912. https://doi.org/10.1149/2.0201610jes.

(151) Sandbeck, D. J. S.; Secher, N. M.; Speck, F. D.; Sørensen, J. E.; Kibsgaard, J.; Chorkendorff, I.; Cherevko, S.; Cherevko, S. Particle Size Effect on Platinum Dissolution: Considerations for Accelerated Stability Testing of Fuel Cell Catalysts. *ACS Catal.* **2020**, *10* (11), 6281–6290. https://doi.org/10.1021/acscatal.0c00779.

(152) Sandbeck, D. J. S.; Inaba, M.; Quinson, J.; Bucher, J.; Zana, A.; Arenz, M.; Cherevko, S. Particle Size Effect on Platinum Dissolution: Practical Considerations for Fuel Cells. *ACS Appl. Mater. Interfaces* **2020**, *12* (23), 25718–25727.

https://doi.org/10.1021/acsami.0c02801.

(153) Yu, K.; Groom, D. J.; Wang, X.; Yang, Z.; Gummalla, M.; Ball, S. C.; Myers, D. J.; Ferreira, P. J. Degradation Mechanisms of Platinum Nanoparticle Catalysts in Proton Exchange Membrane Fuel Cells: The Role of Particle Size. *Chem. Mater.* **2014**, *26* (19), 5540–5548. https://doi.org/10.1021/cm501867c.

(154) Quinson, J.; Röefzaad, M.; Deiana, D.; Hansen, T. W.; Wagner, J. B.; Nesselberger, M.; Crampton, A. S.; Ridge, C. J.; Schweinberger, F. F.; Heiz, U.; Arenz, M. Electrochemical Stability of Subnanometer Pt Clusters. *Electrochim. Acta* **2018**, *277*, 211–217. https://doi.org/10.1016/j.electacta.2018.04.211.

(155) Cherevko, S.; Zeradjanin, A. R.; Topalov, A. A.; Kulyk, N.; Katsounaros, I.; Mayrhofer, K. J. J. Dissolution of Noble Metals during Oxygen Evolution in Acidic Media. *ChemCatChem* **2014**, *6* (8), 2219–2223. https://doi.org/10.1002/cctc.201402194.

(156) Cherevko, S.; Kulyk, N.; Mayrhofer, K. J. J. Durability of Platinum-Based Fuel Cell Electrocatalysts: Dissolution of Bulk and Nanoscale Platinum. *Nano Energy* **2016**, *29*, 275–298. https://doi.org/10.1016/j.nanoen.2016.03.005.

(157) Speder, J.; Zana, A.; Spanos, I.; Kirkensgaard, J. J. K.; Mortensen, K.; Hanzlik, M.; Arenz, M. Comparative Degradation Study of Carbon Supported Proton Exchange Membrane Fuel Cell Electrocatalysts - The Influence of the Platinum to Carbon Ratio on the Degradation Rate. *J. Power Sources* **2014**, *261*, 14–22. https://doi.org/10.1016/j.jpowsour.2014.03.039.

(158) Martens, I.; Vamvakeros, A.; Chattot, R.; Blanco, M. V.; Rasola, M.; Pusa, J.; Jacques, S. D. M.; Bizzotto, D.; Wilkinson, D. P.; Ruffmann, B.; Heidemann, S.; Honkimäki, V.; Drnec, J. X-Ray Transparent Proton-Exchange Membrane Fuel Cell Design for in Situ Wide and Small Angle Scattering Tomography. *J. Power Sources* **2019**, *437*, 226906. https://doi.org/10.1016/j.jpowsour.2019.226906.

(159) Martens, I.; Chattot, R.; Rasola, M.; Blanco, M. V.; Honkimäki, V.; Bizzotto, D.; Wilkinson, D. P.; Drnec, J. Probing the Dynamics of Platinum Surface Oxides in Fuel Cell Catalyst Layers Using in Situ X-Ray Diffraction. *ACS Appl. Energy Mater.* **2019**, *2* (11), 7772–7780. https://doi.org/10.1021/acsaem.9b00982.

(160) Kregar, A.; Kravos, A.; Katrašnik, T. Methodology for Evaluation of Contributions of Ostwald Ripening and Particle Agglomeration to Growth of Catalyst Particles in PEM Fuel Cells. *Fuel Cells* **2020**, *20* (4), 487–498. https://doi.org/10.1002/fuce.201900208.

(161) Shao-Horn, Y.; Sheng, W. C.; Chen, S.; Ferreira, P. J.; Holby, E. F.; Morgan, D. Instability of Supported Platinum Nanoparticles in Low-Temperature Fuel Cells. *Top. Catal.* **2007**, *46* (3–4), 285–305. https://doi.org/10.1007/s11244-007-9000-0.

(162) Quinson, J.; Jensen, K. M. Ø. From Platinum Atoms in Molecules to Colloidal Nanoparticles: A Review on Reduction, Nucleation and Growth Mechanisms. *Adv. Colloid Interface Sci.* **2020**, *286*, 102300. https://doi.org/10.1016/j.cis.2020.102300.

(163) McCrory, C. C. L.; Jung, S.; Peters, J. C.; Jaramillo, T. F. Benchmarking Heterogeneous Electrocatalysts for the Oxygen Evolution Reaction. *J. Am. Chem. Soc.* **2013**, *135* (45), 16977–16987. https://doi.org/10.1021/ja407115p.

(164) Spöri, C.; Briois, P.; Nong, H. N.; Reier, T.; Billard, A.; Kühl, S.; Teschner, D.; Strasser, P. Experimental Activity Descriptors for Iridium-Based Catalysts for the Electrochemical Oxygen Evolution Reaction (OER). *ACS Catal.* **2019**, *9* (8), 6653–6663. https://doi.org/10.1021/acscatal.9b00648.

(165) Yu, H.; Danilovic, N.; Wang, Y.; Willis, W.; Poozhikunnath, A.; Bonville, L.;

Capuano, C.; Ayers, K.; Maric, R. Nano-Size IrOx Catalyst of High Activity and Stability in PEM Water Electrolyzer with Ultra-Low Iridium Loading. *Appl. Catal. B Environ.* **2018**, *239*, 133–146. https://doi.org/10.1016/j.apcatb.2018.07.064.

(166) Harzer, G. S.; Orfanidi, A.; El-Sayed, H.; Madkikar, P.; Gasteiger, H. A. Tailoring Catalyst Morphology towards High Performance for Low Pt Loaded PEMFC Cathodes. *J. Electrochem. Soc.* **2018**, *165* (10), F770–F779. https://doi.org/10.1149/2.0311810jes.

(167) Suermann, M.; Schmidt, T. J.; Büchi, F. N. Comparing the Kinetic Activation Energy of the Oxygen Evolution and Reduction Reactions. *Electrochim. Acta* **2018**, *281*, 466–471. https://doi.org/10.1016/j.electacta.2018.05.150.

(168) Bernt, M.; Hartig-Weiß, A.; Tovini, M. F.; El-Sayed, H. A.; Schramm, C.; Schröter, J.; Gebauer, C.; Gasteiger, H. A. Current Challenges in Catalyst Development for PEM Water Electrolyzers. *Chemie Ing. Tech.* **2020**, *92* (1–2), 31–39. https://doi.org/10.1002/cite.201900101.

(169) Fathi Tovini, M.; Hartig-Weiß, A.; Gasteiger, H. A.; El-Sayed, H. A. The Discrepancy in Oxygen Evolution Reaction Catalyst Lifetime Explained: RDE vs MEA - Dynamicity within the Catalyst Layer Matters. *J. Electrochem. Soc.* **2021**, *168* (1), 014512. https://doi.org/10.1149/1945-7111/abdcc9.

(170) Alia, S. M.; Shulda, S.; Ngo, C.; Pylypenko, S.; Pivovar, B. S. Iridium-Based Nanowires as Highly Active, Oxygen Evolution Reaction Electrocatalysts. *ACS Catal.* **2018**, *8* (3), 2111–2120. https://doi.org/10.1021/acscatal.7b03787.

(171) Spöri, C.; Kwan, J. T. H.; Bonakdarpour, A.; Wilkinson, D. P.; Strasser, P. The Stability Challenges of Oxygen Evolving Catalysts: Towards a Common Fundamental Understanding and Mitigation of Catalyst Degradation. *Angew. Chemie - Int. Ed.* **2017**, *56* (22), 5994–6021. https://doi.org/10.1002/anie.201608601.

(172) Zhang, G.; Wang, H.; Yang, J.; Zhao, Q.; Yang, L.; Tang, H.; Liu, C.; Chen, H.; Lin, Y.; Pan, F. Temperature Effect on Co-Based Catalysts in Oxygen Evolution Reaction. *Inorg. Chem.* **2018**, *57* (5), 2766–2772. https://doi.org/10.1021/acs.inorgchem.7b03168.

(173) Parthasarathy, A.; Srinivasan, S.; Appleby, A. J.; Martin, C. R. Temperature Dependence of the Electrode Kinetics of Oxygen Reduction at the Platinum/Nafion® Interface—A Microelectrode Investigation. *J. Electrochem. Soc.* **1992**, *139* (9), 2530–2537. https://doi.org/10.1149/1.2221258.

(174) Lu, Y.; Wang, W.; Xie, F. Investigation of Oxygen Evolution Reaction Kinetic Process and Kinetic Parameters on Iridium Electrode by Electrochemistry Impedance Spectroscopy Analysis. *J. Electroanal. Chem.* **2020**, *871*, 114281. https://doi.org/10.1016/j.jelechem.2020.114281.

(175) Quinson, J.; Dworzak, A.; Simonsen, S. B.; Theil Kuhn, L.; Jensen, K. M. Ø.; Zana, A.; Oezaslan, M.; Kirkensgaard, J. J. K.; Arenz, M. Surfactant-Free Synthesis of Size Controlled Platinum Nanoparticles: Insights from in Situ Studies. *Appl. Surf. Sci.* **2021**, *549*, 149263. https://doi.org/10.1016/J.APSUSC.2021.149263.

7. Appended Manuscripts

In the following the seven manuscripts discussed in the third chapter are appended together with the supporting information.

Manuscript I:

J. Schröder, S. Neumann, S. Kunz

Visible-Light-Induced Synthesis of "Surfactant-Free" Pt Nanoparticles in Ethylene Glycol as a Synthetic Approach for Mechanistic Studies on Nanoparticle Formation

https://doi.org/10.1021/acs.jpcc.0c06361

Articles on request author-directed link

THE JOURNAL OF PHYSICAL CHEMISTRY C

pubs.acs.org/JPCC Article

Visible-Light-Induced Synthesis of "Surfactant-Free" Pt Nanoparticles in Ethylene Glycol as a Synthetic Approach for Mechanistic Studies on Nanoparticle Formation

Johanna Schröder, Sarah Neumann, and Sebastian Kunz*

Cite This: J. Phys. Chem. C 2020, 124, 21798–21809 Read Online

ACCESS | Metrics & More | Article Recommendations | Supporting Information

ABSTRACT: The alkaline polyol synthesis of "surfactant-free" Pt nanoparticles (NPs) is a straightforward approach to synthesize NPs as colloids. Even challenges such as size control have been successfully addressed in the recent past, but the reduction mechanism remains poorly understood. This work shows that the reduction of the precursors H_2PtCl_6 and H_2PtBr_6 can be performed at low reaction rates using visible light even though neither the precursor nor the solvent exhibits any detectable absorption in the visible range. The possibility of a slowed down visible-light-induced reduction was used for mechanistic investigation on the alkaline polyol approach and compared with other energy sources (thermal, microwaves, and ultraviolet light) to induce the reaction. The obtained insensitivity of the resulting particle size on the reaction kinetics presented here as well as in previous studies demonstrates a clear dependence on the ratio of free OH^- to Pt precursors revealing strong indications that the well-known LaMer model is not a valid mechanistic picture for the polyol process.

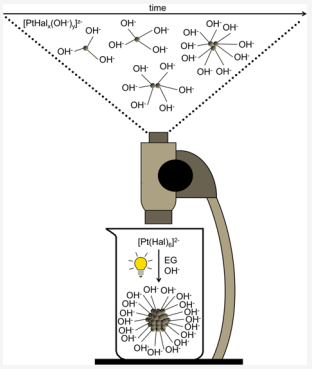

1. INTRODUCTION

Ethylene glycol (EG)-based synthesis of nanoparticles (NPs) under alkaline conditions allows for the preparation of "surfactant-free" colloids with narrow particle size distributions.[1,2] Not only thermal energy but also microwave radiation or ultraviolet (UV) light can be applied to induce the reaction.[2−5] The major advantage of the EG-based synthesis compared to other colloidal methods is that no "surfactants" are needed to obtain small, stable colloids. This makes the approach very attractive for the preparation of model catalysts, and it allows tailoring of the physical properties (particle size, particle loading, and support) of the catalysts.[6] The colloids are formed in alkaline EG by metal precursor (e.g., H_2PtCl_6 and H_2BrCl_6) reduction, while the solvent EG is oxidized. Different oxidation pathways have been discussed for EG. It can be oxidized to glycolaldehyde and glycol acid or to oxalaldehyde and oxalic acid. In addition, EG can degrade by forming two CO molecules that absorb to the NP surface.[2,7] OH^-, which is present in the reaction mixture under alkaline conditions, reacts to form water with the protons that are generated by reduction of the metal precursor.[3] The monomers then form NPs, which are finely dispersed within the reaction medium. An excess of OH^- is needed to stabilize the formed NPs as colloids.[2,4] These NPs can be precipitated by lowering the pH and be redispersed in several organic solvents with high vapor pressures while maintaining the particle size. Consequently, such NPs can be used for coatings, in particular to coat support materials (e.g., Al_2O_3, SiO_2, and carbon) for the preparation of heterogeneous catalysts. Schrader et al. demonstrated that after precipitation, NPs are merely covered by CO, but no organic residuals could be identified.[2] This finding was further confirmed recently for supported catalysts prepared from such colloids using solid-state nuclear magnetic resonance spectroscopy.[8] While surfactants such as polymers (e.g., PVP) that are typically used in colloidal chemistry[9] require harsh conditions to be removed after supporting,[10] CO coverage in supported NPs can be easily replaced by OH^- by adding alkaline water.[11]

Recently, it has been shown that the size of NPs in the polyol synthesis can be controlled by changing the OH^-/Pt ratio.[2−4] However, despite the great potential of the polyol process for catalytic applications[1,12−14] and achievements in terms of size control, the mechanism of NP formation and the control of their size still remain poorly understood.[15] NP formation is usually proposed to follow the LaMer model:[16−19] The dissolved metal precursors are reduced to form the so-called monomers. After reaching supersaturation, small but instable nuclei are formed. As the monomer concentration increases further, a critical concentration is reached where nuclei become large enough to remain stable under the given conditions. This nucleation continues until the concentration of the monomer falls below this nucleation threshold. Below

Received: July 12, 2020
Revised: August 29, 2020
Published: September 17, 2020

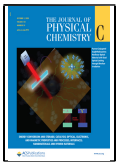

https://dx.doi.org/10.1021/acs.jpcc.0c06361
J. Phys. Chem. C 2020, 124, 21798−21809

the threshold, the monomers are deposited on the stable nuclei resulting in particle growth.[3,15,20] The LaMer model is a simple kinetic model, and several examples have shown its suitability for the specific systems.[16−19] However, evidence has been reported that allows questioning its validity to correctly reflect NP formation in the alkaline polyol synthesis.[4] Quinson et al.[4] described for "surfactant-free" Pt NPs that OH^- not only stabilizes the particles but proposed that it further stops the growth process during the particle formation. Without discussing the formation mechanism, Quinson et al. showed that the ratio of the surface atoms of OH^-/Pt seems to be constant. This indicates that the final particle size is rather determined by the OH^-/Pt ratio than by any kinetic considerations such as the LaMer model.[4] Despite this indication, an improved understanding of what determines the particle size is still missing.[15] As the particle formation and the final particle size seem not to be controlled by kinetics, a slowdown of the NP formation kinetics would be beneficial to gain further insights into relevant mechanistic aspects such as intermediates, etc. Previous reports showed that UV-light-induced NP formation is slower (ca. 2 h) than thermal- or microwave-based reduction (ca. 3 min) but the same mechanisms of EG oxidation were found using the EG method.[3,5] Hence, light-induced NP formation provides an opportunity for further detailed investigations on the NP formation. As the absorbance maximum of the precursor H_2PtCl_6 is found in the UV light region (at ca. 265 nm), the abovementioned reports proposed that UV light as a part of daylight induces NP formation.[3,5] However, in this work we show that NP synthesis does not require UV light. In contrast, it is possible to drive the alkaline polyol process with visible light in the range of 500 nm even though neither the precursor nor the solvent shows any significant absorption in this range. In addition, despite the slowdown of the precursor reduction (to 24 h), the obtained NP sizes are comparable to the particle sizes of the thermal or UV-light-induced reduction. The slow visible-light-induced synthesis enables studying the different metal reduction states and hence the mechanism with respect to the applied metal salt (H_2PtCl_6 and H_2PtBr_6) and the irradiated wavelength. Furthermore, the similar particle sizes obtained despite the use of different energy sources (temperature, microwave, and light) and completely different timescales for the NP formation in the different reduction methods raises questions on the validity of the LaMer model for the alkaline polyol method.

2. EXPERIMENTAL SECTION

2.1. NP Synthesis. *2.1.1. Synthesis of "Surfactant-Free" Pt NPs with Visible Light.* "Surfactant-free" Pt NPs were synthesized following the alkaline EG approach described by Wang et al.[1] In a standard procedure, the metal precursor (0.04 g of H_2PtCl_6 xH_2O (40% Pt, Chempur) or 0.0685 g of H_2PtBr_6 xH_2O (23.35% Pt, Chempur)) was dissolved in 4 mL of EG (99.8%, VWR). 0.5 M NaOH (VWR) (4 mL) in EG was added. In this way, a starting concentration of 0.25 M NaOH was obtained. The OH^- starting concentration describes the NaOH concentration in 8 mL of the reaction mixture before the irradiation. Different OH^- concentrations were obtained respectively by dilution of a 0.5 M NaOH stock solution in EG with EG. The total volume was kept constant at 8 mL. The mixture was filled in a quartz reactor with a cooling jacket. The temperature was kept at 27 °C by using a thermostat to flow water at a constant temperature through the cooling jacket. The reaction mixture was stirred at 600 rpm during irradiation with visible light. A xenon arc lamp (300 W, Lot QuantumDesign) with different filters (Lot QuantumDesign) was used to achieve irradiation maxima at about 400, 450, 500, 550, 600, and 650 nm. Samples were taken after 2, 3, 4, 5, 6, and 24 h.

The lamp spectrum and the filter transmission spectra of the used filters are shown in Figures S19−S22, respectively. The irradiated lamp spectrum is more or less constant over the total range of wavelength used in the present study. However, some spikes are visible at around 450−500 nm. Additionally, the used filters generate transmissions between 65 and 75%. Therefore, the naming of the wavelength is meant as a guide for the experimental setting, as no direct correlation between the wavelength and the energy input can be assumed.

2.1.2. Synthesis of "Surfactant-Free" Pt NPs by Thermal Reduction. In a standard procedure, a metal precursor (0.04 g of H_2PtCl_6 xH_2O (40% Pt, Chempur or Alpha Aesar)) was dissolved in 4 mL of EG in a 50 mL round bottom flask. 0.5 M NaOH (4 mL) in EG was added to obtain a OH^- starting concentration of 0.25 M. Different base concentrations were obtained respectively by dilution of 0.5 M NaOH stock solution in EG with pure EG, but the total volume of 8 mL was kept constant. For the reduction with KOH, 2.050 mL of 40 mM H_2PtCl_6 xH_2O was mixed with 1.945 mL of EG and 4.000 mL of 0.5 mL KOH (Sigma-Aldrich) stock solution in EG. The flask of the thermal reduction with NaOH was equipped with a reflux condenser. The mixture was vigorously stirred at 150 °C using a preheated oil bath and kept at this temperature for 90 min. The yellow precursor solution turned dark brown after about 5 min, indicating the nanoparticle formation. After heating for 90 min, the reaction mixture was cooled to ambient temperature. During the thermal reduction in the absence of any light, the described procedure was performed in the same way, but the flakes were covered with aluminum foil to exclude absorption of light by the reaction mixture.

2.1.3. Cleaning of "Surfactant-Free" NPs. Pt NPs were cleaned by precipitating the "as-prepared" NP dispersion with two aliquots of 1 M aqueous HCl (VWR). The precipitated particles were separated by centrifugation, and the supernatant was removed. The particles were washed once by suspending them in two aliquots of 1 M aqueous HCl. After a second centrifugation, the supernatant was removed again, and the NPs were redispersed in different organic solvents.

2.1.4. NP Deposition on Carbon. A carbon support (Carbot, VXC72R) was dispersed in acetone (VWR). The Pt NPs were cleaned and redispersed in acetone (see Section 2.1.3) and added to the suspension of the carbon support. The solvent was vaporized with a rotary evaporator. Afterward, the carbon deposited NPs were washed with water and acetone to remove solvent residues.

2.1.5. Seed-Mediated Growth Experiments. Different seed-mediated growth experiments were performed by adding (reduced) precursor solutions to different thermally formed Pt NPs. Reduced precursor solutions were obtained by irradiation of a solution of H_2PtCl_6 in alkaline EG (see the standard procedure in Section 2.1.1) with 400 nm for 4 h. For the synthesis of thermally formed Pt NPs, see Section 2.1.2.

2.1.5.1. Exposure of the as-Prepared Thermally Formed Pt NPs to Reduced Precursor Solutions. Reduced H_2PtCl_6 precursor solutions (0.6, 1.2, and 3.0 mL) were added to 0.6 mL of the as-prepared thermally formed Pt NPs to obtain ratios of 1:1, 1:2, and 1:5 with 0.25 M of OH^-. The mixtures

https://dx.doi.org/10.1021/acs.jpcc.0c06361
J. Phys. Chem. C 2020, 124, 21798−21809

were stirred for 5 and 7 days at room light and in the absence of light (covered with aluminum foil).

2.1.5.2. Exposure of Thermally Formed Pt NPs Redispersed in EG to Reduced Precursor Solutions. Reduced H_2PtCl_6 precursors (0.5, 1.0, and 2.5 mL) were added to 0.5 mL of Pt NPs formed by thermal reduction and redispersed in pure EG (see Section 2.1.3) to obtain ratios of 1:1, 1:2, and 1:5. The "pH" is still alkaline in these experiments with a final OH^- concentration of about 0.125, 0.167, and 0.208 M. The mixtures were stirred for 7 days at room light.

2.1.5.3. Exposure of Carbon-Supported Pt NPs to Reduced Precursor Solutions. A dispersion of thermally formed Pt NPs (24 mL) was precipitated and redispersed in acetone (see Section 2.1.3). The NPs were deposited onto 0.433 g of carbon (see Section 2.1.4, carbon was dispersed in 10 mL of acetone). A theoretical loading of about 10 wt % of Pt was obtained. The deposited NPs were washed with water and acetone. After supporting the carbon stick together, a mortar was used to reobtain a fine powder of the NPs supported on carbon. The deposited Pt NPs (0.0997 or 0.0503 g) were dispersed in 1 mL of EG. Reduced H_2PtCl_6 precursor solutions (8 mL) were added to obtain OH^-/Pt ratios of 15.0 and 18.6. The mixture was stirred for 1 week. Afterward, the mixture was centrifuged twice to separate the carbon supported NPs, and the supernatant was removed. The supported NPs were washed with 8 mL of deionized water, and the supernatant was removed. The NPs supported on carbon were dried in an oven at 120 °C for several days to remove any liquid residues.

2.1.5.4. Irradiation of the as-Prepared Thermally Formed Pt NPs Exposed to Precursor Solutions. The as-prepared thermally formed NPs (1 mL) were added to different amounts of 10.25 mM H_2PtCl_6 xH_2O in EG (without additional OH^-). By using 2.2 or 3.0 mL of precursor solution, OH^- concentrations of 0.078 M and 0.063 M NaOH were obtained, respectively, considering the 0.25 M OH^- starting concentration of the thermally formed NPs. The mixtures were irradiated with 500 nm for 3 h and stirred at 27 °C.

2.2. Characterization of NPs. *2.2.1. UV/vis Spectroscopy.* For UV/vis measurements, a Cary 50 Scan UV/vis spectrophotometer from Varian and a UV-1600 PC spectrophotometer from VWR were used. NP dispersions (80 μL) were diluted in 4 mL of EG. The quartz cuvette was cleaned with about 1.5 mL of diluted dispersion. About 2.5 mL of diluted dispersion was used for UV/vis measurement. The spectra were recorded with the empty quartz cuvette as the baseline.

2.2.2. Fourier Transform Infrared Spectroscopy. For Fourier transform infrared (FTIR) spectroscopy, a Thermo Nicolet Avatar 370 was used with a resolution of 4 cm^{-1}. FTIR spectra from the NP dispersions were recorded in attenuated total reflection mode with a Smart Performer Atr unit on a ZnSe crystal plate by taking 16 scans. EG on the ZnSe crystal was used as the background.

2.2.3. Transmission Electron Spectroscopy. Transmission electron spectroscopy (TEM) was performed with a Tecnai F20 S-Twin Microscope (Fei) using an acceleration voltage of 200 kV and a magnification of 150 k. For the measurement of liquid samples, 0.25 or 0.5 mL of the as-prepared NP dispersions were precipitated with two aliquots of 1 M HCl and were redispersed in one aliquot of acetone (see Section 2.1.3). Then, three drops (for lower NP concentrations up to six drops) of that dispersion were diluted with 1 mL of acetone. Afterward, three drops of the diluted acetone dispersions were drop-cast onto the carbon side of the TEM grid (ultrathin Carbon Support Film, Quantifoil, Cu 200 mesh). For the measurement of carbon support samples, the carbon was crushed in a mortar and the TEM grid was covered three times with the NPs supported on carbon. The averaged particle sizes and particle size distributions were determined using ImageJ, counting at least 200 particles.

2.2.4. Mass Spectrometry. A Bruker Esquire-LC ion trap mass spectrometer was used to perform electrospray ionization mass spectrometry (ESI-MS) measurements (synthesis with NaOH), and nano electrospray ionization was performed using a LTQ Orbitrap XL from Thermo (synthesis with KOH). For the sample preparation, 1 mL of the NP dispersion was precipitated and redispersed in EG (see Section 2.1.3) to obtain a metal free system for the mass spectrometry (MS) investigations. The pH of the obtained solution was buffered by adding $NaHCO_3$ (Riedel-de Haën, synthesis with NaOH) or $KHCO_3$ (A.C.S. Reagent, Aldrich, 99.7%, synthesis with KOH). For the MS measurements, the samples synthesized with NaOH were diluted with methanol (VWR) in a ratio of 1:100. The spectra were recorded in the positive ion mode.

3. RESULTS AND DISCUSSION

3.1. Thermal Reduction of H_2PtCl_6 in the Absence of Light. By using the EG method according to Wang et al.,[1] "surfactant-free" Pt NPs are synthesized by thermal reduction of H_2PtCl_6 in EG in the presence of NaOH. The Pt NPs are stable for several months.[1] Kacenauskaite et al.[5] showed that storage of an alkaline H_2PtCl_6 solution in EG does not lead to NP formation, when the solution is not exposed to light. This implies the importance of light for the reaction under ambient conditions. What has not been investigated so far is the thermal reduction of H_2PtCl_6 in the absence of any light to clarify whether the presence of light is a prerequisite for the reaction to occur. We found that thermal reduction of H_2PtCl_6 in the dark at 150 °C for 90 min leads to stable NPs. After precipitation of the NPs, the supernatant was analyzed to determine if the oxidation production of EG is the same as for a thermal reduction in the presence of light. Glycolic acid (m/z = 77, 121, 143), glycolaldehyde (m/z = 83, 105), oxalic acid (m/z = 135, 157), and oxalaldehyde (m/z = 81) besides EG (m/z = 63, 85, 107, 129) were found in the supernatant in the mass spectrum (Figure S1). These species are the same organic oxidation products of EG that are formed in the normal thermal EG method in the presence of light.[7] No significant change in particle size was found when the thermal reduction is performed in the absence of light (Figure 1). We hence conclude that light induction seems not to be the driving force for the NP formation at 150 °C, unlike the thermal energy.

Quinson et al. describes that the thermal reduction of H_2PtCl_6 with KOH leads to stable NPs but, at a high base concentration, a cation effect is observed.[21] The synthesized NPs at 2.5 M KOH (the same base concentration as used before in the thermal reduction) are only stable for several minutes. The mass spectrum of the supernatant after precipitation of the NPs reveals the same oxidation production of EG (m/z = 153) as for NaOH. Glycol acid (m/z = 109, 113), glycolaldehyde (m/z = 97, 115, 169, 205), oxalic acid (m/z = 155), and oxalaldehyde (m/z = 95) were observed. Because of different stabilization effects of the cations (K^+ as compared to Na^+) at the high base concentrations, the two systems are similar but not equivalent. However, the same oxidation mechanism of the organic solvents occurs.

https://dx.doi.org/10.1021/acs.jpcc.0c06361
J. Phys. Chem. C 2020, 124, 21798−21809

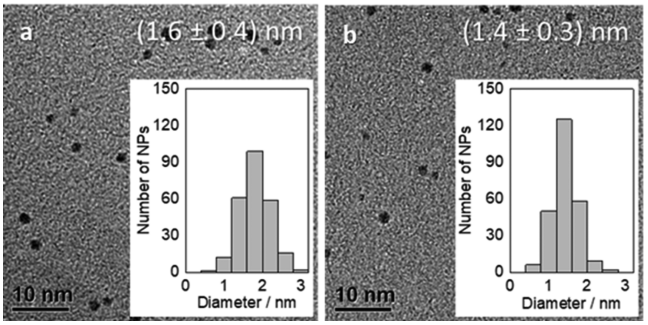

Figure 1. TEM images of Pt NPs, averaged particle sizes, and NP size distributions of NPs generated by thermal reduction of H_2PtCl_6 at 150 °C (a) in the dark and (b) under room light.

3.2. Reduction of H_2PtCl_6 by Visible Light. In the literature, light-induced NP synthesis studies on the alkaline polyol approach are rare and mainly limited to the use of UV light.[3,5] Earlier studies proposed that UV light as part of daylight induces NP formation.[5] This proposal seems reasonable considering that neither EG nor the precursors reveal an absorption band in the visible range. However, as shown in Figure 2, it is possible to form NPs with use of visible

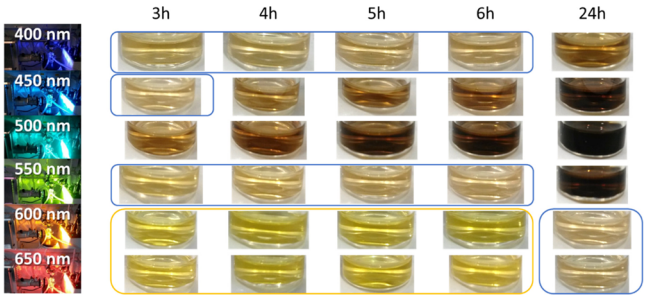

Figure 2. Photos of the time-dependent reduction of H_2PtCl_6 in EG after 3, 4, 5, 6, and 24 h of irradiation with 400, 450, 500, 550, 600, and 650 nm using 0.25 M OH^- as the starting concentration. The solutions that are presumed to be the solved precursor (in yellow) and reduced precursor (in blue) are bordered.

light, but the process is slow (24 h) as compared to the thermal synthesis (ca. 3 min). Mass spectrometric investigations of the supernatant after precipitation of the NPs (24 h, 500 nm) were performed to explore if for the visible-light-induced reduction the same EG oxidation mechanism occurs as for the other reduction methods (thermally,[2] UV light[5]). The data reveal the same organic oxidation products for EG as formed by the thermal EG method in the presence and absence of light (glycolic acid, glycolaldehyde, oxalic acid, and oxalaldehyde, see Figure S2).[7] Therefore, the same mechanism for EG oxidation as for thermally[2] and UV-light-induced NP formation[5] seems to hold for the visible-light-induced reduction. Further investigations of an alkaline EG solution (without Pt) that has been aged for some weeks at room temperature reveal that small amounts of glycolic acid and glycolaldehyde or acetic acid can be found (see Figure S3). This can be related to EG oxidation by oxygen from air.[22,23] After thermal treatment of such an aged alkaline EG solution (stirring for 90 min at 150 °C, the temperature of thermal reduction), oxalic acid is also found (see Figure S4). As the visible-light-induced NP formation was performed at room temperature, the oxalic acid must be traced back to the parallel Pt reduction during the NP synthesis (as no thermal reduction was performed). Consequently, the oxalic acid formed during the light-induced-NP synthesis at room temperature is present because of the NP formation and not the prior solvent oxidation.

Quinson et al.[24] investigated recently the NP synthesis in low boiling point solvents such as ethanol and methanol under UV light. In different studies with those low boiling point solvents, Quinson et al. showed different size effects for hydroxides of different cations (Li^+, Na^+, K^+, and Cs^+) and their concentration as compared to EG[21,24] and a solvent dependent reduction mechanism of ethanol as compared to methanol.[25] Although the reduction of ethanol, methanol, and EG leads to "surfactant-free" Pt NPs, a quite differing mechanism is observed for each of these solvents.

The formation rate for the visible-light-induced reduction shows a clear dependence on the applied wavelength of the light source. After 24 h of irradiation of H_2PtCl_6 (with NaOH as the base), NPs were formed with 400, 450, 500, and 550 nm (Figure 2), but the change of color from yellow (precursor solution) to brown (NPs) (see Figure 2) and the UV/vis absorption intensities after 24 h of reduction (see Figure 3)

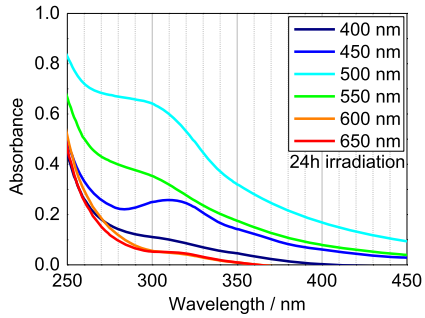

Figure 3. Comparing the UV/vis spectra of NP dispersions after 24 h of irradiation with 400, 450, 500, 550, 600, and 650 nm of H_2PtCl_6 in EG using 0.25 M as the OH^- starting concentration.

imply that the reaction is the fastest for a wavelength of 500 nm. We hence conclude that the absorption maximum of the precursor H_2PtCl_6 at about 265 nm[5] does not necessarily need to be excited to induce the reduction. Irradiation with 500 nm was the only wavelength that led to NP yields high enough to allow for precipitation by adding HCl, and the supernatant was colorless. As only the complete reduction to NPs allows for complete precipitation and hence obtaining a colorless supernatant, it can be concluded that the H_2PtCl_6 reduction is completed after 24 h irradiation with 500 nm. This reaction time, when using visible light, is clearly much longer than those required for a thermal- or microwave-induced reduction.[2,4] The irradiation with 600 and 650 nm did not lead to NPs but probably to a reduced precursor (Figure S5f), as the yellow solution has turned colorless (see Figure 2).

The precursor reduction and NP formation lead to color changes of the solution/dispersion that can be captured optically (Figure 2) and by UV/vis spectroscopy (Figure S5). H_2PtCl_6 dissolved in 0.25 M NaOH in EG exhibits an absorption peak at about 265 nm (Figure S5e) corresponding to the yellow $[PtCl_6]^{2-}$ complex (Figure 2).[5,26] This absorption peak of $[PtCl_6]^{2-}$ decreases with longer irradiation time (Figure S5e,f). When NPs are formed, an absorption peak above 300 nm arises (Figure S5a–d). The time-dependent monitoring of the synthesis reveals an almost colorless

https://dx.doi.org/10.1021/acs.jpcc.0c06361
J. Phys. Chem. C 2020, 124, 21798–21809

intermediate state between the initial yellow solution of the precursor ($[PtCl_6]^{2-}$) and the brown NP dispersion (Figure 2, highlighted in yellow). This colorless state refers presumably to the reduced precursor[27,28] (monomer based on the LaMer model). As even low NP concentrations lead to significant increases of the baseline,[29] the colorless solution can be concluded to be almost completely free of NPs.[27,28,30] In addition, according to the Mie theory, the absorption of such small NPs is higher than their ability to scatter light.[31] So, this reduced precursor could be Pt^{2+}-complexes (as $[PtCl_4]^{2-}$, $[Pt(OH)_4]^{2-}$, or $[PtCl_x(OH)_y]^{2-}$) or even Pt^0. Note that at high OH^- concentrations, no particle formation occurs.[2] It seems hence very unlikely that complexes that exclusively coordinate OH^- act as a reactive species for the particle formation process discussed here. It has been described by Harada et al.[29] that in aqueous ethanol solutions at low pH, NPs are formed by light-induced reduction of $[PtCl_6]^{2-}$ to $[PtCl_4]^{2-}$. According to Wang et al.[32] at high pH levels (in the presence of OH^-) in an alkaline solution, the chlorides in $[PtCl_6]^{2-}$ are substituted by hydroxides, so different hydroxide chloride species up to $[Pt(OH)_6]^{2-}$ are formed. However, Hwang et al.[33] described that in EG at high pH first $[PtCl_4]^{2-}$ is formed from $[PtCl_6]^{2-}$ and heating the mixture for 5 min at 80 °C leads to $[Pt(OH)_4]^{2-}$. The obtained $[Pt(OH)_4]^{2-}$ complexes could be used to deposit Pt onto Ru NPs to form core−shell particles.[33] Generally, depending on the concentration, the exchange of chloride by OH^- must be expected to proceed at least partially as OH^- forms more stable platinum complexes than chloride.[34,35] Considering the results of Hwang et al.,[33] it seems that the exchange of Cl^- with OH^- is fast at 80 °C, leading to a fast NP formation at high temperatures compared to room temperature. This transition of the different intermediates should be visible in the UV/vis spectra. Using highly diluted solutions of the reduced precursor, a small shoulder at about 225 nm may imply the absorbance of an intermediate (Figure S5e,f). According to the literature, the UV/vis absorbance maximum of $[PtCl_4]^{2-}$ in (acidic) aqueous solutions was found in this area (at 217 nm and about 230 nm (shoulder),[36] 215 nm and 225 nm (shoulder),[37] 233 nm,[38] 222−236 nm[39]). There are not many reports about UV/vis data of the hydroxo platinum complexes: One example is the absorbance maximum of $[Pt(OH)_6]^{2-}$ in alkaline water at 200 nm.[40] Although the UV/vis spectra indicate different steps in the NP formation that can also be observed optically (see Figure 2), it cannot be concluded which intermediate is actually formed, but we assume it to be a $[PtCl_xOH_y]^{2-}$ complex. As the different suitable intermediates are complexes of Pt(II), we will refer to the intermediate as the reduced precursor here onward. Despite the different kinetics compared to thermally prepared NPs,[1,2] the size was found to be very similar for both preparation methods (1.4 ± 0.3 nm (Figure 1a) to 1.3 ± 0.5 nm (Figure S11)).

To sum up, the same particle sizes as in thermally,[2] UV light-,[3] or microwave[4]-induced reductions at a constant OH^-/Pt ratio are obtained. Furthermore, during the reduction of $[PtCl_4]^{2-}$, a colorless intermediate is formed that is assumed to be $[PtCl_xOH_y]^{2-}$.

3.3. Reduction of H_2PtBr_6 by Visible Light. The NP formation by thermal reduction of H_2PtBr_6, indicated by the color change from yellow to dark brown, occurs faster (30 s) than that for H_2PtCl_6 (5 min).[41] The change in the thermal reduction is accompanied by a change in particle size of 1.9 ± 0.2 nm for H_2PtBr_6 in less than 30 min as compared to 1.2 ± 0.2 nm for H_2PtCl_6 after 90 min.[41] The use of H_2PtBr_6 was hence also investigated for visible-light-induced reaction. After 24 h of irradiation of H_2PtBr_6 with 400, 450, 500, and 550 nm, the formed NPs could be precipitated, with 600 nm only partially. Thus, the reaction can be concluded to proceed faster with this precursor. Again the absorption maximums of the precursor H_2PtBr_6 at about 315 and 375 nm[36] do not have to be excited to induce the reduction. The NP formation rate has again a maximum at about 450 to 500 nm (Figures 4 and 5) as observed by the visible-light-induced reduction of H_2PtCl_6 (Figure 3).

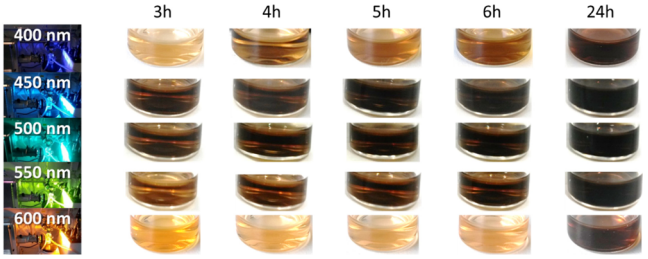

Figure 4. Photos of the time-dependent reduction of H_2PtBr_6 in EG after 3, 4, 5, 6, and 24 h of irradiation with 400, 450, 500, 550, and 600 nm using 0.250 M OH^- as the starting concentration and the corresponding average of the NP diameter after 24 h.

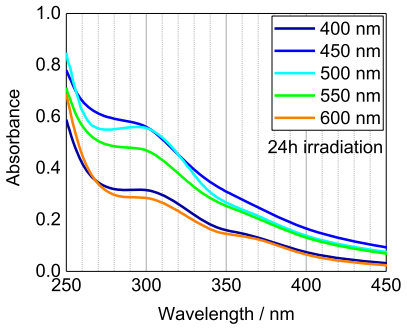

Figure 5. Comparing UV/vis spectra of NP dispersions after 24 h of irradiation with 400, 450, 500, 550, 600, and 650 nm of H_2PtBr_6 in EG using 0.250 M as the OH^- starting concentration.

Because of the faster NP formation with the bromide compared to the chloride containing precursor, an influence on the NP size was expected. However, the particle size at 500 nm (1.6 ± 0.3 nm (Figure S12c)) is in good agreement with the results of Neumann et al. in the thermally induced reduction of H_2PtBr_6 after 1−10 min (1.3 ± 0.2 nm) and of H_2PtCl_6 (1.2 ± 0.2 nm).[41] The particle sizes at 400−600 nm were comparable within the error of the TEM analysis (Figure S12), only after 24 h of irradiation; with 600 nm, not enough NPs were formed for further investigations. In the light-induced NP formation, the particle size does not differ strongly when H_2PtBr_6 is used instead of H_2PtCl_6 at an OH^- starting concentration of 0.25 M NaOH in EG (Figures S11 and S12). Therefore, the halide does not seem to influence the NP size for the slow visible-light-induced NP formation. However, the halide determines the rate of NP formation. The obtained NP size seems independent of the wavelength of the exposed light as long as enough energy is provided to induce the NP formation. The wavelength cannot be directly correlated to the total energy input. However, from the expected different energy input because of the combination of the wavelength-

https://dx.doi.org/10.1021/acs.jpcc.0c06361
J. Phys. Chem. C 2020, 124, 21798−21809

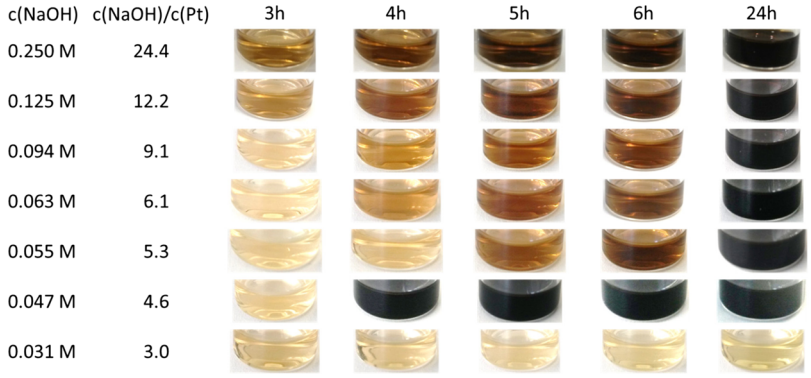

Figure 6. Photos of time-dependent reduction of H_2PtCl_6 in EG after 3, 4, 5, 6, and 24 h of irradiation with 500 nm using 0.250, 0.125, 0.094, 0.063, 0.055, 0.047, and 0.031 M as OH^- starting concentrations. The c(NaOH)/c(Pt) values describe the ratio before the synthesis using the OH^- starting concentration.

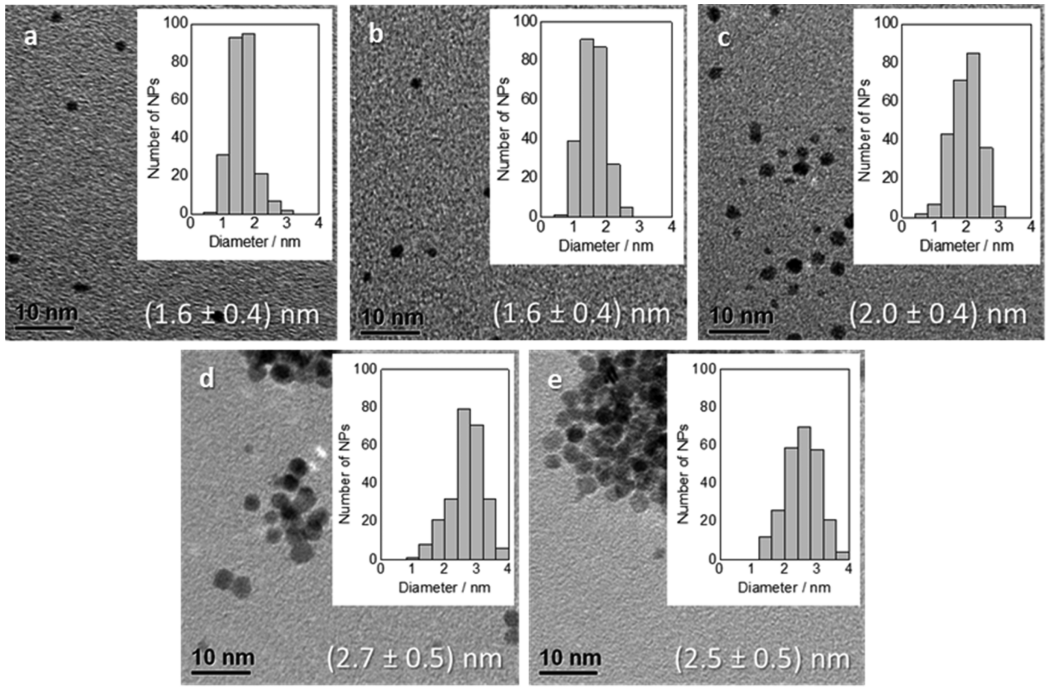

Figure 7. TEM images, averaged particle sizes, and NP size distributions of NPs after exposure of H_2PtCl_6 with 500 nm for 24 h using a NaOH starting concentration of (a) 0.125 M, (b) 0.094 M, (c) 0.063 M, (d) 0.055 M, and (e) 0.047 M. (d) and (e) show agglomeration of NPs on the TEM grid.

dependent photon energy, the lamp spectrum, and the filter transmission spectra per applied wavelength, it can be concluded that the NP size does not depend on the total energy input as long as enough energy is applied to form particles.

The reduction of H_2PtBr_6 is not only faster than that of H_2PtCl_6. During the reduction of H_2PtBr_6, a distinctive absorption maximum at 270 nm is observed (Figure S7) that is not found during the reduction of H_2PtCl_6. The intensity of the absorption maximum of this intermediate is high, while in the H_2PtCl_6 reduction, the absorbance decreases during the intermediate formation. The maximum is not related to the dissolved precursor in the reaction mixture. The H_2PtBr_6 precursor dissolved in the reaction mixture (0.25 M NaOH in EG) shows an absorption maximum at about 315 and 375 nm in the UV/vis spectrum (Figure S7). This is in accordance to the absorbance of $[PtBr_6]^{2-}$.[36] According to Wyk et al.,[36] the $[PtBr_4]^{2-}$ complex shows an absorbance maximum at 270 nm.

If the intermediate during the reduction of $[PtBr_6]^{2-}$ corresponded to a halide-free hydroxo platinum complex, where the halide is completely substituted by hydroxide,[32] the same absorption maximum should be seen as during the reduction of $[PtCl_6]^{2-}$. As UV/vis spectroscopy reveals the presence of different intermediates formed during the precursor reduction of H_2PtCl_6 and H_2PtBr_6, we conclude that the intermediate must partially coordinate the halide. Hence, the intermediate is neither only a Pt ion exclusively coordinating hydroxides nor only a halide containing Pt complex. The intermediates are hence described in the following as $[PtCl_xOH_y]^{2-}$ and $[PtBr_xOH_y]^{2-}$. The results of this work show different formation rates for the two different reductions: Reducing $[PtBr_6]^{2-}$ with the intermediate $[PtBr_xOH_y]^{2-}$ is much faster than the reduction of $[PtCl_6]^{2-}$ with the intermediate $[PtCl_xOH_y]^{2-}$. However, despite the

https://dx.doi.org/10.1021/acs.jpcc.0c06361
J. Phys. Chem. C 2020, 124, 21798−21809

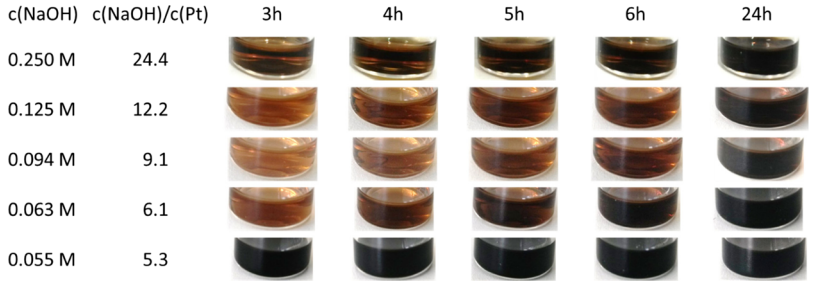

Figure 8. Photos of time-dependent reduction of H_2PtBr_6 in EG after 3, 4, 5, 6, and 24 h of irradiation with 500 nm using 0.250, 0.125, 0.094, 0.063, and 0.055 M as the OH^- starting concentration. The c(NaOH)/c(Pt) values describe the ratio before the synthesis using the OH^- starting concentration.

different kinetics, surprisingly no significant changes in particle size are obtained (see Figures S11 and S12). Although the formation of the intermediate and the formation rate of the NPs (reduction of the intermediate) are dependent on the precursor, the NP formation is halide independent. The LaMer model is a kinetic model, while particle growth by Ostwald ripening is a thermodynamic process. Hence, if the particle formation proceeds via the LaMer model, the final particle size is determined only by kinetics. In the LaMer model, the metal precursors are reduced to form what is referred to as monomers. When supersaturation is reached, nuclei start to form. These are however too small to be stable and redissolve. As a critical concentration is reached, the nuclei become large enough to be stable and the system turns to be heterogeneous (phase 1). Nucleation occurs until the concentration of monomers falls below the nucleation threshold, where the rate of nucleation rapidly decreases to almost zero (phase 2). When the concentration of monomers drops below the nucleation threshold, the stable nuclei act as seeds that grow by deposition of monomers onto the particle surface (phase 3).[42] When the reduction occurs at lower rates, as in the case of the light-induced reduction, the concentration of monomers increases only slowly. The monomer concentration should rapidly fall below the nucleation threshold because the rate of monomer formation cannot keep up with the rate of monomer consumption via nucleation. As a result, a short nucleation period is expected and a long growth phase, which in turn means that large particles are expected. LaMer hence proposes small particles for a fast reaction (thermal reduction) and large NPs for a slow reaction (light-induced). As this proposal cannot be supported by the here presented results, we conclude that the LaMer model is not able to correctly reflect the formation process of the here discussed NPs.

3.4. Reduction of H_2PtCl_6 by Visible Light with Varying OH^- Starting Concentrations. Previous reports demonstrated the influence of the OH^- concentration on the NP size;[2−4] we hence also explored different NaOH/Pt ratios in the reduction of H_2PtCl_6 with NaOH for irradiation with 500 nm. All Pt NP dispersions could be precipitated completely after 24 h, and the supernatant was colorless (0.047−0.25 M NaOH). This indicates a complete reduction of H_2PtCl_6. By lowering the NaOH concentration from 0.250 to 0.063 M NaOH, the rate of NP formation decreases, while the NP size increases from 1.3 ± 0.5 nm to 2.0 ± 0.4 nm (Figures 6 and 7). This finding is basically in agreement with the LaMer model. However, the same trend is also observed by thermally,[2] microwave-,[4] and UV-light-induced Pt NP synthesis,[3] where the reduction occurs at completely different time scales. Considering the above discussion on the LaMer model and the expected effect of temperature on the particle size, the here presented results further support the hypothesis that the LaMer model is not suitable to describe the particle formation for the alkaline EG approach.

Previous results of thermally induced NP formation showed that no stable NPs are formed below a concentration of 0.063 M NaOH.[2] This is explainable by the number of OH^- ions needed to neutralize the formed protons during the reduction.[2] For a concentration of 0.01025 M Pt precursor, 0.0615 M OH^- ions are needed for the neutralization. Hence, the use of OH^- starting concentrations higher than 0.0615 M in the visible-light-induced NP formation leads to the expected basic pH conditions even after several weeks, and hence, the NPs remain stable during that time. At 0.031 M, there is no nucleation, and hence, no NP formation is observed within 24 h, although a color change (the yellow color of the $PtCl_6^-$ complex disappeared) after 3 h indicates a change of the precursor (Figure 6). Hence, it seems that a certain amount of NaOH is needed to exchange the Cl^- in the Pt complex to initiate nucleation. For 0.055 M NaOH (NaOH/Pt = 5.3) and 0.047 M NaOH (NaOH/Pt = 4.6), NPs are formed, but considering what has been reported for thermal reduction, the NPs are expected to precipitate as the OH^- concentration is too low to achieve NP stabilization.[2] However, after irradiation for 24 h, the NPs with 0.055 M and 0.047 M NaOH seem to be stable. Using 0.055 M NaOH compared to 0.063 M NaOH shows a decrease in the rate of the NP formation and an increase of the NP size to 2.7 ± 0.5 nm (Figure 7). The formed particles could be precipitated completely with HCl (colorless supernatant) after the synthesis.[2] Hence, as proposed by Quinson et al.,[4] larger NPs can be formed by decreasing the OH^- concentration in the reaction mixture. However, agglomeration is seen on the TEM grid as there is not enough OH^- to stabilize the particles. To conclude, using the visible-light-induced reduction enables forming NPs in a range of NaOH/Pt ratios where no stable dispersions can be formed by thermal synthesis.[2] At high temperatures, the particle mobility is higher compared to room temperature and the solvent viscosity is lower. We assume that the use of light allows reaching a state that is only kinetically but not thermodynamically stable. Using 0.047 M NaOH, a dark dispersion is already formed after 4 h. The determined NP size is comparable to 0.055 M, but the NPs are agglomerated (Figure 7d). During precipitation of the NPs in 0.047 M NaOH, a dark supernatant is obtained, indicating that precipitation cannot be fully accomplished. The particles could not be redispersed even by adding 0.5 M NaOH. So the sintering of the particles seems to be primarily inhibited by diffusion limitation at room temperature.[43,44] The thermodynamic instability at low base

https://dx.doi.org/10.1021/acs.jpcc.0c06361
J. Phys. Chem. C 2020, 124, 21798−21809

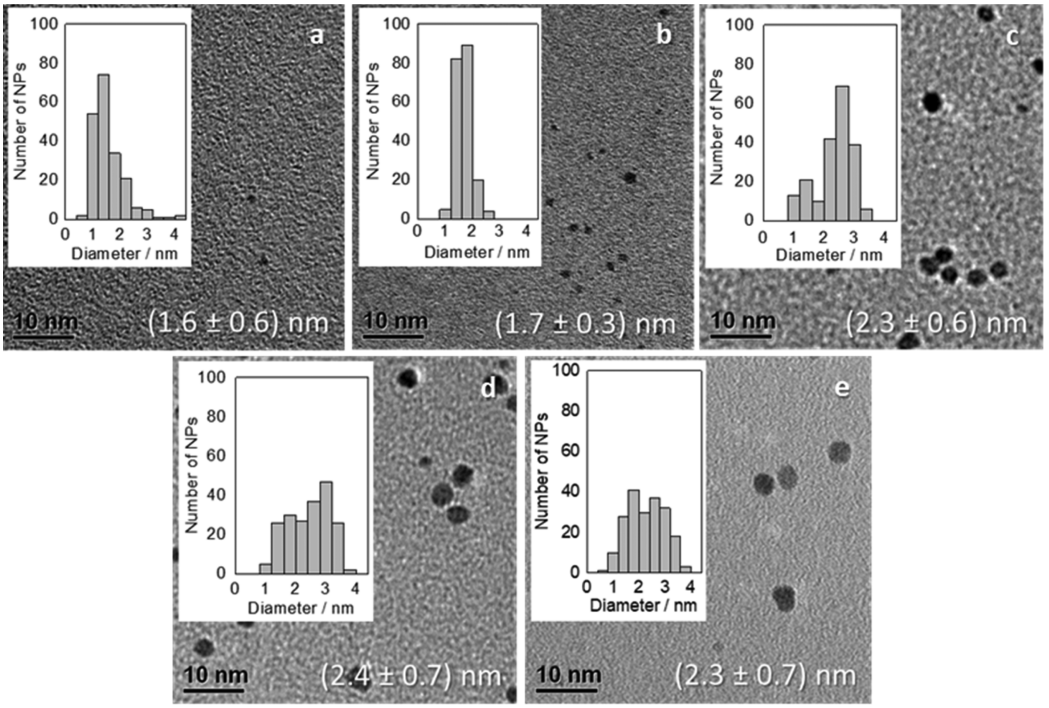

Figure 9. TEM images, averaged particle sizes, and NP size distributions of NPs after exposure of H_2PBr_6 with 500 nm for 24 h using a NaOH starting concentration of (a) 0.125, (b) 0.094, (c) 0.063, (d) 0.055 M, and (e) 0.055 M after 3 h of irradiation.

concentrations allows us to explain why depending on the reaction control larger NP sizes (e.g., 4−5 nm of microwave-induced NPs below NaOH/Pt of 5[4]) can be formed but not stabilized.

3.5. Reduction of H_2PtBr_6 by Visible Light with Varying OH^- Starting Concentrations. The results of this work show that, at a constant OH^-/Pt ratio, the NP formation is faster with the bromide-based precursor, but the NP size is the same as that using the Cl-based precursor. The question is if the variation of the OH^-/Pt ratio by using the bromide-based precursor shows the same change of the NP size as that using H_2PtCl_6. This is expected when the halide and the resulting difference in particle formation rates do not influence the particle size. After 24 h of irradiation of H_2PtBr_6 with 500 nm and different NaOH starting concentrations (between 0.055 and 0.250 M NaOH) all Pt NP dispersions could be precipitated (Figure 8).

The time-dependent UV/vis spectra (Figure S9) during the H_2PtBr_6 reduction by varying the OH^- starting concentration show as mentioned above by varying the irradiated wavelength (Figure S8) an absorbance maximum at 270 nm that is assumed to be an intermediate. This intermediate is hence even at low OH^- concentration formed and not rapidly consumed. The comparison of the UV/vis absorbance after 24 h with varying OH^- starting concentrations is shown in Figure S10, and the reaction time dependent changes are shown in Figure S8. The rate of NP formation decreases from 0.250 to 0.094 M NaOH and increases by lowering the concentration to 0.063 and 0.055 M (Figure 8, Figure S10); this change is similar to the results obtained for H_2PtCl_6 (see Figure 6, Figure S7). In the concentration range where the NP formation rate is decreased, the particle size remains constant within the size error at 1.6−1.7 nm (Figure S12c and Figure 9a,b). In the range where the formation rate is increased (by continuing lowering of the concentration), the particle sizes increase to 2.3−2.4 nm (Figure 9c,d). The particle size increases (for H_2PtBr_6 from 1.6 to 2.4 nm) are comparable to the results of the reduction of H_2PtCl_6 (from 1.3 to 2.7 nm) with varying OH^- starting concentrations (Figures 7 and 9). Using a concentration of 0.055 M shows already after 3 h of irradiation a dark-brown dispersion, and the NPs can be completely precipitated (Figure 8). This is in agreement with the only small changes of the UV/vis absorption spectra (Figure S8d) and the constant particle sizes after 3 h of irradiation (2.3 ± 0.7 nm, Figure 9e) as compared to 24 h (2.4 ± 0.7 nm). For NaOH concentrations below 0.0615 M, instable dispersion should be formed as previously seen for H_2PtCl_6. However, using 0.055 M NaOH with the H_2PtBr_6 precursor led to stable NPs for several weeks. So, it could be assumed that when not enough OH^- is found in the system, the particles are stabilized by the halide. As bromide shows a stronger interaction with Pt than chloride,[45] the differences between chloride and bromide lead to the assumption that bromide stabilizes the surface better than chloride.

In summary, using H_2PtBr_6 instead of H_2PtCl_6 as the precursor for visible-light-induced reduction at room temperature leads to an equivalent increase of NP size with a smaller OH^-/Pt ratio. This particle size control by the OH^-/Pt ratio is also reported in thermally,[2] UV light-[3] and microwave-induced reduction.[4] The increase of NP size by lowering the OH^- content cannot be explained by Ostwald ripening as according to Neumann et al. this process proceeds at higher temperatures (150 °C, after 17 h).[41] Thus, the choice of the metal precursor does not influence the particle size if the reaction is performed in a range, where changes due to Ostwald ripening can be excluded. The formation of the intermediates during the reduction can be observed spectroscopically and leads to the assumption that the halides are partially exchanged with OH^-. The different halide hydroxo complexes lead to the precursor-dependent NP

https://dx.doi.org/10.1021/acs.jpcc.0c06361
J. Phys. Chem. C 2020, 124, 21798−21809

formation rates that however do not determine the final particle size.

3.6. Seed-Mediated Growth Experiments. To further investigate the relevance of the LaMer model, the possibility of seed-mediated growth was tested. According to LaMer, it is possible to let particles grow by exposing NPs to a solution of monomers, low enough in concentration that no nucleation can occur as a competitive reaction pathway.[46] Kunz et al.[47] showed in kinetic studies that the particle size of bimetallic AuPd NPs could be increased by adding different amounts of Au precursor solution to Pd NPs at ambient temperature. In calculations, assuming that the size of all clusters is increased by the same amount within a given time period, the initial size distribution of the Pd clusters is changed by the added Au precursor. The measured particle size increase is in good agreement with predictions based on a pure seed-mediated growth model. This way of seed-mediated growth by exposing NPs to a more noble precursor solution[47] is also shown for bimetallic RuPt NPs by Hwang et al.[33] However, reducing the more noble metal ions in the presence of less noble clusters is thermodynamically restricted.[47]

In the present study, we tried to deposit the reduced precursor of H_2PtCl_6 in several ways and under different conditions onto thermally formed Pt NPs (also by reducing the NaOH concentration) at room temperature in the absence and presence of light (a to c, see Figures S13−S16) over 1 week or under irradiation with 500 nm for 3 h (d, see Figure S17). To exclude diffusion limitations in EG at room temperature, mixtures were vigorously stirred. The thermally formed Pt NPs were used in different ways as seeds: Pt NPs were used as-prepared (a, see Figures S13 and S14, 1.5−1.8 nm), precipitated with HCl and then redispersed in EG (b, see Figure S15, 1.1−1.7 nm), and as carbon supported Pt NPs dispersed in EG (c, see Figure S16, 1.7−1.8 nm). Based on the calculations for the particle growth as per Kunz et al.,[47] NP sizes of 1.8−2.6 nm would be expected (for further information see the Supporting Information). The comparison of the expected particle sizes to those obtained by TEM shows that none of these trails led to a successful seed-mediated growth. The starting OH^- concentration of the seed-mediated growth experiments was in most cases not below 0.125 M. As in this concentration range, the particle size does not change significantly with the OH^- concentration (see Figure 7), and the unsuccessful particle growth is in agreement with the previous OH^--dependent syntheses. In the seed-mediated growth experiment under irradiation with 500 nm (d), the OH^- concentration was below 0.125 M. The wavelength of 500 nm in the experiments should lead after 2 hours of the exposure to reduction of the precursor (Figure 2). However, the expected particle size of 2.1−2.3 nm was also here not reached (see Figure S17, 1.3−1.4 nm).

Hence, the unsuccessful seed-mediated growth experiments of this work give a further indication that the kinetic LaMer model does not seem to describe sufficiently the particle formation process in the EG method. Instead, the process seems thermodynamically controlled.

3.7. Proposed Growth Model. Quinson et al.[4] recently showed that the ratio of OH^- to the number of Pt surface atoms determines the particle size. The here presented results further support this proposal, as the particle size seems merely to depend on the OH^-/Pt ratio independent of different kinetics. In contrast, any proposal for the change in particle size based on the LaMer model fails to explain the here presented results as well as previous studies on thermally, microwave-, and UV-light-induced syntheses. Some conclusions can be drawn from recent reports on the alkaline polyol approach that all seem to support the relevance of the OH^-/Pt ratio for the resulting particle size in combination with the here discussed findings. Based on all these experimental results, we propose the following mechanisms (see Figure 10): NPs

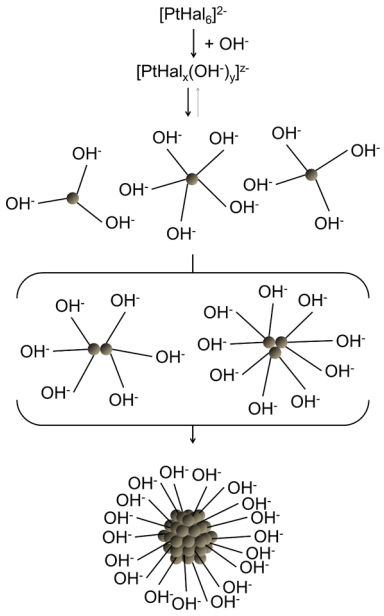

Figure 10. Proposed NP formation mechanism with (I) an intermediate formation by a partial substitution of the halides by hydroxide ions, (II) further reduction to Pt^0 atoms that are stabilized by hydroxide, and (III) dimer and trimer formation of Pt^0 leading to the final NPs with the size determined by the ratio of hydroxide to Pt surface atoms.

synthesized without[3] or with very low NaOH concentrations[2] do not give stable colloidal dispersions, or no particles are formed at all. (I) Hence, probably an intermediate is formed from the precursors where the halide ligands have been partially substituted by OH^-, leading to a halide hydroxo mixed platinum complex as active species. The final particle size is not determined by Ostwald ripening as this process proceeds at higher temperatures (150 °C, after 17 h)[41] but because of other thermodynamic aspects that are controlled by the hydroxide concentration. This dependency of OH^- to Pt surface atoms is supposed to influence already the first formed Pt^0. (II) We assume that the monomers are formed by the reduction of the halide hydroxo platinum complex. The time-dependent UV/vis investigation shows that the intermediate is formed rapidly, but the complete NP formation takes a long time at room temperature under visible light exposure. In addition, during the reduction of H_2PtBr_6, the UV/vis absorption maximum of the intermediate is observable for a quite long time (6 h) (the intermediate of the reduction of H_2PtCl_6 is UV/vis spectroscopically not visible). The monomer formation step is slow compared to the intermediate formation. Hence, it seems that not the reduction of the precursor to the intermediate but the monomer formation (fully reduced precursor) from the intermediate (partially reduced precursor) is the kinetically relevant step. In addition, the monomer formation seems to occur preferentially under exposure to visible light with a wavelength of 500 nm. (III) A

https://dx.doi.org/10.1021/acs.jpcc.0c06361
J. Phys. Chem. C 2020, 124, 21798−21809

freshly formed single atom tries to bind further Pt atoms. If no Pt is available, it will coordinate ligands. Pt is known to bind OH^- quite strongly.[45] At the beginning of the reaction, a higher concentration of OH^- is present for only a few monomers. Thus, the monomers can be stabilized by OH^- coordination. Subsequently formed Pt monomers can either react backward to the intermediate or coalesce with Pt atoms stabilized by OH^- to form dimers, trimers, etc. Such a simultaneous nucleation and growth is in agreement with the Finke–Watzky two-step mechanism.[20,48,49] Since Pt is a noble metal, the formation of a Pt bulk phase is thermodynamically favored over the formation of the intermediate by oxidation. So, the monomers react preferentially to form particles, and their size becomes limited finally by the ratio of OH^- to Pt surface atoms. It was shown before that besides OH^- additionally CO is bound to the surface of the NPs.[2,4] However it is not clear, when the CO starts to appear as a surface binding species. After the visible-light-induced NP synthesis, there was no strong CO absorption band above 2000 cm^{-2} seen in FTIR spectroscopy as compared to the strong signal in the thermal synthesis (see Figure S18).[2] Therefore, only at high temperatures (150 °C), a significant CO amount seems to be present on the Pt surface to stabilize the NPs.

The OH^- amount is not only responsible for the size control but also for stabilizing the NPs.[2] When the chloride-containing precursor is used at a low OH^- concentration, no stable particles could be formed.[2] So, it seems that CO alone cannot sufficiently stabilize the NPs.[2] In the case of bromide, it seems that bromide is additionally stabilizing the particles. This is in line with the fact that bromide can interact stronger with Pt than chloride.[45] Consequently, when not enough OH^- is present in the system to stabilize the NPs, the proposed model is not valid.

The above discussed unsuccessful seed-mediated growth experiments are in agreement with the proposed NP formation mechanism. When the OH concentration is high (seed-mediated growth experiments a to c, Figures S13–S15), no growth of the seeds is expected. Instead, it is assumed that the precursor is reduced and form NPs whose size depends on the ratio of the OH^- to the Pt surface atoms. In the last seed-mediated growth experiment (d, Figure S16), the ratio of OH^- to Pt should basically allow NP growth. However, no growth has occurred. Although OH^- is within the system, there is not enough free OH^- in the solution since OH^- supports the stabilization the NPs (i.e., the seeds) that if otherwise only being covered by CO would aggregate. The OH^- is bound stronger to the NPs; hence, there is not enough free OH^- to form the reactive intermediate. Therefore, the reaction based on our suggested growth mechanism stops and the particle size does not change.

4. CONCLUSIONS

In summary, using the EG method to synthesize NPs by visible light at room temperature leads to the same mechanism of EG oxidation as thermally, microwave-, or UV-light-induced reduction. At a constant OH^-/Pt ratio, the same particle sizes were obtained irrespective of the presence of halides of different metal precursors, the energy source by variation of the wavelength, and the reduction time. Reducing the OH^-/Pt ratio leads to similar particle size increases independent of the presence of halides as long as the reaction proceeds outside a range where Ostwald ripening is known to occur. Because of the same result in particle size despite different timescales and conditions, as well as the unsuccessful seed-mediated growth experiments, the LaMer model seems to be invalid. Instead, we proposed a mechanism assuming that NPs are generated by the agglomeration/sintering of clusters that are formed by the reduction of halide hydroxo platinum complexes.

■ ASSOCIATED CONTENT

Supporting Information

The Supporting Information is available free of charge at https://pubs.acs.org/doi/10.1021/acs.jpcc.0c06361.

ESI-MS spectra; UV/vis spectra; TEM images; seed-mediated growth experiments; FTIR data; transmission spectra of the filters (PDF)

■ AUTHOR INFORMATION

Corresponding Author

Sebastian Kunz − *Institute of Applied and Physical Chemistry (IAPC), Center for Environmental Research and Sustainable Technology, University of Bremen, 28359 Bremen, Germany; Südzucker AG, Central Department Research, Development, and Services (CRDS), 67283 Obrigheim, Germany;* orcid.org/0000-0002-2512-9316; Email: sebkunz@uni-bremen.de

Authors

Johanna Schröder − *Institute of Applied and Physical Chemistry (IAPC), Center for Environmental Research and Sustainable Technology, University of Bremen, 28359 Bremen, Germany; Department of Chemistry and Biochemistry, University of Bern, 3012 Bern, Switzerland*

Sarah Neumann − *Institute of Applied and Physical Chemistry (IAPC), Center for Environmental Research and Sustainable Technology, University of Bremen, 28359 Bremen, Germany*

Complete contact information is available at: https://pubs.acs.org/10.1021/acs.jpcc.0c06361

Notes

The authors declare no competing financial interest.

■ ACKNOWLEDGMENTS

The authors acknowledge the DFG for financial support (BA 1710/15-3 and KU 3152/6-1), and S.K. thanks the "Fonds der Chemischen Industrie (FCI)" for financial support through a Liebig research grant. The authors further thank M. Nowak for technical support, Dr. K. Thiel and the Fraunhofer Institute for Manufacturing Technology and Advanced Materials (IFAM) for technical support with TEM, Dr. T. Dülcks and D. Kemken from the mass spectrometry service from the Institute of Organic and Analytical Chemistry at the University of Bremen, and the mass spectrometry service from the Department of Chemistry and Biochemistry at the University of Bern.

■ REFERENCES

(1) Wang, Y.; Ren, J.; Deng, K.; Gui, L.; Tang, Y. Preparation of Tractable Platinum, Rhodium, and Ruthenium Nanoclusters with Small Particle Size in Organic Media. *Chem. Mater.* **2000**, *12*, 1622–1627.

(2) Schrader, I.; Warneke, J.; Neumann, S.; Grotheer, S.; Swane, A. A.; Kirkensgaard, J. J. K.; Arenz, M.; Kunz, S. Surface Chemistry of "Unprotected" Nanoparticles: A Spectroscopic Investigation on Colloidal Particles. *J. Phys. Chem. C* **2015**, *119*, 17655–17661.

(3) Kacenauskaite, L.; Quinson, J.; Schultz, H.; Kirkensgaard, J. J. K.; Kunz, S.; Vosch, T.; Arenz, M. UV-Induced Synthesis and

Stabilization of Surfactant-Free Colloidal Pt Nanoparticles with Controlled Particle Size in Ethylene Glycol. *ChemNanoMat* **2017**, *3*, 89−93.
(4) Quinson, J.; Inaba, M.; Neumann, S.; Swane, A. A.; Bucher, J.; Simonsen, S. B.; Theil Kuhn, L.; Kirkensgaard, J. J. K. K.; Jensen, K. M. Ø.; Oezaslan, M.; Kunz, S.; Arenz, M. Investigating Particle Size Effects in Catalysis by Applying a Size-Controlled and Surfactant-Free Synthesis of Colloidal Nanoparticles in Alkaline Ethylene Glycol: Case Study of the Oxygen Reduction Reaction on Pt. *ACS Catal.* **2018**, *8*, 6627−6635.
(5) Kacenauskaite, L.; Swane, A. A.; Kirkensgaard, J. J. K.; Fleige, M.; Kunz, S.; Vosch, T.; Arenz, M. Synthesis Mechanism and Influence of Light on Unprotected Platinum Nanoparticles Synthesis at Room Temperature. *ChemNanoMat* **2016**, *2*, 104−107.
(6) Comotti, M.; Li, W. C.; Spliethoff, B.; Schüth, F. Support Effect in High Activity Gold Catalysts for CO Oxidation. *J. Am. Chem. Soc.* **2006**, *128*, 917−924.
(7) Bock, C.; Paquet, C.; Couillard, M.; Botton, G. A.; MacDougall, B. R. Size-Selected Synthesis of PtRu Nano-Catalysts: Reaction and Size Control Mechanism. *J. Am. Chem. Soc.* **2004**, *126*, 8028−8037.
(8) Neumann, S.; Gutmann, T.; Buntkowsky, G.; Paul, S.; Thiele, G.; Sievers, H.; Bäumer, M.; Kunz, S. Insights into the Reaction Mechanism and Particle Size Effects of CO Oxidation over Supported Pt Nanoparticle Catalysts. *J. Catal.* **2019**, *377*, 662−672.
(9) Toshima, N.; Yonezawa, T. Bimetallic Nanoparticles—Novel Materials for Chemical and Physical Applications. *New J. Chem.* **1998**, *22*, 1179−1201.
(10) Huang, W.; Hua, Q.; Cao, T. Influence and Removal of Capping Ligands on Catalytic Colloidal Nanoparticles. *Catal. Lett.*. 2014, *144*, 1355−1369. doi: DOI: 10.1007/s10562-014-1306-5.
(11) Neumann, S.; Grotheer, S.; Tielke, J.; Schrader, I.; Quinson, J.; Zana, A.; Oezaslan, M.; Arenz, M.; Kunz, S. Nanoparticles in a Box: A Concept to Isolate, Store and Re-Use Colloidal Surfactant-Free Precious Metal Nanoparticles. *J. Mater. Chem. A* **2017**, *5*, 6140−6145.
(12) Wang, Y.; Zhang, J.; Wang, X.; Ren, J.; Zuo, B.; Tang, Y. Metal Nanoclusters Stabilized with Simple Ions and Solvents - Promising Building Blocks for Future Catalysts. *Top. Catal.* **2005**, *35*, 35−41.
(13) Corain, B.; Schmid, G.; Toshima, N. *Metal Nanoclusters in Catalysis and Materials Science: The Issue of Size Control*; Elsevier, 2008. doi: DOI: 10.1016/B978-0-444-53057-8.X5001-6.
(14) Wang, X.; Sonström, P.; Arndt, D.; Stöver, J.; Zielasek, V.; Borchert, H.; Thiel, K.; Al-Shamery, K.; Bäumer, M. Heterogeneous Catalysis with Supported Platinum Colloids: A Systematic Study of the Interplay between Support and Functional Ligands. *J. Catal.* **2011**, *278*, 143−152.
(15) Polte, J. Fundamental Growth Principles of Colloidal Metal Nanoparticles − a New Perspective. *CrystEngComm* **2015**, *17*, 6809−6830.
(16) Sugimoto, T.; Shiba, F.; Sekiguchi, T.; Itoh, H. Spontaneous Nucleation of Monodisperse Silver Halide Particles from Homogeneous Gelatin Solution I: Silver Chloride. *Colloids Surfaces A Physicochem. Eng. Asp.* **2000**, *164*, 183−203.
(17) Sugimoto, T.; Shiba, F. Spontaneous Nucleation of Monodisperse Silver Halide Particles from Homogeneous Gelatin Solution II: Silver Bromide. *Colloids Surfaces A Physicochem. Eng. Asp.* **2000**, *164*, 205−215.
(18) Park, B. K.; Jeong, S.; Kim, D.; Moon, J.; Lim, S.; Kim, J. S. Synthesis and Size Control of Monodisperse Copper Nanoparticles by Polyol Method. *J. Colloid Interface Sci.* **2007**, *311*, 417−424.
(19) Chee, S. S.; Lee, J. H. Preparation and Oxidation Behavior of Ag-Coated Cu Nanoparticles Less than 20 Nm in Size. *J. Mater. Chem. C* **2014**, *2*, 5372.
(20) Thanh, N. T. K.; Maclean, N.; Mahiddine, S. Mechanisms of Nucleation and Growth of Nanoparticles in Solution. *Chem. Rev.* **2014**, *114*, 7610−7630.
(21) Quinson, J.; Bucher, J.; Simonsen, S. B.; Kuhn, L. T.; Kunz, S.; Arenz, M. Monovalent Alkali Cations: Simple and Eco-Friendly Stabilizers for Surfactant-Free Precious Metal Nanoparticle Colloids. *ACS Sustainable Chem. Eng.* **2019**, *7*, 13680−13686.
(22) Ranjbar, K.; Abasi, A. Failure Assessment of Crude Oil Preheating Tubes in Mono Ethylene Glycol-Water Mixture Solution. *Eng. Fail. Anal.* **2013**, *31*, 161−167.
(23) Santambrogio, M.; Perrucci, G.; Trueba, M.; Trasatti, S. P.; Casaletto, M. P. Effect of Major Degradation Products of Ethylene Glycol Aqueous Solutions on Steel Corrosion. *Electrochim. Acta* **2016**, *203*, 439−450.
(24) Quinson, J.; Kacenauskaite, L.; Schröder, J.; Simonsen, S. B. B.; Theil Kuhn, L.; Vosch, T.; Arenz, M. UV-Induced Syntheses of Precious Metal Nanoparticles in Alkaline Methanol and Ethanol. *Nanoscale Adv.* **2020**, *2*, 2288−2292.
(25) Quinson, J.; Neumann, S.; Kacenauskaite, L.; Bucher, J.; Kirkensgaard, J. J. K.; Simonsen, S. B.; Theil Kuhn, L.; Zana, A.; Vosch, T.; Oezaslan, M.; Kunz, S.; Arenz, M.; et al. Solvent-Dependent Growth and Stabilization Mechanisms of Surfactant-Free Colloidal Pt Nanoparticles. *Chem. − A Eur. J.* **2020**, *26*, 9012−9023.
(26) Liu, Z.; Ling, X. Y.; Lee, J. Y.; Su, X.; Gan, L. M. Nanosized Pt and PtRu Colloids as Precursors for Direct Methanol Fuel Cell Catalysts. *J. Mater. Chem.* **2003**, *13*, 3049−3052.
(27) Liu, K.; Hou, G.; Mao, J.; Xu, Z.; Yan, P.; Li, H.; Guo, X.; Bai, S.; Zhang, Z. C. Genesis of Electron Deficient Pt1(0) in PDMS-PEG Aggregates. *Nat. Commun.* **2019**, *10*, 996.
(28) Liu, K.; Shen, X.; Bai, S.; Zhang, Z. C. Stable Discrete Pt_1 (0) in Crown Ether with Ultra-High Hydrosilylation Activity. *ChemCatChem* **2020**, *12*, 267−272.
(29) Harada, M.; Einaga, H. Formation Mechanism of Pt Particles by Photoreduction of Pt Ions in Polymer Solutions. *Langmuir* **2006**, *22*, 2371−2377.
(30) Li, H.; Liang, C.; Gao, P.; Hou, G.; Liu, K.; Liu, W.; Jiang, Q.; Bai, S.; Zhang, Z. C. Transportable Mononuclear Metal Atoms as Building Blocks for Bottom-up Material Fabrication: Pt1(0) and Au1(0) Atoms in Stock Solutions. *ChemNanoMat* **2020**, *6*, 1191−1199.
(31) Acharya, R. Interaction of Waves with Medium. In *Satellite Signal Propagation, Impairments and Mitigation*; 2017; pp. 57−86. doi: DOI: 10.1016/b978-0-12-809732-8.00003-x.
(32) Wang, Y.; Wang, Y.; Xu, R. Photochemical Deposition of Pt on CdS for H2 Evolution from Water: Markedly Enhanced Activity by Controlling Pt Reduction Environment. *J. Phys. Chem. C* **2013**, *117*, 783−790.
(33) Hwang, B.-J.; Sarma, L. S.; Chen, C.-H.; Bock, C.; Lai, F.-J.; Chang, S.-H.; Yen, S.-C.; Liu, D.-G.; Sheu, H.-S.; Lee, J.-F. Controlled Synthesis and Characterization of Ru_{Core} −Pt_{Shell} Bimetallic Nanoparticles. *J. Phys. Chem. C* **2008**, *112*, 19922−19929.
(34) Mountain, B. W.; Wood, S. A. Chemical Controls on the Solubility, Transport, and Deposition of Platinum and Palladium in Hydrothermal Solutions: A Thermodynamic Approach. *Econ. Geol.* **1988**, *83*, 492−510.
(35) Holleman, A. F.; und Nils Wiberg, E.; Fischer, G. *Lehrbuch Der Anorganischen Chemie*, 102nd ed.; Walter de Gruyter: Berlin, 2009.
(36) van Wyk, P. H.; Gerber, W. J.; Koch, K. R. A Robust Method for Speciation, Separation and Photometric Characterization of All [PtCl6-NBrn]2- (N=0-6) and [PtCl4-NBrn]2- (N=0-4) Complex Anions by Means of Ion-Pairing RP-HPLC Coupled to ICP-MS/OES, Validated by High Resolution 195Pt NMR Spectroscopy. *Anal. Chim. Acta* **2011**, *704*, 154−161.
(37) Henglein, A.; Ershov, B. G.; Malow, M. Absorption Spectrum and Some Chemical Reactions of Colloidal Platinum in Aqueous Solution. *J. Phys. Chem.* **1995**, *99*, 14129−14136.
(38) Gammons, C. H. Experimental Investigations of the Hydrothermal Geochemistry of Platinum and Palladium.5. Equilibria Between Platinum Metal, Pt(Ii), and Pt(Iv) Chloride Complexes At 25 To 300-Degrees-C. *Geochim. Cosmochim. Acta* **1996**, *60*, 1683−1694.
(39) Murray, P.; Koch, K. R.; Van Eldik, R. Mechanism of Tetrachloroplatinate(Ii) Oxidation by Hydrogen Peroxide in Hydrochloric Acid Solution. *Dalt. Trans.* **2014**, *43*, 6308−6314.
(40) Michel, J. A.; Morris III, W. H.; Lukehart, C. M. Synthesis of Shaped Pt Nanoparticles Using Common Anions or Small Molecules

as Shape-Directing Agents: Observation of a Strong Halide or Pseudo-Halide Effect. *J. Mater. Chem. A* **2015**, *3*, 2012−2018.
(41) Neumann, S.; Schröder, J.; Bizzotto, F.; Arenz, M.; Dworzak, A.; Oezaslan, M.; Bäumer, M.; Kunz, S. Halide-Induced Leaching of Pt Nanoparticles − Manipulation of Particle Size by Controlled Ostwald Ripening. *ChemNanoMat* **2019**, *5*, 462−471.
(42) LaMer, V. K.; Dinegar, R. H. Theory, Production and Mechanism of Formation of Monodispersed Hydrosols. *J. Am. Chem. Soc.* **1950**, *72*, 4847−4854.
(43) Fang, Z. Z. *Sintering of Advanced Materials*; Woodhead Pub, 2010. DOI: 10.1533/9781845699949.
(44) German, R. M. *Thermodynamic and Kinetic Treatments*; 2014. DOI: 10.1016/b978-0-12-401682-8.00007-0.
(45) Markovic, N.; Ross, P. N. Surface Science Studies of Model Fuel Cell Electrocatalysts. *Surf. Sci. Rep.* **2002**, *45*, 117−229.
(46) Xia, Y.; Gilroy, K. D.; Peng, H. C.; Xia, X. Seed-Mediated Growth of Colloidal Metal Nanocrystals. *Angew. Chem., Int. Ed.* **2017**, *56*, 60−95.
(47) Kunz, S.; Iglesia, E. Mechanistic Evidence for Sequential Displacement−Reduction Routes in the Synthesis of Pd−Au Clusters with Uniform Size and Clean Surfaces. *J. Phys. Chem. C* **2014**, *118*, 7468−7479.
(48) Watzky, M. A.; Finke, R. G. Transition Metal Nanocluster Formation Kinetic and Mechanistic Studies. A New Mechanism When Hydrogen Is the Reductant: Slow, Continuous Nucleation and Fast Autocatalytic Surface Growth. *J. Am. Chem. Soc.* **1997**, *119*, 10382−10400.
(49) Besson, C.; Finney, E. E.; Finke, R. G. A Mechanism for Transition-Metal Nanoparticle Self-Assembly. *J. Am. Chem. Soc.* **2005**, *127*, 8179−8184.

https://dx.doi.org/10.1021/acs.jpcc.0c06361
J. Phys. Chem. C 2020, 124, 21798−21809

Supporting Information

Visible-Light-Induced Synthesis of "Surfactant-Free" Pt Nanoparticles in Ethylene Glycol as a Synthetic Approach for Mechanistic Studies on Nanoparticle Formation

Johanna Schröder,[ab] Sarah Neumann,[a] Sebastian Kunz[*ac]

[a] Institute of Applied and Physical Chemistry (IAPC), Center for Environmental Research and Sustainable Technology, University of Bremen, Leobener Strasse 6, 28359 Bremen, Germany

[b] Department of Chemistry and Biochemistry, University of Bern, Freiestrasse 3, 3012 Bern, Switzerland

[c] Südzucker AG, Central Department Research, Development, and Services (CRDS), Wormser Strasse 11, 67283 Obrigheim, Germany

[*] sebkunz@uni-bremen.de

MS Data

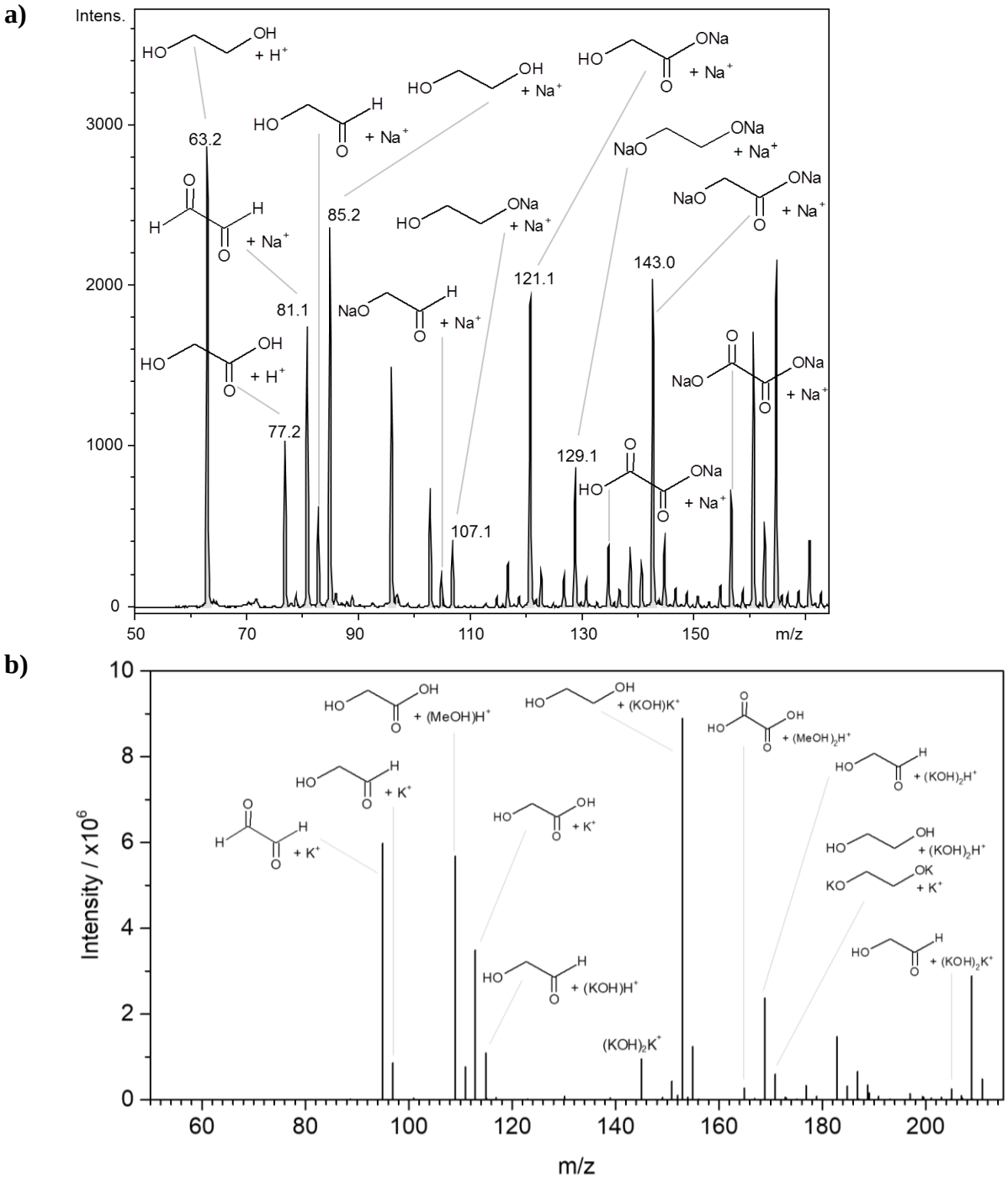

Figure S1: ESI-MS spectrum of the supernatant solvent after precipitating the NPs synthesized by thermal reduction of H_2PtCl_6 a) in the dark using NaOH and b) under room light using KOH. The pH was shifted to alkaline by adding a) $NaHCO_3$ and b) $KHCO_3$. The spectrum was recorded in positive ion mode. The solved species M are detected as quasimolecular ions $[M+H]^+$ or a) $[M+Na]^+$ and b) $[M+K]^+$, $[M+(MeOH)_x+H]^+$, $[M+(KOH)_x+H]^+$, $[M+(KOH)_x+K]^+$.

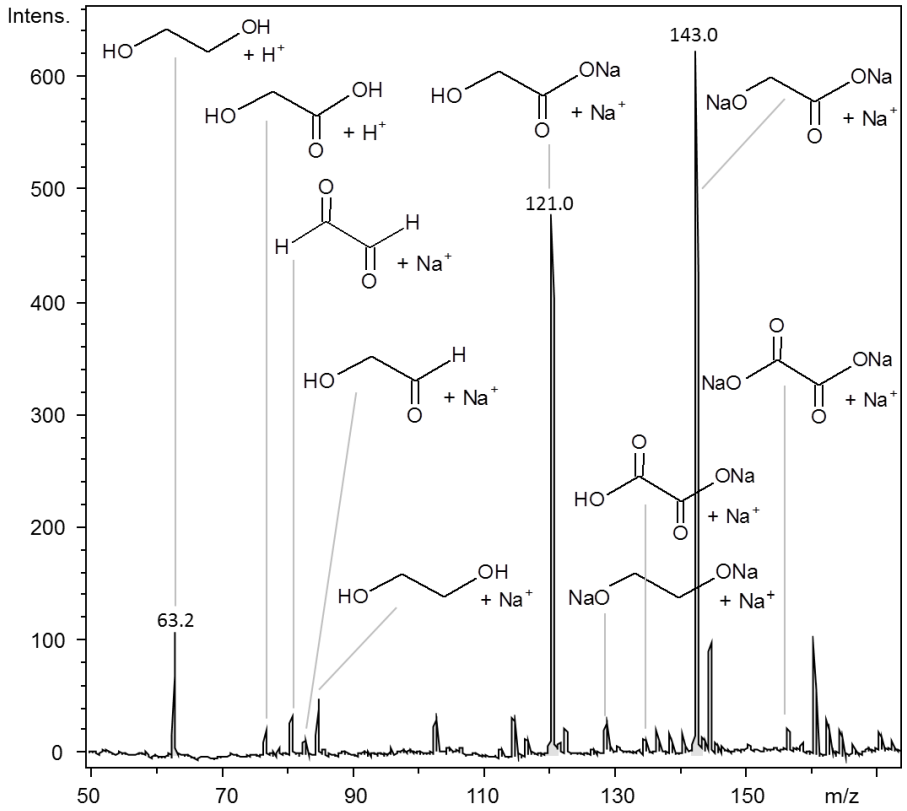

Figure S2: ESI-MS spectrum of the supernatant solvent after precipitating the NPs synthesized by irradiation of H_2PtCl_6 with 500 nm for 24 h. The pH was shifted to alkaline by adding $NaHCO_3$. The spectrum was recorded in positive ion mode. The solved species M are detected as quasimolecular ions $[M+H]^+$ or $[M+Na]^+$.

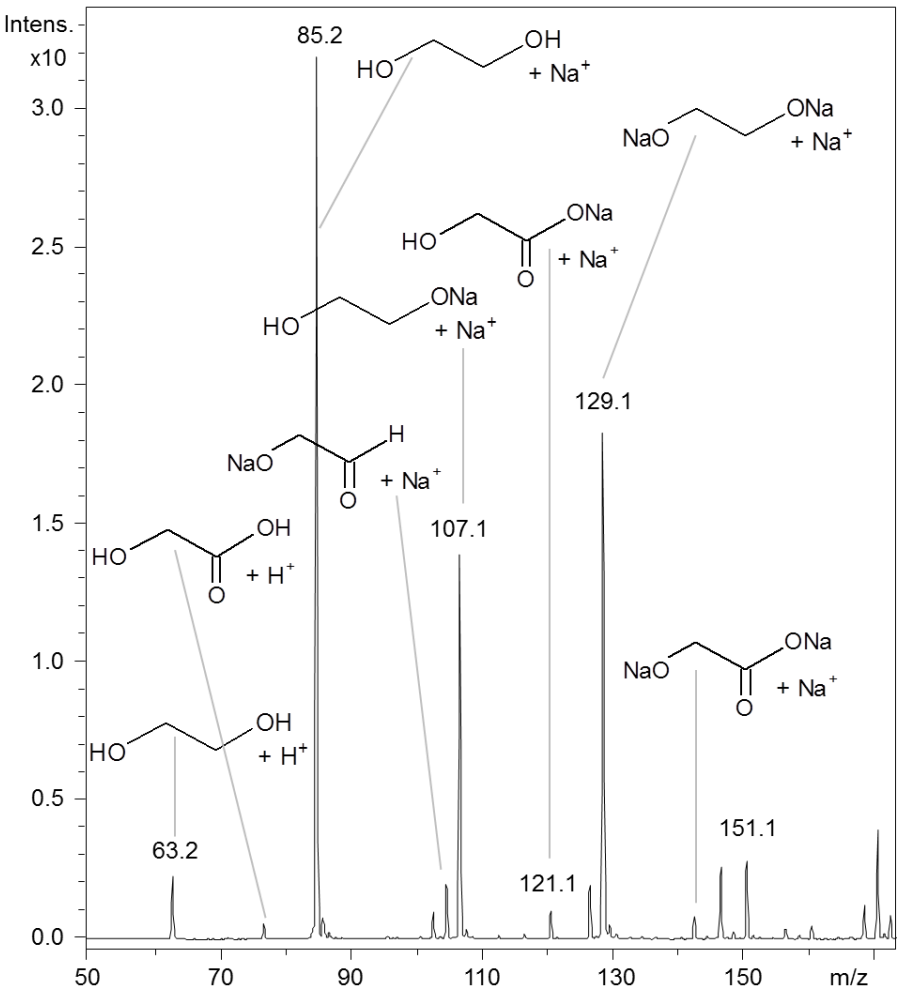

Figure S3: ESI-MS spectrum of 0.25 M NaOH in EG stored in the dark. The spectrum was recorded in positive ion mode. The solved species M are detected as quasimolecular ions $[M+H]^+$ or $[M+Na]^+$.

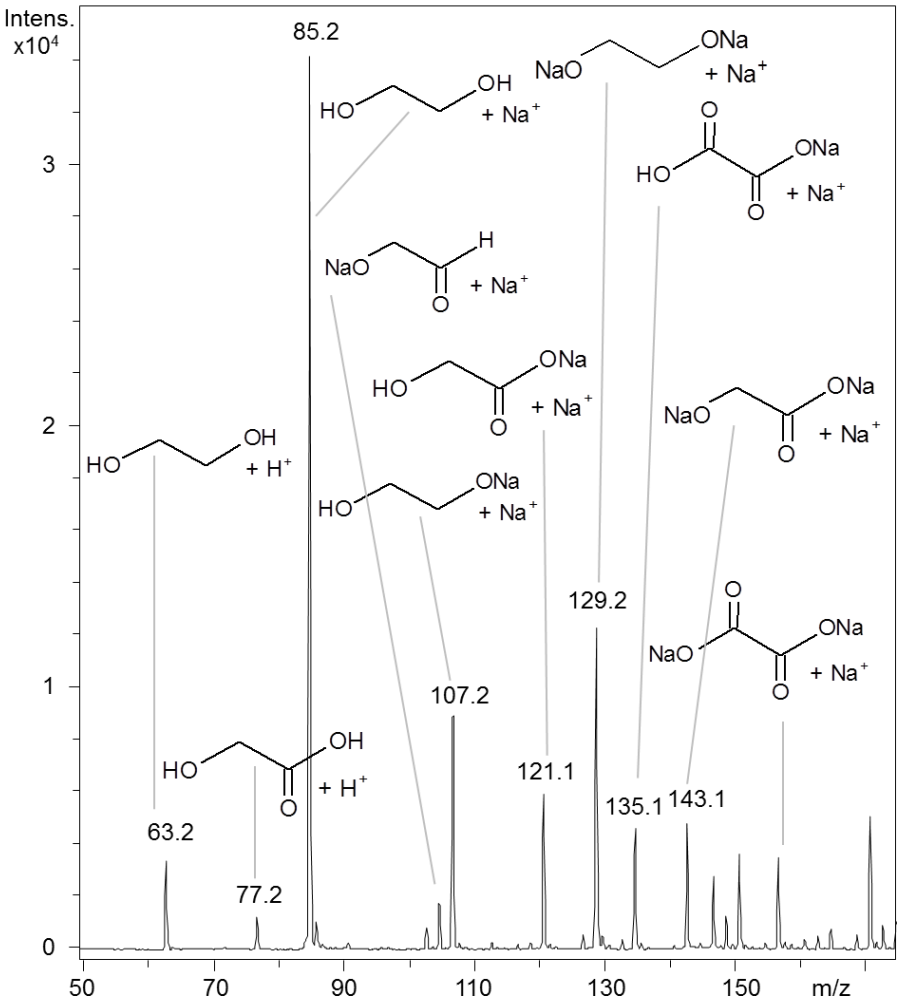

Figure S4: ESI-MS spectrum of 0.25 M NaOH in EG stirred for 1.5 h at 150°C in a preheated oil bath. The spectrum was recorded in positive ion mode. The solved species M are detected as quasimolecular ions $[M+H]^+$ or $[M+Na]^+$.

UV/vis Spectra

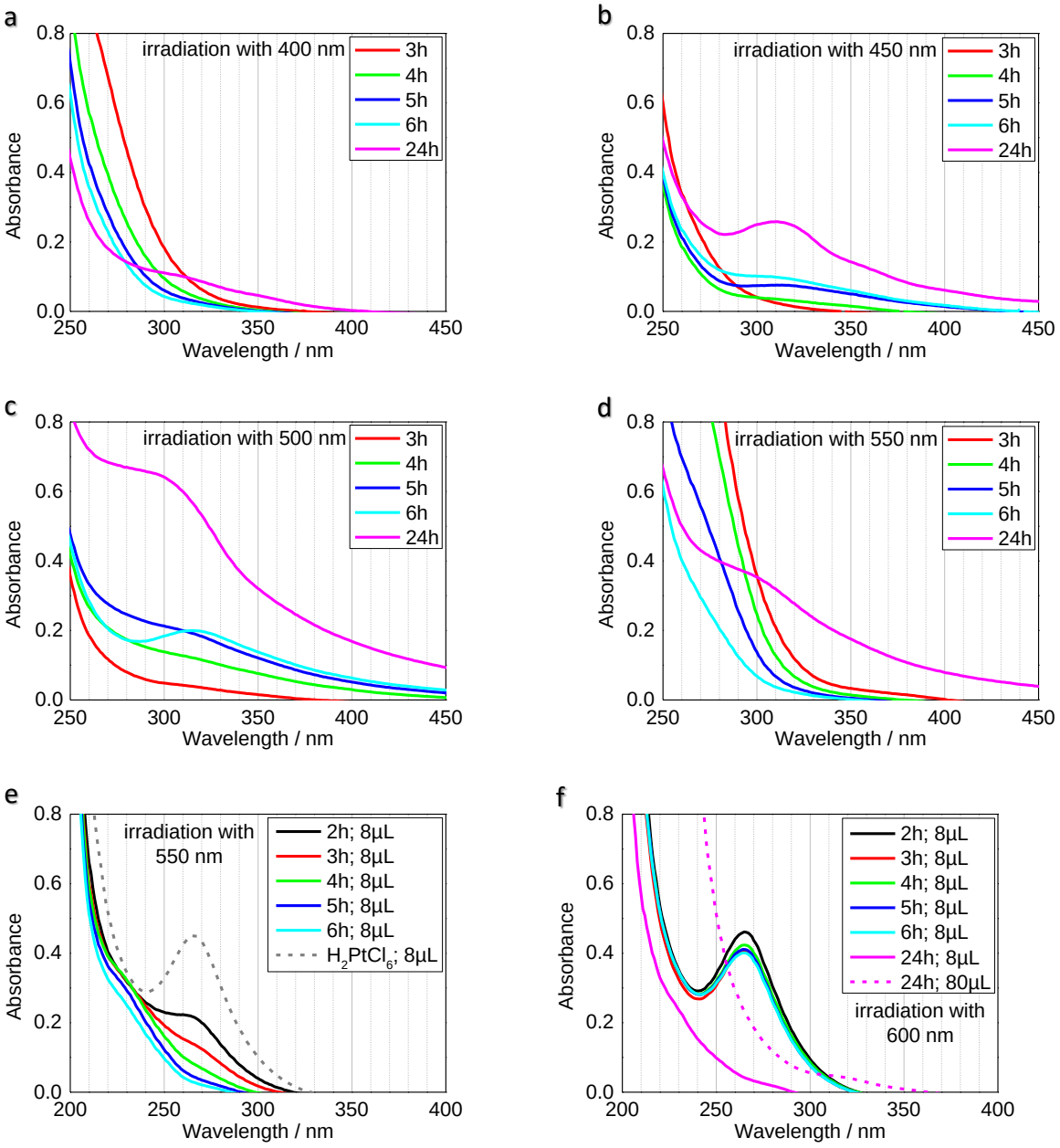

Figure S5: Time-dependent UV/vis spectra of NP dispersions after 2, 3, 4, 5, 6, and 24 h of irradiation with **a** 400, **b** 450, **c** 500, **d/e** 550, and **f** 600 nm of H_2PtCl_6 in EG using 0.250 M as OH^- starting concentration.

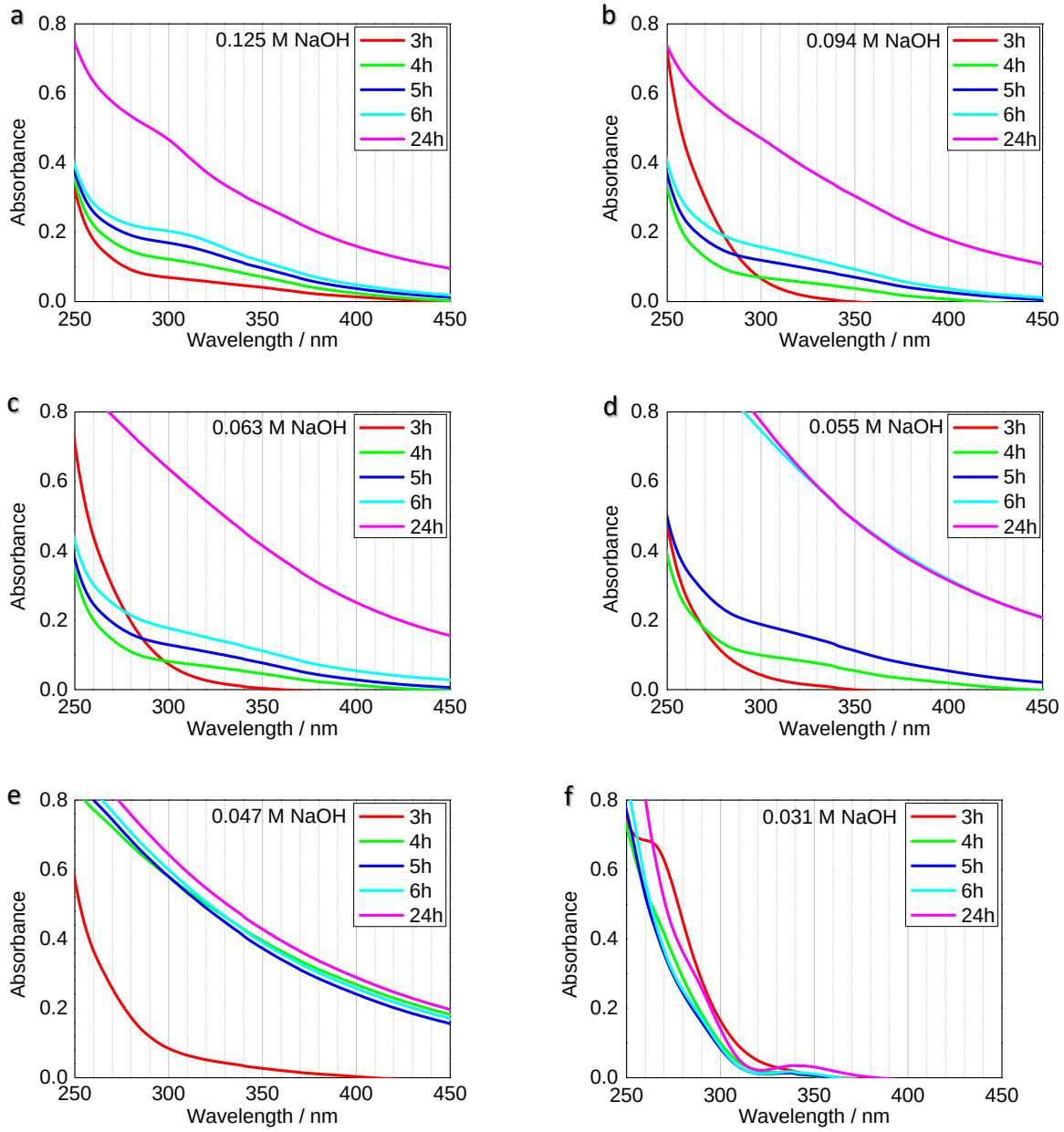

Figure S6: Time-dependent UV/vis spectra of NP dispersions after 2, 3, 4, 5, 6, and 24 h of irradiation with 500 nm of H_2PtCl_6 in EG using **a** 0.125, **b** 0.094, **c** 0.063, **d** 0.055, **e** 0.047, and **f** 0.031 M as OH^- starting concentration.

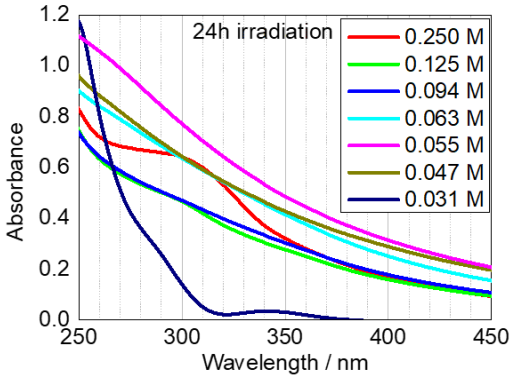

Figure S7: Comparing UV/vis spectra of NP dispersions after 24 h of irradiation with 500 of H_2PtCl_6 in EG using 0.250, 0.125, 0.094, 0.063, 0.055, 0.047, and 0.031 M as OH^- starting concentration.

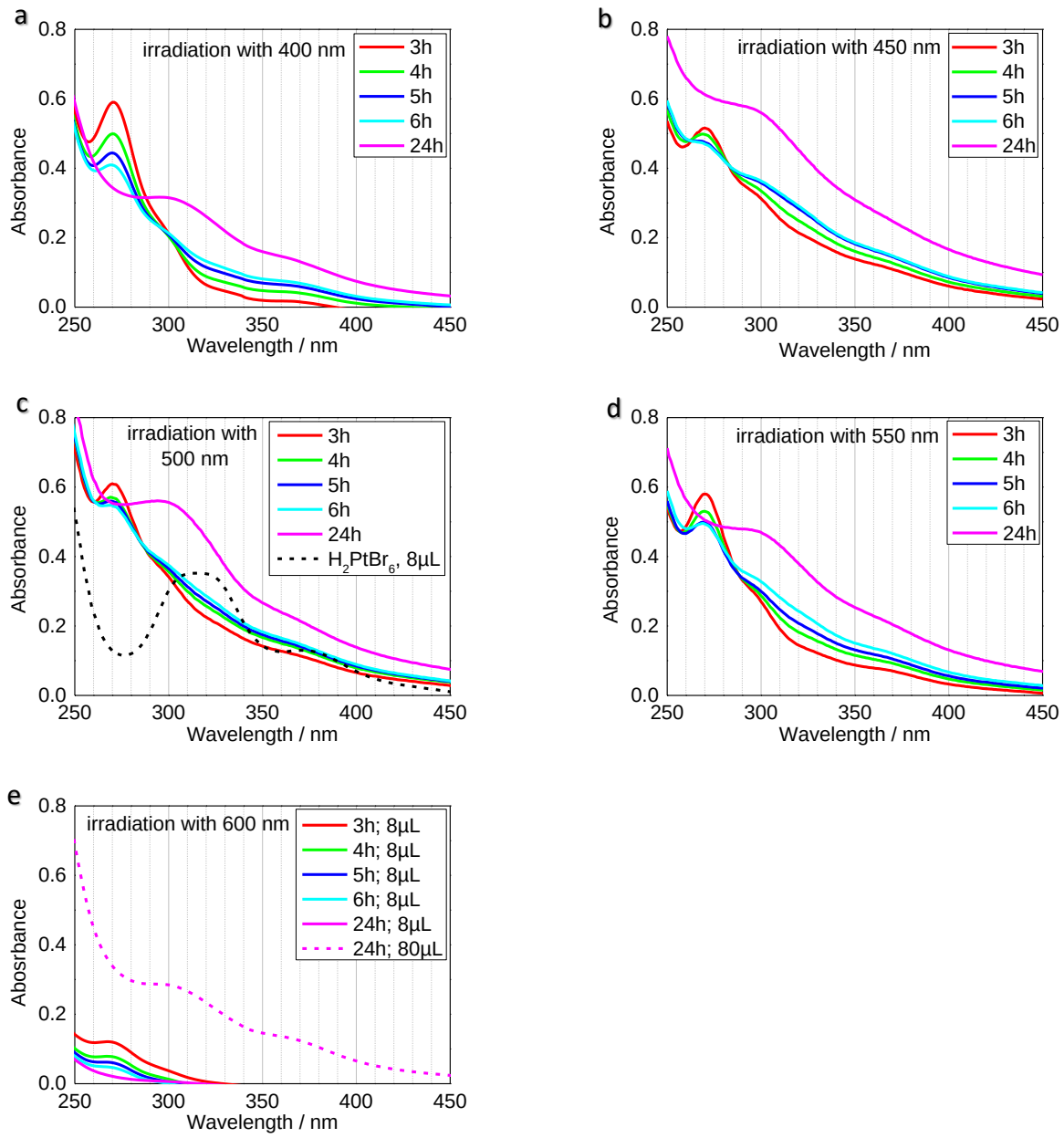

Figure S8: Time-dependent UV/vis spectra of NP dispersions after 2, 3, 4, 5, 6, and 24 h of irradiation with **a** 400, **b** 450, **c** 500, **d** 550, and **e** 600 nm of H_2PtBr_6 in EG using 0.250 M as OH^- starting concentration. The specifications of 8 or 80 µL is related to the dilutions of the sample for UV/vis measurements (s. chapter 2.2.1)

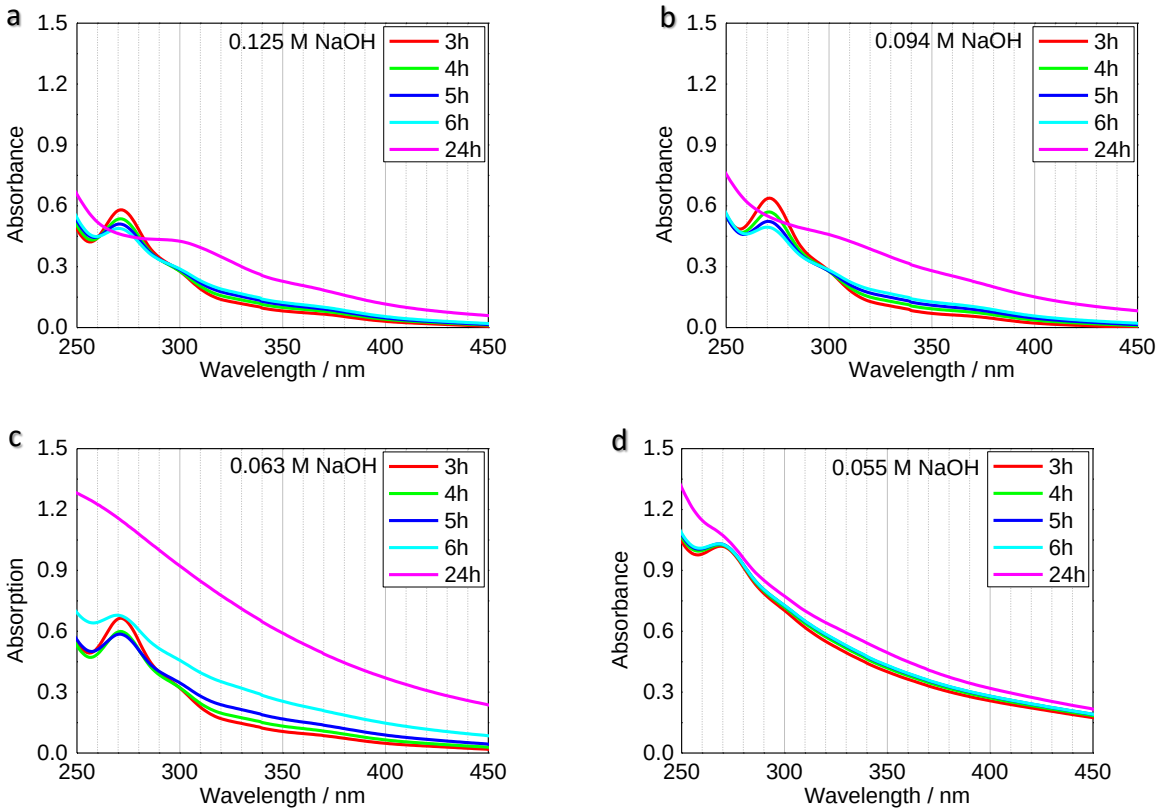

Figure S9: Time-dependent UV/vis spectra of NP dispersions after 2, 3, 4, 5, 6, and 24 h of irradiation with 500 nm of H_2PtBr_6 in EG using **a** 0.125, **b** 0.094, **c** 0.063, and **d** 0.055 M as OH^- starting concentration.

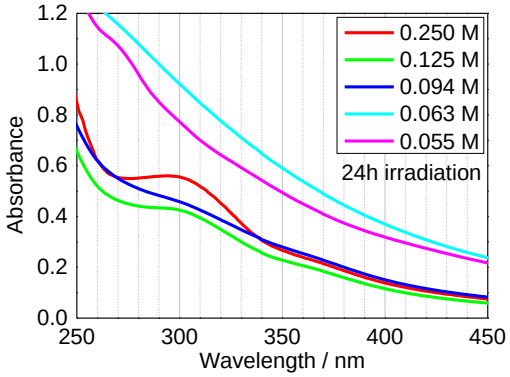

Figure S10: Comparing UV/vis spectra of NP dispersions after 24 h of irradiation with 500 of H_2PtBr_6 in EG using 0.250, 0.063, and 0.055 M as OH^- starting concentration.

TEM Images

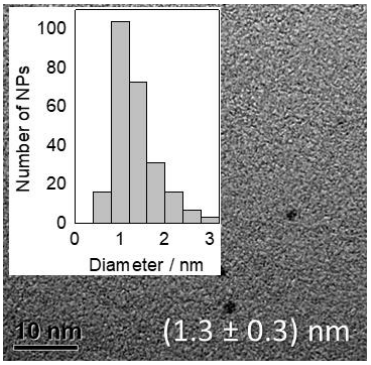

Figure S11: TEM images, averaged particle sizes and NP size distributions of NPs after 24 h of irradiation of H_2PtCl_6 with 500 nm.

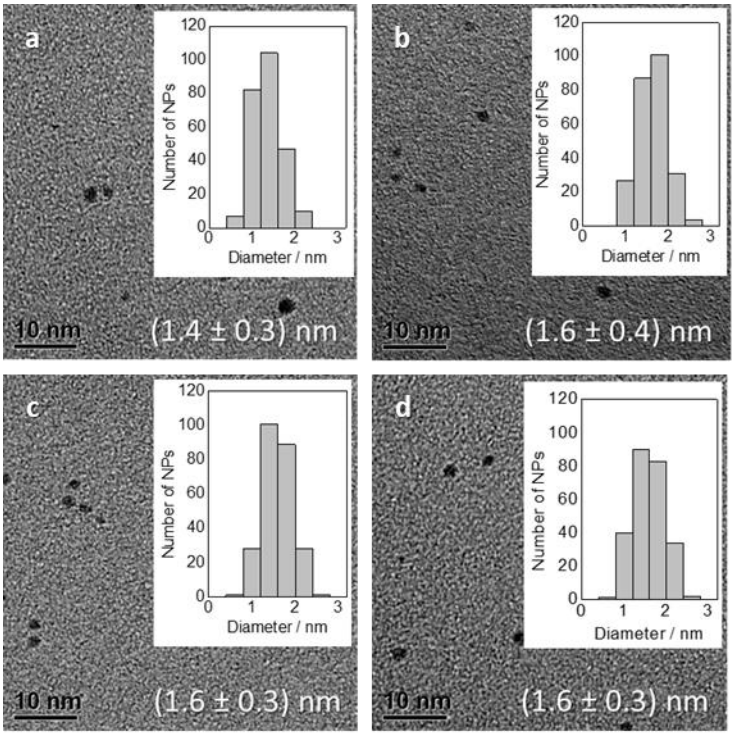

Figure S12: TEM images, averaged particle sizes and NP size distributions of NPs after 24 h of irradiation of H_2PtBr_6 with **a** 400, **b** 450, **c** 500, and **d** 550 nm.

Seed-Mediated Growth Experiments

a) Exposure of as-prepared thermally formed Pt NPs to reduced precursor solutions

First, the reduced precursor solution and the thermally formed Pt NPs were stirred together for 5 or 7 days at room light (**Figure S13**) and in the dark (**Figure S14**). Both were used as-prepared and synthesized with 0.25 M NaOH in EG. So, the same (constant) OH^-/Pt ratio was used. Adding the reduced precursor solution to thermal formed Pt NPs leads to the same averaged particle sizes within the error range (1.5-1.8 nm, **Figure S13** and **Figure S14**). It is assumed that OH^-/Pt ratio determines the particle size. So, this constant OH^-/Pt ratio would explain the constant particle size within the error range and that no seed-mediated growth could be generated.

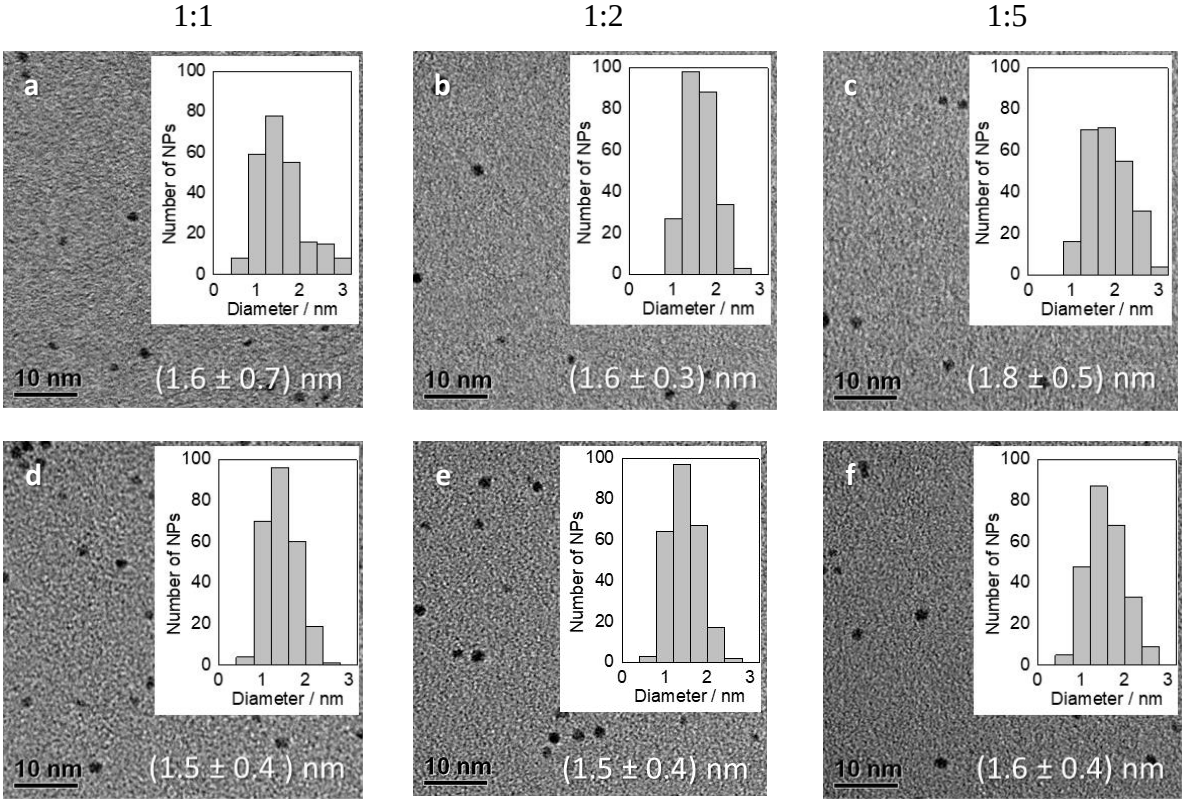

Figure S13: TEM images, averaged particle sizes and NP size distributions of NPs of seed-mediated growth experiments under room light stirring ratios of 1:1, 1:2, 1:5 of reduced H_2PtCl_6 to as-prepared thermally formed Pt NPs for 5 (**a**, **b**, **c**) or 7 (**d**, **e**, **f**) days.

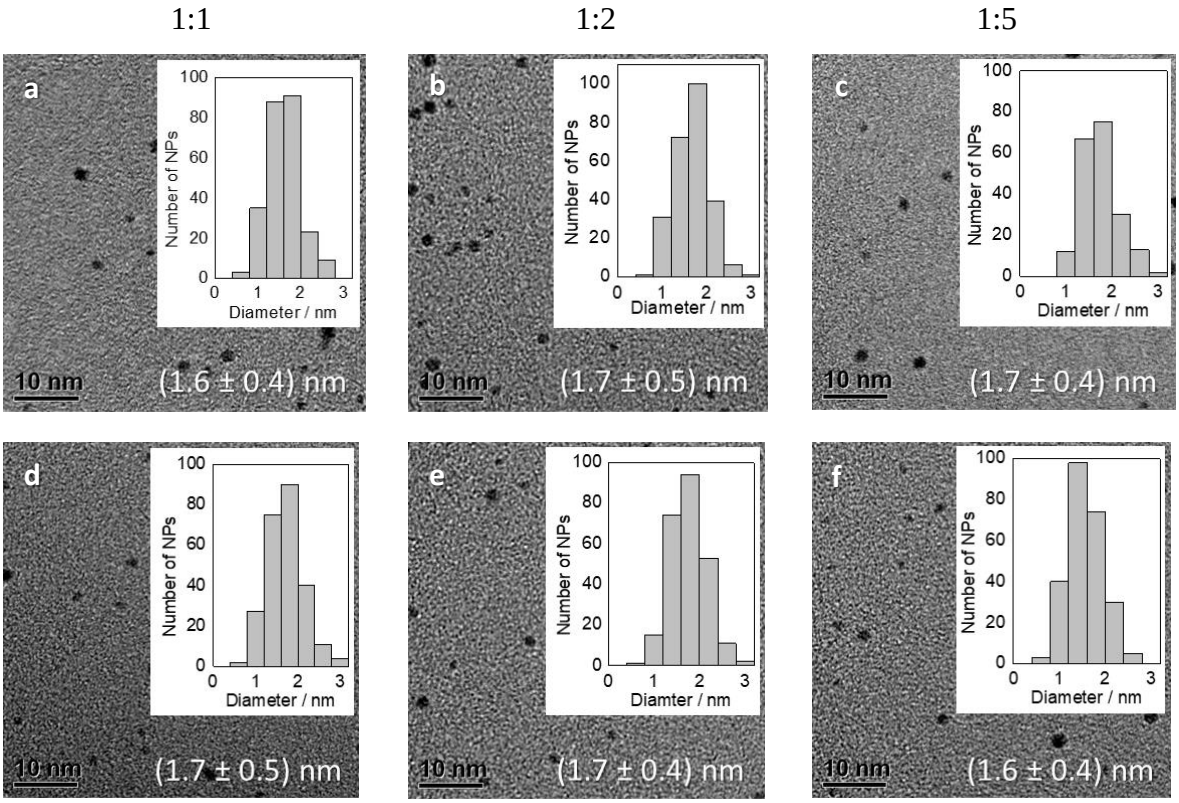

Figure S14: TEM images, averaged particle sizes and NP size distributions of NPs of seed-mediated growth experiments in the dark stirring ratios of 1:1, 1:2, 1:5 of reduced H_2PtCl_6 to as-prepared thermally formed Pt NPs for 5 (**a**, **b**, **c**) or 7 (**d**, **e**, **f**) days.

b) Exposure of thermally formed Pt NPs redispersed in EG to reduced precursor solutions

Then the NaOH concentration was decreased (compared to the standard of 0.25 M) but without obtaining leaching of NPs. Thermally synthesized Pt NPs were precipitated with HCl, it was tried to remove most of the supernatant and NPs were redispersed in EG. Generally, that would be a medium for leaching.[1] However, the reduced precursor solution is in a basic media (0.25 M NaOH in EG as starting concentration), hence leaching should be prevented. Assuming that all HCl was removed after precipitating theoretical OH^- concentrations of about 0.125, 0.167, and 0.208 M were obtained. The particles sizes of 1.1 ± 0.4 (0.125 M NaOH), 1.4 ± 0.3 (0.167 M), and 1.7 ± 0.4 nm (0.208 M) were determined after 7 days of stirring (**Figure S15**). This means that the particle sizes still remained constant within the diameter error.

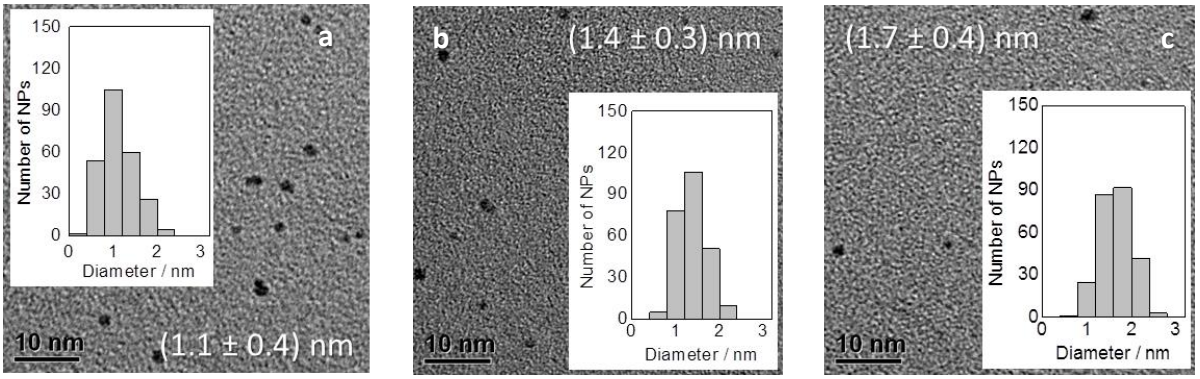

Figure S15: TEM images, averaged particle sizes and NP size distributions of NPs of seed mediated growth experiments of adding different amounts of reduced H_2PtCl_6 to thermally formed Pt NPs redispersed in EG obtaining OH^- concentrations of **a** 0.125, **b** 0.167, and **c** 0.208 M.

c) Exposure of carbon supported Pt NPs to reduced precursor solutions

In the next try thermally synthesized Pt NPs deposited on carbon and dispersed in EG were used as seeds. The deposited NPs were washed by water and acetone to remove residuals of NaCl or NaOH, hence leaching should be prevented again. The deposited Pt NPs (before seed-mediated growth experiments) are showing a particle size of 1.4 ± 0.3 nm. By adding different amounts of reduced precursor solution theoretical OH^-/Pt ratios of 15.0 and 18.6 were obtained. This corresponds to the range of 0.125 to 0.25 M OH^- (**Figure 8**). The obtained particle sizes after one week of stirring were 1.7 ± 0.3 (OH^-/Pt of 15.0) and 1.8 ± 0.4 nm (OH^-/Pt of 18.6) (**Figure S16**). However, the missing growth of both above mentioned experiments is not surprising. All OH^- concentrations were in a range of 0.125 to 0.25 M OH^-. In this range no significant change of NP size is observed (**Figure 8**, section 3.4). Under the assumption that the OH^-/Pt ratio determines the particle size the last two experiments are showing the expected missing of seed-mediated growth.

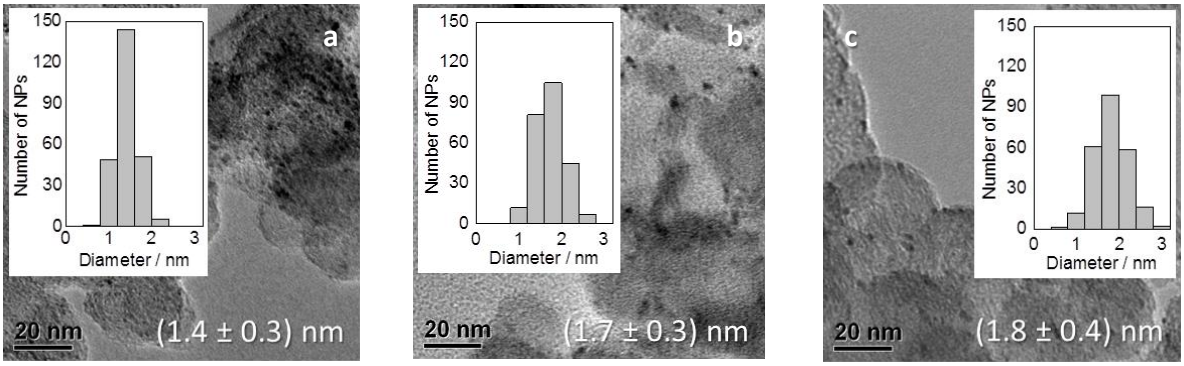

Figure S16: TEM images, averaged particle sizes and NP size distributions of NPs of seed-mediated growth experiments of adding different amounts of reduced H_2PtCl_6 to thermally formed Pt NPs deposited on carbon (**a**) obtaining OH^-/Pt ratios of **b** 15.0 and **c** 18.6.

d) Irradiation of as-prepared thermally formed Pt NPs exposed to precursor solutions

Therefore, the OH^- concentration was reduced below 0.125 M to work in a range of significant particle size (**Figure 8**). A precursor solution in EG was irradiated and stirred with as-prepared thermally synthesized NPs to accelerate the reduction of the precursor at 0.063 and 0.078 M NaOH. The particles sized after 3 h of irritation with 500 nm were 1.4 ± 0.3 (0.063 M OH^-) and 1.3 ± 0.3 nm (0.078 M) (**Figure S17**). The performed irradiation time of the thermally synthesized NPs (as seeds) with the reduced precursor should introduce enough energy to the system to generate seed-mediated growth if it is possible. However, no seed-mediated growth is observable (**Figure S17**), although a range of OH^- concentration was used that leads to significant particle growth during the synthesis (**Figure 8**). Therefore, seed-mediated growth in in the polyol preocess does not seem to be possible.

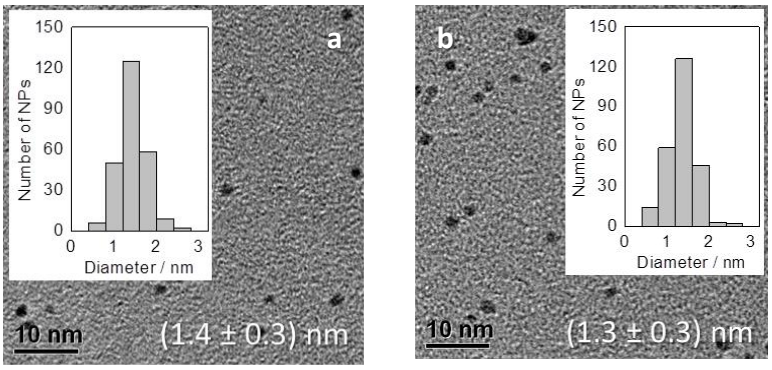

Figure S17: TEM images, averaged particle sizes and NP size distributions of NPs of seed-mediated growth experiments by irradiation of different amount of reduced H_2PtCl_6 with as-prepared thermally formed Pt NPs obtaining OH^- concentrations of **a** 0.063 and **b** 0.078 M.

Expected particle size

For the above described seed-mediated growth experiments the expected particle size was calculated based on Kunz *et al.*[2] assuming that the particles are spherical and the diameter of all seeds is changing by the same value Δd (see **Table S1**). Calculations with the starting particle size distributions as well as the average starting particle size of 1.4 nm (**Figure 1b**) were done. Using the size distributions lead only to an increase of the expected NP size of 0.1 nm as compared to the use of the average of the particle size. Consequently, the faster calculation with the average of the particle size is shown here.

In the synthesis of the "seeds" a Pt concentration of 0.01025 mol L^{-1} was used. So, the amount of Pt per experiment (seed-mediated growth experiments a, b, and d) could be obtained by

$$n(\text{seeds}) = 0.01025 \text{ mol } L^{-1} \times V(\text{solvent seeds})$$

The total Pt volume of the seeds (in nm^3) could be estimated by multiplying the Pt amount and the atomic volume:

$$V(\text{Pt seeds}) = n(\text{seeds}) \times 9.1 \times 10^{21} \text{ nm}^3 \text{ mol}^{-1}$$

The number of atoms in the seeds could be obtained dividing the total volume of the seeds by the volume of 1 atom using the empiric radius of 1 Pt atom of 0.135 nm:

$$N(\text{atoms seeds}) = \frac{V(\text{Pt seeds})}{V(1 \text{ atom})} = \frac{V(\text{Pt seeds})}{\frac{4}{3}\pi \times r(1 \text{ atom})^3}$$

The number of seed is determined by the ratio of the total number of atoms in the seeds and the number of atoms in 1 seed. The number of atoms in 1 seed can be determined by the ratio of the volume of 1 seed and the volume of 1 atom. The volume of 1 seed is calculated using the diameter of 1.4 nm (assuming a spherical particle) and the packing density of 74 % in the centered cubic packing of the NPs:

$$N(\text{seeds}) = \frac{N(\text{atoms seeds})}{N(\text{atoms 1 seed})} = \frac{N(\text{atoms seeds}) \times V(1 \text{ atom})}{V(1 \text{ seed})} = \frac{N(\text{atoms seeds}) \times V(1 \text{ atom})}{\frac{1}{6}\pi \times d(1 \text{ seed})^3 \times 0.74}$$

The total number of atoms in the precursor is calculated in the same way as the total number of atoms in the seeds:

$$N(\text{atoms precursor}) = \frac{V(\text{Pt precursor})}{\frac{4}{3}\pi \times r(1 \text{ atom})^3}$$

$$= \frac{0.01025 \text{ mol } L^{-1} \times V(\text{solvent precursor}) \times 9.1 \times 10^{21} \text{ nm}^3 \text{ mol}^{-1}}{\frac{4}{3}\pi \times r(1 \text{ atom})^3}$$

The new number of atoms in 1 NP after a successful seed-mediated growth experiments was calculated by

$$N(\text{atoms 1 NP after}) = N(\text{atoms 1 seed}) + \frac{N(\text{atoms precursor})}{N(\text{seeds})}$$

The volume was determined by

$$V(\text{1 NP after}) = N(\text{atoms 1 NP after}) \times V(\text{1 atom})$$

and the averaged diameter of the NPs after the growth considering again the packing density of 74 % in the centered cubic packing of the NPs was determined by

$$d(\text{1 NP after}) = \sqrt[3]{\frac{6 \times V(\text{1 NP after})}{\pi \times 0.74}}$$

In the seed-mediated growth experiment d on carbon support NPs were used as seeds. The N(atoms precursor) was calculated with the equation above. The "volume of the seeds" used in one experiments was obtained by ratio of mass used in the experiments and the total mass of the synthesized catalyst multiplied with the total volume of solvent used for the catalyst synthesis using the concentration of 0.002 g_{Pt} mL^{-1} in the NP dispersions:

$$V(\text{solvent seed}) = \frac{m(\text{used catalyst}) \times 24\ \text{mL}}{m(\text{total catalyst})} = \frac{m(\text{used catalyst}) \times 24\ \text{mL}}{m(\text{Pt}) + m(\text{carbon})}$$

$$= \frac{m(\text{used catalyst}) \times 24\ \text{mL}}{(0.002\ g_{Pt}\ mL^{-1} \times 24\ \text{mL}) + m(\text{carbon})}$$

The N(seeds), N(atoms precursor) and d(1 NP after) were determined as before.

Table S1: The calculated total number of atoms N(atoms seeds), the number of seeds N(seeds), the total number of atoms in the precursor N(atoms precursor) and in 1 NP after a theoretical successful deposition of the precursor onto the seeds N(atoms 1 NP after), as well as the following volume V(1 NP after) and the final diameter of d(1 NP after).

Experiments	a			b			c		d	
N(atoms seeds) / 10^{18}	5.4			4.5			45	23	9.1	
N(seeds) / 10^{16}	5.3			4.4			44	22	8.8	
N(atoms precursor) / 10^{18}	5.4	11	27	4.5	9.1	23	72		20	27
N(atoms 1 NP after)	206	309	619	206	346	655	305	468	330	449
V(1 NP after) / nm^3	2.1	3.2	6.4	2.1	3.6	6.8	3.1	4.8	3.4	4.6
d(1 NP after) / nm	1.8	2.0	2.5	1.8	2.1	2.6	2.0	2.3	2.1	2.3

FTIR Data

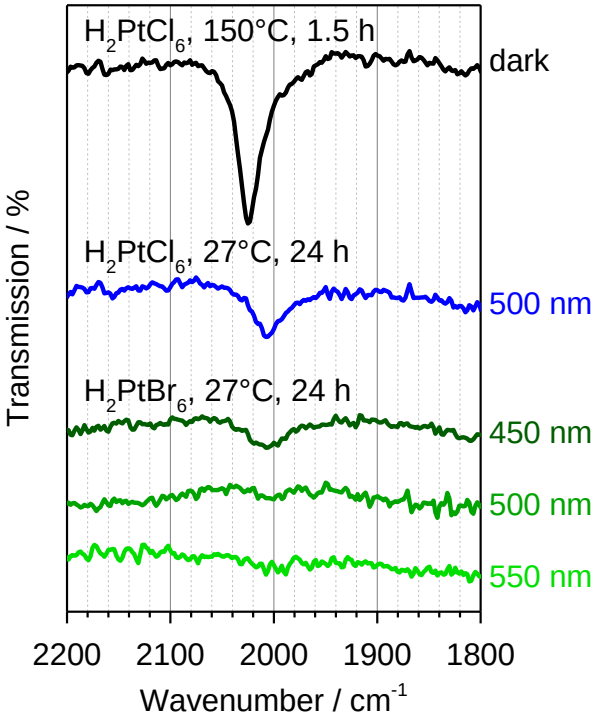

Figure S18: CO absorption bands in the FTIR spectra of as-prepared NPs synthesized in 0.25 M NaOH: the thermal reduction of H_2PtCl_6 performed in the dark for 1.5 h at 150°C (black), after irradiation of H_2PtCl_6 for 24 h at 27°C with 500 nm (blue), and after irradiation of H_2PtBr_6 for 24 h at 27°C with 450, 500, and 550 nm (green).

Spectrum of 300 W xenon arc lamp

The lamp spectrum of the used 300 W xenon arc lamp is provided online by LOT QUANTUM DESIGN in the document "Lamp spectra and irradiance data – Data sheet".[3]

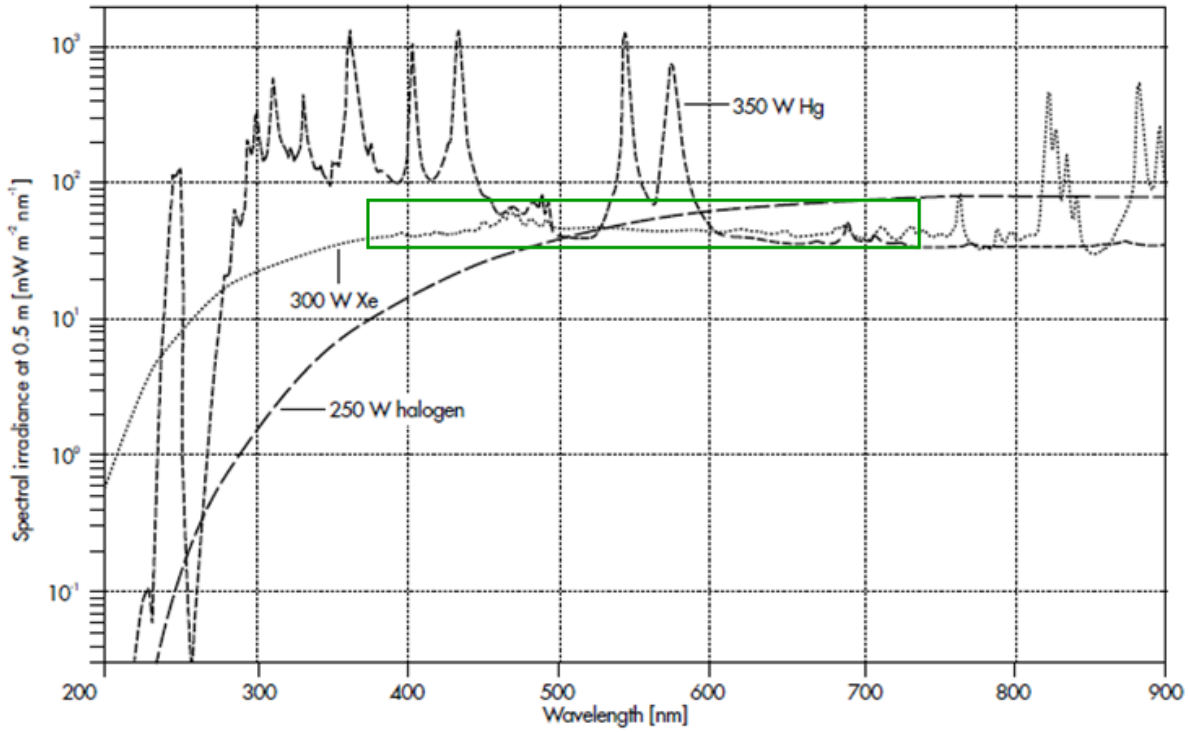

Figure S19: Lamp spectrum of the wavelength dependent irradiance of the used 300 W Xe arc lamp online provided by LOT QUANTUM DESIGN.[3]

Transmission Spectra of the Filters

The transmission spectra of the filters used with a 300 W Xe arc lamp was provided by LOT QUANTUM DESIGN.

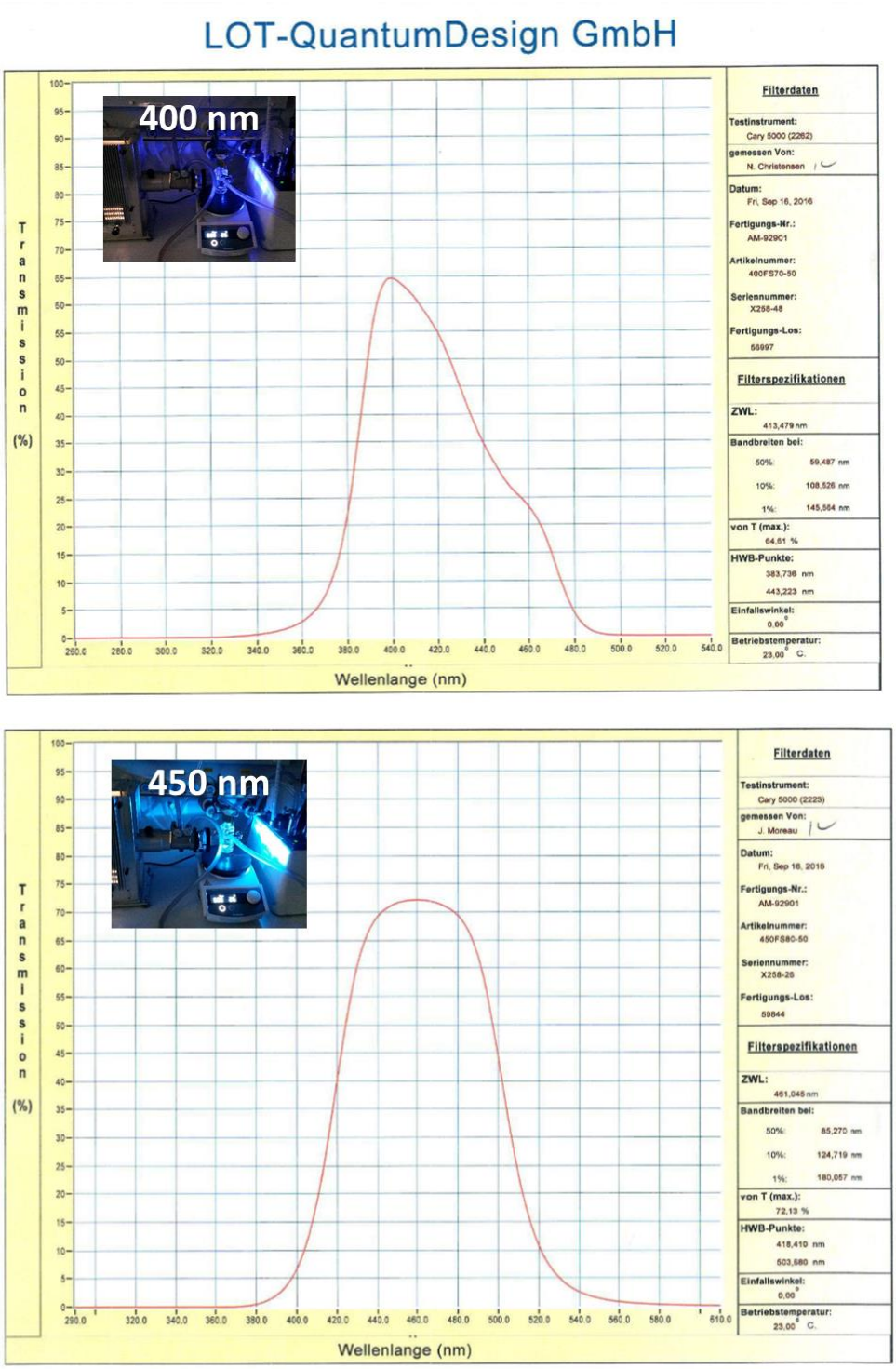

Figure S20: Transmission spectra of two different filters used during the NP synthesis to obtain a wavelength of the irradiated light about 400 and 450 nm.

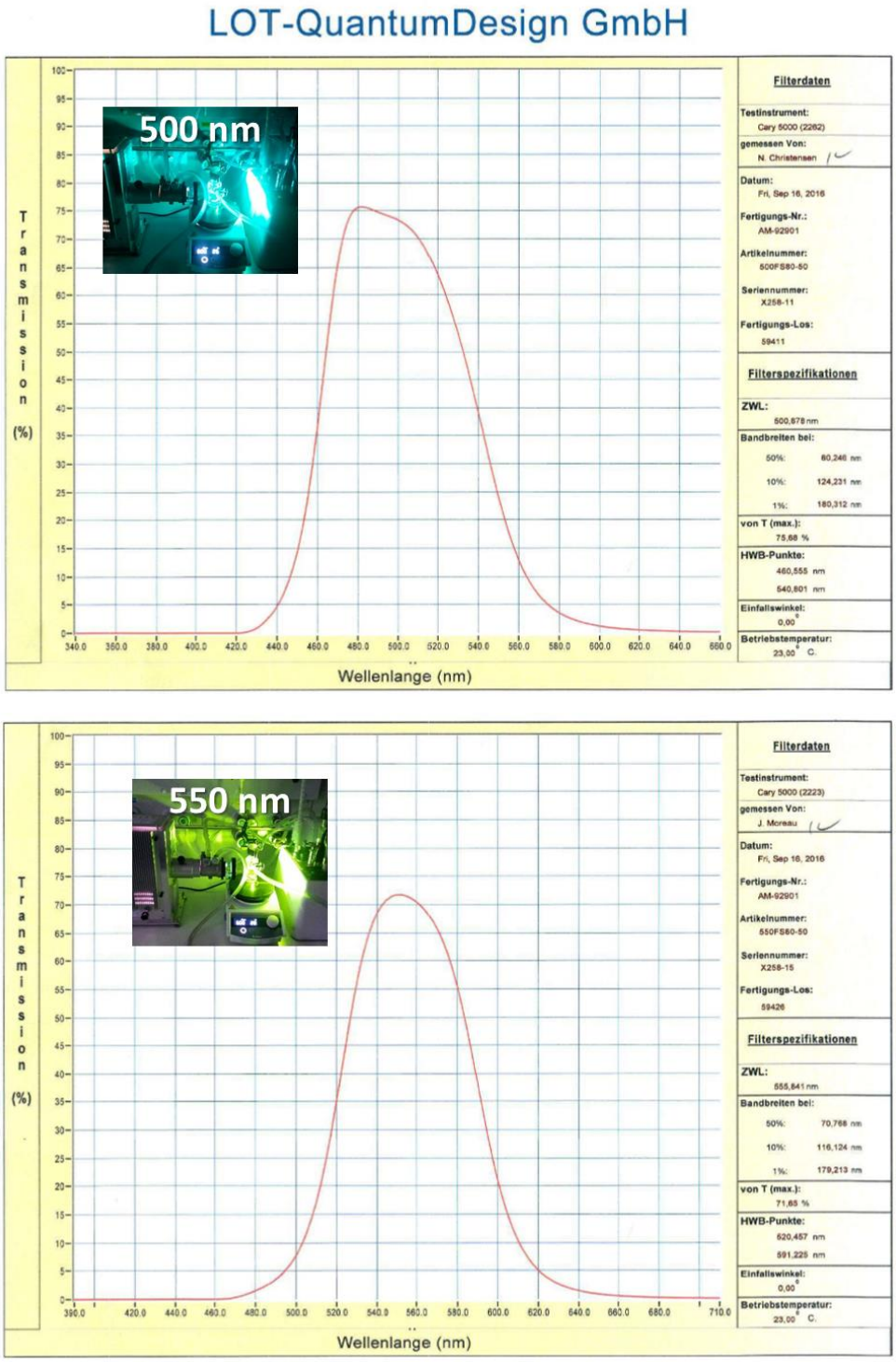

Figure S21: Transmission spectra of two different filters used during the NP synthesis to obtain a wavelength of the irradiated light about 500 and 550 nm.

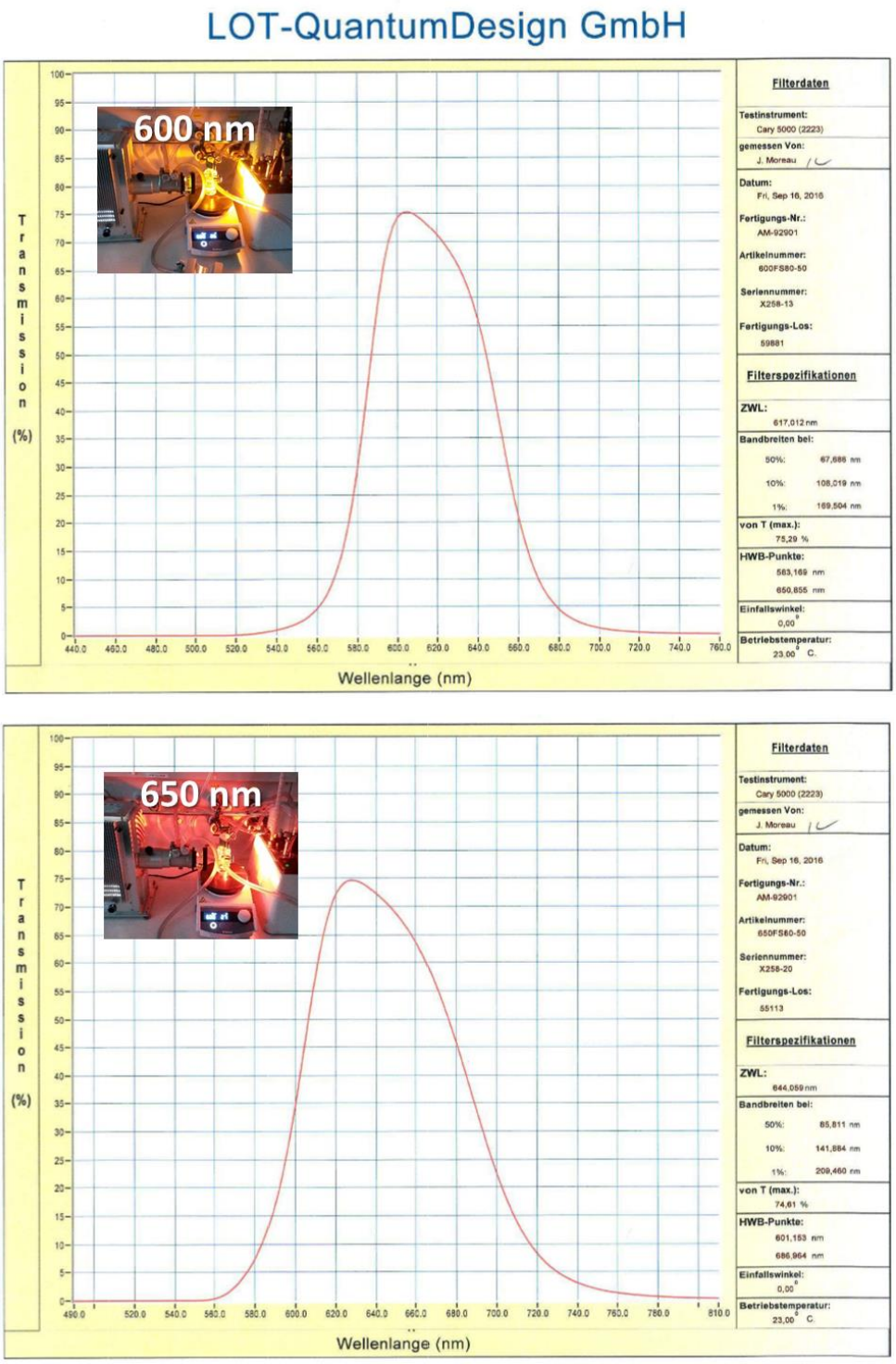

Figure S22: Transmission spectra of two different filters used during the NP synthesis to obtain a wavelength of the irradiated light about 400 and 450 nm.

References

(1) Neumann, S.; Schröder, J.; Bizzotto, F.; Arenz, M.; Dworzak, A.; Oezaslan, M.; Bäumer, M.; Kunz, S. Halide-Induced Leaching of Pt Nanoparticles – Manipulation of Particle Size by Controlled Ostwald Ripening. *ChemNanoMat* **2019**, *5*, 462–471. https://doi.org/10.1002/cnma.201800550.

(2) Kunz, S.; Iglesia, E. Mechanistic Evidence for Sequential Displacement-Reduction Routes in the Synthesis of Pd-Au Clusters with Uniform Size and Clean Surfaces. *J. Phys. Chem. C* **2014**, *118* (14), 7468–7479. https://doi.org/10.1021/jp500537v.

(3) Lot Quantum Design. Lamp spectra and irradiance data - Data sheet https://qd-europe.com/de/en/product/basics/.

Manuscript II:

J. Schröder, S. Neumann, J. Quinson, M. Arenz, S. Kunz

Anion Independent Particle Size Control of Platinum Nanoparticles Synthesized in Ethylene Glycol

The published paper is reprinted from *Nanomaterials,* **2021**, *11*, 2092.

https://doi.org/10.3390/nano11082092 (Open Access)

nanomaterials

MDPI

Communication

Anion Dependent Particle Size Control of Platinum Nanoparticles Synthesized in Ethylene Glycol

Johanna Schröder [1,2,*], Sarah Neumann [1], Jonathan Quinson [3], Matthias Arenz [2] and Sebastian Kunz [1,4,*]

1 Institute of Applied and Physical Chemistry (IAPC), Center for Environmental Research and Sustainable Technology, University of Bremen, Leobener Strasse 6, 28359 Bremen, Germany; SarahNeumann1@gmx.de
2 Department of Chemistry, Biochemistry, and Pharmaceutical Sciences (DCBP), University of Bern, Freiestrasse 3, 3012 Bern, Switzerland; matthias.arenz@unibe.ch
3 Chemistry Department, University of Copenhagen, Universitetsparken 5, 2100 Copenhagen, Denmark; jonathan.quinson@chem.ku.dk
4 Südzucker AG, Central Department Research, Development, and Services (CRDS), Wormser Strasse 11, 67283 Obrigheim, Germany
* Correspondence: johanna.schroeder@unibe.ch (J.S.); sebastian-kunz@web.de (S.K.)

Abstract: The polyol synthesis is a well-established method to form so-called "surfactant-free" nanoparticles (NPs). In the present study, the NP size resulting from the thermal reduction of the precursors H_2PtCl_6, $H_2Pt(OH)_6$, or $Pt(acac)_2$ in presence of the bases NaOH or Na(acac) at different concentrations is studied. It is shown that the size control depends more strongly on the nature of the precursor (metal salt) than on the anion present in the base. The latter is surprising as the concentration of the base anion is often an important factor to achieve a size control. The reduction of H_2PtCl_6 or $H_2Pt(OH)_6$ in presence of NaOH and Na(acac) confirm the observation that the NP size is determined by the OH^-/Pt molar ratio and expands it to the base anion/Pt molar ratio. In contrast, the reduction of $Pt(acac)_2$ in presence of the bases NaOH (previous reports) or Na(acac) (shown in the present work) leads to larger NPs of ca. 3 nm, independent of the concentration of the base anions. Hence, the anion effect observed here seems to originate predominantly from the nature of the precursor (precursor anion dependence) and only for certain precursors as H_2PtCl_6 or $H_2Pt(OH)_6$ the size control depends on the base anion/Pt molar ratio.

Keywords: "surfactant-free" Pt nanoparticle synthesis; polyol process; anion dependent particle size control

Citation: Schröder, J.; Neumann, S.; Quinson, J.; Arenz, M.; Kunz, S. Anion Dependent Particle Size Control of Platinum Nanoparticles Synthesized in Ethylene Glycol. *Nanomaterials* **2021**, *11*, 2092. https://doi.org/10.3390/nano11082092

Academic Editor: Francisco Alonso

Received: 19 July 2021
Accepted: 13 August 2021
Published: 18 August 2021

1. Introduction

The polyol method performed in alkaline ethylene glycol (EG) is a versatile approach to synthesize "surfactant-free" Pt nanoparticle (NP) based tailored catalysts [1–3] for instance for CO oxidation [4,5] or fuel cell studies [6,7]. If desired, the "surfactant-free" particles can subsequently be functionalized with organic surfactants such as different amino acids, e.g., *L*-proline, to increase the catalytic activity [8] or to control the enantiomeric selectivity of hydrogenation reactions [9–11]. In the "surfactant-free" NP synthesis a Pt precursor (metal salt, e.g., H_2PtCl_6) is reduced in presence of a base like NaOH while the solvent EG is oxidized. The oxidation mechanisms of EG to form glycolaldehyde, glycol acid, oxalaldehyde, and oxalic acid have been described and additionally two CO molecules absorbing to the NP surface are formed [12,13]. The OH^- of the base is neutralized by the protons formed during the reduction of the metal precursor to form water, as shown in Figure 1 [14].

The influence of the anion OH^- as additive within the reaction mixture on the stability and size control was mentioned before in different studies [7,13,15]. Quinson et al. [16] investigated the influence of the cations Li^+, Na^+, K^+, and Cs^+ in the hydroxide base and showed that the particle size and stability is not affected in EG. Neumann et al. [4]

observed that the presence of halides in the precursors H_2PtCl_6 and H_2PtBr_6 induces leaching leading to a size increase during the thermal reduction in presence of NaOH at 150 °C during 17 h. In contrast, the size of the halide free precursor $Pt(acac)_2$ (acac− as abbreviation for the acetylacetonate anion) remains constant [4]. Due to the larger leaching ability of bromide as compared to chloride, the thermal reduction of H_2PtBr_6 (as compared to H_2PtCl_6) results in a larger particle size for prolonged reaction times. Furthermore, the use of the halide-free precursor $Pt(acac)_2$ leads to substantially larger particles of about 3 nm [4]. Schröder et al. [15] showed that the use of the precursors H_2PtCl_6 or H_2PtBr_6 in presence of NaOH under conditions where Ostwald ripening can be excluded, i.e., reduction induced by visible light at room temperature, results in a comparable size control by the OH^-/Pt ratio. The results of Neumann et al. [4] and Schröder et al. [15] indicate an influence of the precursor anions on the particle size. The size resulting of the reduction of the precursors H_2PtCl_6 [7,13,15] or $Pt(acac)_6$ [4] in the presence of NaOH were investigated before.

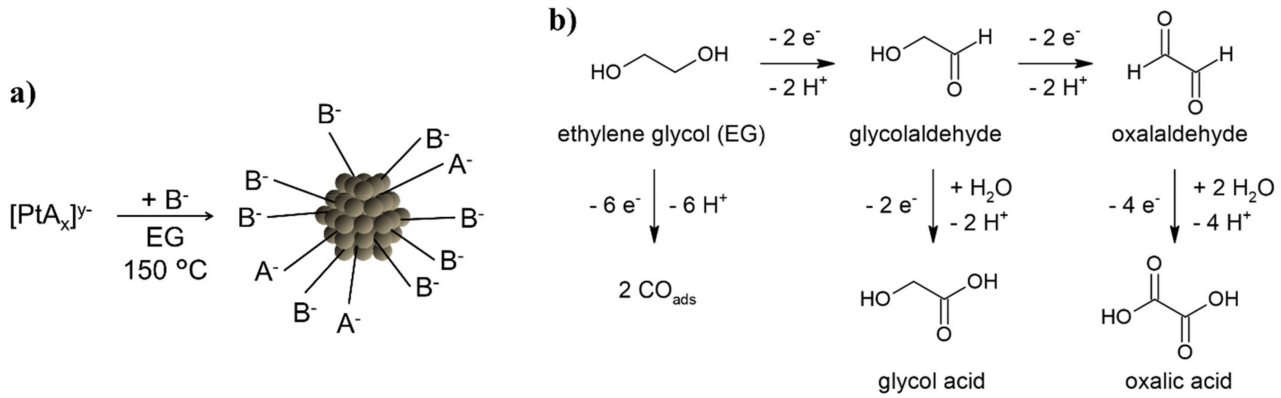

Figure 1. Scheme of the thermally induced polyol process: (**a**) the precursor with the anion A^- is reduced in presence of the base anion B^- in EG at 150 °C to form NPs. For instance, during the reduction of $[Pt(OH)_6]^{2-}$ the anions are $A^- = B^- = OH$; (**b**) different oxidation mechanisms of EG.

In the present study, the precursors H_2PtCl_6 or $Pt(acac)_2$, were reduced in presence of the base Na(acac), and $H_2Pt(OH)_6$ in presence of the bases NaOH or Na(acac). By doing so, the influence of the nature of the base anion of NaOH or Na(acac) and its concentration on the particle size in the reduction of the precursors H_2PtCl_6, $H_2Pt(OH)_6$, or $Pt(acac)_2$ are compared. It is observed that, as mentioned by Quinson et al. [7], the size control by tuning the OH^-/Pt ratio seems to be applicable to the base anion/Pt molar ratio for the precursors H_2PtCl_6 and $H_2Pt(OH)_6$. In contrast, a comparable large particle size of ca. 3 nm is obtained here in the reduction of $Pt(acac)_2$ in presence of Na(acac) or in the reduction of $Pt(acac)_2$ in presence of NaOH as shown by Neumann et al. [4]. This clearly shows the importance of the careful selection of the nature of the precursor (the precursor anion) compared to the nature of the base anion in order to achieve size control in ''surfactant-free" NP synthesis.

2. Experimental Section

2.1. NP Synthesis

In general, for the polyol process, a metal salt (precursor) is reduced in presence of a base in EG. The thermal reduction is performed in a preheated oil bath at 150 °C, see Figure 1 [4,7,13]. In the present study H_2PtCl_6, $H_2Pt(OH)_6$, or $Pt(acac)_2$ were used as precursors and NaOH or Na(acac) as bases. Details about the syntheses are found in the following.

2.1.1. Synthesis of "Surfactant-Free" Pt NPs by Thermal Reduction of H_2PtCl_6 in Presence of Na(acac)

H_2PtCl_6 xH_2O (0.04 g, 40% Pt, Chempur, Karlsruhe, Germany, or AlphaAesar, Haverhill, MA, USA) was dissolved in 4 mL of EG (99.8%, VWR, Radnor, PA, USA) in a 50 mL round bottom flask. 4 mL of 0.5 M Na(acac) ($C_5H_7NaO_2$ xH_2O, 95%, AlphaAesar, Haverhill, MA, USA) in EG was added to obtain an $acac^-$ starting concentration of 0.25 M, i.e., an $acac^-$/Pt ratio of 24.4. Because of the impurities in the base (only a purity of 95%) proportionately more Na(acac) was dissolved in EG. During dissolution overnight, the solution turned light yellow. Different base concentrations between 0.055 and 0.5 M were obtained by diluting 0.5 M Na(acac) in EG leading to $acac^-$/Pt ratios between 5.4 and 48.8. As the total volume of the added base was kept constant at 4 mL, the reaction mixture was in total 8 mL. The flasks were equipped with a reflux condenser. The mixture was vigorously stirred at 150 °C for 10 min using a preheated oil bath. The precursor solution turned dark brown after about 1–2 min indicating the NP formation. Previously unpublished results showed that at lower Na(acac) amounts the particles became instable even after keeping the synthesis temperature at 150 °C for 20 min. After the heating procedure, the reaction mixture was cooled to ambient temperature.

2.1.2. Synthesis of "Surfactant-Free" Pt NPs by Thermal Reduction of $H_2Pt(OH)_6$ in Presence of NaOH or Na(acac)

For the reduction in presence of NaOH the precursor $H_2Pt(OH)_6$ (0.0286 g, 56% Pt, ChemPur, Karlsruhe, Germany) was dissolved in 4 mL of EG. To obtain the desired base starting concentrations the amount of OH^- in the precursor was considered and the 0.5 M NaOH (VWR, Radnor, PA, USA) stock solution in EG was diluted with EG to a total volume of 4 mL. The applied Pt concentration of 10.25 mM in the total volume of 8 mL led to an OH^- concentration of around 0.072 M for $H_2Pt(OH)_6$. Therefore, OH^- concentrations between 0.078 and 0.5 M were used for thermal reduction of $H_2Pt(OH)_6$, leading to OH^-/Pt ratios of 7.6 to 48.8, respectively.

For the reduction in presence of Na(acac) the precursor $H_2Pt(OH)_6$ (0.0138 g, 57.94% Pt, ChemPur, Karlsruhe, Germany) was dissolved in 4 mL of EG. The 0.5 M Na(acac) stock solution was diluted by EG. Because of the impurity of the base (only a purity of 95%) proportionately more Na(acac) was dissolved in EG. During dissolution overnight, the solvent turned light yellow. For example, 4 mL of 0.5 M Na(acac) in EG was added to obtain an $acac^-$ starting concentration of 0.25 M, leading to an $acac^-$/Pt ratio of 48.8.

As the total volume of the added bases was kept constant at 4 mL, the volume of the reaction mixtures in both synthesis approaches with the two different bases was in total 8 mL. The flask was equipped with a reflux condenser. $H_2Pt(OH)_6$ is insoluble at room temperature in EG, it stays turbid even after one week of stirring in the dark. The solution and reduction step of $H_2Pt(OH)_6$ in EG could not be separated from each other as the white turbidity changed first to yellow and then brown turbidity before the brown dispersions were obtained by heating up. Therefore, the turbid mixture was vigorously stirred at 150 °C for 90 min using a preheated oil bath. The precursor solution of $H_2Pt(OH)_6$ in presence of NaOH turned dark brown after about 1 to 25 min (the lower the OH^- concentration, the faster the reduction) indicating NP formation. The precursor solution of $H_2Pt(OH)_6$ in presence of Na(acac) turned dark brown after about 90–120 s. After the heating procedure, the reaction mixture was cooled to ambient temperature.

2.1.3. Synthesis of "Surfactant-Free" Pt NPs by Thermal Reduction of $Pt(acac)_2$ in Presence of Na(acac)

$Pt(acac)_2$ (0.0161 g, 49.6% Pt, FluoroChem, Hadfield, United Kingdom) was dissolved in 4 mL of EG. To obtain the desired Na(acac) starting concentrations the amount of $acac^-$ in the precursor was considered and 0.5 M Na(acac) stock solution in EG was diluted with EG to a total volume of 4 mL. The applied Pt concentration of 10.24 mM in 4 mL led to an $acac^-$ concentration of around 20.48 mM in $Pt(acac)_2$. Therefore, OH^- concentrations between 0.047 and 0.5 M were used for the thermal reduction of $Pt(acac)_2$ leading to $acac^-$/Pt ratios

of 4.6 to 48.9, respectively. As the total volume of the added base was kept constant at 4 mL, the reaction mixture was in total 8 mL. The flask was equipped with a reflux condenser. The $Pt(acac)_2$ precursor was dissolved at 100 °C for 20 min, resulting in a yellow solution. The mixture was vigorously stirred at 150 °C for 150 min using a preheated oil bath. The precursor solution turned dark brown after about 50 min. After the heating procedure, the reaction mixture was cooled to ambient temperature.

2.1.4. Cleaning of "Surfactant-Free" NPs

Pt NPs were cleaned flocculating the "as-prepared" NP dispersion with two aliquots of 1 M aqueous HCl (VWR, Radnor, PA, USA). The flocculated particles were separated by centrifugation. The supernatant was removed. The particles were washed once by suspending them in 2 aliquots of 1 M aqueous HCl. After a second centrifugation, the supernatant was removed again. The NP were redispersed in acetone for further analysis.

2.2. Characterization of Nanoparticles

Transmission Electron Spectroscopy (TEM)

TEM was performed with a Tecnai F20 S-Twin Microscope (Fei, Hillsboro, OR, USA) using an acceleration voltage of 200 kV and a magnification of 150 k or with a Jeol 2100 microscope (Jeol Ltd. Akishima, Japan) operated at 200 kV (the latter only for particles synthesized by the reduction of $H_2Pt(OH)_6$ in presence of Na(acac)). For the measurement of liquid NP samples, 0.25 or 0.5 mL of as-prepared NP dispersions were flocculated with 2 aliquots of 1 M HCl and redispersed in 1 aliquots of acetone (see Section 2.1.4). 3 drops of that dispersion were diluted with 1 mL acetone and 3 drops of the diluted acetone dispersions were drop-casted onto the carbon side of the TEM grid (ultrathin Carbon Support Film, Cu 200 mesh, Quantifoil, Großlöbichau, Germany). The averaged particle sizes, the standard deviation, and histograms of the particle sizes distributions were determined using ImageJ counting at least 200 particles.

3. Results and Discussion

3.1. Thermal Reduction of Pt Precursors with Varying OH^- Concentrations

Schrader et al. [13] and Quinson et al. [7] showed the importance of OH^- in the reduction of the precursor H_2PtCl_6 to obtain stable colloids and to determine the size of NPs in the "surfactant-free" Pt NP synthesis in EG. Recently, the size control by OH^- in the reduction of H_2PtCl_6 and H_2PtBr_6 was used for mechanistic investigations [5]. So far, the size control by OH^- in the reduction of H_2PtCl_6 was only investigated in the presence of different cations [16] or halides [4,15]. In the present work a halide-free precursor $H_2Pt(OH)_6$ was reduced in presence of NaOH to investigate if in a halide-free system the NP size is still controlled by a certain OH^-/Pt ratio as reported before [7,13,15]. The solution and reduction step of the precursor $H_2Pt(OH)_6$ used in the present study could not be separated from each other as by heating up the white turbidity changed first to yellow and then brown turbidity before brown dispersions were obtained. Nevertheless, it has been attempted to perform an equivalent procedure to the standard thermal reduction of H_2PtCl_6 and H_2PtBr_6 [4,13]. $H_2Pt(OH)_6$ and NaOH in EG were stirred at 150 °C in a preheated oil bath adjusting the amount of added NaOH in EG with respect to the amount of OH^- of the precursor to obtain the desired OH^-/Pt ratios (see the experimental section for more details).

The particles obtained in the reduction of $H_2Pt(OH)_6$ in presence of NaOH at a OH^-/Pt ratio of 48.8 were not stable, they already sintered and as a consequence flocculated after less than 10 min during the synthesis as observed before in the reduction of H_2PtCl_6 in presence of NaOH [13]. The reaction mixtures of $H_2Pt(OH)_6$ after 25, 30, 35, and 90 min of synthesis using an OH^-/Pt ratio of 24.4 showed after 3 days of storage some particle flocculation, but the majority of the NPs remained dispersed in the solution. The NP dispersions with an OH^-/Pt ratio of 12.2 (after 10, 15, 20, 90 min synthesis time), 9.2, and 7.6 (after 5, 10, 15, 90 min synthesis time) remained stable. The thermal reduction

observable by the color change from yellow to brown becomes faster as the OH^-/Pt ratio decreases (24.4: after about 25 min, 12.2: about 8 min, 9.2: about 1.5 min, 7.6: about 1 min). In the thermal reduction of H_2PtCl_6 in the presence of NaOH also at high OH^-/Pt ratios the color change to dark brown indicating the NP formation occurs after ca. 3 min [7,13]. This different behavior in reduction time implies that in the absence of halides a different mechanism may occur in the polyol process as compared to the one proposed recently [15]. It seems that in the thermal reduction the halide plays a decisive role to initiate the reduction. After a short time of synthesis, when the NPs have been formed indicated by the color change to a dark dispersion, narrow size distributions were obtained. The particle sizes remained the same between the OH^-/Pt ratios of 7.6 and 9.2, i.e., 1.4 ± 0.3 nm, after 5 min and also for an OH^-/Pt ratio of 12.2 after 10 min, see Figure 2.

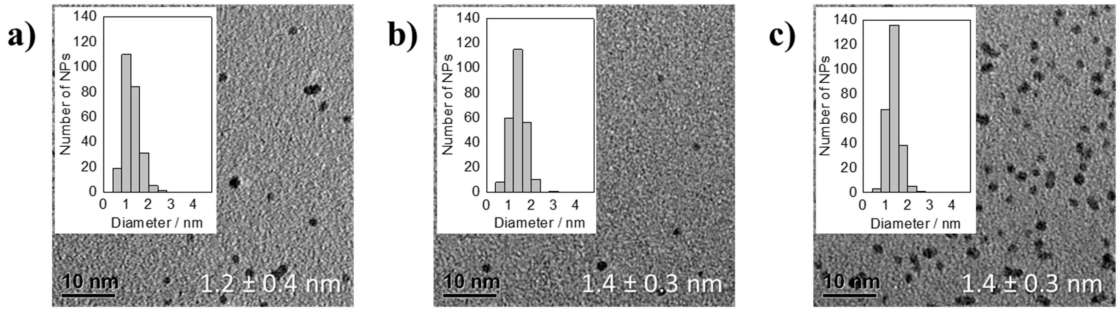

Figure 2. TEM micrographs of averaged particle sizes together with the standard deviation and NP size distributions of thermally formed Pt NPs by using $H_2Pt(OH)_6$ as precursor in presence of NaOH with different OH^-/Pt ratios of: (**a**) 12.2 (after 10 min of synthesis), (**b**) 9.2 (after 5 min), and (**c**) 7.6 (after 5 min).

The particles continued to grow, and quite broad particle size distributions were obtained after 90 min, see Figure 3. At an OH^-/Pt ratio of 24.4 the particle size of 1.6 ± 0.4 nm is comparable to the other polyol syntheses at an equal OH^- starting concentration [4,7,13,15,16]. The particle size increase by lowering the OH^- concentration is comparable to previous observations [7,15]. At an OH^-/Pt ratio of 12.2 the size of 2.0 ± 0.7 nm is however slightly larger as compared to 1.4 ± 0.3 nm (OH^-/Pt ratio of 12.5) that was described before by Quinson et al. [7] in a chloride containing system. Additionally, at an OH^-/Pt ratio of 9.2 the particle size remained constant at a diameter of about 2.5 nm while in the chloride containing system with OH^-/Pt ratios of 6.3 and 10 particle sizes of 2.5 ± 0.3 and 2.1 ± 0.6 nm were reached, respectively [7]. The slightly different particle size together with the larger standard deviation in size could be explained by the lack of chloride that limits the amount of leached Pt species during the reduction and/or the low solubility of $H_2Pt(OH)_6$ in the EG that leads to entangled dissolution and reduction in the NP synthesis.

In summary, at 150 °C in the absence of halides when $H_2Pt(OH)_6$ is used as precursor and NaOH as base, an influence of the OH^-/Pt ratio to the NP size is shown (see a summary of the size results in Table S1). This behavior is similar to what is observed in the reduction of H_2PtCl_6 in presence of NaOH [4,7,13,15,16]. However, the particle sizes in the reduction of $H_2Pt(OH)_6$ are slightly larger as compared to the halide containing systems using H_2PtCl_6. Therefore, changing the precursor anion from Cl^- to OH^- has only a modest effect on the particle size. In contrast, Neumann et al. [4] showed that the precursor anion $acac^-$ leads to a substantial size increase in the presence of the base anion OH^-, as the thermal reduction of the precursor $Pt(acac)_2$ in presence of NaOH resulted in particle sizes of ca. 3 nm. This may indicate an influence of the precursor anion within the reduction process. This effect is investigated further in the next section.

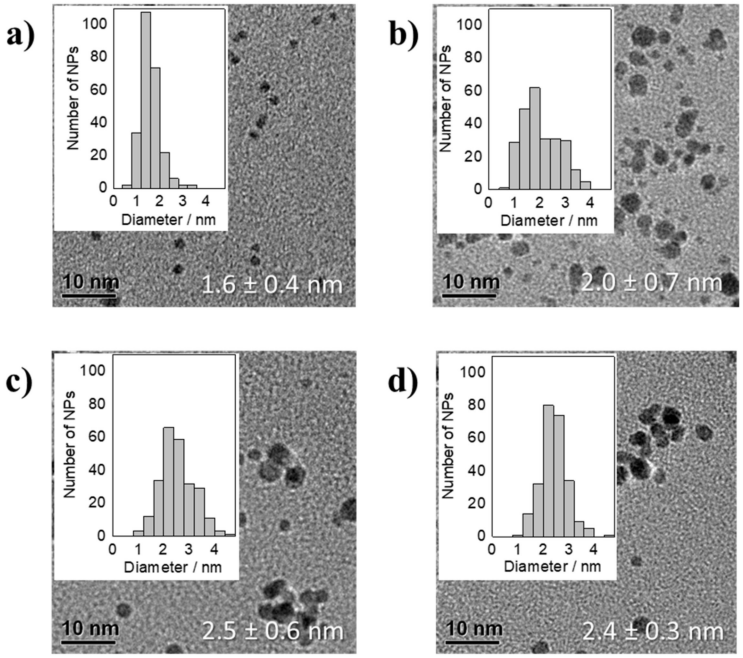

Figure 3. TEM micrographs of averaged particle size together with the standard deviation and NP size distribution of thermally formed Pt NPs by using $H_2Pt(OH)_6$ as precursor in presence of NaOH with different OH^-/Pt ratios of: (**a**) 24.4, (**b**) 12.2, (**c**) 9.2, and (**d**) 7.6 after 90 min of synthesis.

3.2. Thermal Reduction of Pt Precursors with Varying Acac⁻ Concentrations

In the previous section a slightly different behavior depending on the precursor was shown and hence the precursor anions in the reduction mixture seem to affect the particle size as well. It is now investigated whether a different base anion shows a comparable trend in size control depending on the precursor or if the base anion/Pt molar ratio control the size as it is the case in the previous results. As the precursor $Pt(acac)_2$ contains the organic anion $acac^-$ that is substantially larger as compared to the inorganic and small OH^- anion, Na(acac) was used as base for the reduction of the three precursors H_2PtCl_6, $H_2Pt(OH)_6$, $Pt(acac)_2$.

By changing the base from inorganic NaOH to organic Na(acac) the thermal reduction of H_2PtCl_6 occurred substantially faster (about 1 min of reduction) and heating periods longer than 20 min led to sintering and flocculation of the NPs. This is different to the previous experiments. The presence of $acac^-$ and chloride anions seem not to be able to take over the stabilizing role that OH^- fulfills in the experiments using H_2PtCl_6 or H_2PtBr_6 as precursors. Therefore, it can be assumed that the NPs might be less protected against an attack by chloride resulting in Ostwald ripening as discussed by Neumann et al. [4] or coalescence. While the NPs sintered during longer reduction times, after 10 min the $acac^-$/Pt ratios of 48.8, 24.4, 12.2, 9.2, 6.1 and 5.4 led to stable NPs with sizes within the size error of 1.4–1.9 nm determined by TEM analysis, see Figure 4. The obtained particle sizes in Figure 4 were slightly smaller at low OH^-/Pt as compared to the size reported for the reduction of H_2PtCl_6 in presence of NaOH [7]. Using an $acac^-$/Pt ratio of 4.6 and 2.4 did not lead to stable NPs. The NPs already sintered during the thermal reduction, but at the higher $acac^-$ concentrations the dispersions remained stable for several days. Interestingly, although the reduction rate and stability are affected using Na(acac), in the reduction of H_2PtCl_6 the particle size was comparable to the system with NaOH as base and no Ostwald ripening was observed. Hence, the smaller NPs might be obtained due to leaching induced by chloride without a following Ostwald ripening, which was observed also by Neumann et al. [4] only after longer reaction times.

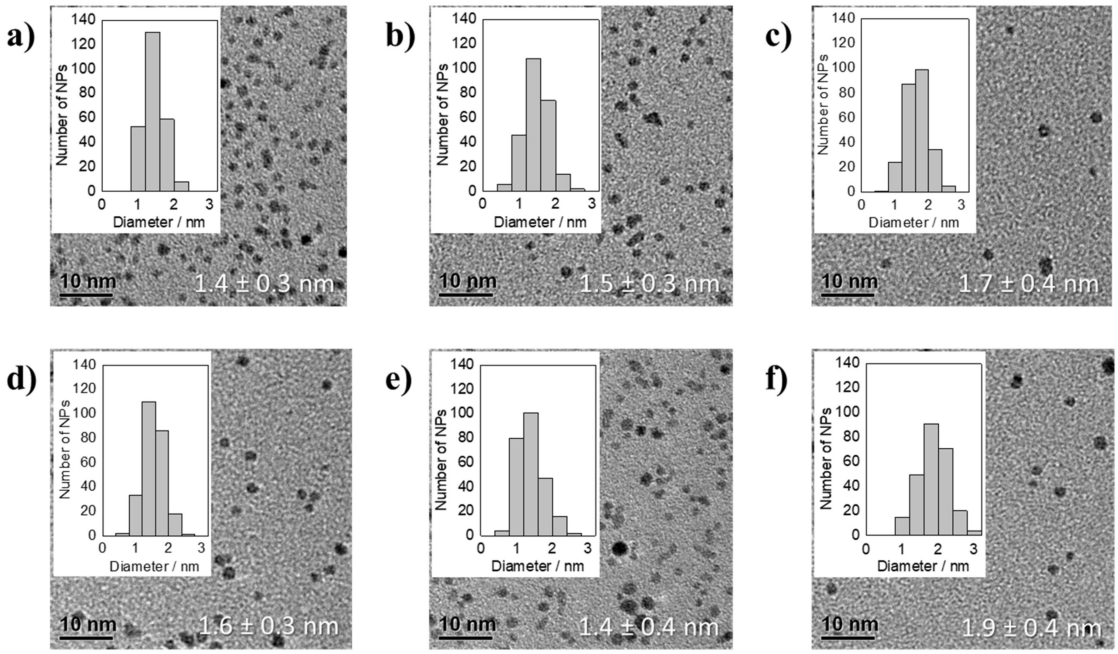

Figure 4. TEM micrographs of averaged particle size together with the standard deviation and NP size distribution of thermally formed Pt NPs by using H_2PtCl_6 as precursor in presence of Na(acac) with different $acac^-$/Pt ratios of: (**a**) 48.8, (**b**) 24.4, (**c**) 12.2, (**d**) 9.2, (**e**) 6.1, and (**f**) 5.4 after 10 min of synthesis.

The reduction of $H_2Pt(OH)_6$ in presence of Na(acac) led to stable particles after 90 min at 150 °C between $acac^-$/Pt ratios of 4.6 and 48.8. At $acac^-$/Pt ratios of 28.8 and 24.4 the particle size was constant at 1.7 ± 0.5 and 1.7 ± 0.4 nm, respectively, see Figure 5. Decreasing the $acac^-$/Pt ratio led to an increase in size to 2.2 ± 0.7 nm at an $acac^-$/Pt ratio of 4.6. The size increase in Figure 5 was comparable to the reduction of $H_2Pt(OH)_6$ in presence of NaOH, see Figure 3, but the results suggest that slightly smaller particle sizes are reached. In conclusion, the presence of Na(acac) in the reduction of $H_2Pt(OH)_6$ leads to slightly smaller particles in comparison to the use of NaOH, compare Figure 5 to Figure 3. As compared to the reduction of H_2PtCl_6 no chloride was present that could induce leaching. Hence, the smaller particles must be explained by an interaction of $acac^-$ and OH^- as "ligands" stabilizing the Pt NP surface against coalescence.

Reducing $Pt(acac)_2$ in the presence of Na(acac) leads after 150 min of synthesis to NP dispersions that remained stable for several hours, but the TEM analysis showed a fast particles agglomeration, see Figure 6. In addition, after one day in most samples a yellow to light brown solid was found depositing on the wall and the bottom of the glass vials. The solid is probably an organic based compound that might contain $acac^-$ and precipitates as it is not anymore soluble in EG at room temperature. The $acac^-$/Pt ratio of 48.9 did not lead to stable particles. The NP size at an $acac^-$/Pt ratio of 24.4 was 3.1 ± 0.6 nm, see Figure 6. In the range of an $acac^-$/Pt ratio between 4.6 and 24.4 the particle size varied between 2.9 ± 0.4 and 3.7 ± 0.7 nm at an $acac^-$/Pt ratio of 5.4 and 6.1, respectively. At a particle size of above 3 nm, NPs also synthesized by H_2PtCl_6 in presence of NaOH by Quinson et al. [7] showed aggregation on the TEM grid. Interestingly, to reach such sizes substantially lower OH^-/Pt ratios of 5.5 or lower were necessary [7]. This might be explainable by the substantially larger size of the acac− as compared to the OH^- anion, as less $acac^-$ can be located on the Pt NP surface due to sterically hindering of the "ligands". Hence, even at higher $acac^-$ concentration substantially less anions are needed to completely saturate the surface resulting in less negative charge located on the surface. Due to the less negative charge density the Coulomb repulsion between the NPs is reduced, which increases the probability of agglomeration.

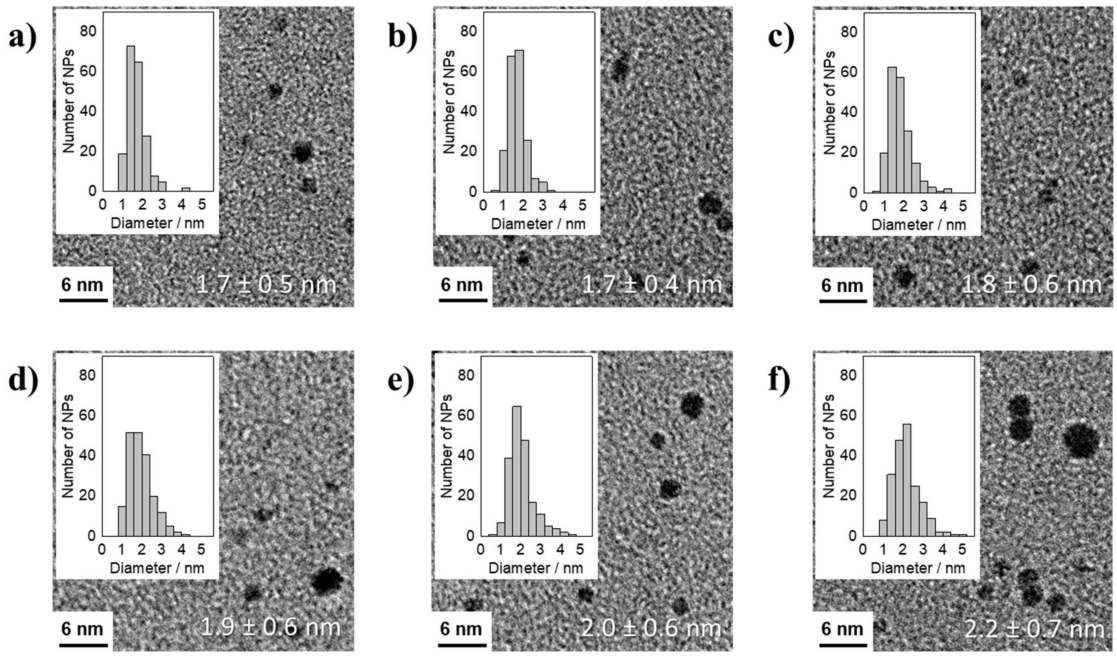

Figure 5. TEM micrographs of averaged particle size together with the standard deviation and NP size distributions of thermally formed Pt NPs by using $H_2Pt(OH)_6$ as precursor in presence of Na(acac) with different $acac^-$/Pt ratios of: (**a**) 48.8, (**b**) 24.4, (**c**) 12.2, (**d**) 9.2, (**e**) 6.1, and (**f**) 4.6 after 90 min of synthesis.

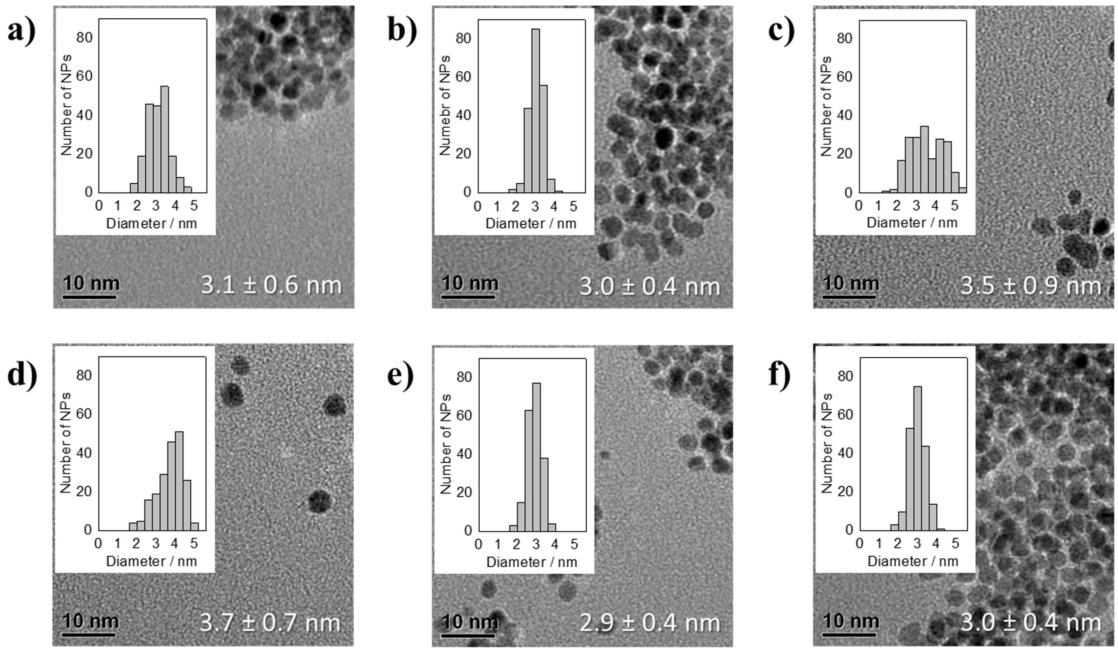

Figure 6. TEM micrographs of averaged particle size together with the standard deviation and NP size distribution of thermally formed Pt NPs by using $Pt(acac)_2$ as precursor in presence of Na(acac) with different $acac^-$/Pt ratios of: (**a**) 24.4, (**b**) 12.2, (**c**) 9.1, (**d**) 6.1, (**e**) 5.4, and (**f**) 4.6 after 150 min of synthesis.

The size of the particles obtained from the reduction of $Pt(acac)_2$ in presence of Na(acac) are consistent with the sizes obtained by Neumann et al. [4] of 3.0 ± 0.3 nm for reducing $Pt(acac)_2$ in presence of NaOH as base in EG. Consequently, it seems that it is not the presence of $acac^-$ but the use of the $Pt(acac)_2$ precursor that leads to a substantial particle increase. Considering the previous experiments, the base anion seems to be less

important for the particle size but mainly the nature of the precursor (oxidation state, bonding strength, etc.) determines the size control. The nature of the precursor itself would be expected to be only important in the first step of the reduction mechanism. Assuming a size control determined by the Pt salt could be explained by the following: The Pt precursor influences the reduction rate, i.e., how fast the coordinated Pt can be reduced or how fast the "ligands" are exchanged with base anions. The latter depends on the ligand properties and in particular on the binding properties of the discussed anions (OH^-, $acac^-$, or chloride) to Pt. This is important for the (further) reduction and growth process as the precursor anions are expected to be located or to be bond to the surface during the particle formation. Small precursor anions (OH^-) lead to smaller particles, see Figure 3 to Figure 5, while larger precursor anions ($acac^-$) lead to larger particles, see Figure 6 and a summary of the size results in Table S1. Using larger anions, less "ligands" can be located at or adsorbed to the Pt surface. As a result, less charge is present at the particle surface to stabilize even at higher anion concentrations thus larger NPs are formed. As the use of $Pt(acac)_2$ independent of the amount of NaOH or Na(acac) led to the same large particles, the sterically demanding $acac^-$ (from the precursor) seems to bind strongly to the Pt, determining the size independent of other anions present within the reaction medium. Therefore, the size determining step seems to be the shielding of the $acac^-$ limiting the number of bound $acac^-$ "ligands" to the Pt, hence leading to a size increase, or, e.g., hindering the "ligand" exchange by OH^- when NaOH is used as base.

4. Conclusions

Comparison of the NP sizes obtained in thermal reduction of the precursors H_2PtCl_6, $H_2Pt(OH)_6$, and $Pt(acac)_2$ in presence of NaOH or Na(acac) in EG revealed that the nature of base anions does not substantially influence the size. Instead, the precursor anion or the nature of the metal salt seem to play a more important role in the particle size control. Interestingly, the thermal reduction of $Pt(acac)_2$ leads to large particles of about 3 nm independent of the NaOH or Na(acac) concentration in EG, while the size control of H_2PtCl_6 and $H_2Pt(OH)_6$ depends on the OH^-/Pt or $acac^-$/Pt ratio.

Supplementary Materials: The following are available online at https://www.mdpi.com/article/10.3390/nano11082092/s1. Table S1. Overview of the averaged particle sizes and standard deviations determined from TEM images reducing different precursors in presence of the bases NaOH and Na(acac) depending on the ratio of the anion of the base to Pt. * When the precursor contains the same anion as the base the amount is considered in the anion/Pt ratio. # Some base anion/Pt ratios led to instable particles.

Author Contributions: J.S. designed the experiments together with S.K.; S.N. and J.Q. provided TEM images that were analyzed by J.S.; S.K. and M.A. supervised the research; J.S. and S.K. wrote the first draft of the paper, that was read, and commented on by all authors. All authors have read and agreed to the published version of the manuscript.

Funding: This research was funded by the DFG (KU 3152/6-1) and the Swiss National Science Foundation (SNSF, project No. 200021_1847429). S.K. thanks the "Fonds der Chemischen Industrie (FCI)" for financial support through a Liebig research grant. J.Q. has received funding from the European Union's Horizon 2020 research and innovation program under the Marie Skłodowska-Curie grant agreement No 840523 (CoSolCat).

Data Availability Statement: The data presented in this study are available on request from the corresponding author.

Acknowledgments: The authors thank L. Theil Kuhn and S. B. Simonsen, Technical University of Denmark (DTU) for access to TEM facilities.

Conflicts of Interest: The authors declare no conflict of interest.

References

1. Wang, Y.; Zhang, J.; Wang, X.; Ren, J.; Zuo, B.; Tang, Y. Metal Nanoclusters Stabilized with Simple Ions and Solvents—Promising Building Blocks for Future Catalysts. *Top. Catal.* **2005**, *35*, 35–41. [CrossRef]
2. Wang, X.; Sonström, P.; Arndt, D.; Stöver, J.; Zielasek, V.; Borchert, H.; Thiel, K.; Al-Shamery, K.; Bäumer, M. Heterogeneous Catalysis with Supported Platinum Colloids: A Systematic Study of the Interplay between Support and Functional Ligands. *J. Catal.* **2011**, *278*, 143–152. [CrossRef]
3. Neumann, S.; Grotheer, S.; Tielke, J.; Schrader, I.; Quinson, J.; Zana, A.; Oezaslan, M.; Arenz, M.; Kunz, S. Nanoparticles in a Box: A Concept to Isolate, Store and Re-Use Colloidal Surfactant-Free Precious Metal Nanoparticles. *J. Mater. Chem. A* **2017**, *5*, 6140–6145. [CrossRef]
4. Neumann, S.; Schröder, J.; Bizzotto, F.; Arenz, M.; Dworzak, A.; Oezaslan, M.; Bäumer, M.; Kunz, S. Halide-Induced Leaching of Pt Nanoparticles—Manipulation of Particle Size by Controlled Ostwald Ripening. *ChemNanoMat* **2019**, *5*, 462–471. [CrossRef]
5. Neumann, S.; Gutmann, T.; Buntkowsky, G.; Paul, S.; Thiele, G.; Sievers, H.; Bäumer, M.; Kunz, S. Insights into the Reaction Mechanism and Particle Size Effects of CO Oxidation over Supported Pt Nanoparticle Catalysts. *J. Catal.* **2019**, *377*, 662–672. [CrossRef]
6. Speder, J.; Altmann, L.; Roefzaad, M.; Bäumer, M.; Kirkensgaard, J.J.K.K.; Mortensen, K.; Arenz, M. Pt Based PEMFC Catalysts Prepared from Colloidal Particle Suspensions—A Toolbox for Model Studies. *Phys. Chem. Chem. Phys.* **2013**, *15*, 3602. [CrossRef] [PubMed]
7. Quinson, J.; Inaba, M.; Neumann, S.; Swane, A.A.; Bucher, J.; Simonsen, S.B.; Theil Kuhn, L.; Kirkensgaard, J.J.K.; Jensen, K.M.Ø.; Oezaslan, M.; et al. Investigating Particle Size Effects in Catalysis by Applying a Size-Controlled and Surfactant-Free Synthesis of Colloidal Nanoparticles in Alkaline Ethylene Glycol: Case Study of the Oxygen Reduction Reaction on Pt. *ACS Catal.* **2018**, *8*, 6627–6635. [CrossRef]
8. Schrader, I.; Warneke, J.; Backenköhler, J.; Kunz, S. Functionalization of Platinum Nanoparticles with L-Proline: Simultaneous Enhancements of Catalytic Activity and Selectivity. *J. Am. Chem. Soc.* **2015**, *137*, 905–912. [CrossRef] [PubMed]
9. Schrader, I.; Neumann, S.; Himstedt, R.; Zana, A.; Warneke, J.; Kunz, S. The Effect of Particle Size and Ligand Configuration on the Asymmetric Catalytic Properties of Proline-Functionalized Pt-Nanoparticles. *Chem. Commun.* **2015**, *51*, 16221–16224. [CrossRef] [PubMed]
10. Šulce, A.; Backenköhler, J.; Schrader, I.; Piane, M.D.; Müller, C.; Wark, A.; Ciacchi, L.C.; Azov, V.; Kunz, S. Ligand-Functionalized Pt Nanoparticles as Asymmetric Heterogeneous Catalysts: Molecular Reaction Control by Ligand-Reactant Interactions. *Catal. Sci. Technol.* **2018**, *8*, 6062–6075. [CrossRef]
11. Šulce, A.; Flaherty, D.W.; Kunz, S. Kinetic Analysis of the Asymmetric Hydrogenation of SS-Keto Esters over $α$-Amino Acid-Functionalized Pt Nanoparticles. *J. Catal.* **2019**, *374*, 82–92. [CrossRef]
12. Bock, C.; Paquet, C.; Couillard, M.; Botton, G.A.; MacDougall, B.R. Size-Selected Synthesis of PtRu Nano-Catalysts: Reaction and Size Control Mechanism. *J. Am. Chem. Soc.* **2004**, *126*, 8028–8037. [CrossRef] [PubMed]
13. Schrader, I.; Warneke, J.; Neumann, S.; Grotheer, S.; Swane, A.A.; Kirkensgaard, J.J.K.; Arenz, M.; Kunz, S. Surface Chemistry of "Unprotected" Nanoparticles: A Spectroscopic Investigation on Colloidal Particles. *J. Phys. Chem. C* **2015**, *119*, 17655–17661. [CrossRef]
14. Kacenauskaite, L.; Quinson, J.; Schultz, H.; Kirkensgaard, J.J.K.; Kunz, S.; Vosch, T.; Arenz, M. UV-Induced Synthesis and Stabilization of Surfactant-Free Colloidal Pt Nanoparticles with Controlled Particle Size in Ethylene Glycol. *ChemNanoMat* **2017**, *3*, 89–93. [CrossRef]
15. Schröder, J.; Neumann, S.; Kunz, S. Visible-Light-Induced Synthesis of "Surfactant-Free" Pt Nanoparticles in Ethylene Glycol as a Synthetic Approach for Mechanistic Studies on Nanoparticle Formation. *J. Phys. Chem. C* **2020**, *124*, 21798–21809. [CrossRef]
16. Quinson, J.; Bucher, J.; Simonsen, S.B.; Kuhn, L.T.; Kunz, S.; Arenz, M. Monovalent Alkali Cations: Simple and Eco-Friendly Stabilizers for Surfactant-Free Precious Metal Nanoparticle Colloids. *ACS Sustain. Chem. Eng.* **2019**, *7*, 13680–13686. [CrossRef]

Supplementary Materials

Communication

Anion Dependent Particle Size Control of Platinum Nanoparticles Synthesized in Ethylene Glycol

Johanna Schröder [1,2,*], Sarah Neumann [1], Jonathan Quinson [3], Matthias Arenz [2] and Sebastian Kunz [1,4,*]

[1] Institute of Applied and Physical Chemistry (IAPC), Center for Environmental Research and
Sustainable Technology, University of Bremen, Leobener Strasse 6, 28359 Bremen, Germany
[2] Department of Chemistry, Biochemistry, and Pharmaceutical Sciences (DCBP), University of Bern,
Freiestrasse 3, 3012 Bern, Switzerland
[3] Chemistry Department, University of Copenhagen, Universitetsparken 5, 2100 Copenhagen, Denmark;
[4] Südzucker AG, Central Department Research, Development, and Services (CRDS), Wormser Strasse 11, 67283 Obrigheim, Germany
* Correspondence: johanna.schroeder@unibe.ch (J.S.); sebastian-kunz@web.de (S.K.)

Table S1. Overview of the averaged particle sizes and standard deviations determined from TEM images reducing different precursors in presence of the bases NaOH and Na(acac) depending on the ratio of the anion of the base to Pt. * When the precursor contains the same anion as the base the amount is considered in the anion/Pt ratio. # Some base anion/Pt ratios led to instable particles.

Precursor		**$H_2Pt(OH)_6$**			**H_2PtCl_6**	**$Pt(acac)_2$**
Base		**NaOH** *		**Na(acac)**	**Na(acac)**	**Na(acac)** *
Reduction time		10 min	90 min	90 min	10 min	150 min
base anion/Pt molar ratio *	48.8	-	-	1.7 ± 0.5	1.4 ± 0.3	- #
	24.4	- #	1.6 ± 0.4	1.7 ± 0.4	1.5 ± 0.3	3.1 ± 0.6
	12.2	1.2 ± 0.4	2.0 ± 0.7	1.8 ± 0.6	1.7 ± 0.4	3.0 ± 0.4
	9.2	1.4 ± 0.3	2.5 ± 0.6	1.9 ± 0.5	1.6 ± 0.3	3.5 ± 0.9
	7.6	1.4 ± 0.3	2.4 ± 0.3	-	-	-
	6.1	-	-	2.0 ± 0.6	1.4 ± 0.4	3.7 ± 0.7
	5.4	-	-	2.2 ± 0.7	-	2.9 ± 0.4
	4.6	-	-	- #	1.9 ± 0.4	3.0 ± 0.4
	2.4	-	-	- #	-	-

Manuscript III:

J. Schröder, J. Quinson, J. K. Mathiesen, J. J. K. Kirkensgaard, S. Alinejad, V. A. Mints, K. M. Ø. Jensen, M. Arenz

A new Approach to Probe the Degradation of Fuel Cell Catalysts under Realistic Conditions: Combining Tests in a Gas Diffusion Electrode Setup with Small Angle X-Ray Scattering

The published paper is reprinted from *J. Electrochem. Soc.*, **2020**, *167*, 134515.

https: doi.org/10.1149/1945-7111/abbdd2

Journal of The Electrochemical Society, 2020 **167** 134515
1945-7111/2020/167(13)/134515/8/$40.00 © 2020 The Electrochemical Society ("ECS"). Published on behalf of ECS by IOP Publishing Limited

A New Approach to Probe the Degradation of Fuel Cell Catalysts under Realistic Conditions: Combining Tests in a Gas Diffusion Electrode Setup with Small Angle X-ray Scattering

Johanna Schröder,[1,2] Jonathan Quinson,[3] Jette K. Mathiesen,[3] Jacob J. K. Kirkensgaard,[4] Shima Alinejad,[1] Vladislav A. Mints,[1] Kirsten M. ∅. Jensen,[3] and Matthias Arenz[1,*,z]

[1]*Department of Chemistry and Biochemistry, University of Bern, 3012 Bern, Switzerland*
[2]*Institute of Applied and Physical Chemistry (IAPC), Center for Environmental Research and Sustainable Technology, University of Bremen, 28359 Bremen, Germany*
[3]*Department of Chemistry, University of Copenhagen, 2100 Copenhagen, Denmark*
[4]*Department of Food Science, University of Copenhagen, 958 Frederiksberg, Denmark*

A new approach for efficiently investigating the degradation of fuel cell catalysts under realistic conditions is presented combining accelerated stress tests (ASTs) in a gas diffusion electrode (GDE) setup with small angle X-ray scattering (SAXS). GDE setups were recently introduced as a novel testing tool combining the advantages of classical electrochemical cells with a three-electrode setup and membrane electrode assemblies (MEAs). SAXS characterization of the catalyst layer enables an evaluation of the particle size distribution of the catalyst and its changes upon applying an AST. The straight-forward approach not only enables stability testing of fuel cell catalysts in a comparative and reproducible manner, it also allows mechanistic insights into the degradation mechanism. Typical metal loadings for proton exchange membrane fuel cells (PEMFCs), i.e. 0.2 mg_{Pt} cm^{-2}_{geo}, are applied in the GDE and the degradation of the overall (whole) catalyst layer is probed. For the first time, realistic degradation tests can be performed comparing a set of catalysts with several repeats within reasonable time. It is demonstrated that independent of the initial particle size in the pristine catalyst, for ASTs simulating load cycle conditions in a PEMFC, all catalysts degrade to a similar particle size distribution.
 [DOI: 10.1149/1945-7111/abbdd2]

Manuscript submitted May 12, 2020; revised manuscript received September 10, 2020. Published October 12, 2020.

Supplementary material for this article is available online

Proton exchange membrane fuel cells (PEMFCs) are a promising alternative to replace combustion engines[1–3] with the development of fuel-cells vehicles. A key component of this technology are using nanoparticles (NPs), nowadays typically Pt-alloys (e.g. PtCo in the Mirai automobile from Toyota),[4–6] supported on high surface carbon as catalysts.[3] For a long time, the main research focus was to improve the catalyst activity leading to the development of several different types of highly active catalysts.[7] More recently, the performance at high current densities and the effect of high oxygen mass transfer resistances has gained increasing attention.[8] It was established that the oxygen mass transfer resistance decreases by increasing the metal dispersion on the support material, i.e. the decrease in particle size of the catalyst.[8] However, besides a high activity, a sufficient stability of the catalysts is required for applications.[1,9] Today, most degradation studies are either performed under idealized conditions, or they lack statistics and comparative character. Hence an efficient, i.e. fast and realistic, testing of fuel cell catalysts is needed to bridge catalyst development to their application in fuel cells. Ideally the testing is not of pure descriptive behavior, but also mechanistic insights are provided.

To simulate the use of catalysts under realistic conditions and at the same time accelerate their degradation, stability investigations are performed using accelerated stress tests (AST), e.g. following protocols recommended by the Fuel Cell Commercialization Conference of Japan (FCCJ).[10,11] Usually such measurements are either performed in classical electrochemical cells with a three-electrode setup[12] or in membrane electrode assemblies (MEAs).[13] Both approaches have advantages and disadvantages. Classic electrochemical cells enable relatively fast screening at the expense of a somewhat unrealistic "environment" (e.g. liquid electrolyte). MEAs offer a more realistic "environment" but require significantly more advanced facilities such as a complete hydrogen infrastructure in the laboratory. In addition, MEA testing is very time consuming and therefore usually not combined with spectroscopic tools in a comparative manner, i.e. comparing different catalysts and showing several repeats for each sample. A powerful methodology to combine the advantages of both approaches for an efficient testing fuel cell catalysts under realistic conditions is the gas diffusion electrode (GDE) setup.[14,15] Alinejad et al.[15] recently presented the benefits to perform AST protocols in gas diffusion setups by following the loss in catalyst active surface area as function of the electrochemical treatment.

In the here presented work, a significant advancement of this approach is achieved by using realistic catalyst layers applied in MEA testing and by combining such tests with the analysis of the catalyst layer via small angle X-ray scattering (SAXS). The known electrochemical degradation mechanisms of (1) migration of particles followed by coalescence and potentially sintering, (2) metal dissolution, (3) electrochemical Ostwald ripening, where large particles grow at the expense of small ones, and (4) particle detachment from the support[16] have a direct effect on the particle size distribution of the catalysts. The understanding of the degradation mechanism is key to propose and develop mitigation strategies. Commonly, the determination of the particle size is done by (scanning) transmission electron microscopy ((S)TEM) and to observe the change of selected particles before and after the treatment identical location (IL) (S)TEM is performed using rotating disk electrode (RDE)[16–18] or GDE setups.[15] However, while (S)TEM is a local method, SAXS offers the benefits to analyze the particle size distribution after performing the AST in the whole catalyst layer[19,20] and even without further dismantling of the GDE as we demonstrate in the present study. In the present work, load-cycle conditions were simulated in an AST protocol by applying potential steps between 0.6 and 1.0 V_{RHE} in oxygen saturated atmosphere at 25 °C and 50 °C in a GDE setup. The combination of electrochemical measurements and SAXS analysis allows to determine the loss in active surface area and to relate it to a change in particle size as function of operation temperature and initial NP size distribution. We demonstrate with this study that the combination of GDE and SAXS is an efficient way to test fuel cell catalysts in a comparative manner under realistic conditions and enable mechanistic insights into the catalyst degradation.

*Electrochemical Society Member.
[z]E-mail: matthias.arenz@dcb.unibe.ch

Experimental

Chemicals, materials, and gases.—Ultrapure Milli-Q water (resistivity > 18.2 MΩ·cm, total organic carbon (TOC) < 5 ppb) from a Millipore system was used for catalyst ink formation, diluting the acid, and the cleaning of the GDE cell. For preparing the catalysts ink isopropanol (IPA, 99.7 + %, Alfa Aesar), commercial Pt/C catalysts (TEC10E20A (1–2 nm Pt/C, 19.4 wt% Pt), TEC10E50E (2–3 nm Pt/C, 46.0 wt% Pt), TEC10E50E-HT (4–5 nm Pt/C, 50.6 wt% Pt), Tanaka kikinzoku kogyo), and Nafion dispersion (D1021, 10 wt.%, EW 1100, Fuel Cell Store) was used.

The GDE was prepared using a Nafion membrane (Nafion 117, 183 μm thick, Fuel Cell Store), two gas diffusion layers (GDL) (Sigracet 39AA, 280 μm thick, Fuel Cell Store; with a microporous layer (MPL): Sigracet 39BC, 325 μm thick, Fuel Cell Store). In this study the Nafion membrane was always pretreated. Circles with a diameter of 2 cm were cut from a sheet of Nafion membrane. Those cutoff membranes were treated in 5 wt.% H_2O_2 (Hänseler, 30 min, 80 °C), rinsed with Milli-Q water, treated in Milli-Q water (30 min, 80 °C), rinsed again with Milli-Q water, and treated in 8 wt.% H_2SO_4 (30 min, 80 °C). After final rinsing of the cutoff membranes with Milli-Q water, they were kept in a glass vial filled with Milli-Q water.

Diluted 70% perchloric acid ($HClO_4$, 99.999% trace metals basis, Sigma Aldrich) as electrolyte and the gases Ar (99.999%), O_2 (99.999%), and CO (99.97%) from Air Liquide were used in the electrochemical measurements.

Gas diffusion electrode setup.—An in-house gas diffusion electrode setup as described before[14,15] was used in the electrochemical measurements. The GDE was placed on top of the flow field in the stainless-steel cell body with the Nafion membrane upwards. The upper cell part above the Nafion membrane is made of polytetrafluoroethylene (PTFE). A platinum wire was used as a counter electrode (CE) and a reversible hydrogen electrode (RHE) as a reference electrode (RE). The CE was placed inside a glass capillary with a glass frit on the bottom to avoid the trapping of gas bubbles in the hole of the Teflon cell and hence helping to improve the reproducibility of the measurement. All potentials in this study are referred to the RHE potential.

In an initial cleaning the Teflon upperpart was soaked in acid (H_2SO_4:HNO_3 = 1:1, v:v) overnight. After rinsing it with ultrapure water, it was boiled twice in ultrapure water. Between the measurements the Teflon upper part, the RE, and the glass capillary were boiled once in ultrapure water.

Catalyst synthesis and ink formation.—Three commercial Tanaka catalysts with different particle sizes and metal loadings were used. The ink was formed by dispersing the catalysts in a mixture of Milli-Q water and IPA (water/IPA ratio of 3:1) to obtain about 5 ml of ink with a Pt concentration of 0.5 mg ml^{-1}. The mixture was sonicated for 5 min in a sonication bath to get a suitable dispersion. 23–98 μl of Nafion was added (Nafion/carbon mass ratio of 1). The dispersion was again sonicated for 5 min in a sonication bath.

Vacuum filtration and pressing of GDE.—The Sigracet 39BC gas diffusion layer (GDL) was placed in a vacuum filtration setup between a glass funnel and a sand core filter. All this was placed on a collecting bottle as described by Yarlagadda et al.[21] 4 ml of the inks were diluted with 7 ml of Milli-Q water and 29 ml of IPA (water-IPA ratio of 1:3, Pt concentration of 0.05 mg l^{-1}). The mixture was sonicated for 1 min. The 40 ml diluted ink were filled in a funnel. A jet water pump was used to deposit the catalyst on top of the GDL. When the collected solvent was not colorless it was refilled into the funnel and the vacuum filtration was started again. Afterwards, the GDE was dried at least overnight on air. By this procedure a theoretical Pt loading of 0.208 mg_{Pt} $cm^{-2}{}_{geo}$ was generated.

The Nafion membrane was pressed on top of the GDE. Therefore, a Teflon sheet was placed on top of a Teflon block and afterwards the GDL without MPL (∅ 2 cm), GDL with MPL (∅ 2 cm with hole of ∅ 3 mm) and the catalyst on the GDL from the vacuum filtration (∅ 3 mm) in the hole. A Nafion membrane (to avoid later the leaking of the electrolyte into the GDE) was rinsed with Milli-Q water, dried and followed by a second Teflon sheet and a second Teflon block placed on top. Everything was placed between two metal blocks and the pressing was performed at 2 tons for 10 min.

Electrochemical measurement.—The electrochemical measurements were performed with a computer controlled parallel potentiostat (ECi-242, NordicElectrochemistry). Two measurements could be performed in parallel by splitting the gas inlet after humidification of the gas. Hence the gas inlet of two GDE setups was connected to the same bubbler. 4 M $HClO_4$ aqueous solution in the upper Teflon compartment of the GDE setup was used as electrolyte and different temperatures (25 °C or 50 °C) were applied using a fan in an isolated Faraday cage. Before performing the AST protocols first 20 cyclic voltammograms (CVs) in Argon (Ar, with a scan rate of 500 mV s^{-1}, 0.06–1.1 V_{RHE}) were performed to assess if the assembling of the cell was successful. For cleaning the surface, afterwards CVs in oxygen (O_2) were performed: 20 CVs with 500 mV s^{-1}, then ca. 50 CVs with 50 mV s^{-1} until a stable CV was obtained. The resistance between the working electrode (WE) and RE (ca. 10 Ω) was compensated to around 2 Ω by using the analog positive feedback scheme of the potentiostat. The resistance was determined online using an AC signal (5 kHz, 5 mV)[22] Before starting the measurement, to make sure that the O_2 was completely replaced, CVs in Ar (50 CVs, 500 mV s^{-1}) were done. The wished temperature for the following AST was adjusted.

To investigate the degradation mechanism(s) of the Pt/C electrocatalysts, ASTs as reported by Alinejad et al.[15] were used. The applied electrode potential was stepped between 0.6 and 1.0 V_{RHE} and hold for three seconds, respectively to simulate the load-cycle conditions. The surface loss of the catalysts during the AST was determined by comparing the ECSA obtained from the CO stripping voltammetry before and after the AST of at least three reproducible measurements. The ECSA values in m^2 $g_{Pt}{}^{-1}$ were determined using the theoretical Pt loading of 0.208 mg_{Pt} $cm^{-2}{}_{geo}$ and the surface area (in cm^2) determined by CO stripping. The CO stripping was performed by subtracting the Ar background and using a baseline correction between the chosen peak limits to avoid any influence of capacitive currents from the carbon support as shown by Inaba et al.[23] ASTs were performed in O_2 with 9000 steps at 25 °C or 5000 steps at 50 °C.

SAXS analysis.—A SAXSLab instrument (Niels Bohr Institute, University of Copenhagen, Denmark) equipped with a 100XL + micro-focus sealed X-ray tube (Rigaku) producing a photon beam with a wavelength of 1.54 Å was used for SAXS data acquisition.[20,24] A 2D 300 K Pilatus detector from Dectris was used to record the scattering patterns and the samples did not show anisotropy. The two-dimensional scattering data were azimuthally averaged, normalized by the incident radiation intensity, the sample exposure time and the transmission using the Saxsgui software. Data were then corrected for background and detector inhomogeneities using standard reduction software. Samples were sealed between two 5–7 μm thick mica windows in dedicated sample cells and measurements performed in vacuum. The background measurement was made with a GDL Sigracet 39BC without NPs.

The radially averaged intensity I(q) is given as a function of the scattering vector $q = 4\pi\cdot\sin(\theta)/\lambda$, where λ is the wavelength and 2θ is the scattering angle. The background corrected scattering data were fitted using a power law to take into account the behavior at low q value and a model of polydisperse spheres described by a volume-weighted log-normal distribution. This model leads to satisfying results for 13 samples out of 36 samples. The remaining data were then best fitted by adding a second model of polydisperse

spheres also described by a volume-weighted log-normal distribution (for 11 samples out of 36). A structure factor contribution was sometimes needed to properly model the data for the 2 polydisperse sphere models (6 samples out of 36). We employed a hard-sphere structure factor $F(R,\eta)$ as described in Ref. 25. The scattering data are fitted to the following general expression:

$$I(q) = A \cdot q^{-n} + C_1 \cdot F(R_1, \eta_1) \cdot \int P_{S1}(q, R) V_1(R) D_1(R) dR + C_2 \int P_{S2}(q, R) V_2(R) D_2(R) dR$$

where $A \cdot q^{-n}$ corresponds to the power law where A and n are free parameters; C_1 and C_2 are scaling constants, Ps_1 and Ps_2 the sphere form factors, V_1 and V_2 the particle volumes and D_1 and D_2 the log-normal size distribution. The sphere form factor is given by[26,27]:

$$Ps(q, R) = \left(3\frac{\sin(qR) - qR\cos(qR)}{(qR)^3}\right)^2$$

and the log-normal distribution by:

$$D(R) = \frac{1}{R\sigma\sqrt{2\pi}} \exp\left(\frac{-\left[\ln\left(\frac{R}{R_0}\right)\right]^2}{2\sigma^2}\right)$$

where σ is the variance and R_0 the geometric mean of the log-normal distribution. The fitting was done using home written MATLAB code. The free parameters in the model are: A, n, R_1, R_2, σ_1, σ_2, C_1, C_2, η_1. The values obtained for these parameters are reported in Table SI. In 13 out 36 samples, only 5 free parameters where needed, and a one population model was enough to describe the sample. For 3 samples a model adding a structure factor with 6 free parameters gave a better fit. After ASTs however and in particular for the initially 1–2 nm Pt/C catalysts, better fits were obtained with 8 free parameters considering 2 spheres populations. In 3 cases a better fit was obtained with 9 free parameters. In order to account for the two populations, the reported probability density functions were weighted by the relative surface contribution of the spheres as detailed in SI. The scattering data and corresponding fits are reported in Figs. S1–S4 (available online at stacks.iop.org/JES/167/134515/mmedia) and Table SI. In the discussion, we refer to the average diameter of the particle and use the standard deviation relative to the evaluation of this average diameter based on three independent measurements as error to compare the catalyst sizes. In other words, the values quoted in the manuscript read as $\langle d \rangle \pm \sigma_{\langle d \rangle}$ where $\langle d \rangle$ is the average diameter retrieved from three independent measurements and $\sigma_{\langle d \rangle}$ a measure of how reproducible this estimation of $\langle d \rangle$ is from three independent measurements. The relative deviation relative to $\langle d \rangle$ (σ_d), i.e. how broad the distribution is around the value $\langle d \rangle$, was between 10 and 30%, see details in Table SI.

The "starting size" was analyzed from three samples of 3 mm diameter punched from catalyst film on the GDL after vacuum filtration. Three samples with reproducible ECSAs after the AST were analyzed by punching a circle with a diameter of 5 mm around the GDE (of 3 mm) with the Nafion membrane on top. The background sample was obtained by performing the AST protocol on a catalyst free "GDE" by using a circle with a diameter of 3 mm Sigracet 39BC as "GDE" (pressing was performed the same way as before).

TEM analysis.—TEM micrographs were obtained using a Jeol 2100 operated at 200 kV. Samples were characterized by imaging at least 5 different areas of the TEM grid at minimum 3 different magnifications. The size (diameter) of the NPs was estimated using the imageJ software and considering at least 200 NPs. The samples Pt/C were diluted in ethanol before being drop casted onto a holey carbon support film of Cu 300 mesh grids (Quantifoil).

Pair distribution function (PDF) analysis.—Data acquisition: X-ray total scattering data were obtained at beamline 11-ID-B, Advanced Photon Source (APS), Argonne National Laboratory, USA. The samples were mounted on a flat plate sample holder, so that data were collected in transmission geometry using a Perkin-Elmer flat panel detector with a pixel size of 200 × 200 μm in the RA-PDF setup.[28] A wavelength of 0.2115 Å was used, and the sample-to-detector distance was calibrated using a CeO_2 standard. Fit2D was used to calibrate the experimental geometry parameters and azimuthally integrate the scattering intensities to 1D scattering patterns.[29,30]

PDF modelling: X-ray total scattering data were Fourier transformed with xPDFsuite to obtain PDFs using the Q-range from 0.9 Å -1 to 22.0 Å-1.[31] The scattering signal from the carbon substrate and Nafion membrane was subtracted before the Fourier transform. The scattering signal from the carbon substrate was measured independently, while that from the MEA membrane was determined from the data obtained from the largest nanoparticles after O_2 exposure by subtracting out the well-known Pt contribution in reciprocal space. Analysis and refinement of the obtained PDFs was performed using PDFgui, in which a least-square optimization procedure is performed between a theoretical PDF and the experimental PDF from a model.[32] The refined parameters included the unit cell, d2-parameter describing local correlated atomic movement, scale factor, a spherical particle diameter and the atomic displacement parameters (ADPs) for Pt.

Results and Discussion

An efficient catalyst testing must be fast, performed under realistic conditions, and conducted to allow several repeats for each catalyst sample. To assess the Pt NP size evolution in Pt/C catalysts, SAXS is so far mainly used in combination with RDE testing in addition to the local technique (S)TEM.[19,20] Although single RDE measurements are fast, the testing conditions are far from the ones in fuel cell devices[14,15]; a liquid electrolyte is employed, which respective type of anions[33–35] and pH values[36,37] influence Pt dissolution while the catalyst film thickness (loading on the glassy carbon tip) is significantly lower than in a fuel cell. Furthermore, to reach sufficient signal to noise ratios for the SAXS analysis, the catalyst layer must be collected from several RDE measurements. This renders the study of the effect of stability tests on the NP size impractical and time consuming. The conditions in MEA testing are realistic but time consuming and rarely performed with several repeats of different catalysts. Among the very few in situ SAXS studies reported, most require exposure of the electrocatalyst to liquid electrolyte flow or are performed in a MEA.[38–44] In setups exposing the catalyst to liquid electrolyte flow the risk of a mechanical delamination and incomplete catalyst utilization is given. For an analysis of the catalyst layers in MEA, a dismantling is necessary to avoid probing anode and cathode catalyst at the same time. Due to the complexity of the experiments and the limited measurement time at Synchrotron beamlines, to the best of our knowledge in no in situ SAXS study statistical data concerning the reproducibility of the measurements is tested by performing three repeats per sample. These limitations call for further improvement.

In contrast, the GDE setup provides more realistic conditions than the RDE method but is at the same time a more simple and faster methodology than flow cell or MEA measurements.[14,15] Several repeats of the measurements can be performed and their reproducibility be discussed. Therefore, in this work, a GDE setup is used to investigate the degradation of three commercial Tanaka Pt/C catalysts with different NP size distributions ranging from 1–2 to 4–5 nm (hereafter denoted as 1–2 nm Pt/C, 2–3 nm Pt/C, and 4–5 nm Pt/C) that are often used as benchmark catalysts in RDE testing.[45]

TEM micrographs of the three catalyst powders are displayed in Fig. 1. In a recent work we showed that ASTs can be performed in our GDE setup but the used catalyst loading was comparable to loadings for RDE measurements and hence far from realistic fuel cell loadings.[15] In the present work, the catalyst film on the GDL (i.e. the GDE) is prepared by vacuum filtration as described by Yarlagadda et al.[21] to reach typical catalyst loadings for fuel cells in cars of 0.2 mg_{Pt} cm^{-2}_{geo}.[8] ASTs are performed at 25 °C (9000 steps in O_2 between 0.6 and 1.0 V_{RHE}, 3 s holding) and additionally at 50 ° C (with a reduced number of degradation steps to 5000 to reach a comparable loss in surface area) to generate more realistic fuel cell conditions.[4] In the SI it is demonstrated that with the established procedure, reproducible particle size distributions of the different Pt/C catalysts could be determined before (Fig. S5) as well as after the ASTs (Fig. S6). The same reproducibility is observed for the determined values of the electrochemically active surface area (ECSA), see relatively low standard deviations from the measurements of three catalyst films in Table I. By analyzing the electrochemical measurements recorded in the GDE setup, (Fig. 2 and Table I) and comparing the ECSA values of the catalysts with the ones reported from RDE measurements in literature it is further confirmed that the catalyst layer is fully utilized.[45] This is of utmost importance for the SAXS analysis, which otherwise would be misleading as parts of the catalyst layer that were not be under electrochemical control would not be subjected to any degradation and hence would not show any change in the particle size distributions. In addition, it is observed that going from 25 °C to 50 °C, the peak potential of the CO stripping is shifted to lower electrode potentials and the established initial ECSA is slightly reduced (see Fig. 2 and Table I). This finding is in agreement with the expected effect of higher temperature reducing the equilibrium coverage of adsorbents and facilitating the oxidation of CO.[46] Based on the average of the mean particle sizes obtained from SAXS data analyses "theoretical" surface areas before the AST can be calculated (see Table SIII in SI). Comparing the experimental ECSA established by the CO stripping and "theoretical" surface areas uncovers that although large NPs have in total less surface area, a higher fraction of the surface area is accessible for catalytic reactions as compared to the small NPs.

As prepared, the catalysts with the smaller NPs exhibit higher initial ECSA than the catalyst with larger NPs (see Table I). At the same time, the smaller NPs experience a larger ECSA loss upon applying the AST: 43 ± 1 and 34 ± 1% for 1–2 and 2–3 nm Pt/C, respectively as compared to 4 ± 1% for 4–5 nm Pt/C at 25 °C. An increase in temperature accelerates the loss in ECSA considerably (AST duration of 10 h at 50 °C as compared to 16 h 40 at 25 °C). Interestingly, the 4–5 nm Pt/C catalyst is very stable. Its ECSA loss upon applying the AST is very small, i.e. after more than 16 h of AST at 25 °C it is less than 5% and thus almost negligible. Increasing the temperature to 50 °C, the ECSA loss increases to 16% (note that the testing time was shorter, i.e. 10 h), but is still minor as compared to the ECSA loss of the 1–2 and 2–3 Pt/C catalysts of 53 ± 1 and 48 ± 2%, respectively. Another highly important observation results from a comparison of the ECSA loss at 25 °C (see Fig. 2). In our previous study by Alinejad et al.,[15] we used the same AST protocol but significantly lower catalyst loadings on the GDL. With catalyst loadings typical for RDE testing[47] (i.e. ca. 8 $\mu g\ cm^{-2}_{geo}$ vs 0.2 $mg\ cm^{-2}_{geo}$ here), significantly higher ECSA losses are observed, i.e. 48 ± 2% with lower loading as compared to 34 ± 1% in this study for the 2–3 nm Pt/C catalyst and 18 ± 1% with lower loading as compared to 4 ± 1% here for the 4–5 nm Pt/C catalyst (see Table I and Figs. S5–S6). Such dependence of the degradation on the film thickness was observed previously in our laboratory in RDE measurements (not published) as well as in Pt dissolution measurements determined via scanning flow cell (SFC) measurements coupled to inductively coupled plasma mass spectrometry (ICP-MS).[48,49] The influence of the catalyst film thickness on the observed Pt dissolutions rates was assigned to differences in the probability of re-deposition of the Pt ions.[48] The influence of different iR-drops for different catalyst loadings is considered to be small. An active compensation scheme of the potentiostat allows to limit the uncompensated resistance to similar, reproducible values (see electrochemical measurements in experimental part). However, as larger currents are obtained with a thicker catalyst layer, the same

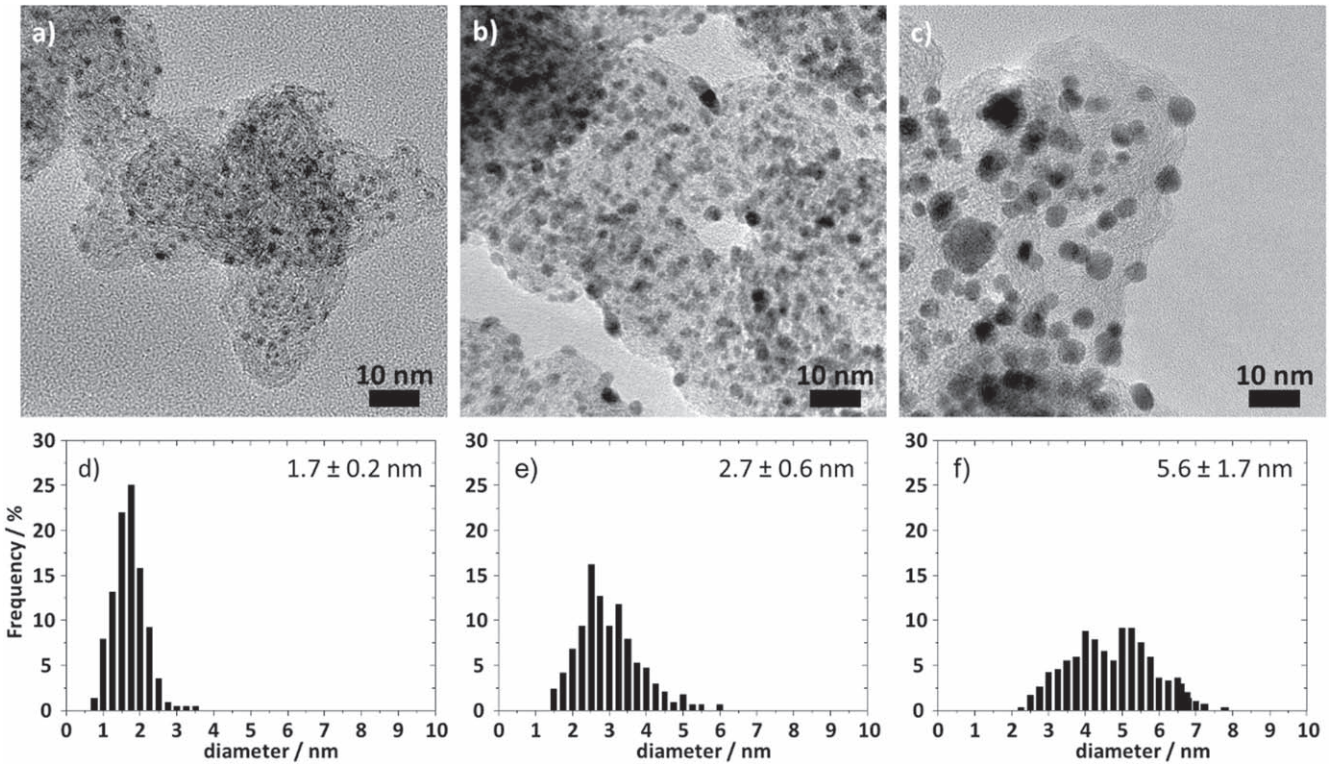

Figure 1. TEM micrographs and size distributions of the commercial 1–2 nm (a), (d), 2–3 nm (b), (e), and 4–5 nm (c), (f) Pt/C catalyst powders.

Table I. Experimental ECSA before and after AST of commercial Pt/C catalysts at T = 25 °C (9000 steps between 0.6 and 1.0 V_{RHE}) and 50 °C (5000 steps between 0.6 and 1.0 V_{RHE}) in oxygen and determined ECSA loss after the AST of three reproducible repeats. The error indicates the standard deviation of the three measurements.

T/°C	Pt/C Catalysts	ECSA/$m^2\ g^{-1}_{Pt}$		surface loss/%
		before AST	after AST	
25	1–2 nm	109 ± 4	62 ± 3	43 ± 1
	2–3 nm	81 ± 1	54 ± 1	34 ± 1
	4–5 nm	57 ± 1	55 ± 1	4 ± 1
50	1–2 nm	90 ± 2	43 ± 2	53 ± 1
	2–3 nm	67 ± 4	35 ± 3	48 ± 2
	4–5 nm	50 ± 2	42 ± 1	16 ± 2

uncompensated resistance leads to larger deviations between "applied and real potential." Nevertheless, the effect should be minor for the upper potential (1.0 V) in the AST as no ORR takes place at this potential. The lower potential (0.6 V), however, should be affected. Consequently, it is difficult to disregard any influence of the uncompensated resistance.

Comparing the GDE studies with different catalyst loading, typically resulting in different film thickness, it can be concluded that although identical trends in stability of the two different catalysts are observed, an extrapolation of the results to fuel cell conditions is more difficult if very thin catalyst films are used since phenomena such as re-deposition of Pt ions do not occur. Therefore, the here presented results highlight the importance of realistic conditions for degradation studies.

Further, crucial mechanistic information concerning the change in the NP size distribution after applying the AST can be extracted from the SAXS data. Representative size distributions are shown in Fig. 3 and repeats in the SI. In the following we refer to the average diameter of the particle and use the standard deviation relative to the evaluation of this average diameter based on three independent measurements as error to compare the catalyst sizes (see Table SI). It should be noticed that in contrast to size histograms plotted in a TEM analysis, minor changes in the fitting parameters lead to deviations in the log-normal plots that might suggest large deviations between the individual measurements. However, we observed that for a given set of conditions, the three individual repeats were consistent: a comparable average diameter and deviation with only small variations between the repeated measurements was observed. For one of the catalyst samples (2–3 nm Pt/C at 50 °C) larger deviations between the individual repeats are observed.

As a result of the AST treatments (at 25 °C or 50 °C) the size distribution (established by SAXS) of all catalysts increases as it is expected from the ECSA loss determined in the CO stripping measurements. For the 1–2 nm Pt/C catalyst the increase in size is most dramatic, an increase from 2.08 ± 0.04 to 4.86 ± 0.43 (AST in O_2 at 25 °C) and 6.06 ± 0.54 nm (AST in O_2 at 50 °C) is determined, while for the 2–3 nm Pt/C catalyst an increase from 2.97 ± 0.09 to 5.24 ± 0.02 (25 °C) and 5.58 ± 1.67 nm (50 °C) is observed. Only the 4–5 nm Pt/C catalyst shows a relative moderate increase in particle size, i.e. from 5.88 ± 0.13 to 6.25 ± 0.47 (25 °C) and 6.63 ± 0.03 nm (50 °C) in line with the very moderate ECSA loss. The size increase of the smaller Pt NPs after the AST is furthermore confirmed by applying PDF analysis (see SI). Interestingly, after applying the AST at 50 °C the "end of treatment" particle sizes of all three Pt/C catalysts are very similar, i.e. they are all in the range of 5.6–6.6 nm. The results demonstrate that, as expected, the degradation and the particle growth are more significant for catalysts with small NPs.[50]

The obtained results are unfortunately difficult to compare to literature as there still no common procedure for AST protocols in RDE measurements, e.g. potential scanning not following the FCCJ protocols was performed on the 2–3 nm Pt /C catalyst on Vulcan C by Kocha et al.[51] (0.025–1.0 V_{RHE}) and on Ketjen black by Mayrhofer et al.[52] (0.4–1.4 V_{RHE}). Speder et al.[19,53] applied load cycles but also on homemade catalysts and Zana et al.[18] performed IL-TEM on homemade catalysts. For MEA measurements the following results are reported: Based on a TEM analysis Yano et al.[54] report that after load cycles in MEA a comparable particle size increase from 2.2 ± 0.5 nm to 6.5 ± 2.3 nm occurs for the 2–3 nm C^{-1} catalyst. Tamaki et al.[55] reported after 10,000 cycles a particle size increase from 3.2 ± 0.8 nm to 7.9 ± 4.6 nm.

In our GDE study, we document for the first time to the best of our knowledge that the "end of treatment" particle size of around 6 nm is rather independent from the "starting size" but depends on the temperature, i.e. after the AST protocol under realistic conditions at 50 °C all three catalysts exhibit more or less the same size distribution. This is an important finding considering that increasing the power density in PEMFCs for mobile applications is of high priority.[8] Currently a large performance loss is observed at high-current density (>1 A cm^{-2}) and it is proposed that a resistive oxygen mass transfer term can be addressed among others through high and stable Pt dispersion (i.e. small NPs).[8] Our results indicate a serious limitation for such efforts to decrease oxygen mass transfer resistances by increasing the catalyst dispersion (i.e. NP size) unless strategies are found and successfully implemented to inhibit the growth in particle size under operation. At the same time the presented GDE methodology provides an easy means to screen test the behavior of different catalysts under realistic conditions.

Focusing on the degradation mechanism, the observed particle size distribution after degradation reported in Fig. 3 is consistent with the established loss in surface area (see Table I). While the surface loss could be in general a consequence of all degradation mechanisms (migration/coalescence, metal dissolution, Ostwald ripening, particle detachment), the observed increase in particle size can occur due to electrochemical Ostwald ripening and particle coalescence. The dependence of the degradation (ECSA loss) on the catalyst layer thickness (catalyst loading on GDL) indicates a significant contribution of electrochemical Ostwald ripening. However, the tail of the size distributions to large sizes (maximum at small size) after the AST at 25 °C could be an indication for coalescence,[56] while tailing to small NP sizes (maximum at large size) after the AST at 50 °C could signify Ostwald ripening.[57,58] The shoulder in the particle size distribution after the AST at 25 °C for 2–3 nm Pt/C, consistent with the "end of treatment size" after the AST at 50 °C, on the other hand might be an indication for coalescence followed by Ostwald ripening into spherical particles under the AST treatment and therefore coalescence might be difficult to detect in the "end of treatment" catalyst. Such a simultaneous occurrence of both growth mechanisms complicates the interpretation of the tailed size distributions[13] and the results do not allow an unambiguous separation of Ostwald ripening and coalescence. To sum up, the strong dependency of the ECSA loss on the catalyst layer thickness makes Ostwald ripening more likely, but coalescence cannot be excluded. Particle detachment, by comparison, leads to a loss in surface area while maintaining the size distribution[52]; a scenario that would best fit to the behavior of the 4–5 nm Pt/C catalyst, but certainly not for the other two catalysts. Mayrhofer et al.[52] showed in IL-TEM that the main degradation mechanism of the 4–5 nm Pt/C catalyst at room temperature and exposure to liquid electrolyte is particle detachment. However, at this point the occurrence of particle detachment in the GDE setup cannot be proven. Metal dissolution (without re-deposition) would lead to a decrease in particle size and is not observed in any of the Pt/C catalysts, i.e. the determined size distributions exhibit very low probability towards small particle sizes. A deposition of the dissolved Pt-ions in the Nafion membrane as observed in MEA measurements seems unlikely, as in the MEA the process is caused by the hydrogen gas crossover.[13] In the GDE measurements, a hydrogen gas crossover through the Nafion membrane is not expected as the measured gas flow at the gas inlet and outlet are

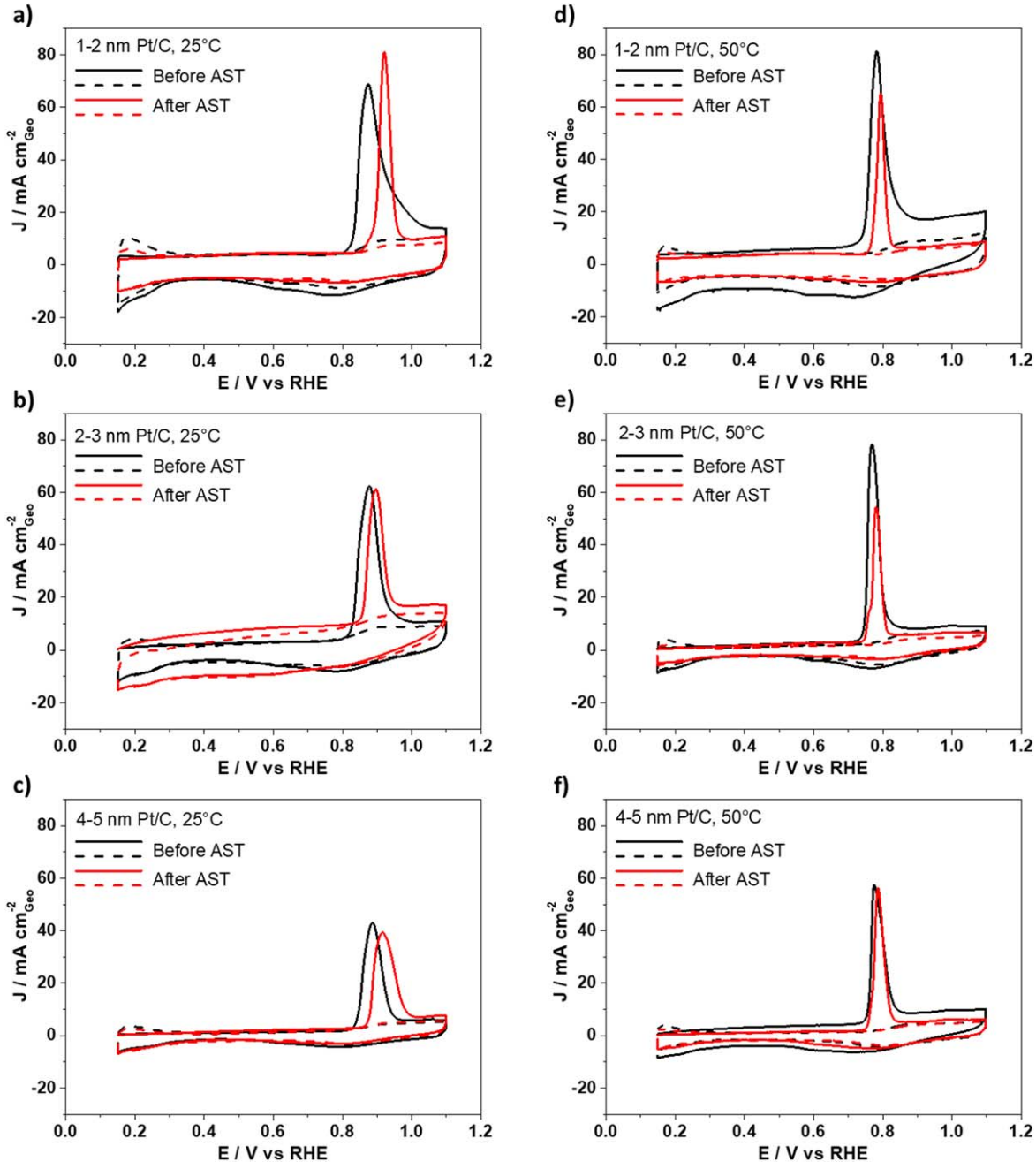

Figure 2. Representative CO stripping curves (solid lines) and subsequent cyclic voltammograms in Ar (dash lines) of commercial 1–2 nm (a), (d), 2–3 nm (b), (e), and 4–5 nm (c), (f) Pt/C catalysts before (black lines) and after (red lines) ASTs in O_2 at 25 °C ((a)–(c) 9000 steps between 0.6 and 1.0 V_{RHE}, 3 s holding) or 50 °C ((d)–(f) 5000 steps between 0.6 and 1.0 V_{RHE}, 3 s holding).

constant and the electrolyte above the membrane is not purged with hydrogen. Therefore, more likely this observation might be related to a (small) component of loss in surface area due to particle detachment.

Conclusions

In summary, in the present work we demonstrate the strength of the application of GDE setups—as compared to classical electrochemical cells or MEAs—for the investigation of catalyst degradation under realistic conditions. In the GDE setup, only one half-cell reaction of a fuel cell, e.g. the oxygen reduction reaction (ORR), is investigated, thus separating anode and cathode degradation. Without further disassembling (as opposed to MEA measurements) or sample collection (in contrast to RDE measurements), the catalyst layer can be investigated by SAXS measurements even without removing the Nafion membrane.

Applying conditions close to MEA testing (regarding the setup,[15] loading,[8] and temperature[4]) the degradation mechanism can be analyzed based on the change in the size distribution and the ECSA obtained by CO stripping. It is found that after applying the ASTs, catalysts with small NPs exhibit significant degradation and particle growth. While this is an expected result, comparing the investigations with previous ones, it is found that the amount of degradation depends on the film thickness; thin films exhibit more degradation than thicker films. The main mechanism seems particle growth based on either coalescence and/or electrochemical Ostwald ripening whereas only for the 4–5 Pt/C catalyst there is a weak indication of particle loss at the applied conditions. The here introduced combination of GDE and SAXS offers a straight-forward

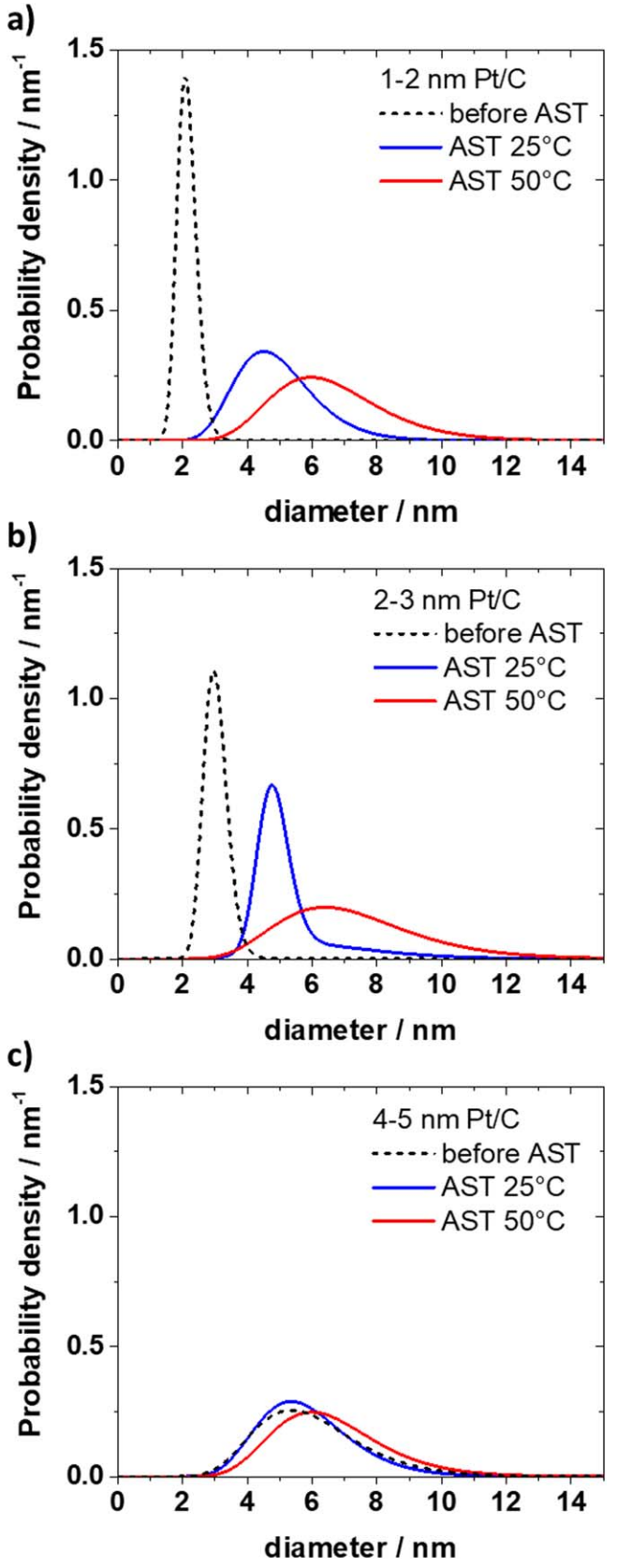

Figure 3. Representative SAXS particle size distributions of commercial 1–2 nm (a), 2–3 nm (b), and 4–5 nm (c) Pt/C catalyst before (dash black lines) and after ASTs in O_2 at 25 °C (blue lines, 9000 steps between 0.6 and 1.0 V_{RHE}, 3 s holding) or 50 °C (red lines, 5000 steps between 0.6 and 1.0 V_{RHE}, 3 s holding).

way for comparative studies of the degradation of several different fuel cell catalysts allowing several repeats. The approach therefore offers significant advantages over RDE and MEA measurements and thus will aid the quest for developing improved PEMFC catalysts.

Acknowledgments

This work was supported by the Swiss National Science Foundation (SNSF) via the project No. 200021_184742. J.S. acknowledges the German Research Foundation (DFG) for financial support (KU 3152/6–1) and the German Academic Exchange Service (DAAD) for financial support through a scholarship for an academic exchange to the University of Bern. J.Q and K.M.Ø.J thank the Villum foundation for financial support through a Villum Young Investigator grant. J.Q. and M.A. thank Dr Luise Theil Kuhn and Dr Søren B. Simonsen, technical University of Denmark (DTU) for access to TEM facilities. J.Q., K.M.Ø.J. and J.J.K.K. acknowledge local support and continued access to the University of Copenhagen SAXSLab facility. Use of the Advanced Photon Source was supported by the U. S. Department of Energy, Office of Science, Office of Basic Energy Sciences, under Contract No. DE-AC02–06CH11357 (proposal GUP-65450).

ORCID

Johanna Schröder https://orcid.org/0000-0001-5461-4751

References

1. I. Katsounaros, S. Cherevko, A. R. Zeradjanin, and K. J. J. J. Mayrhofer, *Angew. Chemie - Int. Ed.*, **53**, 102 (2014).
2. T. Reier et al., *J. Am. Chem. Soc.*, **137**, 13031 (2015).
3. M. K. Debe, *Nature*, **486**, 43 (2012).
4. T. Yoshida and K. Kojima, *Electrochem. Soc. Interface*, **24**, 45 (2015).
5. V. R. Stamenkovic, B. S. Mun, M. Arenz, K. J. J. Mayrhofer, C. A. Lucas, G. Wang, P. N. Ross, and N. M. Markovic, *Nat. Mater.*, **6**, 241 (2007).
6. D. Wang, H. L. Xin, R. Hovden, H. Wang, Y. Yu, D. A. Muller, F. J. DiSalvo, and H. D. Abruña, *Nat. Mater.*, **12**, 81 (2013).
7. B. Han, C. E. Carlton, A. Kongkanand, R. S. Kukreja, B. R. Theobald, L. Gan, R. O'Malley, P. Strasser, F. T. Wagner, and Y. Shao-Horn, *Energy Environ. Sci.*, **8**, 258 (2015).
8. A. Kongkanand and M. F. Mathias, *J. Phys. Chem. Lett.*, **7**, 1127 (2016).
9. A. Marcu, G. Toth, S. Kundu, L. C. Colmenares, and R. J. Behm, *J. Power Sources*, **215**, 266 (2012).
10. A. Ohma, K. Shinohara, A. Iiyama, T. Yoshida, and A. Daimaru, *ECS Trans.*, **41**, 775 (2019).
11. Y.-C. Park, K. Kakinuma, M. Uchida, D. A. Tryk, T. Kamino, H. Uchida, and M. Watanabe, *Electrochim. Acta*, **91**, 195 (2013).
12. T. Nagai, H. Murata, and Y. Morimoto, *J. Electrochem. Soc.*, **161**, F789 (2014).
13. P. J. Ferreira et al., *J. Electrochem. Soc.*, **152**, A2256 (2005).
14. M. Inaba, A. W. Jensen, G. W. Sievers, M. Escudero-Escribano, A. Zana, and M. Arenz, *Energy Environ. Sci.*, **11**, 988 (2018).
15. S. Alinejad, M. Inaba, J. Schröder, J. Du, J. Quinson, A. Zana, and M. Arenz, *J. Phys.: Energy*, **2**, 024003 (2020).
16. J. C. Meier, C. Galeano, I. Katsounaros, A. A. Topalov, A. Kostka, F. Schüth, and K. J. J. Mayrhofer, *ACS Catal.*, **2**, 832 (2012).
17. K. Hartl, M. Hanzlik, and M. Arenz, *Energy Environ. Sci.*, **4**, 234 (2011).
18. A. Zana, J. Speder, M. Roefzaad, L. Altmann, M. Bäumer, and M. Arenz, *J. Electrochem. Soc.*, **160**, F608 (2013).
19. J. Speder, A. Zana, I. Spanos, J. J. K. K. Kirkensgaard, K. Mortensen, M. Hanzlik, and M. Arenz, *J. Power Sources*, **261**, 14 (2014).
20. J. Speder, L. Altmann, M. Roefzaad, M. Bäumer, J. J. K. K. Kirkensgaard, K. Mortensen, and M. Arenz, *Phys. Chem. Chem. Phys.*, **15**, 3602 (2013).
21. V. Yarlagadda, S. E. McKinney, C. L. Keary, L. Thompson, B. Zulevi, and A. Kongkanand, *J. Electrochem. Soc.*, **164**, F845 (2017).
22. G. K. H. Wiberg, K. J. J. Mayrhofer, and M. Arenz, *Fuel Cells*, **10**, 575 (2010).
23. M. Inaba, J. Quinson, J. R. Bucher, and M. Arenz, *J. Vis. Exp.*, **133**, e57105 (2018).
24. J. Quinson et al., *ACS Catal.*, **8**, 6627 (2018).
25. T. Zemb and P. Lindner, *Neutron, X-rays and Light. Scattering Methods Applied to Soft Condensed Matter*, ed. T. Zemb and P. Lindner (Elsevier, Amsterdam) p. 552 (2002).
26. K. Kajiwara and Y. Hiragi, *Analytical Spectroscopy Library*, **7**, 353 (1996).
27. P. R. A. F. Garcia, O. Prymak, V. Grasmik, K. Pappert, W. Wlysses, L. Otubo, M. Epple, and C. L. P. Oliveira, *Nanoscale Adv.*, **2**, 225 (2020).
28. P. J. Chupas, X. Qiu, J. C. Hanson, P. L. Lee, C. P. Grey, and S. J. L. Billinge, *J. Appl. Crystallogr.*, **36**, 1342 (2003).
29. A. P. Hammersley, S. O. Svensson, M. Hanfland, A. N. Fitch, and D. Häusermann, *High Press. Res.*, **14**, 235 (1996).
30. A. P. Hammersley, *J. Appl. Crystallogr.*, **49**, 646 (2016).
31. X. Yang, P. Juhas, C. L. Farrow, and S. J. L. Billinge, (2014), arXiv:http://arxiv.org/abs/1402.3163.

32. C. L. Farrow, P. Juhas, J. W. Liu, D. Bryndin, E. S. Boin, J. Bloch, T. Proffen, and S. J. L. Billinge, *J. Phys. Condens. Matter*, **19**, 335219 (2007).
33. S. Mitsushima, Y. Koizumi, S. Uzuka, and K.-I. Ota, *Electrochim. Acta*, **54**, 455 (2008).
34. J. Omura, H. Yano, M. Watanabe, and H. Uchida, *Langmuir*, **27**, 6464 (2011).
35. T. Lopes, J. Chlistunoff, J.-M. Sansiñena, and F. H. Garzon, *Int. J. Hydrogen Energy*, **37**, 5202 (2012).
36. Y. Furuya, T. Mashio, A. Ohma, M. Tian, F. Kaveh, D. Beauchemin, and G. Jerkiewicz, *ACS Catal.*, **5**, 2605 (2015).
37. A. A. Topalov, S. Cherevko, A. R. Zeradjanin, J. C. Meier, I. Katsounaros, and K. J. J. Mayrhofer, *Chem. Sci.*, **5**, 631 (2014).
38. K. N. Wood, S. T. Christensen, S. Pylypenko, T. S. Olson, A. A. Dameron, K. E. Hurst, H. N. Dinh, T. Gennett, and R. O'hayre, *MRS Commun.*, **2**, 85 (2012).
39. T. Binninger et al., *J. Electrochem. Soc.*, **163**, H906 (2016).
40. M. Povia, J. Herranz, T. Binninger, M. Nachtegaal, A. Diaz, J. Kohlbrecher, D. F. Abbott, B.-J. Kim, and T. J. Schmidt, *ACS Catal.*, **8**, 7000 (2018).
41. J. A. Gilbert, N. N. Kariuki, R. Subbaraman, A. J. Kropf, M. C. Smith, E. F. Holby, D. Morgan, and D. J. Myers, *J. Am. Chem. Soc.*, **134**, 14823 (2012).
42. H.-G. G. Haubold, X. H. Wang, G. Goerigk, and W. Schilling, *J. Appl. Crystallogr.*, **30**, 653 (1997).
43. J. Tillier, T. Binninger, M. Garganourakis, A. Patru, E. Fabbri, T. J. Schmidt, and O. Sereda, *J. Electrochem. Soc.*, **163**, H913 (2016).
44. X. Tuaev, S. Rudi, V. Petkov, A. Hoell, and P. Strasser, *ACS Nano*, **7**, 5666 (2013).
45. M. Nesselberger, S. Ashton, J. C. Meier, I. Katsounaros, K. J. J. Mayrhofer, and M. Arenz, *J. Am. Chem. Soc.*, **133**, 17428 (2011).
46. E. Herrero, J. M. Feliu, S. Blais, Z. Radovic-Hrapovic, and G. Jerkiewicz, *Langmuir*, **16**, 4779 (2000).
47. M. Inaba, J. Quinson, and M. Arenz, *J. Power Sources*, **353**, 19 (2017).
48. G. P. Keeley, S. Cherevko, and K. J. J. Mayrhofer, *ChemElectroChem*, **3**, 51 (2016).
49. O. Kasian, S. Geiger, K. J. J. Mayrhofer, and S. Cherevko, *Chem. Rec.*, **19**, 2130 (2019).
50. E. F. Holby, W. Sheng, Y. Shao-Horn, and D. Morgan, *Energy Environ. Sci.*, **2**, 865 (2009).
51. S. S. Kocha, K. Shinozaki, J. W. Zack, D. J. Myers, N. N. Kariuki, T. Nowicki, V. Stamenkovic, Y. Kang, D. Li, and D. Papageorgopoulos, *Electrocatalysis*, **8**, 366 (2017).
52. K. J. J. Mayrhofer, J. C. Meier, S. J. Ashton, G. K. H. Wiberg, F. Kraus, M. Hanzlik, and M. Arenz, *Electrochem. Commun.*, **10**, 1144 (2008).
53. J. Speder, A. Zana, I. Spanos, J. J. K. K. Kirkensgaard, K. Mortensen, and M. Arenz, *Electrochem. Commun.*, **34**, 153 (2013).
54. H. Yano, M. Watanabe, A. Iiyama, and H. Uchida, *Nano Energy*, **29**, 323 (2016).
55. T. Tamaki, A. Minagawa, B. Arumugam, B. A. Kakade, and T. Yamaguchi, *J. Power Sources*, **271**, 346 (2014).
56. C. G. Granqvist and R. A. Buhrman, *J. Appl. Phys.*, **47**, 2200 (1976).
57. A. Baldan, *J. Mater. Sci.*, **37**, 2379 (2002).
58. Y. Zhai, H. Zhang, D. Xing, and Z.-G. Shao, *J. Power Sources*, **164**, 126 (2007).

Supporting Information

A new approach to probe the degradation of fuel cell catalysts under realistic conditions: combining tests in a gas diffusion electrode setup with small angle X-ray scattering

Johanna Schröder[a,b], Jonathan Quinson[c], Jette K. Mathiesen[c], Jacob J. K. Kirkensgaard[d], Shima Alinejad[a], Vladislav A. Mints[a], Kirsten M. Ø. Jensen[c], Matthias Arenz[a,z,*]

[a] Department of Chemistry and Biochemistry, University of Bern, Freiestrasse 3, 3012 Bern, Switzerland

[b] Institute of Applied and Physical Chemistry (IAPC), Center for Environmental Research and Sustainable Technology, University of Bremen, Leobener Strasse 6, 28359 Bremen, Germany

[c] Department of Chemistry, University of Copenhagen, Universitetsparken 5, 2100 Copenhagen, Denmark

[d] Department of Food Science, University of Copenhagen, Rolighedsvej 26, 1958 Frederiksberg, Denmark

[*] Electrochemical Society Member

[z] E-mail: matthias.arenz@dcb.unibe.ch

SAXS data

The average volume of nanoparticle from population 1 and from population 2, $\langle V \rangle_1$ and $\langle V \rangle_2$ respectively, lead to define volume fraction of population 1, Φ_{V1}, and volume fraction of population 2, Φ_{V2}, as:

$$\Phi_{V1} = \frac{N_1 \langle V \rangle_1}{N_1 \langle V \rangle_1 + N_2 \langle V \rangle_2} = 1 - \Phi_{V2}$$

$$\frac{\Phi_{V1}}{\Phi_{V2}} = \frac{N_1 < V >_1}{N_2 < V >_2}$$

$$\frac{N_1}{N_2} = \frac{\Phi_{V1} < V >_2}{\Phi_{V2} < V >_1}$$

where N_1 and N_2 are the number of nanoparticles in the population 1 or 2 respectively.

From the SAXS data acquisition we have the relationship between the retrieved coefficient C_1 and C_2 given by $C_i = k. \Phi_{vi}. \langle V \rangle_i$ where i=1 or 2 and k is a constant.

$$k = \frac{C_1}{\Phi_{V1} < V >_1} = \frac{C_2}{\Phi_{V2} < V >_2} = \frac{C_2}{(1 - \Phi_{V1}) < V >_2}$$

$$\frac{\Phi_{V1}}{1 - \Phi_{V1}} = \frac{C_1 < V >_2}{C_2 < V >_1}$$

$$\Phi_{V1} = \frac{1}{1 + \frac{C_2 < V >_1}{C_1 < V >_2}}$$

In order to weight the probability density function by the area or surface fractions we consider $\langle A \rangle_1$ and $\langle A \rangle_2$ as the average area of the nanoparticles from population 1 and 2, respectively:

$$\Phi_{A1} = \frac{N_1 \langle A \rangle_1}{N_1 \langle A \rangle_1 + N_2 \langle A \rangle_2} = 1 - \Phi_{A2} = \frac{1}{1 + \frac{N_2 \langle A \rangle_2}{N_1 \langle A \rangle_1}}$$

$$\Phi_{A1} = \frac{1}{1 + \frac{\Phi_{V2} < V >_1 < A >_2}{\Phi_{V1} < V >_2 < A >_1}}$$

$$\Phi_{A1} = \frac{1}{1 + \frac{C_2 (< V >_1)^2 < A >_2}{C_1 (< V >_2)^2 < A >_1}}$$

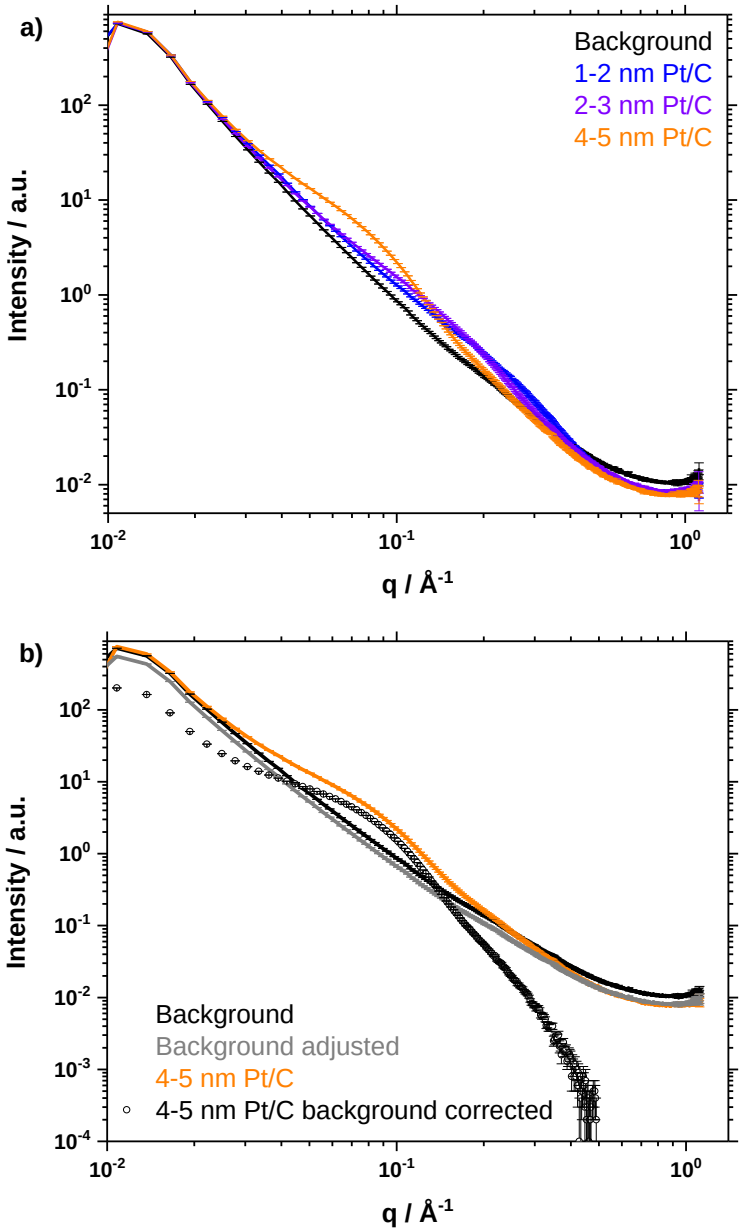

Figure S1: (a) Examples of SAXS measurements for different Pt/C catalyst with Pt NP size of 1-2 nm, 2-3 nm or 4.5 nm as indicated. The small error bars for the intensities on the Y axis indicate the quality of the data. At high q values the deviation increased since fewer pixels contribute to each q-value as the pixel are closer to the detector edges. The background measured is in dark. (b) Example of background subtraction.

The clear shift of the 'bump' in the SAXS measurements towards higher q values is consistent with a larger NP size for the samples with an increasing size order 1-2 nm < 2-3 nm < 4-5 nm Pt/C. For background subtraction the background and sample intensities were corrected to overlap at high q values.

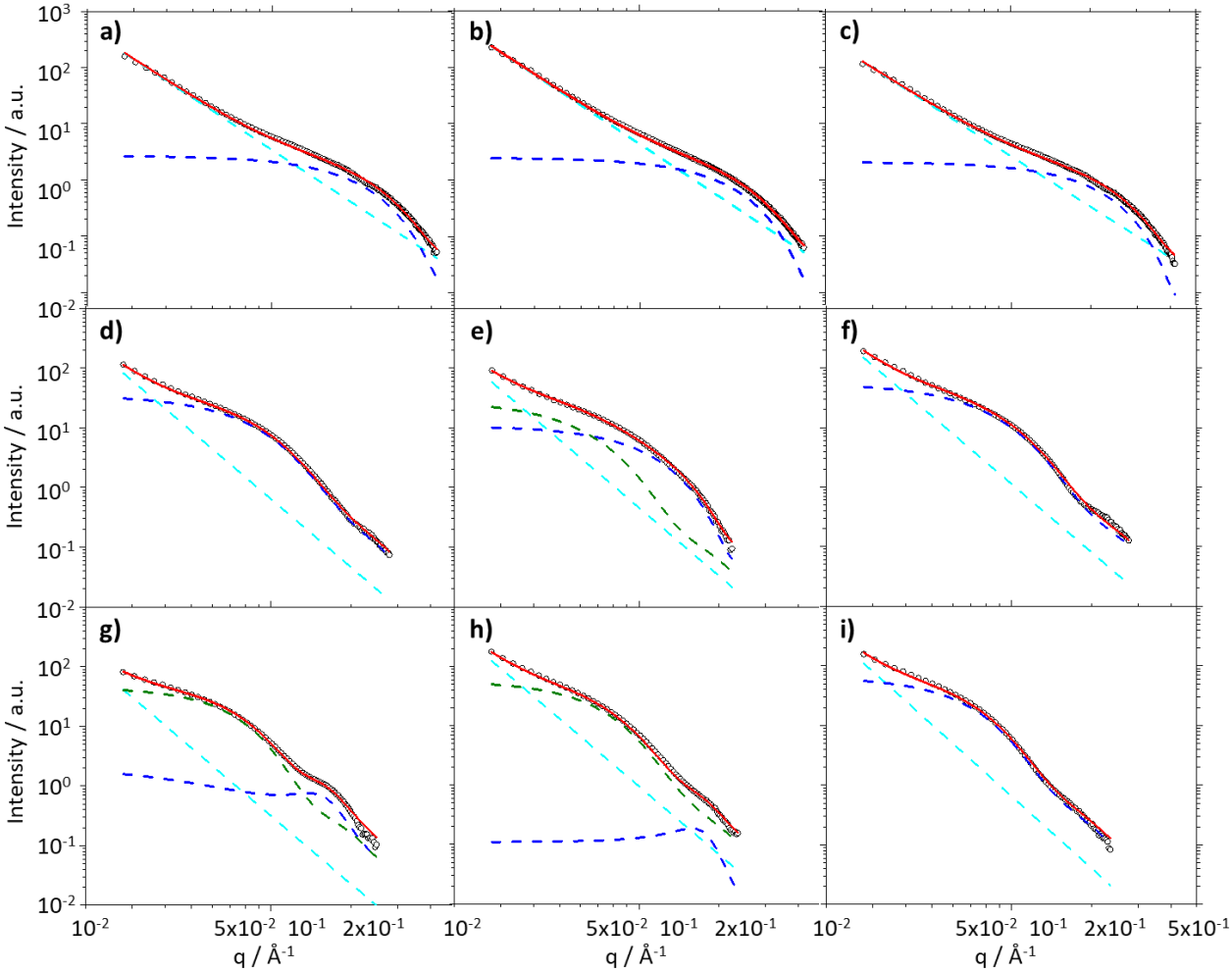

Figure S2: SAXS data fitting for the commercial 1-2 nm Pt/C catalyst before AST (a, b, c), after AST at 25 °C (d, e, f, 9000 steps between 0.6 and 1.0 V_{RHE}, 3 s holding) and 50 °C (g, h, i, 5000 steps): data (black circles), power law (cyan dash line), spheres 1 (blue dash line), sphere 2 (green dash line), fit (red line).

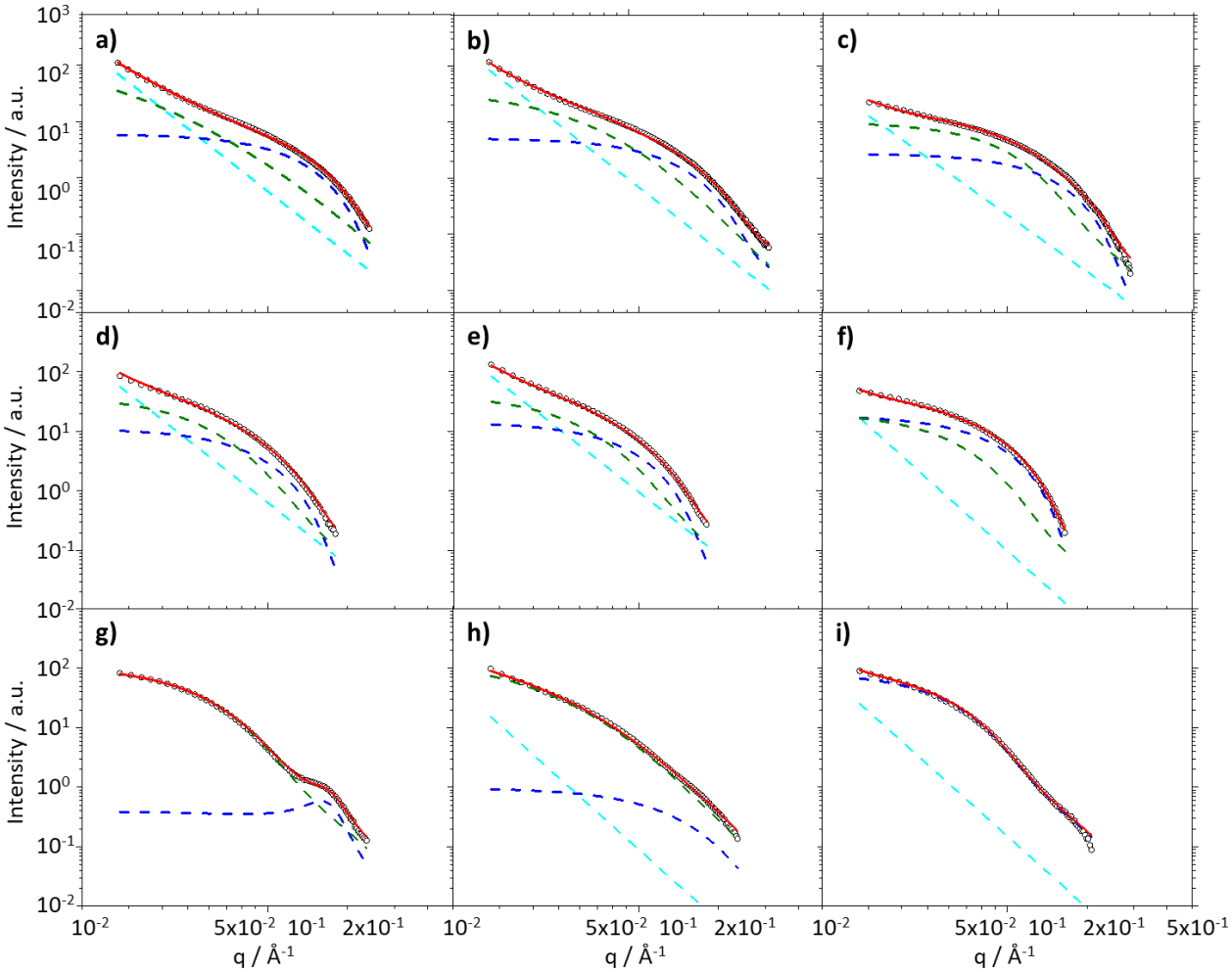

Figure S3: SAXS data fitting for the commercial 2-3 nm Pt/C catalyst before AST (a, b, c), after AST at 25 °C (d, e, f, 9000 steps between 0.6 and 1.0 V_{RHE}, 3 s holding) and 50 °C (g, h, i, 5000 steps): data (black circles), power law (cyan dash line), spheres 1 (blue dash line), sphere 2 (green dash line), fit (red line).

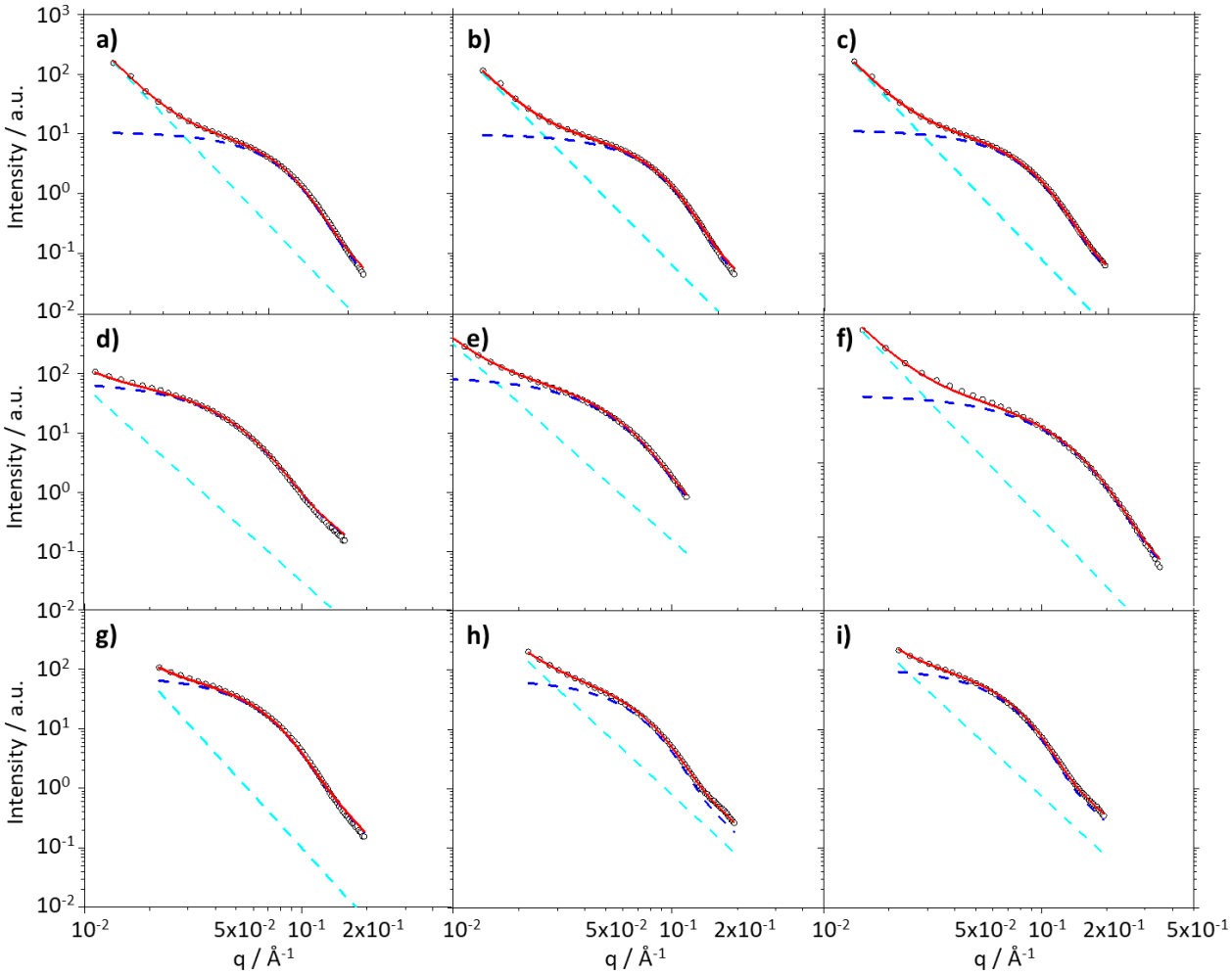

Figure S4. SAXS data fitting for the commercial 4-5 nm Pt/C catalyst before AST (a, b, c), after AST at 25 °C (d, e, f, 9000 steps between 0.6 and 1.0 V_{RHE}, 3 s holding) and 50 °C (g, h, i, 5000 steps): data (black circles), power law (cyan dash line), spheres 1 (blue dash line), sphere 2 (green dash line), fit (red line).

Table S1: Fitting parameters for SAXS data. The testing conditions are detailed in the text and Figure S1-S4 (the number of steps correspond to step between 0.6 and 1.0 V_{RHE}, 3 s holding). The determined size and distribution are based on the mean particle diameter.

		Sample	Figure S	Power law		1st population				2nd population			Size and distribution					
				A x 10^6	n	R_1	σ_1	C_1	η_1	R_2	σ_2	C_2	d_{sample}[A] / nm	σ_{sample}[B] / nm	Average diameter: $<d>$[C] / nm	Average deviation of σ_{sample}: $<\sigma>$[D] / nm	Standard deviation of $<d>$: $\sigma_{d\text{-}a,b,c}$[E] / nm	Standard deviation of $<d>$: $\sigma_{<d>}$[F] / nm
1-2 nm	Before AST	1a	5a-A	370	3.0	10.3	0.14	0.006	-	-	-	-	2.08	0.29	2.08	0.26	0.15	0.04
		1b	5a-B	300	3.1	10.1	0.13	0.005	-	-	-	-	2.04	0.27				
		1c	5a-C	300	3.0	10.5	0.11	0.004	-	-	-	-	2.11	0.23				
	25 °C 9000 steps	1d	5b-A	8.5	3.8	25.0	0.30	0.014	-	-	-	-	5.23	1.61	4.86	1.14	0.70	0.43
		1e	5b-B	7.0	3.8	20.0	0.14	0.006	-	33	0.23	0.005	4.39	0.54				
		1f	5b-C	18	3.8	24.0	0.25	0.018	-	-	-	-	4.95	1.26				
	50 °C 5000 steps	1g	5c-A	4	3.8	19.0	0.50	0.004	0.28	32	0.22	0.013	5.96	1.23	6.06	1.42	0.84	0.54
		1h	5c-B	15	3.8	17.5	0.20	0.001	0.32	31	0.26	0.016	5.57	1.21				
		1i	5c-C	5	4.0	32.0	0.27	0.017	-	-	-	-	6.64	1.83				
2-3 nm	Before AST	2a	6a	25	3.5	15.0	0.12	0.006	-	20	0.80	0.006	3.05	0.36	2.97	0.40	0.23	0.09
		2b		30	3.5	13.5	0.17	0.006	-	19	0.50	0.008	2.88	0.48				
		2c		16	3.2	13.5	0.10	0.004	-	18	0.30	0.006	2.99	0.37				
	25 °C 9000 steps	2d	6b	20	3.5	24.0	0.10	0.005	-	32	0.30	0.006	5.24	0.59	5.24	0.54	0.31	0.02
		2e		30	3.5	24.0	0.10	0.006	-	31	0.30	0.007	5.22	0.60				
		1f		1	4.0	25.0	0.08	0.007	-	31	0.25	0.004	5.25	0.43				
	50 °C 5000 steps	2g	6c	0	3.7	18.5	0.30	0.003	0.35	34	0.30	0.017	5.42	1.21	5.58	1.55	0.94	1.67
		2h		0.9	4.0	14.0	0.25	0.001	-	28	0.50	0.014	4.00	1.19				
		2i		2	3.7	35 .0	0.30	0.017	-	-	-	-	7.32	2.25				
4-5 nm	Before AST	3a	7a	13	3.8	29.0	0.28	0.032	0.05	-	-	-	6.03	1.72	5.88	1.68	0.97	0.13
		3b		13	3.7	28.0	0.27	0.030	0.04	-	-	-	5.81	1.60				
		3c		12	3.8	27.8	0.289	0.034	0.04	-	-	-	5.80	1.71				
	25 °C 9000 steps	3d	7b	8	3.8	28.5	0.25	0.020	-	-	-	-	5.88	1.49	6.25	1.59	0.92	0.47
		3e		5	4.0	29.5	0.25	0.020	-	-	-	-	6.09	1.55				
		3f		2	4.0	32.8	0.25	0.015	-	-	-	-	6.77	1.72				
	50 °C 5000 steps	3g	7c	1	4.0	32.0	0.28	0.014	-	-	-	-	6.66	1.90	6.63	1.78	1.03	0.03
		3h		32	3.4	32.0	0.26	0.014	-	-	-	-	6.62	1.75				
		3i		30	3.4	32.0	0.25	0.022	-	-	-	-	6.60	1.68				

(A) evaluated as $d_{sample} = 0.2\, e^{(ln(R)+\frac{\sigma^2}{2})}$ for a one size population, evaluated as $d_{sample} = 0.2\, \varphi_{A1}.\, e^{\left(\ln(R_1)+\frac{{\sigma_1}^2}{2}\right)} + 0.2\, \varphi_{A2}.\, e^{\left(\ln(R_2)+\frac{{\sigma_2}^2}{2}\right)}$ for a 2 sizes population

(B) evaluated as $\sigma_{sample} = 0.2\, \sqrt{(e^{\sigma^2}-1)e^{(2\ln(R)+\sigma^2)}}$ for a one size population, evaluated as $\sigma_{sample} = 0.2\, \sqrt{{\varphi_{A1}}^2.[(e^{{\sigma_1}^2}-1)e^{(2\ln(R_1)+{\sigma_1}^2)}] + {\varphi_{A2}}^2.[(e^{{\sigma_2}^2}-1)e^{(2\ln(R_2)+{\sigma_2}^2)}]}$

(C) evaluated as the mean value for 3 measurement $\langle d \rangle = \frac{d_a+d_b+d_c}{3}$

(D) evaluated as the mean value for 3 measurements $\langle \sigma \rangle = \frac{\sigma_a+\sigma_b+\sigma_c}{3}$

(E) evaluated as $\sigma_{d\text{-}a,b,c} = \frac{1}{3}\sqrt{{\sigma_a}^2 + {\sigma_b}^2 + {\sigma_c}^2}$

(F) evaluated as the deviation relative to the mean value diameter estimation from 3 measurements

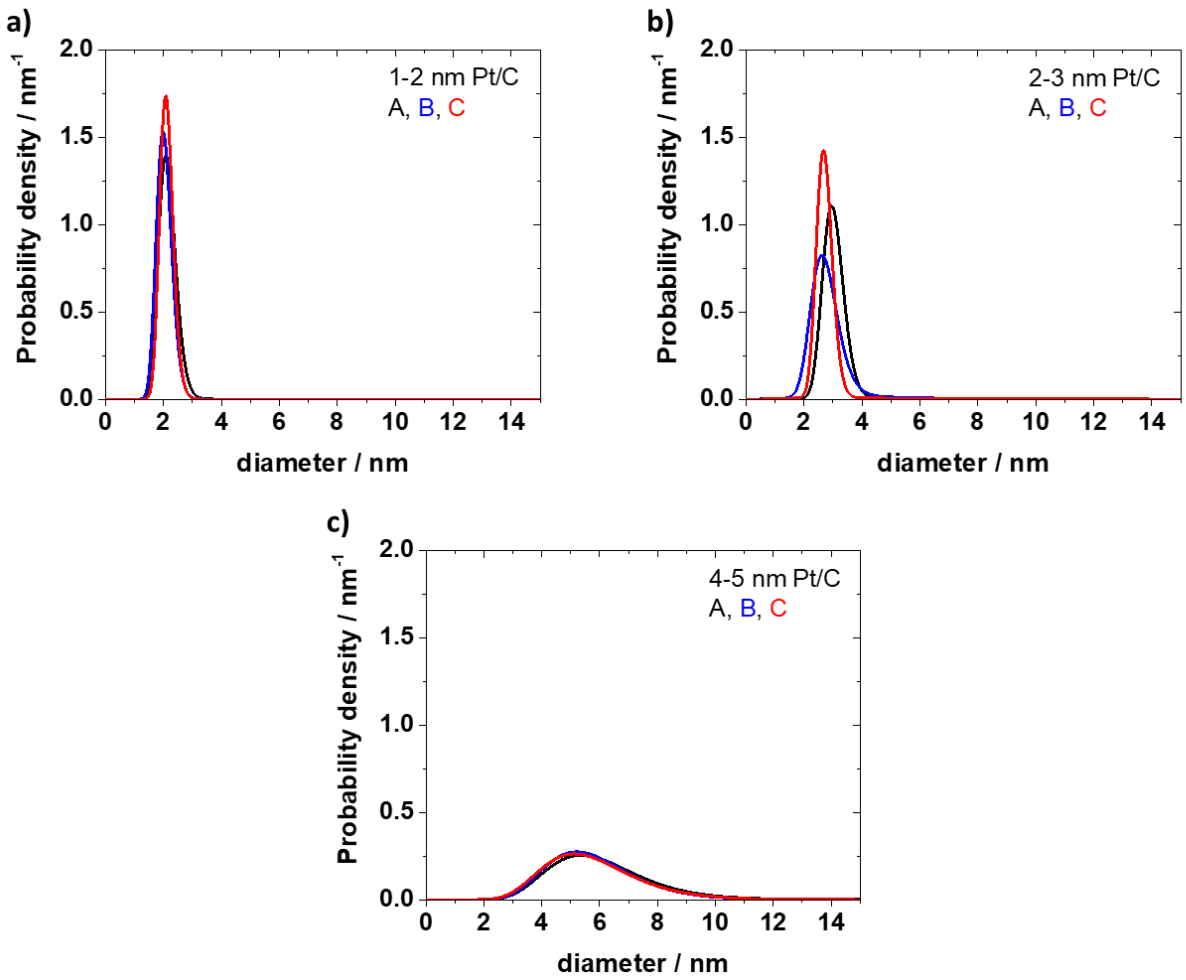

Figure S5: Particle size distributions obtained from SAXS data analysis for the commercial 1-2 nm (a), 2-3 nm (b), and 4-5 nm (c) Pt/C catalysts before AST. A, B, and C are independent repeats of the same condition.

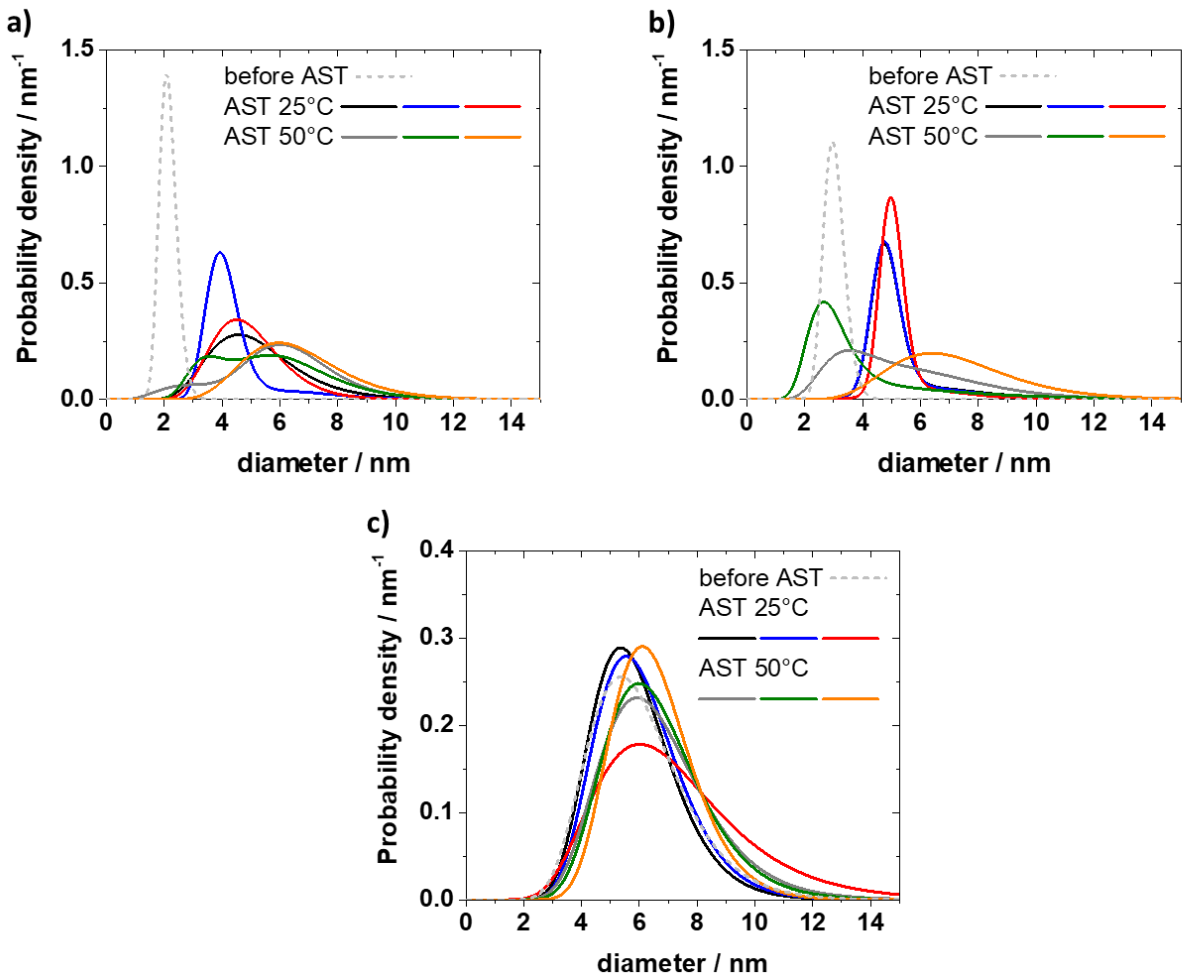

Figure S6: Particle size distributions obtained from SAXS data analysis for the commercial 1-2 nm (a), 2-3 nm (b), and 4-5 nm (c) Pt/C catalysts before and after AST in O2 at 25 °C (9000 steps between 0.6 and 1.0 VRHE, 3 s holding) or 50 °C (5000 steps between 0.6 and 1.0 V_{RHE}, 3 s holding) with three independent repeats for each AST condition.

Calculation of ESCA for low catalyst loading

In the previous work by Alinejad *et al.* [1] the exact Pt loading could not be directly controlled due to the limitations in the spray coating procedure for the preparation of the working electrode. The theoretical Pt loading of 0.208 mg_{Pt} cm^{-2}_{geo} and the absolute surface area (in cm^2) determined by CO stripping for this work can be used to estimate (by the rule of three) the loading by comparison with the minimum and maximum absolute surface area of the 2-3 and 4-5 nm Pt/C catalysts reported by Alinejad *et al.* [1]. Based on the absolute values of the Pt surface area, the loading is estimated to vary between 6.2 and 7.7 µg cm^{-2}_{geo} (see **Table S2**) without any influence on the observed ECSA loss.

Table S2: Comparison of the measured surface area by CO stripping and the ECSA for low and high catalyst loadings on the GDL of 2-3 nm and 4-5 Pt/C in the GDE setup.

Pt/C catalysts	Low loading on GDL from reference [1]		High loading on GDL (this work)	
	Surface area / cm^2	Loading / μg_{Pt} cm^{-2}_{geo}	Surface area / cm^2	Loading / mg_{Pt} cm^{-2}_{geo}
2-3 nm	0.42	7.3	11.9 ± 0.2	0.208
	0.44	7.7		
4-5 nm	0.25	6.2	8.4 ± 0.3	0.208
	0.28	6.9		

Calculation of theoretical surface area

The theoretical Pt loading is 0.208 mg_{Pt} cm^{-2}_{geo} and the area of a GDE A_{GDE} is 0.07 cm^2 (diameter of 3 mm). This leads to a Pt amount $m_{Pt\ GDE}$ of $1.47 \cdot 10^{-5}$ g_{Pt} per experiment. This Pt amount has a total volume $V_{Pt\ GDE}$ of $6.85 \cdot 10^{-7}$ cm^3. Based on the particle sizes of **Table S3** the volume of one Pt NP $V_{Pt\ NP}$ (assumed to be spherical) can be calculated. The number of particles per catalysts $N_{NP\ total}$ are calculated by:

$$N_{NP\ total} = \frac{V_{Pt\ GDE}}{V_{Pt\ NP}}$$

Multiplying the surface area $A_{Pt\ NP}$ of one Pt NP by $N_{NP\ total}$ leads to the total theoretical surface area per catalyst $A_{Pt\ catalyst}$. By considering the theoretical Pt loading 0.208 mg_{Pt} cm^{-2}_{geo} the theoretical surface area $A_{Pt\ catalyst}$ in mg_{Pt} cm^{-2}_{geo} and hence the difference between experimentally obtained ECSA and theoretical surface area ΔA can be determined.

Table S3: Averages of mean particle sizes obtained from the SAXS data analysis. Volumes of one NP based on the averages of the mean particle sizes and the total number of NPs based on the ratio of the Pt volume in the GDE and the volume of one Pt NP. Surface areas of one NP and of all NPs in the whole catalyst based on the averages of the mean particle sizes. Theoretical surface of the Pt NPs per catalysts and the difference between experimental ECSA and theoretical surface area.

Pt/C catalysts	$d_{Pt\ NP}$ / nm	$V_{Pt\ NP}$ / nm^3	$N_{NP\ total}$ / 10^{12}	$A_{Pt\ NP}$ / 10^{-17} m^2	$A_{Pt\ catalyst}$ / 10^{-4} m^2	$A_{Pt\ catalyst}$ / $m^2\ g^{-1}_{Pt}$	ΔA / $m^2\ g^{-1}_{Pt}$
1-2 nm	2.1	5	150	1.3	20	135	-26
2-3 nm	2.8	11	60	2.5	15	100	-19
4-5 nm	5.7	95	7.2	10	7.3	49	8

Analysis of X-ray total scattering data

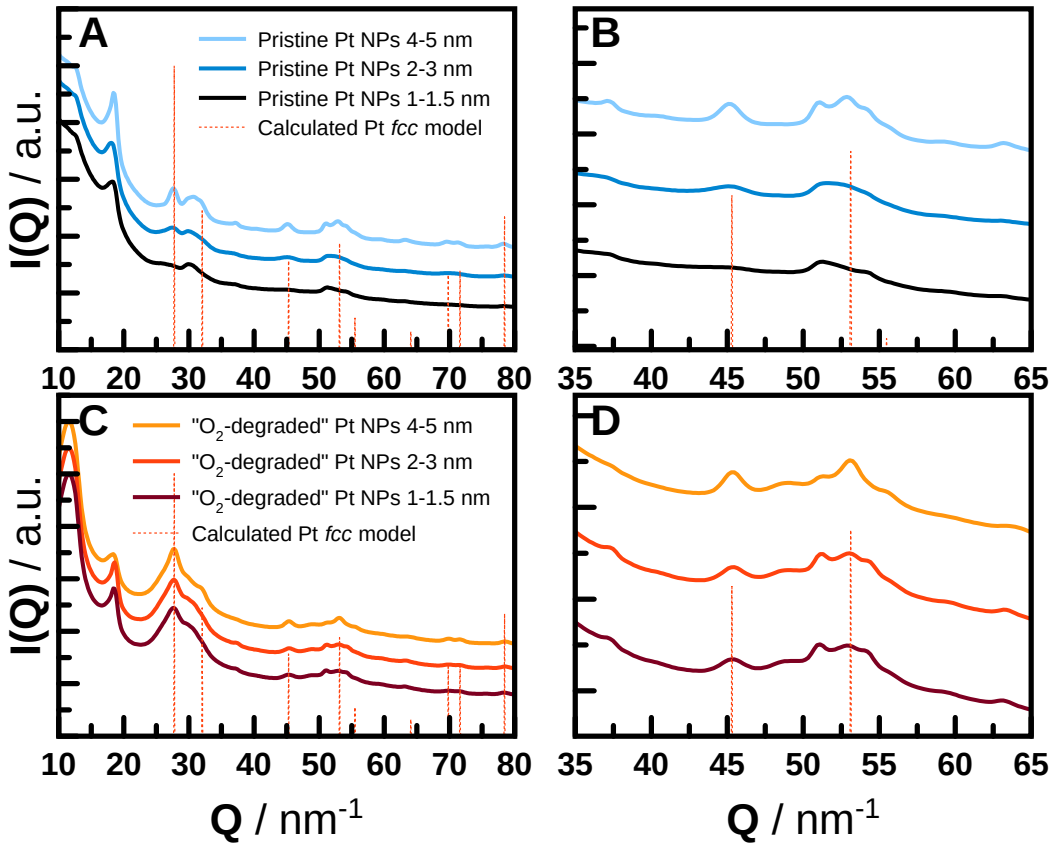

Figure S7: X-ray scattering data in reciprocal space, I(Q), of A-B) pristine supported Pt NPs and C-D) supported Pt NPs after the AST at 25°C.

Figure S7 shows the total scattering data obtained from the samples before and after O_2 degradation**.** The data show a significant background signal from the carbon support and membrane, but a scattering signal from Pt NPs can also be identified. The size of the NPs is reflected in the width of the Pt Bragg peaks, where broad peaks indicate small NPs. As seen in

Figure S7B, the peaks arising from Pt (highlighted in red) are broader for the smallest Pt NPs (i.e. 1-2 nm and 2-3 nm), than for the 4-5 nm Pt NPs, as expected. However, after the AST, the width of Pt peaks (highlighted) in the smallest Pt NPs are found to become narrower showing growth of the Pt NPs (

Figure S7C and D). Similar peak widths are observed for all three Pt samples after the AST, and the width of the 4-5 nm Pt NPs appears uninfluenced by the degradation step.

The data from the samples after the AST were analyzed in real-space by modelling the reduced PDFs, G(r). The PDFs were modelling using a *fcc* Pt model assuming a spherical crystallite size. The results

from the modelling is given in **Figure S8** and **Table S4.** The Pt crystallite size refined to approx. 4 nm for all three samples (**Figure S8** and **Table S4**).

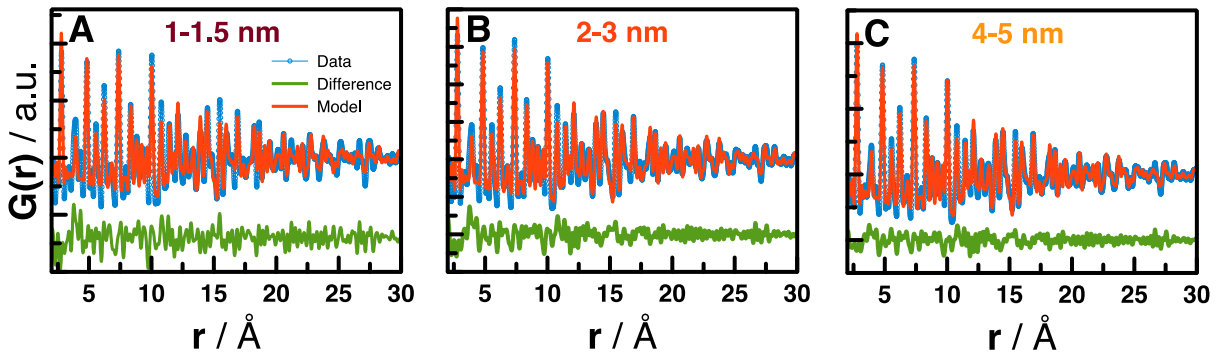

Figure S8: PDF refinements of Pt/C catalysts after the AST at 25°C.

Table S4: Refined values obtained from the PDF refinement after the AST at 25°C.

Pt/C catalysts	Cell / Å	d / Å	d / nm	Rw
1-2 nm	3.935	44	4.4	0.37
2-3 nm	3.932	42	4.2	0.28
4-5 nm	3.931	40	4.0	0.23

References

1. S. Alinejad, M. Inaba, J. Schröder, J. Du, J. Quinson, A. Zana, and M. Arenz, *J. Phys. Energy*, **2**, 024003 (2020).

Manuscript IV:

J. Schröder,* J. Quinson,* J. J. K Kirkensgaard, M. Arenz

*equally contributing

Operando SAXS Study of a Pt/C Fuel Cell Catalyst with an X-ray Laboratory Source

The published paper is reprinted from *J. Phys. D: Appl. Phys.*, **2021**, *54*, 294004.

https://doi.org/10.1088/1361-6463/abfa39

IOP Publishing Journal of Physics D: Applied Physics

J. Phys. D: Appl. Phys. **54** (2021) 294004 (7pp) https://doi.org/10.1088/1361-6463/abfa39

Operando SAXS study of a Pt/C fuel cell catalyst with an X-ray laboratory source

Johanna Schröder[1,5], **Jonathan Quinson**[2,5,*], **Jacob J K Kirkensgaard**[3,4] **and Matthias Arenz**[2,*]

[1] Department of Chemistry, Biochemistry and Pharmaceutical Sciences, University of Bern, Bern, Switzerland
[2] Department of Chemistry, University of Copenhagen, Copenhagen, Denmark
[3] Department of Food Science, University of Copenhagen, Frederiksberg, Denmark
[4] Niels Bohr Institute, University of Copenhagen, Copenhagen, Denmark

E-mail: jonathan.quinson@chem.ku.dk and matthias.arenz@dcb.unibe.ch

Received 17 January 2021, revised 30 March 2021
Accepted for publication 21 April 2021
Published 14 May 2021

Abstract

Small-angle X-ray scattering (SAXS) is a powerful technique to investigate the degradation of catalyst materials. Ideally such investigations are performed *operando*, i.e. during a catalytic reaction. An example of *operando* measurements is to observe the degradation of fuel cell catalysts during an accelerated stress test (AST). Fuel cell catalysts consist of Pt or Pt alloy nanoparticles (NPs) supported on a high surface area carbon. A key challenge of *operando* SAXS measurements is a proper background subtraction of the carbon support to extract the information of the size distribution of the Pt NPs as a function of the AST treatment. Typically, such *operando* studies require the use of synchrotron facilities. The background measurement can then be performed by anomalous SAXS or in a grazing incidence configuration. In this work we present a proof-of-concept study demonstrating the use of a laboratory X-ray diffractometer for *operando* SAXS. Data acquisition of *operando* SAXS with a laboratory X-ray diffractometer is desirable due to the general challenging and limited accessibility of synchrotron facilities. They become even more crucial under the ongoing and foreseen restrictions related to the COVID-19 pandemic. Although, it is not the aim to completely replace synchrotron-based studies, it is shown that the background subtraction can be achieved by a simple experimental consideration in the setup that can ultimately facilitate *operando* SAXS measurements at a synchrotron facility.

Supplementary material for this article is available online

Keywords: *operando* spectroscopy, small-angle X-ray scattering, fuel cell catalyst, degradation

(Some figures may appear in color only in the online journal)

1. Introduction

Proton exchange membrane fuel cells (PEMFCs) are seen as an important renewable alternative of combustion engines, especially for large vehicles and heavy duty trucks [1–4]. For an efficient conversion of the hydrogen fuel to electric power, highly active catalysts are required. PEMFC catalysts are often composed of Pt or Pt alloy nanoparticles (NPs) [5, 6]. Besides a high catalytic activity, efficient catalysts also require sufficient stability [2, 7]. The stability of catalysts is often investigated by performing accelerated stress tests (ASTs) to decrease the testing time [8, 9]. Such ASTs were recently performed on commercial Pt catalysts in gas diffusion electrode (GDE) setups [10–12] simulating load cycles and start-stop conditions as recommended by the Fuel Cell Commercialization Conference of Japan [13, 14] under realistic mass transport conditions. To determine changes in particle size as result

[5] Equally contributing authors.
[*] Authors to whom any correspondence should be addressed.

of the AST protocol the measurements in the GDE setup were coupled to *ex situ* small-angle X-ray scattering (SAXS) [11, 12]. However, *ex situ* measurements provide only the possibility to determine the particle size at few points in time (i.e. at the beginning and the end of treatment). To establish a time-resolved picture of catalyst degradation the number of samples would need to be enormously increased.

To obtain a deeper insight into time-resolved phenomena, *in situ* [15–17] or *operando* [18–20] SAXS is necessary, which is typically performed at synchrotron X-ray sources. Beamtime for *operando* SAXS measurements at a synchrotron facility to investigate time-resolved degradation mechanisms is unfortunately limited, challenging to get granted, and typically requires a long time until the proposals are accepted, and the measurements can be performed. Furthermore, planning a beamtime at a synchrotron can be costly and logistically challenging. For instance, equipment must be shipped to the synchrotron facility, making the measurements rather inflexible already under normal circumstances. The COVID-19 pandemic made planned travelling basically impossible in 2020 and currently restricts most measurements at synchrotrons to remote operation which is even more challenging. Being able to study the time resolved degradation of catalysts with *operando* SAXS using a laboratory X-ray source would not be only at the moment but also for the future very helpful; it is resource-efficient to reduce travelling and research costs. Additionally, the use of a laboratory source gives the possibility for better designed experiments, e.g. more and more reliable repeats. At a synchrotron repeating measurements and checking the reproducibility of measurements is often limited due to the scarce beamtime. It can take months before experiments can be repeated.

In this work an *operando* SAXS and X-ray absorption spectroscopy cell was used with some adjustments to the firstly introduced version by Binninger *et al* [18] for measurements at synchrotron X-ray sources. This *operando* cell was used in this study in a laboratory X-ray source to perform electrochemical ASTs and investigate the time resolved degradation of a Pt NP catalyst with two distinguishable size populations by SAXS. An important point to obtain reasonable data for the particle size probability densities retrieved from SAXS measurements is a proper background subtraction, implying a careful background measurement. Using laboratory X-ray sources, the background measurement usually requires a separate experiment leading often to difficulties in normalization of the curves [21]. At synchrotron facilities anomalous SAXS can be performed by tuning the X-ray energy to subtract elemental scattering energies [21]. Alternatively the measurements can be performed in grazing incidence [22–24]. These two choices, however, are not available for measurements at laboratory X-ray sources. Tillier *et al* [19] thus measured the background *ex situ* on a Pt-free carbon electrode performing the same degradation protocol as on the sample which led to the measurement of a suitable background.

Here we present a new design of the working electrode in the *operando* cell. In this study, the catalyst film as well as a catalyst-free part of the substrate (i.e. the background) experience the same electrochemical treatment during the AST, enabling an *operando* SAXS background measurement. It is demonstrated that with such a design *operando* studies of catalyst degradation can be performed even with less powerful X-ray sources. The same technique can also be used to facilitate *operando* SAXS measurements at a synchrotron facility.

2. Experimental

2.1. Chemicals and materials

For the catalyst ink formation and the cleaning of the cell ultrapure Milli-Q water (resistivity >18.2 MΩ cm, total organic carbon <5 ppb) from a Millipore system was used. The catalysts ink was prepared with isopropanol (IPA, 99.7+ %, Alfa Aesar), commercial Pt/C catalysts (TEC10E20A (1–2 nm Pt/C, 19.4 wt% Pt) and TEC10E50E-HT (4–5 nm Pt/C, 50.6 wt% Pt), Tanaka kikinzoku kogyo), and Nafion dispersion (D1021, 10 wt. %, EW 1100, Fuel Cell Store). The working electrode (WE) was prepared by a gas diffusion layer (GDL) with a microporous layer (MPL) on top (Freudenberg H23C8, 0.230 μm thick) and a leather punching tool (Takagi Co., 4 907 052 141 636, diameter of 3 mm) was used to cut the GDL to the desired size. In the electrochemical measurements 0.1 M $HClO_4$ prepared from 70% perchloric acid ($HClO_4$, Suprapur®, Merck) was used as electrolyte.

2.2. Catalyst synthesis

The catalyst mixture with two size populations on different carbon flakes was obtained by mixing 10.31 mg TEC10E20A and 5.97 mg TEC10E50E-HT (Pt mass ratio of 40:60 (small:large NPs)). The ink with a Pt concentration of 0.5 mg ml^{-1} was formed by dispersing the catalysts in 10 ml of a mixture of Milli-Q water and IPA (water/IPA ratio of 3:1) as described before [11]. The mixture was sonicated for 10 min in a sonication bath to get a good dispersion. 53 μL of Nafion was added (Nafion/carbon mass ratio of 0.5). The dispersion was again sonicated for 10 min in a sonication bath.

2.3. Catalyst film preparation

The Freudenberg GDL was placed in a vacuum filtration setup between a glass funnel and a sand core filter. All this was placed on a collecting bottle as described by Yarlagadda *et al* [25]. 4 mL of the inks were diluted with 7 ml of Milli-Q water and 29 ml of IPA (water-IPA ratio of 1:3, Pt concentration of 0.05 mg l^{-1}). The mixture was sonicated for 1 min. The diluted ink was then filled in a funnel. A diaphragm vacuum pump (Vacuubrand, MZ 2C, max. 1.7 m^3 h^{-1} and 9.0 mbar) was used to deposit the catalyst on top of the GDL (duration for the filtering was ca. 4 h). Afterwards, the GDE was dried and stored in air. By this procedure a theoretical Pt loading of 0.208 mg $cm^{-2}{}_{geo}$, typically used for commercial fuel cells [26] is obtained.

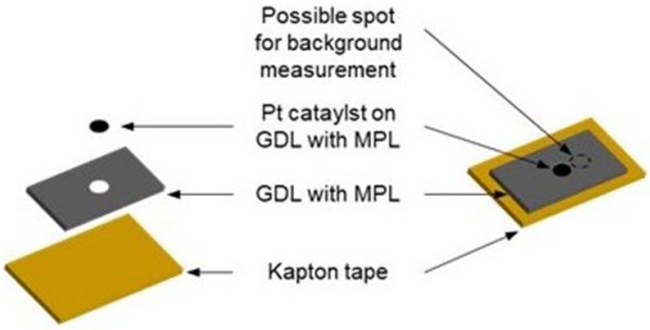

Figure 1. Sketch of the WE (diameter of 5 mm) consist of the Pt catalyst on a GDL with a MPL placed in the middle of a GDL and glued to Kapton tape.

2.4. Degradation study in operando cell

The cell used for *operando* SAXS is adapted from the one reported by Binninger *et al* [18]. As counter electrode (CE) the Freudenberg GDL was used and as reference electrode an Ag wire. To prepare the WE a circle (diameter of 5 mm) was punched inside a rectangle of the Freudenberg GDL. This rectangle was fixed on a Kapton tape (MPL was placed upside). A circle (diameter of 5 mm) of the catalyst film deposited on the GDL by vacuum filtration was placed in the hole, see figure 1. The electrolyte (0.1 M $HClO_4$) exposed to air was manually pulled through the cell before and after an electrochemical measurement by drawing up a 50 ml syringe. For the AST measurement the potential was stepped between 0.6 and 1.0 V_{RHE} with 3 s holding time at each potential. The applied potential was adjusted to the open circuit potential of the cell: 0.422 V (steps between 0.12 and 0.52 V_{Ag}), 0.415 V (0.11 and 0.51 V_{Ag}), 0.406 V (0.10 and 0.50 V_{Ag}), 0.394 V (0.09 and 0.49 V_{Ag}), and 0.406 (0.10 and 0.50 V_{Ag}). The resistance during the measurement was determined online using an AC signal (5 kHz, 5×10^{-5} A) [27]. Details about the AST protocol and data are found in the SI, see figures S1 and S2 (available online at stacks.iop.org/JPD/54/294004/mmedia).

2.5. SAXS

The size change of NPs supported on carbon was assessed by SAXS measurements as previously reported [11, 12]. SAXS measurements were performed at the Niels Bohr Institute, University of Copenhagen, Denmark, on a Ganesha instrument (SAXSLab). The Ganesha is equipped with a 100XL+ microfocus sealed X-ray tube (Rigaku), producing a photon beam with a wavelength of 1.54 Å, and a two-dimensional (2D) 300 K Pilatus detector (Dectris). The detector is situated inside a large continuous vacuum chamber, where it can be moved to adjust the distance between sample and detector. For the present experiment, the sample detector distance was set to cover a q-range of 0.0159–0.7428 $Å^{-1}$ calibrated using silver behenate. Motorized scatterless slits allow to tune the collimation and for the present study a two-slit configuration was used with 0.9 mm and 0.4 mm squares as first and second pinholes, respectively, resulting in a beam with ca. 10 M photons/second hitting the sample. The 2D scattering data were azimuthally averaged, normalized by the incident radiation intensity, the sample exposure time, and the transmission. Using a standard SAXSGUI reduction software, the data were then corrected for the background and detector inhomogeneities. The samples consisting of the NPs on the GDL were placed in the *operando* cell and the cell exposed to the beam produced by the lab source. The cell itself was not under vacuum, but the detector was placed in a chamber under vacuum (on the left of the image in figure 2). The background was measured next to the Pt catalyst (see figure 1) by manually moving the *operando* cell. A fast SAXS measurement of 15 s was performed to confirm that a metal-free spot was subjected to the beam.

The data analysis after background subtraction (acquired in a part of the sample without Pt NPs) was performed as described previously [11, 12, 28, 29] using a polydisperse spheres model. The radially averaged intensity $I(q)$ is expressed as a function of the scattering vector $q = 4\pi \cdot \sin(\theta)/\lambda$, where λ is the wavelength, and 2θ is the scattering angle. The background-corrected scattering data were fitted using a power law to consider the behavior at low q value and a model of one or two polydisperse spheres described by a volume-weighted log-normal distribution. The scattering data are fitted to the following expression:

$$I(q) = A \cdot q^{-n} + C_1 \cdot \int P_{s1}(q, R)\, V_1(R)\, D_1(R)\, \mathrm{d}R + C_2 \cdot \int P_{s2}(q, R)\, V_2(R)\, D_2(R)\, \mathrm{d}R$$

where $A \cdot q^{-n}$ corresponds to the power law with A and n as free parameters, C_1 and C_2 are scaling constants, P_{s1} and P_{s2} the sphere form factors, V_1 and V_2 the particle volumes and D_1 and D_2 the log-normal size distribution. The sphere form factor is given by [30, 31]:

$$P_s(q,R) = \left(3\frac{\sin(qR) - qR\cos(qR)}{(qR)^3}\right)^2$$

and the log-normal distribution by:

$$D(R) = \frac{1}{R\sigma\sqrt{2\pi}}\mathrm{emp}\left(\frac{-\left[\ln\left(\frac{R}{R_0}\right)\right]^2}{2\sigma^2}\right)$$

where σ is the variance and R_0 (evaluated in Å) the geometric mean of the log-normal distribution. The fitting was done using a home written MATLAB code. The free parameters in the model are A, n, C_1, R_1, σ_1, C_2, R_2, σ_2. The values obtained for these parameters are reported in table S1. In order to account for the two populations, the reported probability density functions were weighted by the relative surface contribution of the spheres as detailed in the SI. The scattering data and corresponding fits are reported in figures S3–S6.

The scattering intensities were recorded for 15 min per measurement, with and without electrolyte in the *operando* cell, before the AST and after 150, 300, 450, 600, and 900 steps

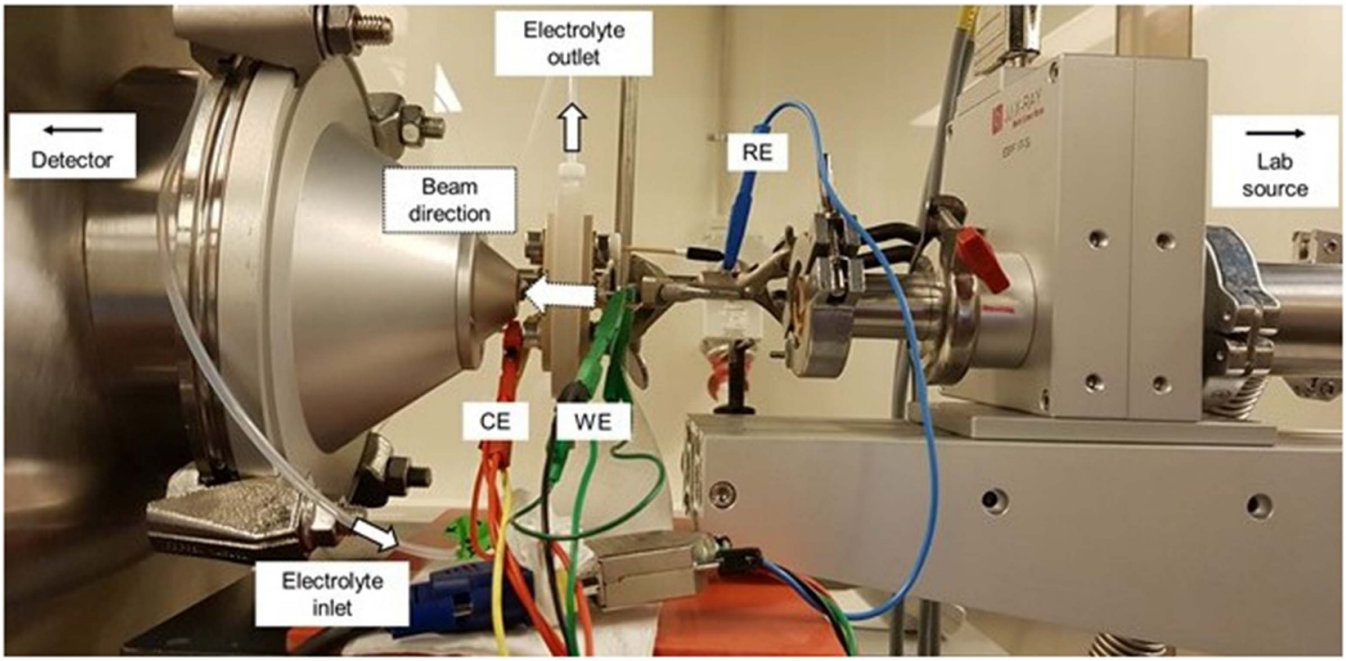

Figure 2. Experimental setup of the *operand* cell placed in the beam made by the SAXS lab source. Different from the picture a silver wire was used as reference electrode (RE).

of electrochemical treatments, as detailed below and indicated in the different figures.

3. Results and discussion

As discussed in the introduction, establishing a proper background using a laboratory X-ray source for SAXS is often difficult due to the need for separate (*ex situ*) measurements of the background and sample scattering data [21]. In this study, we demonstrate a simple design that enables to record the background data by moving the cell slightly horizontally to switch between the beam spot hitting the catalyst or the catalyst-free GDL next to the catalyst sample (i.e. *operando*), respectively. With the help of the specific WE configuration, see also the experimental part and figure 1, the catalyst and the 'blank' WE on which the background data are recorded, receive the same electrochemical treatment.

To prove the concept, two commercial Pt NP catalysts supported on carbon (Pt/C) consisting of two distinguishable size populations were mixed together. This mixed catalyst powder enables to investigate the influence of background subtraction over a range of particle sizes. Additionally, particle size dependent dissolution rates [32, 33] or degradation mechanisms [34] were reported before. Due to the two size populations the degradation mechanism of Ostwald ripening is expected to be favored, i.e. that the small particles grow at the expense of large ones [35].

Figure 3 compares different background scattering data that were measured in the described assembly before subjecting the WE to the electrolyte (red line), after introducing electrolyte to the SAXS cell (blue line), and after the electrochemical AST study (black line). After introducing the electrolyte to the

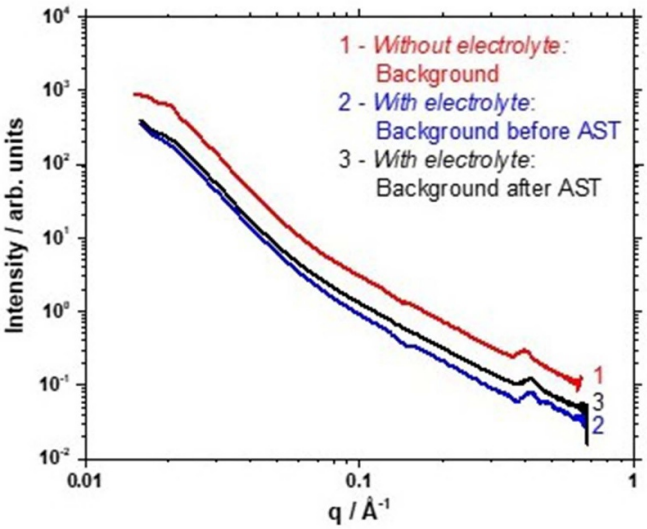

Figure 3. Overview of signal intensity for the SAXS measurements for backgrounds acquired under different conditions as indicated.

operando cell an AST protocol with potential steps consisting of 3 s holds at 0.6 and 1 V_{RHE}, respectively, was applied, see figures S1 and S2, to observe the degradation of the catalyst film with the Pt/C consisting of two size populations. The difference in the obtained probability density function for the size distributions of the Pt/C catalysts is demonstrated in figure 4. The received probability density functions are shown for using background data collected at the blank GDL exposed to electrolyte, but before applying the AST (figure 3(a)) as well as when using background data collected after exposing the blank GDL to the same electrochemical treatment as the sample

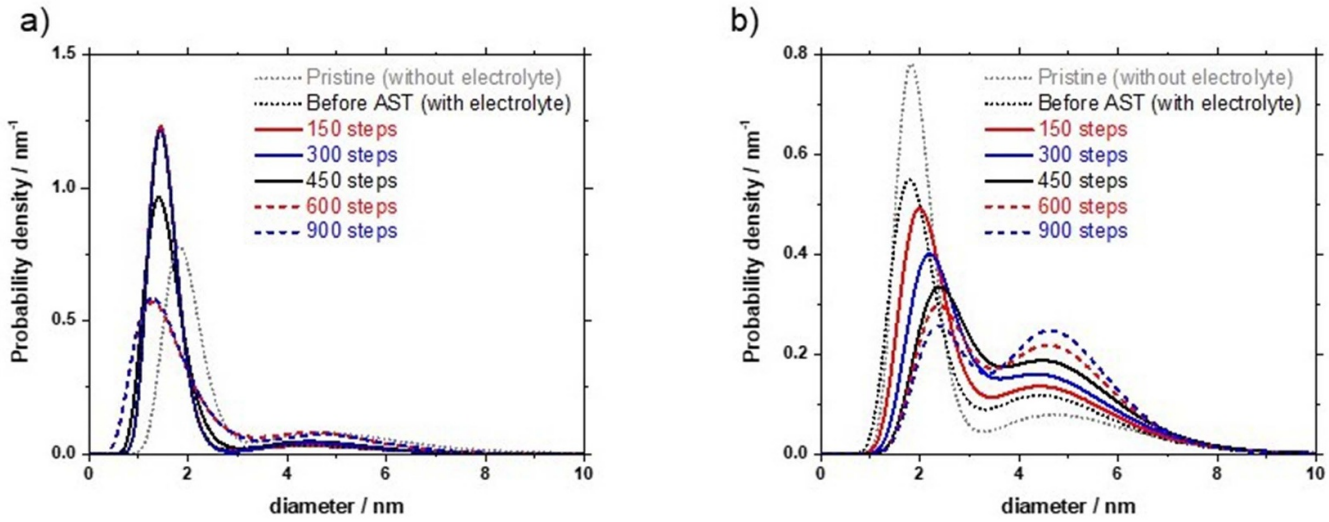

Figure 4. Probability density function received from SAXS data analysis using as background scattering data measured (a) before and (b) after the electrochemical test.

(figure 3(b)). In addition, the probability density functions for the pristine *ex situ* Pt/C sample are shown in both figures.

It is directly apparent that recording the background data before applying the AST as done in figure 3 is not optimal. Although one can distinguish the two size populations of the mixed catalyst, see figure 4, and follow the change in the populations, there is a clear difference between the size probability density of the pristine *ex situ* sample (measured without electrolyte) and the one before applying the electrochemical AST treatment (measured with electrolyte). This effect is pronounced for the population of the smaller Pt NPs and might have several origins: it could be that the electrolyte was not in a steady state within the cell or that the metal-free spot chosen for the background measurement was not adequately selected. However, the likely explanation is that since the intensity scales with the square of the volume, small NPs are more sensitive to the added scattering and absorption from the electrolyte. It then becomes easier to account for the 'larger NPs' in presence of electrolyte. This leads to probability densities where the larger NPs account for more of the size distribution than the smaller ones, see figure 4. Nevertheless, it also leads to an erroneous estimation of the average particle size of the smaller Pt NPs, see table S1. In addition, no strong difference in the average particle size of the small NPs is seen during the complete AST; after 600 potential steps only the size distribution widens, see figure 4 and table S1. This trend is not expected based on previous investigations where at least some changes in the average particle size are reported [11].

By comparison, using background data of the GDL that experienced the same electrochemical treatment as the catalyst, the mean particle size of the two size populations of the pristine sample (without electrolyte) are as expected at the same size position as for the set of data measured before the AST but with electrolyte, see figures 4 and S7. Nevertheless, also with a proper background subtraction, a difference between the pristine sample and the one in presence of the electrolyte is observed. In particular a decrease of the probability density of the population with small particle size at the expense of the one with larger size is seen. This observation could be an indication for particle dissolution followed by Ostwald ripening. Indeed, it is observed in scanning flow cell measurements coupled to inductively coupled plasma mass spectrometry that upon the contact of a Pt/C catalyst with an electrolyte Pt dissolution is induced [8, 36]. Applying the AST, it is observed that the size population of the small particles increases from 2.0 ± 0.5 nm to 2.6 ± 0.6 nm, while the large particles remain constant at 5.0 ± 1.4 before and 5.0 ± 1.1 nm after 900 steps. This behavior of particle growth of small particles (1–2 nm) and stable larger NPs (4–5 nm) is consistent with results observed recently in a GDE setup investigating both catalysts independently by *ex situ* SAXS [11]. It could not be distinguished between the degradation mechanisms of particle dissolution with subsequent Ostwald ripening or particle coalescence; both mechanisms were in agreement with the observed NP growth. Therefore, the comparison of the initial and end of treatment size populations between *ex situ* (GDE setup [11]) and *in situ* SAXS (*operando* cell) seem to show that the presence of the second size population in the catalyst mixture in the *operando* cell does not have an influence on the degradation mechanism. However, the catalyst mixture in the *operando* SAXS result in a continuous size increase and reduced probability density of the small population, while the probability density of the large particles increases at the same time. Consequently, *operando* SAXS points toward a continuous process of Pt dissolution with subsequent Ostwald ripening as compared to particle coalescence.

4. Conclusion

It is demonstrated how using a SAXS laboratory X-ray source not only enables a proper background subtraction, but also high-quality degradation data can be obtained. Our approach has a strong benefit because beamtimes and the flexibility

of the experiments at synchrotron X-ray sources are limited. There is often too little room for optimization of the experimental design during synchrotron beamtime to implement spontaneous ideas and to repeat experiments under optimized conditions can take quite a long time. In addition, the synchrotron beamtime itself includes travelling and the transport of materials to the synchrotron beamline which can be a large cost factor for research groups and is virtually impossible during the current COVID-19 pandemic. In contrast, experiments using a laboratory X-ray source can be performed on-site at universities and repeats of experiments can be more easily planned. Last but not least, on-site experiments offer a great opportunity to perform preliminary studies to optimize chances to secure synchrotron beamtimes by improving beamtime proposals as well as to make the most of the valuable time at synchrotrons if the proposal is granted.

Data availability statement

All data that support the findings of this study are included within the article (and any supplementary files).

Acknowledgments

This work was supported by the Swiss National Science Foundation (SNSF) via the Project No. 200021_184742 and the Danish National Research Foundation Center for High Entropy Alloys Catalysis (CHEAC) DNRF-149.

ORCID iDs

Johanna Schröder https://orcid.org/0000-0001-5461-4751
Jonathan Quinson https://orcid.org/0000-0002-9374-9330
Matthias Arenz https://orcid.org/0000-0001-9765-4315

References

[1] Gröger O, Gasteiger H A and Suchsland J P 2015 Review-electromobility: batteries or fuel cells? *J. Electrochem. Soc.* **162** A2605–22
[2] Stacy J, Regmi Y N, Leonard B and Fan M 2017 The recent progress and future of oxygen reduction reaction catalysis: a review *Renew. Sustain. Energy Rev.* **69** 401–14
[3] Nazir H *et al* 2020 Is the H_2 economy realizable in the foreseeable future? Part III: H_2 usage technologies, applications, and challenges and opportunities *Int. J. Hydrog. Energy* **45** 28217–39
[4] Ruf Y, Baum M, Zorn T, Menzel A and Rehberger J 2020 Study report: fuel cells hydrogen trucks—heavy-duty's high performance green solution study summary Published 15 December 2020 by fuel cells and hydrogen joint undertaking (FCH JU) and Roland Berger (available at: www.fch.europa.eu/publications/study-fuel-cells-hydrogen-trucks) (Accessed 24 March 2021)
[5] Yoshida T and Kojima K 2015 Toyota MIRAI fuel cell vehicle and progress toward a future hydrogen society *Electrochem. Soc. Interface* **24** 45–9
[6] Pollet B G, Kocha S S and Staffell I 2019 Current status of automotive fuel cells for sustainable transport *Curr. Opin. Electrochem.* **16** 90–5
[7] Katsounaros I, Cherevko S, Zeradjanin A R and Mayrhofer K J J 2014 Oxygen electrochemistry as a cornerstone for sustainable energy conversion *Angew. Chem., Int. Ed.* **53** 102–21
[8] Pizzutilo E, Geiger S, Grote J-P, Mingers A, Mayrhofer K J J, Arenz M and Cherevko S 2016 On the need of improved accelerated degradation protocols (ADPs): examination of platinum dissolution and carbon corrosion in half-cell tests *J. Electrochem. Soc.* **163** F1510–4
[9] Yano H, Watanabe M, Iiyama A and Uchida H 2016 Particle-size effect of Pt cathode catalysts on durability in fuel cells *Nano Energy* **29** 323–33
[10] Alinejad S, Inaba M, Schröder J, Du J, Quinson J, Zana A and Arenz M 2020 Testing fuel cell catalysts under more realistic reaction conditions: accelerated stress tests in a gas diffusion electrode setup *J. Phys. Energy* **2** 024003
[11] Schröder J, Quinson J, Mathiesen J K, Kirkensgaard J J K, Alinejad S, Mints V A, Jensen K M Ø and Arenz M 2020 A new approach to probe the degradation of fuel cell catalysts under realistic conditions: combining tests in a gas diffusion electrode setup with small angle X-ray scattering *J. Electrochem. Soc.* **167** 134515
[12] Alinejad S, Quinson J, Schröder J, Kirkensgaard J J K and Arenz M 2020 Carbon-supported platinum electrocatalysts probed in a gas diffusion setup with alkaline environment: how particle size and mesoscopic environment influence the degradation mechanism *ACS Catal.* **10** 13040–9
[13] Ohma A, Shinohara K, Iiyama A, Yoshida T and Daimaru A 2019 Membrane and catalyst performance targets for automotive fuel cells by FCCJ membrane, catalyst, MEA WG *ECS Trans.* **41** 775–84
[14] Park Y-C, Kakinuma K, Uchida M, Tryk D A, Kamino T, Uchida H and Watanabe M 2013 Investigation of the corrosion of carbon supports in polymer electrolyte fuel cells using simulated start-up/shutdown cycling *Electrochim. Acta* **91** 195–207
[15] Harada M, Tamura N and Takenaka M 2011 Nucleation and growth of metal nanoparticles during photoreduction using *in situ* time-resolved SAXS analysis *J. Phys. Chem.* C **115** 14081–92
[16] Wu L, Willis J J, McKay I S, Diroll B T, Qin J, Cargnello M and Tassone C J 2017 High-temperature crystallization of nanocrystals into three-dimensional superlattices *Nature* **548** 197–201
[17] Quinson J *et al* 2020 Solvent-dependent growth and stabilization mechanisms of surfactant-free colloidal Pt nanoparticles *Chem. Eur. J.* **26** 9012–23
[18] Binninger T *et al* 2016 Electrochemical flow-cell setup for *in situ* X-ray investigations: I. Cell for SAXS and XAS at synchrotron facilities *J. Electrochem. Soc.* **163** H906–12
[19] Tillier J, Binninger T, Garganourakis M, Patru A, Fabbri E, Schmidt T J and Sereda O 2016 Electrochemical flow-cell setup for *in situ* X-ray investigations: II. Cell for SAXS on a multi-purpose laboratory diffractometer *J. Electrochem. Soc.* **163** H913–20
[20] Povia M, Herranz J, Binninger T, Nachtegaal M, Diaz A, Kohlbrecher J, Abbott D F, Kim B-J and Schmidt T J 2018 Combining SAXS and XAS to study the *operando* degradation of carbon-supported Pt-nanoparticle fuel cell catalysts *ACS Catal.* **8** 7000–15
[21] Binninger T, Garganourakis M, Han J, Patru A, Fabbri E, Sereda O, Kötz R, Menzel A and Schmidt T J 2015 Particle-support interferences in small-angle X-ray scattering from supported-catalyst materials *Phys. Rev. Appl.* **3** 024012(6)
[22] Chaâbane N, Lazzari R, Jupille J, Renaud G and Avellar Soares E 2012 CO-induced scavenging of supported Pt nanoclusters: a GISAXS study *J. Phys. Chem.* C **116** 23362–70

[23] Ruge M, Drnec J, Rahn B, Reikowski F, Harrington D A, Carlà F, Felici R, Stettner J and Magnussen O M 2017 Structural reorganization of Pt(111) electrodes by electrochemical oxidation and reduction *J. Am. Chem. Soc.* **139** 4532–9

[24] Khalakhan I, Bogar M, Vorokhta M, Kúš P, Yakovlev Y, Dopita M, Sandbeck D J S, Cherevko S, Matolínová I and Amenitsch H 2020 Evolution of the PtNi bimetallic alloy fuel cell catalyst under simulated operational conditions *ACS Appl. Mater. Interfaces* **12** 17602–10

[25] Yarlagadda V, McKinney S E, Keary C L, Thompson L, Zulevi B and Kongkanand A 2017 Preparation of PEMFC electrodes from milligram-amounts of catalyst powder *J. Electrochem. Soc.* **164** F845–9

[26] Kongkanand A and Mathias M F 2016 The priority and challenge of high-power performance of low-platinum proton-exchange membrane fuel cells *J. Phys. Chem. Lett.* **7** 1127–37

[27] Wiberg G K H, Mayrhofer K J J and Arenz M 2010 Investigation of the oxygen reduction activity on silver—a rotating disc electrode study *Fuel Cells* **10** 575–81

[28] Quinson J *et al* 2018 Investigating particle size effects in catalysis by applying a size-controlled and surfactant-free synthesis of colloidal nanoparticles in alkaline ethylene glycol: case study of the oxygen reduction reaction on Pt *ACS Catal.* **8** 6627–35

[29] Speder J, Altmann L, Roefzaad M, Bäumer M, Kirkensgaard J J K K, Mortensen K and Arenz M 2013 Pt based PEMFC catalysts prepared from colloidal particle suspensions—a toolbox for model studies *Phys. Chem. Chem. Phys.* **15** 3602

[30] Kajiwara K and Hiragi Y 1996 Chapter 6 Structure analysis by small-angle X-ray scattering *Analytical Spectroscopy Library* vol 7 H Saish0 and Y Gohshi and (Amsterdam: Elsevier) pp 353–404

[31] Garcia P R A F, Prymak O, Grasmik V, Pappert K, Wlysses W, Otubo L, Epple M and Oliveira C L P 2020 An *in situ* SAXS investigation of the formation of silver nanoparticles and bimetallic silver–gold nanoparticles in controlled wet-chemical reduction synthesis *Nanoscale Adv.* **2** 225–38

[32] Sandbeck D J S, Inaba M, Quinson J, Bucher J, Zana A, Arenz M, Arenz M and Cherevko S 2020 Particle size effect on platinum dissolution: practical considerations for fuel cells *ACS Appl. Mater. Interfaces* **12** 25718–27

[33] Sandbeck D J S, Secher N M, Speck F D, Sørensen J E, Kibsgaard J, Chorkendorff I and Cherevko S 2020 Particle size effect on platinum dissolution: considerations for accelerated stability testing of fuel cell catalysts *ACS Catal.* **10** 6281–90

[34] Yu K, Groom D J, Wang X, Yang Z, Gummalla M, Ball S C, Myers D J and Ferreira P J 2014 Degradation mechanisms of platinum nanoparticle catalysts in proton exchange membrane fuel cells: the role of particle size *Chem. Mater.* **26** 5540–8

[35] Quinson J *et al* 2018 Electrochemical stability of subnanometer Pt clusters *Electrochim. Acta* **277** 211–7

[36] Cherevko S, Zeradjanin A R, Topalov A A, Kulyk N, Katsounaros I and Mayrhofer K J J 2014 Dissolution of noble metals during oxygen evolution in acidic media *ChemCatChem* **6** 2219–23

Supporting information

Operando SAXS Study of a Pt/C Fuel Cell Catalysts with an X-ray Laboratory Source

Johanna Schröder[1+], Jonathan Quinson[2+*], Jacob J. K. Kirkensgaard[3,4], Matthias Arenz[1*]

[1] Department of Chemistry and Biochemistry, University of Bern, Freiestrasse 3, 3012 Bern, Switzerland

[2] Department of Chemistry, University of Copenhagen, Universitetsparken 5, 2100 Copenhagen, Denmark

[3] Department of Food Science, University of Copenhagen, Rolighedsvej 26, 1958 Frederiksberg, Denmark

[4] Niels Bohr Institute, University of Copenhagen, Universitetsparken 5, 2100 Copenhagen, Denmark

[+] equally contributing authors

[*] corresponding authors

Accelerated stress test

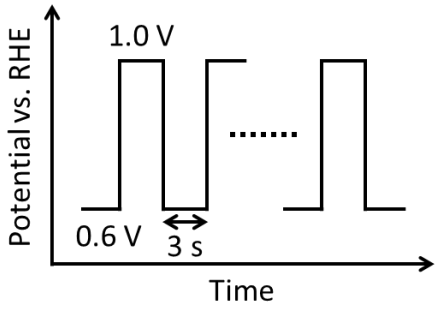

Figure S1. Sketch of the AST protocol applied in the *operando* cell.

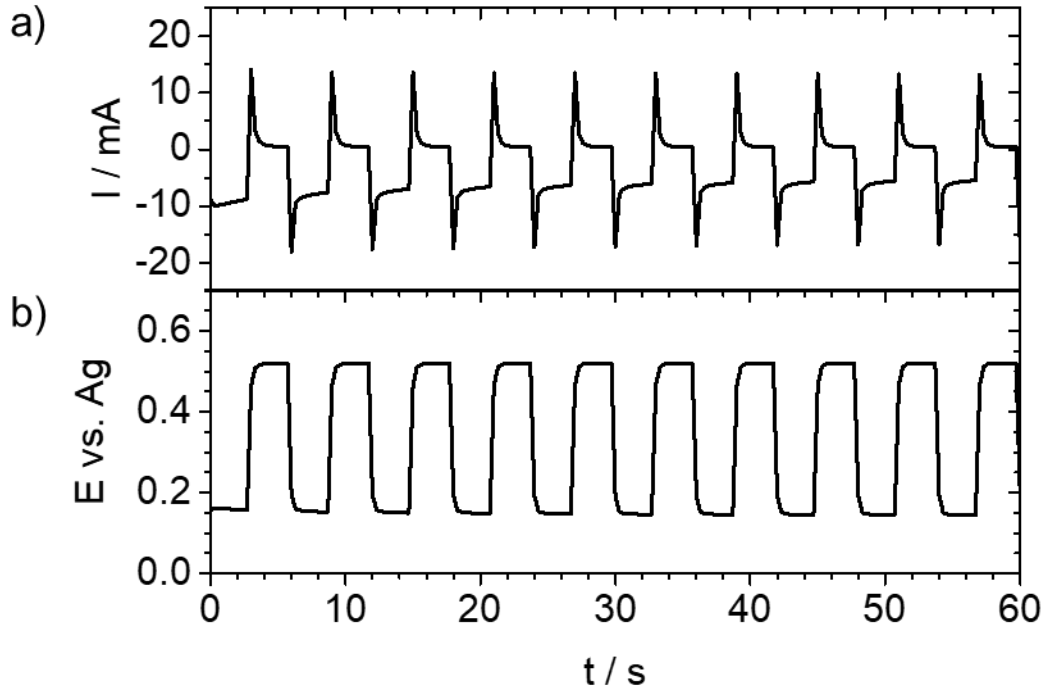

Figure S2. Examples of the a) applied (corrected) potential E vs. the Ag reference electrode and b) the measured current I during the AST at room temperature under air.

SAXS data

The average volume of nanoparticle from population 1 and from population 2, $\langle V \rangle_1$ and $\langle V \rangle_2$ respectively, lead to define volume fraction of population 1, Φ_{V1}, and volume fraction of population 2, Φ_{V2}, as:

$$\Phi_{V1} = \frac{N_1 \langle V \rangle_1}{N_1 \langle V \rangle_1 + N_2 \langle V \rangle_2} = 1 - \Phi_{V2}$$

$$\frac{\Phi_{V1}}{\Phi_{V2}} = \frac{N_1 < V >_1}{N_2 < V >_2}$$

$$\frac{N_1}{N_2} = \frac{\Phi_{V1} < V >_2}{\Phi_{V2} < V >_1}$$

where N_1 and N_2 are the number of nanoparticles in the population 1 or 2 respectively.

From the SAXS data acquisition we have the relationship between the retrieved coefficient C_1 and C_2 given by $C_i = k.\ \Phi_{vi}.\ \langle V \rangle_i$ where i=1 or 2 and k is a constant.

$$k = \frac{C_1}{\Phi_{V1} < V >_1} = \frac{C_2}{\Phi_{V2} < V >_2} = \frac{C_2}{(1 - \Phi_{V1}) < V >_2}$$

$$\frac{\Phi_{V1}}{1 - \Phi_{V1}} = \frac{C_1 < V >_2}{C_2 < V >_1}$$

$$\Phi_{V1} = \frac{1}{1 + \frac{C_2 < V >_1}{C_1 < V >_2}}$$

In order to weight the probability density function by the area or surface fractions we consider $\langle A \rangle_1$ and $\langle A \rangle_2$ as the average area of the nanoparticles from population 1 and 2, respectively:

$$\Phi_{A1} = \frac{N_1 \langle A \rangle_1}{N_1 \langle A \rangle_1 + N_2 \langle A \rangle_2} = 1 - \Phi_{A2} = \frac{1}{1 + \frac{N_2 \langle A \rangle_2}{N_1 \langle A \rangle_1}}$$

$$\Phi_{A1} = \frac{1}{1 + \frac{\Phi_{V2} < V >_1 < A >_2}{\Phi_{V1} < V >_2 < A >_1}}$$

$$\Phi_{A1} = \frac{1}{1 + \frac{C_2 (< V >_1)^2 < A >_2}{C_1 (< V >_2)^2 < A >_1}}$$

Table S1: Fitting parameters for SAXS data.

		Power law		1st population			2nd population			Diameters and deviation / nm [A.B]					
	Sample	A x 10^6	n	R_1 (Å)	σ_1	C_1	R_2 (Å)	σ_2	C_2	**d_1**	**σ_1**	**d_2**	**σ_2**	**d**	**σ**
Without electrolyte	Pristine	22	4	9.5	0.20	0.0050	25.5	0.28	0.047	1.9	0.4	5.3	1.5	2.9	0.5
With electrolyte and background recorded before EC	Before EC	-	-	7.5	0.20	0.0035	22.5	0.30	0.016	1.5	0.3	4.7	1.4	1.9	0.
	150 steps	-	-	7.5	0.20	0.0045	23.5	0.27	0.018	1.5	0.3	4.9	1.3	1.8	0.3
	300 steps	-	-	7.5	0.20	0.0044	23.5	0.22	0.017	1.5	0.3	4.8	1.1	1.9	0.3
	450 steps	-	-	7.5	0.25	0.0042	23.5	0.23	0.017	1.5	0.4	4.8	1.1	2.0	0.4
	600 steps	250	2	7.5	0.40	0.0047	24	0.23	0.019	1.6	0.7	4.9	1.1	2.3	0.6
	900 steps	250	2	7.5	0.40	0.0049	25	0.22	0.019	1.6	0.7	5.1	1.1	2.3	0.6
With electrolyte and background recorded after EC	Before EC	7	4	9.5	0.25	0.0016	24	0.27	0.016	2.0	0.5	5.0	1.4	3.1	0.6
	150 steps	4	4	10.5	0.23	0.0016	24	0.27	0.016	2.2	0.5	5.0	1.4	3.3	0.6
	300 steps	3	4	11.5	0.23	0.0016	24	0.27	0.016	2.4	0.6	5.0	1.4	3.6	0.7
	450 steps	3	4	12.5	0.23	0.0017	24.5	0.25	0.016	2.6	0.6	5.1	1.3	3.9	0.7
	600 steps	2	4	12.5	0.23	0.0015	24.5	0.23	0.016	2.6	0.6	5.0	1.2	4.0	0.7
	900 steps	2	4	12.5	0.23	0.0013	24.5	0.22	0.017	2.6	0.6	5.0	1.1	4.1	0.7

(A) evaluated as **d** = $0.2\, e^{(ln(R)+\frac{\sigma^2}{2})}$ for a one size population, evaluated as **d**= $0.2\, \varphi_{A1}.e^{\left(\ln(R_1)+\frac{{\sigma_1}^2}{2}\right)} + 0.2\, \varphi_{A2}.e^{\left(\ln(R_2)+\frac{{\sigma_2}^2}{2}\right)}$ for a 2 sizes population

(B) evaluated as $\boldsymbol{\sigma}= 0.2\sqrt{(e^{\sigma^2}-1)e^{(2\ln(R)+\sigma^2)}}$ for a one size population,

evaluated as $\boldsymbol{\sigma}= 0.2\sqrt{{\varphi_{A1}}^2.[(e^{{\sigma_1}^2}-1)e^{(2\ln(R_1)+{\sigma_1}^2)}]+{\varphi_{A2}}^2.[(e^{{\sigma_2}^2}-1)e^{(2\ln(R_2)+{\sigma_2}^2)}]}$ for a two sizes populations

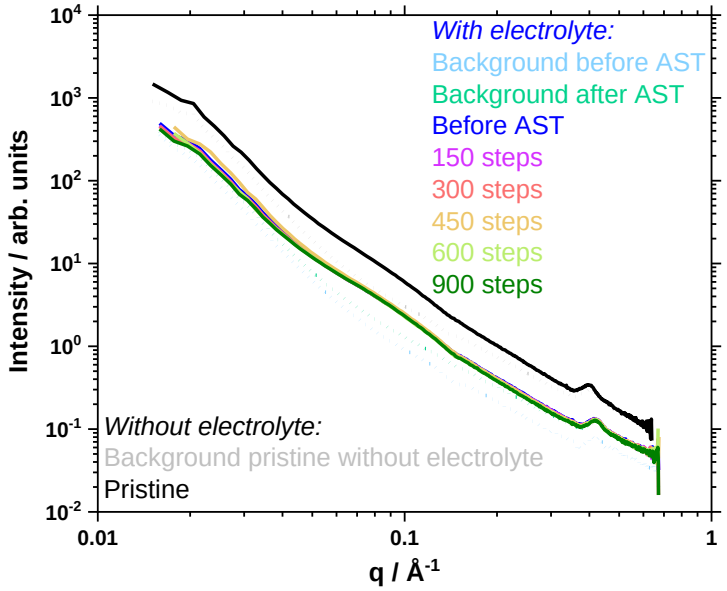

Figure S3. Overview of signal intensity for the SAXS measurements. Backgrounds are in dotted line, samples measured for different electrochemical treatment are reported as indicated.

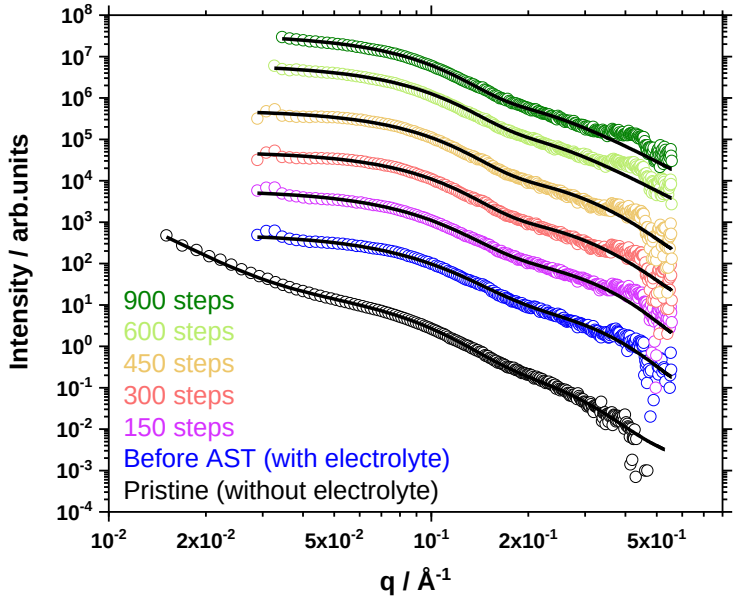

Figure S4. Overview of signal intensity for the SAXS measurements and fits after background subtraction for a background measured before electrochemical testing. The fit for the sample measured without electrolyte is also displayed.

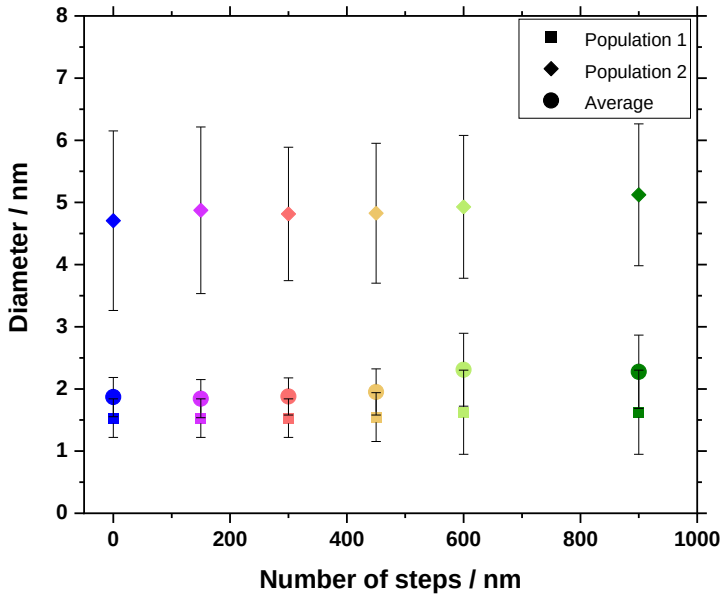

Figure S5. Diameter of the nanoparticles retrieved from SAXS data analysis using as background a background measured before electrochemical test, as a function of the number of steps for electrochemical testing and using a model taking into account two size populations.

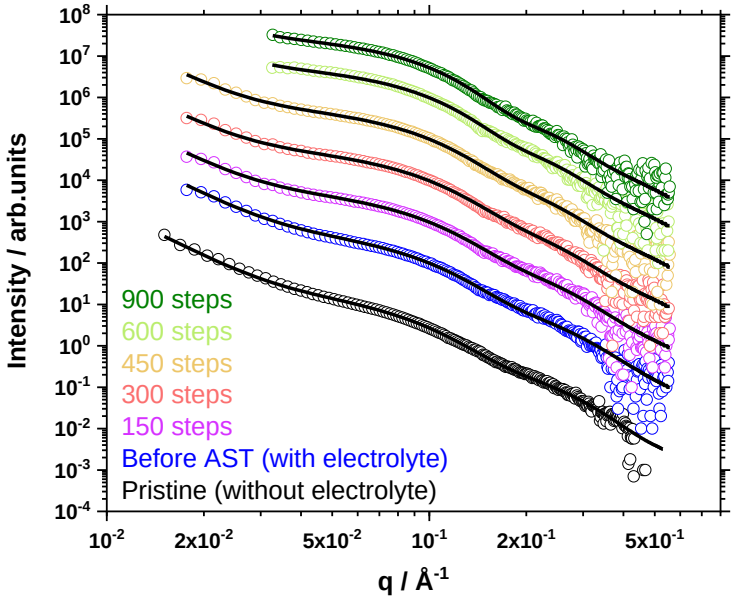

Figure S6. Overview of signal intensity for the SAXS measurements and fits after background subtraction for a background measured after electrochemical testing. The fit for the sample measured without electrolyte is also displayed.

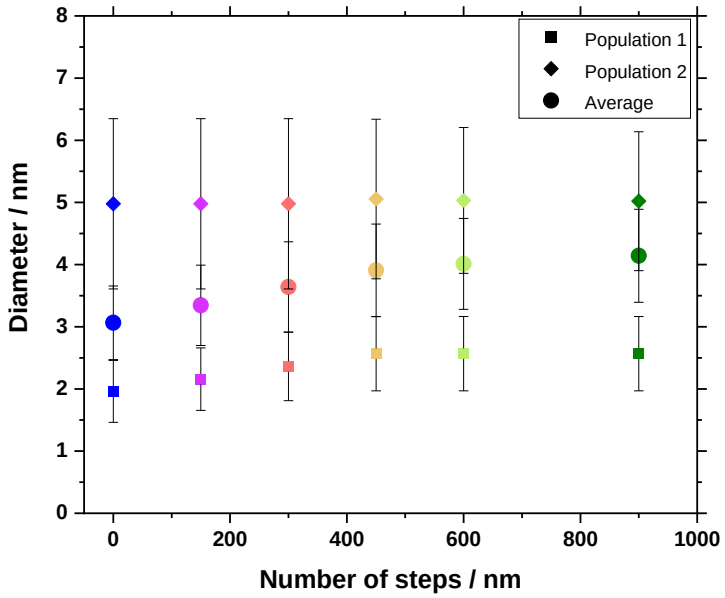

Figure S7. Diameter of the nanoparticles retrieved from SAXS data analysis using as background a background measured after electrochemical test, as a function of the number of steps for electrochemical testing and using a model taking into account two size populations.

Manuscript V:

J. Schröder, R. K. Pittkowski, I. Martens, R. Chattot, J. Drnec, J. Quinson, J. J. K. Kirkensgaard, M. Arenz

Tracking the Catalyst Layer Depth Dependent Electrochemical Degradation of a Bimodal Pt/C Fuel Cell Catalyst: A Combined *Operando* Small- and Wide-Angle X-Ray Scattering Study

In preparation.

Tracking the Catalyst Layer Depth-Dependent Electrochemical Degradation of a Bimodal Pt/C Fuel Cell Catalyst: A Combined *Operando* Small- and Wide-Angle X-Ray Scattering Study

Johanna Schröder,[a] Rebecca K. Pittkowski,[a,b] Isaac Martens,[c] Raphael Chattot,[c] Jakub Drnec,[c] Jonathan Quinson,[b] Jacob J. K. Kirkensgaard,[d,e] Matthias Arenz[a*]

[a] Department of Chemistry and Biochemistry, University of Bern, Freiestrasse 3, 3012 Bern, Switzerland

[b] Department of Chemistry, University of Copenhagen, Universitetsparken 5, 2100 Copenhagen Ø, Denmark

[c] European Synchrotron Radiation Facility (ESRF), 71 Avenue des Martyrs, 38000 Grenoble, France

[d] Niels Bohr Institute, University of Copenhagen, Universitetsparken 5, 2100 København Ø, Denmark

[e] Department of Food Science, University of Copenhagen, Rolighedsvej 26, 1958 Frederiksberg, Denmark

[*] Corresponding author: matthias.arenz@dcb.unibe.ch

Abstract

The combination of *operando* small- and wide-angle X-ray scattering (SAXS, WAXS) in grazing incidence configuration is presented as a new approach to provide depth-dependent insights into the changes in mean particle sizes and phase fractions occurring for fuel cell catalysts during accelerated stress tests (ASTs). As fuel cell catalyst, a bimodal Pt/C catalyst was chosen that consists of two distinguishable particle size populations. The presence of the two different sizes should favor and uncover electrochemical Ostwald ripening as the major degradation mechanism, i.e., it is expected that the size of the larger particles in the Pt/C catalyst grows at the expense of the smaller particles. The grazing incidence mode performed at the European Synchrotron Radiation Facility (ESRF) at the ID31 beamline revealed an intertwinement of the depth dependent degradation. While the larger particles show the same particle size changes close to the electrolyte-catalyst interface and within the catalyst layer, for the smaller Pt nanoparticles a different degradation scenario is observed. At the electrolyte-catalyst interface, the smaller particles increase in size while their phase fraction decreases during the AST. However, in the inner catalyst layer the phase fraction of smaller particles increases instead of decreases. The results of a depth-dependent degradation strongly suggest the need for a depth-dependent catalyst design for future improvement of the catalyst stability.

Keywords

Small-angle X-ray scattering (SAXS); wide-angle X-ray scattering (WAXS); fuel cell catalyst degradation; accelerated stress test (AST); bimodal Pt/C catalyst

1. Introduction

Proton exchange membrane fuel cells (PEMFCs) offer a sustainable alternative to conventional combustion engines.[1] Highly active precious metal based catalysts are typically used as state-of-the-art, e.g., PtCo catalysts in the Mirai vehicle from Toyota.[2] The translation of new PEMFC catalysts into their "real-life" application requires not only a high activity but also sufficient long-term catalyst stability of the costly catalyst.[3,4] Therefore, stability investigations and suitable degradation protocols to simulate realistic application conditions recently received increasing attention.[5–9] To reduce the time needed to induce catalyst degradation, accelerated stress tests (ASTs) are performed in fundamental screening studies.[10–13] The performed ASTs can induce different electrochemical degradation mechanisms that affect the nanoparticle (NP) size of the degrading catalyst: (1) migration of particles followed by coalescence, (2) metal dissolution, (3) electrochemical Ostwald ripening, i.e., the growth of larger particles at the expense of smaller ones, and (4) particle detachment from the support.[14,15] The particle size of fuel cell catalysts is commonly determined by (scanning) transmission electron microscopy ((S)TEM). To observe the change of some specific particles before and after the treatment, identical location (IL) (S)TEM is performed.[16–24] By comparison, in small-angle X-ray scattering (SAXS) studies the particle size change can be investigated in larger volume as compared to the limited number of NPs and local characterization that is achieved by only (S)TEM.[25–30] For example, *ex situ* SAXS was recently performed after applying AST protocols in a gas diffusion electrode (GDE) setup[20,28,29] that eliminates mass transport limitations as compared to the rotating disk electrodes (RDEs) commonly used in fundamental research studies.[31] However, both (S)TEM and SAXS were not clearly demonstrating the degradation mechanism of electrochemical Ostwald ripening which has been considered as one of the main degradation mechanisms in membrane electrode assemblies (MEA).[5,10,32]

In the present study, the depth-dependent (in the following also referred to as z-direction, see Figure S1) degradation within a catalyst layer was investigated by combining *operando* SAXS and wide-angle X-ray scattering (WAXS). The aims were to reveal degradation phenomena such as Ostwald ripening as well as to probe if the degradation is homogeneous within the catalyst layer. To generate a system that should favor electrochemical Ostwald ripening, a catalyst with two distinguishable Pt NP size distributions (bimodal catalyst) was prepared by mixing two commercial catalysts.[33]. Using

an *operando* cell with grazing incidence configuration[34] at the ID31 beamline at the European Synchrotron Radiation Facility (ESRF) in Grenoble, load cycle conditions of PEMFCs were simulated as AST following a protocol recommended by the Fuel Cell Commercialization Conference of Japan (FCCJ).[12,35] In the separate analysis of *operando* SAXS and WAXS data, both techniques revealed different limitations in studying the change in size distribution of the bimodal catalyst. However, combining both SAXS and WAXS enabled determining the mean particle sizes as well as the respective phase fractions of the two populations. The mean particle sizes of both size populations were determined by SAXS, and those values were used as input for the Rietveld refinement of the WAXS data. Studying the degradation close to the electrolyte-catalyst interface, a phenomenon in line with Ostwald ripening is observed. However, investigation of the *operando* data in a middle depth within the catalyst layer unexpectedly revealed an increase of both the mean particle size and phase fraction of the smaller population. Based on the revealed depth-dependent catalyst degradation, a depth-dependent design of catalyst layers could be an important strategy to improve catalyst stability.

2. Experimental section

2.1. Chemicals, materials, and gases

For the catalyst ink formation, ultrapure Milli-Q water (resistivity > 18.2 MΩ·cm, total organic carbon (TOC) < 5 ppb) from a Millipore system was used. Isopropanol (IPA, 99.7+ %, Alfa Aesar), commercial Pt/C catalysts (TEC10E20A (1-2 nm Pt/C, 19.4 wt% Pt) and TEC10E50E-HT (4-5 nm Pt/C, 50.6 wt% Pt), Tanaka kikinzoku kogyo), and Nafion dispersion (D1021, 10 wt. %, EW 1100, Fuel Cell Store) were used for the preparation of the catalyst ink. The working electrolyte (WE) was prepared using a gas diffusion layers (GDL) with a microporous layer (MPL) on top (Freudenberg H23C8, 0.230 µm thick). In the electrochemical measurements diluted 70 % perchloric acid ($HClO_4$, suprapur, Sigma Aldrich) as electrolyte and the gas argon (BIP ultrahigh purity, Air Liquide) were used. The two commercial Pt/C catalysts were dispersed in ethanol (absolute, VWR) and drop cast on holey C support film of Cu 300 mesh grids (Quantifoil). The spectrochemical cell was cleaned by briefly immersing it in diluted Caro's acid at room temperature.

2.2. Catalyst synthesis and ink formation

The two commercial Pt/C catalysts (TEC10E20A and TEC10E50E-HT) were mixed in a Pt mass ratio of 0.4:0.6 to obtain the catalyst mixture with two size populations on different carbon (C) flakes (bimodal Pt/C catalyst). In the following the two populations are referred to as the "smaller" and the "larger" population, respectively. The catalyst mixture was dispersed in a mixture of Milli-Q water

and IPA (water/IPA volume ratio of 3:1) to prepare about 5 mL of ink (Pt concentration of 0.5 mg/mL). To generate a suitable dispersion for further use, the mixture was sonicated for 5 min in a sonication bath (Bioblock Scientific, T 310/H, 35 kHz). After adding 38.5 µL of Nafion (Nafion/carbon mass ratio of 1), the dispersion was again sonicated for 5 min in a sonication bath.

2.3. Preparation of working electrode

The Freudenberg GDL was placed between a glass funnel and a sand core filter in a vacuum filtration setup. As described by Yarlagadda *et al.*[36] all this was placed on a collecting bottle. 4 mL of the prepared ink was diluted with 7 mL of Milli-Q water and 29 mL of IPA (water/IPA volume ratio of 1:3, Pt concentration of 0.05 mg/L). After 1 min of sonication in a sonication bath, the diluted ink was filled in a funnel. The catalyst was deposited on top of the GDL using a diaphragm vacuum pump (Vacuubrand, MZ 2C, max. 1.7 m^3/h and 9.0 mbar). The GDE was dried and stored in air. By this procedure, a nominal Pt loading of 0.208 mg cm^{-2}_{geo} was generated. For the electrochemical measurement, the GDE after vacuum filtration was cut in circles with a diameter of 1 cm.

2.3.1. Electrochemical cell and measurement

A transmission diffraction cell introduced before[34] was used with Ar saturated 0.1 M $HClO_4$ as electrolyte. The electrolyte was degassed in a bubbler before being introduced into the top of the cell, pumped out of the top of the cell, and recirculated back to the bubbler.

Activation of the catalyst was done by 10 cyclic voltammograms (CVs) between 0.06 and 1.0 V versus reversible hydrogen electrode (V_{RHE}) using a scan rate of 50 mV/s. ASTs applying potential steps between 0.6 and 1.0 V_{RHE} (3 s holding per potential) simulating load-cycle conditions in a fuel cell vehicle were performed.

2.4. Transmission electron microscopy (TEM)

TEM was performed with a Jeol 2100 microscope, operated at 200 kV. At least five different areas of the TEM grid were imaged at a minimum of three different magnifications. The NP diameter was determined by measuring at least 200 NPs with the imageJ software. The Pt/C catalysts were dispersed in ethanol and drop cast onto Quantifoil grids.

2.5. Small-angle X-ray scattering (SAXS)

The SAXS and WAXS pattern were collected with a 77.0 keV beam and reduced as described previously.[37] The beam size was focused to approximately 5 x 2 µm (horizontal x vertical). In grazing-incidence mode a depth profile was performed, see Figure S1 and S2 as an example. Three different

depths were analyzed (referred to as depth 4, 8, and 12). Depth 4 was chosen as it is the first layer showing Pt pattern in WAXS, i.e., the layer closest to the electrolyte, and the SAXS pattern of depth 4 were analyzed using depth 3 as background. Depth 8 shows the maximum intensity in the SAXS diffraction i.e., the layer in the middle of the catalyst layer, and was analyzed using depth 18 as background. Depth 12 is deeper inside the catalyst layer and was analyzed using depth 18 as background.

An initial scan was performed before electrolyte was added to the cell. To ensure that the surface of the particles was fully reduced, the cell was held at 0.6 V_{RHE} during X-ray data collection. Details about the measurement protocol during AST can be found in the SI, see Table S1.

The SAXS data analysis after background subtraction was performed as described previously [27,29,38–40] using a polydisperse spheres model. The radially averaged intensity I(q) is expressed as a function of the scattering vector $q = 4\pi \cdot \sin(\theta)/\lambda$, where λ is the wavelength and 2θ is the scattering angle. The background-corrected scattering data were fitted using a model of one or two polydisperse spheres described by a total volume distributed (i.e., volume-weighted) log-normal distribution. A hard-sphere form factor $F(R_2,\eta_2)$ was used.[41] The scattering data are fitted to the following expression:

$$I(q)= C_1 \cdot \int P_{s1}(q,R) V_1(R) D_1(R) dR + C_2 \cdot F(R_2,\eta_2) \int P_{s2}(q,R) V_2(R) D_2(R) dR$$

C_1 and C_2 are scaling constants, P_{s1} and P_{s2} the sphere form factors, V_1 and V_2 the particle volumes and D_1 and D_2 the log-normal size distribution. The normalized sphere form factor is given by: [42,43]

$$P_s(q,R)= \left(3\frac{\sin(qR)-qR\cos(qR)}{(qR)^3}\right)^2$$

and the log-normal distribution by:

$$D(R)=\frac{1}{R\sigma\sqrt{2\pi}}\exp\left(\frac{-\left[\ln\left(\frac{R}{R_0}\right)\right]^2}{2\sigma^2}\right)$$

where σ is the variance and R_0 (evaluated in Å) the geometric mean of the log-normal distribution. The fitting was done using a home-written MATLAB code (available on request). The free parameters in the model are C_1, R_1, σ_1, C_2, R_2, σ_2, η_2. The values obtained for these parameters are reported in Table S2. To account for the two populations, the reported probability density functions were weighted by the relative surface contribution of the spheres (to point out the electrochemical contribution of the population) as detailed in the SI. Details about the determination of the mean particle sizes and deviation for the log-normal distributions are found in Table S2.

2.6. Wide-angle X-ray scattering (WAXS)

WAXS analysis was done by performing Rietveld refinement using GSAS-II[44], as previously described[34]. The structural model used for refinement consisted of two platinum *fcc* phases (Fm-3m) of the same lattice constant *a*. The lattice constant was obtained from refinement with a single *fcc* phase (a = 3.9046(6)). The mean particle sizes obtained from SAXS were used as input parameter in the WAXS refinement as the volume-weighted average number of coherent scattering domains, which are calculated from the full-width-at-half-maximum of reflections refined with only Lorentzian line shapes.[34] In this approach, we assume that no strain effects contribute to the broadening of reflections in the diffraction pattern. The contribution of the instrumental profile to broadening of the Bragg peaks can be neglected based on the refinement of the CeO_2 calibrant: For the ceria NIST standard (380 nm), the instrumental profile contributes less than 10 % to the width of the Bragg peaks. Therefore, no instrumental profile correction was included for the Rietveld refinement of the nanoparticles as the effect is insignificant compared to the peak broadening from the platinum nanoparticles and a complex model is further needed to account for the cell geometry.[22] The background was described by a diffraction pattern from the grazing incident scan with minimal platinum content (depth 3) to describe the carbon background correctly.

The phase fraction is determined based on the crystallite sizes used as input values during the Rietveld refinement, which is not identical to the SAXS mean particle size. Therefore, we studied the influence of slight variations of the input values of the crystallite sizes. The input domain sizes were shifted by ± 0.5 or ± 1.0 nm in three different ways in the WAXS refinement of the diffraction pattern of different depths, see Figure S7. First, the mean particle size of the larger population is changed by ± 0.5 and ± 1.0 nm while the size of the smaller population is kept constant. Second the size of the larger population is kept constant while the size of the smaller population is changed by ± 0.5 nm. Third, the sizes of both populations are changed at the same time in the same direction by ± 0.5 nm. The fractions obtained by varying the input domain sizes are found in the SI. These tests confirmed that the observed trend for the change in the two particle population fractions is not an artifact of using the input of mean particle sizes from the SAXS fitting as the crystallite size. Details about the WAXS measurement protocol during AST are found in the SI.

3. Results and discussion

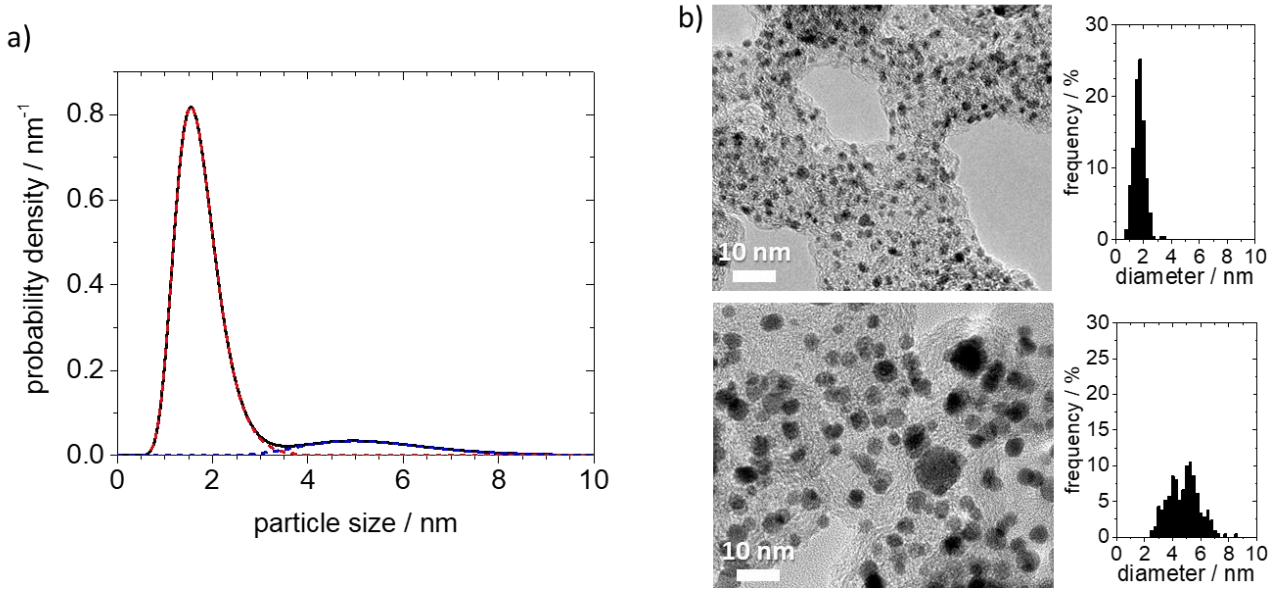

Figure 1. a) Calculated probability density function of the particle size of the as-prepared bimodal catalyst (black line) together with the probability densities of the separate size populations (dashed red and blue lines of the small and large size population, respectively) in a depth close to the electrolyte-catalyst interface derived from the SAXS data. b) TEM micrographs and size histograms of the two individual Pt/C catalysts that were mixed to obtain the bimodal Pt/C catalyst.

The aim of this work is to investigate the depth-dependent degradation mechanism(s) within a Pt/C fuel cell catalyst layer subjected to simulated load-cycle conditions. As main analytical tool, a combination of *operando* SAXS and WAXS was used to obtain precise information on the mean particle sizes and crystallite size fractions as a function of the duration of the AST protocol. To induce and uncover electrochemical Ostwald ripening, i.e., the growth of larger NPs at the expense of smaller ones, a bimodal Pt/C catalyst obtained by mixing two different commercial Pt/C catalysts with distinguishable size populations, was studied, see Figure 1. The here applied grazing-incidence mode allows a straightforward selection not only of different spots at the same depth (same x-y planes) in the catalyst layer, but additionally z-scans can be performed[45] to investigate if the degradation depends on the distance of the NPs to the electrolyte-catalyst interface, see Figure S1 for a scheme of the x-, y-, z-directions relative to the electrolyte-catalyst interface.

Before discussing the influence of the AST protocol on the catalyst particles, we first introduce the combination of SAXS and WAXS analysis based on the pristine catalyst in a z-direction close to the electrolyte-catalyst interface, see grey scattering and diffraction data in Figure 2. Based on the fact that the bimodal Pt/C catalyst is the result of mixing two individually characterized Pt/C catalysts in

known metal ratio (0.4:0.6 based on metal weight percentage of the two catalysts), the determined mean particle sizes and phase fractions in the bimodal Pt/C catalysts can be compared to the "expected values". The analysis shows that the mean particle size of both populations of the bimodal catalyst can be determined by SAXS data analysis with high accuracy. However, a quantitative analysis of the relative number of NPs in the two size populations was difficult. The particle diameters and their standard deviations retrieved from the log-normal distributions obtained from the SAXS data are 1.7 ± 0.5 and 5.5 ± 1.5 nm, see Figure 1a, Figure 3a, and Table S2 for details about the fitting parameters. Comparing the individual catalysts in Figure 1 with the prepared bimodal catalyst, it is demonstrated that the SAXS results are in good agreement with the TEM data of ca. 2 and ca. 5 nm average size. Although the expected relative number of NPs in the two size populations could be fitted to the SAXS data, in simulations the fit is ambiguous in this respect, i.e., no one-to-one correspondence between the intensities of the two populations of the same scattering data is found. However, this is not the case for the mean particle sizes, which remain the similar in simulations of different phase fractions of the two populations.

To address this limitation, we took advantage of WAXS data. The WAXS diffraction patterns clearly show the typical Bragg peaks of the platinum *fcc* phase which are convoluted with the signals of the carbon and polymer background at low 2θ angles, see Figure S2. From an angular range of six 2θ onwards, the platinum reflections are virtually free of background and can readily be analyzed by Rietveld refinement.[45] Simultaneously varying both the fraction and crystallite size of the two populations of Pt NPs in the Rietveld refinement of WAXS data was not feasible due to the intertwining of these variables, as only one population with an average coherent domain size was obtained. Therefore, we used the mean particle size of the two populations derived by the SAXS fitting as pre-defined input values in the Rietveld refinement of the WAXS data. Two platinum phases of different coherent domain sizes (input of SAXS mean particle sizes) were used as the structural model in the Rietveld refinement. Although, the mean particle size derived from the SAXS fitting is not identical with the coherent domain size in diffraction, the two parameters are closely related.[34] In this way the fractions of the platinum phases, i.e., their mass ratios, can be determined for the two size populations of Pt NPs. A representative refinement showing the two platinum phases of the structural model with different crystallite sizes is depicted in Figure S6. The obtained ratio of the smaller to the larger population of 0.44:0.56 in the pristine sample close to electrolyte-catalyst interface obtained from the combined SAXS and WAXS data analysis is in good agreement with the theoretical ratio of 0.4:0.6 expected from the sample preparation procedure, see Figure 3b. Thus, the combination of *operando* SAXS and WAXS simultaneously generates the data to readily evaluate

both the size evolution of the two size populations and the fractions of the two size platinum crystallite domains of the bimodal Pt/C catalyst.

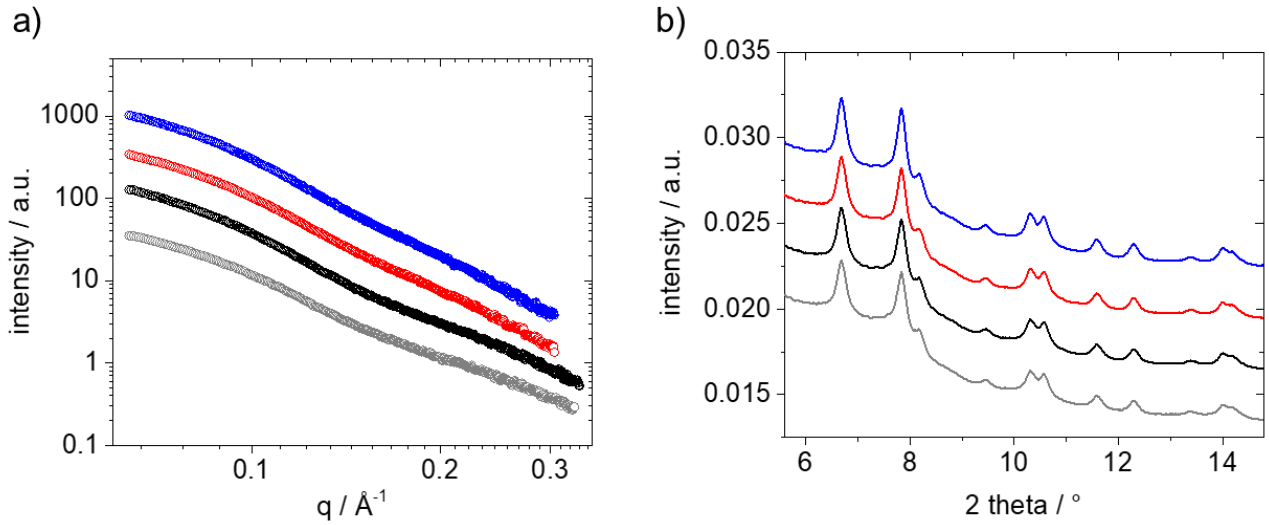

Figure 2. a) Background subtracted SAXS scattering data and b) WAXS diffractograms in an angular range from 5 to 15 ° 2 theta in the depth close to the electrolyte-catalyst interface: initial (grey), after catalyst cleaning (black), after 2500 AST cycles (red), after 5000 AST cycles (blue). The increase of the height and narrowing of the peaks of the diffractogram during the AST protocol imply an increase in particle size, which is in agreement with the mean particle size results. The data in a) and b) are shown with a vertical offset to improve visibility of the different datasets.

Before addressing the results on the influence of the AST protocol in detail, it should be mentioned that, at the beginning of an electrochemical experiment Pt/C catalysts typically need to be cleaned by cycling the electrode potential, see experimental section for details. Insertion of the catalyst into the *operando* cell[34], establishing electrochemical contact, and the applied cleaning procedure slightly affects the starting conditions. This effect can be seen by the fact that after electrolyte contact and the cleaning CVs the fraction of smaller NPs increases from 0.44:0.56 to 0.48:0.52 with respect to the larger size population, see Figure 3a, while the mean particle sizes remain relatively less affected as can be seen from the SAXS fitting, see Figure 3b. Such finding could be related to a pronounced Pt NP loss upon electrolyte contact during the cleaning CVs. Pt dissolution upon establishing electrochemical contact has been described by Pizzutilo *et al.*[8] by coupling scanning flow cells (SFC) with inductively coupled plasma mass spectrometry (ICP-MS). Interestingly, here the change in phase fraction and the absence of changes in mean particle size of the two populations suggest a particle loss phenomenon with a higher loss of NPs in the large population. A preferential detachment of the larger particles would be in line with previous investigations by Mayrhofer *et al.*[10] and Hartl *et al.*[16]

who demonstrated particle loss for the exact same catalyst that constitutes the larger fraction in the present work, see also discussion below. The periodically performed CVs, recorded after the AST treatment (see Table S1 for the related protocol) to determine the H_{upd} and to confirm electrochemical contact, however, did not influence the mean particle size; see overlap of the blue filled circles (after CV) and the blue circles in Figure 3a. Therefore, in the following all changes observed during the measurements are assigned to the applied AST protocol.

The effect of the AST treatment on the catalyst is analyzed first at a depth close to the electrolyte-catalyst interface. Representative *operando* SAXS and WAXS data of the initial Pt/C catalyst, after catalyst cleaning, after 2500, and after 5000 AST cycles are shown in Figure 2. Based on the mean particle size changes obtained from the SAXS data (see Figure S4 and Table S2) three main observations are made, see Figure 3a. First, both populations of the catalyst located in the catalyst layer close to the electrolyte-catalyst interface increase in size. Second, at the beginning of the AST, the increase in size per treatment cycle is more pronounced than at the end of the AST. Third, the increase in size of the population of the larger particles is less pronounced (from 5.48 ± 1.45 to 5.87 ± 1.61 nm, size increase of around 7 %) than the size increase of the smaller particles (1.76 ± 0.48 to 2.42 ± 0.79, size increase of around 50 %), see Figure 3a. The observation of a more pronounced size increase at the beginning of the AST as compared to that during the AST is in line with previous findings.[3,8,18] But the finding that both distributions increase in size is not in obvious agreement with an electrochemical Ostwald ripening process. In particular, when Ostwald ripening would occur between the two size populations, a homogeneous dissolution of Pt NPs in the smaller population could be expected to lead to a decrease in the mean particle size of this population. Hence, the observed behavior is more in line with a preferential dissolution of smaller Pt NPs *within* the small population thus shifting the average particle size to larger values. The increase in average particle size of the large population then can be explained by either electrochemical Ostwald ripening or the same phenomena, i.e., preferential dissolution of smaller NPs *within* the large population. So, dissolution of the smaller particles followed by Ostwald ripening seems to occur *within* but not between both populations. As a consequence, Ostwald ripening is a very local process in the nanometer scale that does not include pronounced redeposition of dissolved Pt ions on neighboring catalyst flakes of the two different catalysts. Such mechanism would be an agreement with the Pt species being mobile on the carbon support as previously proposed by Ferreira *et al.*[5] Diffusion of soluble Pt species on a larger scale does not lead to Ostwald ripening, however, in an MEA environment to Pt precipitation due to hydrogen crossover.

If there would be a substantial Ostwald ripening process between the two populations, the relative number of particles in the two populations should dramatically change as a result of the AST treatment.

Analyzing the relative number of particles in the two populations, i.e., the phase fraction, it is seen that indeed the phase fraction of the smaller size population decreases when applying the AST protocol. The relatively small change in phase fraction, however, suggests that the observed effect is more likely the sole result of a particle size dependent Pt dissolution. Additionally, during the AST protocol, preferential NP dissolution within both populations leads to an increase in the mean particle size. Due to the size difference of both populations, the absolute number of particles in the small population decreases with respect to the large population.

Trying to understand the depth dependence of the degradation mechanism, the changes of the particle size and the phase fraction were also analyzed in a "middle depth" with respect to the electrolyte-catalyst interface.

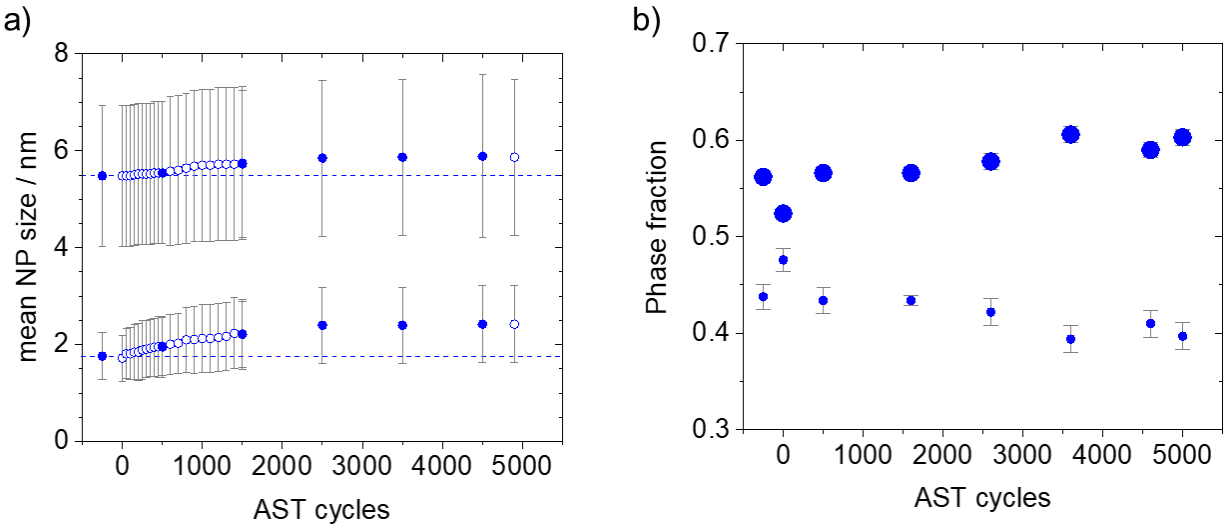

Figure 3. a) Mean particle size of the bimodal Pt NP/C catalyst in the depth close to the electrolyte-catalyst interface plotted together with the standard deviation of a log-normal distribution applying load-cycle conditions as AST protocol in an operando cell after the AST cycles (blue open circles) and after performed CVs (blue filled cycles). b) Phase fractions of the two size populations (small and large circles, for the smaller and larger size populations, respectively) obtained from Rietveld refinement of in the depth close to electrolyte-catalyst interface, keeping the particle sizes determined via SAXS constant. The data points of the pristine sample are given on the x-axis for a negative AST number.

It is seen that in both depths (close to the electrolyte-catalyst interface and in the middle catalyst depth) the mean particle size of both populations increases with the AST treatment. This confirms that the complete catalyst layer is electrochemically active and thus connected, see Figure 4a. Based

on the observations we can identify four common characteristics for the two depths analyzed. First, the particle size and the size change during the AST of the larger population are similar in the two depths. Second, the particle size of the smaller size population increases in a more pronounced way than the particle size of the larger population (from 2.43 ± 0.67 to 3.52 ± 0.68 nm (size increase of around 45 %) and from 5.50 ± 1.17 to 5.99 ± 1.15 nm (size increase of around 9 %) in the middle catalyst layer depth). Third, the relatively size increases of the two population are comparable in the depth close to the electrolyte-catalyst interface (7 and 50 % for the small and large population, see blue circles in Figure 4a) or in the middle of the catalyst layer (9 and 45 %, see black circles). Fourth, the particle size change of the larger population seems to be independent of the depth. However, there is also a distinct difference between the two depths. Close to the electrolyte interface, the smaller population is characterized by a slightly smaller particle size than the smaller population in the middle depth. This size difference is apparent already before the start of the AST protocol. On the contrary, comparing the scattering data at two different positions of the same depth in the middle of the catalyst layer in Figure S5, it is confirmed that these observations are representative for the macroscopic catalyst layer, i.e., the changes in particle size of the two populations are identical at both x-y positions in the layer.

The obtained ratio of the smaller to the larger population of 0.46:0.54 in the pristine sample in the middle of the catalyst layer is comparable to the theoretical ratio of 0.4:0.6. Again, after electrolyte contact and the cleaning CVs, the fraction of the smaller NPs increases to 0.51:0.49 with respect to the larger size population, see Figure 4b, while the mean particle sizes remain unchanged as can be seen from the SAXS fitting, see Figure 4a. This phenomenon is similar to that observed in the depth close to the electrolyte-catalyst interface, see Figure 3a und b. However, applying the AST, the phenomenon of an increase in the fraction of smaller NPs continues during further AST cycles. It is found that the fraction of the smaller as compared to the larger population in the middle of the catalyst layer continuously increases to reach a value of 0.6:0.4 at the end of treatment, see Figure 3c. Concomitantly, the particle sizes in both populations increase, see Figure 3a.

This behavior of the Pt/C catalyst in the middle of the catalyst layer is unexpected. It would be more intuitive to observe a growth of the NPs and a decrease of the smaller NP fraction, e.g., when Ostwald ripening is the main degradation process. Therefore, we analyzed additional data obtained from different z-directions at a third depth closer to the GDL, i.e., deeper inside the catalyst layer. The analysis of the SAXS and WAXS data in the depth far away from the electrolyte-catalyst interface show the same unexpected results in change of the mean particle sizes and the phase fractions as observed in the middle catalyst layer, see Figure 4a and c. To explain those observations, several scenarios can be considered. An enhanced dissolution of the larger particles seems to be unlikely. In

addition, a migration of smaller particles from the upper catalyst layers could explain the observation but seems unlikely as well. However, a preferential particle detachment due to support oxidation as documented before of the same catalyst with larger particles[10,16] could explain the findings.

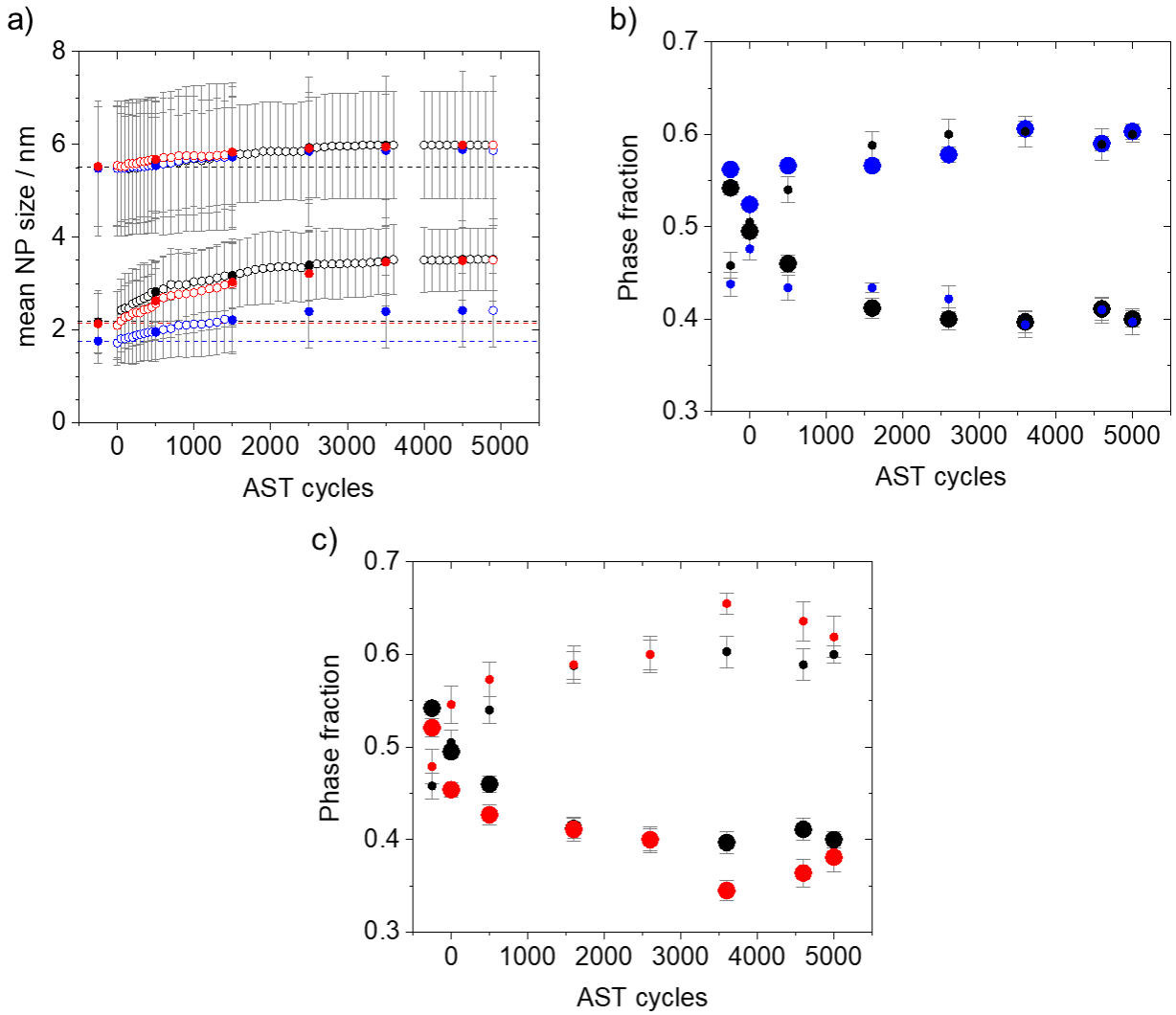

Figure 4. a) Mean particle size of the bimodal Pt NP/C catalyst plotted together with the standard deviation of a log-normal distribution applying load-cycles conditions as AST protocol in an *operando* cell after the AST cycles (empty circles) and after CVs (filled circles) close to the electrolyte (blue), in the middle depth (black), and deeper inside the catalyst layer (red). Phase fractions of the two size populations (small and large circles, for the smaller and larger size populations, respectively) obtained from Rietveld refinement of the different depth keeping the particle sizes determined via SAXS constant, b) close to the electrolyte (blue) and in the middle catalyst layer (black), c) in the middle (black) and deeper inside the catalyst layer (red) (the red filled circles are placed in front of the red circles, due to an overlap the black circles are sometimes covered). The data points of the pristine sample are given on the x-axis for a negative AST number.

In this context, it is important to point out that refinement of the diffraction pattern yields a relative and not an absolute number for both populations. Hence, the increase in the fraction of the smaller population could also be explained by a loss of the larger particles. Such a particle detachment of larger particles followed by dissolution but without redeposition was observed before by Mayrhofer *et al.*[10] and Hartl *et al.*[16] by performing IL-TEM in an RDE setup. Stronger support-particle interaction of the larger particles due to the larger contact area with the support, as compared to smaller ones, could indicate that larger particles interact more strongly with the support and might migrate and detach less.[46] However, the support-particle interaction is determined by other factors, e.g., by the degree of graphitization of the carbon support.[47] The observed preferential particle detachment of larger NPs indicates a degradation scenario based on the support-particle interaction being a combination of both the nature of particles and support. Assuming such a possible detachment of the larger NPs inside the catalyst layer, the NPs have a certain probability to redeposit onto the support during their pathway through the pores of the catalyst layer. Hence, the number of larger particles inside the catalyst layer is decreasing while it is increasing closer to the electrolyte.

4. Conclusion

The combination of *operando* SAXS and WAXS in grazing incidence configuration is used to investigate catalyst layer depth-dependent degradation of a fuel cell catalyst subjected to ASTs. A bimodal Pt/C catalyst was chosen that consists of two distinguishable particle size populations to maximize the chance to observe the expected electrochemical Ostwald ripening where the size of the larger particles in the Pt/C catalyst grows at the expense of the smaller particles. However, it is seen that the degradation mechanism is more complex. The degradation of the Pt/C catalyst close to the catalyst-electrolyte layer shows features that can be associated with preferential dissolution of small Pt particles and potentially with Ostwald ripening via Pt species mobile on the carbon support. Starting the AST, the average particle size of the smaller population slightly increases while the phase fraction decreases during the AST. The increase in average size indicates that within the population smaller particles preferentially dissolve and Pt species redeposit on the nanometer scale, the decrease in phase fraction indicates that dissolution is more pronounced in the small population.

However, in the inner catalyst layer, the phase fraction of the smaller particles increases instead. Furthermore, the mean particle size of the small population is larger at the inner catalyst layer. By comparison, the mean particle size of the larger population seems homogenous across the catalyst layer and in all cases a slight increase in size is observed during the AST. Although the increase in phase fraction of the smaller particles is difficult to explain at this point, the results show that the degradation of the Pt/C catalyst within the layers is far from being homogeneous. This raises the

question if the liquid electrolyte has any influence on the observed mechanism. Interestingly, it is seen that contacting the catalyst with the electrolyte and applying cleaning cycles, the same increase in phase fraction of the smaller particles is observed. It can be speculated that the contact of the electrolyte leads to a pronounced particle loss mechanism, as has previously been observed. In any case, the fact that the observed change in phase fraction is not associated with an increase in mean size suggests that this degradation process is not intrinsically size-dependent but more related to the different catalyst synthesis procedures of both catalysts, in particular - the 'HT' from the commercial name implied - heat treatment (TEC10E50E-HT) of the larger population may lead to a pronounced degradation upon contact to the electrolyte and by applying cleaning cycles.

In conclusion, the results suggest that Ostwald ripening is a nanoscale phenomenon most likely triggered by Pt species mobile on the carbon support. Longer scale phenomena in an MEA are related to Pt reduction via hydrogen cross-over. A significant contribution to the degradation, however, is also related to the anchoring of the nanoparticles on the support. Both effects seem to have different dependences on the distance to the solid-liquid interface. The combination of *operando* SAXS and WAXS in grazing incidence configuration is a powerful tool that also could be used to study new degradation inhibition strategies such as the design of gradient composition and particle size distributions. Furthermore, the approach demonstrated here can be easily transferred to mechanistic studies of catalyst systems with two or more size populations consisting of different metal particles.

Acknowledgements

This work was supported by the Swiss National Science Foundation (SNSF) via the project No. 200021_184742 and the Danish National Research Foundation Center for High Entropy Alloy Catalysis (CHEAC) DNRF-149. S. B. Simonsen and L. Theil Kuhn, Technical University of Denmark, are thanked for access to TEM. The authors also thank ESRF for beamtime at ID31 beamline and H. Isern and F. Russelo for technical support.

References

(1) Pollet, B. G.; Kocha, S. S.; Staffell, I. Current Status of Automotive Fuel Cells for Sustainable Transport. *Current Opinion in Electrochemistry*. Elsevier August 1, 2019, pp 90–95. https://doi.org/10.1016/j.coelec.2019.04.021.

(2) Yoshida, T.; Kojima, K. Toyota MIRAI Fuel Cell Vehicle and Progress Toward a Future Hydrogen Society. *Electrochem. Soc. Interface* **2015**, *24* (2), 45–49. https://doi.org/10.1149/2.F03152if.

(3) Marcu, A.; Toth, G.; Kundu, S.; Colmenares, L. C.; Behm, R. J. Ex Situ Testing Method to

Characterize Cathode Catalysts Degradation under Simulated Start-up/Shut-down Conditions – A Contribution to Polymer Electrolyte Membrane Fuel Cell Benchmarking. *J. Power Sources* **2012**, *215*, 266–273. https://doi.org/10.1016/j.jpowsour.2012.05.010.

(4) Katsounaros, I.; Cherevko, S.; Zeradjanin, A. R.; Mayrhofer, K. J. J. J. Oxygen Electrochemistry as a Cornerstone for Sustainable Energy Conversion. *Angew. Chemie - Int. Ed.* **2014**, *53* (1), 102–121. https://doi.org/10.1002/anie.201306588.

(5) Ferreira, P. J.; la O', G. J.; Shao-Horn, Y.; Morgan, D.; Makharia, R.; Kocha, S.; Gasteiger, H. A.; La O', G. J.; Shao-Horn, Y.; Morgan, D.; Makharia, R.; Kocha, S.; Gasteiger, H. A. Instability of Pt/C Electrocatalysts in Proton Exchange Membrane Fuel Cells. *J. Electrochem. Soc.* **2005**, *152* (11), A2256. https://doi.org/10.1149/1.2050347.

(6) Borup, R.; Meyers, J.; Pivovar, B.; Kim, Y. S.; Mukundan, R.; Garland, N.; Myers, D.; Wilson, M.; Garzon, F.; Wood, D.; Zelenay, P.; More, K.; Stroh, K.; Zawodzinski, T.; Boncella, J.; McGrath, J. E.; Inaba, M.; Miyatake, K.; Hori, M.; Ota, K.; Ogumi, Z.; Miyata, S.; Nishikata, A.; Siroma, Z.; Uchimoto, Y.; Yasuda, K.; Kimijima, K. I.; Iwashita, N. Scientific Aspects of Polymer Electrolyte Fuel Cell Durability and Degradation. *Chemical Reviews*. American Chemical Society October 2007, pp 3904–3951. https://doi.org/10.1021/cr050182l.

(7) Castanheira, L.; Silva, W. O.; Lima, F. H. B. B.; Crisci, A.; Dubau, L.; Maillard, F. Carbon Corrosion in Proton-Exchange Membrane Fuel Cells: Effect of the Carbon Structure, the Degradation Protocol, and the Gas Atmosphere. *ACS Catal.* **2015**, *5* (4), 2184–2194. https://doi.org/10.1021/cs501973j.

(8) Pizzutilo, E.; Geiger, S.; Grote, J.-P.; Mingers, A.; Mayrhofer, K. J. J.; Arenz, M.; Cherevko, S. On the Need of Improved Accelerated Degradation Protocols (ADPs): Examination of Platinum Dissolution and Carbon Corrosion in Half-Cell Tests. *J. Electrochem. Soc.* **2016**, *163* (14), F1510–F1514. https://doi.org/10.1149/2.0731614jes.

(9) Geiger, S.; Kasian, O.; Ledendecker, M.; Pizzutilo, E.; Mingers, A. M.; Fu, W. T.; Diaz-Morales, O.; Li, Z.; Oellers, T.; Fruchter, L.; Ludwig, A.; Mayrhofer, K. J. J.; Koper, M. T. M.; Cherevko, S. The Stability Number as a Metric for Electrocatalyst Stability Benchmarking. *Nat. Catal.* **2018**, *1* (7), 508–515. https://doi.org/10.1038/s41929-018-0085-6.

(10) Mayrhofer, K. J. J.; Meier, J. C.; Ashton, S. J.; Wiberg, G. K. H.; Kraus, F.; Hanzlik, M.; Arenz, M. Fuel Cell Catalyst Degradation on the Nanoscale. *Electrochem. commun.* **2008**, *10* (8), 1144–1147. https://doi.org/10.1016/j.elecom.2008.05.032.

(11) Zana, A.; Speder, J.; Reeler, N. E. A.; Vosch, T.; Arenz, M. Investigating the Corrosion of

High Surface Area Carbons during Start/Stop Fuel Cell Conditions: A Raman Study. *Electrochim. Acta* **2013**, *114*, 455–461. https://doi.org/10.1016/j.electacta.2013.10.097.

(12) Ohma, A.; Shinohara, K.; Iiyama, A.; Yoshida, T.; Daimaru, A. Membrane and Catalyst Performance Targets for Automotive Fuel Cells by FCCJ Membrane, Catalyst, MEA WG. *ECS Trans.* **2011**, *41* (1), 775–784. https://doi.org/10.1149/1.3635611.

(13) Schröder, J.; Quinson, J.; Kirkensgaard, J.; Alinejad, S.; Mints, V.; Jensen, K.; Arenz, M. A New Approach to Probe the Degradation of Fuel Cell Catalysts Under Realistic Conditions: Combining Tests in a Gas Diffusion Electrode Setup with Small Angle X-Ray Scattering. *J. Electrochem. Soc.* **2020**. https://doi.org/10.26434/chemrxiv.12263804.

(14) Meier, J. C.; Galeano, C.; Katsounaros, I.; Topalov, A. A.; Kostka, A.; Schüth, F.; Mayrhofer, K. J. J. Degradation Mechanisms of Pt/C Fuel Cell Catalysts under Simulated Start–Stop Conditions. *ACS Catal.* **2012**, *2* (5), 832–843. https://doi.org/10.1021/cs300024h.

(15) Cherevko, S.; Kulyk, N.; Mayrhofer, K. J. J. Durability of Platinum-Based Fuel Cell Electrocatalysts: Dissolution of Bulk and Nanoscale Platinum. *Nano Energy* **2016**, *29*, 275–298. https://doi.org/10.1016/j.nanoen.2016.03.005.

(16) Hartl, K.; Hanzlik, M.; Arenz, M. IL-TEM Investigations on the Degradation Mechanism of Pt/C Electrocatalysts with Different Carbon Supports. *Energy Environ. Sci.* **2011**, *4* (1), 234–238. https://doi.org/10.1039/C0EE00248H.

(17) Hodnik, N.; Zorko, M.; Bele, M.; Hočevar, S.; Gaberšček, M. Identical Location Scanning Electron Microscopy: A Case Study of Electrochemical Degradation of PtNi Nanoparticles Using a New Nondestructive Method. *J. Phys. Chem. C* **2012**, *116* (40), 21326–21333. https://doi.org/10.1021/jp303831c.

(18) Zana, A.; Speder, J.; Roefzaad, M.; Altmann, L.; Baumer, M.; Arenz, M.; Bäumer, M.; Arenz, M. Probing Degradation by IL-TEM: The Influence of Stress Test Conditions on the Degradation Mechanism. *J. Electrochem. Soc.* **2013**, *160* (6), F608–F615. https://doi.org/10.1149/2.078306jes.

(19) Arenz, M.; Zana, A. Fuel Cell Catalyst Degradation: Identical Location Electron Microscopy and Related Methods. *Nano Energy* **2016**, *29*, 299–313. https://doi.org/10.1016/j.nanoen.2016.04.027.

(20) Alinejad, S.; Inaba, M.; Schröder, J.; Du, J.; Quinson, J.; Zana, A.; Arenz, M. Testing Fuel Cell Catalysts under More Realistic Reaction Conditions: Accelerated Stress Tests in a Gas Diffusion Electrode Setup. *J. Phys. Energy* **2020**, *2* (2), 024003. https://doi.org/10.1088/2515-7655/ab67e2.

(21) Schonvogel, D.; Hülstede, J.; Wagner, P.; Kruusenberg, I.; Tammeveski, K.; Dyck, A.;

Agert, C.; Wark, M. Stability of Pt Nanoparticles on Alternative Carbon Supports for Oxygen Reduction Reaction. *J. Electrochem. Soc.* **2017**, *164* (9), F995. https://doi.org/10.1149/2.1611709JES.

(22) Souza, N. E.; Bott-Neto, J. L.; Rocha, T. A.; da Silva, G. C.; Teixeira-Neto, E.; Gonzalez, E. R.; Ticianelli, E. A. Support Modification in Pt/C Electrocatalysts for Durability Increase: A Degradation Study Assisted by Identical Location Transmission Electron Microscopy. *Electrochim. Acta* **2018**, *265*, 523–531. https://doi.org/10.1016/J.ELECTACTA.2018.01.180.

(23) Lafforgue, C.; Maillard, F.; Martin, V.; Dubau, L.; Chatenet, M. Degradation of Carbon-Supported Platinum-Group-Metal Electrocatalysts in Alkaline Media Studied by in Situ Fourier Transform Infrared Spectroscopy and Identical-Location Transmission Electron Microscopy. *ACS Catal.* **2019**, 5613–5622. https://doi.org/10.1021/acscatal.9b00439.

(24) Yu, H.; Zachman, M.; Myers, D.; Mukundan, R.; Zhang, H.; Zelenay, P.; Neyerlin, K.; Cullen, D. Elucidating Fuel Cell Catalyst Degradation Mechanisms by Identical-Location Transmission Electron Microscopy. *Microsc. Microanal.* **2021**, *27* (S1), 974–976. https://doi.org/10.1017/S1431927621003706.

(25) Speder, J.; Zana, A.; Spanos, I.; Kirkensgaard, J. J. K. K.; Mortensen, K.; Hanzlik, M.; Arenz, M. Comparative Degradation Study of Carbon Supported Proton Exchange Membrane Fuel Cell Electrocatalysts - The Influence of the Platinum to Carbon Ratio on the Degradation Rate. *J. Power Sources* **2014**, *261*, 14–22. https://doi.org/10.1016/j.jpowsour.2014.03.039.

(26) Inaba, M.; Quinson, J.; Arenz, M. PH Matters: The Influence of the Catalyst Ink on the Oxygen Reduction Activity Determined in Thin Film Rotating Disk Electrode Measurements. *J. Power Sources* **2017**, *353*, 19–27. https://doi.org/10.1016/j.jpowsour.2017.03.140.

(27) Quinson, J.; Inaba, M.; Neumann, S.; Swane, A. A.; Bucher, J.; Simonsen, S. B.; Theil Kuhn, L.; Kirkensgaard, J. J. K.; Jensen, K. M. Ø.; Oezaslan, M.; Kunz, S.; Arenz, M. Investigating Particle Size Effects in Catalysis by Applying a Size-Controlled and Surfactant-Free Synthesis of Colloidal Nanoparticles in Alkaline Ethylene Glycol: Case Study of the Oxygen Reduction Reaction on Pt. *ACS Catal.* **2018**, *8* (7), 6627–6635. https://doi.org/10.1021/acscatal.8b00694.

(28) Schröder, J.; Quinson, J.; Mathiesen, J. K.; Kirkensgaard, J. J. K.; Alinejad, S.; Mints, V. A.; Jensen, K. M. Ø.; Arenz, M. A New Approach to Probe the Degradation of Fuel Cell Catalysts under Realistic Conditions: Combining Tests in a Gas Diffusion Electrode Setup with Small Angle X-Ray Scattering. *J. Electrochem. Soc.* **2020**, *167* (13), 134515.

https://doi.org/10.1149/1945-7111/abbdd2.

(29) Alinejad, S.; Quinson, J.; Schröder, J.; Kirkensgaard, J. J. K.; Arenz, M. Carbon-Supported Platinum Electrocatalysts Probed in a Gas Diffusion Setup with Alkaline Environment: How Particle Size and Mesoscopic Environment Influence the Degradation Mechanism. *ACS Catal.* **2020**, *10* (21), 13040–13049. https://doi.org/10.1021/acscatal.0c03184.

(30) Binninger, T.; Garganourakis, M.; Han, J.; Patru, A.; Fabbri, E.; Sereda, O.; Kötz, R.; Menzel, A.; Schmidt, T. J. Particle-Support Interferences in Small-Angle X-Ray Scattering from Supported-Catalyst Materials. *Phys. Rev. Appl.* **2015**, *3* (2), 024012(6). https://doi.org/10.1103/PhysRevApplied.3.024012.

(31) Ehelebe, K.; Seeberger, D.; Paul, M. T. Y.; Thiele, S.; Mayrhofer, K. J. J.; Cherevko, S. Evaluating Electrocatalysts at Relevant Currents in a Half-Cell: The Impact of Pt Loading on Oxygen Reduction Reaction. *J. Electrochem. Soc.* **2019**, *166* (16), F1259–F1268. https://doi.org/10.1149/2.0911915jes.

(32) Speder, J.; Zana, A.; Spanos, I.; Kirkensgaard, J. J. K.; Mortensen, K.; Hanzlik, M.; Arenz, M. Comparative Degradation Study of Carbon Supported Proton Exchange Membrane Fuel Cell Electrocatalysts - The Influence of the Platinum to Carbon Ratio on the Degradation Rate. *J. Power Sources* **2014**, *261*, 14–22. https://doi.org/10.1016/j.jpowsour.2014.03.039.

(33) Quinson, J.; Röefzaad, M.; Deiana, D.; Hansen, T. W.; Wagner, J. B.; Nesselberger, M.; Crampton, A. S.; Ridge, C. J.; Schweinberger, F. F.; Heiz, U.; Arenz, M. Electrochemical Stability of Subnanometer Pt Clusters. *Electrochim. Acta* **2018**, *277*, 211–217. https://doi.org/10.1016/j.electacta.2018.04.211.

(34) Martens, I.; Chattot, R.; Rasola, M.; Blanco, M. V.; Honkimäki, V.; Bizzotto, D.; Wilkinson, D. P.; Drnec, J. Probing the Dynamics of Platinum Surface Oxides in Fuel Cell Catalyst Layers Using in Situ X-Ray Diffraction. *ACS Appl. Energy Mater.* **2019**, *2* (11), 7772–7780. https://doi.org/10.1021/acsaem.9b00982.

(35) Park, Y.-C.; Kakinuma, K.; Uchida, M.; Tryk, D. A.; Kamino, T.; Uchida, H.; Watanabe, M. Investigation of the Corrosion of Carbon Supports in Polymer Electrolyte Fuel Cells Using Simulated Start-up/Shutdown Cycling. *Electrochim. Acta* **2013**, *91*, 195–207. https://doi.org/10.1016/j.electacta.2012.12.082.

(36) Yarlagadda, V.; McKinney, S. E.; Keary, C. L.; Thompson, L.; Zulevi, B.; Kongkanand, A. Preparation of PEMFC Electrodes from Milligram-Amounts of Catalyst Powder. *J. Electrochem. Soc.* **2017**, *164* (7), F845–F849. https://doi.org/10.1149/2.1461707jes.

(37) Martens, I.; Vamvakeros, A.; Martinez, N.; Chattot, R.; Pusa, J.; Blanco, M. V.; Fisher, E. A.; Asset, T.; Escribano, S.; Micoud, F.; Starr, T.; Coelho, A.; Honkimäki, V.; Bizzotto, D.;

Wilkinson, D. P.; Jacques, S. D. M.; Maillard, F.; Dubau, L.; Lyonnard, S.; Morin, A.; Drnec, J. Imaging Heterogeneous Electrocatalyst Stability and Decoupling Degradation Mechanisms in Operating Hydrogen Fuel Cells. *ACS Energy Lett.* **2021**, 2742–2749. https://doi.org/10.1021/ACSENERGYLETT.1C00718.

(38) Schröder, J.; Quinson, J.; Mathiesen, J. K.; Kirkensgaard, J. J. K.; Alinejad, S.; Mints, V. A.; Jensen, K. M. Ø.; Arenz, M. A New Approach to Probe the Degradation of Fuel Cell Catalysts under Realistic Conditions: Combining Tests in a Gas Diffusion Electrode Setup with Small Angle X-Ray Scattering. *J. Electrochem. Soc.* **2020**, *167* (13), 134515. https://doi.org/10.1149/1945-7111/abbdd2.

(39) Speder, J.; Altmann, L.; Roefzaad, M.; Bäumer, M.; Kirkensgaard, J. J. K. K.; Mortensen, K.; Arenz, M. Pt Based PEMFC Catalysts Prepared from Colloidal Particle Suspensions – a Toolbox for Model Studies. *Phys. Chem. Chem. Phys.* **2013**, *15* (10), 3602. https://doi.org/10.1039/c3cp50195g.

(40) Schröder, J.; Mints, V. A.; Bornet, A.; Berner, E.; Fathi Tovini, M.; Quinson, J.; Wiberg, G. K. H.; Bizzotto, F.; El-Sayed, H. A.; Arenz, M. The Gas Diffusion Electrode Setup as Straightforward Testing Device for Proton Exchange Membrane Water Electrolyzer Catalysts. *JACS Au* **2021**, *1* (3), 247–251. https://doi.org/10.1021/jacsau.1c00015.

(41) Zemb, T.; Lindner, P. *Neutron, X-Rays and Light. Scattering Methods Applied to Soft Condensed Matter*, 1st Editio.; Zemb, T., Lindner, P., Eds.; Elsevier: Amsterdam, 2002.

(42) Kajiwara, K.; Hiragi, Y. Chapter 6 Structure Analysis by Small-Angle X-Ray Scattering. *Anal. Spectrosc. Libr.* **1996**, *7* (C), 353–404. https://doi.org/10.1016/S0926-4345(96)80007-1.

(43) Garcia, P. R. A. F.; Prymak, O.; Grasmik, V.; Pappert, K.; Wlysses, W.; Otubo, L.; Epple, M.; Oliveira, C. L. P. An in Situ SAXS Investigation of the Formation of Silver Nanoparticles and Bimetallic Silver–Gold Nanoparticles in Controlled Wet-Chemical Reduction Synthesis. *Nanoscale Adv.* **2020**, *2* (1), 225–238. https://doi.org/10.1039/C9NA00569B.

(44) Toby, B. H.; Von Dreele, R. B. GSAS-II : The Genesis of a Modern Open-Source All Purpose Crystallography Software Package. *J. Appl. Crystallogr.* **2013**, *46* (2), 544–549. https://doi.org/10.1107/S0021889813003531.

(45) Martens, I.; Vamvakeros, A.; Chattot, R.; Blanco, M. V.; Rasola, M.; Pusa, J.; Jacques, S. D. M.; Bizzotto, D.; Wilkinson, D. P.; Ruffmann, B.; Heidemann, S.; Honkimäki, V.; Drnec, J. X-Ray Transparent Proton-Exchange Membrane Fuel Cell Design for in Situ Wide and Small Angle Scattering Tomography. *J. Power Sources* **2019**, *437*, 226906.

https://doi.org/10.1016/j.jpowsour.2019.226906.

(46) Kregar, A.; Kravos, A.; Katrašnik, T. Methodology for Evaluation of Contributions of Ostwald Ripening and Particle Agglomeration to Growth of Catalyst Particles in PEM Fuel Cells. *Fuel Cells* **2020**, *20* (4), 487–498. https://doi.org/10.1002/fuce.201900208.

(47) Shao-Horn, Y.; Sheng, W. C.; Chen, S.; Ferreira, P. J.; Holby, E. F.; Morgan, D. Instability of Supported Platinum Nanoparticles in Low-Temperature Fuel Cells. *Top. Catal.* **2007**, *46* (3–4), 285–305. https://doi.org/10.1007/s11244-007-9000-0.

Supporting information

Tracking the Catalyst Layer Depth-Dependent Electrochemical Degradation of a Bimodal Pt/C Fuel Cell Catalyst: A Combined *Operando* Small- and Wide-Angle X-Ray Scattering Study

Johanna Schröder,[a] Rebecca K. Pittkowski,[a,b] Isaac Martens,[c] Raphael Chattot,[c] Jakub Drnec,[c] Jonathan Quinson,[b] Jacob J. K. Kirkensgaard,[d,e] Matthias Arenz[a]

[a] Department of Chemistry and Biochemistry, University of Bern, Freiestrasse 3, 3012 Bern, Switzerland

[b] Department of Chemistry, University of Copenhagen, Universitetsparken 5, 2100 Copenhagen Ø, Denmark

[c] European Synchrotron Radiation Facility (ESRF), 71 Avenue des Martyrs, 38000 Grenoble, France

[d] Niels Bohr Institute, University of Copenhagen, Universitetsparken 5, 2100 København Ø, Denmark

[e] Department of Food Science, University of Copenhagen, Rolighedsvej 26, 1958 Frederiksberg, Denmark

[*] corresponding author: matthias.arenz@dcb.unibe.ch

SAXS and WAXS AST measurement protocol

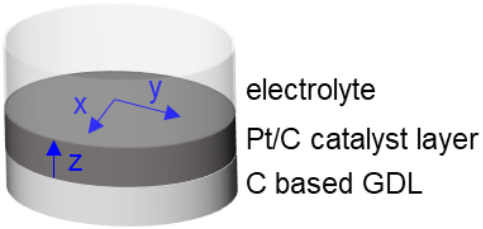

Figure S1. Orientation of the x-, y-, z-directions in the catalyst layer depending on the distance of the NPs to the electrolyte-catalyst interface.

Table S1. SAXS and WAXS measurement protocol during AST including the sample No. *after CVs for catalyst cleaning.

Cycle	**SAXS**		**WAXS**	
	Pos 1 (-17.0)	Pos 2 (-17.2)	Pos 1 (-17.0)	Pos 2 (-17.2)
Pristine	10	11	6	7
After CV*	16	17	18	19
50	20	21		
100	22	23		
150	24	25		
200	26	27		
250	28	29		
300	30	31		
350	32	33		
400	34	35		
450	36	37		
500	38	39		
After CV	40	41	42	43
600	44	45		
700	46	47		
800	48	49		
900	50	51		

Cycle	SAXS		WAXS	
	Pos 1 (-17.0)	Pos 2 (-17.2)	Pos 1 (-17.0)	Pos 2 (-17.2)
1000	52	53		
1100	54	55		
1200	56	57		
1300	58	59		
1400	60	61		
1500	62	63		
After CV	64	65	66	67
1600	68	69		
1700	70	71		
1800	72	73		
1900	74	75		
2000	76	77		
2100	78	79		
2200	80	81		
2300	82	83		
2400	84	85		
2500	86	87		
After CV	88	89	90	91
2600	92	93		
2700	94	95		
2800	96	97		
3000	98	99		
3100	100	101		
3200	102	103		
3300	104	105		
3400	106	107		

Cycle	SAXS		WAXS	
	Pos 1 (-17.0)	Pos 2 (-17.2)	Pos 1 (-17.0)	Pos 2 (-17.2)
3500	108	109		
3600	110	111		
After CV	112	113	114	115
3700	116	-		
4100	124	125		
4200	126	127		
4300	128	129		
4400	130	131		
4500	132	133		
4600	134	135		
After CV	136	137	138	139
4700	140	141		
4800	142	143		
4900	144	145		
5000	146	147	150	151

SAXS and WAXS raw data

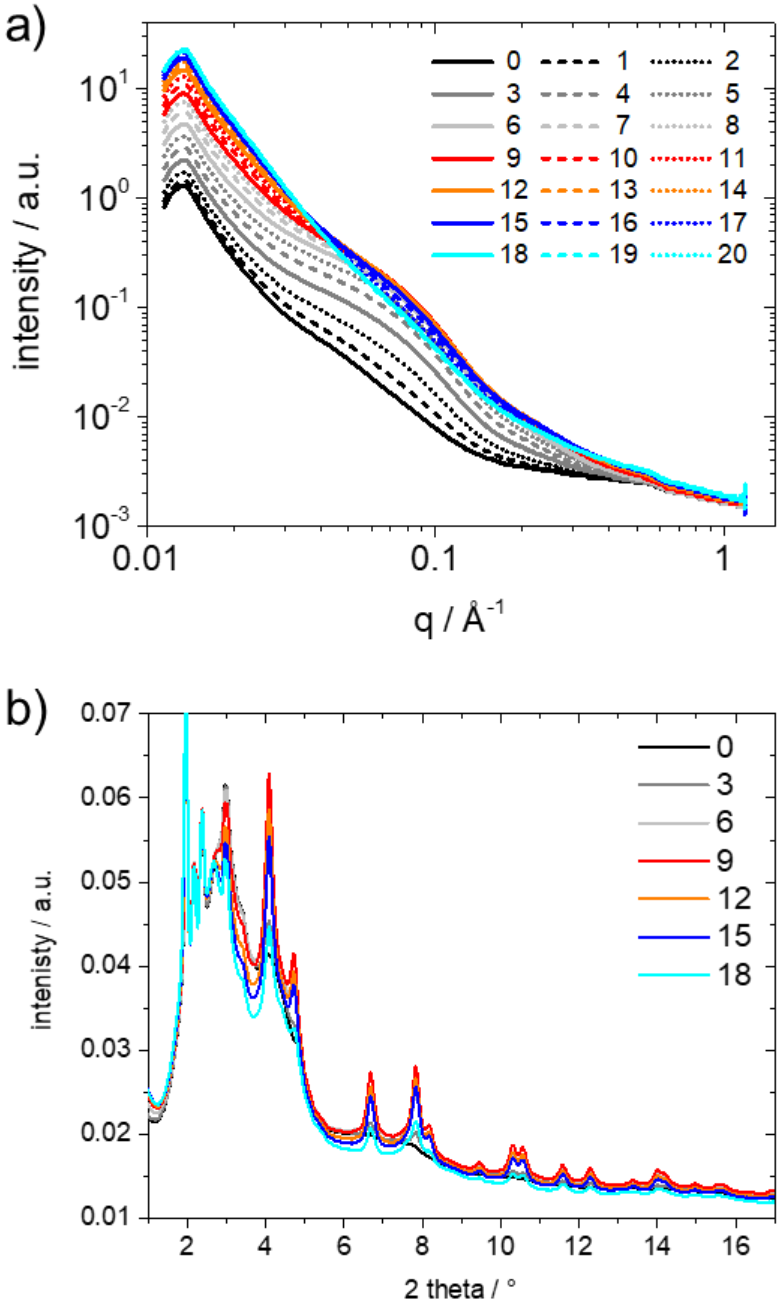

Figure S2. Depth profile of a) SAXS data and b) WAXS diffraction pattern in the initial catalyst layer. In the WAXS data intense scattering from the carbon support is observed until 6 ° 2 theta.

Details SAXS analysis and results

The average volume of nanoparticle from population 1 and from population 2, $<V>_1$ and $<V>_2$ respectively, lead to define volume fraction of population 1, Φ_{V1}, and volume fraction of population 2, Φ_{V2}, as:

$$\Phi_{V1} = \frac{N_1 < V >_1}{N_1 < V >_1 + N_2 < V >_2} = 1 - \Phi_{V2}$$

$$\frac{\Phi_{V1}}{\Phi_{V2}} = \frac{N_1 < V >_1}{N_2 < V >_2}$$

$$\frac{N_1}{N_2} = \frac{\Phi_{V1} < V >_2}{\Phi_{V2} < V >_1}$$

where N_1 and N_2 are the number of nanoparticles in the population 1 or 2 respectively.

From the SAXS data acquisition we have the relationship between the retrieved coefficient C_1 and C_2 given by $C_i = k.\ \Phi_{vi}.\ <V>_i$ where i=1 or 2 and k is a constant.

$$k = \frac{C_1}{\Phi_{V1} < V >_1} = \frac{C_2}{\Phi_{V2} < V >_2} = \frac{C_2}{(1 - \Phi_{V1}) < V >_2}$$

$$\frac{\Phi_{V1}}{1 - \Phi_{V1}} = \frac{C_1 < V >_2}{C_2 < V >_1}$$

$$\Phi_{V1} = \frac{1}{1 + \frac{C_2 < V >_1}{C_1 < V >_2}}$$

In order to weight the probability density function by the area or surface fractions we consider $<A>_1$ and $<A>_2$ as the average area of the nanoparticles from population 1 and 2, respectively:

$$\Phi_{A1} = \frac{N_1 < A >_1}{N_1 < A >_1 + N_2 < A >_2} = 1 - \Phi_{A2} = \frac{1}{1 + \frac{N_2 < A >_2}{N_1 < A >_1}}$$

$$\Phi_{A1} = \frac{1}{1 + \frac{\Phi_{V2} < V >_1 < A >_2}{\Phi_{V1} < V >_2 < A >_1}}$$

$$\Phi_{A1} = \frac{1}{1 + \frac{C_2 (< V >_1)^2 < A >_2}{C_1 (< V >_2)^2 < A >_1}}$$

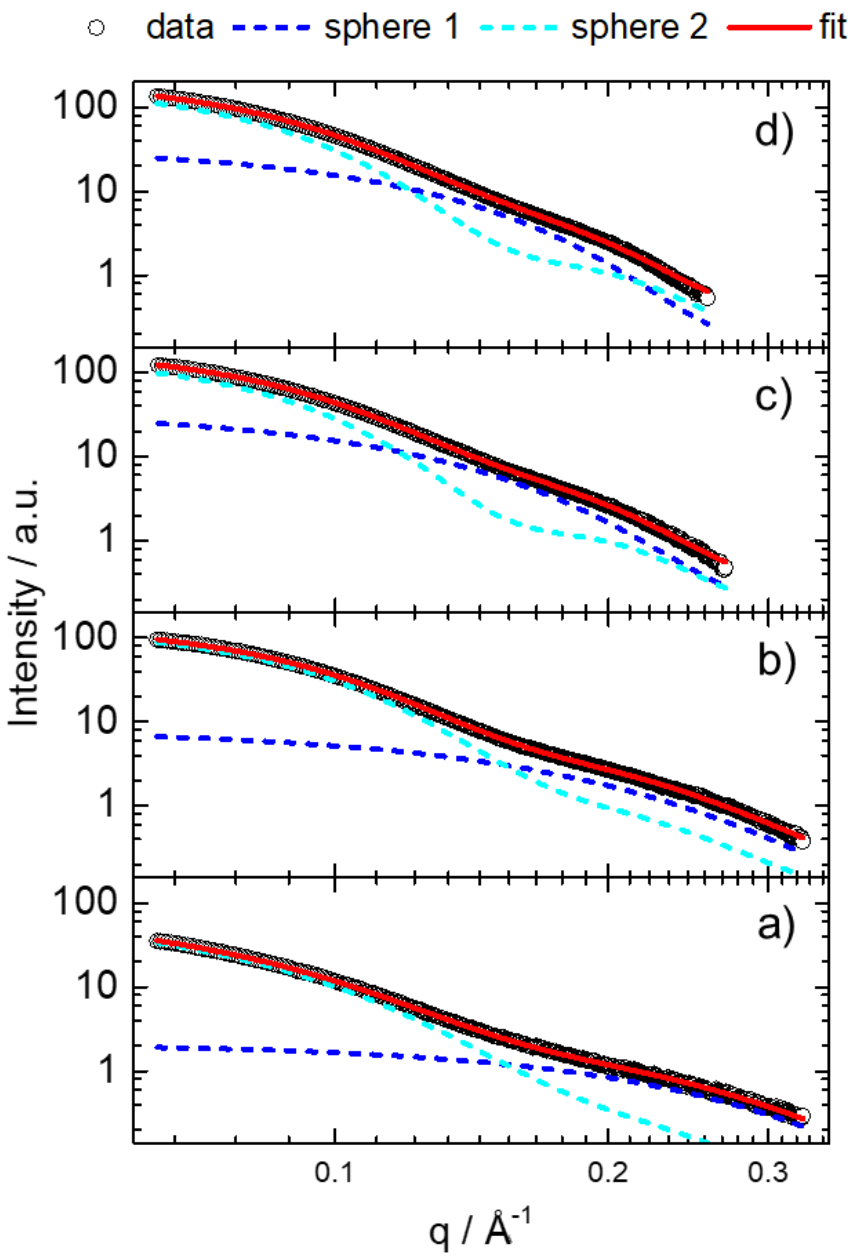

Figure S3. Representative SAXS fitting in the middle depth of the catalyst layer: **a)** initial, **b)** after activation, **c)** after 2500 cycles, **d)** after 5000 cycles.

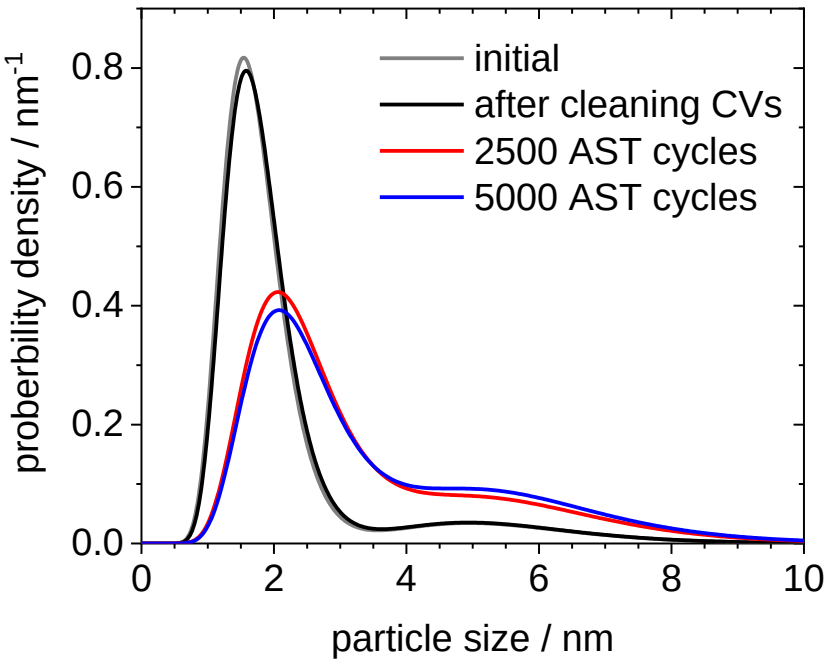

Figure S4. Probability densities obtained from the fitting of the SAXS data in a depth close to the electrolyte-catalyst interface: initial (grey), after activation (black), after 2500 cycles (red), after 5000 cycles (blue).

Table S2. Fitting parameters for SAXS data.

Sample No._depth	1st population			2nd population				Diameter and deviation / nm *			
	R_1 (Å)	σ_1	C_1 / 10^{-4}	R_2 (Å)	σ_2	C_2 / 10^{-4}	η_2	**d_1**	**σ_1**	**d_2**	**σ_2**
0010_0004	8.3	0.27	0.53	26.5	0.36	2.15	-	1.72	0.47	5.48	1.45
0016_0004	8.5	0.27	0.58	26.5	0.26	2.25	0.010	1.76	0.48	5.48	1.45
0020_0004	8.7	0.28	0.57	26.5	0.26	2.25	-	1.81	0.52	5.48	1.45
0022_0004	8.7	0.29	0.5.7	26.5	0.26	2.25	-	1.81	0.54	5.48	1.45
0024_0004	8.8	0.30	0.55	26.5	0.26	2.25	-	1.84	0.56	5.50	1.46
0026_0004	8.8	0.31	0.55	26.7	0.26	2.30	0.010	1.85	0.59	5.52	1.46
0028_0004	9.0	0.31	0.56	26.7	0.26	2.30	0.005	1.88	0.60	5.52	1.46
0030_0004	9.1	0.30	0.55	2.67	0.26	2.30	0.005	1.90	0.58	5.52	1.46
0032_0004	9.2	0.30	0.55	26.7	0.26	2.30	-	1.92	0.60	5.52	1.46
0034_0004	9.3	0.30	0.56	26.8	0.26	2.30	-	1.95	0.60	5.52	1.47
0036_0004	9.3	0.31	0.55	26.8	0.26	2.35	-	1.95	0.62	5.54	1.47
0038_0004	9.3	0.31	0.55	26.8	0.26	2.35	-	1.95	0.62	5.54	1.47
0040_0004	9.4	0.30	0.56	26.8	0.26	2.40	0.010	1.97	0.60	5.54	1.47
0044_0004	9.6	0.30	0.54	26.9	0.27	2.40	0.010	2.01	0.62	5.58	1.53
0046_0004	9.7	0.30	0.55	27.0	0.27	2.45	0.010	2.03	0.62	5.60	1.54
0048_0004	10.0	0.32	0.58	27.2	0.27	2.45	0.010	2.10	0.66	5.64	1.55
0050_0004	10.0	0.32	0.59	2.74	0.27	2.50	0.020	2.11	0.69	5.68	1.56
0052_0004	10.1	0.32	0.58	27.5	0.27	2.55	0.020	2.13	0.70	5.70	1.56
0054_0004	10.1	0.32	0.58	27.5	0.27	2.60	0.030	2.13	0.70	5.70	1.56
0056_0004	10.2	0.32	0.59	27.6	0.27	2.60	0.020	2.15	0.71	5.72	1.57
0058_0004	10.3	0.32	0.59	27.6	0.27	2.60	0.020	2.17	0.71	5.72	1.57
0060_0004	10.6	0.32	0.58	27.6	0.27	2.55	0.020	2.23	0.73	5.72	1.57
0062_0004	10.5	0.32	0.59	27.7	0.27	2.58	0.020	2.21	0.73	5.75	1.58
0064_0004	10.6	0.30	0.61	27.7	0.26	2.60	0.020	2.22	0.68	5.73	1.52
0088_0004	11.4	0.32	0.63	28.2	0.27	2.80	0.030	2.40	0.79	5.85	1.61
0112_0004	11.4	0.32	0.59	28.3	0.27	2.90	0.030	2.40	0.79	5.87	1.61
0136_0004	11.5	0.32	0.52	28.3	0.28	2.75	0.030	2.42	0.79	5.89	1.68
0146_0004	11.5	0.32	0.50	28.3	0.27	2.75	0.030	2.42	0.79	5.87	1.61
0010_0008	10.0	0.33	1.11	26.9	0.23	6.00	0.04	2.11	0.72	5.52	1.29

Sample No._depth	1st population			2nd population				Diameter and deviation / nm *			
	R_1 (Å)	σ_1	C_1 / 10^{-4}	R_2 (Å)	σ_2	C_2 / 10^{-4}	η_2	**d_1**	**σ_1**	**d_2**	**σ_2**
0016_0008	10.4	0.30	1.17	26.9	0.23	6.20	0.05	2.18	0.67	5.52	1.29
0020_0008	11.7	0.27	1.25	26.9	0.21	5.90	0.04	2.43	0.67	5.50	1.17
0022_0008	11.8	0.30	1.36	26.9	0.20	5.90	0.03	2.47	0.76	5.49	1.11
0024_0008	11.9	0.30	1.40	26.9	0.21	6.10	0.03	2.47	0.76	5.48	1.16
0026_0008	12.3	0.29	1.45	27.0	0.20	6.10	0.03	2.57	0.76	5.51	1.11
0028_0008	12.6	0.26	1.45	26.9	0.20	6.10	0.02	2.61	0.69	5.49	1.11
0030_0008	12.7	0.28	1.50	27.2	0.20	6.20	0.04	2.64	0.75	5.55	1.12
0032_0008	12.9	0.28	1.55	27.2	0.20	6.20	0.03	2.68	0.77	5.55	1.12
0034_0008	13.2	0.25	1.52	27.2	0.20	6.1	0.03	2.72	0.69	5.55	1.12
0036_0008	13.5	0.25	1.55	27.4	0.20	6.20	0.03	2.80	0.71	5.57	1.01
0038_0008	13.6	0.25	1.66	27.4	0.18	6.00	0.02	2.81	0.66	5.57	1.01
0040_0008	13.7	0.23	1.64	27.4	0.18	6.00	0.02	2.83	0.63	5.60	1.07
0044_0008	14.0	0.24	1.75	27.6	0.19	6.15	0.03	2.88	0.70	5.62	1.08
0046_0008	14.4	0.26	1.89	2.78	0.19	6.00	0.03	2.98	0.79	5.66	1.09
0048_0008	14.4	0.25	1.90	27.6	0.18	6.00	0.02	2.97	0.75	5.61	1.02
0050_0008	14.5	0.23	1.85	2.78	0.18	6.10	0.02	2.98	0.69	5.65	1.03
0052_0008	14.8	0.23	1.95	28.0	0.18	6.20	0.03	3.04	0.71	5.69	1.03
0054_0008	14.9	0.22	1.90	27.8	0.18	6.20	0.02	3.05	0.68	5.65	1.03
0056_0008	15.0	0.22	1.98	28.0	0.18	6.20	0.03	3.07	0.68	5.69	1.03
0058_0008	15.2	0.23	2.05	28.2	0.18	6.20	0.03	3.12	0.73	5.73	1.04
0060_0008	15.4	0.23	2.12	28.3	0.18	6.25	0.04	3.16	0.74	5.75	1.04
0062_0008	15.4	0.22	2.00	28.3	0.18	6.25	0.03	3.16	0.70	5.75	1.04
0064_0008	15.5	0.23	2.10	28.3	0.18	6.20	0.03	3.18	0.71	5.75	1.04
0068_0008	15.7	0.22	2.10	28.5	0.18	6.30	0.04	3.22	0.72	5.79	1.05
0070_0008	15.9	0.22	2.22	28.5	0.18	6.30	0.04	3.26	0.73	5.79	1.05
0072_0008	16.1	0.23	2.25	28.6	0.18	6.20	0.04	3.30	0.77	5.81	1.05
0074_0008	16.2	0.23	2.30	28.8	0.18	6.20	0.04	3.33	0.78	5.85	1.03
0076_0008	16.3	0.23	2.30	28.8	0.18	6.20	0.04	3.35	0.78	5.85	1.03
0078_0008	16.4	0.22	2.30	28.8	0.18	6.20	0.04	3.36	0.75	5.85	1.06
0080_0008	16.4	0.23	2.25	28.8	0.18	6.30	0.04	3.37	0.78	5.85	10.3

Sample No._depth	1st population			2nd population				Diameter and deviation / nm *			
	R_1 (Å)	σ_1	C_1 / 10^{-4}	R_2 (Å)	σ_2	C_2 / 10^{-4}	η_2	**d_1**	**σ_1**	**d_2**	**σ_2**
0082_0008	16.4	0.22	2.30	28.8	0.18	6.20	0.03	3.36	0.75	5.85	1.03
0084_0008	16.3	0.22	2.30	28.8	0.18	6.30	0.03	3.34	0.74	5.85	1.06
0086_0008	16.5	0.22	2.20	28.9	0.18	6.40	0.04	3.38	0.75	5.87	1.07
0088_0008	16.6	0.22	2.40	29.2	0.18	6.40	0.05	3.40	0.76	5.94	1.08
0092_0008	16.7	0.22	2.4	29.2	0.18	6.40	0.05	3.42	0.76	5.94	1.08
0094_0008	16.7	0.21	2.3	29.2	0.19	6.55	0.05	3.41	0.73	5.95	1.14
0096_0008	16.7	0.22	2.4	29.3	0.19	6.55	0.05	3.42	0.76	5.97	1.14
0098_0008	16.7	0.22	2.35	29.3	0.19	6.60	0.05	3.42	0.76	5.97	1.14
0100_0008	16.8	0.21	2.35	29.3	0.19	6.60	0.05	3.43	0.73	5.97	1.14
0102_0008	16.8	0.21	2.3	29.3	0.19	6.70	0.05	3.43	0.73	5.97	1.14
0104_0008	16.8	0.21	2.35	29.4	0.19	6.80	0.05	3.43	0.73	5.99	1.15
0106_0008	16.9	0.21	2.3	29.4	0.19	6.80	0.05	3.46	0.73	5.99	1.15
0108_0008	17.0	0.20	2.3	29.4	0.19	6.80	0.05	3.47	0.70	5.99	1.15
0110_0008	17.1	0.20	2.35	29.4	0.19	6.85	0.05	3.49	0.70	5.99	1.15
0112_0008	17.1	0.21	2.35	29.4	0.19	6.85	0.06	3.50	0.74	5.99	1.15
0116_0008	17.2	0.21	2.45	29.4	0.19	6.80	0.05	3.52	0.75	5.99	1.15
0124_0008	17.2	0.20	2.30	29.4	0.19	6.75	0.06	3.51	0.71	5.99	1.15
0126_0008	17.2	0.19	2.30	29.4	0.19	6.85	0.06	3.50	0.67	5.99	1.15
0128_0008	17.2	0.19	2.30	29.4	0.19	6.85	0.05	3.50	0.67	5.99	1.15
0130_0008	1.72	0.19	2.30	29.4	0.19	6.85	0.05	3.50	0.67	5.99	1.15
0132_0008	17.2	0.19	2.30	29.4	0.19	6.90	0.05	3.50	0.67	5.99	1.15
0134_0008	17.3	0.19	2.35	29.4	0.19	6.90	0.05	3.52	0.68	5.99	1.15
0136_0008	17.3	0.19	2.35	29.4	0.19	7.00	0.05	3.52	0.68	5.99	1.15
0140_0008	17.3	0.19	2.30	29.4	0.19	7.00	0.05	3.52	0.68	5.99	1.15
0142_0008	17.3	0.19	2.30	29.4	0.19	7.10	0.05	3.52	0.68	5.99	1.15
0144_0008	17.3	0.19	2.30	29.4	0.19	7.10	0.05	3.52	0.68	5.99	1.15
0146_0008	17.3	0.19	2.35	29.4	0.19	7.20	0.05	3.52	0.68	5.99	1.15
0011_0010	10.6	0.33	0.87	26.9	0.23	5.10	0.06	2.32	0.69	5.49	1.22
0017_0010	11.1	0.29	0.95	26.8	0.22	5.10	0.05	2.24	0.76	5.52	1.29
0041_0010	13.8	0.22	1.46	27.5	0.19	5.60	0.04	2.83	0.63	5.60	1.07

Sample No._depth	1st population			2nd population				Diameter and deviation / nm *			
	R_1 (Å)	σ_1	C_1 / 10^{-4}	R_2 (Å)	σ_2	C_2 / 10^{-4}	η_2	**d_1**	**σ_1**	**d_2**	**σ_2**
0065_0010	15.5	0.22	1.90	28.5	0.19	5.75	0.05	3.18	0.71	5.80	1.08
0089_0010	16.6	0.18	2.00	29.1	0.19	5.90	0.06	3.37	0.61	5.93	1.14
0113_0010	17.2	0.17	2.10	27.4	0.19	6.30	0.06	3.49	0.60	5.99	1.15
0137_0010	17.3	0.14	2.05	29.4	0.18	6.40	0.05	3.49	0.49	5.98	1.08
0147_0010	17.4	0.13	1.85	29.4	0.19	6.20	0.06	3.51	0.46	5.99	1.15
0010_0012	9.9	0.34	1.04	27.0	0.23	5.15	0.030	2.10	0.73	5.54	1.29
0016_0012	10.2	0.30	1.10	26.9	0.23	5.30	0.030	2.13	0.65	5.52	1.29
0020_0012	10.5	0.30	1.15	26.9	0.23	5.35	0.030	2.20	0.67	5.52	1.29
0022_0012	10.9	0.29	1.15	26.9	0.23	5.35	0.030	2.27	0.67	5.52	1.29
0024_0012	11.0	0.30	1.22	27.2	0.23	5.40	0.030	2.30	0.70	5.59	1.30
0026_0012	11.3	0.29	1.22	27.2	0.23	5.50	0.030	2.36	0.70	5.59	1.30
0028_0012	11.4	0.29	1.22	27.2	0.23	5.50	0.030	2.38	0.70	5.59	1.30
0030_0012	11.4	0.28	1.23	27.4	0.23	5.60	0.035	2.37	0.68	5.63	1.31
0032_0012	11.7	0.28	1.25	27.4	0.23	5.60	0.035	2.43	0.69	5.63	1.31
0034_0012	11.8	0.28	1.26	27.5	0.23	5.60	0.035	2.45	0.70	6.65	1.32
0036_0012	12.0	0.28	1.30	27.6	0.23	5.60	0.035	2.50	0.71	5.67	1.32
0038_0012	12.3	0.28	1.34	27.6	0.22	5.60	0.040	2.57	0.76	5.66	1.26
0040_0012	12.5	0.32	1.50	27.7	0.22	5.35	0.030	2.63	0.86	5.68	1.26
0044_0012	12.8	0.32	1.55	27.9	0.22	5.40	0.030	2.69	0.88	5.72	1.27
0046_0012	13.0	0.32	1.60	27.9	0.22	5.40	0.030	2.73	0.92	5.72	1.27
0048_0012	13.2	0.31	1.60	28.1	0.22	5.45	0.030	2.77	0.88	5.76	1.28
0050_0012	13.3	0.30	1.60	28.1	0.22	5.50	0.030	2.78	0.85	5.76	1.28
0052_0012	13.4	0.30	1.60	28.1	0.22	5.60	0.035	2.80	0.86	5.76	1.28
0054_0012	13.6	0.30	1.65	28.1	0.21	5.50	0.035	2.85	0.87	5.75	1.22
0056_0012	13.8	0.30	1.70	28.1	0.21	5.50	0.035	2.89	0.86	5.75	1.22
0058_0012	13.9	0.30	1.75	28.2	0.21	5.50	0.030	2.91	0.89	5.77	1.22
0060_0012	14.2	0.30	1.80	28.3	0.20	5.40	0.030	2.97	0.91	5.77	1.17
0062_0012	14.3	0.30	1.80	28.4	0.21	5.45	0.030	2.99	0.92	5.80	1.23
0064_0012	14.5	0.30	1.90	28.6	0.20	5.45	0.040	3.03	0.93	5.84	1.18
0088_0012	15.5	0.27	1.95	29.0	0.20	5.70	0.040	3.22	0.88	5.92	1.20

Sample No._depth	1st population			2nd population				Diameter and deviation / nm *			
	R_1 (Å)	σ_1	C_1 / 10^{-4}	R_2 (Å)	σ_2	C_2 / 10^{-4}	η_2	$\mathbf{d_1}$	$\boldsymbol{\sigma_1}$	$\mathbf{d_2}$	$\boldsymbol{\sigma_2}$
0112_0012	16.7	0.27	2.25	29.2	0.19	5.55	0.030	3.46	0.95	5.94	1.14
0136_0012	17.0	0.24	2.25	29.4	0.19	5.55	0.020	3.50	0.85	5.99	1.15
0146_0012	17.0	0.25	2.25	29.4	0.19	5.70	0.020	3.51	0.89	5.99	1.15

* The diameter and standard deviation are evaluated as $\mathbf{d} = 0.2\, e^{(ln(R)+\frac{\sigma^2}{2})}$ and $\boldsymbol{\sigma} = 0.2\sqrt{(e^{\sigma^2}-1)e^{(2\ln(R)+\sigma^2)}}$ separately for both size populations for a log-normal distribution. The factor 0.2 comes from changing the unit from Å to nm and the radius to the diameter.

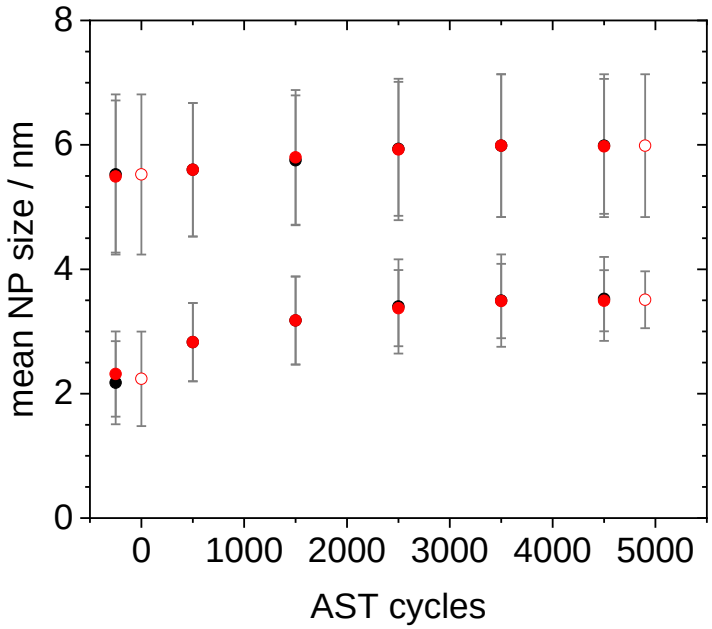

Figure S5. a) Mean particle size of the bimodal Pt NP/C catalyst plotted together with the standard deviation of a log-normal distribution applying load-cycles conditions as AST protocol in an operando cell after the AST cycles (empty circles) and after CVs (filled circles) at the first (black) and second (red) position in the middle catalyst layer.

Details WAXS analysis and results

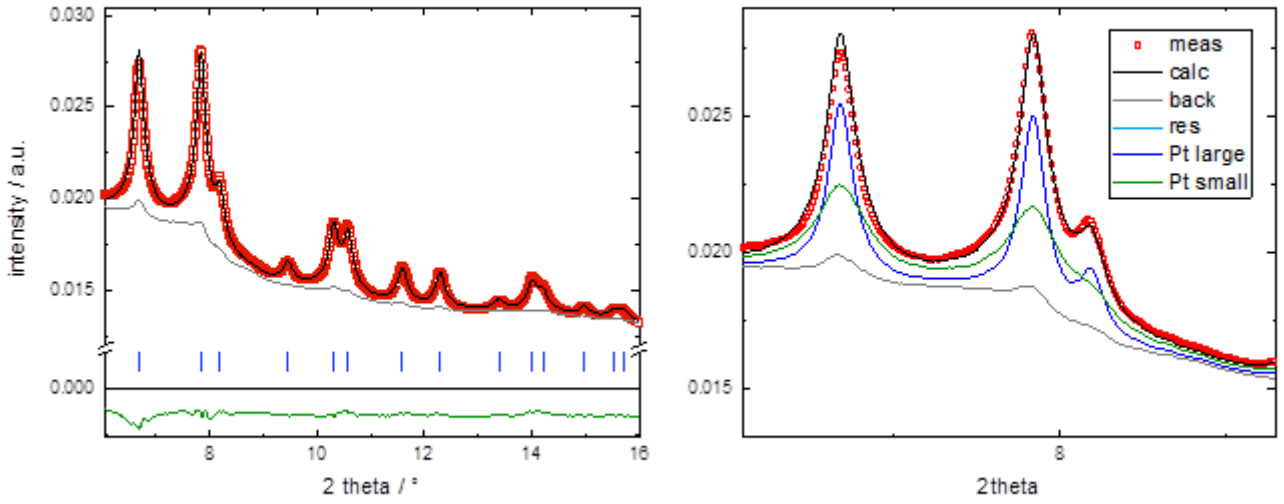

Figure S6. Representative Rietveld refinement of WAXS data based on the structural model including two platinum fcc phases (the blue dashes indicate the position of platinum reflections) of equal lattice parameter (a = 3.9046) with two different coherent domain sizes (2.1 nm and 5.4 nm) in an angular range from six to sixteen two theta (R_{wp} = 0.25 %).

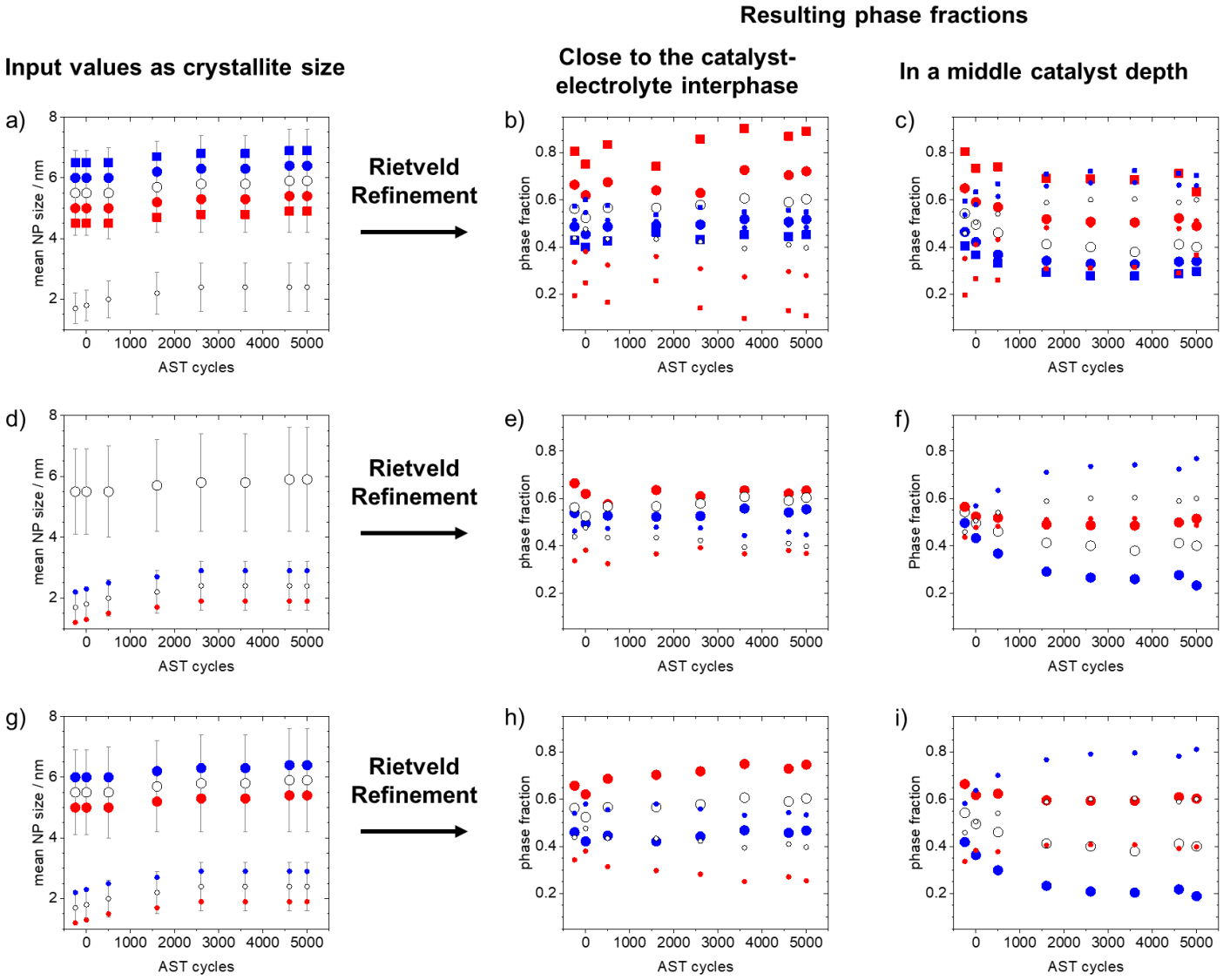

Figure S7. Change of mean particle size obtained by SAXS (a, d, g; mean particle sizes (open circle), increased sizes (in blue), decreased sizes (in red)) in the different catalyst layer depths: close to electrolyte (b, e, h), in the middle of the catalyst layer (c, f, i).

Manuscript VI:

J. Quinson, L. Kacenauskaite, J. Schröder, S. B. Simonsen, L. Theil Kuhn, T. Vosch, M. Arenz

UV-Induced Syntheses of Surfactant-Free Precious Metal Nanoparticles in Alkaline Methanol and Ethanol

The published paper is reproduced from *Nanoscale Advances*, **2020**, *2*, 2288-2292 with permission from the Royal Society of Chemistry.

https://doi.org/10.1039/D0NA00218F (Open Access)

Nanoscale Advances

ROYAL SOCIETY OF CHEMISTRY

COMMUNICATION

View Article Online
View Journal | View Issue

Cite this: *Nanoscale Adv.*, 2020, **2**, 2288

Received 18th March 2020
Accepted 8th May 2020

DOI: 10.1039/d0na00218f

rsc.li/nanoscale-advances

UV-induced syntheses of surfactant-free precious metal nanoparticles in alkaline methanol and ethanol†

Jonathan Quinson, ‡*[a] Laura Kacenauskaite,‡[a] Johanna Schröder,[b] Søren B. Simonsen, [c] Luise Theil Kuhn, [c] Tom Vosch [a] and Matthias Arenz *[b]

Surfactant-free UV-induced syntheses of Pt and Ir nanoparticles in alkaline methanol and ethanol are presented. Small size nanoparticles *ca.* 2 nm in diameter are obtained without surfactants in a wide range of base concentration.

Introduction

Nanoparticles (NPs) are key catalysts in many chemical processes.[1] In particular, precious metal NPs are in high demand for automotive,[2] energy[3] or environmental applications.[4] To best address specific needs and tailor specific features, simple synthesis strategies are crucial. In particular, the synthesis of NPs <10 nm in diameter made of precious metals like Pt or Ir plays a key role in catalysis.[5,6] Size control at the nanoscale is important to tune catalyst properties like activity,[3] selectivity[7] and stability.[3] In most colloidal syntheses, surfactants are used to achieve size control, stabilize the NPs and avoid agglomeration.[8] The later however need to be removed for catalytic applications[9] which is often performed by approaches only partially successful. In this respect surfactant-free syntheses of nanomaterials[10] and colloids bear promising features.[11]

A recently reported wet chemical surfactant-free synthesis is suitable to obtain precious metal NPs with superior catalytic activity.[12–14] This was for instance demonstrated with Pt NPs for hydrogenation reaction and Ir NPs for the oxygen evolution reaction.[12,15] The synthesis is performed at low temperature (<80 °C) and does not require harsh chemicals. Only a mono-alcohol (*e.g.* methanol or ethanol), a metal complex (*e.g.* H_2PtCl_6 or $IrCl_3$) and a base (*e.g.* NaOH) are needed. So far, mainly microwave assisted synthesis has been studied and a strong focus was given to methanol as solvent. To finely tune the size of the NPs, we study here the UV-induced synthesis of Pt and Ir NPs in alkaline methanol and ethanol and compare the results with a micro-wave oven synthesis previously reported using alkaline methanol as solvent.[12] The general approach is illustrated in Fig. 1a. Specific attention is given to NP size control and the stability of the colloids obtained without surfactants. The size of the NPs was evaluated by transmission electron microscopy (TEM). Insight into the reaction mechanism in different solvents is given by Fourier-transform infra-red absorption spectroscopy (FTIR) and head space gas chromatography coupled to mass spectrometry (GC-MS).

Results

We recently investigated the use of UV-light[16,17] to obtain surfactant-free precious metal NPs like Pt, based on the polyol synthesis using ethylene glycol as solvent.[18–20] UV-light is used in this context to induce the reduction of a metal complex like $H_2Pt(IV)Cl_6$ or $Ir(III)Cl_3$ to metallic Pt(0) or Ir(0) NPs,

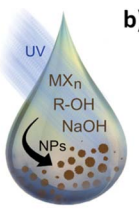

b)

Solvent	NaOH/Pt	<d> / nm	σ /nm
Methanol	0	2.6	0.8
Methanol	25	3.3	1.1
Methanol	125	2.1	0.5
Ethanol	0	2.4	0.4
Ethanol	25	2.4	0.6
Ethanol	125	2.5	0.9

Fig. 1 (a) Schematic of the UV-induced synthesis of Pt NPs by the mono-alcohol process. MX_n represents a molecular precious metal precursor, R–OH represent a mono-alcohol solvent. (b) Average diameter $\langle d \rangle$ and standard deviation σ, obtained for different solvents and different NaOH concentration for 2 mM H_2PtCl_6.

[a]*Department of Chemistry, University of Copenhagen, Universitetsparken 5, 2100 Copenhagen Ø, Denmark. E-mail: jonathan.quinson@chem.ku.dk*

[b]*Department of Chemistry and Biochemistry, University of Bern, Freiestrasse 3, CH-3012 Bern, Switzerland*

[c]*Department of Energy Conversion and Storage, Technical University of Denmark, Fysikvej Bldg. 310, DK-2800 Kgs. Lyngby, Denmark*

† Electronic supplementary information (ESI) available: Experimental section, GC-MS, fluorescence measurements and detailed Ir investigation. See DOI: 10.1039/d0na00218f

‡ These authors equally contributed to the work.

respectively.[13,21] A simple strategy to achieve size control in the surfactant-free synthesis of platinum NPs is to vary the concentration of NaOH or more precisely the NaOH/Pt molar ratio.[11] To compare the mono- with the poly-alcohol process, we performed experiments in methanol and ethanol as solvents for the same NaOH concentrations and H_2PtCl_6 concentration as previous studies with UV-induced synthesis in alkaline ethylene glycol.[16,17] This allows to investigate the effects of the different solvents for the UV-induced synthesis of Pt NPs under alkaline conditions.

First, the influence of solvent and NaOH/Pt molar ratio on the size control was studied. The size obtained in methanol and ethanol is summarised in Fig. 1b. 2 mM of H_2PtCl_6 and concentration of NaOH of 0, 50 and 250 mM were used. If methanol is used as solvent, the average diameter size is 2.6 ± 0.8 nm, 3.3 ± 1.1 nm and 2.1 ± 0.5 nm respectively. If ethanol is used as solvent, the effect of NaOH/Pt ratio on the size is less pronounced yielding NPs with diameter of 2.4 ± 0.4 nm, 2.4 ± 0.6 nm and 2.5 ± 0.9 nm, respectively.

The weak effect of the NaOH/Pt molar ratio on size control is in agreement with previous reports for the mono-alcohol process used there but performed using a microwave synthesis.[12,13] It is however in contrast with the UV-induced polyol process where the NaOH/Pt molar ratio leads to a clear size control: as the NaOH/Pt molar ratio increases, the size and size distribution decreases in alkaline ethylene glycol.[11,16,17]

Second, the general formation mechanism of the NPs was investigated to address these differences. The reduction of Pt(IV) in H_2PtCl_6 typically proceeds first *via* a reduction to Pt(II), followed by further reduction to Pt(0) and formation of NPs while the solvent or sacrificial agents get oxidised.[22,23] Head-space GC analysis, see Fig. S1,† confirms that during the reaction, oxidation products of methanol like formic acid (in absence of NaOH), methyl formate (in presence of NaOH) and CO_2 are detected. These products are consistent degradation products of formaldehyde expected to be the main product formed under the photo-degradation of H_2PtCl_6 in methanol, as previously reported without using a base.[23] In ethanol, whether or not a base is used, the same products like acetaldehyde are detected. In parallel to the nucleation and formation of NPs, ethanol undergoes further chemical reactions evidenced by fluorescence measurements whereas methanol remains free of fluorescent species after the NPs are formed, see Fig. S2.† In respect to the formation of fluorescent species alkaline methanol seems to be a 'cleaner' solvent since less side reactions seem to occur.

Another important property of colloidal NPs is their stability. Without a base and for microwave synthesis, large agglomerates are formed in the mono-alcohols upon reduction of H_2PtCl_6. In alternative syntheses, for instance in ethanol–water mixture,[24] a deposition of the Pt NPs on the cell walls is observed and no colloidal dispersions are obtained if no surfactants are used. In contrast here, using UV-induced synthesis, small size NPs with a diameter around 2.5 nm are obtained in absence of NaOH and in absence of surfactant, see Fig. 2. The size of the NPs is in agreement with NPs observed in a recent study focusing on the reduction of H_2PtCl_6 with methanol under UV radiation.[23] More importantly, the NPs obtained here are stable as colloids. This is

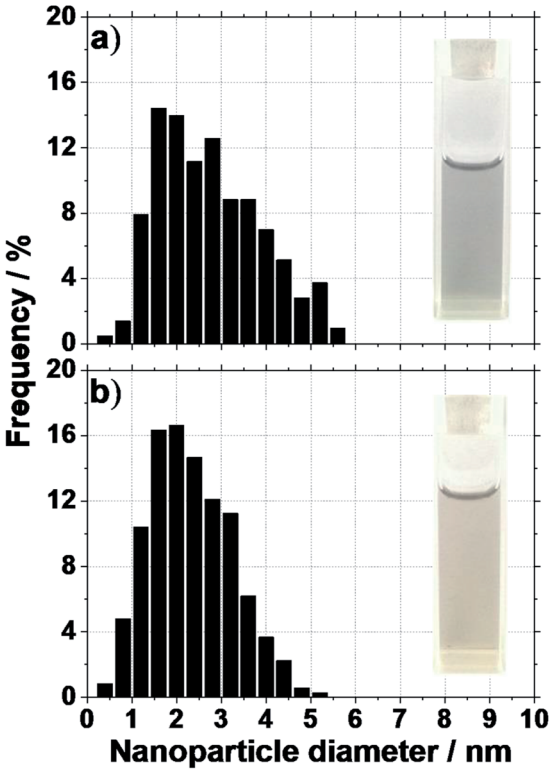

Fig. 2 Size distribution of Pt NPs obtained after 2 hours UV irradiation of a solution of 2 mM H_2PtCl_6 without NaOH in (a) methanol and (b) ethanol. Images of the solution after UV-irradiation are also displayed (volume is 3 mL).

attributed to the milder conditions (*versus* microwave synthesis) for the reaction to proceed and the relatively low concentration of H_2PtCl_6 used.

In alkaline conditions, stable colloids are also obtained. In agreement with previous reports in poly-[25] or mono-alcohols,[13] electrostatic stabilization of the surfactant-free NPs *e.g.* by OH^- groups account for the colloidal stability. The photo-reduction of H_2PtCl_6 to size controlled and stable colloidal NPs by mono-alcohols is typically performed and studied in aqueous media, in presence of photo-activators or polymers[24,26–28] and typically without adding a base. The need for additives under these conditions to initialize the photo-reaction or to stabilize the colloids is largely stressed in the literature.[24,26] However additives are typically detrimental for further applications *e.g.* in catalysis.[29] Surfactants need to be removed in typically hazardous and time consuming steps.[8] It is therefore a significant achievement to obtain surfactant-free colloidal NPs by photo-induced synthesis in alcohol-only solutions.

The NPs prepared are conveniently 'unprotected' in the meaning of previous terminology.[25] This implies that in the surfactant-free synthesis that is the mono-alcohol process, the resulting NPs are functionalized with CO and OH/OH^- groups. FTIR characterization reveals that the methanol synthesized NPs express CO functional groups (clear absorption peak between 2000-2100 cm^{-1}) whereas the ethanol based synthesis do not show a strong signal, even though a small signal

appearing as 'bump' just below 2000 cm^{-1} could indicate some CO species, see Fig. 3a. This is attributed to the more facile oxidation of the one-carbon molecule that is methanol to CO, compared to the formation of CO from the two carbon molecule that is ethanol. A pronounced shift of the CO peak position in methanol-prepared NPs towards larger wavenumber is observed: shift from 2030 cm^{-1} with NaOH to 2086 cm^{-1} without NaOH. This shift is consistent with a larger NP size[25,30] achieved in absence of a base and consistent with TEM characterization.

A different surface functionalization accounts for more stable colloidal solutions of Pt NPs obtained in methanol *versus* ethanol. Since the NPs obtained in ethanol are less 'protected' by CO groups they show less stability and a direct consequence is that they tend to agglomerate. An indirect effect of this different surface functionalization is observed during the preparation of TEM grids where NPs prepared in ethanol tend to form large aggregates (made of individual NPs), see Fig. 3d and e. The NPs obtained in methanol tend to be more isolated and individual on the TEM grid, see Fig. 3b and c. The NPs are also protected by OH^- groups due to the alkaline conditions. As a consequence, the NPs appear more distant from each other on the TEM grids when prepared in alkaline conditions, Fig. 3b and c.

At last, size control is an important feature to take into account to design synthesis strategies. An option to achieve size control in the mono-alcohol process is to add water to the reaction mixture.[12] Using a microwave reactor, adding water in the range 0–80% (volume%) lead to a size increase from *ca.* 2 nm to *ca.* 5 nm.[12] This size control is more easily achieved at high (*e.g.* 2.5 mM) H_2PtCl_6 concentration but difficult to probe at low (*e.g.* 0.5 mM) H_2PtCl_6 concentration: under microwave synthesis the solvent quickly reaches reflux conditions and a fine size control is challenging to achieve.

The UV-induced synthesis differs in that respect. Results presented in Fig. 4 were obtained using 0.5 mM H_2PtCl_6 and 10 mM NaOH. Different volume fraction of (1) 0%, (2) 20%, (3) 50%, (4) 80% and (5) 100% H_2O in methanol are used. The pictures of the solutions before and after exposure time of 2 hours under UV-light, see Fig. 4a and b respectively. For 0%, 20% and 50% water the solutions turn brown upon UV-irradiation indicative of successful NP formation. The reaction mixture containing 80% is not as brown as for the other syntheses. For 100% water the reaction does not proceed. This can be attributed to the need for a suitable alcohol–Pt ratio in order to perform the reduction of the salt while the alcohol gets oxidized for the synthesis to proceed.[13,14]

For 0% water the size is 1.4 ± 0.3 nm whereas for 50% water the size is 1.7 ± 0.3 nm, see Fig. 4c. This indicates that addition of water can control to some extent the size of the NPs in the

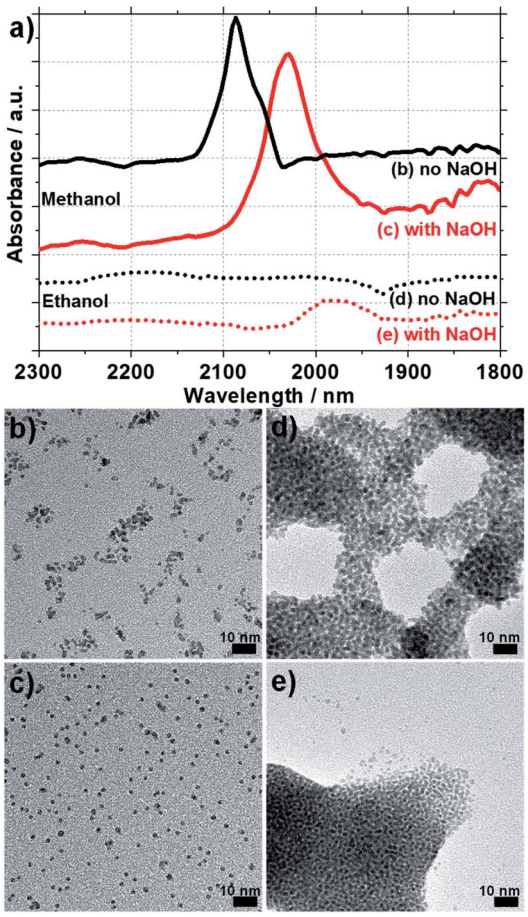

Fig. 3 (a) IR absorption spectra of Pt NP suspensions obtained with 2 mM H_2PtCl_6 without and with 250 mM NaOH in methanol and ethanol as indicated. (b–e) TEM micrographs of the Pt NPs in methanol (b) without and (c) with 250 mM NaOH and in ethanol (d) without and (e) with 250 mM NaOH.

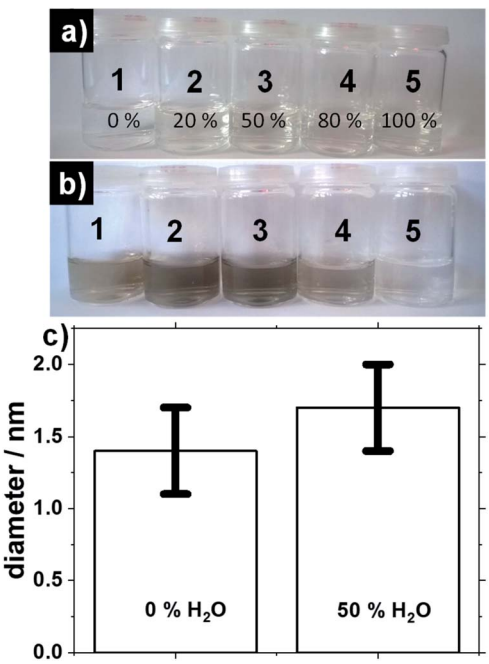

Fig. 4 Pictures of reaction mixture containing 0.5 mM H_2PtCl_6 and 10 mM NaOH in methanol (a) before and (b) after 2 hours exposure to UV-light when the solvent is methanol and (1) 0%, (2) 20%, (3) 50%, (4) 80% and (5) 100% water. (c) Average diameter obtained for the experimental conditions of 0% and 50% water in alkaline methanol.

case of UV-induced synthesis, even in the case of low H_2PtCl_6 concentration selected here to achieve a fine size control. UV-induced synthesis offers milder reaction conditions (*e.g.* lower overall temperature, no need for reflux conditions) than a microwave oven which can explain why even at low Pt concentration a fine size control is achieved by adding water.

We previously showed that Ir NPs obtained in alkaline methanol show surprisingly high catalytic activity.[12,15] The general approach presented here using UV-light is also suitable to obtain Ir NPs, see Fig. S3.† Despite using different precursors (Na_2IrCl_6, H_2IrCl_6, or $IrCl_3$), solvents (methanol, ethanol, water), amounts of water (10–25% in volume), NaOH concentrations (0–44 mM), temperatures (10–40 °C), times of synthesis (up to 24 h) and gas atmosphere (air, 5% H_2 in Ar, Ar, CO) or seed-mediated growth approaches, see Fig. S4 and details in ESI,† the size of the NPs was always in the range 1.0–1.7 nm without clear size control. The synthesis in ethanol is often significantly faster than in methanol. Adding NaOH increases slightly and working in Ar containing gas atmospheres increases significantly the NP formation rate. In contrast, a CO atmosphere is slowing down the NP formation. Different duration time of synthesis and changing reaction parameters lead to the same NP size ranges regardless of the formation kinetics. It therefore seems to be a general challenge to control the size of Ir NPs. Nevertheless, UV-induced synthesis is here shown to be suitable to produce very small Ir NPs.

Conclusions

UV-induced or thermally induced syntheses of Pt and Ir NPs by the mono-alcohol surfactant-free process show similar features. In both type of synthesis, Pt NP size control is not simply achieved by varying the NaOH concentration whereas adding water seems to give a finer size control. The NPs obtained are 'unprotected', *i.e.* show mainly CO and/or OH/OH^- functionalization. An advantageous feature of the UV-induced synthesis is that the reaction proceeds under milder reaction conditions (*e.g.* lower overall temperature). As a result, the formation of Pt NPs for instance can be achieved without NaOH. The overall synthesis is then extremely simple to obtain stable colloidal NPs of *ca.* 2–2.5 nm. For Ir NPs, the size control is generally more challenging to achieve while NPs with size < 2 nm are easily obtained. The mono-alcohol process combined with UV-induced synthesis is a promising synthesis route to further study NP formation and produce surfactant-free precious metal NPs.

Conflicts of interest

There are no conflicts to declare.

Acknowledgements

M. Johnson, M. Santella, B. Wegge Laursen and T. Just Sørensen, all University of Copenhagen, are thanked for their help and use of equipment and N. Schären, University of Bern, for performing most of the Ir NP syntheses. M. A. acknowledges support from the Villum Foundation in form of a block stipend as well as support from the Swiss National Science Foundation (SNSF) *via* the project no. 200021_184742. J.S. thanks the DFG for financial support (KU 3152/6-1). J.Q. has received funding from the European Union's Horizon 2020 research and innovation programme under the Marie Skłodowska-Curie grant agreement no 703366 (SELECTRON).

Notes and references

1 S. Olveira, S. P. Forster and S. Seeger, *J. Nanotechnol.*, 2014, 324089.
2 A. Ohma, K. Shinohara, A. Liyama, T. Yoshida and A. Daimaru, *ECS Trans.*, 2011, **41**, 775.
3 E. Antolini, *Appl. Catal., B*, 2016, **181**, 298.
4 T. Pradeep and Anshup, *Thin Solid Films*, 2009, **517**, 6441.
5 B. I. Kharisov, H. V. R. Dias, O. V. Kharissova and A. Vazquez, *J. Nanopart. Res.*, 2014, **16**, 2665.
6 M. Navlani-Garcia, D. Salinas-Torres, K. Mori, Y. Kuwahara and H. Yamashita, *Catal. Surv. Asia*, 2019, **23**, 127.
7 I. Schrader, S. Neumann, R. Himstedt, A. Zana, J. Warneke and S. Kunz, *Chem. Commun.*, 2015, **51**, 16221.
8 Z. Q. Niu and Y. D. Li, *Chem. Mater.*, 2014, **26**, 72.
9 D. G. Li, C. Wang, D. Tripkovic, S. H. Sun, N. M. Markovic and V. R. Stamenkovic, *ACS Catal.*, 2012, **2**, 1358.
10 J. Quinson, M. Inaba, S. Neumann, A. Swane, J. Bucher, S. Simonsen, L. Theil Kuhn, J. Kirkensgaard, K. Jensen, M. Oezaslan, S. Kunz and M. Arenz, *ACS Catal.*, 2018, **8**, 6627.
11 Y. R. Ouyang, H. J. Cao, H. J. Wu, D. B. Wu, F. Q. Wang, X. J. Fan, W. Y. Yuan, M. X. He, L. Y. Zhang and C. M. Li, *Appl. Catal., B*, 2020, **265**, 118606.
12 J. Quinson, S. Neumann, T. Wannmacher, L. Kacenauskaite, M. Inaba, J. Bucher, F. Bizzotto, S. B. Simonsen, L. T. Kuhn, D. Bujak, A. Zana, M. Arenz and S. Kunz, *Angew. Chem., Int. Ed.*, 2018, **57**, 12338.
13 J. Quinson, L. Kacenauskaite, J. Bucher, S. B. Simonsen, L. T. Kuhn, M. Oezaslan, S. Kunz and M. Arenz, *ChemSusChem*, 2019, **12**, 1229.
14 J. Quinson, J. Bucher, S. B. Simonsen, L. T. Kuhn, S. Kunz and M. Arenz, *ACS Sustainable Chem. Eng.*, 2019, **7**, 13680.
15 F. Bizzotto, J. Quinson, A. Zana, J. Kirkensgaard, A. Dworzak, M. Oezaslan and M. Arenz, *Catal. Sci. Technol.*, 2019, **9**, 6345.
16 L. Kacenauskaite, J. Quinson, H. Schultz, J. J. K. Kirkensgaard, S. Kunz, T. Vosch and M. Arenz, *ChemNanoMat*, 2017, **2**, 89.
17 J. Quinson, L. Kacenauskaite, T. L. Christiansen, T. Vosch, M. Arenz and K. M. Ø. Jensen, *ACS Omega*, 2018, **3**, 10351.
18 H. Dong, Y. C. Chen and C. Feldmann, *Green Chem.*, 2015, **17**, 4107.
19 F. Fievet, S. Ammar-Merah, R. Brayner, F. Chau, M. Giraud, F. Mammeri, J. Peron, J.-Y. Piquemal, L. Sicarda and G. Viaub, *Chem. Soc. Rev.*, 2018, **47**, 5187.
20 Y. Wang, J. W. Ren, K. Deng, L. L. Gui and Y. Q. Tang, *Chem. Mater.*, 2000, **12**, 1622.
21 T. S. Rodrigues, M. Zhao, T. H. Yang, K. D. Gilroy, A. G. M. da Silva, P. H. C. Camargo and Y. N. Xia, *Chem.–Eur. J.*, 2018, **24**, 16944.

22 S. M. Chen, Q. Y. Yang, H. H. Wang, S. Zhang, J. Li, Y. Wang, W. S. Chu, Q. Ye and L. Song, *Nano Lett.*, 2015, **15**, 5961.
23 M. Wojnicki and P. Kwolek, *J. Photochem. Photobiol., A*, 2016, **314**, 133.
24 M. Harada and H. Einaga, *Langmuir*, 2006, **22**, 2371.
25 I. Schrader, J. Warneke, S. Neumann, S. Grotheer, A. A. Swane, J. J. K. Kirkensgaard, M. Arenz and S. Kunz, *J. Phys. Chem. C*, 2015, **119**, 17655.
26 N. Toshima, K. Nakata and H. Kitoh, *Inorg. Chim. Acta*, 1997, **265**, 149.
27 M. Harada, K. Okamoto and M. Terazima, *Langmuir*, 2006, **22**, 9142.
28 M. Harada and Y. Kamigaito, *Langmuir*, 2012, **28**, 2415–2428.
29 M. Cargnello, C. Chen, B. T. Diroll, V. V. T. Doan-Nguyen, R. J. Gorte and C. B. Murray, *J. Am. Chem. Soc.*, 2015, **137**, 6906.
30 E. A. Baranova, C. Bock, D. Ilin, D. Wang and B. MacDougall, *Surf. Sci.*, 2006, **600**, 3502.

Electronic Supplementary Material (ESI) for Nanoscale Advances.

Supplementary information for

UV-induced syntheses of surfactant-free precious metal nanoparticles in alkaline methanol and ethanol

Jonathan Quinson,[a]*† Laura Kacenauskaite,[a†] Johanna Schröder,[b] Søren B. Simonsen,[c] Luise Theil Kuhn,[c] Tom Vosch[a] and Matthias Arenz [b]*

[a.] *Department of Chemistry, University of Copenhagen, Universitetsparken 5, 2100 Copenhagen Ø, Denmark*
[b.] *Department of Chemistry and Biochemistry, University of Bern, Freiestrasse 3 CH-3012 Bern, Switzerland*
[c.] *Department of Energy Conversion and Storage, Technical University of Denmark, Fysikvej Bldg. 310, DK-2800 Kgs. Lyngby, Denmark*
† *These authors equally contributed to the work.*

1. Experimental Section

Pt nanoparticle synthesis

For the synthesis of the Pt nanoparticles the mono-alcohol synthesis was used. Unless otherwise specified the nanoparticles were obtained using 2 mM $H_2PtCl_6 \cdot 6H_2O$ (99,9 % Alfa Aesar) in alkaline NaOH (98.9%, Fisher Chemical) methanol (≥ 99.8 %, Sigma-Aldrich) or ethanol (99.9 %, Kemetyl) at a concentration indicated in the text and for a volume of typically 3 mL.
The reaction mixtures were placed in quartz cuvettes and placed in home-built container equipped with controllable cooling system (T max = 40 °C) and 10 standard UV mercury lamps (PL-L- 24 W/10/4P Hg, Philips) for 2 hours (unless otherwise specified).

Ir nanoparticle synthesis

It is important to note that regardless of the approach chosen, the size of the nanoparticle evaluated by TEM was always in the range 1.0-1.7 nm without clear size control.

For the Ir nanoparticle synthesis a homebuilt UV set-up was used. In a typical experiment four UV-C lamps (TUV PL-S 9W/2P, Philips) were placed around a double jacket Quartz glass reactor. 4.4 mM Ir ($IrCl_3$, 99.8 %, Alfa Aesar; H_2IrCl_6, 99.9%, Stream Chemicals; Na_2IrCl_6, ≥ 99.9 %, Acros Organics), NaOH (0, 22, or 44 mM; from pellets, Hänseler), and Millipore water (0, 10, or 25 %) in ethanol (100 %, VWR) or methanol (≥ 99.8 %, Fisher Chemicals) were used. The reactor was closed with a septum to enable the introduction of gas (for 90s; 5% H_2 in Ar) into the reaction mixture to obtain a hydrogen/argon saturated atmosphere before the reduction. The reaction mixture was stirred with a magnetic stirring bar. The temperatures of 10, 20 or 40°C of the reactor were controlled by a continuous water flow through the double jacket. The inside of the set-up was cooled down by ventilation. Pictures were taken of the reaction mixture in the reactor before the reduction and then by interrupting the irradiation for less than 1 min and disconnecting the water cooling tubes after 10 minutes up to 24 h.

For the interest of the reader we detail here our attempts to perform seed mediated growth. Experiments were performed in ethanol and methanol to attempt increase the nanoparticle size by the deposition of fresh monomer on pre-formed seeds as summarized in **Table S1** and detailed below.

Table S1: Overview of the performed seed-mediated growth experiments concerning the seed and monomer solution, as well as the treatment of the mixture for the different solvents.

Solvent	Seed	Monomer	Treatment
Methanol	S1: MW, NaOH S2: UV, NaOH, H_2	M1: UV, NaOH	M1: no UV, no H_2 M2: no UV, H_2 M3: UV, no H_2 M4: UV, H_2
Ethanol		M2:no NaOH M3: NaOH	

$IrCl_3$ precursor (monomer) was added to 1 mL of pre-formed nanoparticles (seeds). The seeds were synthesized (S1) with 4.4 mM $IrCl_3$ and 44 mM NaOH heated for 3 min at 160 °C using a microwave (MW) reactor (CEM Discover SP, 100 W) or (S2) by 1h UV-C irradiation at 20°C (90 s H_2 in Ar). The monomer in methanol (green solution detailed below) was formed by (M1) reducing 4.4 mM $IrCl_3$ and 44 mM NaOH at 20°C for 1 h under UV-C light. As monomer sources in ethanol, (M2) 1 mL of 8.8 mM $IrCl_3$ or (M3) 2 mL of 4.4 mM $IrCl_3$ and 44 mM NaOH were used. The mixtures were afterwards treated in different ways. In the thermal treatments the mixtures were kept for 6h at 40°C (T1) without or (T2) with H_2 (5% in Ar, 90s) pre-treatment. In the UV light treatments, the mixtures were irradiated for 1h at 20°C with UV-C light (T3) without or (T4) with or H_2 (5% in Ar, 90s) introduced before synthesis.

FTIR characterization

The as-synthesised colloidal solutions were characterized by FTIR absorption spectroscopy. The colloidal suspensions in alkaline mono-alcohol were placed in a cell allowing to record IR absorption spectra of liquid in an attenuated total reflectance mode. Infrared spectra were captured using a Nicolet 6700 FT-IR (Thermo Electra Corporation) with a zinc selenide prism. All spectra were recorded with a resolution of 4 cm^{-1} and averaging over 100 scans. Background spectra of methanol or ethanol were measured and subtracted from the spectra recorded for the colloidal suspension. The difference spectra are reported.

Gas-chromatography coupled to mass spectroscopy (GC-MS) characterization

Head-space GC-MS was used to charaterise possible low boiling point species formed during the nanoparticle formation. A headspace sampler (Agilent G1888 Network Headspace Sampler) connected to a GC (Agilent 6890N Network GC System) equipped with an Agilent 19091S-433 non-polar column (HP-5ms (5%-phenyl) methyl poly siloxane, 30.0 m, 250 µm, 0.25µm) was connected to a mass spectrometer (Agilent 5973 inert Mass Selective Detector). Chromatographs were acquired with a ramp from 30 to 140 °C at 20 °C min^{-1}.

TEM characterization

For TEM the Pt nanoparticles were washed and re-dispersed in pure methanol or ethanol, the Ir nanoparticles (or reaction mixtures) were used as prepared without washing. Small drops of colloids then were placed on carbon coated copper grids (300 mesh grids, Quantifoil) and dried in room conditions. TEM images were taken using a Jeol 2100 microscope operated at 200 kV. Samples were characterized by taking images at different magnification (at least 3) in different areas (at least 3) of the TEM grids and the size analysis was performed by measuring the size of at least 100 nanoparticles.

Fluorescence measurements

In all cases the samples were first diluted to a suitable concentration before spectroscopic measurements (typically 0.1 mM of metal precursor). An excitation wavelength of 360 nm was used with a Cary Eclipse fluorescence spectrophotometer (Agilent Technologies). Reported spectra are not corrected for detector response to different wavelengths.

2. Results

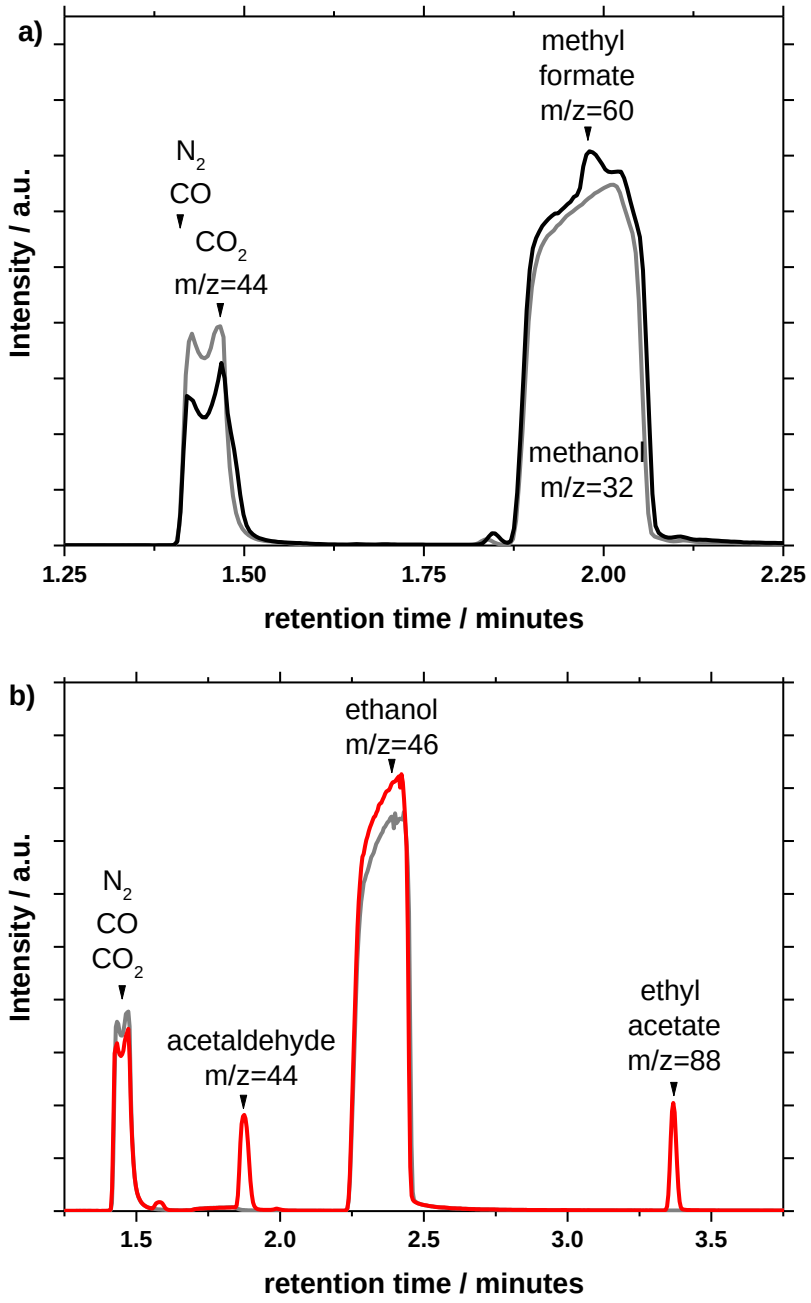

Fig. S1. Head space GC-MS chromatographs of (a) methanol (grey) and H_2PtCl_6 in alkaline methanol after UV irradiation (black) and (b) ethanol (grey) and H_2PtCl_6 in alkaline ethanol after UV irradiation (red).

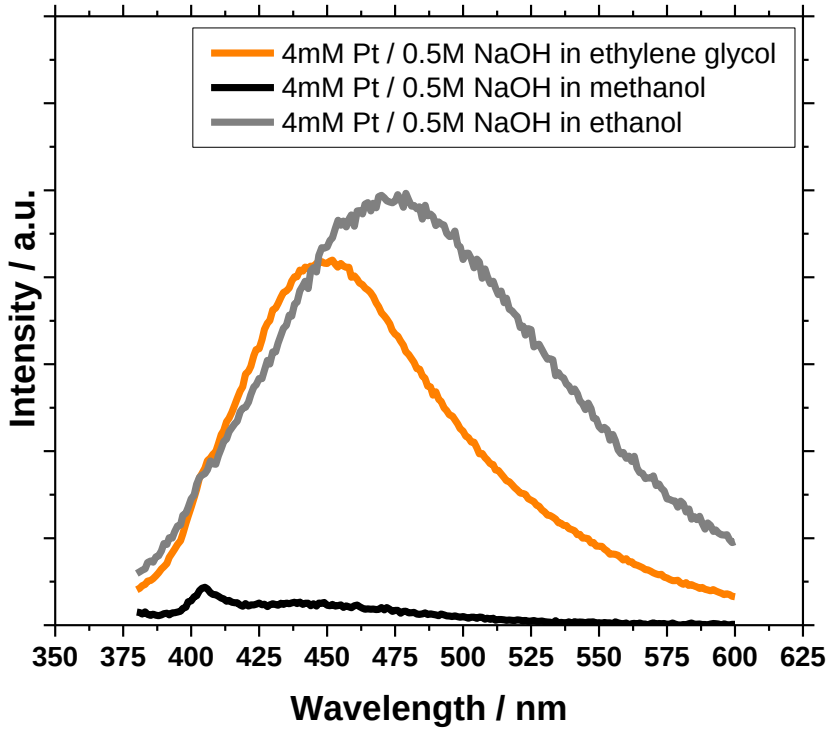

Fig. S2. Fluorescence spectra of alkaline solution of H_2PtCl_6 in different solvents after irradiation for a same period of time by UV light. The precursor used was H_2PtCl_6 and the concentration indicated are the final concentrations in the reaction mixture. Excitation wavelength of 360 nm. Emission peak around 410 nm correspond to Raman scattering from the solvent.

The formation of fluorescent species can be attributed to side reaction of the solvent with NaOH and formation for instance of carbon dots[1] or polymers for instance by aldol condensation in alkaline ethanol. The formation of fluorescent by-products is not observed in methanol.

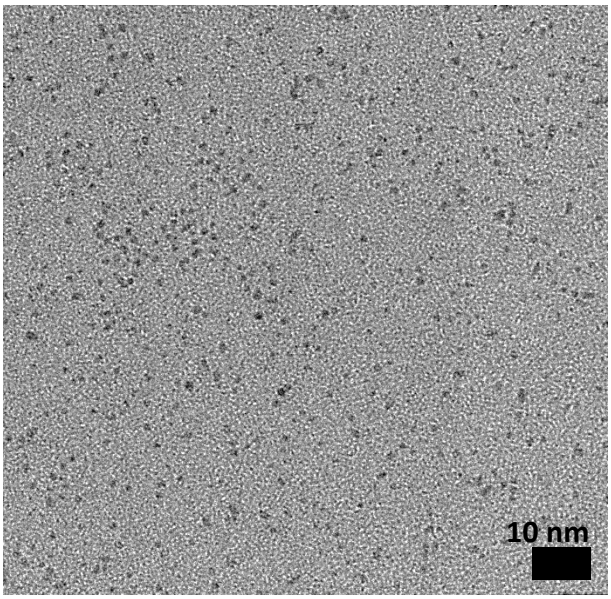

Fig. S3. TEM micrograph representative of Ir NPs obtained using UV-light.

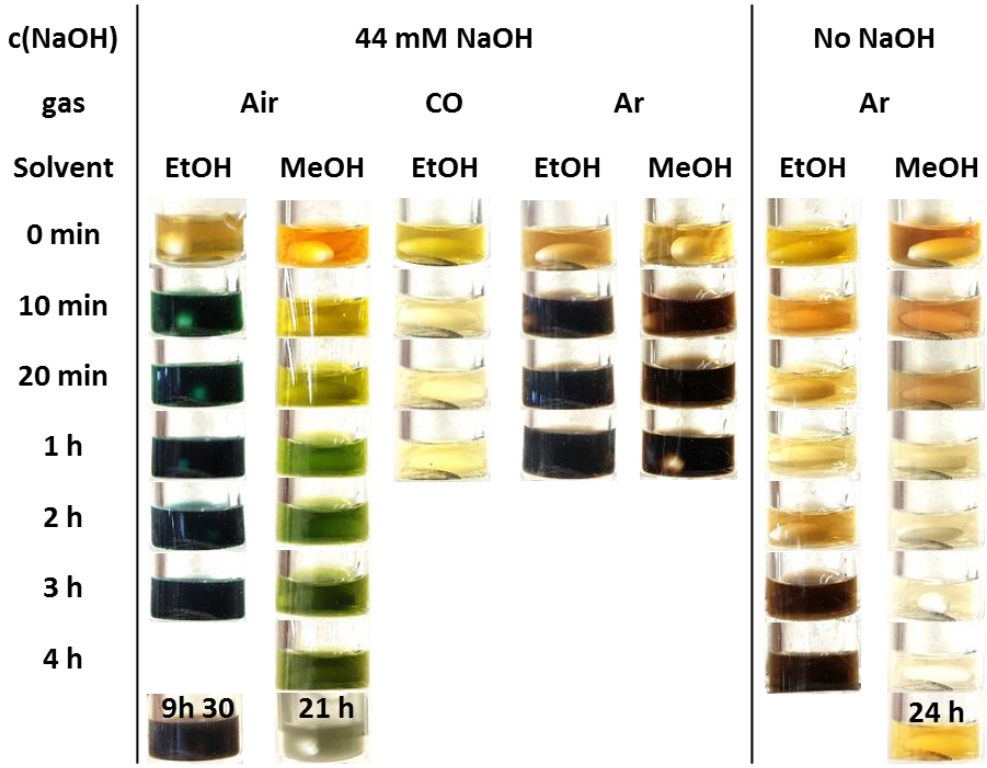

Fig. S4. Photos of the synthesis mixtures and nanoparticle dispersions under different conditions using 4.4 mM H_2IrCl_6 as precursor is ethanol and methanol before the reduction (0 min) and after 10 min to 24 h irradiation with UV-C light.

References

1. Gao, X. H.; Lu, Y. Z.; Zhang, R. Z.; He, S. J.; Ju, J.; Liu, M. M.; Li, L.; Chen, W., One-pot synthesis of carbon nanodots for fluorescence turn-on detection of Ag+ based on the Ag+-induced enhancement of fluorescence. *Journal of Materials Chemistry C* **2015,** *3* (10), 2302-2309.

Manuscript VII:

J. Schröder, V. A. Mints, A. Bornet, E. Berner, M. Fathi Tovini, J. Quinson, G. K. H. Wiberg, F. Bizzotto, H. A. El-Sayed, M. Arenz

The Gas Diffusion Electrode Setup as Straightforward Testing Device for Proton Exchange Membrane Water Electrolyzer Catalysts

https://pubs.acs.org/doi/10.1021/jacsau.1c00015 (Open Access)

JACS Au
AN OPEN ACCESS JOURNAL OF THE AMERICAN CHEMICAL SOCIETY

ACS AUTHORCHOICE

pubs.acs.org/jacsau

Letter

The Gas Diffusion Electrode Setup as Straightforward Testing Device for Proton Exchange Membrane Water Electrolyzer Catalysts

Johanna Schröder, Vladislav A. Mints, Aline Bornet, Etienne Berner, Mohammad Fathi Tovini, Jonathan Quinson, Gustav K. H. Wiberg, Francesco Bizzotto, Hany A. El-Sayed, and Matthias Arenz*

Cite This: https://dx.doi.org/10.1021/jacsau.1c00015

Read Online

ACCESS | Metrics & More | Article Recommendations | Supporting Information

ABSTRACT: Hydrogen production from renewable resources and its reconversion into electricity are two important pillars toward a more sustainable energy use. The efficiency and viability of these technologies heavily rely on active and stable electrocatalysts. Basic research to develop superior electrocatalysts is commonly performed in conventional electrochemical setups such as a rotating disk electrode (RDE) configuration or H-type electrochemical cells. These experiments are easy to set up; however, there is a large gap to real electrochemical conversion devices such as fuel cells or electrolyzers. To close this gap, gas diffusion electrode (GDE) setups were recently presented as a straightforward technique for testing fuel cell catalysts under more realistic conditions. Here, we demonstrate for the first time a GDE setup for measuring the oxygen evolution reaction (OER) of catalysts for proton exchange membrane water electrolyzers (PEMWEs). Using a commercially available benchmark IrO_2 catalyst deposited on a carbon gas diffusion layer (GDL), it is shown that key parameters such as the OER mass activity, the activation energy, and even reasonable estimates of the exchange current density can be extracted in a realistic range of catalyst loadings for PEMWEs. It is furthermore shown that the carbon-based GDL is not only suitable for activity determination but also short-term stability testing. Alternatively, the GDL can be replaced by Ti-based porous transport layers (PTLs) typically used in commercial PEMWEs. Here a simple preparation is shown involving the hot-pressing of a Nafion membrane onto a drop-cast glycerol-based ink on a Ti-PTL.

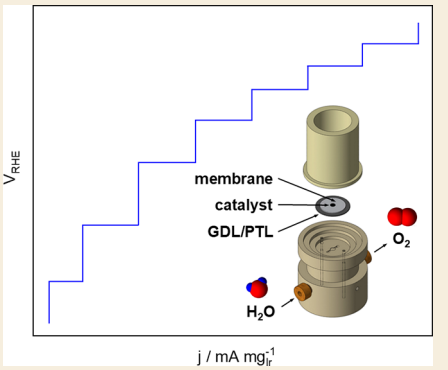

KEYWORDS: *oxygen evolution reaction, gas diffusion electrode setup, water electrolyzer, iridium-based catalysts, Ti porous transport layer, performance screening*

PEMWEs coupled to renewable energy sources such as wind and solar are a promising technology for energy conversion and long-term storage because of their higher current density as compared with alkaline electrolysis cells (AECs).[1−3] For PEMWEs, the preferred anode materials are Ir and Ir alloys because of the combination of high activity and stability of IrO_2.[4−6] As Ir is one of the rarest precious metals,[7] an efficient testing platform requiring only small amounts of Ir to screen PEMWE catalysts is necessary to optimize the anode performance. In this work, an in-house developed GDE setup[8−11] previously used for oxygen reduction reaction (ORR) studies is adapted to enable OER measurements. In this modified setup, the stainless-steel body is replaced by polychlorotrifluoroethylene for enhanced chemical stability at high voltages (see Figure 1 for the scheme of the developed GDE setup for straightforward OER measurements and Figures S1−S2).

The GDE consists of a catalyst layer deposited on top of a carbon GDL by vacuum filtration as introduced by Yarlagadda et al.[12] The vacuum filtration enables a reproducible film quality with catalyst loadings comparable to PEMWEs.[7,13] Element mapping by energy-dispersive X-ray spectroscopy (EDS) reveals a clearly separated IrO_2 layer on top of the microporous carbon layer (MPL) of the GDL (see Figure 2).

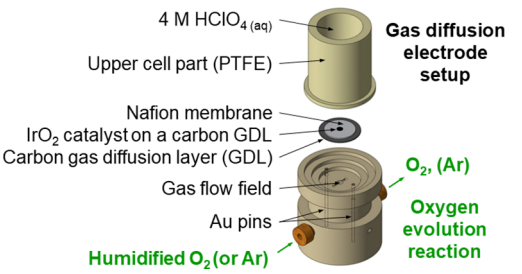

Figure 1. Scheme of the developed GDE setup for straightforward OER measurements.

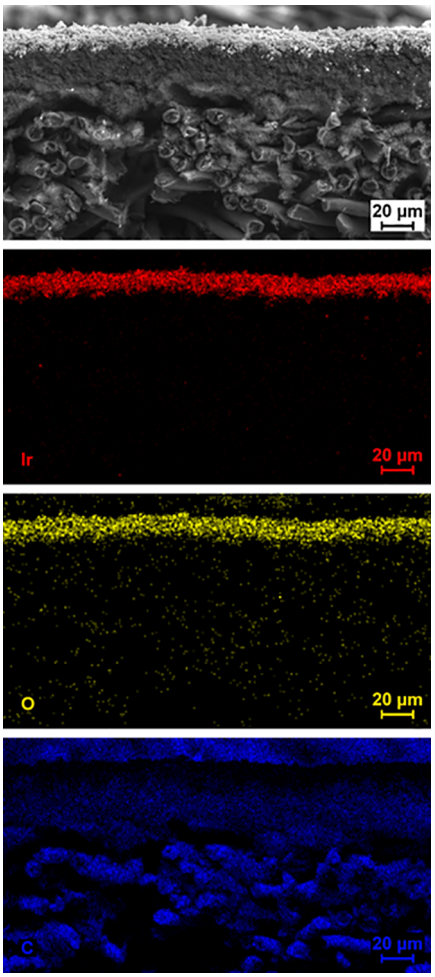

Figure 2. SEM cross-section of an activated IrO_2 catalyst film deposited on a GDL in combination with EDS mapping of iridium (Ir, red), oxygen (O, yellow), and carbon (C, blue). A clear separation of the catalyst film, the carbon containing MPL, and the carbon fibers of the GDL is apparent.

To establish a measurement protocol for the new GDE setup, the influence of several experimental parameters such as the gas flow rate, gas atmosphere (Ar, O_2), substrate, and temperature on the measured reaction rate were investigated (see Table S1 for a summary). In addition, the results were compared to conventional RDE measurements.[14−17]

The influence of the reactant gas flow (humidified Ar) on the observed OER activity is shown in Figure S4. Based on the measurements, possible mass transport limitations can be identified. The results demonstrate that the apparent OER activities and Tafel slopes are relatively constant (41.4 ± 0.9 mV dec^{-1}) over a wide range of the reactant gas flow (40−190 mL min^{-1}). Only for low flow rates (10 mL min^{-1}), the observed OER rates are inhibited and the Tafel slope shows nonlinear behavior. These observations indicate mass transport limitations at too low flow rates because of a lack of water transported to the catalyst or the difficulty in removing produced O_2 from the surface. Hence, in the following, a flow rate of 40 mL min^{-1} was used to ensure sufficient reactant mass transport.

On the basis of the investigations, we established a measurement protocol, where a set current (normalized to the mass of the precious metal catalyst) is applied and the electrode potential is recorded as a function of time (see Figure S4). Given the controlled current, the average of the *iR*-corrected potential of the last 60 s (when not stated differently) of every step is defined as the OER.

Thus, conducted OER measurements with a commercial IrO_2 benchmark catalyst are presented in Figure 3. In Figure 3a, we compare GDE measurements to conventional RDE measurements at 30 °C in an O_2 atmosphere. It is seen that the determined mass activities and Tafel slopes are similar in both setups. At 1.48 V_{RHE}, mass activities of 4.3 and 4.9 mA mg_{Ir}^{-1} are determined for the galvanostatic GDE and potentiostatic RDE measurements, respectively, which is comparable to the values reported by Alia et al.[18,19] The determined Tafel slopes are 45.4 ± 1.0 and 39.2 ± 0.4 mV dec^{-1}, respectively.

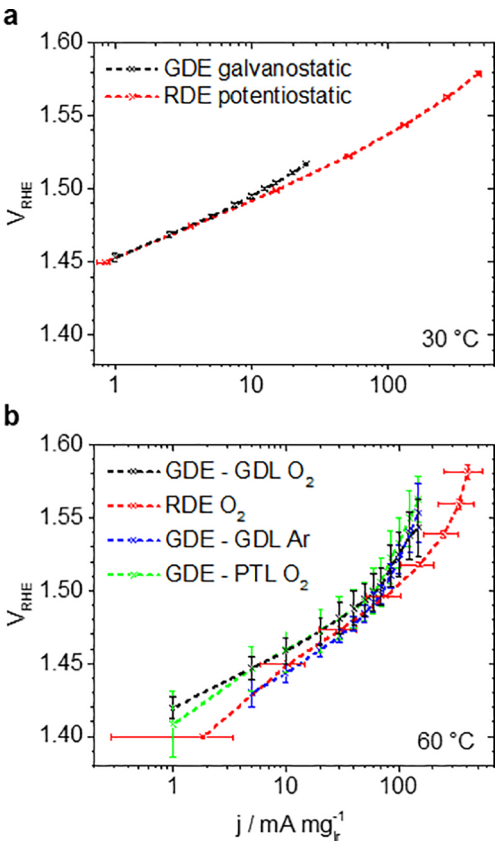

Figure 3. Tafel plots of OER mass activity j of the IrO_2 catalyst. Comparison of GDE (galvanostatic, 4 M $HClO_4$, 1 mg_{Ir} cm^{-2}_{geo}) and RDE (potentiostatic in O_2 atmosphere, 0.1 M $HClO_4$, 50 μg_{Ir} cm^{-2}_{geo}) measurements (a) at 30 °C in O_2 and (b) 60 °C using a GDL in O_2 and Ar or Ti-PTL in O_2 atmosphere in the GDE setup. The error bars show the standard deviation of three independent measurements; the data points are connected by dashed lines as guide for the eye.

In Figure 3b, the results at an increased temperature of 60 °C are shown. In a RDE setup, potentiodynamic measurements reveal performance degradation during continuous cycling (see Figure S5), and potentiostatic measurements show a large standard deviation for the measured current density. By comparison, in the GDE setup, three independent measurements confirm a good reproducibility of the obtained OER activities under steady-state conditions (see also Table S1). The fast performance degradation, as seen in the RDE, is most likely inhibited in the GDE setup because of the use of a

https://dx.doi.org/10.1021/jacsau.1c00015
JACS Au XXXX, XXX, XXX−XXX

Nafion membrane avoiding direct contact of the catalyst to the liquid electrolyte leading to a more realistic setup in the GDE comparable to a PEMWE. Furthermore, it is demonstrated that the OER activity can be conveniently studied in O_2 or Ar gas atmosphere. The latter leads to apparent activity improvements, which can be understood by the influence of the O_2 partial pressure in the Nernst equation. The same effect influences the Tafel behavior. In O_2 atmosphere and 60 °C, a Tafel slope of 41.1 ± 4.8 mV dec^{-1} is observed at low current densities, which at higher current densities increases significantly. This observation is linked to oxygen bubble formation, which leads to inhibited OER rates.[20,21] As a consequence, with increasing oxygen formation rates (i.e., higher current densities), the apparent OER activity in Ar atmosphere decreases and approaches that in O_2. Interestingly, nonlinearities in the Tafel slope at low current densities, which are often observed in potentiodynamic RDE measurements,[22] are not apparent in the GDE setup.

Most importantly, no fundamental difference is observed if these OER activity measurements are performed with a catalyst film deposited onto a carbon GDL or Ti-PTL, justifying the substantially less complex GDL approach for catalyst screening; see more details about the film preparation in the SI. To further corroborate that carbon corrosion of the GDL does not pose a problem during the activity measurement, the current density was increased stepwise from 1 to 10 mA mg_{Ir}^{-1} and held at 10 mA mg_{Ir}^{-1} for 1 h. Figure 4 shows that even with the

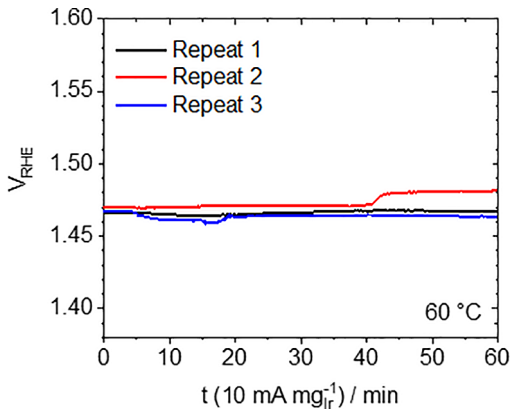

Figure 4. Stability measurements of IrO_2/GDL applying 10 mA mg_{Ir}^{-1} for 1 h.

carbon-based GDL, it is possible to perform such suggested stability measurements,[23] although the potential increase in repeat 2 (of three independent samples) can probably be traced back to bubble formation or carbon degradation. Hence the GDL is a suitable substrate for determining the activity of OER catalysts in screening-type studies.

For long-term stability measurements under harsher conditions, catalyst-coated membranes (CCMs) pressed to Ti-PTLs might be used.[24,25] However, CCM preparation is time-consuming and needs special equipment; hence, it is not available in all laboratories for a fast screening test protocol. Because of the high porosity of the PTL, vacuum filtration or drop-casting using an ink of water and IPA as for the GDLs preparation is not possible. A simple alternative to CCM preparation is to use a glycerol-based catalyst ink. To completely avoid the ink permeation into the PTL, Teflon was sprayed on top of the PTL before drop-casting (note that the MPL on top of the carbon fiber structure of the GDL also contains Teflon). Furthermore, as compared with the GDL preparation, the temperature during pressing needs to be increased; otherwise, a poor electric connection between Nafion membrane and PTL can lead to high resistances of several hundred ohms. However, a homemade hot-press was sufficient to enable the use of a PTL and achieve results comparable to the GDL approach (see Figure 5b). Therefore,

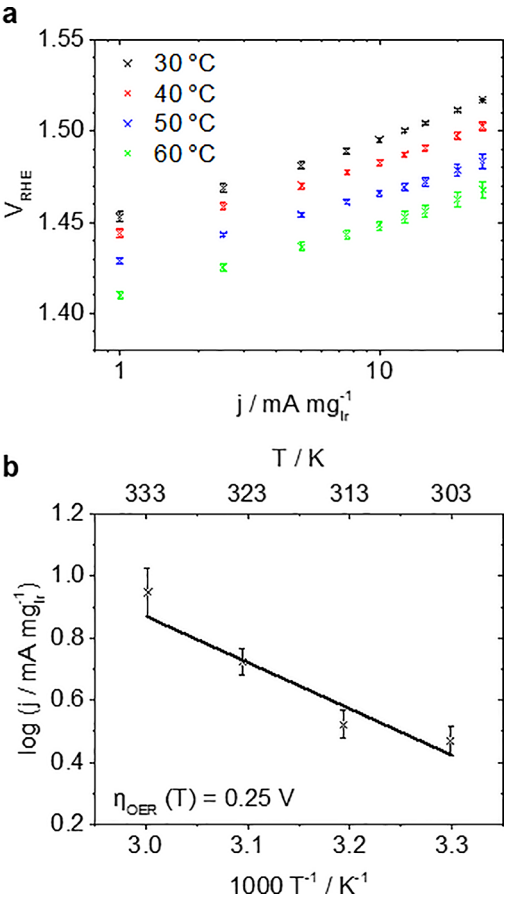

Figure 5. (a) Temperature-dependent OER mass activity j plotted as Tafel plots obtained in a GDE setup applying current steps versus V_{RHE}. (b) The corresponding Arrhenius plot at an overpotential η_{OER} of 0.25 V.

the use of a PTL is possible in the presented GDE setup even without specialized equipment. However, because of the simple hot-pressing, the membrane can peel off with time at high O_2 formation rates. Additionally, because of the high costs of the PTL, we believe that the GDL approach is more suitable for a first activity screening.

To complete the IrO_2 catalyst characterization, the temperature dependency was investigated between 30 and 60 °C. In Figure 5a, it is shown that, as expected, the OER rate increases with temperature.[26] Furthermore, comparable Tafel slopes (38.5−45.4 mV dec^{-1}) are observed, indicating that the OER reaction mechanism is the same in the investigated temperature range. Hence, the electrochemical activation energy E_A can be estimated assuming Arrhenius behavior. For a rough estimation, the formal E_A determined with respect to the reference potential of the used reversible hydrogen reference electrode (RHE) can be used (see SI). For a more precise determination, the temperature-dependent shift of the

https://dx.doi.org/10.1021/jacsau.1c00015
JACS Au XXXX, XXX, XXX−XXX

reversible oxygen potential versus RHE needs to be considered. This correction is also required when determining the exchange current density j_0. The precise Tafel slope allows for an extrapolation of the linear fits to the reversible potential to determine j_0 for the OER. In conventional, potentiodynamic RDE measurements, determining j_0 for the OER is daring and usually not pursued because an extrapolation of the measured current densities over several orders of magnitude is required. Error margins in the Tafel slope therefore can lead to substantial uncertainties of several orders of magnitude. For the determination of the temperature-dependent reversible potential $E_{rev,T}$ different equations can be found (e.g., from Parthasarathy et al.[27] or from Bratsch).[28] The latter contains an approximation of the exact dependence. Determining $E_{rev,T}$ using the equation of Parthasarathy et al.[27] j_0 of 10.6 ± 6.0, 3.5 ± 1.8, 2.1 ± 1.2, and 7.2 ± 3.8 × 10^{-9} A mg_{Ir}^{-1} are obtained for 30, 40, 50, and 60 °C, respectively. It should be noted that three independent samples were measured while consecutively applying the four temperatures. Determining $E_{rev,T}$ following Bratsch[28] leads to comparable but slightly higher values of j_0 (see Tables S2−S3). The obtained j_0 are comparable to 7.3 × 10^{-9} A mg_{Ir}^{-2} calculated from the data reported by Lu et al.[22] The limitation of the extrapolation, however, is apparent from the increase in j_0 going from 50 to 60 °C. For the determination of E_A at constant overpotential, $E_{rev,T}$ has been calculated according to Parthasarathy et al.[27] (see Figure S6 for a Arrhenius plot according to the correction by Bratsch[28]). The linear fit of the Arrhenius plot at an overpotential η_{OER} of 0.25 V (Figure 5b) leads to E_A of 28.5 ± 6.6 kJ mol^{-1} being a bit lower than 47 kJ mol^{-1} reported by Suermann et al.[29] in a PEMWE, which is mainly related to the point at 30 °C. Using kinetic data of four temperatures certainly only allows a rough estimation. Nevertheless, this example shows the potential of the presented GDE approach to provide high quality data.

To sum up, we demonstrate a new strategy to test OER catalysts in a GDE setup. The GDE setup is a more straightforward technique than RDE[10,11] and the GDE cell can be built in any research workshop (see technical drawings in SI). Depositing the catalyst onto a carbon GDL is suitable for OER steady-state activity screening and allows the determination of key kinetic data. In contrast to conventional potentiodynamic RDE measurements, the catalyst layers contain Nafion and exhibit realistic loadings comparable to PEMWEs. Accurate Tafel slopes can be obtained and extrapolated to determine the exchange current density. Even short-term stability tests are feasible with carbon GDL, which are cost-efficient substrates for catalyst screening. Furthermore, the GDE setup can be used for more elaborate stability screenings using Ti-PTLs as substrate and performing a simple hot-pressing procedure.

■ ASSOCIATED CONTENT

Supporting Information

The Supporting Information is available free of charge at https://pubs.acs.org/doi/10.1021/jacsau.1c00015.

Experimental (chemicals, materials, and gases; gas diffusion electrode setup; rotating disk electrode setup; ink formation; catalyst film preparation; electrochemical measurements; characterization), OER activity measurements (GDE and RDE data; Tafel plot determination; exchange current density and activation energy), XPS and TEM measurements (PDF)

■ AUTHOR INFORMATION

Corresponding Author

Matthias Arenz − *Department of Chemistry, Biochemistry and Pharmaceutical Sciences, University of Bern, 3012 Bern, Switzerland;* orcid.org/0000-0001-9765-4315; Email: matthias.arenz@dcb.unibe.ch

Authors

Johanna Schröder − *Department of Chemistry, Biochemistry and Pharmaceutical Sciences, University of Bern, 3012 Bern, Switzerland;* orcid.org/0000-0001-5461-4751

Vladislav A. Mints − *Department of Chemistry, Biochemistry and Pharmaceutical Sciences, University of Bern, 3012 Bern, Switzerland*

Aline Bornet − *Department of Chemistry, Biochemistry and Pharmaceutical Sciences, University of Bern, 3012 Bern, Switzerland;* orcid.org/0000-0001-9850-2735

Etienne Berner − *Department of Chemistry, Biochemistry and Pharmaceutical Sciences, University of Bern, 3012 Bern, Switzerland*

Mohammad Fathi Tovini − *Chair of Technical Electrochemistry, Department of Chemistry and Catalysis Research Center, Technical University Munich, 85748 Garching, Germany*

Jonathan Quinson − *Department of Chemistry, University of Copenhagen, 2100 Copenhagen, Denmark;* orcid.org/0000-0002-9374-9330

Gustav K. H. Wiberg − *Department of Chemistry, Biochemistry and Pharmaceutical Sciences, University of Bern, 3012 Bern, Switzerland*

Francesco Bizzotto − *Department of Chemistry, Biochemistry and Pharmaceutical Sciences, University of Bern, 3012 Bern, Switzerland*

Hany A. El-Sayed − *Chair of Technical Electrochemistry, Department of Chemistry and Catalysis Research Center, Technical University Munich, 85748 Garching, Germany;* orcid.org/0000-0002-8769-8258

Complete contact information is available at: https://pubs.acs.org/10.1021/jacsau.1c00015

Author Contributions

G.K.H.W. designed the GDE setup for the OER measurements. J.S., M.A., H.A.E.-S. designed the electrochemical experiments in the GDE setup, prepared and performed by J.S. V.A.M. performed the RDE measurements. J.S. prepared the samples for TEM and XPS measurements. J.Q. performed TEM and M.F.T. XPS measurements and analysis. E.B. did the SEM and EDS measurements. A.B. did initial tests on the hot pressing. F.B. did initial OER tests in the GDE setup. H.A.E.-S. and M.A. supervised the research. J.S. and M.A. wrote the first draft of the paper, read, and commented by all authors.

Notes

The authors declare no competing financial interest.

■ ACKNOWLEDGMENTS

This Project has received funding from the European Union's Horizon 2020 Research and Innovation program under grant agreement N. 861960 ("Recycalyse" project) and the Swiss National Science Foundation (SNSF) via the project No. 200021_184742. J.Q acknowledges the European Union's Horizon 2020 research and innovation program under the

https://dx.doi.org/10.1021/jacsau.1c00015
JACS Au XXXX, XXX, XXX−XXX

Marie Skłodowska-Curie grant agreement No. 840523 (CoSolCat). J.Q. and M.A. thank Dr. L. Theil Kuhn and Dr. S. B. Simonsen, Technical University of Denmark (DTU) for access to TEM facilities. H.A.E.-S. and M.F.T. gratefully acknowledge the German Ministry of Education and Research for financial support of this work within the innoKA project (BMWi, 03ET6096A). Dr. Nedjeljko Seselj of Danish Power Systems (DPS) is acknowledged for his advice concerning the catalyst film formation on the PTL.

REFERENCES

(1) Buttler, A.; Spliethoff, H. Current Status of Water Electrolysis for Energy Storage, Grid Balancing and Sector Coupling via Power-to-Gas and Power-to-Liquids: A Review. *Renewable and Sustainable Energy Reviews* **2018**, *82*, 2440−2454.

(2) Babic, U.; Suermann, M.; Büchi, F. N.; Gubler, L.; Schmidt, T. J. Critical Review—Identifying Critical Gaps for Polymer Electrolyte Water Electrolysis Development. *J. Electrochem. Soc.* **2017**, *164* (4), F387−F399.

(3) Schmidt, O.; Gambhir, A.; Staffell, I.; Hawkes, A.; Nelson, J.; Few, S. Future Cost and Performance of Water Electrolysis: An Expert Elicitation Study. *Int. J. Hydrogen Energy* **2017**, *42* (52), 30470−30492.

(4) Fabbri, E.; Habereder, A.; Waltar, K.; Kötz, R.; Schmidt, T. J. Developments and Perspectives of Oxide-Based Catalysts for the Oxygen Evolution Reaction. *Catal. Sci. Technol.* **2014**, *4* (11), 3800−3821.

(5) Antolini, E. Structural Parameters of Supported Fuel Cell Catalysts: The Effect of Particle Size, Inter-Particle Distance and Metal Loading on Catalytic Activity and Fuel Cell Performance. *Applied Catalysis B: Environmental* **2016**, *181*, 298−313.

(6) McCrory, C. C. L.; Jung, S.; Peters, J. C.; Jaramillo, T. F. Benchmarking Heterogeneous Electrocatalysts for the Oxygen Evolution Reaction. *J. Am. Chem. Soc.* **2013**, *135* (45), 16977−16987.

(7) Carmo, M.; Fritz, D. L.; Mergel, J.; Stolten, D. A Comprehensive Review on PEM Water Electrolysis. *Int. J. Hydrogen Energy* **2013**, *38* (12), 4901−4934.

(8) Wiberg, G. K. H.; Fleige, M.; Arenz, M. Gas Diffusion Electrode Setup for Catalyst Testing in Concentrated Phosphoric Acid at Elevated Temperatures. *Rev. Sci. Instrum.* **2015**, *86* (2), 024102.

(9) Inaba, M.; Jensen, A. W.; Sievers, G. W.; Escudero-Escribano, M.; Zana, A.; Arenz, M. Benchmarking High Surface Area Electrocatalysts in a Gas Diffusion Electrode: Measurement of Oxygen Reduction Activities under Realistic Conditions. *Energy Environ. Sci.* **2018**, *11* (4), 988−994.

(10) Alinejad, S.; Inaba, M.; Schröder, J.; Du, J.; Quinson, J.; Zana, A.; Arenz, M. Testing Fuel Cell Catalysts under More Realistic Reaction Conditions: Accelerated Stress Tests in a Gas Diffusion Electrode Setup. *J. Phys. Energy* **2020**, *2* (2), 024003.

(11) Schröder, J.; Quinson, J.; Mathiesen, J. K.; Kirkensgaard, J. J. K.; Alinejad, S.; Mints, V. A.; Jensen, K. M. Ø.; Arenz, M. A New Approach to Probe the Degradation of Fuel Cell Catalysts under Realistic Conditions: Combining Tests in a Gas Diffusion Electrode Setup with Small Angle X-Ray Scattering. *J. Electrochem. Soc.* **2020**, *167* (13), 134515.

(12) Yarlagadda, V.; McKinney, S. E.; Keary, C. L.; Thompson, L.; Zulevi, B.; Kongkanand, A. Preparation of PEMFC Electrodes from Milligram-Amounts of Catalyst Powder. *J. Electrochem. Soc.* **2017**, *164* (7), F845−F849.

(13) Pan, L.; Ott, S.; Dionigi, F.; Strasser, P. Current Challenges Related to the Deployment of Shape-Controlled Pt Alloy Oxygen Reduction Reaction Nanocatalysts into Low Pt-Loaded Cathode Layers of Proton Exchange Membrane Fuel Cells. *Curr. Opin. Electrochem.* **2019**, *18*, 61−71.

(14) Bernt, M.; Hartig-Weiß, A.; Tovini, M. F.; El-Sayed, H. A.; Schramm, C.; Schröter, J.; Gebauer, C.; Gasteiger, H. A. Current Challenges in Catalyst Development for PEM Water Electrolyzers. *Chem. Ing. Tech.* **2020**, *92* (1−2), 31−39.

(15) Oakton, E.; Lebedev, D.; Povia, M.; Abbott, D. F.; Fabbri, E.; Fedorov, A.; Nachtegaal, M.; Copéret, C.; Schmidt, T. J. IrO2-TiO2: A High-Surface-Area, Active, and Stable Electrocatalyst for the Oxygen Evolution Reaction. *ACS Catal.* **2017**, *7* (4), 2346−2352.

(16) Reier, T.; Oezaslan, M.; Strasser, P. Electrocatalytic Oxygen Evolution Reaction (OER) on Ru, Ir, and Pt Catalysts: A Comparative Study of Nanoparticles and Bulk Materials. *ACS Catal.* **2012**, *2* (8), 1765−1772.

(17) Oh, H. S.; Nong, H. N.; Reier, T.; Bergmann, A.; Gliech, M.; Ferreira De Araújo, J.; Willinger, E.; Schlögl, R.; Teschner, D.; Strasser, P. Electrochemical Catalyst-Support Effects and Their Stabilizing Role for IrOx Nanoparticle Catalysts during the Oxygen Evolution Reaction. *J. Am. Chem. Soc.* **2016**, *138* (38), 12552−12563.

(18) Alia, S. M.; Rasimick, B.; Ngo, C.; Neyerlin, K. C.; Kocha, S. S.; Pylypenko, S.; Xu, H.; Pivovar, B. S. Activity and Durability of Iridium Nanoparticles in the Oxygen Evolution Reaction. *J. Electrochem. Soc.* **2016**, *163* (11), F3105−F3112.

(19) Alia, S. M.; Shulda, S.; Ngo, C.; Pylypenko, S.; Pivovar, B. S. Iridium-Based Nanowires as Highly Active, Oxygen Evolution Reaction Electrocatalysts. *ACS Catal.* **2018**, *8* (3), 2111−2120.

(20) El-Sayed, H. A.; Weiß, A.; Olbrich, L. F.; Putro, G. P.; Gasteiger, H. A. OER Catalyst Stability Investigation Using RDE Technique: A Stability Measure or an Artifact? *J. Electrochem. Soc.* **2019**, *166* (8), F458−F464.

(21) Hartig-Weiss, A.; Tovini, M. F.; Gasteiger, H. A.; El-Sayed, H. A. OER Catalyst Durability Tests Using the Rotating Disk Electrode Technique: The Reason Why This Leads to Erroneous Conclusions. *ACS Appl. Energy Mater.* **2020**, *3*, 10323.

(22) Lu, Y.; Wang, W.; Xie, F. Investigation of Oxygen Evolution Reaction Kinetic Process and Kinetic Parameters on Iridium Electrode by Electrochemistry Impedance Spectroscopy Analysis. *J. Electroanal. Chem.* **2020**, *871*, 114281.

(23) Spöri, C.; Kwan, J. T. H.; Bonakdarpour, A.; Wilkinson, D. P.; Strasser, P. The Stability Challenges of Oxygen Evolving Catalysts: Towards a Common Fundamental Understanding and Mitigation of Catalyst Degradation. *Angewandte Chemie - International ed.* **2017**, *56*, 5994−6021.

(24) Rakousky, C.; Reimer, U.; Wippermann, K.; Carmo, M.; Lueke, W.; Stolten, D. An Analysis of Degradation Phenomena in Polymer Electrolyte Membrane Water Electrolysis. *J. Power Sources* **2016**, *326*, 120−128.

(25) Bühler, M.; Holzapfel, P.; McLaughlin, D.; Thiele, S. From Catalyst Coated Membranes to Porous Transport Electrode Based Configurations in PEM Water Electrolyzers. *J. Electrochem. Soc.* **2019**, *166* (14), F1070−F1078.

(26) Zhang, G.; Wang, H.; Yang, J.; Zhao, Q.; Yang, L.; Tang, H.; Liu, C.; Chen, H.; Lin, Y.; Pan, F. Temperature Effect on Co-Based Catalysts in Oxygen Evolution Reaction. *Inorg. Chem.* **2018**, *57* (5), 2766−2772.

(27) Parthasarathy, A.; Srinivasan, S.; Appleby, A. J.; Martin, C. R. Temperature Dependence of the Electrode Kinetics of Oxygen Reduction at the Platinum/Nafion® Interface—A Microelectrode Investigation. *J. Electrochem. Soc.* **1992**, *139* (9), 2530−2537.

(28) Bratsch, S. G. Standard Electrode Potentials and Temperature Coefficients in Water at 298.15 K. *J. Phys. Chem. Ref. Data* **1989**, *18* (1), 1−21.

(29) Suermann, M.; Schmidt, T. J.; Büchi, F. N. Comparing the Kinetic Activation Energy of the Oxygen Evolution and Reduction Reactions. *Electrochim. Acta* **2018**, *281*, 466−471.

https://dx.doi.org/10.1021/jacsau.1c00015
JACS Au XXXX, XXX, XXX−XXX

Supporting information

The Gas Diffusion Electrode Setup as Straightforward Testing Device for Proton Exchange Membrane Water Electrolyzer Catalysts

Johanna Schröder[a], Vladislav A. Mints[a], Aline Bornet[a], Etienne Berner[a], Mohammad Fathi Tovini[b], Jonathan Quinson[c], Gustav K. H. Wiberg[a], Francesco Bizzotto[a], Hany A. El-Sayed[b], Matthias Arenz[a]*.

[a] Department of Chemistry, Biochemistry and Pharmaceutical Sciences, University of Bern, Freiestrasse 3, 3012 Bern, Switzerland

[b] Chair of Technical Electrochemistry, Department of Chemistry and Catalysis Research Center, Technical University Munich, Lichtenbergstrasse 4, 85748 Garching, Germany.

[c] Department of Chemistry, University of Copenhagen, Universitetsparken 5, 2100 Copenhagen, Denmark.

Experimental

Chemicals, materials, and gases

For the catalyst ink formation, dilution of the acid, and the cleaning of the GDE cell ultrapure Milli-Q water (resistivity > 18.2 MΩ·cm, total organic carbon (TOC) < 5 ppb) from a Millipore system was used. For the preparation of the catalyst inks isopropanol (IPA, 99.7+ %, Alfa Aesar), glycerol (sigma, for molecular biology, ≥ 99 %), commercial IrO_2 (Alfa Aesar, Iridium(IV) oxide, Premion®, 99.99% metals basis, Ir 84.5% min, MFCD00011065) and Nafion dispersion (D1021, 10 wt.%, EW 1100, Fuel Cell Store) were used.

The GDE was prepared using a Nafion membrane (Nafion 117, 183 µm thick, Fuel Cell Store), two carbon gas diffusion layers (GDL) (Freudenberg H23, 0.210 mm thick, Fuel Cell Store; with a microporous layer (MPL): Freudenberg H23C8, 0.230 mm thick), a porous transport layer (PTL) (Sintered titanium, Mott Corporation, USA) and Teflon (polytetrafluorethylene, PTFE) spray (BOLA Fluorkunststoff spray, Bohlender). The used Nafion membrane was always pretreated. Cutoff membranes (diameter of 2 cm) were treated in 5 wt.% H_2O_2 (Hänseler, 30 min, 80 °C), rinsed with Milli-Q water, treated in Milli-Q water (30 min, 80 °C), again rinsed with Milli-Q water, treated in 8 wt.% H_2SO_4 (30 min, 80 °C) and finally rinsed with Milli-Q water. Afterwards the cutoff membranes were stored in a with Milli-Q water filled glass vial.

The electrochemical measurements were performed using diluted 70% perchloric acid ($HClO_4$, GDE: 99.999% trace metals basis, Sigma Aldrich; RDE: Suprapur, Merck) as electrolyte and the gas argon (Ar) or oxygen (O_2) from Air Liquide (99.999 %).

Gas diffusion electrode setup

For the electrochemical measurements an in-house developed GDE setup was used. The GDE was placed above a flow-field of a Polychlorotrifluoroethylene (PCTFE) cell body with the Nafion membrane upwards. The upper cell part made of Teflon was placed above the Nafion membrane. Two Au pins (Conrad Electronic, 1025-M-1.5N-AU-1.5) were placed vertical inside the cell body and a plastic disk as base was screwed into the cell body to push the Au pins into the GDE. Two screws were used to enable an electric contact via Au pins to the GDE (i.e. working electrode (WE)). The previously stainless steel lower cell body[1] was for this study replaced by PCTFE. The main advantages of this replacement are the higher chemical resistance due to prevention of corrosion of the cell body (by acid and water) that in the past sometimes led to iron signals during potentiodynamic measurements. While the corrosion of

the flow field was easily visible and could be removed by a fast grinding the rusting of the internal parts (from gas inlet to outlet) was really challenging. Therefore, the high chemical resistance of PCTFE against $HClO_4$ is an important improvement. The only corroding components in the new setup are the easily replaceable Au pins.

A platinum wire was used as a counter electrode (CE) and a reversible hydrogen electrode (RHE) as a reference electrode (RE). The CE was placed inside a glass capillary with a glass frit on the bottom to avoid the trapping of gas bubbles in the hole of the Teflon cell and thus helping to improve the reproducibility of the measurement. The CE inside the frit and the RE were placed in the upper cell part inside the electrolyte. The position of the CE was fixed with a holder to keep a constant position and preventing the falling out of the upper cell part. All potentials in this study are referred to the RHE potential.

The Teflon upper cell body was initially cleaned by soaking it overnight in acid (H_2SO_4:HNO_3 = 1:1, v:v) following by rinsing and twice boiling in ultrapure water. Between measurements, it was boiled once in ultrapure water together with the RE, and the glass capillary.

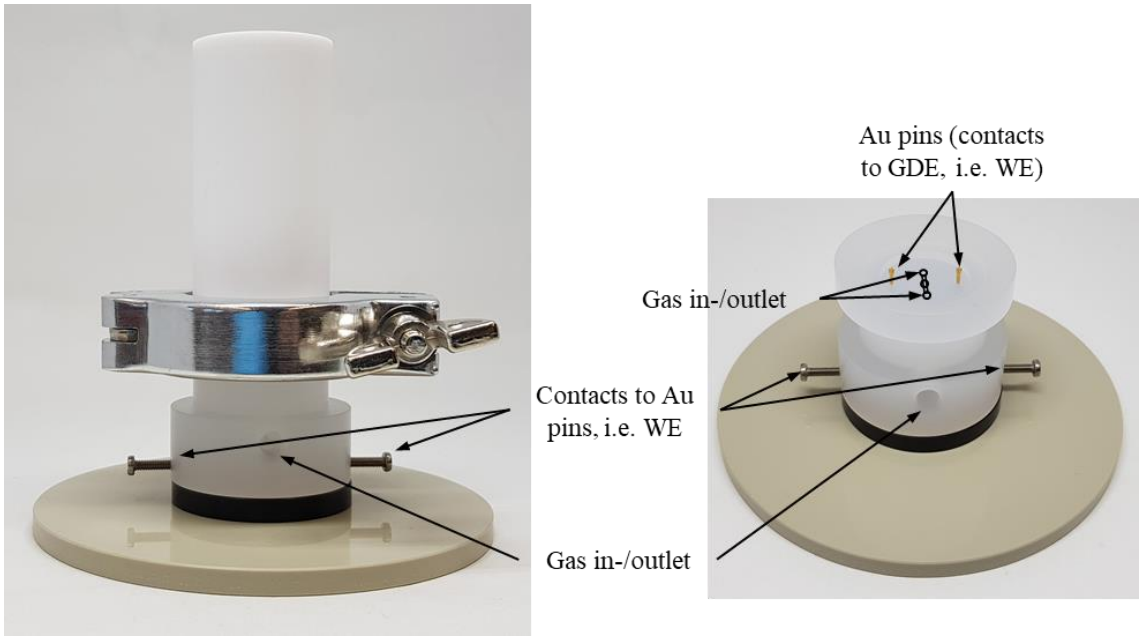

Figure S1. Pictures of the developed GDE setup for OER measurements consisting of a PCTFE cell body, two screws as contacts to the Au pins, i.e. the WE, and a PTFE upper cell body.

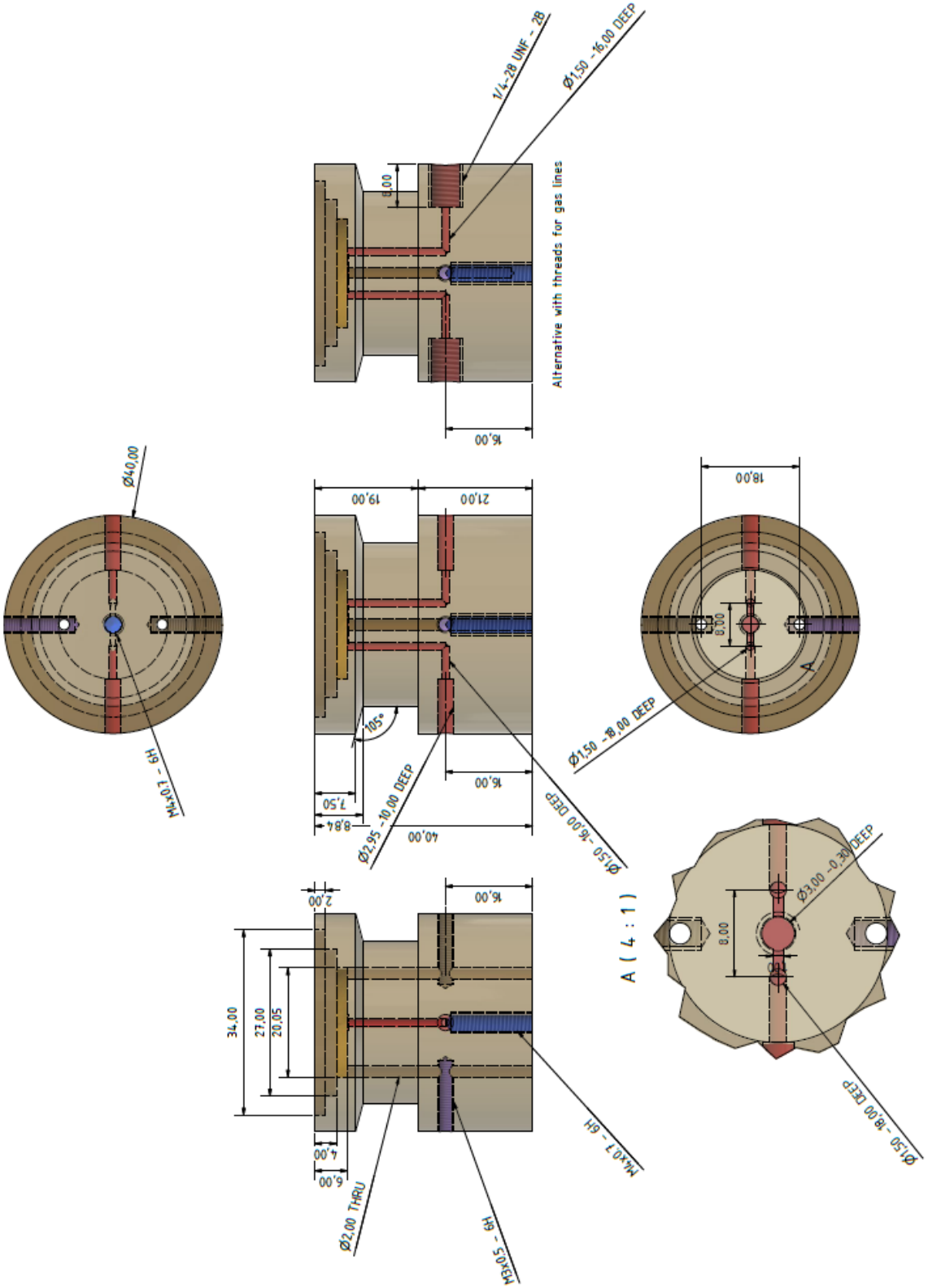

Figure S2. Technical drawing of the GDE setup.

Rotating disk electrode setup

The RDE experiments were carried out in a three-electrode glass cell setup. For the 60 °C measurement a glass jacket cell setup was used. A trapped hydrogen RHE electrode serves as a RE and a platinum mesh served as CE. The RE was separated from the working compartment via a Luggin capillary to reduce the iR drop, whereas the CE was separated with a zirconia frit to prevent hydrogen crossover.

Ink formation

For RDE and the GDL film preparation the catalyst was dispersed in a mixture of Milli-Q water and IPA (water/IPA ratio of 3:1). For the GDE film preparation an Ir concentration of 14 mg_{Ir} mL^{-1} and for the RDE of 654 μg_{Ir} mL^{-1} was used. To obtain a suitable dispersion the mixture was sonicated for 10 min in a sonication bath (inks for GDE) or horn sonicator (inks for RDE). Nafion was added to the ink for the GDE to reach 10 wt.% with regard to the catalyst and the dispersion was again sonicated for 10 min in a sonication bath.

For the PTL film preparation the catalyst was dispersed in a glycerol ink using a concentration of 28 mg_{Ir} mL^{-1}. 2.5 g glycerol and 69.5 µL of Nafion (to reach 10 wt % with regard to the catalyst) were stirred (680 rpm) for 30 min (glass vial was covered in aluminum foil). 46.5 mg of catalyst and 1.75 g of the glycerol-Nafion mixture was stirred (1200 rpm) for 30 min (glass vial was covered in aluminum foil).

Catalyst film preparation

Vacuum filtration and pressing of GDE

The Freudenberg H23C8 carbon gas diffusion layer (GDL) was placed between a glass funnel and a sand core filter (diameter 1.5 cm) in a vacuum filtration setup. This was placed on a collecting bottle as described by Yarlagadda et al.[2] 0.506 (0.253, or 0.126) mL of the inks of the commercial catalyst were diluted with 3.155 (1.580, or 0.789) mL of Milli-Q water and 10.476 (5.238, or 2.620) mL of IPA (water-IPA ratio of 1:3, Ir concentration of 0.5 mg_{Ir} mL^{-1}). The mixture was sonicated for 1 min. The diluted ink was filled in a funnel. A membrane water pump was used to deposit the catalyst on top of the GDL. The GDE was dried at least overnight on air. By this procedure theoretical Ir loading of 4 (2, or 1) mg_{Ir} cm^{-2}_{geo} was generated.

The Nafion membrane was pressed on top of the GDE: A Teflon or paper sheet was placed on top of a Teflon block and afterwards a GDL with MPL (Ø 2 cm with hole of Ø 3 mm) and the catalyst deposited on the GDL by vacuum filtration (Ø 3 mm) into the hole. A Nafion

membrane (to avoid later the leaking of the electrolyte into the GDE) was rinsed with Milli-Q water, dried and followed by a second Teflon sheet and a second Teflon block placed on top. Everything was placed between two metal blocks and the pressing was performed at 2 tons for 10 min. Afterwards the pressed GDE was placed on top of the GDL without MPL (Ø 2 cm) in the cell body (see Figure S3). The second GDL was not pressed together with the other parts of the WE as sometimes it stuck to the Teflon sheets leading to nonuniform thicknesses of the GDLs. The additional GDL was placed so that the WE (of 3 mm diameter) remained in position and did not fall down what would lead to a loss in connection. As the WE was only pressed but not under increased temperature (i.e. no hot-pressing) in previous experiments it sometimes did not stay in the middle of the hole of the upper GDL.

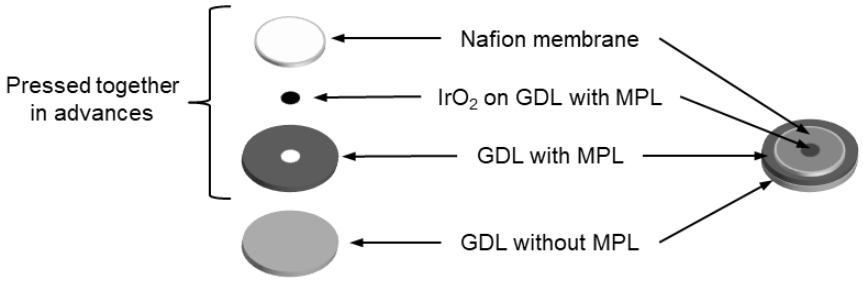

Figure S3. Illustration of the arrangement of the GDLs used in this study

Film preparation with PTL

Teflon spray was sprayed on PTL cutoffs (Ø 2 cm) and dried under a hood. Afterwards 2.52 µL of 28 mg_{Ir} mL^{-1} of the glycerol-based ink was drop casted in the middle of the PTL disk and placed on a glass petri dish for 13.5 h at 135 °C in an oven.

The Nafion membrane was pressed in a simple homemade hot-pressing setup on the PTL: An aluminum foil was placed in a metal autoclave reactor, the Nafion membrane on top of the PTL (catalyst film upside) and a second aluminum foil was added. The pressing was performed by pressing a metal piece on top of the aluminum foil with a metal screw-tube combination by closing three screws of the metal cap. The pressing setup was placed for 5 min on a hot plate of 135°C.

RDE film preparation

The alkaline ink was mixed for 5 min using an Ultra Turrax (IKA, T18 digital) at 20’000 rpm. 14.98 µL of the ink were drop casted onto the glassy carbon (GC) disk to achieve a theoretical

loading of 50 μg_{Ir} cm^{-2}_{geo}. The electrodes were then dried under humidified (H_2O/IPA ratio of 3:1) Ar flow.

Electrochemical measurements

Electrochemical measurements in GDE setup

For the electrochemical measurements, a computer controlled parallel potentiostat (ECi-242, NordicElectrochemistry ApS) was used. The gas was humidified by passing a bubbler filled with Milli-Q water and the gas inlet was connected to the cell body. The gas flow rate was determined with a mass flow controller (7000 flowmeter, Ellutia Chromatography Solutions). As electrolyte 4 M $HClO_4$ aqueous solution were used in the upper Teflon compartment of the GDE and different temperatures (30, 40, 50, or 60 °C) were applied using a fan in an isolated Faraday cage. After assembling the setup, one or two cyclic voltammograms (CV) were recorded while purging the electrode with humidified gas (with a scan rate of 10 mV s^{-1}, 1.2-1.6 V_{RHE}) to check if the assembling of the cell was successful. Afterwards humidified gas was purged for 10-20 min to reach the desired temperature before starting any experiments. For guaranteeing the complete oxidation of the Ir based catalyst the electrode potential was hold at 1.6 V_{RHE} for 5 min. Before starting the measurement, a current of 1 mA mg_{Ir}^{-1} was applied for 5-10 min. The measurement series consisted of current steps with 2 or 5 min holding per current. Different current densities were applied: 1, 2.5, 5, 7.5, 10, 12.5, 15, 20, and 25 mA mg_{Ir}^{-1} for temperature dependent measurements (30-60 °C); 1, 5, 10, 20, 30, 40, 50, 60, 70, 85, 100, 125, and 150 mA mg_{Ir}^{-1} for 60 °C measurements (O_2 vs. Ar atmosphere, GDL vs. PTL substrate); 0.25, 1.25, 2.5, 5, 7.5, 12.5, and 17, 5 mA mg_{Ir}^{-1} for 40 °C measurements in Ar. The resistance during the measurement was determined online using an AC signal (5 kHz, 5 x 10^{-5} A)[3]. The activity was analyzed of the iR corrected data averaging the potential of the last 60 s (of 2 min holding) or last 100 s (of 5 min holding) of each current step. Each measurement was repeated three times with a new WE and setup.

Electrochemical measurement in RDE setup

The potential and current are measured with a computer controlled potentiostat. As standard an electrolyte of 0.1 M $HClO_4$ was used.

Care needs to be taken to keep the electrochemical cell clean. A suitable procedure is to store in between the experiments the glassware in acidic 1 g L^{-1} $KMnO_4$ solution. Prior to the experiments this solution is removed, and the glassware rinsed with a diluted H_2SO_4/H_2O_2

solution to remove residual MnO_2. Finally, the glassware is boiled three times in ultrapure water.

During measurement, the cell is degassed by bubbling O_2 through the solution for 20 minutes prior to the start of the experiment. This O_2 flow is also maintained throughout the whole experiment. The WE is inserted into the solution under potentiostatic control at 1.0 V_{RHE}.

As the potentiostat has an active iR compensation scheme such as positive feedback, the iR drop in the cell is adjusted first. For this the potential is kept at 1.0 V_{RHE}, and the impedance resistance at 5 kHz with 5 mV amplitude is measured. This measured resistance is then reduced to 5 ohms by adjusting the feedback loop of the potentiostat. Afterwards an electrochemical impedance spectrum (EIS) is taken between 1 Hz to 50 kHz with an amplitude of 5 mV to evaluate the apparent solution resistance. If the potentiostat has no active iR compensation only the latter step (EIS) is taken. The solution resistance from the impedance spectrum is employed to post-correct the data for the iR drop.

In the following step the electrode is activated by holding it at 1.65 V_{RHE} for 10 minutes at a RDE rotation of 3600 rpm. This activation is important to completely oxidize the catalyst and avoid additional oxidation current during OER evaluation that could be misinterpreted as activity.

The rotation is maintained until all electrochemical experiments are finished. After the activation, 5 consecutive CV cycles at 10 mV s^{-1} between 1.0 and 1.6 V_{RHE}. When the CVs were finished, a potentiostatic experiment is performed, in which each potential is hold for 2 minutes. The potentials are: 1.0, 1.1, 1.2, 1.3, 1.4, 1.45, 1.475, 1.5, 1.525, 1.55, 1.575, 1.6, 1.575, 1.55, 1.525, 1.5, 1.475, 1.45, 1.4, 1.3, 1.2, 1.1, 1.0 V_{RHE}. Following this experiment 3 CV cycles between 1.0 and 1.6 V_{RHE} are measured at 10 mV s^{-1}.

Characterization

Determination of the OER overpotential

For temperature dependent measurement the potential versus RHE was converted to the OER overpotential:

$$\eta_{OER} = E_{rev,T} - E_{RHE}$$

For the determination of the reversible potential the equation of Parthasarathy et al.[4] was used (calories were converted into joules) with T as temperature (in K), n = 2 transferred electrons to produce one mol of water, F as Faraday constant:

$$E_{rev,T} = \frac{-\Delta G^0}{n\,F} = \frac{295600 + 33.5\,T\ln(T) - 388.4\,T}{n\,F}$$

X-ray photoelectron spectroscopy (XPS)

XPS was performed on a Kratos Axis Supra spectrometer using monochromatic Al K_α radiation at an energy of 1486.6 eV. The spectra were recorded at a total power of 225 W, 15 kV and 15 mA anode current. Pristine IrO_2 catalysts were drop-casted on a copper tape in a floating mode on a stainless-steel sample bar and then outgassed during overnight in an ultrahigh vacuum chamber so that the pressure in the chamber during the analysis was less than 1.0×10^{-8} Torr. The catalyst coated GDEs with a loading of 2 mg_{Ir} cm_{geo}^{-2} after activity measurement were grinded into powder by a mortar and pestle and drop-casted the same way as the raw catalysts for the XPS analysis. The narrow Ir 4f spectra were collected using a step size of 0.05 eV, a pass energy of 20 eV and the represented data are the average of 10 recorded spectra. All the binding energy values are corrected using the carbon signal (C 1s = 284.8 eV).

Scanning electron microscope (SEM) and energy-dispersive X-ray spectroscopy (EDS)

After performing the oxidation step of the catalyst with a loading of 2 mg_{Ir} cm_{geo}^{-2}, a circle of 5 mm was punched around the GDE as described before.[5] The dried sample was detached from the Nafion membrane and fixed with Cu-adhesive tape (3M #1182 electrical tape) on the sample holder. Before cutting with a scalpel the coated GDL was dipped for 10 s in liquid nitrogen.

The measurements of the cross-section were performed on a Zeiss GeminiSEM 450 using SmartSEM 6.05 software with EDS Photodetector Ultim max 65 from Oxford instruments using AZTec 4.2 software. As scan parameters for the EDS maps a WD (working distance) of 8.8 mm, accelerating voltage of 15 kV and a probe current of 200 pA were used.

Transmission electron microscopy (TEM)

TEM was performed using a Jeol 2100 microscope operated at 200 kV. The sample was prepared by drop casting a dispersion of the IrO_2 catalyst on carbon coated copper grids (300 mesh grids, Quantifoil) and dried in air at room temperature.

OER activity measurements

GDE and RDE data

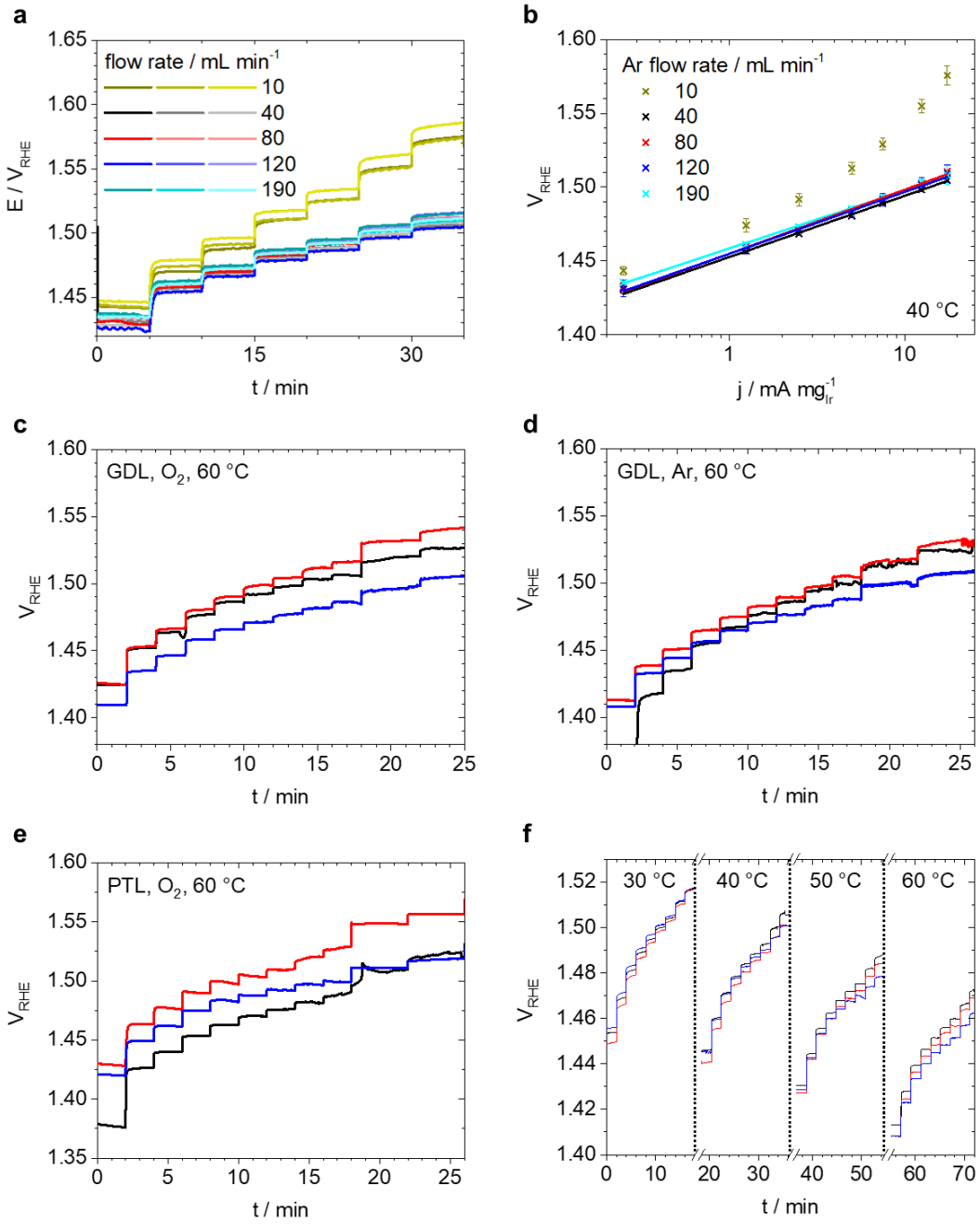

Figure S4. The three repetitions of the galvanostatic measurements of the commercial IrO_2 in the GDE setup applying current steps under humidified (a) Ar at different flow rates at 40°C, (c) O_2 at 60 °C, (d) Ar at 60 °C, (e) O_2 at 60 °C using a Ti-PTL, and (f) O_2 in T dependent measurements (the breaks in the t axis is due to the heating up to higher T). (b) The corresponding OER mass activity j plotted of the different flow rates as Tafel plots (using the average of the iR corrected potential of the last 100 s of every step is defined as OER activity). Unless specified otherwise differently C based GDLs were used as substrate.

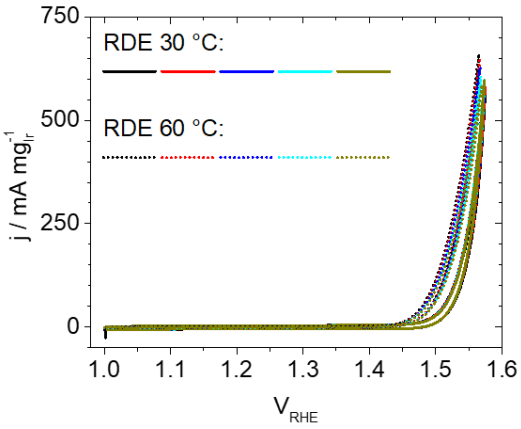

Figure S5. Five consecutive scans of linear scanning voltammetry (LSV) in RDE setup using the IrO_2 catalyst at 30 °C as compared to 60 °C.

Tafel plot determination

The Tafel slope was obtained from the slopes of the linear fit in the J(E) plots. For the determination of the Tafel slope in **Error! Reference source not found.** the data of the three (GDE) repetitions (not the average of all measurements) were used. The Tafel slope at 60 °C was determined for the RDE results out of current densities between 0.8-100 mA mg_{Ir}^{-1} and in the GDE (GDL: O_2 and Ar; PTL: O_2) up to 40 mA mg_{Ir}^{-1}. The deviation of the Tafel slope was obtained from the error of the slope.

The linear fits from the three repetitions in the Tafel plots were used for the determination of the activity at a certain potential.

Table S1. Tafel slopes of the GDE measurements of the IrO_2 catalyst depending on the flow rate, gas atmosphere, substrate, and temperature.

Substrate	**T / °C**	**Gas atmosphere**	**Loading / mg_{Ir} cm^{-2}_{geo}**	**Flow rate / mL min^{-1}**	**Tafel slope / mV dec^{-1}**
GDL	40	Ar	4	10	-
GDL	40	Ar	4	40	40.2 ± 0.5
GDL	40	Ar	4	80	41.8 ± 0.7
GDL	40	Ar	4	120	41.9 ± 1.5
GDL	40	Ar	4	190	39.9 ± 1.0
GDL	60	O_2	1	40	41.1 ± 4.8
GDL	60	Ar	1	40	50.3 ± 6.7
PTL	60	O_2	1	40	44.5 ± 15.9
GDL	30	O_2	1	40	45.4 ± 1.0
GDL	40	O_2	1	40	41.5 ± 1.0
GDL	50	O_2	1	40	38.5 ± 1.1
GDL	60	O_2	1	40	40.7 ± 1.5

In the Figures 3 and 5 of the Tafel plots the average of three measurements are shown.

Exchange current density and activation energy

The linear fits from the Tafel plots of all three repeats, see

Table S2, were used to determine the current density at the reversible potential. First a constant, temperature independent, reversible potential of E_{rev}=1.23 V was assumed. Additionally, the temperature dependent reversible potential was determined by Parthasarathy et al.[4] and by an equation of Bratsch[6], see Table S3. The reported exchange current densities in Table S3 are the averaged values and standard variation of the three repeats.

Table S2. Intercept and slope determined by the linear fits in the Tafel plot from the three repeats of the temperature dependent measurements in the GDE setup.

T / K	**Intercept = V_{RHE}**	**Slope = V_{RHE} log(J)$^{-1}$**
303.15	1.4543 ± 0.0011	0.0436 ± 0.0011
	1.4515 ± 0.0014	0.0450 ± 0.0014
	1.4473 ± 0.0014	0.0476 ± 0.0014
313.15	1.4438 ± 0.0016	0.0421 ± 0.0016
	1.4442 ± 0.0007	0.0394 ± 0.0007
	1.4389 ± 0.0010	0.0429 ± 0.0011
323.15	1.4287 ± 0.0012	0.0403 ± 0.0012
	1.4261 ± 0.0010	0.0399 ± 0.0010
	1.4288 ± 0.0004	0.0351 ± 0.0004
333.15	1.4115 ± 0.0011	0.0414 ± 0.0012
	1.4073 ± 0.0011	0.0427 ± 0.0011
	1.4075 ± 0.0006	0.0379 ± 0.0007

Table S3. The exchange current densities determined from the different reversible potentials for the four temperatures obtained from the averaged log (j) of the three repeats.

Method to determine E_{rev}	**T / K**	**E_{rev} / V_{RHE}**	**J_0 / 10^{-9} A mg_{Ir}^{-1}**
Parthasarathy *et al.*[4]	303.15	1.2224	10.6 ± 6.0
	313.15	1.2140	3.5 ± 1.8
	323.15	1.2056	2.1 ± 1.2
	333.15	1.1972	7.2 ± 3.8
Bratsch[6]	303.15	1.2249	12.0 ± 6.7
	313.15	1.2164	4.1 ± 2.0
	323.15	1.2080	2.4 ± 1.3
	333.15	1.1995	8.2 ± 4.3
Constant E_{rev}	303.15	1.23	15.5 ± 8.6
	313.15	1.23	8.5 ± 4.1
	323.15	1.23	8.7 ± 4.6
	333.15	1.23	44.2 ± 20.6

Afterwards the temperature dependent Tafel plots of each repetition is used to determine log(J) at the reversable potential E_{rev} = 0.25 V assuming a constant E_{rev} and additionally the temperature dependent E_{rev} values from Table S4 were used. The average of log(J) at the standard deviations of the three repeats are plotted against the inverse temperature as Arrhenius plot, see Figure S6. The product of the temperature T and the logarithm of the exchange current density log(J) was used to determine with the gas constant R the activation energy E_A (in kJ mol^{-1}) at the reversible potential by:

$$E_A = -\ 2.3\ 10^{-3}\ T\ R\ \log(j)$$

The deviation of the activation energy was determined from the error of the slope "b" of the linear fit by error propagation via:

$$\left|\frac{\partial E_A}{\partial b}\right| \Delta b = \left|\frac{\partial}{\partial b}(-2.3\ R\ b)\right| \Delta b = |-2.3\ R|\ \Delta b$$

Table S4. Averaged values of log(J) from the Tafel plots at an overpotential of 0.25 V using the OER overpotential from the temperature dependent measurements in the GDE setup and Arrhenius plot to determine the activation energy.

Method to determine E_{rev}	**T / K**	**η=0.25 V / V_{RHE}**	**log(j / mA mg_{Ir}^{-1}) at η=0.25 V**	**Arrhenius plots η=0.25 V**	
				T log(J) / K	**E_A / kJ mol^{-1}**
Parthasarathy et al.[4]	303.15	1.4724	0.4695 ± 0.0457	-1492.3 ± 346.0	28.5 ± 6.6
	313.15	1.4640	0.5218 ± 0.0439		
	323.15	1.4556	0.7231 ± 0.0408		
	333.15	1.4472	0.9479 ± 0.0763		
Bratsch[6]	303.15	1.4749	0.5240 ± 0.0438	-1494.3 ± 338.0	28.6 ± 6.5
	313.15	1.4664	0.5810 ± 0.0429		
	323.15	1.4580	0.7855 ± 0.0437		
	333.15	1.4495	1.0038 ± 0.0786		
Constant E_{rev}	303.15	1.48	0.6370 ± 0.0397	-3509.7 ± 464.2	67.1 ± 8.9
	313.15	1.48	0.9091 ± 0.0385		
	323.15	1.48	1.3610 ± 0.0757		
	333.15	1.48	1.7555 ± 0.1123		

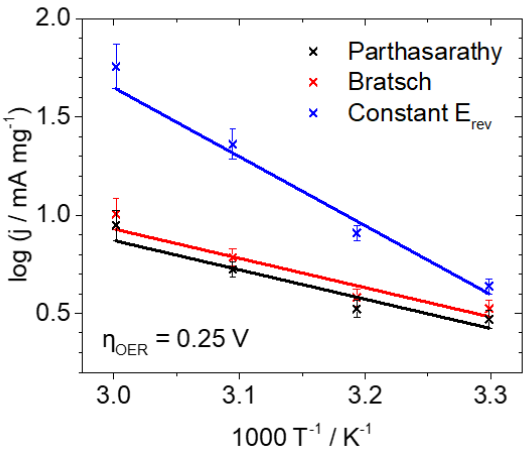

Figure S6. Arrhenius plot of the temperature dependent measurements at the OER overpotential η = 0.25 V. The reversible potential was determined by the equation of Parthasarathy et al.[4] (black), Bratsch[6] (red), or a constant value of 1.23 V (blue) was used.

XPS and TEM measurement

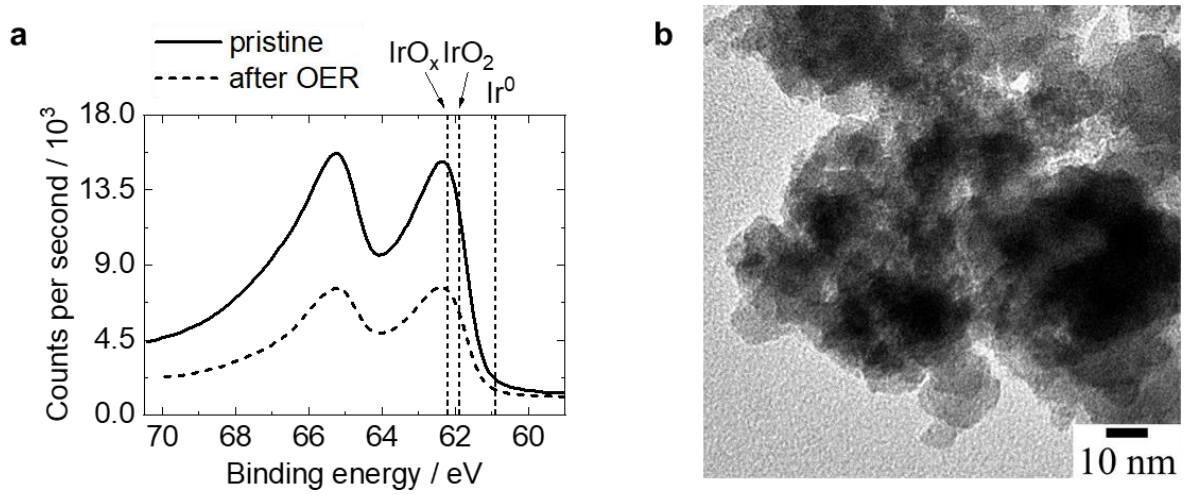

Figure S7. (a) XPS measurements of the binding energy of the IrO_2 catalysts, pristine (solid line) and after OER (dash line). The Ir 4f signals of Ir^0, IrO_2, and IrO_x are marked by the black dash lines.[7,8] (b) TEM micrograph of the IrO_2 catalyst.

The XPS data of the pristine catalyst (before the activation and activity measurement) shows that the IrO_2 only contain iridium oxide IrO_x (62.3 eV due to Pfeifer et al.[7]) and not metallic Ir^0 (60.8 eV due to Freakley et al.[8]), see Figure S7a. As expected after the OER performance (including the activation step before) no change in oxidation state was observed.

References

(1) Inaba, M.; Jensen, A. W.; Sievers, G. W.; Escudero-Escribano, M.; Zana, A.; Arenz, M. Benchmarking High Surface Area Electrocatalysts in a Gas Diffusion Electrode: Measurement of Oxygen Reduction Activities under Realistic Conditions. *Energy Environ. Sci.* **2018**, *11* (4), 988–994. https://doi.org/10.1039/C8EE00019K.

(2) Yarlagadda, V.; McKinney, S. E.; Keary, C. L.; Thompson, L.; Zulevi, B.; Kongkanand, A. Preparation of PEMFC Electrodes from Milligram-Amounts of Catalyst Powder. *J. Electrochem. Soc.* **2017**, *164* (7), F845–F849. https://doi.org/10.1149/2.1461707jes.

(3) Wiberg, G. K. H.; Mayrhofer, K. J. J.; Arenz, M. Investigation of the Oxygen Reduction Activity on Silver - A Rotating Disc Electrode Study. *Fuel Cells* **2010**, *10* (4), 575–581. https://doi.org/10.1002/fuce.200900136.

(4) Parthasarathy, A.; Srinivasan, S.; Appleby, A. J.; Martin, C. R. Temperature Dependence of the Electrode Kinetics of Oxygen Reduction at the Platinum/Nafion®

Interface—A Microelectrode Investigation. *J. Electrochem. Soc.* **1992**, *139* (9), 2530–2537. https://doi.org/10.1149/1.2221258.

(5) Schröder, J.; Quinson, J.; Mathiesen, J. K.; Kirkensgaard, J. J. K.; Alinejad, S.; Mints, V. A.; Jensen, K. M. Ø. Ø.; Arenz, M. A New Approach to Probe the Degradation of Fuel Cell Catalysts under Realistic Conditions: Combining Tests in a Gas Diffusion Electrode Setup with Small Angle X-Ray Scattering. *J. Electrochem. Soc.* **2020**, *167* (13), 134515. https://doi.org/10.1149/1945-7111/abbdd2.

(6) Bratsch, S. G. Standard Electrode Potentials and Temperature Coefficients in Water at 298.15 K. *J. Phys. Chem. Ref. Data* **1989**, *18* (1), 1–21. https://doi.org/10.1063/1.555839.

(7) Pfeifer, V.; Jones, T. E.; Velasco Vélez, J. J.; Massué, C.; Arrigo, R.; Teschner, D.; Girgsdies, F.; Scherzer, M.; Greiner, M. T.; Allan, J.; Hashagen, M.; Weinberg, G.; Piccinin, S.; Hävecker, M.; Knop-Gericke, A.; Schlögl, R. The Electronic Structure of Iridium and Its Oxides. *Surf. Interface Anal.* **2016**, *48* (5), 261–273. https://doi.org/10.1002/sia.5895.

(8) Freakley, S. J.; Ruiz-Esquius, J.; Morgan, D. J. The X-Ray Photoelectron Spectra of Ir, IrO2 and IrCl3 Revisited. *Surf. Interface Anal.* **2017**, *49* (8), 794–799. https://doi.org/10.1002/sia.6225.

(9) Oh, H. S.; Nong, H. N.; Reier, T.; Bergmann, A.; Gliech, M.; Ferreira De Araújo, J.; Willinger, E.; Schlögl, R.; Teschner, D.; Strasser, P. Electrochemical Catalyst-Support Effects and Their Stabilizing Role for IrOx Nanoparticle Catalysts during the Oxygen Evolution Reaction. *J. Am. Chem. Soc.* **2016**, *138* (38), 12552–12563. https://doi.org/10.1021/jacs.6b07199.

(10) Oakton, E.; Lebedev, D.; Povia, M.; Abbott, D. F.; Fabbri, E.; Fedorov, A.; Nachtegaal, M.; Copéret, C.; Schmidt, T. J. IrO2-TiO2: A High-Surface-Area, Active, and Stable Electrocatalyst for the Oxygen Evolution Reaction. *ACS Catal.* **2017**, *7* (4), 2346–2352. https://doi.org/10.1021/acscatal.6b03246.

Declaration of consent

on the basis of Article 18 of the PromR Phil.-nat. 19

Name/First Name: Schröder, Johanna

Registration Number: 19-125-954

Study program: PhD Program Chemistry and Molecular Sciences

Bachelor ☐ Master ☐ Dissertation ☑

Title of the thesis: Electrocatalysts for Fuel Cells and Water Electrolyzers: From Synthesis to Performance Evaluation at Realistic Reaction Conditions

Supervisor: Prof. Dr. Matthias Arenz

I declare herewith that this thesis is my own work and that I have not used any sources other than those stated. I have indicated the adoption of quotations as well as thoughts taken from other authors as such in the thesis. I am aware that the Senate pursuant to Article 36 paragraph 1 litera r of the University Act of September 5th, 1996 and Article 69 of the University Statute of June 7th, 2011 is authorized to revoke the doctoral degree awarded on the basis of this thesis.
For the purposes of evaluation and verification of compliance with the declaration of originality and the regulations governing plagiarism, I hereby grant the University of Bern the right to process my personal data and to perform the acts of use this requires, in particular, to reproduce the written thesis and to store it permanently in a database, and to use said database, or to make said database available, to enable comparison with theses submitted by others.

Bern/24.09.2021

Place/Date

Johanna Schröder

Signature